

PhD Thesis

School of Chemistry

Cardiff University



Organic Transformations Utilising *in-situ* Hydrogen
Peroxide Synthesis: An Experimental and
Theoretical Study

Thesis submitted in accordance with the
requirements of Cardiff University for the degree of
doctor in philosophy by:

James Singleton

2020

Abstract

The research presented within this thesis focused on the utilisation of hydrogen peroxide for a subsequent oxidation reaction. Hydrogen peroxide (H_2O_2) is considered a 'green' oxidant as it can be easily degraded to form water. To complete the utilisation, the H_2O_2 was made via the direct synthesis route, in a one-pot synthesis reaction. Furthermore, this *in-situ* technique decreases the complexity of the simulated manufacturing process as only one reactor is required.

The first part of this thesis focused on experimentally investigating the utilisation of H_2O_2 for the ammoximation reaction. Cyclohexanone was used as the target molecule for this ammoximation reaction. Cyclohexanone oxime is an important precursor to the manufacturing process of the plastic nylon-6. The tandem-catalyst system used comprised of a supported gold-palladium (AuPd) catalyst, with a low loading (0.66 wt%, 1:1), and a Titanium Silicalite-1 (TS-1) molecular sieve. The first catalyst synthesised the H_2O_2 needed to form hydroxylamine (NH_2OH), which was synthesised using the TS-1. In a non-catalytical reaction at 353.15 K, NH_2OH reacted with cyclohexanone. In the present work, a series of the H_2O_2 synthesis catalysts were made and investigated for both the direct H_2O_2 synthesis reaction, and the cyclohexanone ammoximation reaction utilising *in-situ* direct H_2O_2 synthesis.

The second part of this thesis focused on computationally investigating the utilisation of H_2O_2 for the epoxidation reaction. The key advantage of this method of investigation is that catalytic performance can be estimated to a good degree of accuracy, which in turn can provide information on how to synthesise a highly active and selective catalyst. Propene was used as the target molecule as it was a computationally simple molecule to use, and propene oxide is an important precursor to numerous manufacturing processes, such as the production of polyurethane and propene glycol.

Using Density Functional Theory, surfaces of Au and Pd were used to represent the facets of those catalysts. The surfaces were cut at Miller indices (111) and (100). The reactions studied and presented in this work were the direct H_2O_2 synthesis reaction and the propene epoxidation utilising *in-situ* direct H_2O_2 synthesis. Both parts of the research in this thesis could be used to inform future work on catalytic *in-situ* H_2O_2 synthesis and its subsequent utilisation.

Acknowledgements

I would like to express my gratitude to my research supervisors Dr. David Willock and Dr. Jonathan Bartley, and Prof. Graham Hutchings' "Hydrogen Peroxide Team" who offered me the opportunity to conduct this research as a member of the Cardiff Catalysis Institute. The training, guidance, insights and support I have received throughout this work was vital and conducive to this research.

I would like to thank members of the Cardiff Catalysis Institute, students, post-doctoral researchers, and lecturers alike, for their advice and support during my time at this Institute and had the pleasure of working alongside. In particular, I would like to thank Dr. Sam Francis, Dr. Claire Mitchell, Dr. Caitlin Crombie, Dr. Dávid Kovačič, Ollie Kennedy-Britten, Connie Black, Dr. Josh Kirsopp, Dr. Richard Lewis, Dr. Ouardia Adkim, Dr. Alhaji Mala, Dr. Sachin Nanavati, Dr. Matt Turner, Dr. Rob Armstrong, Dr. David Morgan, Dr. Greg Davies, Dr. Tom Davies, Dr. Meenakshisundaram Sankar, Prof. Philip Davies, and the members of staff in both the School of Chemistry's Workshop and Post-Graduate Research Office. Furthermore, I would like to thank the School of Chemistry and Cardiff University for the invaluable experience I have received.

A special thank you goes to Dr. Arunabhiram Chutia and Dr. Meenakshisundaram Sankar for their insights, guidance, and support. I would like to extend my gratitude to Cardiff University and UBE Industries Ltd. for their financial support of the two parts of this research. Without it, this work could not have been completed. I would like to thank HPC Wales and ARCCA for providing the computing time necessary for the completion of the computational calculations.

Finally, I would like to thank my family, partner, and friends for their incalculable support through the most demanding of times. I will be forever in their debt.

"Success or failure is individual; its effect is felt together. Regardless, it is the determination and perseverance to continue that is what we should all strive towards. That continuation leads to the betterment of a united human race."

Table of Contents

Abstract.....	i
Acknowledgements	iii
Table of Contents.....	iv
1. Introduction	1
1.1. Concepts and Principles of Catalysis	1
1.2. Support Materials for Heterogeneous Catalysts.....	8
1.2.1. Support Materials.....	8
1.2.2. Titanium Silicalite-1	9
1.3. Concepts and Principles of Density Functional Theory	10
1.3.1. First Principles	10
1.3.2. Hartree-Fock.....	11
1.3.3. Hohenberg and Kohn.....	12
1.3.4. Kohn and Sham	13
1.3.5. Total Energy Calculations	15
1.3.6. Vienna <i>Ab-Initio</i> Simulation Package	16
1.3.7. Long Range Dispersion Correction	18
1.3.8. Bulk and Surface Calculations	19
1.4. Oxidation Chemistry Background and History.....	22
1.4.1. Hydrogen Peroxide	22
1.4.2. Current Method of Synthesis.....	24
1.4.3. Alternative Methods	25
1.4.4. Direct Synthesis of Hydrogen Peroxide.....	27
1.5. Heterogeneous Catalysis for the Direction Synthesis of Hydrogen Peroxide Research.....	29

1.5.1. Reaction Conditions for the Direct Synthesis of Hydrogen Peroxide	29
1.5.2. Experimental Research for Palladium- and Gold-Palladium Catalysts	31
1.5.3. Research Supported by Computational Methods for Palladium- and Gold-Palladium Catalysts	45
1.6. Project Aims	56
1.7. References	57
2. Experimental and Computational Methods.....	68
2.1. Experimental Methods.....	68
2.1.1. Catalyst Preparation.....	68
2.1.2. Direct Hydrogen Peroxide Synthesis	68
2.1.3. Cyclohexanone Ammoximation utilising <i>in-situ</i> Direct Hydrogen Peroxide Synthesis.....	69
2.1.4. Analytical Methods	69
2.1.4.1. Gas Chromatography	69
2.1.4.2. Gas Chromatography for Gas-Phase Samples	72
2.1.4.3. Gas Chromatography for Liquid-Phase Samples	73
2.1.5. Catalyst Characterisation Techniques	74
2.1.5.2. Scanning Electron Microscopy	74
2.1.5.2. Field Emission Gun-Scanning Electron Microscopy.....	77
2.1.5.3. Energy Dispersive X-Ray Spectroscopy	78
2.1.5.4. X-Ray Photoelectron Spectroscopy.....	78
2.1.5.5. Powder X-Ray Diffraction.....	80
2.1.6. Errors and Limitations.....	82

2.2. Computational Methods	90
2.2.1. Optimisation of Parameters.....	91
2.2.1.1. Energy Cut-Off	91
2.2.1.2. Bulk Modulus, Expansion Factor and Miller Indices	92
2.2.1.3. Calculation Parameters	98
2.2.2. Geometry Optimisation Calculations	100
2.2.3. Interaction, Deformation and Adsorption Energies	101
2.2.4. Density of States Calculations.....	102
2.3. References.....	103
2.4. Appendix	105
2.4.1. Gas Chromatography Calibrations	105
2.4.2. Settings for INCAR Files	108
3. Ammoximation of Cyclohexanone utilising <i>in-situ</i> Hydrogen Peroxide Synthesis	113
3.1. Introduction	113
3.1.1. Cyclohexanone Ammoximation.....	113
3.2. Results and Discussion.....	116
3.2.1. Different Support Study.....	116
3.2.1.1. Catalyst Experiments.....	116
3.2.1.2. Catalyst Characterisation	121
3.2.2. Reaction Time Study.....	153
3.2.2.1. Catalyst Experiments.....	153
3.2.3. Different Amounts of TS-1 with P25 Titanium Dioxide Supported Catalyst Study.....	157
3.2.3.1. Catalyst Experiments	157

3.2.4. Different Phases of Titanium Dioxide Support Study	158
3.2.4.1. Catalyst Experiments	159
3.2.4.2. Catalyst Characterisation.....	162
3.3. Conclusions	168
3.4. Future Research	171
3.5. References	172
3.6. Appendix.....	177
3.6.1. Scanning Electron Microscopy	177
3.6.1.1. 0.33 wt% Au-0.33 wt% Pd/P25 Titanium Dioxide Catalyst.....	178
3.6.1.2. 0.33 wt% Au-0.33 wt% Pd/Zirconium Dioxide Catalyst	183
3.6.1.3. 0.33 wt% Au-0.33 wt% Pd/Silicon Dioxide Catalyst	184
3.6.1.4. 0.33 wt% Au-0.33 wt% Pd/ACS TS-1 Catalyst.....	185
3.6.2. X-ray Photoelectron Spectroscopy	186
4. Epoxidation of Propene utilising <i>in-situ</i> Hydrogen Peroxide	
Synthesis.....	191
4.1. Introduction	191
4.1.1. Propene Oxide.....	191
4.2. Results and Discussion	201
4.2.1. Gold.....	202
4.2.1.1. Gold (111).....	202
4.2.1.2. Gold (100).....	223
4.2.2. Palladium.....	243
4.2.2.1. Palladium (111).....	244
4.2.2.2. Palladium (100).....	268

4.2.3. Gold and Palladium Adsorption Site Analysis	290
4.2.3.1. Adsorption of Hydrogen	290
4.2.3.2. Dissociation of Hydrogen	291
4.2.3.3. Adsorption of Oxygen	293
4.2.3.4. Dissociation of Oxygen	295
4.2.3.5. Adsorption of Hydrogen Peroxide	295
4.2.3.6. Dissociation of Hydrogen Peroxide	297
4.2.3.7. Adsorption of Propene	299
4.2.3.8. Adsorption of Propene Oxide	301
4.3. Conclusions.....	302
4.4. Future Research	304
4.5. References	305
5. Conclusions and Future Work.....	309
5.1. Conclusions.....	309
5.2. Future Work.....	315
5.3. References	318

1. Introduction

1.1. Concepts and Principles of Catalysis

Catalysis is important as it forms part of everyone's everyday lives. They are within living organisms as well as playing a role for human activities, needs and desires. The various materials that people interact with each day will most likely have been involved in catalysis. For example, the plastic needed for computer casings would have been manufactured with the use of a catalyst.¹

There are three types of catalysis: biocatalysis, homogeneous catalysis and heterogeneous catalysis. Biocatalysis occurs within living cells, usually as enzymatic processes. Homogeneous catalysis occurs when the catalyst and the reactant molecules are in the same phase, normally in the liquid phase as metal complexes. Heterogeneous catalysis occurs when the catalyst and reactant molecules are in different phases, typically a solid catalyst with liquid phase or dissolved reactants.¹

All three types have unique characteristics and advantages. Biocatalysis is extremely selective, but has a limited span of operating conditions, depending on the biocatalyst's prerequisites for temperature and environment. Therefore, this type of catalysis is limited by the conditions required. Homogeneous catalysis can be selective and be up scaled to produce chemicals in bulk. However, the expensive ligands for the metal centres as well as the costly recovery of the catalysts from the reaction mixture make these processes expensive.¹

Finally, heterogeneous catalysis provides selectivity for certain catalytic reactions, potential industrial scale use, and catalyst recovery. Nevertheless, it does not come without its flaws. For example, the reproducibility of catalysts made using carbon-based (C) supports has been well documented. Only through research can these desirable qualities be attained.¹ This work will focus on heterogeneous catalysis.

A catalyst is a chemical species that increases the rate at which the equilibrium of a reaction is reached without being chemically changed at the end of the reaction. This is achieved by the catalyst offering an alternate reaction pathway that decreases the activation energy (E_a) (Fig. 1.1). This is of significance to industry as costly reaction conditions, such as high reaction pressures, can be reduced.²

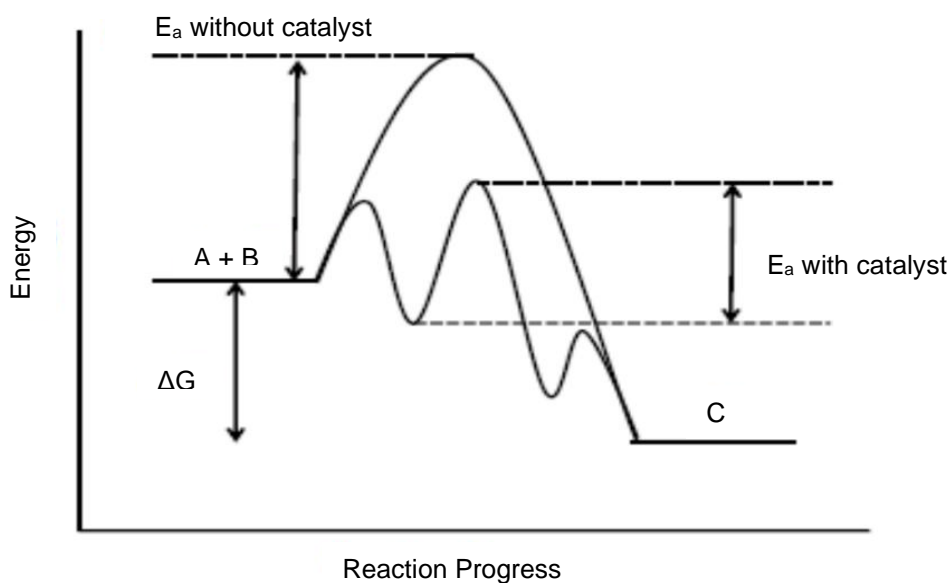


Figure 1.1. Reaction coordinate profiles demonstrating the effect that catalyst can have on a generic reaction ($A + B \rightarrow C$). Images adapted from reference.²

It can be seen in Fig 1.1 that the peaks signify transition states, and the troughs signify the stable intermediates as the reaction proceeds. The effect of a catalyst can also be depicted within a Maxwell-Boltzmann distribution (Fig. 1.2). A larger proportion of molecules have the energy to overcome the E_a barrier(s) in the presence of a catalyst compared to those that are not.^{1,2}

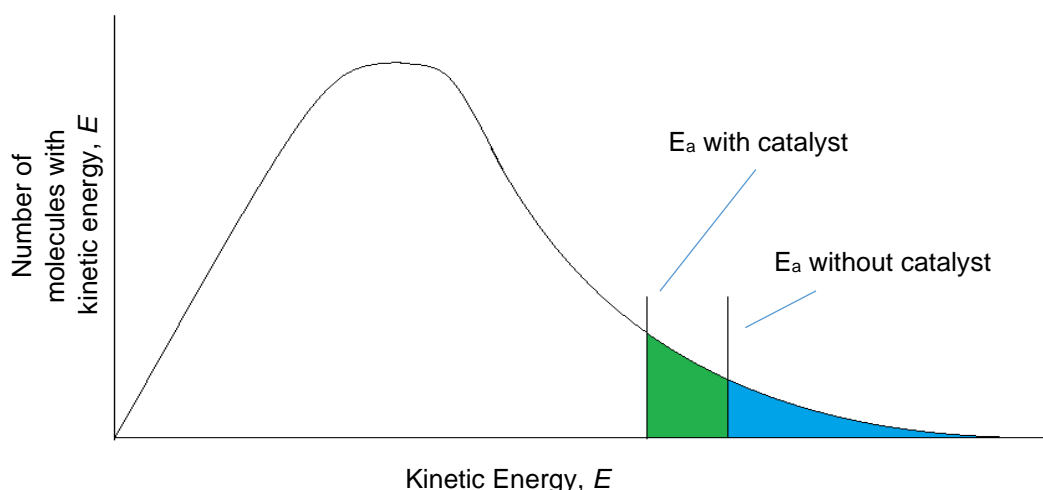


Figure 1.2. Maxwell-Boltzmann Distribution of a catalysed and uncatalysed reaction, with the activation energy indicated for each reaction.

Although E_a may have been decreased by the catalyst, this does not necessarily mean a reaction will occur; energy is still required even with the reduced E_a barrier. In addition, if a reaction is either thermodynamically or kinetically unfavourable, this will hinder the reaction from proceeding. For example, there may be an energy requirement for the reaction to proceed as it may not occur spontaneously or happens too slowly under standard conditions. The thermodynamic probability can be determined by the change in Gibb's free energy (ΔG). This is the product of the change in enthalpy (ΔH), the temperature (T) and the change in entropy (ΔS), as defined in equation (1.1):

$$\Delta G = \Delta H - T\Delta S \quad (1.1)$$

The change in Gibb's free energy provides information regarding the spontaneity of a reaction, the change in enthalpy provides information on whether a reaction is exothermic or endothermic and change in entropy is the change in the level of disorder of a system. If ΔG of a reaction is positive at a given T , the reaction is unlikely to proceed, and if ΔG of a reaction is negative at a given T , the reaction is likely to occur.

As defined in equations (1.2)-1.4), ΔG can also provide information on the equilibrium constant, and thus, the relative concentrations of the reactant and product molecules of a given reaction at equilibrium. For a given reaction:



$$K = \frac{[C][D]}{[A][B]} \quad (1.3)$$

$$\Delta G = -RT \ln K \quad (1.4)$$

where K is the equilibrium constant, $[A]$ is the concentration of chemical species A and R is the molar gas constant ($8.314 \text{ J mol}^{-1} \text{ K}^{-1}$).

For example, if ΔG has a large negative value, it suggests that there will be a larger number of products relative to the number of reactant molecules, possibly in excess, indicating that the reaction has gone to completion. The value of ΔG also remains unaffected by the addition of a catalyst to a reaction mixture as the enthalpy between reactant(s) and product(s) remain constant; only the rates of the reaction steps are affected.^{1,2}

Kinetics determine the rates of individual reaction steps. Catalysts affect this by increasing the rate at which equilibrium of a reaction step is reached. For example, the oxidation state of a heterogeneous catalyst and the surface functional groups, which directly affect its active sites, affect its performance for a given reaction.^{1,2} It is also determined by the reaction mechanism a catalytic reaction undergoes, which is discussed below.

Control of both thermodynamics and kinetics is of the utmost importance, especially for industrial processes. Having a stable product that takes weeks to produce or having a product that takes minutes to synthesise but is unstable are both not commercially viable. Catalysts can aid in this control with their activity and selectivity towards a desired product. The activity of a catalyst governs how much of a reactant is converted at a set time interval; the selectivity of a catalyst determines how much reactant is converted into desirable product. The product of conversion and selectivity gives information about the yield of a reaction that a catalyst can provide.^{1,2}

For example:



In this example, A is the target reactant, C is the desirable product and the reaction is entropically favourable. Conversion is defined as:

$$\text{Conversion} = \frac{n_{A_0} - n_{A_t}}{n_{A_0}} \quad (1.6)$$

where n_{A_0} is the number of moles of molecule A at the start of the reaction, denoted by 0, and n_{A_t} is the number of moles of molecule A at a time after the start of the reaction, denoted by t .

Using the number of moles is advantageous as this value can be directly or (through a small calculation) indirectly obtained from the analytical equipment (*i.e.*, Gas Chromatography (GC)). The higher the conversion, the greater the proportion of reactant molecules are being converted into product molecules. However, a high conversion does not necessarily mean that the reactants are converted into desirable products. This is where selectivity is introduced to provide that data. Selectivity is defined as:

$$\text{Selectivity} = \frac{nC_t}{\sum nPr_t} \quad (1.7)$$

where nC_t is the number of moles of molecule C at a time after the start of the reaction, denoted by t , and nPr_t is the number of moles of product molecules at the same time, denoted by t .

The higher the selectivity, the greater the amount of desirable product is being made compared to the other products within the reaction. However, it does not give information on conversion for the reaction. This is where yield combines both conversion and selectivity to provide a succinct value to a catalyst's performance. Yield provides information on the amount of desirable product that can be potentially recovered from the reaction mixture, and is defined as:

$$\text{Yield} = \text{Conversion} \times \text{Selectivity} \quad (1.8)$$

Nevertheless, yield can only provide an estimate on the rate of catalyst's turnover throughout the reaction. It provides information of how much product can potentially be recovered from the reaction mixture. The rate of a reaction can change over time as the number of reactant molecules decrease and the number of product molecules increase with time. The rate at the start of the reaction (*i.e.*, initial rate) will be different to that of the rate toward the end of the reaction (Fig. 1.3).

It can be seen that the initial rate of the reaction is faster than that of the rate during the reaction at time t , which is indicated by the difference in the gradients of the rate constants for the formation of product molecules (Fig. 1.3, blue and green lines). In this example, the steeper the gradient for the rate constant, the faster the reaction is proceeding during that interval of time.

The rate of the catalytic reaction during an interval of time can be defined by the following equations:

$$A_{Act} = \frac{-\delta[A]}{\delta t} \quad (1.9)$$

$$C_{Act} = \frac{\delta[C]}{\delta t} \quad (1.10)$$

where A_{Act} is the rate activity of the molecule it's assigned to (*i.e.*, A) and δ is the change of the subject it is assigned to (in this case, either concentration of a molecule ($[A]$ or $[C]$) or time of the reaction, t).¹⁻⁴

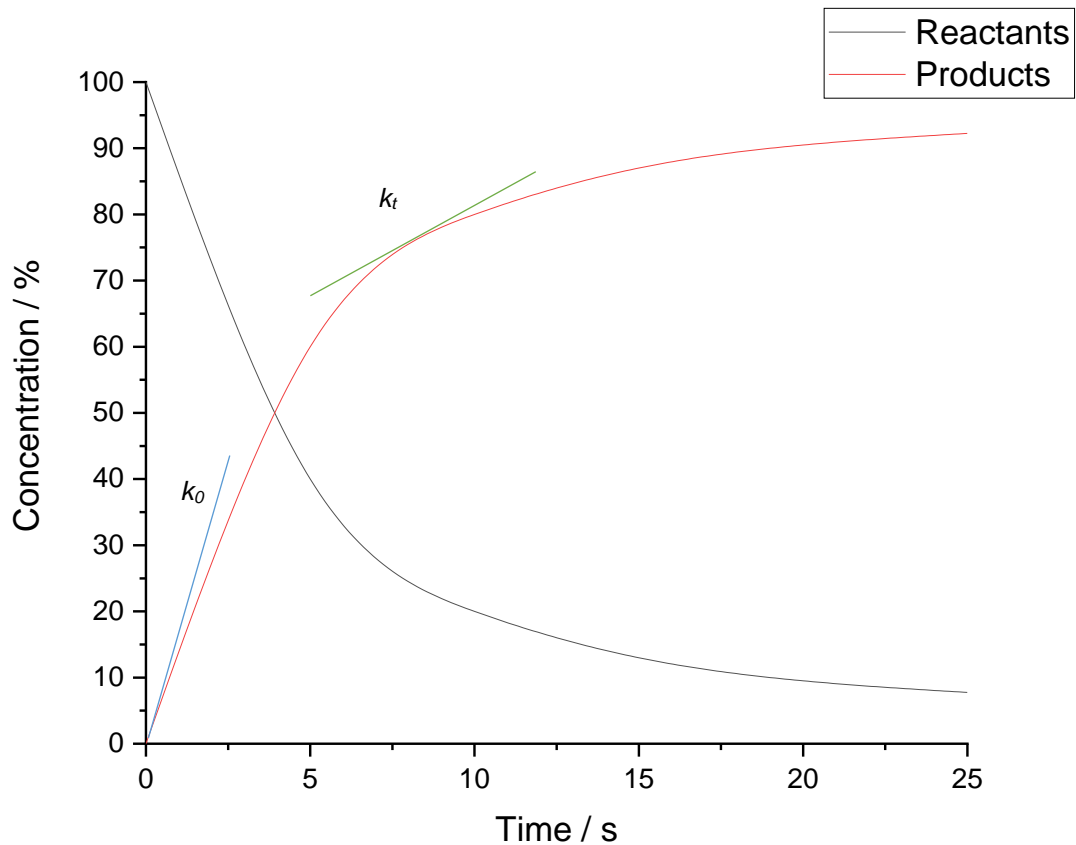


Figure 1.3. An example of a concentration-time graph showing the change in concentrations for both reactant(s) and product(s) in a 1:1 reaction, where k_0 represents the rate constant for the initial rate of the formation of products (blue line) and k_t represents the rate constant of the formation of products at a certain time, t (green line).

The information provided by equations (1.6)-(1.10) indicate the performance of a catalyst. Further information can be collected and applied to industrial processes with fixed volume reactors. Turnover number (TON) is the number of product molecules an active site can produce, as defined in equation (1.11). Turnover frequency (TOF) is the value of TON per time interval, as defined in equations (1.12) and (1.13). TOF gives more valuable information as it provides the intrinsic activity of the catalyst over time.

$$TON = \frac{n_A}{S} \quad (1.11)$$

where n_A is the number of moles of reactant, A is the reactant molecule from the reaction equation (1.5) and S is the number of active sites.

$$TOF = \frac{TON}{t} \quad (1.12)$$

$$TOF = \frac{n_A}{m_s \times t} \quad (1.13)$$

where m_s is the mass of the active sites.

All these equations provide specific pieces of information that contribute to understanding by what degree a catalyst has performed. A highly active, highly selective and highly stable catalyst is vital for industrial-scale production of chemical commodities.¹⁻⁴

With information that can be garnered from a catalyst, understanding how catalysis is carried out from a mechanistic viewpoint is important. The process of heterogeneous catalysis normally follows a particular order to make product molecules. This order of a simple catalytic process is: adsorption of the reactant molecule(s), the catalytic reaction of the molecule(s), followed by their desorption (Fig. 1.4).¹ There are two more potential steps in the catalytic process not depicted in Fig. 1.4: dissociation of the molecule(s) (*i.e.*, the reactant molecules' bond(s) break) to a more favourable transition state may occur after adsorption; or desorption does not occur and further catalytic reactions occur to form undesirable by-products.¹

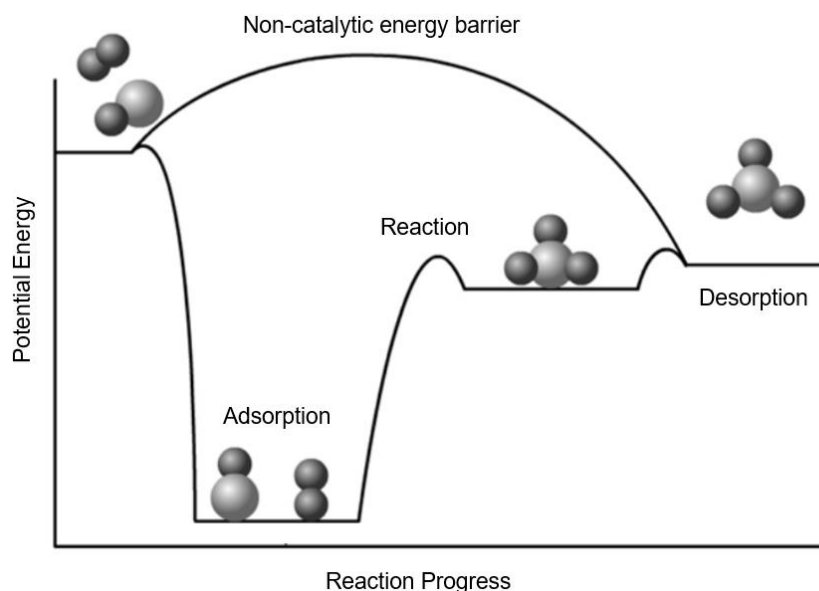


Figure 1.4. Potential energy diagram comparing a catalysed and non-catalysed reaction, demonstrating the individual steps through a catalytic reaction. Image adapted from reference.¹

The catalytic process described can occur slightly differently depending on the catalyst's mechanism. There are three main types of mechanism for heterogeneous

catalysts: Langmuir-Hinshelwood (LH), Eley-Rideal (ER) or Mars van Krevelen (MvK). An LH mechanism occurs when the reactant molecules adsorb simultaneously; an ER mechanism happens when the reactant molecules adsorb in sequence. An MvK mechanism is altogether different as the catalyst donates a constituent part of itself into the reactant molecule to form a product. A reactant molecule will then replenish the catalyst's structure. The latter mechanism will not be focused on in detail.¹

These mechanisms are important as they have different reaction rate equations. An LH mechanism's reaction rate is at its optimum when both the surface coverage of *A* and *B* are equal. An ER mechanism's reaction rate is at its optimum when the surface coverage of *A* and [*B*] are high.^{1,2} It is important to understand what mechanism the catalyst undergoes as optimal conditions need to be established to avoid wasting materials and energy and to make the process as efficient as possible.

1.2. Support Materials for Heterogeneous Catalysts

1.2.1. Support Materials

A support material is a structure that provides a surface for metal precursors to seed and to subsequently grow into nanoparticles. The addition of a support differentiates homogeneous and heterogeneous catalysis. Homogeneous catalysts are usually metal centres surrounded by ligands that provide their unique properties and characteristics, and the catalysts are kept within the same state as the reactants. Heterogeneous catalysts are solid materials and are in a different phase to the reactants. The catalysts can either be colloids, solid acid catalysts, such as a zeolite, or supported nanoparticles, all of which are normally powders that can be manipulated into different forms like pellets and extrudates.¹ The current work will focus on the use of solid acid catalysts and supported metal nanoparticles.

Burch *et al.*⁵ conducted a study in which palladium (Pd) was supported on a C support and various metal oxide (MO_x) supports (*i.e.*, TiO₂, α-Al₂O₃, Fe₂O₃/Al₂O₃, WO₃/Al₂O₃ and F/Al₂O₃) that were tested for the direct synthesis of hydrogen peroxide (H₂O₂). The MO_x supports gave higher conversions and selectivities compared to the C-supported catalyst. In particular, TiO₂ gave the highest selectivity at 66 %.⁵

Metal oxides provide some notably superior characteristics, such as high thermal decomposition temperatures, high melting points or their ability to maintain their surface area at high reaction temperatures.³ Catalysts with MO_x supports usually have synergy with the metal nanoparticles they support. This synergy refers to the

metal-support interaction (MSI), which has been studied extensively.¹ According to Junction Effect theory, transportation of electrons occurs from the lower energy valence band of one material to the Fermi energy level of the other material, once the two materials are in contact with one another. In this instance, the support and the nanoparticle. This electron transfer aids with the catalytic process on or at the nanoparticle, changing the oxidation state and electronic properties of the nanoparticle.⁶

1.2.2. Titanium Silicalite-1

Titansilicalite-1 (TS-1) is a zeolite, like ZSM-5, with a mordenite framework inverted (MFI) structure. However, unlike H-ZSM-5, TS-1 lacks the strongly acidic sites, which the aluminium (Al) in the aluminosilicate provides, instead being replaced by titanium (Ti) sites. For example, Drago *et al.*⁷ credited the inability for epoxide ring opening exhibited by TS-1 to the lack of the strongly acidic sites; H-ZSM-5 had this ability. Moreno *et al.*⁸ showed high selectivity for benzyl alcohol oxidation utilising *in-situ* direct H₂O₂ synthesis with TS-1. The three-dimensional system of channels (Fig. 1.5.a) has channel areas of 0.28 nm² and 0.30 nm², meaning that the TS-1 can provide excellent shape selectivity and can act as a molecular sieve.^{7,9} It is also highly stable in the presence of water (H₂O) without compromising the active sites.

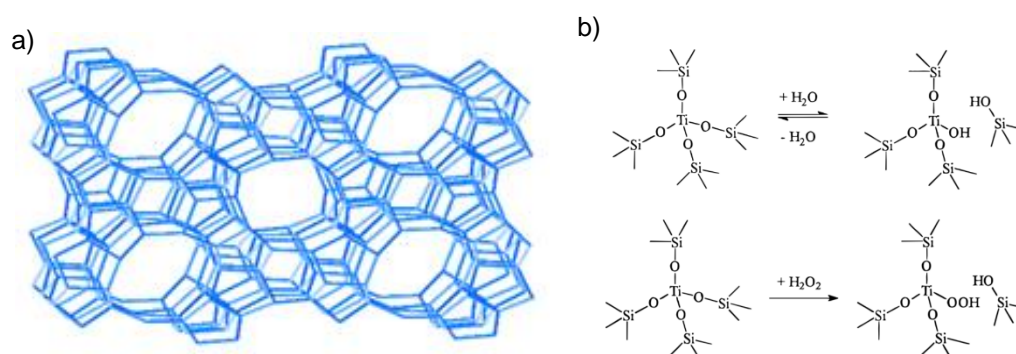


Figure 1.5. The structure of TS-1 showing **a)** the general structure of channels within an MFI structure and **b)** the local geometry of the tetrahedral Ti⁴⁺ site interacting with H₂O and H₂O₂. Images adapted with permission from references.^{7,9}

TS-1 has an approximate Si/Ti ratio of 30.00:1.00 (~1.00 wt% Ti), with the Ti atoms in lone tetrahedral configurations (Ti⁴⁺) and no Ti-O-Ti bonds contained within the structure (Fig. 1.5.b). At low temperatures, the reaction of H₂O₂ with TS-1 can lead

to dissociation of the H₂O₂ to form a hydroperoxyl (OOH) group bonded to the exposed Ti site (Ti-OOH), leaving the H to bond with the adjacent SiO site (SiOH) (Fig. 1.5.b).⁹⁻¹² The Ti-OOH can complete catalytic oxidation; for example, an ammonia (NH₃) source can be oxidised to form hydroxylamine (NH₂OH), which is required for cyclohexanone ammoximation.^{3,13-18} Sirijaraensre *et al.*¹⁹ showed that defective Ti sites were critical to produce the OOH species. Further discussion on the use of this material has been described in Chapter 4.

1.3. Concepts and Principles of Density Functional Theory

1.3.1. First Principles

First principles or *ab-initio* calculations are the foundations for Density Functional Theory (DFT). They describe the interactions between electrons and nuclei, which largely describes the characteristics of different elements and systems. These calculations are derived from quantum mechanics; primarily, from the Schrödinger equation (1.14).^{20,21}

$$\hat{H}\Psi(\mathbf{r}, \mathbf{R}, t) = E\Psi(\mathbf{r}, \mathbf{R}, t) \quad (1.14)$$

where \hat{H} is the Hamiltonian operator, Ψ is the wavefunction (describes an isolated system's quantum state), E is the energy of the system, \mathbf{r} and \mathbf{R} are the coordinates of the electron and nucleus, respectively, and t is time.

Theoretically, it should be possible to solve this equation for every atom within a system. However, it is almost impossible to solve for any atomic system larger than the hydrogen (H) atom with an increasing number of variables, making the system far more complicated.^{20,21}

This challenge can be made easier by circumventing time from equation (1.14). From the whole system of electrons, only their ground states are studied and observed, and therefore, the system's potential energy can remain constant. Further simplification can be achieved by discounting any interactions of the nucleus altogether as any change in the nucleus will instantly affect the electrons. The nucleus or nuclei of the system are considered constant parameters as they are preserved in their spatial vectors.^{20,21}

The separation of the electronic and nuclear coordinates is known as the Born-Oppenheimer approximation, defined by equation (1.15):

$$E_{atom} = E_{nucleus} + E_{electron} \quad (1.15)$$

where E is the energy associated with either the atom, the atom's nucleus, or the atom's electrons.

The Born-Oppenheimer approximation (1.15) can be applied to the *time-dependent* Schrödinger equation (1.14) to form the *time-independent* Schrödinger equation, defined by equation (1.16):

$$\hat{H}(r)\Psi(r) = E\Psi(r) \quad (1.16)$$

where r is the coordinates for the atoms' or systems' electron(s).

Within equation (1.16), the Ψ contains E of the system, meaning that the latter can be calculated, provided that the correct Ψ and \hat{H} are selected.^{20,21}

1.3.2. Hartree-Fock

The Hartree-Fock (HF) theory looks to solve the *time-independent* Schrödinger equation (1.16). It does this based on several assumptions:

- A linear combination of a finite number of one-electron orbitals provides the solution.
- A single Slater determinant (*i.e.*, an expression of the Ψ of a multiple sub-atomic particle system) describes each energy.
- Correlation is zero between electrons of opposite spin.
- Born-Oppenheimer approximation remains true.
- Relativistic effects are small.
- Any trial Ψ will always have an energy equal to or greater than the true value.

Based on these assumptions and calculations of a value for the system energy at a particular set of nuclear coordinates, the Ψ can be estimated. This is done by varying the values for the Ψ calculated until they reach convergence. This method optimises the Ψ and describes the energy of the system. The HF method works well

for simple systems as the Ψ of a system can be defined as a product of one-electron states. However, the interaction energy between electrons is oversimplified with a mean field approximation, which neglects the exchange and correlation energies (described below). As a system becomes more complex, the band gaps are overestimated, thus, inaccuracies arise.^{20,21}

1.3.3. Hohenberg and Kohn

In 1964, Hohenberg and Kohn gave two theorems about how to calculate the system's energy without the need of the Ψ .²² This was completed by studying the electron densities of the atoms within the system. The first theorem underlined that a unique external potential, where interaction between electrons and nuclei, could be provided by the ground state electron density of the system, as defined by equation (1.17):

$$\rho(r) \Leftrightarrow U_{ext} \tag{1.17}$$

where $\rho(r)$ is the electron density and U_{ext} is the external potential.

The electron-electron interaction energy and the electron kinetic energy, defined as the internal energy, is universal and not reliant on U_{ext} . Provided that the system is in the ground state, U_{ext} and the $\rho(r)$ can be defined. As the internal energy is universal, a universal functional should be used. Both $\rho(r)$ and U_{ext} can be used to determine the different \hat{H} and Ψ , which leads to the determination of the properties of the system. The principles described form the basis of DFT.²⁰⁻²⁴

The second theorem governs the system's minimum energy deduction, related to the method that finds the system's ground state. This is completed by use of the variational principle, which allows for the estimation of the energy of a system's ground state by selecting the variational parameters. The number and type of the variational parameters affects the accuracy of the Ψ and, by extension, the $\rho(r)$. The ground state $\rho(r)$ and energy of the system can be calculated by varying the $\rho(r)$, minimising the energy for a given U_{ext} , as defined by equation (1.18):

$$E[\rho(r)] = F[\rho(r)] + E_{ext}[\rho(r)] \geq E_{gs} \tag{1.18}$$

where $E[\rho(r)]$ is the system's current energy, $F[\rho(r)]$ is the system's internal energy, $E_{ext}[\rho(r)]$ is the external energy as a function of the current $\rho(r)$ and E_{gs} is the energy of the ground state (*gs*).

The limitation of this theorem is that this can only work for non-degenerate ground states.²⁰⁻²⁴ However, Levy proved the theorems for degenerate ground states by generalising and simplifying them using a constrained-search formulation, which could consider all the v -representable densities in a multi-density system.²³⁻²⁵

1.3.4. Kohn and Sham

Developing the mathematics further, the Kohn-Sham method was brought to fruition to address the issue of the electronic kinetic energy as a function of $\rho(r)$.²⁶ This method formed the majority of DFT in use today. To remove the electronic kinetic energy, a system of single electrons could be used, derived from the work of Hohenberg and Kohn.²⁰⁻²⁴ The \hat{H} from the *time-independent* Schrödinger equation for the n -electron system should be considered to comprehend and use the Kohn-Sham method, as defined by equation (1.19):

$$\hat{H} = -\frac{1}{2} \sum_{i=1}^n \nabla_i^2 - \sum_{I=1}^N \sum_{i=1}^n \frac{Z_I}{|R_I - r_i|} + \sum_{i=1}^n \sum_{i>j}^n \frac{1}{|r_i - r_j|} \quad (1.19)$$

where R_I are the coordinates of the nuclei, Z_I is the charge of the nuclei and r_i and r_j are the electron's coordinates.

The terms expressed in equation (1.19) are as follows: kinetic energy of the system, external potential, and electron-electron interaction potential (*i.e.*, Hartree potential). To remove any self-interaction, the latter is summed over as follows: $i \neq j$. Therefore, the summation below in equation (1.20) can be used to consider the energy of the system:

$$E = E_{kin} + E_{ext} + E_H + E_x \quad (1.20)$$

where E_{kin} is the kinetic energy, E_{ext} is the external energy, E_H is the Hartree energy and E_x is the exchange energy.

In equation (1.21), the exchange correlation energy is defined as the sum of the exchange energy (the interactions between electrons of the same spin), and the correlation energy (the interaction between the electrons of opposite spin regardless of orbital).

$$E_{xc} = E_x + E_c \quad (1.21)$$

where E_{xc} is the exchange-correlation energy, E_x is the exchange energy and E_c is the correlation energy.

The correlation energy consists of two parts: the kinetic energy of the electron-electron interaction and the energy of this correlation.^{20,21} This is defined in equation (1.22):

$$E_c = E_{kin}^{int} + E_c^{int} \quad (1.22)$$

where E_c is the correlation energy of a system, E_{kin}^{int} is the kinetic energy of the electron-electron interactions and E_c^{int} is the energy of the correlation of the interactions.

Kohn and Sham further assumed that it should be possible to find a model system of non-interacting electrons with the same density of interacting electrons within a real system. The energy of a system could be divided into interacting and non-interacting electrons. This gave the standard energy used in DFT with the inclusion of the exchange-correlation energy, derived from equation (1.21) to give equation (1.23):

$$E = E_{kin}^{non} + E_{ext} + E_H + E_{xc} \quad (1.23)$$

where E_{kin}^{non} is the kinetic energy of the non-interacting system.

As the first three components of equation (1.23) can be calculated simply, the last term contains the system's quantum effects without an explicit solution.²⁶ The only action that can be completed to deal with E_{xc} is to approximate it using a model. Two main methods could be used to complete the approximation: Local Density Approximation (LDA) and Generalised Gradient Approximation (GGA).^{20,21}

LDA works by dividing the total $\rho(r)$ into smaller uniform parts. It is possible to calculate E_{xc} by adding each part together, as $\rho(r)$ is constant for each part for the system. Unfortunately, this method of approximation has several issues, such as the inability to correctly approximate transition metal ground states. Thus, this method is not widely used.²⁷

On the other hand, GGA works by taking the gradient of $\rho(r)$ at a given point to provide a more accurate and realistic view of the system's $\rho(r)$. A common functional for this approximation is the Perdew, Burke and Ernzerhof (PBE) functional, which can accurately calculate the properties of most systems.²⁸ However, the disadvantages of this functional is that it produces errors for certain organometallic complexes' binding energies and does not include long range effects. Nevertheless, GGA is an accepted method of approximation for DFT calculations.

When completing calculations, a compromise must always be met. Usually, the more accurate a calculation is, the more computationally costly it will be. Other functionals are available that do not have the disadvantages (*i.e.*, accuracy) that the PBE functional has, but they usually suffer from being more computationally costly.^{20,21}

1.3.5. Total Energy Calculations

An iterative method is utilised to calculate the system's ground state $\rho(r)$. This is an effective method for this calculation. For a multi-atomic system, the $\rho(r)$ of each atom is constructed, providing the electronic configuration and an estimate of $\rho(r)$ of the system. Subsequently, the \hat{H} for the Kohn-Sham energy is assessed, as observed in equation (1.24):

$$\hat{H}_{ks}\rho(r) = E_{kin}^{non}(\rho(r)) + U_{ext}(\rho(r)) + U_H(\rho(r)) + U_{xc}(\rho(r)) \quad (1.24)$$

where \hat{H}_{ks} denotes the Kohn-Sham Hamiltonian operator.

Following this, the Kohn-Sham equation can be solved, as defined by equation (1.25):

$$\hat{H}_{ks}\phi_i = E_{i\phi_i} \quad (1.25)$$

Both equations (1.24) and (1.25) are similar to equations (1.23) and (1.16), respectively. Solving the Kohn-Sham equation (1.25) will provide a new KS orbital, with a new $\rho(r)$ and a new system energy. The repeated process continues until the energy converges within a predetermined limit (*e.g.*, the HF optimiser). Once

convergence has been reached, the system's total energy can be calculated with the resultant atomic forces used to optimise the atoms' positions.^{20,21,26}

1.3.6. Vienna *Ab-Initio* Simulation Package

Vienna *Ab-Initio* Simulation Package (VASP) can use the Projector Augmented Wave (PAW) method, with a plane wave basis set and pseudopotentials.^{27,28} The package is used to simulate materials and their interactions with other chemical species, based on their properties that can be established using Kohn-Sham. Using an effective iterative matrix diagonalisation method in tandem with Pulay-Broyden charge density mixing, the Kohn-Sham equations can be calculated for a system's ground state properties.

Completing this method provides accurate approximations for transition metal systems, with optimisation of the system's geometry utilising the atoms' forces. Using the PAW method in VASP can gain access to the full wavefunction as the density functional is being calculated, utilising only the valence electrons as the core electrons are substituted for the PAW pseudopotentials.^{20,21}

The periodic system of atoms, which is optimised using the calculated energy from the density functional used, is optimised within two loops. The first loop optimises the wavefunction and the density (*i.e.*, energy convergence); the second attempts to optimise the atomic positions and force (*i.e.*, force convergence). These optimisations are achieved by one of three ways: a blocked algorithm; a Residual Minimisation Method-Direct Inversion in Iterative Subspace (RMM-DIIS); or a hybridisation of both. The outer loop can be optimised by two possible methods: Quasi-Newton-Raphson or Conjugate Gradient. Both deal with the minimisation of the atomic positions and forces. The former estimates the linear equations and optimises the system; the latter is a common method for the optimisation of linear equations.²⁹

It is impossible to calculate for an infinite number of electrons for macroscopic materials, and therefore, there is an intrinsic requirement to decrease the number of atoms. This is completed by using Periodic Boundary Conditions, and unit cells are defined to duplicate the material in three dimensions. The properties of the system within the unit cell must be changed from real space to reciprocal space (or *k*-space). This is completed by the following method (Fig. 1.6):

1. Reduction of the material into a supercell (multiple unit cells).
2. Expansion of the supercell by the Periodic Boundary Conditions.
3. Transformation of the supercell into reciprocal space, contained within the first Brillouin zone.
4. Using the reciprocal lattice vector, k , in which the electron density features have a wavelength larger than that of the unit cell dimensions, and the plane wave vector, G , in which the plane wave basis set selected has wavelengths smaller than the periodic distance that describe the electron density features local to the unit cell, the wavefunctions are mapped.
5. Conversion of the first Brillouin zone to the irreducible Brillouin zone (simplest form).
6. Mapping of the Brillouin zone is done by using a grid of k -points.
7. Integration/summation/extrapolation of the k -points to attain the infinite system's properties.³⁰

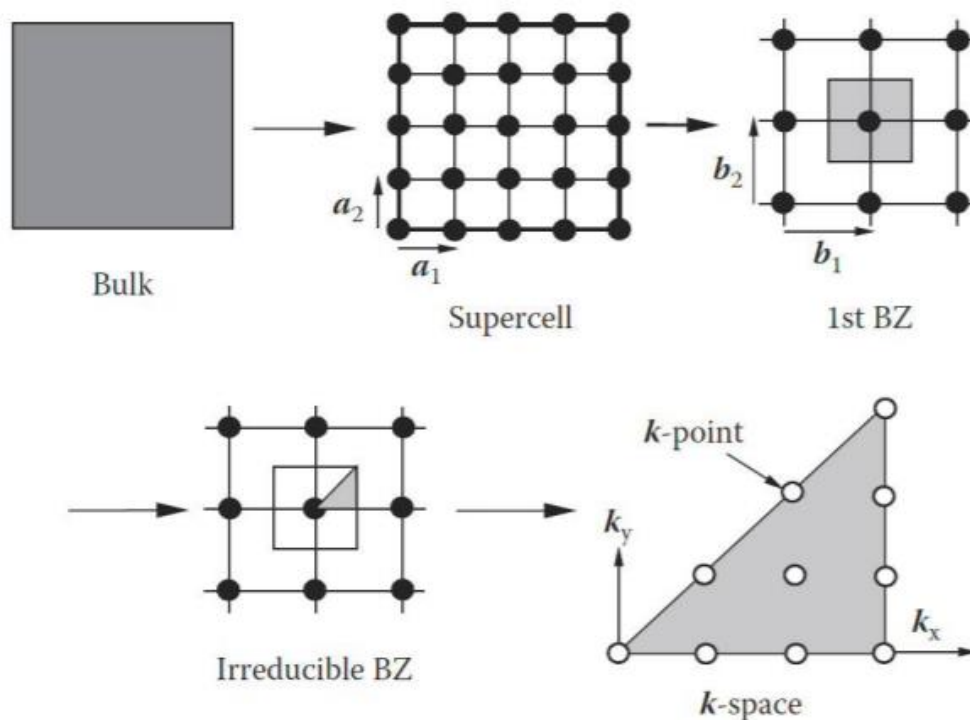


Figure 1.6. Periodic Boundary Conditions used for the treatment of solid materials. Image adapted with permission from reference.³⁰

A plane wave basis set, which builds up the crystal orbitals that describe the one-electron states, and a periodic wavefunction are added to one another to create a simulated wavefunction. This is to try to duplicate the true wavefunction of the solid in reciprocal space. The wavefunction is considered a true replication of the real

wavefunction as the number of summed plane waves, to the periodic function, rises to infinity. Alas, an energy cut-off of the plane waves is required as summing an infinite number of wavefunctions is impossible. The energy cut-off limits the number of plane waves used in the basis set, as it is systematically increased until the system energy convergence has reached an acceptable level. This is completed using a plane wave energy cut-off test, where different energy cut-offs are selected for a predetermined period of time.^{20,21}

In addition to determining the plane wave cut-off, the number of k -points within the k -point sampling grid needs to be determined in a similar fashion. To achieve this, the size of the grid is changed, with the total number of k -points for each lattice vector correlated to the size of that lattice vector. More k -points are required for the smaller directions (a , b , and c) of unit cells. However, using more k -points is computationally expensive, and a single k -point is adequate to describe the Brillouin zone for larger systems. Increasing the k -point sampling grid will exponentially increase the computational time for a calculation, thus, selecting the right k -point sampling grid is important.^{20,21}

1.3.7. Long Range Dispersion Corrections

As previously discussed DFT using VASP can provide good optimisation, however, it does have its limitations. For example, long range dispersion (van der Waals) forces are not accurately calculated in a standard DFT calculation. The correction can be included in the calculation by adding the energy of the correction to the standard Kohn-Sham energy calculated, as defined by equation (1.26). The Grimme D3 corrections can be a good way to estimate the dispersion forces.³¹

$$E_{DFT_{D3}} = E_{DFT} + E_{D3} \quad (1.26)$$

where $E_{DFT_{D3}}$ is the energy from the Grimme D3 corrected system, E_{DFT} is the energy determined from the standard DFT calculation and E_{D3} is the energy of the dispersion corrections.

To calculate E_{D3} , the corrections for the positions of the atoms within the system and their respective forces have to be considered and determined, as defined by equations (1.27)-(1.29):

$$E_{D3} = -\frac{1}{2} \sum_{i=1}^N \sum_{j=1}^N \sum_L' \left(f_{d,6}(r_{ij,L}) \frac{C_{6ij}}{f_{ij,L}^6} + f_{d,8}(r_{ij,L}) \frac{C_{8ij}}{r_{ij,L}^8} \right) \quad (1.27)$$

where N is the number of atoms in the system, L is the translation number across the unit cells, $f_{d,n}$ is a damping function (where 6 and 8 represent the n th orders), $r_{ij,L}$ is the internuclear distance, C_{6ij} and C_{8ij} are geometry dependent dispersion coefficients, and i and j are atom indexes.

$$f_{d,6} = \frac{s_n}{1+6\left(\frac{r_{ij}}{s_{R,n} R_{0ij}}\right)^{-\alpha_n}} \quad (1.28)$$

where s_n is the damping function parameters, $s_{R,n}$ is the order-dependent scaling factor of the cut-off radii R_{0ij} , and α_n is the “steepness” parameter.

$$R_{0ij} = \sqrt{\frac{C_{8ij}}{C_{6ij}}} \quad (1.29)$$

With all the above, it is possible to estimate the long-range dispersion of a system.

1.3.8. Bulk and Surface Calculations

The interactions between an adsorbate molecule and a catalyst are of interest. Studying catalysis computationally can provide much information on the mechanisms of a catalytic reaction. The surface chemistry is more important than the bulk of a material. However, the bulk of the catalyst must first be correctly calculated before studying its surface.^{20,21}

After optimisation of the correct parameters to use (*i.e.*, the k -point sampling grid and the energy cut-off), the atom's positions and the size of the unit cell also need to be optimised. VASP can effortlessly compute the former; the latter requires more complex calculations. VASP has a built-in optimiser that can change the unit cell size and provide the bulk modulus data. Use of the Murnaghan equation to state the optimal unit cell size can then be deployed. As the unit cell size is fluctuating, the energy cut-off needs to be multiplied by 1.3 of its value to account for the Pulay stress when running the optimisations through VASP. Pulay stress is borne out of the plane wave basis set being periodic within the cell. If the cell dimensions are changed, the

basis set also changes, which can lead to forces on the system. Using a higher energy cut-off limits this as the effect would not occur as the basis set nears completion.

The lattice parameters or the cell dimensions of the bulk of the material must first be optimised before cuts using Miller indices are performed. A measure of the material's resistance to compression or pressure must be determined. This is called the bulk modulus. The compression is changed incrementally by changing the volume *via* the cell dimensions (*i.e.*, as the cell volume increases, the pressure decreases, and vice versa), as defined by equation (1.30):

$$B_0 = -V \frac{\delta P}{\delta V} \quad (1.30)$$

where B_0 is the bulk modulus, V is the cell volume, δP is the change in cell pressure and δV is the change in cell volume.

To simulate the pressure in the *ab-initio* calculations, the same force must be applied to all faces of the material within the cell (Fig. 1.7 and equation (1.31)).

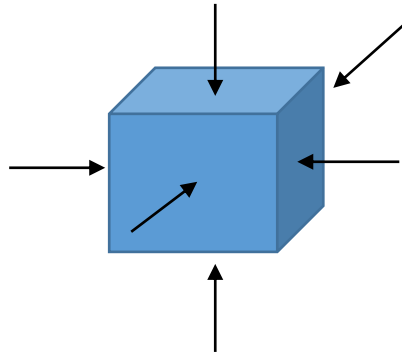


Figure 1.7. Representation of forces applied to a material within a cell.

$$P = \frac{F}{A} \quad (1.31)$$

where F is the force applied to each face and A is the total area of the material.

If the material moves a small distance as the force is applied, the latter can be related to the change in potential energy, as defined by equations (1.32) and (1.33):

$$F = -\frac{\delta E}{\delta x} \quad (1.32)$$

$$P = -\frac{1}{A} \frac{\delta E}{\delta x} = -\frac{\delta E}{\delta V} \quad (1.33)$$

where A is the area, δE is the change in potential energy and δx is the change in distance.

This means that B_0 can be defined by the energy, as defined by equation (1.34):

$$B_0 = V \frac{\partial^2 E}{\partial V^2} \quad (1.34)$$

where $\frac{\partial^2 E}{\partial V^2}$ is the second derivative of the potential energy with respect to the volume.

Using VASP, a second-order polynomial can be created plotting the energy against the volume, under the assumption that the calculation has taken place in the material's elastic region. A relationship between E and V can be established, as defined by equations (1.35)-(1.37):

$$E = aV^2 + bV + c \quad (1.35)$$

$$\frac{\partial E}{\partial V} = 2aV + b \quad (1.36)$$

$$\frac{\partial^2 E}{\partial V^2} = 2a \quad (1.37)$$

where a , b and c are the indeterminates.

The x^2 coefficient from the plot provides the second derivative. From equations (1.34) and (1.37), the indeterminates at the parabolic minimum can be used to provide an answer to the B_0 , as defined by equation (1.38):

$$B_0 = \frac{-b}{2a} = -b \quad (1.38)$$

From equation (1.38), the B_0 is dependent on the linear coefficient and V is dependent on the quadratic term. It is important to note the B_0 has a sensitivity towards k -point sampling. Checking the convergence of the B_0 with k -point sampling must be done to ensure the accuracy of the calculations. Analysis of the B_0 with strain by Murnaghan leads to the following equation (1.39):

$$E = E_0 + \frac{B_0 V}{B'_0} \left[\frac{\left(\frac{V_0}{V}\right)^{B'_0}}{B'_0 - 1} + 1 \right] - \frac{V_0 B_0}{B'_0 - 1} \quad (1.39)$$

where E_0 is the energy of the cell at the minimum of the curve, B'_0 is the pressure derivative of the bulk modulus at V_0 , and V_0 is the volume of the cell at the minimum of the curve.

Values of E_0 and V_0 can be obtained from the quadratic plot with a preliminary guess of B'_0 being made from known values for common solids. The four variables E_0 , B_0 , B'_0 and V_0 can be altered by control of a least-squares comparison with calculated data. This will lead to the optimal set being obtained.

The Murnaghan fit solver is a more accurate way for estimating the lattice parameters than manually solving the Murnaghan plot. However, to gain accurate results for a system, using the solver requires multiple data points for the Murnaghan equation. More computational time and cost is expended as more calculations need to be completed.

1.4. Oxidation Chemistry Background and History

1.4.1. Hydrogen Peroxide

Hydrogen peroxide is an important, commodity chemical as it has many uses, such as paper bleaching, disinfectant and propellants (Fig. 1.8).^{32–35} It is an environmentally friendly or “green” solvent as it degrades into H_2O and oxygen (O_2). Hydrogen peroxide can serve as a central intermediate in many vital reactions.³⁶ For example, the ammoximation of cyclohexanone to form cyclohexanone oxime, which

is an important intermediate for the production of nylon-6,³⁷ or the epoxidation of propene, which is an intermediate for the production of polymers, such as polyurethane.³⁸ With an increasing demand for H₂O₂ to be synthesised, the estimated amount of this product is to rise to 5.7 million tons per year by 2022.³⁹ The industry turned to researching how to more efficiently create this chemical commodity.

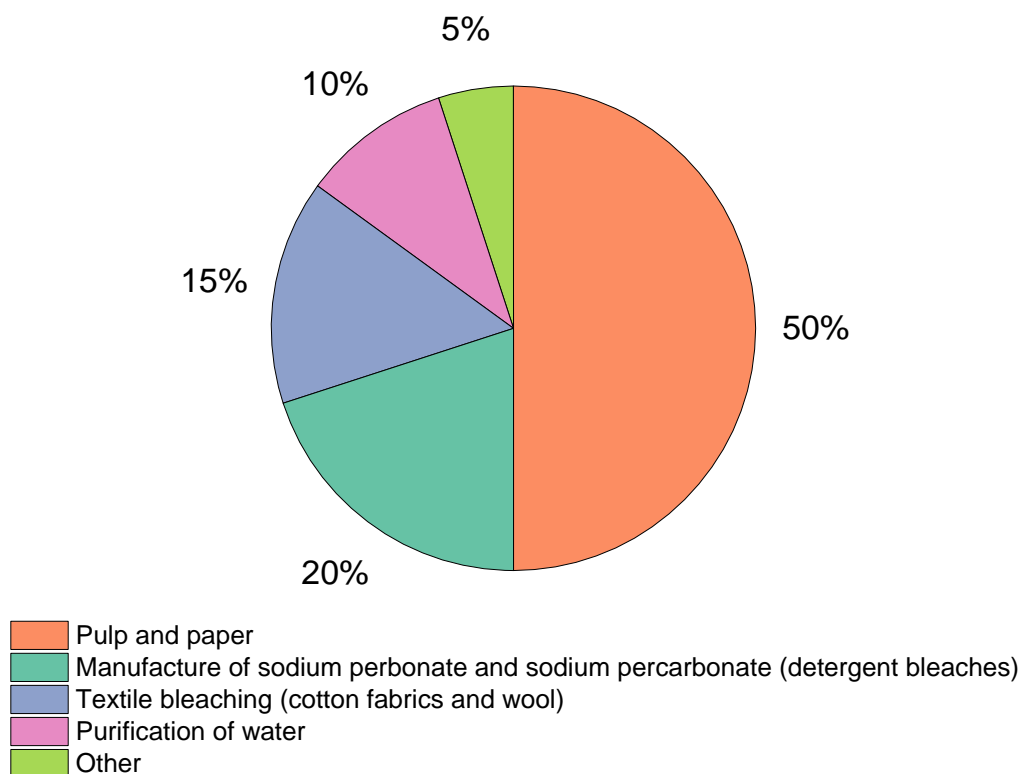
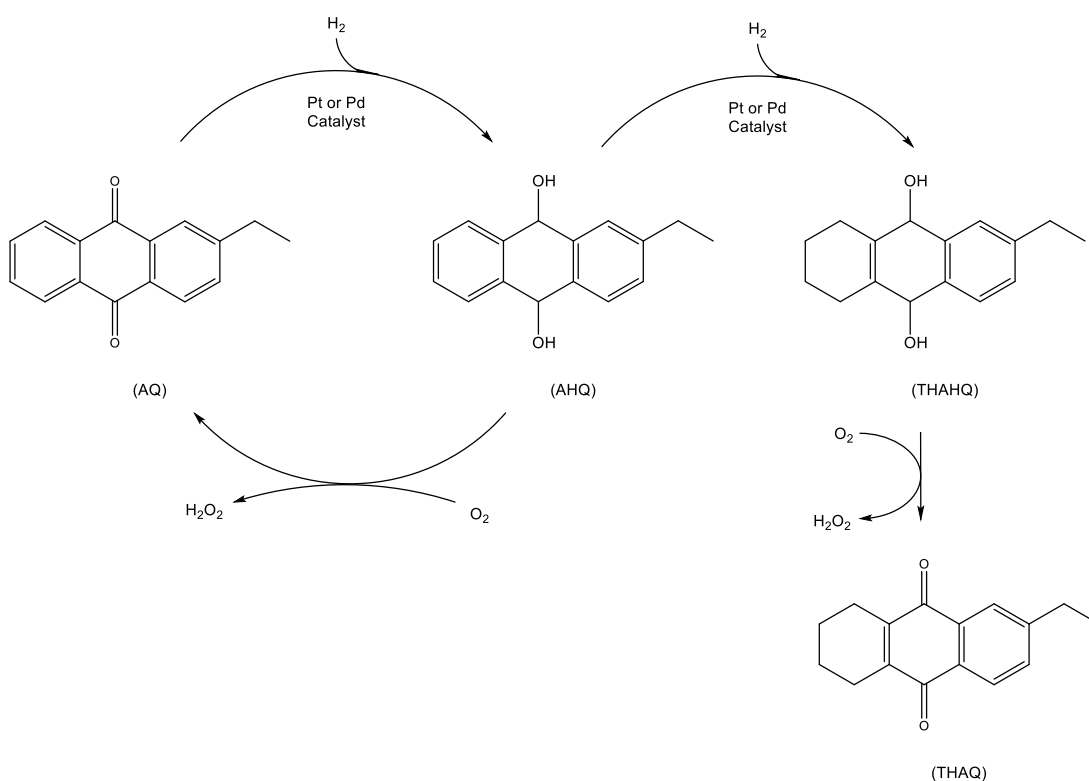


Figure 1.8. Chart to show the use of H₂O₂ in 2014. Image adapted with permission from reference.³⁵

With the discovery of H₂O₂ in 1818 by Louis-Jacques Thenard, it has become an important industrial chemical and its demand is growing significantly as it is environmentally friendly upon decomposition.^{32,34,35} At that time, there were a number of techniques being used to create this commodity, such as the hydrolysis of barium peroxide with sulphuric acid. Other methods included the oxidation of methylbenzyl alcohol or isopropanol, electrolysis of sulphates, cathodic reduction of O₂ and the auto-oxidation (AO) of organic compounds. Although the electrolysis of ammonium sulphate was a good technique for the production of H₂O₂ on a massive scale, it became largely overshadowed by the AO of H₂, also known as the anthraquinone process.^{32,34,35}

1.4.2. Current Method of Synthesis

The anthraquinone process was first commercialised by the German company I.G. Farbenindustrie in 1939.⁴⁰ The process involved an alkylated anthraquinol being oxidised by O_2 to H_2O_2 with the analogous anthraquinone (AQ). The quinone was then reduced to the anthrohydroquinone (AHQ) or anthraquinol, which was achieved by utilising a Pd-based hydrogenation catalyst and H_2 , completing the catalytic cycle. Nevertheless, further hydrogenation led to the production of 5,6,7,8-tetrahydroanthrahydroquinone (THAHQ). Further auto-oxidation can lead to the synthesis of H_2O_2 and tetrahydroanthraquinone (THAQ)⁴⁰ (Scheme 1.1).³²



Scheme 1.1. Anthraquinone auto-oxidation reactions for the synthesis of H_2O_2 . Image adapted with permission from reference.³²

The reason for this successful and long-standing process is due to its financial viability on an industrial scale, with more than three million tons being produced each year.⁴¹ The demand for this chemical commodity has been increasing approximately 4 % each year.³² Furthermore, the extraction of H_2O_2 from the solution is simple. With the addition of H_2O , the H_2O_2 changes phase, from the organic to the aqueous phase, and can then be distilled under low pressure to acquire the desired product and remove impurities.³²

Unfortunately, there are limitations to this process. Diluted amounts of H₂O₂ (usually ~30.00 wt%) are yielded, meaning that further treatments are needed for higher concentrations. Additionally, deactivation of the Pd-based hydrogenation catalyst and the AQ catalyst occurs during this process.⁴²

The former occurs by poisoning by impurities, such as carbon monoxide (CO) or halides,⁴³ and the latter occurs through further hydrogenation of the AHQ and subsequent auto-oxidation of the THAHQ.^{32,33} This leads to large amounts of toxic organic waste being produced. This issue can only be resolved through exhaustive clean-up steps in removing the organic waste. Another problem arises as this waste needs to be disposed of carefully, which means the cost of this process increases.^{32,33,42,44}

The storage of a chemical that has the potential to explode with a small amount of heat leads to more hindrances occurring in this process, increasing the cost of such a chemical process. This factor means that users cannot justify the production of H₂O₂ on-site. A single site is required for the synthesis and distribution of H₂O₂, meaning that a more efficient process (both financially and environmentally) is needed for the industrial-scale production and use of H₂O₂.

1.4.3. Alternative Methods

As with all processes, there are other means to obtaining a desired product. There are four other methods that can be used to produce H₂O₂. The first technique is the plasma method in which non-equilibrated H₂ and O₂ plasmas in the gas-phase react.^{32,45} A high selectivity for H₂O₂ and high conversion of the reactant gases can be achieved through the use of this method, as demonstrated by Zhou *et al.*⁴⁵ This group achieved a selectivity of ~56 % based on H₂ and a yield of ~33 % by using an atmospheric pressure dielectric barrier discharge reactor to create the H₂ and O₂ plasmas.

The benefits of the plasma method are as follows: no other chemicals are needed for the reaction; no issues regarding diffusion; it is a safe and environmentally friendly process; and the reaction is carried out in the gas-phase only.³² However, with this method, the gas concentrations have to be above the explosive limit, which poses a serious danger. Unfortunately, the formation of plasmas is energy intensive and produces low yields of H₂O₂. This all leads to the method not being economically viable.^{32,33}

The second technique is the fuel cell method in which O_2 is reduced to H_2O_2 in a three-phase system. The three phases are solid electrodes (*i.e.*, cathode and anode), an aqueous electrolyte and gaseous O_2 . The major advantages of this technique is that electrical energy can be generated from this process and that the H_2 and O_2 are fed separately due to the electrolyte membrane, meaning that a potentially violent and explosive reaction is avoided.^{32,33}

The fuel cell method was studied further by Yamanaka *et al.*⁴⁶ from the original fuel cell design realised and constructed by William Grove in 1838.⁴⁷ This research group produced a fuel cell that gave a selectivity of 93 %, where H_2 activation and the subsequent H_2O_2 synthesis was performed by C and platinum (Pt), and a cationic membrane was used to avert the mass transfer of H_2O_2 .⁴⁶ The rarity and high cost of using Pt has led to the investigation of cheaper alternatives such as the graphene nano-platelets synthesised from graphite.⁴⁸ Jeon *et al.*⁴⁸ prepared the nanoplatelets by ball-milling graphite with chlorine (Cl_2), bromine (Br_2) and iodine (I_2), which demonstrated a high activity and selectivity for the Oxygen Reduction Reaction (ORR). In addition, these stable nanoplatelets did not suffer from CO poisoning and DFT calculations agreed with the experimental data as the O=O bond from adsorbed O_2 was weakened by the charge transfer from certain halogenated edges of the nanoplatelets.⁴⁸ Nevertheless, more research is required for this process if it is to become a commercially viable technique.

The last technique is the supercritical carbon dioxide (CO_2) method.^{32,33} The reaction is completed by a fluid-solid two-phase system, whereby both homogeneous⁴⁹ and heterogeneous catalysts⁵⁰ can be used to aid the reaction. For the homogeneous catalyst, a Pd^0 and Pd^{2+} were the main constituents,⁴⁹ for the heterogeneous catalyst, a 0.35 wt% Pd/TS-1 catalyst was used.⁵⁰ The gas and liquid phases combine to form the fluid phase reducing the traditional three-phase system to two. This occurs due to H_2 and O_2 being miscible in the supercritical CO_2 at a temperature ≥ 304.15 K, which decreases the resistivity of mass transfer. This means that the use of supercritical CO_2 is a much more environmentally benign and efficient process, and has many other advantages (*e.g.*, abundance, inertness and low toxicity).^{32,33}

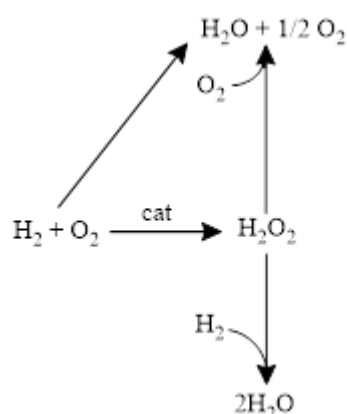
Nevertheless, there are inconsistencies in the literature for the supercritical CO_2 method for the direct synthesis of H_2O_2 as decomposition rates are too fast at temperatures > 304.15 K. Though the use of supercritical CO_2 has many advantages, this one hindrance dominates the whole process.^{32,33} In addition, the high pressures

required to make supercritical CO₂ is expensive, and therefore, makes this process less economically viable.^{32,33}

1.4.4. Direct Synthesis of Hydrogen Peroxide

In 1914, Henkel and Weber were granted the first patent for the direct synthesis of H₂O₂, however, little development was formulated and carried out due to the hazards that were brought with the highly flammable and explosive nature of H₂ and O₂. The explosive limits of H₂ and O₂ are between 4 and 95 %, and therefore, safety precautions had to be undertaken.^{32,33,51,52}

At this time, it was known that Pd could catalyse the liquid-phase reaction to form H₂O₂ from H₂ and O₂. Although it could be carried out at close to room temperature, there were unwanted side reactions that could occur. These reactions are the decomposition and hydrogenation of H₂O₂ that form H₂O, as well as the direct synthesis of H₂O (Scheme 1.2).^{32,33,41,51-53}



Scheme 1.2. Reaction pathways for the direct synthesis of H₂O₂ with a catalyst (cat).

Unfortunately, these reactions are thermodynamically favourable, and therefore, are likely to occur. Their exothermic nature also means that they can incur potential hazards considering the flammable and explosive reaction mixture.^{32,33,41,51-53} The theoretical enthalpy and Gibb's free energy values for the desired and unwanted reactions involved in the direct synthesis of H₂O₂ are presented below:

(i) non-selective oxidation of H₂ to H₂O

$$(\Delta H_{298\text{ K}} = -241.6 \text{ kJ mol}^{-1}, \Delta G_{298\text{ K}} = -237.2 \text{ kJ mol}^{-1})$$

(ii) decomposition of H₂O₂

$$(\Delta H_{298\text{ K}} = -105.8 \text{ kJ mol}^{-1}, \Delta G_{298\text{ K}} = -116.8 \text{ kJ mol}^{-1})$$

(iii) hydrogenation of H₂O₂

$$(\Delta H_{298\text{ K}} = -211.5 \text{ kJ mol}^{-1}, \Delta G_{298\text{ K}} = -354.0 \text{ kJ mol}^{-1})$$

(iv) selective oxidation of H₂ to H₂O₂

$$(\Delta H_{298\text{ K}} = -135.9 \text{ kJ mol}^{-1}, \Delta G_{298\text{ K}} = -120.4 \text{ kJ mol}^{-1})' \text{ (Scheme 1.2)}.^{32}$$

In 1961, Pospelova *et al.*⁵⁴ studied the effect of additional acid (*i.e.*, nitric acid (HNO₃) and hydrochloric acid (HCl)) to Pd catalysts and discovered they produced high yields of H₂O₂. This result was to be expected as the H₂O₂ decomposition is catalysed by the addition of base, preventing this reaction pathway from occurring.^{54–56} These findings indicated that acid promoters present in a H₂O₂ solvent system improved H₂ selectivity. Further investigation by Choudhary *et al.*⁵⁷ demonstrated the effects on the decomposition of H₂O₂, with 5.00 wt% Pd/C catalyst, using a series of acids under aqueous conditions.

In the 1960's, Imperial Chemical Industries (ICI) Ltd. was granted a patent for their technique for the direct synthesis of H₂O₂, followed by Tokuyama Soda Company for their improved method as H₂O₂ was synthesised in the aqueous phase. Throughout the 1970's, research progressed slowly until the 1980's as demand for H₂O₂ increased due to its environmentally benign by-product: H₂O.

In 1988, Gosser and Schwartz could produce solutions of H₂O₂ with a concentration greater than 35.00 wt% over a Pd catalyst, which was significantly higher than most yields at that time. This procedure was completed at a higher pressure, above the explosive limit for H₂ and O₂ gas mixtures. Before the 1990's, most research conducted for the direct synthesis of H₂O₂ was conducted above the explosive limit. Due to safety precautions, most developments in this area of research have been carried out below the explosive limit ([H₂] <4 vol%).^{4,32,33} The diluent gas used must be relatively inert to avoid the gas contributing to the synthesis, hydrogenation or decomposition (the latter terms collectively known as degradation) of H₂O₂ in any way to give an accurate representation of the catalyst's performance. An example of an inert diluent gas is nitrogen (N₂).^{3,4,32,33}

To date, the only successes were realised by Du Pont throughout the 1980's.^{32,33,44} Although there are many different laboratories working on this issue,

there has been no successful, industrial-scale production of H_2O_2 via the direct synthesis route. The explanation for this is due to the explosive limits of H_2 and O_2 mixtures that require diluting each gas to low amounts. The other reason for no industrial-scale H_2O_2 production is that the catalysts' abilities to activate H_2 can also promote the hydrogenation and decomposition pathways of H_2O_2 .

From the different methods discussed, the obvious contender to produce H_2O_2 is the catalytic direct synthesis route. It could be manufactured locally to avoid large volumes of high concentrations H_2O_2 being transported over long distances. The direct synthesis route for H_2O_2 production is also atom efficient.^{32,33}

1.5. Heterogeneous Catalysis for the Direct Synthesis of Hydrogen Peroxide Research

1.5.1. Reaction Conditions for the Direct Synthesis of Hydrogen Peroxide

Landon *et al.*⁵⁸ studied a variety of effects for the direct synthesis of H_2O_2 . At 274.15 K with a Pd catalyst supported on sulphonated C, the stirring speed of the autoclave was investigated first and showed that at 800 rpm, the gas-liquid mass transfer was at its maximum leading to a higher conversion of H_2 . Different catalyst masses were also researched and demonstrated an overall increase in H_2 conversion, H_2O_2 selectivity and H_2O_2 yield by increasing the catalyst mass. The influence of temperature was explored and showed that increasing the reaction temperature increased the H_2 conversion. However, it decreased the H_2O_2 selectivity and yield due to the decomposition, hydrogenation, or direct synthesis of H_2O pathways becoming more favourable. Further exploration using halides, comparisons with gold (Au) catalysts, and a comparison between the standard conditions and supercritical CO_2 was conducted.⁵⁸

The use of CO_2 was noted by Solsona *et al.*⁵⁹ as being a stabiliser for direct H_2O_2 synthesis. The diluent gas not only ensured that the H_2 was kept below the explosive limit but was also in equilibrium with carbonic acid (H_2CO_3) when dissolved in H_2O . The acid stabilised the H_2O_2 and reduced its rate of degradation to H_2O and O_2 . Edwards *et al.*^{4,33,60} demonstrated that different solvents and different solvent mixtures had a significant effect on the production of H_2O_2 . The research showed that,

with a 2.50 wt% Au-2.50 wt% Pd/TiO₂ catalyst, a water/methanol (H₂O/CH₃OH) solvent mixture at 20 vol.% gave a marked increase in H₂O₂ productivity.

Choudhary *et al.*⁵⁷ also reported the effect of potassium halides and acids for the direct synthesis of H₂O₂ from several studies. Regardless of the support material used for the Pd catalysts, the trend for halides increasing the conversion of H₂ was as follows: KBr < KCl < no halide < KF. However, the selectivity towards H₂O₂ decreased with this trend. KI hindered the yield of H₂O₂ as it poisoned the catalyst. The K⁺ counter ion promoted the production of H₂O₂, similar to the H⁺, but the halide ion also affected the synthesis, hydrogenation and decomposition sites on the catalysts, giving rise to the trend observed.⁶¹⁻⁶³ Additionally, an optimum concentration for each halide was determined for the synthesis reaction (*i.e.*, 0.94 mmol dm⁻³ KBr vs 1.5 mmol dm⁻³ KCl).

Liu *et al.*⁶⁴ studied the effect of temperature on the solubility of H₂ gas in liquid CH₃OH. The temperature range studied was between 293.15-413.15 K and it was found that with increasing temperature that the solubility of H₂ increased. These values were confirmed experimentally by a barometric method that involved the precise measurements of the temperature, the volumes of liquid and gas, and the total pressure change due to gas adsorption.

Henry's law states that the amount of a particular gas dissolved in a set volume and the type of liquid is proportional to the partial pressure of the gas in equilibrium with the liquid at constant temperature.⁶⁵ The mole fractions and Henry's law constants of H₂ in CH₃OH at different temperatures were calculated using the following equations:

$$n(H_2) = \frac{\Delta P(H_2) \cdot V_g}{RT} \quad (1.40)$$

$$x(H_2) = \frac{n(H_2)}{n(CH_3OH) + n(H_2)} \quad (1.41)$$

$$H(H_2) = \frac{P(H_2)}{x(H_2)} \quad (1.42)$$

where $n(H_2)$ is the number of moles of H₂ in CH₃OH, $\Delta P(H_2)$ is change in partial pressure of H₂, V_g is the volume of gas, R is the molar gas constant (8.314 J mol⁻¹ K⁻¹), T is the temperature, $x(H_2)$ is the mole fraction of H₂ in CH₃OH, $n(CH_3OH)$ is the number of moles of CH₃OH, and $H(H_2)$ is the Henry's law constant for H₂ in CH₃OH.⁶⁴

However, the trend stated above does not occur for O₂ in CH₃OH, or H₂ or O₂ in H₂O. These gases with these solvents decrease in solubility as temperature increases as the gases move out of the liquid phase.^{66,67} These effects are important when considering temperature for the direct H₂O₂ synthesis, as well as the solvent system to be used.

1.5.2. Experimental Research for Palladium- and Gold-Containing Catalysts

Palladium has been shown to be an active catalyst for the direct synthesis of H₂O₂. There have been several studies to uncover the mechanism, both experimentally and computationally, with regards to how H₂O₂ is produced over a supported-Pd catalyst.⁶⁸⁻⁷¹ Huerta *et al.*⁶⁸ investigated the effect of different reaction conditions for direct H₂O₂ synthesis over 5.00, 10.00 and 30.00 wt% Pd/C catalysts, such as the liquid and gas flow rates, total catalyst amount, pressure, temperature and bromide concentration (Br⁻). It was found that with higher mass transfer parameters or a larger amount of catalyst was detrimental for direct H₂O₂ synthesis, meaning that the conditions that allowed for low H₂ consumption should not be used to attain higher yields. The group also discovered that a greater number of Pd sites across the catalytic reactor bed led to greater hydrogenation values. Huerta *et al.*⁶⁸ found that the optimal temperature for the synthesis of H₂O₂ was discovered (at ~298.15 K, 6.1 mol_{H₂O₂} kg_{cat}⁻¹ h⁻¹). However, with a higher temperature came a greater amount of hydrogenation of the H₂O₂. To avoid this increased hydrogenation, H₂ consumption needed to be slower across the reactor bed.⁶⁸

Wilson *et al.*⁶⁹ conducted research into how varying the pressures of H₂ and O₂ would affect the production of H₂O₂ and H₂O. The group also explored what the effect of differing the H⁺ concentration would have on the previously stated reactions. These experiments were carried out to gain greater insight into the mechanism of direct H₂O₂ synthesis and its hydrogenation over a Pd/SiO₂ catalyst.⁶⁹

From the data collected, it was concluded that H₂O₂ synthesis did not occur *via* a classic Langmuir-Hinshelwood (LH) mechanism. Instead, the mechanism proceeded *via* a heterolytic reaction route, not dissimilar to a two-electron ORR. The H₂ molecules were adsorbed to the surface of the catalysts and were heterolytically cleaved to form H⁺ ions and the electrons were transferred to the Pd cluster. Subsequently, O₂ was adsorbed to the surface, accepting the electrons from the Pd

cluster to form a superoxide ion. The superoxide ion subsequently reacted with the two H^+ ions to form H_2O_2 .⁶⁹

This mechanism was theorised as it was found that the varying pressures of the reacting gases were inconsistent with a typical L-H mechanism. The differing H^+ concentration made a significant impact on the productivity of H_2O_2 indicating that a proton-electron transfer was responsible for the synthesis of H_2O_2 (CH_3OH : $\sim 15 \text{ mol}_{H_2O_2} \text{ kg}_{\text{cat}}^{-1} \text{ h}^{-1}$).⁶⁹ The counter-ion was less important in this process. In addition, the peroxy species was destroyed by the O=O bond cleavage that occurred, which subsequently formed H_2O . However, a reaction that contained no H_2 gas and only H^+ ions with O_2 was not carried out. This experiment would have provided the necessary information to confirm whether the H_2 gas was undergoing heterolytic cleavage, which was the linchpin in the proposed mechanism (Scheme 1.3).⁶⁹



Scheme 1.3. Wilson *et al.*'s proposed mechanism of direct H_2O_2 synthesis over a Pd cluster via two half-reactions. Image adapted with permission from reference.⁶⁹ Further permission related to the material excerpted should be directed to the American Chemical Society (ACS).

Gibb's free energy and enthalpy values were calculated from the experimental data of the syntheses of H_2O_2 and H_2O indicating that the formation of H_2O was more dependent on the electronic properties of the surface compared to the formation of H_2O_2 . This meant that selectivity towards H_2O_2 could be raised by increasing the number of coordinated surface atoms.⁶⁹

Burch *et al.*⁵ contradicted the previously mentioned work and offered a different mechanism of catalysis. This group stated that a reduced metal (Pd) surface could only produce H_2O_2 effectively. It was also stated that oxidised surfaces led to H_2O formation and that promoters are essential for selectivity towards H_2O_2 for a Pd catalyst.

The group studied a wide range of catalysts for the direct synthesis of H_2O_2 . Different support materials with different metal loadings were tested and only one catalyst was not supported by a MO_x (*i.e.*, C). Various cosolvents were also tested with the 5.00 wt% Pd/C, with the highest conversion exhibited with diethyl ether, but the greatest selectivity was exhibited by using ethylene glycol. The solvent composition was vital to the solubility of H_2 and O_2 as well as the catalyst's hydrophilicity or hydrophobicity.

Clearly, there appears to be contradictions in the literature that requires resolution. A comprehensive study examining the mechanism of oxidised, reduced, and untreated metal catalysts would give clarity to the scientific community.

Another study conducted by Gemo *et al.*⁷⁰ investigated the effect of different reactors on the direct synthesis of H_2O_2 using a 0.50 wt% Pd/K2621 (K2621 is a PS-DVB macroporous resin). It was found that the batch and semi-batch reactors worked dependent on the operational temperature, unlike the trickle bed reactor (TBR). The E_a values of the direct synthesis, decomposition, and hydrogenation pathways of H_2O_2 was calculated for each reactor showing that the E_a of these two reactions were relatively close in the TBR. This information led them to believe that mass transfer had a greater effect in the TBR than in the batch and semi-batch reactors, meaning mass transfer should be controlled by a greater extent to stop the unwanted hydrogenation and decomposition reactions.⁷⁰

Gemo *et al.*⁷⁰ suggested that a greater concentration of H_2 in the liquid phase, a shorter contact time and gas-liquid recirculation would reduce H_2O production and increase H_2O_2 synthesis. Reactor design was investigated; multiple injection points for the H_2 could be placed throughout a continuous reactor to increase H_2O_2 synthesis. It was suggested that there was a rate dependence on the amount of H_2 present for the direct synthesis pathway.⁷⁰

Additionally, the group suggested that porosity should be given as much weight in catalyst design as the particle size and oxidation state of the metal(s). This was related to the mass transfer dependence on direct H_2O_2 synthesis. The group also stated that the PdO sites 'seem responsible'⁷⁰ for the synthesis of unwanted H_2O . The synthesis and hydrogenation of H_2O_2 was dependent on the amount of O_2 and H_2 adsorbed on the surface of the catalyst and the amount of H_2O_2 in the solution. The amounts of both adsorbed reactant gases for the synthesis pathway indicated that an ER mechanism was taking place.⁷⁰

To summarise, Gemo *et al.*⁷⁰ indicated that the direct H₂O₂ synthesis catalysts needed to be designed and created for the correct reactor as well as distributing H₂ equally across the reactor. This group emphasised that chemistry and chemical engineering involved with the direct synthesis of H₂O₂ needed to be complementary to one another and were equally important.⁷⁰

There are a variety of preparation techniques for synthesising catalysts and many variables that can be changed. A common example of the former is the wet impregnation technique, and a common example of the latter is to change the calcination temperature. The variables can be altered either before, during or after the preparation of a catalyst (*i.e.*, pre-, peri- and post-preparation treatment).

Gudarzi *et al.*⁷² demonstrated the effect of the Pd content on Pd/ACC (activated carbon cloth) catalysts, the pH of the precursor on oxidised and non-oxidised catalysts, and the effect of calcination and reduction temperatures. The catalysts were produced *via* the wet impregnation method. This method is normally completed by heating the metal precursor(s) to a temperature below 373.15 K and adding the support material in until it has dried. The dried catalyst can then undergo post-preparation treatments, such as calcination. When multiple metal precursors are used with this preparation technique, it commonly produces a random alloy morphology when another metal is introduced. For example, AuPd catalysts.

The group concluded that two important characteristics were responsible for the inherent activities and selectivities displayed by the catalysts: the oxidation state of Pd and the surface chemistry of the support, defined by how much of and which functional groups were on the surface. The PdO gave rise to a more active, and more importantly, a more selective catalyst than Pd⁰. The former concurrently reduced the rate of H₂O formation and increased the rate of H₂O₂ production. The oxidised support gave rise to better selectivities than the non-oxidised support, which indicated that the support with O-containing functional groups on the surface also helped with the enhanced selectivities observed. Interestingly, damage to these functional groups was observed when the catalyst was reduced with H₂ at 458.15 K or calcined in air at temperatures above 463.15 K. Decreasing the pH of the metal precursor increased the adsorption of the Pd anions as the pH of the precursor was less than the pH for the isoelectric point (pI) of the support.⁷²

Another method of catalyst preparation is deposition-precipitation (DP). This technique uses a Brønsted-Lowry base to modify the precursor by increasing the pH, which in turn causes the charge of the precursor to be opposite to that of the support,

thus, increasing the electrostatic attraction to one another. An example of this method can be found in the work of Melada's research group,^{73,74} where Pd was evenly distributed over a carbon-coated α -alumina (Al_2O_3) membrane supported on microporous α - Al_2O_3 .

This research showed that there was an inherent safety issue as H_2 and O_2 were only in contact with one another when near the Pd. Productivities of H_2O_2 were high compared to other work ($\sim 222 \text{ mol}_{\text{H}_2\text{O}_2} \text{ kg}_{\text{Pd}}^{-1} \text{ h}^{-1}$).^{3,4,33,60,75,76} Particle size was controlled to give a range of different sizes, and an optimum size (8 nm) was determined by the amounts of synthesis and degradation of H_2O_2 that occurred. Melada's research group^{73,74} also attributed the improved selectivity towards H_2O_2 to the existence of PdO, similarly to Gudarzi *et al.*'s work.⁷²

Although Pd catalysts have shown great activity for H_2O_2 synthesis, the matter of selectivity away from the undesirable pathways (hydrogenation or decomposition of H_2O_2 and direct H_2O formation) needs to be attained for the industry to fully embrace this as a competitor. The addition of other metals could offer this enhanced selectivity. Gold catalysis has been at the forefront of research since the 1980's, following Haruta's and Hutchings' work and research.^{32,33,77,78} Gold was found to be selective for numerous reactions, in particular, CO oxidation.

The incorporation of other metals into a Pd catalyst has afforded enhanced selectivity and activity. This has been largely due to the altered electronics and morphology of the nanoparticles, which directly affected the sites for catalysis. Depending on the metal used, electrons can be transferred to or from the Pd. As the atomic radii of the metals are different to Pd's, this can force how the atoms are arranged in the nanoparticle. Another consideration is the affinity of the metals to themselves and other elements. Gold notoriously agglomerates with itself and forms large Au-rich nanoparticles.^{79,80}

Sol-immobilisation (S_{IM}) is another preparation technique for catalyst synthesis. Colloids are metal nanoparticles with organic stabilisers; these metal nanoparticles can be bound to a support material to form a heterogeneous catalyst. It has been reported that particle size can be controlled well by altering the amount and type of precursor, reductant, and stabiliser. The reductant reduces the oxidation state of the metal in the metal salt (e.g., Au^{3+} to Au^0). The stabiliser is usually a chemical species with a significant amount of electronegative groups (e.g., hydroxyl (OH) groups in polyvinyl alcohol (PVA)) that halts nanoparticle growth at a particular size and prevents their aggregation. The type of stabiliser used affects the nanoparticle

size. Although this catalyst preparation technique would be of great significance to the industry, it cannot be sustained on such a large scale.^{81,82}

Pritchard *et al.*⁸³ studied 1.00 wt% AuPd catalysts prepared by S_{IM} supported on activated carbon (AC) for both the direct synthesis of H₂O₂ and benzyl alcohol oxidation. With two- and 30-minute reactions completed, the S_{IM} catalysts were capable of superior productivities compared to wet impregnation and DP catalysts. More importantly, the two-minute reactions produced even higher productivities than the 30-minute reactions (386 and 120 mol_{H₂O₂} kg_{cat}⁻¹ h⁻¹, respectively).

Table 1.1. Direct Synthesis and Hydrogenation of H₂O₂ using Carbon-Supported AuPd catalysts prepared by S_{IM}. Table adapted with permission from reference.⁸³

Au/Pd Molar Ratio	H ₂ O ₂ Productivity / mol _{H₂O₂} kg _{cat} ⁻¹ h ⁻¹	H ₂ O ₂ Hydrogenation / mol _{H₂O₂} kg _{cat} ⁻¹ h ⁻¹
1:0	4	27
7:1	20	64
3:1	38	214
2:1	73	238
1:1	156	522
1:1.85	158	546
1:2	188	617
1:3	162	650
1:7	162	683
0:1	120	360

Direct synthesis reaction conditions: catalyst (0.01 g) in CH₃OH (5.60 g) and H₂O (2.90 g) solvent, 5 % H₂/CO₂ (2.89 MPa) and 25 % O₂/CO₂ (1.11 MPa), 30 minutes, 120 rpm, 275.15 K. Hydrogenation reaction conditions: catalyst (0.01 g) in CH₃OH (5.60 g) and H₂O (2.90 g) solvent, 5 % H₂/CO₂ (2.89 MPa), 30 minutes, 120 rpm, 275.15 K.

From the mono- and bi-metallic catalysts used, it was clear that Pd was the active component as the Au-only catalyst had low productivity and hydrogenation

values (4 and 27 mol_{H₂O₂} kg_{cat}⁻¹ h⁻¹, respectively). However, it was noted that when AuPd bi-metallic catalysts were used, increasing the amount of Pd led to an increased amount of H₂O₂ hydrogenation as the highest Au/Pd ratio studied (1:7) gave an H₂O₂ hydrogenation value of 683 mol_{H₂O₂} kg_{cat}⁻¹ h⁻¹ (Table 1.1).

Using Transmission Electron Microscopy (TEM), this group observed that this preparation method gave catalysts with smaller nanoparticle sizes than the wet impregnation technique. This suggested that the smaller nanoparticles exhibited by these catalysts were responsible for their increased catalytic performance.

Differing ratios of Au and Pd were used for the S_{IM} catalysts, supported on AC, that affected the particle size, dispersion, and morphology of the nanoparticles. This in turn affected the activity and selectivity towards H₂O₂ synthesis. The AuPd (1:1) catalysts gave the largest mean particle size (4.9 nm) and one of the highest productivity values for the 30-minute reaction (156 mol_{H₂O₂} kg_{cat}⁻¹ h⁻¹) (Table 1.1).

However, it was not one of the most selective catalysts in the series, as it gave a high hydrogenation value (522 mol_{H₂O₂} kg_{cat}⁻¹ h⁻¹). An optimum ratio of Au/Pd was determined (1:1.85), based on the amount of synthesis and hydrogenation of H₂O₂ that occurred (158 and 546 mol_{H₂O₂} kg_{cat}⁻¹ h⁻¹, respectively) (Table 1.1).

These catalysts were prepared with the simultaneous addition of both metals, which can also be called coimpregnation. This produced a random alloy nanoparticle. However, the metals can be added sequentially, providing a core-shell morphology, altering the catalytic capabilities of the nanoparticles.

Another method of catalyst preparation is the modified-impregnation (M_{IM}) technique.⁸⁴ This method is similar to the wet impregnation technique, but concentrated HCl is added and diluted to a set concentration by H₂O, and reduction *via* heat treatment is favoured. The use of excess Cl⁻ ions improves the dispersion of certain metals and the subsequent reduction removes the Cl from the surface, as it has been attributed to decreased catalytic activity.⁸⁵

Sankar *et al.*⁸⁴ created 1.00 wt% AuPd/TiO₂ catalysts *via* the M_{IM} method. The increased dispersion of the metals and the narrow particle size distribution (2-6 nm) led to an increased activity for the direct synthesis of H₂O₂. This increase was almost four-fold compared to the conventional wet coimpregnation (C_{IM}) and S_{IM} catalysts. The Au/Pd ratio could to some extent be controlled by the concentration of Cl⁻ ions. Selection of the Pd precursor was critical to the selectivity

of the catalyst as the anions and cations affected the nanoparticle seeding process (Table 1.2).

Table 1.2. 'Effect on the Hydrogen Peroxide activity^a of using different palladium precursors in the synthesis of the' 0.50 wt% Au-0.50 wt% Pd/TiO₂ catalyst.⁸⁴ Table adapted with permission from reference.⁸⁴

Pd Precursor	Productivity / mol _{H₂O₂} kg _{cat} ⁻¹ h ⁻¹	Hydrogenation / mol _{H₂O₂} kg _{cat} ⁻¹ h ⁻¹
PdCl ₂	99	230
Na ₂ PdCl ₄	87	136
Pd(NO ₃) ₂	100	583
PdBr ₂ ^b	59	173
PdCl ₂ ^c	32	nd ^d

^aReaction conditions: 5 % H₂/CO₂ and 25 % O₂/CO₂, 50 % H₂/O₂ at 3.7 MPa, CH₃OH (5.6 g), H₂O (2.9 g), catalyst (0.01 g), 275.15 K, 1200 rpm, 30 min. ^bGold precursor is AuBr₃ in the presence of an excess of HBr. ^c This catalyst was prepared in aqueous solution of 0.19 M H₃PO₄. ^dnd = Not determined.¹⁸⁴

The catalyst synthesised using excess Cl⁻ ions from 0.58 M HCl was not only reproducible, but also, a reusable catalyst. This was significant to the industry as it meant that a catalyst for this reaction could be produced without the need for expensive stabilisers or additives. Using higher concentrations or changing the cation to Na⁺ led to higher activities, but non-reusable catalysts.

Although it is possible to change the morphology of the nanoparticles depending on the entry of the metal precursor to give rise to either a random alloy or core-shell morphology (together or sequentially, respectively), the degree to which this can happen is dependent on the technique used. There is a lack of control with C_{IM} as seeding of the metals depends on the precursor (pH, counterions). However, DP and S_{IM} offer greater control as there are more variables to control, altering the catalyst's morphology, which directly affects its performance.

Miedziak *et al.*⁸⁶ continued the research of Kondrat *et al.*⁸⁷ by further studying the effect of different metal loadings for a AuPd catalyst for the direct synthesis of H₂O₂. The catalysts were prepared by the physical grinding of metal acetate precursors and calcined at 623.15 K.⁸⁶ The research demonstrated that higher H₂O₂ yields were afforded with higher loadings of metal, from 1.00 wt% to 5.00 wt% AuPd

catalyst (~ 18 to $\sim 93 \text{ mol}_{\text{H}_2\text{O}_2} \text{ kg}_{\text{cat}}^{-1} \text{ h}^{-1}$, respectively), with the exception of 10.00 wt% AuPd catalyst in which a decrease in conversion was observed ($\sim 68 \text{ mol}_{\text{H}_2\text{O}_2} \text{ kg}_{\text{cat}}^{-1} \text{ h}^{-1}$). However, they also had reduced selectivity compared to the lower metal loaded catalysts (< 5.00 wt%). The amount of hydrogenation was significantly higher with increasing metal loadings, from 1.00 wt% to 10.00 wt% AuPd (~ 20 to $\sim 1270 \text{ mol}_{\text{H}_2\text{O}_2} \text{ kg}_{\text{cat}}^{-1} \text{ h}^{-1}$, respectively).⁸⁶

The group hypothesised that with the higher metal loaded catalysts the additional metal did not contribute to the reaction and was present only as a spectator. With larger metal loadings, the nanoparticles were larger, and therefore, more of the metal was not at the surface but within the bulk or core of the nanoparticles.⁸⁶ Nevertheless, the increased amount of metal did contribute to the catalyst's performance as higher levels of the undesirable hydrogenation reaction was observed. Further investigation into the spectator metal atoms or nanoparticles needs to be conducted as the level of H_2O_2 hydrogenation and the amount of spectator metal increased with increasing metal loading.

With this preparation method, the catalysts showed a greater dispersion of Au than Pd, which is unusual due to Au's affinity for itself.^{79,80} However, the nanoparticle size was typically high for Au (≥ 165 nm). These characteristics were attributed to the concentration of Au precursor, where higher concentrations display these characteristics.⁸⁶

Alba-Rubio *et al.*⁵¹ researched the preparation of Pd/SiO₂ catalysts *via* electroless deposition to subsequently add Au to the catalyst *via* the same technique. Electrostatic interaction of the $[\text{Pd}(\text{NH}_3)_4](\text{NO}_3)_2$ precursor and the support were enhanced by the differing pH and pI as the precursor was basic and the SiO₂ was acidic. Addition of the Au was similar; however, an acidic Au precursor was used, meaning that a strong base was required to increase the pI of the precursor as well as reach the pI of SiO₂ to prevent deposition onto the support.

The idea of depositing Au onto Pd to give a core-shell morphology in this fashion was sound, however, not all the Au deposited onto the nanoparticles and Pd leached out of them. Through CO chemisorption, it was noted that the Au was binding to the low coordination Pd sites where CO is normally chemisorbed. In fact, the addition of Au did not aid with the activity or selectivity towards H_2O_2 production, and only increased the rate of synthesis and hydrogenation per Pd site when the dispersion of the Pd was low.⁵¹

Alba-Rubio *et al.* claimed that electroless deposition was a good preparation technique for AuPd catalysts. Nevertheless, the lack of enhancement to activity or selectivity would suggest otherwise as other, well-established preparation methods exist.^{32,42,88,89}

Comparisons can be drawn between different research groups' studies on the catalysis of direct H₂O₂ synthesis.³³ However, it is vital to note that reaction conditions and weight loadings of the catalysts differ, meaning that direct comparisons may not always be made. In addition, the catalyst preparation methods and treatments vary between the different groups' studies (Table 1.3).³³

Edwards *et al.*^{90–92} studied the pre-treatment of a TiO₂,⁹¹ SiO₂,⁹² and an AC support⁹⁰ used for a 5.00 wt% AuPd (1:1) catalyst, using HNO₃ (2 %). The latter showed an unusually high H₂ selectivity (<95 %), without decomposition or hydrogenation of the high concentrations of H₂O₂ formed. The reason for this high selectivity was due to a large amount of small Pd-rich nanoparticles (2-6 nm) present on the support. Additionally, the oxidation state of the Pd within these particles was also crucial in the enhanced selectivity, in which Pd²⁺ was more selective than Pd⁰.^{33,72,90–92}

Gemo *et al.*⁹³ demonstrated the Al doped SBA-15-supported catalysts led to increased activity and selectivity. This was credited to an increased number of Brønsted-Lowry acid sites in the support material. This work supported the mechanism proposed by Wilson *et al.*⁶⁹ as H⁺ was one part of the ORR reaction on the Pd clusters.

Park *et al.*^{94,95} studied Pd supported on tungstophosphoric acid, after precipitation with Cs⁺, for direct H₂O₂ synthesis catalysts. These catalysts gave a higher H₂O₂ selectivity (~44 %) compared to other Pd-only catalyst, without the need of an acid promoter. As the amount of additional Cs was varied, increasing amounts of Cs gave a high selectivity value (~48 %). This was attributed to the acidic nature of the catalyst, further enhanced by Cs, which supported the work of Gemo *et al.*⁹³

Abate *et al.*⁹⁶ demonstrated increased Pd dispersion on an N-doped carbon nanotube (CNT) support. It was thought that the N increased the acidity of the support, similar to Edwards *et al.* work.^{90–92} In addition, the smaller Pd particles caused by the increased acidity led to their increased stabilisation on the support material. The activity towards H₂O₂ was high (128 mol_{H₂O₂} kg_{cat}⁻¹ h⁻¹), comparable to that of the acid pre-treated 5.00 wt% AuPd/TiO₂ (110 mol_{H₂O₂} kg_{cat}⁻¹ h⁻¹) (Table 1.3). Although the

selectivity towards H_2O_2 of this catalyst under the reaction conditions used was significantly smaller than that of Edwards *et al.*'s 2.5 % Au-2.5 % Pd/C catalyst,⁷⁸ it was significantly higher than the Pd-only heteropolyacid catalysts synthesised by Park *et al.*⁸¹ (77 %, ⁹⁶ <95 %⁷⁸ and ~48 %, ⁸¹ respectively).

Menegazzo *et al.*⁹⁷ observed a similar characteristic to the work of Gemo *et al.*,⁹³ with the presence of acidic sites on the support material. With the 1.50 wt% Pd/SiO₂ catalyst, Menegazzo *et al.*⁹⁷ showed that the existence of OH groups at the acid sites on the surface of the support led to a greater dispersion of smaller Pd nanoparticles. However, it was noted that SiO₂ is not an ideal support for Au, which is in part due to their similar pI's.^{71,72} Nevertheless, Edwards *et al.*⁸⁵ demonstrated that a 5.00 wt% AuPd/SiO₂ catalyst, with an acid pre-treated support, could compete with catalysts that have different supports, such as a pre-treated TiO₂ (83 and 110 mol_{H₂O₂} kg_{cat}⁻¹ h⁻¹, respectively).^{97,98}

From the results discussed in the aforementioned studies,⁹⁰⁻⁹⁷ it would appear that the 2.5 % Au-2.5 % Pd/C, with the support pre-treated with HNO₃ (2 %) was the better catalyst with its high activity and high selectivity (110 mol_{H₂O₂} kg_{cat}⁻¹ h⁻¹, <95 %, respectively), provided that the differing reaction conditions are neglected in this analysis. However, carbon supports are notorious for their inconsistent reproducibility (Table 1.3).³²

Table 1.3. 'Comparison of productivities for a selection of catalysts reported in the literature.' Table adapted with permission from reference.³³

Reference	Catalyst	Temperature / K	Pressure / Bar	Solvent	Reaction time / h	Productivity / mol _{H₂O₂} kg _{cat} ⁻¹ h ⁻¹
Edwards ⁹⁰	2.50 wt% Au-2.50 wt% Pd/C (2% HNO ₃) (0.01 g)	275.15	40	H ₂ O + CH ₃ OH	0.5	160
Gemo ⁹³	1.00 wt% Pd-0.19 wt% Au/ Al-SBA15 (0.15 g)	283.15	17.5	CH ₃ OH	0.25	90
Park ⁹⁴	Pd _{0.15} Cs _{2.5} H _{0.2} PW ₁₂ O ₄₀ (1.00 g)	301.15	10	CH ₃ OH + H ₃ PO ₄ + NaBr	6	5.9
Park ⁹⁵	Cs _{2.5} H _{0.2} PW ₁₂ O ₄₀ /Pd/ MCF (1.00 g)	301.15	10	CH ₃ OH + H ₃ PO ₄ + 1.5 NaBr	6	6.8
Abate ⁹⁶	0.90 wt% Pd/N-CNT (0.03 g)	298.15	10	CH ₃ OH + H ₂ SO ₄	1.5	128
Menegazzo ⁹⁷	1.50 wt% Pd/SiO ₂ (0.0135 g)	293.15	1.0	CH ₃ OH + H ₂ SO ₄	5	11.4
Edwards ⁹¹	2.50 wt% Au-2.50 wt% Pd/TiO ₂ (2% HNO ₃) (0.01 g)	275.15	40	H ₂ O + CH ₃ OH	0.5	110
Edwards ⁹²	2.50 wt% Au-2.50 wt% Pd/SiO ₂ (2% HNO ₃) (0.01 g)	275.15	40	H ₂ O + CH ₃ OH	0.5	83

Note: the weight of the catalysts used are stated in parentheses.

Edwards *et al.*⁹⁸ studied a variety of differently loaded AuPd catalysts supported on CeO₂ via the C_{IM} method. However, what was unique about this research was the addition of Pt to the catalysts. Whilst maintaining a total metal loading of 5.00 wt%, it was observed that there was enhanced activity towards H₂O₂ synthesis with these catalysts. The black marks visible on the ternary composition diagrams are the loadings of the catalysts tested by Edwards *et al.* (Fig. 1.9).⁹⁸

It was important to note that the best tri-metallic H₂O₂ synthesis catalyst (159 mol_{H₂O₂} kg_{cat}⁻¹ h⁻¹ with 2.35 wt% Au-2.35 wt% Pd-0.30 wt% Pt/CeO₂) (Fig 1.9.a) in this study was not necessarily the most selective as there was a high level of hydrogenation (177 mol_{H₂O₂} kg_{cat}⁻¹ h⁻¹) (Fig. 1.9.b). By comparison, the 2.50 wt% Au-2.30 wt% Pd-0.20 wt% Pt/CeO₂ catalyst was superior in relation to being selective as the amount of hydrogenation was low (11 mol_{H₂O₂} kg_{cat}⁻¹ h⁻¹). However, the activity towards H₂O₂ had also decreased (86 mol_{H₂O₂} kg_{cat}⁻¹ h⁻¹) and comparable to that of the 2.50 wt% Au-2.50 wt% Pd/SiO₂ catalyst, with an HNO₃ pre-treated support catalyst in Edwards *et al.* previous study (Fig. 1.9).⁹²

From the perspective of utilising each metal, Pd was the active component for the mono-, bi- and tri-metallic catalysts, unlike Au and Pt that showed little to no activity towards H₂O₂ synthesis in either mono-metallic catalysts. Furthermore, the AuPt catalyst showed an inability to synthesise H₂O₂ in large amounts. With the increased activity, however, the disadvantage of using Pd became apparent as selectivity decreased with greater hydrogenation. All the mono-, bi- and tri-metallic catalysts with varying amounts of Au, Pd and Pt had the ability to hydrogenate H₂O₂, with Au credited being the least hydrogenating metal (Fig. 1.9).

The results of varying the AuPd ratio showed that where there was a significant increase in direct H₂O₂ synthesis, there was an even larger increase in its degradation. The reason for the improved activity and selectivity was that the Pt induced the formation of core-shell structures that gave a beneficial electronic effect. Scanning-Transmission Electron Microscopy-Energy Dispersive X-ray spectroscopy (STEM-EDX) analyses were used to support this.⁹⁸

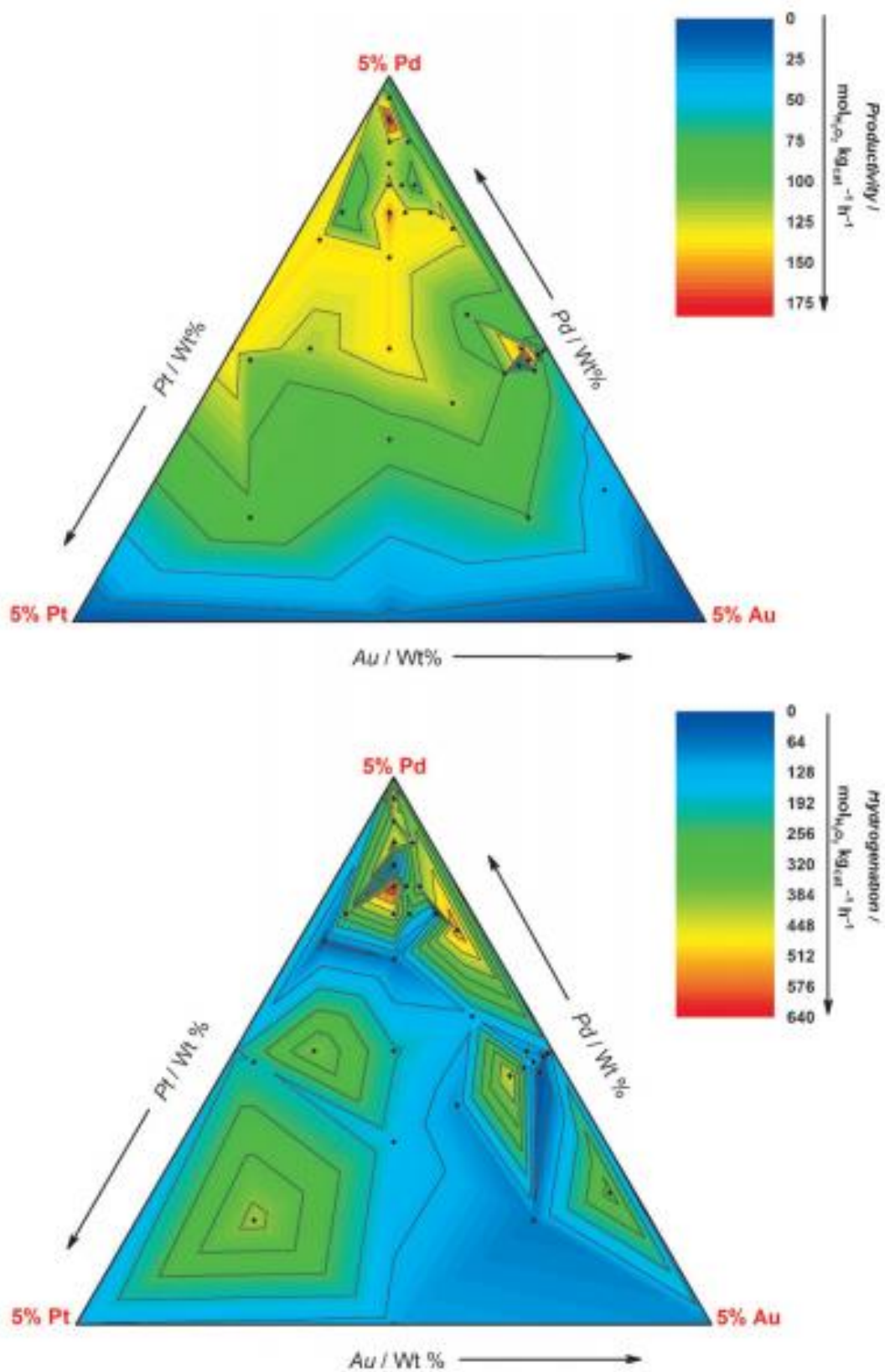


Figure 1.9. Ternary composition diagrams demonstrating the effect of the different metal loadings on a) the H_2O_2 synthesis reaction; and b) on the hydrogenation/decomposition of H_2O_2 with the same catalysts. Image adapted with permission from reference.⁹⁸

When conducting experimental catalytic research, there are important aspects that chemical manufacturers will consider for the use of catalysts in their processes that should also be considered by the research groups. These qualities of a catalyst are its reproducibility, stability, and reusability. A catalyst will not be used on a large scale if it cannot be reproduced with the same efficacy, is unstable under desired reaction conditions or can only be used once before it must be disposed of. However, research into a wide variety of catalysts is vital in understanding how the catalysis occurs and can accomplish these goals.

It should also be noted that chemical manufacturers seek to reduce the cost of their production, inclusive of the use of materials. As with all precious metals, additional metals included in the catalyst increase the cost of the catalyst. Furthermore, the cost of additional chemicals, such as acid promoters, will also be avoided by manufacturers. Although understanding how catalysis occurs for certain reactions on different materials is of great importance, it is also important to be mindful of how useful those catalysts will be at an industrial level.

1.5.3. Research Supported by Computational Methods for Palladium- and Gold-Containing Catalysts

Deguchi *et al.*⁷¹ investigated the effects of acid and base promoters for the direct synthesis for H₂O₂ over a 5.00 wt% Pd/C catalyst. In particular, the particle size of the metal, the catalyst support, the pressures of the O₂ and H₂ and the effect of H⁺ and Br⁻ ions were studied. This study was part of a series of studies that this group had conducted to determine the mechanism of the synthesis, decomposition and hydrogenation of H₂O₂.^{71,99-101}

The kinetics of the direct H₂O₂ synthesis and decomposition as well as the adsorption of Br⁻ ions were explored.⁷¹ This was complimented by DFT calculations using the Pd cluster model.¹⁰² The results confirmed the theorised mechanisms where reduced Pd at the surface were the active sites, of which there were two categories. The first category was the 'corner' and 'edge' Pd sites that were less coordinatively saturated and the 'face' Pd sites that were more coordinatively saturated. The DFT calculations that were completed suggested that the 'corner' and edge' sites favoured H₂O₂ decomposition, whereas the 'face' sites favoured synthesis of H₂O₂. This was confirmed through the calculated energy profiles of each reaction.⁷¹

Deguchi *et al.*⁷¹ noted that H⁺ and Br⁻ inhibited the decomposition pathway by site blocking the 'corner' and 'edge' Pd sites. It was discovered that a greater concentration of H⁺ ions led to an increase in selectivity towards direct H₂O₂ synthesis (at 10⁻¹ M [H⁺], ~95 % selectivity). Additionally, the lower pIs for the support used led to an increase in H₂ consumption and selectivity towards direct H₂O₂ synthesis and decreased the amount of decomposition. This was due to the protonation of the support changing the surface of the Pd cluster(s).⁷¹

This group also found that larger Pd particles coupled with a lower dispersion of the particles led to a decreased activity but was more selective towards the synthesis route as less 'corner' and 'edge' Pd sites existed. Furthermore, simulations that were run for this catalysed reaction indicated that it could not be scaled up for industrial purposes as mass transfer was a major issue.⁷¹ However, this could be rectified with better catalyst design, for example, Gemo *et al.*⁷⁰ suggested to increase the porosity of the catalyst to overcome this obstacle.

After analysing the studies that have been completed, it was clear that there were contradictory mechanisms of the direct synthesis of H₂O₂.⁶⁸⁻⁷¹ For instance, the site blocking that was proposed by Huerta *et al.*⁶⁸ stated that Br⁻ deactivated the catalyst entirely for synthesis and decomposition of H₂O₂, whereas Deguchi *et al.*⁷¹ stated that site blocking only occurred at the 'corner' and 'edge' Pd sites, which were responsible for decomposition and not the direct synthesis of H₂O₂. Although the catalysts may have had different supports, the theory regarding site blocking still applies and would need further investigation to determine which proposed mechanism is correct.

From Gemo *et al.*'s study,⁷⁰ it was concluded that an ER mechanism may have taken place as the rate of synthesis was dependent on the amount of adsorbed H₂ and O₂ on the surface of the catalyst. The mechanism proposed was different from the proposed mechanism by Wilson *et al.*⁶⁹, where an ORR occurred at the Pd surface. It is apparent that the mechanism for the direct synthesis of H₂O₂ is still not known and debated.

Huerta *et al.*⁶⁸ proposed a theory of the effect of Br⁻ and how it affected H₂O₂ production. The study suggested that site blocking for H₂O₂ synthesis and hydrogenation was instigated by sodium bromide (NaBr). Moreover, the Br⁻ ions caused the surface of the catalyst to reorganise itself and the Pd was leached from the catalyst. The group thought that with the other optimised reaction conditions, NaBr

could be used to switch off the hydrogenation of H₂O₂, but still attain a high synthesis value. However, the highest value this group could attain was ~0.16 wt% H₂O₂.⁶⁸

Wells *et al.*¹⁰³ studied the direct synthesis of H₂O₂ over a neutral Au trimer using the Gaussian98 suite of programs and the Becke and Perdew-Wang 1991 (BPW91) correlation energy functional. The Los Alamos LANL2DZ effective core pseudopotentials (ECPs), with the valence double zeta basis set for Au and D95 valence double zeta basis sets for H₂ and O₂, were also utilised. Greater accuracy of the system could be acquired using the BPW91 functional compared to the B3LYP, however, the group predicted that the trimer with adsorbates would have lower energy differences due to the cancellation of systematic errors within such a narrow molecular range. Superposition errors of the basis sets were not calculated as they had a relatively constant energetic offset across the cluster models and were a minor factor to consider. Previous work by the group using the same pseudopotentials, coupled with experimental results, that described the behaviour of the small Au clusters and O₂ accurately. Using the synchronous transit-guided quasi-Newton (STQN) method and the reactant and product geometries as its starting points, all transition states were identified.

Key observations from this study were that the O=O bond did not break to form H₂O₂ and the largest energy barrier was the desorption of H₂O₂. Again, this was another study that supports Au as a highly selective element to use in catalysis. However, the issue of the lack of H₂O₂ desorption meant that it may not be the most ideal metal to use in a catalyst. This study only considered Au trimers, which is vastly different to the nanoparticles of heterogeneous catalysts.¹⁰³

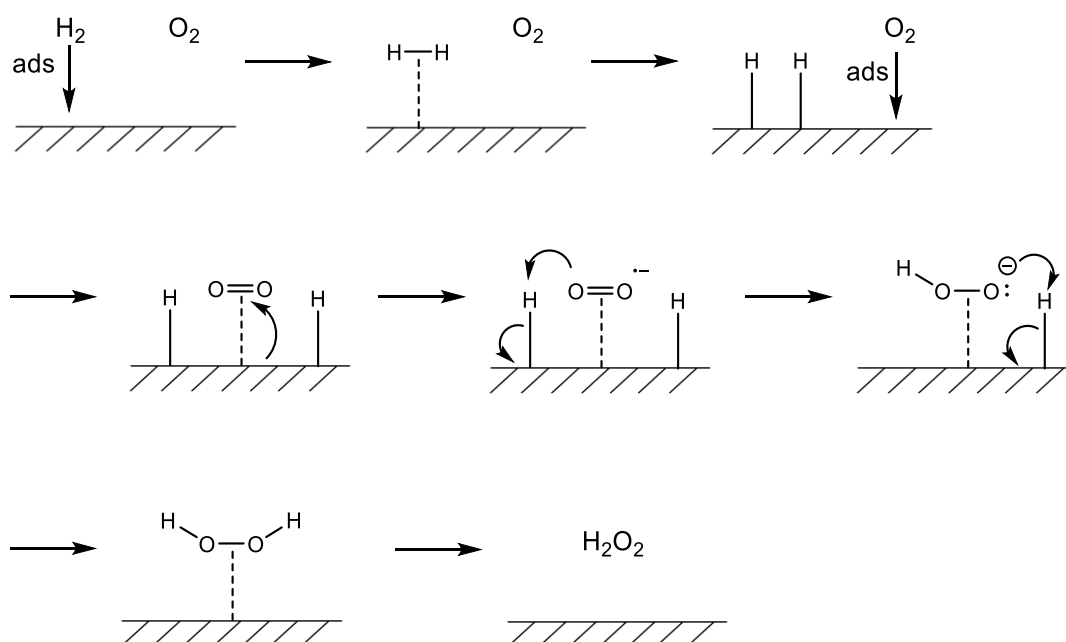
Staykov *et al.*¹⁰⁴ investigated the direct synthesis of H₂O₂ over Pd and Au/Pd catalysts in 2008. The group used first principle DFT methods to propose a two-step mechanism of the reaction, involving superoxo formation over Pd followed by its reaction with H atoms. This was a similar mechanism to the one proposed by Wilson *et al.*⁶⁹

However, the differences between the studies arise through further explanation of the mechanism; electron donation from the Pd *d*-orbital to the π -orbital of the O₂ molecule occurred as they overlapped, and a significant electron density was found.¹⁰⁴ This resulted in a stable chemisorption state. With Staykov *et al.*'s work, the mechanism proposed showed that the superoxo species was formed, having a weaker and longer O=O bond, and it reacted with the dissociated H atoms

subsequently to form the OOH and H₂O₂ species (Scheme 1.4).¹⁰⁴ This is different to Wilson *et al.*'s mechanism for direct H₂O₂ synthesis over a Pd cluster as the dissociated H atoms are H⁺ ions and predicted a two-electron transfer through the Pd nanoparticle to form the superoxo species (Scheme 1.3).⁶⁹

The activity can be measured by the increasing length of the O=O bond on the metal surface.¹⁰⁴ For Au, no increase was observed as it could not be optimised and agreed with experimental data. For Au with small amounts of Pd, an increase of 0.09 Å was observed in O=O bond and for Pd only, an increase of 0.13 Å in the O=O bond length and its resulting dissociation was observed. The longest O=O bond length increase was observed with Pd and small amounts of Au, with 0.17 Å. This meant that the latter composition provided the optimum conditions for catalytic H₂O₂ formation, however, it also made it suitable for undesirable O₂ dissociation.

The AuPd catalyst had a greater E_a barrier for O₂ dissociation than the Pd catalyst due to the increased distance between the O₂ molecule and surface, which in turn was caused by the larger radius of the Au atom compared to the Pd atom. The calculations determined that a larger E_a was required for O₂ dissociation because of the increased distance over the Au atom on the surface. This result was of significance as it explained the enhanced selectivity for H₂O₂ synthesis attributed to AuPd catalysts (Scheme 1.4).¹⁰⁴



Scheme 1.4. Reaction scheme of Staykov *et al.*'s proposed mechanism for direct H₂O₂ synthesis over Pd and AuPd surfaces.¹⁰⁴

However, the same cannot be said for H₂ dissociation over the surface with the inclusion of Au. As the E_a was low due to the short distances between the H₂ molecule and the surface, the inclusion of Au into the Pd surface only increased the E_a of H₂ dissociation by ~6.00 kcal mol⁻¹ (~25.10 kJ mol⁻¹). This meant that Au cannot inhibit H-H bond dissociation in an AuPd catalyst. Because of the low E_a of H₂ dissociation, this was the first step in the mechanism after H₂ adsorption (Scheme 1.4).

The work conducted by Staykov *et al.*¹⁰⁴ did not include any MSI(s) that may have occurred or a solvent that may take a vital role in the catalysis involved. These components are needed for a true understanding of the reaction mechanism. Nevertheless, Wilson *et al.*'s proposed mechanism⁶⁹ was supported by the work of Staykov *et al.*¹⁰⁴

Ford *et al.*¹⁰⁵ completed a systematic study of the reduction of O₂ by H₂ on eight late transition and noble metals (Au, Ag, Cu, Pt, Pd, Ni, Ir and Rh) using DFT. The study observed the reactivity of the metals for this catalytic reaction at the gas-solid interface. All the metals had the (111) facet as it was the most thermodynamically stable and all had face-centred cube (fcc) structures that allowed consistency throughout the study. Several forms of hydrogenated O were investigated as possible reaction intermediates may have existed during the reaction. The properties of the reaction intermediates were studied, and a detailed ORR network was constructed using the calculated reaction energies and E_a barriers from multiple possible intermediate reaction pathways. This resulted in identifying the most probable reaction mechanism on each metal.

As an H atom is bonded to the adsorbed O₂, it forms an OOH radical, which adsorbed to the surface more strongly than O₂. For the Pd and Pt surfaces, the preferred and most stable configuration of the OOH was to bind to a single metal atom; for Cu, Au, and Ag, OOH preferred to bind to two metal atoms with the OH tilted away from the surface. The point of binding was at the non-hydrogenated O of the OOH species. For Rh, Ni and Ir, the OOH spontaneously dissociated into O and OH, which suggested that further hydrogenation reactions of OOH could not take place.¹⁰⁵

As H₂O₂ could not be formed on either Rh, Ni and Ir, eight metals of interest turned to five. Ford *et al.*¹⁰⁵ found that HOOH bound weaker to Ag and Au than Pt, Pd and Cu (~0.10 eV) (Fig. 1.10). The isomer of H₂O₂ studied was the aquoxyl group (OOHH), which was found to be stable on Au and Ag, unlike the other metals. The OOHH species does not exist in the gas phase, meaning its binding energies could

not be calculated directly. This group found that the OOHH was 1.00-1.20 eV less stable than HOOH on Ag and Au.¹⁰⁵

Four mechanisms were proposed to account for the different intermediates and products formed. The first was the dissociative mechanism that involves the dissociation of O₂ and its subsequent hydrogenation to form OH and H₂O. The second was the peroxy mechanism that involved the formation of OOH and its subsequent decomposition to OH and O. The third was the peroxide mechanism that involves the hydrogenation of OOH to H₂O₂. At this juncture, the H₂O₂ could desorb or undergo O-O scission. The latter was required before any further hydrogenation could occur and no stable HOOHH species was found. The last mechanism was the aquoxyl mechanism that involved the further hydrogenation of OOH to form OOHH and its subsequent O-O bond scission, forming a H₂O and adsorbed O. The latter three mechanisms were considered associative mechanisms. The last mechanism could not be completed by Cu, Pt, and Pd as the O-O bond scission and hydrogenation occurred simultaneously, meaning that the OOHH intermediate was not formed.¹⁰⁵

It was observed that Au and Ag favoured OOH formation ($E_a = 0.25$ eV and 0.20 eV, respectively) over O-O dissociation ($E_a = 2.04$ eV and 1.22 eV, respectively), thus, the associative mechanism for O₂ reduction was favoured. However, for Pt, Pd and Cu, the E_a barriers for O-O dissociation ($E_a = 0.71$ eV, 0.84 eV and 0.23 eV, respectively) and the reduction reactions ($E_a = 0.29$ eV, 0.63 eV and 0.44 eV, respectively) were significantly closer, causing competition between the dissociative mechanism and the associative mechanisms. Cu marginally favoured O₂ dissociation; Pd had nearly identical E_a barriers for both types of reaction pathway, and Pt marginally favoured O₂ hydrogenation (Fig. 1.10).¹⁰⁵

Au demonstrated that H₂O₂ formation was more favourable than OOH dissociation, O-O bond scission or hydrogenation. Additionally, O-O bond scission in H₂O₂ was the least exothermic reaction step for Au. These characteristics led to the suggestion that H₂O₂ production was at its most selective on Au compared to the other metals (Fig. 1.10), in accordance with Hutching *et al.*'s work.⁷⁷ The selectivity regimes for O₂ reduction were divided into three categories: metals that bind O weakly (Au); moderately (Pt and Pd); and strongly (Rh, Cu, Ir and Ni). This may explain the activity and selectivity observed in Edwards *et al.*'s work,⁹⁸ with the Pt-promoted AuPd catalysts. Plauck *et al.*¹⁰⁶ also investigated Pd promoted H₂O₂ decomposition and drew the same conclusions.

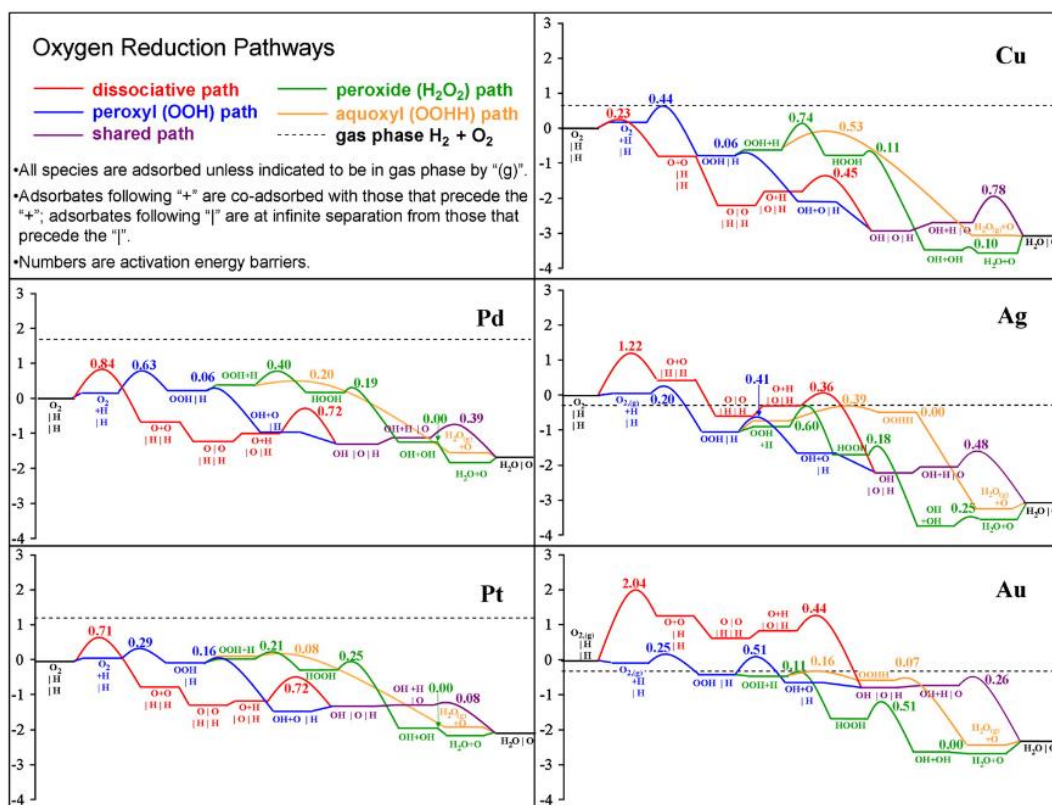


Figure 1.10. ‘The 2D potential energy surfaces for oxygen reduction by hydrogen on (111) facet of fcc metals via the dissociative-, peroxy-, peroxide-, and aquoxyl-mechanisms. The purple line indicates the merge of the dissociative and peroxy pathways. The ordinate is relative energy (in eV). Dashed lines indicate the energy of gas-phase $\text{H}_2 + \text{O}_2$. All species are adsorbed unless indicated to be in gas phase by “(g)”. Adsorbates connected by “+” are coadsorbed, ‘and adsorbates separated by “|” are infinitely separated from each other. Numbers are activation energy barriers (in eV).’ Image adapted with permission from reference.¹⁰⁵

Jirkovský *et al.*¹⁰⁷ devised an approach that could lead to the preferable pathway of producing H_2O_2 from O_2 reduction. DFT modelling was used to assess the best alloy candidate using Pd, Pt or Rh as the ‘guest’ atom to the Au ‘host’. From the study, isolated alloying atoms of Rh, Pt or Rh within the Au surface should have enhanced the H_2O_2 yield compared to the Au only surface, but this was not the case. The $\text{Au}_{1-x}\text{Pd}_x$ nanoalloys were investigated with varied Pd content that could predict the selectivity towards H_2O_2 , and by increasing the amount of Pd to 8 conc.%, it led to a H_2O_2 selectivity of ~95 %. However, the environment required for this electrocatalytic production of H_2O_2 with this high selectivity must be compatible with the same environment required for a proton exchange membrane. A greater amount of Pd onto the surface led to a large decrease in H_2O_2 selectivity, to the extent where a pure Pd surface readily supported H_2O formation.¹⁰⁷

This work was in close agreement with Staykov *et al.*'s and Ford *et al.*'s studies.^{104,105} All three groups showed the catalytic performance towards H₂O₂ synthesis yielded by noble metals, and in particular, by Au. Although these pieces of literature support one another, there are limitations to the work, such as the assumptions made, details neglected and their ability to be applied to the “real-world.” For example, Staykov *et al.*⁹² reported an E_a barrier of 1.22 kcal mol⁻¹ (or 0.052 eV) for the first reduction step of the oxygen species, whereas Ford *et al.*⁹³ reported an E_a barrier of 0.63 eV for the same reaction step. However, the difference between the studies was due to the existence of the superoxo species present in the mechanism Staykov *et al.*⁹² proposed, which was not present in Ford *et al.*'s work.⁹³

Nevertheless, other studies have been conducted for the activation of O₂ on metal nanoparticles. Shang *et al.*¹⁰⁸ studied the aerobic oxidation of phenylethanol over Au nanoparticles. The group demonstrated that Au nanoparticles could active O₂ at liquid-solid interface through the extensive use of DFT calculations coupled with the periodic continuum solvation model.

A complete reaction network of aerobic alcohol oxidation was created. The Au nanoparticle facilitated the α-C-H bond dissociation and was the rate-determining step. The surface H because of this cleavage was then removed by O₂ to form OOH and H₂O₂. Due to the simple proton-shift equilibrium, the Au nanoparticles became negatively charged at the steady state.

Although a reaction mechanism was devised, it was observed that there was a degree of sensitivity regarding the nanoparticles' surroundings. It was discovered that the presence of H₂O can double the adsorption energy of O₂ to the edge sites of the nanoparticle due to the strongly polarising nature of H₂O in adsorption. This relates to the affinity of H₂O and O₂ as O₂ readily dissolves in H₂O. In addition, the O₂ activation only occurred after H was present on the surface.¹⁰⁷

Thetford *et al.*¹⁰⁹ used DFT to study the adsorption to ten-atom Au nanoparticles support on rutile TiO₂(110). It was discovered that H₂O₂ effortlessly decomposed to two OH species over the Au nanoparticle. The interaction with the surface OH components on the TiO₂ support provided a low E_a barrier to an OOH species existing on the surface. The group theorised that the H₂O₂ formation occurred at the interface between the support and the nanoparticle and the hydroxylated surface's influence on this metal-support region.

This research could be considered as a step closer to a “real-world” situation than other works previously discussed as the observations were of nanoparticles on

a support material rather than a surface of atoms. It may not conform with the research of other groups but does bring the scientific community closer to more accurate answers that help in better understanding the catalysis.¹⁰⁹ The work showed that Au does not provide the greatest selectivity when investigating ten-atom clusters, unlike the Au surface research that was conducted by Ford *et al.*¹⁰⁵

Li *et al.*¹¹⁰ looked at computational models through DFT for Pd and Au@Pd catalysts for the decomposition of H₂O₂, OH hydrogenation and H₂O₂ hydrogenation. The first reaction mentioned was completed by dissociation of the H₂O₂ molecule into two OH groups followed by a disproportionation reaction to form O and H₂O. The last reaction step was found to be energetically unfavourable, and therefore, unlikely to occur. The discovery that H₂O₂ dissociation was irreversible and facile was key as inhibition of the dissociation sites would be needed to improve selectivity towards direct H₂O₂ synthesis.

The E_a barrier for the H₂O₂ dissociation over a Pd(111) surface was less than the desorption energy. Interestingly, the Au@Pd surface had inverted characteristics, meaning that the selectivity towards direct H₂O₂ synthesis was enhanced; a behaviour that was observed both experimentally and computationally.^{32,33,42,104,105,107,109,111} The reason for this increased selectivity was due to the Au diminishing the interaction between the surface and the H₂O₂. The same behaviour was observed when pre-adsorbed H was on the Pd surface.¹¹²

Xu *et al.*¹¹³ studied 55-atom nanoparticles comprised of Pd, and introducing dopant metals (transition metals) into the particle to replace some of the Pd atoms. Using DFT and Sabatier analyses, the valence electrons of the Pd-shell was found to be an intrinsic factor for the particle's activity and selectivity for the direct synthesis of H₂O₂. The dopant metals had the capability to finely tune the activity and selectivity, which was determined by the amount of and electronegativity of the dopant.

Within this research, one of the particles was a AuPd (1:1) particle. This particle was arranged in a core-shell configuration with the core as the dopant metal. The adsorption of H and H₂ of this bi-metallic particle was superior to the mono-metallic nanoparticles by ~2.00 eV, whereas O or O₂ did not readily adsorb to the surface of the particles. However, this was not the most catalytically active particle that was observed.¹¹³ Pt₂Au₂₃Pd₃₀ particle was seen to be the most active and selective, which was supported by Edwards *et al.*'s research.⁹⁸

The reason for these characteristics and behaviours was due to the dopant's ability to withdraw electrons from the Pd.¹¹³ This led to decreased repulsion from the

particles and the adsorbates could readily interact with the particles. However, other dopants (W, Pb, Ru and Mo) could be competitors to Au within this bi-metallic particle, having displayed similar activities and selectivities.

Nugraha *et al.*¹¹⁴ researched, through DFT calculations, Pd(111) and AuPd alloy materials for the direct synthesis of H₂O₂. Only one or three dopant metal atoms were incorporated into the alloy. It was found that the OOH and O₂ species gave rise to more desirable pathways compared to O, with decreased adsorptions observed for the bi-metallic alloy. The rationale for this was that the electronics of the dopant metal interfered with the Pd and suppressed the O=O scission.

Similar activities and selectivity values were observed between the Pd-only and the alloy materials. However, the desorption of H₂O₂ was largely decreased for the alloy. This provided an indicator of the relative rates of the different steps throughout the reaction mechanism, as the AuPd alloy had an increased rate of desorption compared to the Pd-only material as the E_a barrier was lower.¹¹⁴ This might explain the experimental and other computational results observed by other research groups.^{32,33,42,104,105,107,109,111} A Hg alloy was also studied in a similar fashion, with similar activities and selectivity values observed.¹¹⁴

Todorovic *et al.*¹¹⁵ studied Pd(111), Pt(111) PdH(211) and AuPd(221) using DFT, and subsequent Nudged Elastic Band calculations (NEBs), for direct H₂O₂ synthesis. The Pd-only and AuPd surfaces gave similar results to that of Nugraha's research group's, where O=O scission for O₂ can be switched off with the addition of dopant metal(s).¹¹⁴ This was seen clearly in the Potential Energy Surface (PES) diagrams. In simplistic terms, a PES plots the molecular energy against the molecular geometry (Fig. 1.11).

On both Pd(111) and Au_{0.89}Pd_{0.11}(221), H₂ readily adsorbed and dissociated, but by different degrees ($\Delta G = \sim 2.00$ and ~ 0.05 eV, respectively). The similarities dissipate at this point as O-O bond scission was more favourable than the H₂O₂ synthesis pathway on the Pd surface (E_a = ~ 0.60 and ~ 0.50 eV, respectively). As H₂O₂ was synthesised on Pd, after the first hydrogenation step, the E_a barrier for OOH dissociation was lower than that of the second hydrogenation step, meaning that H₂O₂ destruction was more likely to occur (E_a = ~ 0.20 and ~ 1.00 eV, respectively) (Fig. 1.11).

By comparison, the first hydrogenation step in H₂O₂ synthesis was the favoured pathway over O-O bond scission on the AuPd surface (E_a = ~ 0.19 and ~ 1.45 eV, respectively). However, for both Pd and AuPd surfaces, the

dissociation of H_2O_2 after its synthesis was likely to occur as the E_a barriers for its dissociation was considerably lower than its desorption (for Pd, $E_a = \sim 0.10$ and ~ 0.30 eV, respectively) (for AuPd, $E_a = \sim 0.09$ and ~ 0.45 eV, respectively) (Fig. 1.11).

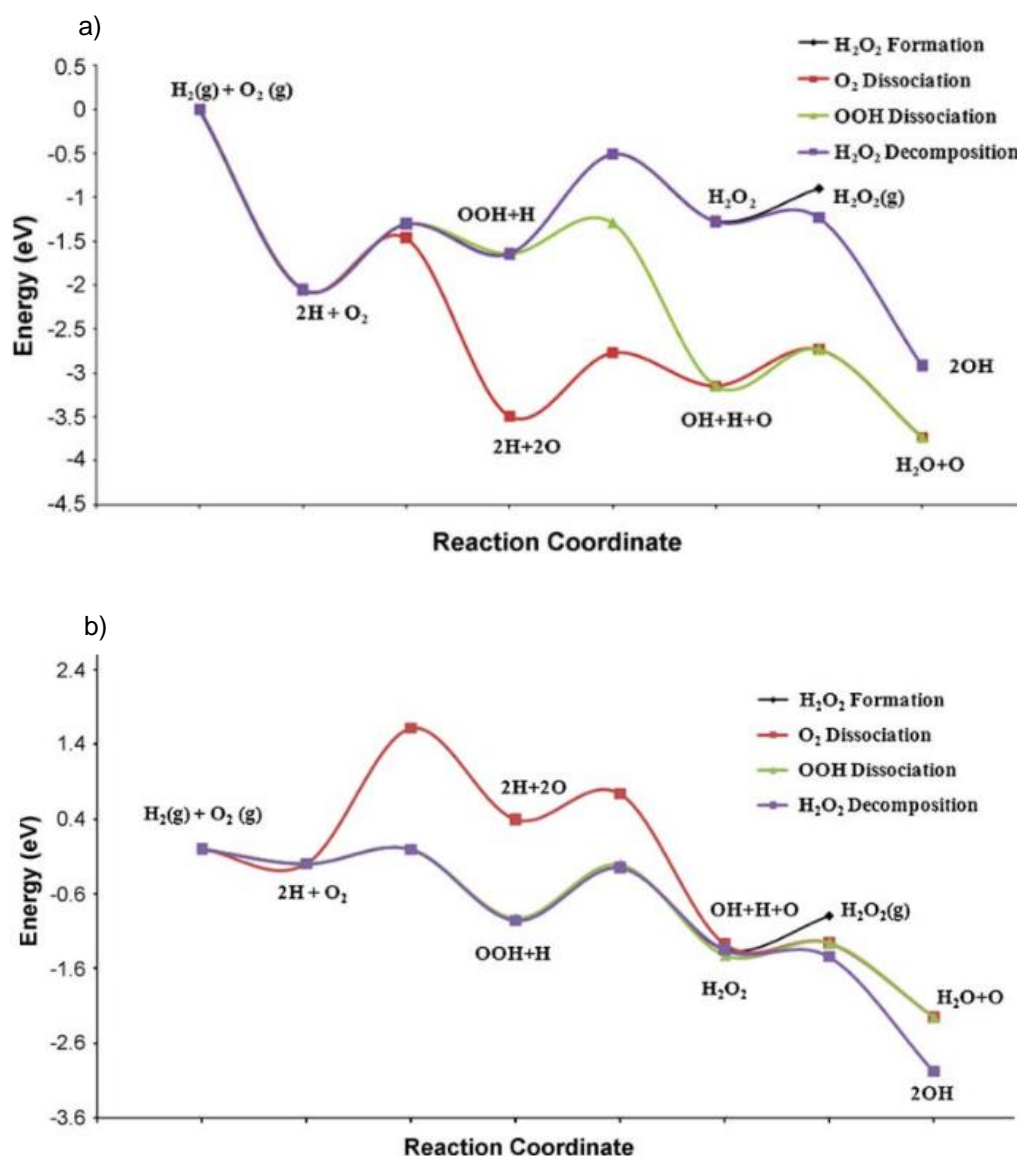


Figure 1.11. Potential energy surface diagrams and their associated reaction mechanisms, where **a)** is for Pd(111), and **b)** is for Au_{0.89}Pd_{0.11}(221). With reference to gas phase H_2 and O_2 , the reaction mechanism species and E_a barriers have been plotted. Images adapted with permission from reference.¹¹⁵

Interestingly, both the OOH dissociation and H_2O_2 decomposition pathway follow the same energy profile in the mechanism for the alloy, unlike the mono-metallic surface. This would indicate that these two surfaces follow different mechanisms, as the former can more readily activate H_2 (Fig. 1.11). Another study that supported the

findings of both Nugraha *et al.*¹¹⁴ and Todorovic *et al.*¹¹⁵ was conducted by Ham *et al.*¹¹⁶ The latter also found that the addition of Au quelled the O=O scission of O₂.

There is a serious lack of computational research with alloyed metals, in a 1:1 ratio, for the direct synthesis of H₂O₂. The majority of the research has been focused towards the effect of an additional metal as a dopant, with only a few atoms being included within the structure.^{113–116} Until such research has been published that focuses upon the former, it is not possible to draw comparisons between the mono-metallic and alloyed metal catalysts. However, what can be gleaned from the literature is that mono- and bi-metallic (and by further extension multi-metallic) catalysts follow different reaction pathways that lead to different characteristics being exhibited; a quality that is key in catalyst design.

1.6. Project Aims

The aims of the project are as follows:

1. To study and understand the catalysis involved for Au- and Pd-based catalyst systems in the utilisation of *in-situ* direct H₂O₂ synthesis for the ammoximation of cyclohexanone and for the epoxidation of propene;
2. Through catalyst design, optimise a direct H₂O₂ synthesis catalyst to achieve high yields of H₂O₂ under basic conditions and at high temperatures (353.15 K) in a three-reaction one-pot synthesis;
3. Through catalyst design, optimise a catalyst system to achieve high yields of cyclohexanone oxime in a three-reaction one-pot synthesis;
4. Through DFT calculations, study and appreciate the catalysis involved for the reaction steps of direct H₂O₂ synthesis over Au and Pd surfaces, with a focus on the local geometric and electronic properties;
5. And through DFT calculations, study and understand the catalysis involved for the reaction steps of the epoxidation of propene utilising H₂O₂ as the oxidant (from direct H₂O₂ synthesis) over Au and Pd surfaces, with a focus on the local geometric and electronic properties.

1.7. References

- 1 M. Bowker, *The Basis and Applications of Heterogeneous Catalysis*, Oxford University Press, 1998.
- 2 G. J. Price, *Thermodynamics of chemical processes*, Oxford University Press, Second Ed., 2018.
- 3 R. J. Lewis, *PhD Thesis Title: The application of Cs-exchanged tungstophosphoric acid as an additive in the direct synthesis of hydrogen peroxide and the use of Au-Pd/TS-1 in a one-pot approach to cyclohexanone oxime production*, Cardiff University, 2016.
- 4 J. K. Edwards, *PhD Thesis Title: Direct synthesis of hydrogen peroxide from hydrogen and oxygen over catalysts containing gold*, Cardiff University, 2006.
- 5 R. Burch and P. R. Ellis, An investigation of alternative catalytic approaches for the direct synthesis of hydrogen peroxide from hydrogen and oxygen, *Appl. Catal. B Environ.*, 2003, **42**, 203–211.
- 6 J. C. Frost, Junction effect interactions in methanol synthesis catalysts, *Nature*, 1988, **334**, 577–580.
- 7 R. S. Drago, S. C. Dias, J. M. McGilvray and A. L. M. L. Mateus, Acidity and hydrophobicity of TS-1, *J. Phys. Chem. B*, 1998, **102**, 1508–1514.
- 8 I. Moreno, N. F. Dummer, J. K. Edwards, M. Alhumaimess, M. Sankar, R. Sanz, P. Pizarro, D. P. Serrano and G. J. Hutchings, Selective oxidation of benzyl alcohol using in situ generated H₂O₂ over hierarchical Au-Pd titanium silicalite catalysts, *Catal. Sci. Technol.*, 2013, **3**, 2425–2434.
- 9 Structure Commission of the International Zeolite Association, MFI: Framework Type, <https://europe.iza-structure.org/IZA-SC/framework.php?STC=MFI>, (accessed 20 April 2020).
- 10 E. Ntainjua N., J. K. Edwards, A. F. Carley, J. A. Lopez-Sanchez, J. A. Moulijn, A. A. Herzing, C. J. Kiely and G. J. Hutchings, The role of the support in achieving high selectivity in the direct formation of hydrogen peroxide, *Green Chem.*, 2008, **10**, 1162.
- 11 C. R. A. Catlow, S. A. French, A. A. Sokol and J. M. Thomas, Computational approaches to the determination of active site structures and reaction mechanisms in heterogeneous catalysts, *Philos. Trans. R. Soc. London A Math. Phys. Eng. Sci.*, 2005, **363**, 913–936.

- 12 J. M. Thomas and G. Sankar, The role of synchrotron-based studies in the elucidation and design of active sites in titanium - Silica epoxidation catalysts, *Acc. Chem. Res.*, 2001, **34**, 571–581.
- 13 G. Rapp and H. Fuchs, *United States Patent: MANUFACTURE OF CYCLOHEXANONE OXIME*, 1976.
- 14 L. Dal Pozzo, G. Fornasari and T. Monti, TS-1, catalytic mechanism in cyclohexanone oxime production, *Catal. Commun.*, 2002, **3**, 369–375.
- 15 P. Roffia, M. Padovan, G. Leofanti, M. A. Mantegazza and G. De Alberti, *United States Patent (19) Roffia et al. (54 CATALYTIC PROCESS FOR THE MANUFACTURE OF OXIMES*, 1987.
- 16 M. Taramasso, S. Donato Milanese, G. Perego and B. Notari, *United States Patent: PREPARATION OF POROUS CRYSTALLINE SYNTHETIC MATERIAL COMPRISED OF SILICON AND TITANIUM OXIDES*, 1982.
- 17 H. Ichihashi and H. Sato, The development of new heterogeneous catalytic processes for the production of epsilon-caprolactam, *Appl. Catal. a-General*, 2001, **221**, 359–366.
- 18 C. Meng, S. Yang, G. He, G. Luo, X. Xu and H. Jin, The Reaction Mechanism of Acetaldehyde Ammoximation to Its Oxime in the TS-1/H₂O₂ System, *Catalysts*, 2016, **6**, 109.
- 19 J. Sirijaraensre and J. Limtrakul, Mechanisms of the ammonia oxidation by hydrogen peroxide over the perfect and defective Ti species of TS-1 zeolite, *Phys. Chem. Chem. Phys.*, 2013, **15**, 18093.
- 20 F. Jensen, *Introduction to Computational Chemistry*, John Wiley & Sons, Ltd, West Sussex, England, 3rd edn., 2017.
- 21 C. J. Cramer, *Essentials of Computational Chemistry: Theories and Models*, John Wiley & Sons, Ltd, West Sussex, England, 2nd edn., 2004.
- 22 P. Hohenberg and W. Kohn, Inhomogeneous Electron Gas, *Phys. Rev.*, 1964, **136**, 864–871.
- 23 R. G. Parr and W. Yang, *Density-Functional Theory of Atoms and Molecules*, Oxford University Press, 1st edn., 1989.
- 24 A. Szabo and N. S. Ostlund, *Modern Quantum Chemistry: Introduction to Advanced Electronic Structure Theory*, Dover Publications, 2nd edn., 1982.

- 25 M. Levy, Universal variational functionals of electron densities, first-order density matrices, and natural spin-orbitals and solution of the v-representability problem, *Proc. Natl. Acad. Sci. U. S. A.*, 1979, **76**, 6062–6065.
- 26 W. Kohn and L. J. Sham, Self-Consistent Equations Including Exchange and Correlation Effects*, *Phys. Rev.*, 1965, **140**, 1133–1138.
- 27 C. Reece, *PhD Thesis Title: Kinetic Analysis and Modelling in Heterogeneous Catalysis*, 2017.
- 28 J. P. Perdew, K. Burke and M. Ernzerhof, Generalized gradient approximation made simple, *Phys. Rev. Lett.*, 1996, **77**, 3865–3868.
- 29 K. E. Atkinson, *An introduction to numerical analysis*, 2nd edn., 1989.
- 30 J. G. Lee, *Computational materials science : an introduction*, CRC Press, 2nd edn., 2016.
- 31 S. Grimme, J. Antony, S. Ehrlich and H. Krieg, A consistent and accurate ab initio parametrization of density functional dispersion correction (DFT-D) for the 94 elements H-Pu, *J. Chem. Phys.*, 2010, **132**, 154104.
- 32 C. Samanta, Direct synthesis of hydrogen peroxide from hydrogen and oxygen: An overview of recent developments in the process, *Appl. Catal. a- General*, 2008, **350**, 133–149.
- 33 J. K. Edwards, S. J. Freakley, R. J. Lewis, J. C. Pritchard and G. J. Hutchings, Advances in the direct synthesis of hydrogen peroxide from hydrogen and oxygen, *Catal. Today*, 2015, **248**, 3–9.
- 34 M. Abdollahi and A. Hosseini, in *Encyclopedia of Toxicology: Third Edition*, 2014, pp. 967–970.
- 35 C. H. Stone, Hydrogen peroxide, <https://www.essentialchemicalindustry.org/chemicals/hydrogen-peroxide.html>, (accessed 22 April 2020).
- 36 P. A. CARSON, *Hazardous Chemicals Handbook*, Butterworth-Heinemann, 2002.
- 37 D. Y. Murzin, N. V. Kul'kova, V. G. Kotova and M. Y. Kvyatkovskaya, Kinetic study of cyclohexanone ammoxidation in the liquid phase on titanium silicates, *Kinet. Catal.*, 1998, **39**, 702–705.

- 38 E. Kertalli, L. S. S. va. Rijnsoever, V. Paunovic, M. F. N. D'Angelo, J. C. Schouten and T. A. Nijhuis, Propylene epoxidation with hydrogen peroxide in acidic conditions, *Chem. Eng. Sci.*, 2016, **156**, 36–43.
- 39 I. Global Industry Analysts, Hydrogen Peroxide Market Trends, http://www.strategyr.com/MarketResearch/Hydrogen_Peroxide_Market_Trends.asp, (accessed 7 December 2017).
- 40 Y. Yi, L. Wang, G. Li and H. Guo, *Catal. Sci. Technol.*, 2016, **6**, 1593–1610.
- 41 J. M. Campos-Martin, G. Blanco-Brieva and J. L. G. Fierro, Hydrogen peroxide synthesis: an outlook beyond the anthraquinone process, *Angew. Chem. Int. Ed. Engl.*, 2006, **45**, 6962–6984.
- 42 R. J. Lewis and G. J. Hutchings, Recent Advances in the Direct Synthesis of H₂O₂, *ChemCatChem*, 2019, **11**, 298–308.
- 43 Q. Chen, Development of an anthraquinone process for the production of hydrogen peroxide in a trickle bed reactor—From bench scale to industrial scale, *Chem. Eng. Process. Process Intensif.*, 2008, **47**, 787–792.
- 44 S. Ranganathan and V. Sieber, *Catalysts*, 2018, **8**.
- 45 J. Zhou, H. Guo, X. Wang, M. Guo, J. Zhao, L. Chen and W. Gong, Direct and continuous synthesis of concentrated hydrogen peroxide by the gaseous reaction of H₂/O₂ non-equilibrium plasma, 2005, 1631–1633.
- 46 I. Yamanaka, T. Onizawa, S. Takenaka and K. Otsuka, Direct and Continuous Production of Hydrogen Peroxide with 93 % Selectivity Using a Fuel-Cell System, *Angew. Chemie Int. Ed.*, 2003, **42**, 3653–3655.
- 47 *Philosophical Magazine*, Taylor & Francis., 1838.
- 48 I.-Y. Jeon, H.-J. Choi, M. Choi, J.-M. Seo, S.-M. Jung, M.-J. Kim, S. Zhang, L. Zhang, Z. Xia, L. Dai, N. Park and J.-B. Baek, Facile, scalable synthesis of edge-halogenated graphene nanoplatelets as efficient metal-free electrocatalysts for oxygen reduction reaction, *Sci. Rep.*, 2013, **3**, 1810.
- 49 D. Hâncu and E. J. Beckman, Generation of hydrogen peroxide directly from H₂ and O₂ using CO₂ as the solvent, 2001, **003**, 80–86.
- 50 Q. L. Chen and E. J. Beckman, Direct synthesis of H₂O₂ from O₂ and H₂ over precious metal loaded TS-1 in CO₂, *Green Chem.*, 2007, **9**, 802–808.
- 51 A. C. Alba-Rubio, A. Plauck, E. E. Stangland, M. Mavrikakis and J. A. Dumesic, Direct Synthesis of Hydrogen Peroxide Over Au-Pd Catalysts Prepared by Electroless Deposition, *Catal. Letters*, 2015, **145**, 2057–2065.

- 52 J. K. Edwards, S. J. Freakley, A. F. Carley, C. J. Kiely and G. J. Hutchings, Strategies for Designing Supported Gold-Palladium Bimetallic Catalysts for the Direct Synthesis of Hydrogen Peroxide, *Acc. Chem. Res.*, 2014, **47**, 845–854.
- 53 H. Q. An, G. Y. Wang, Y. J. Wang and X. Q. Zhao, Performance of Transition Metal Modified Pd/TS-1 in Direct Synthesis of Hydrogen Peroxide from H₂ and O₂, *Chinese J. Inorg. Chem.*, 2010, **26**, 405–412.
- 54 T. Pospelova and N. Kobozev, Catalytic Synthesis of Hydrogen Peroxide from the Elements on Palladium III: the Active Centers of Hydrogen Peroxide Decomposition on Palladium, *Zhurnal Fiz. Khimii*, 1961, **35**, 1192–1197.
- 55 T. Pospelova, N. Kobozev and E. Eremin, Palladium Catalyzed Synthesis of Hydrogen Peroxide from the Elements I: Conditions for the Formation of Hydrogen Peroxide, *Zhurnal Fiz. Khimii*, 1961, **35**, 298–305.
- 56 T. Pospelova and N. Kobozev, Palladium Catalyzed Synthesis of Hydrogen Peroxide from the Elements II: the Active Centers of Palladium in the Synthesis of H₂O₂, *Zhurnal Fiz. Khimii*, 1961, **35**, 535–542.
- 57 V. R. Choudhary and C. Samanta, Role of chloride or bromide anions and protons for promoting the selective oxidation of H₂ by O₂ to H₂O₂ over supported Pd catalysts in an aqueous medium, *J. Catal.*, 2006, **238**, 28–38.
- 58 P. Landon, P. J. Collier, A. F. Carley, D. Chadwick, A. J. Papworth, A. Burrows, C. J. Kiely and G. J. Hutchings, Direct synthesis of hydrogen peroxide from H₂ and O₂ using Pd and Au catalysts, 2003, **5**, 1917–1923.
- 59 B. E. Solsona, J. K. Edwards, P. Landon, A. F. Carley, A. Herzing, C. J. Kiely and G. J. Hutchings, Direct synthesis of hydrogen peroxide from H₂ and O₂ using Al₂O₃ supported Au-Pd catalysts, *Chem. Mater.*, 2006, **18**, 2689–2695.
- 60 J. K. Edwards, A. Thomas, B. E. Solsona, P. Landon, A. F. Carley and G. J. Hutchings, Comparison of supports for the direct synthesis of hydrogen peroxide from H₂ and O₂ using Au-Pd catalysts, *Catal. Today*, 2007, **122**, 397–402.
- 61 V. R. Choudhary, C. Samanta and T. V. Choudhary, Factors influencing decomposition of H₂O₂ over supported Pd catalyst in aqueous medium, *J. Mol. Catal. A Chem.*, 2006, **260**, 115–120.

- 62 V. R. Choudhary and P. Jana, Direct oxidation of H₂ to H₂O₂ over Br and F-promoted Pd/Al₂O₃ in aqueous acidic medium: Influence of the concentration of Br and F and the method of incorporation of the two halogens in the catalyst, *Appl. Catal. A Gen.*, 2007, **329**, 79–85.
- 63 V. R. Choudhary and P. Jana, Direct H₂-to-H₂O₂ oxidation over highly active/selective Br-F-Pd/Al₂O₃ catalyst in aqueous acidic medium: Influence of process conditions on the H₂O₂ formation, *Appl. Catal. A Gen.*, 2009, **352**, 35–42.
- 64 Q. Liu, F. Takemura and A. Yabe, Solubility of hydrogen in liquid methanol and methyl formate at 20 °C to 140 °C, *J. Chem. Eng. Data*, 1996, **41**, 1141–1143.
- 65 ChemEngineering - Henry's Law, <https://chemengineering.wikispaces.com/Henry%27s+Law>, (accessed 10 July 2017).
- 66 C. L. Young, Ed., *Hydrogen and deuterium*, Pergamon Press, Oxford ; New York, 1st ed., 1981.
- 67 R. Battino and International Union of Pure and Applied Chemistry, Eds., *Oxygen and Ozone*, Pergamon, Oxford ; New York, 1st ed., 1981.
- 68 I. Huerta, P. Biasi, J. Garcia-Serna, M. J. Cocero, J. P. Mikkola and T. Salmi, Continuous H₂O₂ direct synthesis process: an analysis of the process conditions that make the difference, *Green Process. Synth.*, 2016, **5**, 341–351.
- 69 N. M. Wilson and D. W. Flaherty, Mechanism for the Direct Synthesis of H₂O₂ on Pd Clusters: Heterolytic Reaction Pathways at the Liquid-Solid Interface, *J. Am. Chem. Soc.*, 2016, **138**, 574–586, <https://pubs.acs.org/doi/10.1021/jacs.5b1>.
- 70 N. Gemo, T. Salmi and P. Biasi, The use of modelling to understand the mechanism of hydrogen peroxide direct synthesis from batch, semibatch and continuous reactor points of view, *React. Chem. Eng.*, 2016, **1**, 300–312.
- 71 T. Deguchi, H. Yamano and M. Iwamoto, Kinetic and mechanistic studies on direct H₂O₂ synthesis from H₂ and O₂ catalyzed by Pd in the presence of H⁺ and Br⁻ in water: A comprehensive paper, *Catal. Today*, 2015, **248**, 80–90.

- 72 D. Gudarzi, W. Ratchananusorn, I. Turunen, T. Salmi and M. Heinonen, Preparation and study of Pd catalysts supported on activated carbon cloth (ACC) for direct synthesis of H₂O₂ from H₂ and O₂, *Top. Catal.*, 2013, **56**, 527–539.
- 73 S. Melada, F. Pinna, G. Strukul, S. Perathoner and G. Centi, Palladium-modified catalytic membranes for the direct synthesis of H₂O₂: preparation and performance in aqueous solution, *J. Catal.*, 2005, **235**, 241–248.
- 74 S. Abate, G. Centi, S. Melada, S. Perathoner, F. Pinna and G. Strukul, Preparation, performances and reaction mechanism for the synthesis of H₂O₂ from H₂ and O₂ based on palladium membranes, *Catal. Today*, 2005, **104**, 323–328.
- 75 S. Chinta and J. H. Lunsford, A mechanistic study of H₂O₂ and H₂O formation from H₂ and O₂ catalyzed by palladium in an aqueous medium, *J. Catal.*, 2004, **225**, 249–255.
- 76 A. Gervasini, P. Carniti, F. Desmedt and P. Miquel, Liquid Phase Direct Synthesis of H₂O₂: Activity and Selectivity of Pd-Dispersed Phase on Acidic Niobia-Silica Supports, *ACS Catal.*, 2017, **7**, 4741–4752.
- 77 B. Nkosi, N. J. Coville and G. J. Hutchings, Vapour phase hydrochlorination of acetylene with group VIII and IB metal chloride catalysts, *Appl. Catal.*, 1988, **43**, 33–39.
- 78 M. Haruta, T. Kobayashi, H. Sano and N. Yamada, Novel Gold Catalysts for the Oxidation of Carbon Monoxide at a Temperature far Below 0 °C, *Chem. Lett.*, 1987, **16**, 405–408.
- 79 C. G. Bathomarco, K. N. Franke and A. P. Ferreira, Aspects of the interaction between Au and Fe in supported catalysts applied to the preferential CO oxidation, , DOI:10.1016/j.cattod.2018.12.025.
- 80 Z. Li, W. Ma and Q. Zhong, Insight into Deactivation Reasons for Nanogold Catalysts Used in Gas-Phase Epoxidation of Propylene, *Catal. Letters*, **1**, 3.
- 81 A. Villa, D. Wang, D. S. Su and L. Prati, Gold sols as catalysts for glycerol oxidation: The role of stabilizer, *ChemCatChem*, 2009, **1**, 510–514.
- 82 M. Comotti, W. C. Li, B. Spliethoff and F. Schüth, Support effect in high activity gold catalysts for CO oxidation, *J. Am. Chem. Soc.*, 2006, **128**, 917–924.

- 83 J. Pritchard, L. Kesavan, M. Piccinini, Q. He, R. Tiruvalam, N. Dimitratos, J. A. Lopez-Sanchez, A. F. Carley, J. K. Edwards, C. J. Kiely and G. J. Hutchings, Direct Synthesis of Hydrogen Peroxide and Benzyl Alcohol Oxidation Using Au-Pd Catalysts Prepared by Sol Immobilization, *Langmuir*, 2010, **26**, 16568–16577.
- 84 M. Sankar, Q. He, M. Morad, J. Pritchard, S. J. Freakley, J. K. Edwards, S. H. Taylor, D. J. Morgan, A. F. Carley, D. W. Knight, C. J. Kiely and G. J. Hutchings, Synthesis of Stable Ligand-free Gold-Palladium Nanoparticles Using a Simple Excess Anion Method, *ACS Nano*, 2012, **6**, 6600–6613.
- 85 M. Bowker, A. Nuhu and J. Soares, High activity supported gold catalysts by incipient wetness impregnation, *Catal. Today*, 2007, **122**, 245–247.
- 86 P. J. Miedziak, S. A. Kondrat, N. Sajjad, G. M. King, M. Douthwaite, G. Shaw, G. L. Brett, J. K. Edwards, D. J. Morgan, G. Hussain and G. J. Hutchings, Physical mixing of metal acetates: Optimisation of catalyst parameters to produce highly active bimetallic catalysts, *Catal. Sci. Technol.*, 2013, **3**, 2910–2917.
- 87 S. A. Kondrat, G. Shaw, S. J. Freakley, Q. He, J. Hampton, J. K. Edwards, P. J. Miedziak, T. E. Davies, A. F. Carley, S. H. Taylor, C. J. Kiely and G. J. Hutchings, Physical mixing of metal acetates: A simple, scalable method to produce active chloride free bimetallic catalysts, *Chem. Sci.*, 2012, **3**, 2965–2971.
- 88 E. N. Ntainjua, M. Piccinini, J. C. Pritchard, J. K. Edwards, A. F. Carley, C. J. Kiely and G. J. Hutchings, Direct synthesis of hydrogen peroxide using ceria-supported gold and palladium catalysts, *Catal. Today*, 2011, **178**, 47–50.
- 89 S. J. Freakley, M. Piccinini, J. K. Edwards, E. N. Ntainjua, J. A. Moulijn and G. J. Hutchings, Effect of Reaction Conditions on the Direct Synthesis of Hydrogen Peroxide with a AuPd/TiO₂ Catalyst in a Flow Reactor, *ACS Catal.*, 2013, **3**, 487–501.
- 90 J. K. Edwards, B. Solsona, E. N. N, A. F. Carley, A. A. Herzing, C. J. Kiely and G. J. Hutchings, Switching Off Hydrogen Peroxide Hydrogenation in the Direct Synthesis Process, *Science (80-.)*, 2009, **323**, 1037–1041.
- 91 J. K. Edwards, E. Ntainjua, A. F. Carley, A. A. Herzing, C. J. Kiely and G. J. Hutchings, Direct Synthesis of H₂O₂ from H₂ and O₂ over Gold, Palladium, and Gold-Palladium Catalysts Supported on Acid-Pre-treated TiO₂, *Angew. Chemie-International Ed.*, 2009, **48**, 8512–8515.

- 92 J. K. Edwards, S. F. Parker, J. Pritchard, M. Piccinini, S. J. Freakley, Q. He, A. F. Carley, C. J. Kiely and G. J. Hutchings, Effect of acid pre-treatment on AuPd/SiO₂ catalysts for the direct synthesis of hydrogen peroxide, *Catal. Sci. Technol.*, 2013, **3**, 812–818.
- 93 N. Gemo, P. Biasi, P. Canu, F. Menegazzo, F. Pinna, A. Samikannu, K. Kordás, T. O. Salmi and J. P. Mikkola, Reactivity aspects of SBA15-based doped supported catalysts: H₂O₂ direct synthesis and disproportionation reactions, *Top. Catal.*, 2013, **56**, 540–549.
- 94 S. Park, T. J. Kim, Y. M. Chung, S. H. Oh and I. K. Song, Direct synthesis of hydrogen peroxide from hydrogen and oxygen over insoluble Pd_{0.15}M_{2.5}H_{0.2}PW₁₂O₄₀ (M = K, Rb, and Cs) heteropolyacid catalysts, *Res. Chem. Intermed.*, 2010, **36**, 639–646.
- 95 S. Park, D. R. Park, J. H. Choi, T. J. Kim, Y. M. Chung, S. H. Oh and I. K. Song, Direct synthesis of hydrogen peroxide from hydrogen and oxygen over insoluble Cs_{2.5}H_{0.5}PW₁₂O₄₀ heteropolyacid supported on Pd/MCF, *J. Mol. Catal. A Chem.*, 2010, **332**, 76–83.
- 96 S. Abate, R. Arrigo, M. E. Schuster, S. Perathoner, G. Centi, A. Villa, D. Su and R. Schlögl, Pd nanoparticles supported on N-doped nanocarbon for the direct synthesis of H₂O₂ from H₂ and O₂, *Catal. Today*, 2010, **157**, 280–285.
- 97 F. Menegazzo, M. Signoretto, G. Frison, F. Pinna, G. Strukul, M. Manzoli and F. Boccuzzi, When high metal dispersion has a detrimental effect: Hydrogen peroxide direct synthesis under very mild and nonexplosive conditions catalyzed by Pd supported on silica, *J. Catal.*, 2012, **290**, 143–150.
- 98 J. K. Edwards, J. Pritchard, L. Lu, M. Piccinini, G. Shaw, A. F. Carley, D. J. Morgan, C. J. Kiely and G. J. Hutchings, The Direct Synthesis of Hydrogen Peroxide Using Platinum-Promoted Gold-Palladium Catalysts, *Angew. Chemie-International Ed.*, 2014, **53**, 2381–2384.
- 99 T. Deguchi and M. Iwamoto, Kinetics and Simulation Including Mass-Transfer Processes of Direct H₂O₂ Synthesis from H₂ and O₂ over Pd/C Catalyst in Water Containing H⁺ and Br⁻ Ions, *Ind. Eng. Chem. Res.*, 2011, **50**, 4351–4358.
- 100 T. Deguchi and M. Iwamoto, Reaction mechanism of direct H₂O₂ synthesis from H₂ and O₂ over Pd/C catalyst in water with H⁺ and Br⁻ ions, *J. Catal.*, 2011, **280**, 239–246.

- 101 T. Deguchi, H. Yamano and M. Iwamoto, Dynamics of direct H₂O₂ synthesis from H₂ and O₂ on a Pd nano-particle catalyst protected with polyvinylpyrrolidone, *J. Catal.*, 2012, **287**, 55–61.
- 102 T. Deguchi and M. Iwamoto, Catalytic Properties of Surface Sites on Pd Clusters for Direct H₂O₂ Synthesis from H₂ and O₂: A DFT Study, *J. Phys. Chem. C*, 2013, **117**, 18540–18548.
- 103 D. H. Wells, W. N. Delgass and K. T. Thomson, Formation of hydrogen peroxide from H₂ and O₂ over a neutral gold trimer: a DFT study, *J. Catal.*, 2004, **225**, 69–77.
- 104 A. Staykov, T. Kamachi, T. Ishihara and K. Yoshizawa, Theoretical study of the direct synthesis of H₂O₂ on Pd and Pd/Au surfaces, *J. Phys. Chem. C*, 2008, **112**, 19501–19505.
- 105 D. C. Ford, A. U. Nilekar, Y. Xu and M. Mavrikakis, Partial and complete reduction of O₂ by hydrogen on transition metal surfaces, *Surf. Sci.*, 2010, **604**, 1565–1575.
- 106 A. Plauck, E. E. Stangland, J. A. Dumesic and M. Mavrikakis, Active sites and mechanisms for H₂O₂ decomposition over Pd catalysts, *Proc. Natl. Acad. Sci.*, 2016, **113**, E1973–E1982.
- 107 J. S. Jirkovský, I. Panas, E. Ahlberg, M. Halasa, S. Romani and D. J. Schiffrin, Single atom hot-spots at Au-Pd nanoalloys for electrocatalytic H₂O₂ production, *J. Am. Chem. Soc.*, 2011, **133**, 19432–19441.
- 108 C. Shang and Z. P. Liu, Origin and activity of gold nanoparticles as aerobic oxidation catalysts in aqueous solution, *J. Am. Chem. Soc.*, 2011, **133**, 9938–9947.
- 109 A. Thetford, G. J. Hutchings, S. H. Taylor and D. J. Willock, in *Proceedings of the Royal Society A: Mathematical, Physical and Engineering Sciences*, 2011, vol. 467, pp. 1885–1899.
- 110 J. Li, T. Ishihara and K. Yoshizawa, Theoretical revisit of the direct synthesis of H₂O₂ on Pd and Au@Pd surfaces: A comprehensive mechanistic study, *J. Phys. Chem. C*, 2011, **115**, 25359–25367.
- 111 A. Roldan, D. Torres, J. M. Ricart and F. Illas, On the effectiveness of partial oxidation of propylene by gold: A density functional theory study, *J. Mol. Catal. A Chem.*, 2009, **306**, 6–10.

- 112 J. Li, A. Staykov, T. Ishihara and K. Yoshizawa, Theoretical Study of the Decomposition and Hydrogenation of H₂O₂ on Pd and Au@Pd Surfaces: Understanding toward High Selectivity of H₂O₂ Synthesis, *J. Phys. Chem. C*, 2011, **115**, 7392–7398.
- 113 H. Xu, D. Cheng and Y. Gao, Design of High-Performance Pd-Based Alloy Nanocatalysts for Direct Synthesis of H₂O₂, *ACS Catal.*, 2017, **7**, 2164–2170.
- 114 M. Nugraha, M. C. Tsai, W. N. Su, H. L. Chou and B. J. Hwang, Descriptor study by density functional theory analysis for the direct synthesis of hydrogen peroxide using palladium-gold and palladium-mercury alloy catalysts, *Mol. Syst. Des. Eng.*, 2018, **3**, 896–907.
- 115 R. Todorovic and R. J. Meyer, A comparative density functional theory study of the direct synthesis of H₂O₂ on Pd, Pt and Au surfaces, *Catal. Today*, 2011, **160**, 242–248.
- 116 C. H. Hyung, S. H. Gyeong, H. Jonghee, W. N. Suk and H. L. Tae, On the role of Pd ensembles in selective H₂O₂ formation on PdAu alloys, *J. Phys. Chem. C*, 2009, **113**, 12943–12945.

2. Experimental and Computational Methods

2.1. Experimental Methods

2.1.1. Catalyst Preparation

The 0.33 wt% Au-0.33 wt% Pd catalysts were supported onto five different materials (*i.e.*, TiO₂ (Degussa P25), SiO₂ (Fisher Scientific), ZrO₂ (Aldrich), Anatase (Aldrich) and Rutile (Aldrich)) *via* an incipient wetness method using aqueous solutions of PdCl₂ (Aldrich) and HAuCl₄·3H₂O (Aldrich). An aqueous solution of HAuCl₄·3H₂O (0.27 mL, 12.25 mg mL⁻¹) and an aqueous solution of PdCl₂ (0.80 mL, 6 mg mL⁻¹) were simultaneously added to TiO₂ (0.99 g). The paste that was formed was subsequently dried at 368.15 K for 16 h, ground and calcined in static air at 673.15 K for 3 h.¹⁻³

2.1.2. Direct Hydrogen Peroxide Synthesis

Catalyst testing was performed using a stainless-steel autoclave (Parr Instruments) with an overhead stirrer (0-2000 rpm), which had provision for measurement of temperature and pressure. The autoclave had a volume of 100 mL and a maximum working pressure of 14 MPa. For the standard reaction conditions used previously,⁴ a polytetrafluoroethylene (PTFE) liner was used to complete the experiments without interference from the autoclave as PTFE is non-reactive. The autoclave was charged with the catalyst (0.01 g) and solvent mixture (5.60 g of CH₃OH and 2.90 g of H₂O) and purged three times with 5% H₂/CO₂. The autoclave was then filled with 2.89 MPa of 5% H₂/CO₂ and 1.11 MPa of 25% O₂/CO₂, giving a total pressure of 4 MPa.

Once the desired temperature (275.15 K) had been reached, stirring (1200 rpm) was commenced and experiments were carried out for 30 minutes. The H₂O₂ yield was determined by titration of aliquots of the final filtered solution with acidified Ce(SO₄)₂ (710-3 mol L⁻¹). The Ce(SO₄)₂ solutions were standardised against (NH₄)₂Fe(SO₄)₂·6H₂O using ferroin as indicator.¹⁻³

2.1.3. Cyclohexanone Ammoximation utilising *in-situ* Direct Hydrogen Peroxide Synthesis

Catalyst testing was performed using a stainless-steel autoclave (Parr Instruments) with an overhead stirrer (0-2000 rpm) and had provision for measurement of temperature and pressure. The autoclave had a volume of 100 mL and a maximum working pressure of 14 MPa. For the standard reaction conditions that were used previously, a PTFE liner was used to complete the experiments without interference from the autoclave as PTFE is non-reactive. The autoclave was charged with the direct H₂O₂ synthesis catalyst (0.075 g), TS-1 (0.075 g), solvent mixture (5.90 g *tert*-butanol (tBA) and 7.50 g H₂O), ammonium hydrogen carbonate (NH₄HCO₃) (0.32 g) and cyclohexanone (0.20 g). The direct H₂O₂ synthesis catalyst and TS-1 together were tandem catalysts. The TS-1-supported catalyst did not have additional TS-1 for these experiments. The autoclave was purged three times with 5% H₂/N₂ before being charged with 5 % H₂/N₂ (2.89 MPa) and 25 % O₂/N₂ (1.11 MPa) at a total pressure of 4 MPa. During heating, the autoclave was stirred (100 rpm) to ensure homogeneous heating. At the desired temperature (353.15 K), stirring (800 rpm) was commenced and experiments were carried out for a set time interval (Chapter 3 – 1.5, 3.0, 4.5 and 6.0 h). After the reaction had finished, the autoclave was cooled while stirring was continued (100 rpm) and once it had reached the desired temperature (rt), gas- and liquid-phase samples were taken for analysis.⁵

2.1.4. Analytical Methods

2.1.4.1. Gas Chromatography

Gas chromatography (GC) is an analytical technique that can separate and subsequently study liquid- or gas-phase chemical species (*i.e.*, analytes), where the former is vapourised before the separation process. A GC has different components that aid in this separation, which are described below (Fig. 2.1).

The sample must be introduced into the column *via* an injection port or inlet, of which there are various types. One such type is a split injection, which restricts the amount of sample that can pass through to the column and can cause sensitivity issues. Splitless injection allows all the sample to pass to the column, increasing the signal of each analyte.

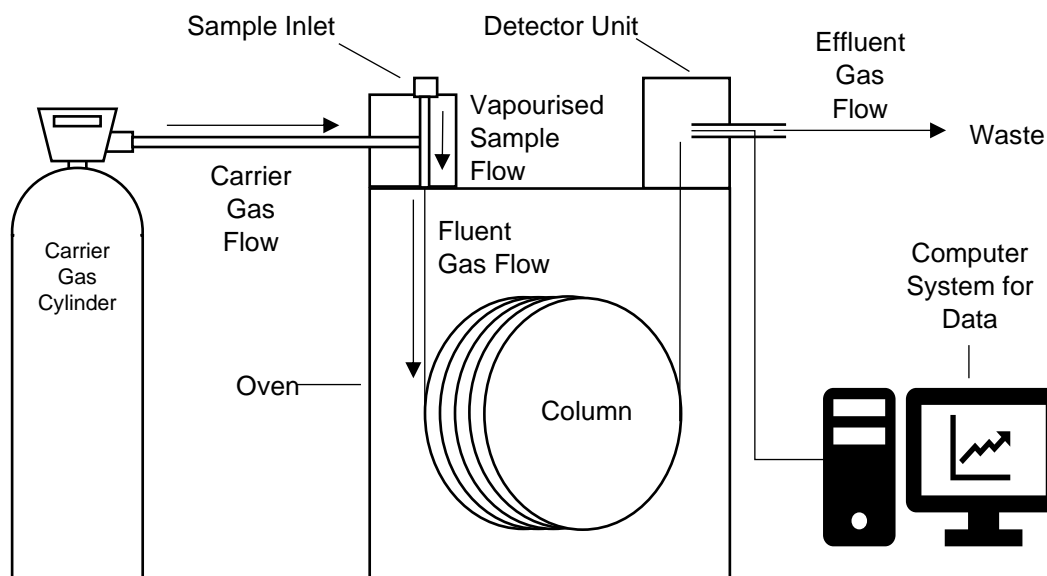


Figure 2.1. Basic schematic diagram of a GC analyser.

The chemical species analysed from a reaction are usually as a mixture, hence the need for separation. A standard must be introduced to analyse the sample quantitatively. An external standard is a chemical species that has been analysed separately to the sample; an internal standard is a chemical species that has been analysed with the sample, either being added before or after the reaction.

The signal produced by each chemical species detected produces a peak. The area under each peak is proportional to the amount of each chemical species present in the sample. The concentration of the analyte is determined by integrating the area of the peak. A calibration curve is required, where known concentrations of a known species is passed through the GC to produce a linear calibration curve or by determining the relative response factor of an analyte.

An inert gas (*i.e.*, eluent) is required to make the analytes move without interfering with the components of the mixture. Together, this is called the mobile phase (*i.e.*, fluent), which moves through the column that contains the stationary phase. As the fluent leaves the GC to waste, it is called the effluent gas. The stationary phase is the material lining the column that separates the analytes within the mobile phase.

There are two types of columns: packed and open tubular (*i.e.*, capillary). Packed columns have inert, finely divided, solid support material coated with a liquid stationary phase. There are a further two types of open tubular columns:

support-coated open tubular (SCOT) and wall-coated open tubular (WCOT). The former has its inner wall lined with support material in a thin layer with the stationary phase adsorbed onto it; the latter has its walls of the capillary tube coated with stationary phase.

The column is housed in an oven that is thermostatically controlled, with a wide range of temperatures that can be used. The ovens can be programmed to remain at a constant temperature or have a ramp rate implemented to increase the rate of separation. This separation occurs by selecting the correct column for the analytes within the sample. Polarity of chemical species is related to its boiling point: the higher the boiling point, the lower the vapour pressure, meaning the retention time increases as it spends less time in the gas phase. If a chemical species is highly polar and passes through a highly polar column, it will have a longer retention time as the amount and strength of interaction will increase, and vice versa. Each analyte will have a different polarity to the next, thus, they will move through the column at different rates, consequently separating them.

Many methods of detection exist that produce a signal as an analyte is being passed to the detector. The signal of each analyte is compiled to form a chromatogram for data analysis by the user. Two types of detectors are the Thermal Conductivity Detector (TCD) and the Flame Ionisation Detector (FID).

A TCD operates by heat loss caused by the analyte passing over the detector filament. The detector filament is kept at a constant temperature. As the temperature is decreased by a volume of analyte, a certain amount of current is required to raise the temperature of the filament back to its norm. The amount of current required equates to a signal being produced on the chromatogram.

An FID operates by mixing air, H₂ and the separated analyte together, to then be subsequently burnt through a small metal jet. The jet is the anode and the cathode (*i.e.*, collector) is above the tip of the flame, forming an electrolytic cell. The analytes, usually organic compounds, pyrolyse leading to ion and electron formation. Detection of the charged ions causes a current to be produced. The current produces a signal for the chromatogram, just like a TCD.

Finally, the computer system interprets the signals from the detector to generate a chromatogram. The chromatogram will display the peaks for each separated analyte. Opportunities can arise by further developing the separation method should peak overlap occur or further data analysis that can provide quantitative data in addition to the qualitative data acquired.

2.1.4.2. Gas Chromatography for Gas-Phase Samples

For the cyclohexanone ammoximation experiments, H₂ conversion was determined by taking a gas-phase sample that could then be analysed using a Varian 3800 GC system with a TCD and a Porapak-Q (packed) column (303.15 K, 22-minute total run time, Ar carrier gas (30 mL min⁻¹)). A calibration was completed by using a blank gas sample where all conditions are the same for a reaction carried out in the reactor, but with no catalysts present (*i.e.*, blank-H₂ or H₂-blank sample, as H₂ was the chemical species of interest), to which all subsequent catalytic reaction samples could be compared. The total number of moles and the corresponding GC counts for H₂ at the start of the reaction were known, and the GC counts for the remaining H₂ after a reaction in the presence of catalyst was determined, it was possible to determine the number of moles of H₂ that had been converted by the catalyst. For example, if the number of moles of H₂ at the beginning of the reaction is 5.00 mmoles that give a total count of 500 from the GC, and the counts of H₂ after a reaction in the presence of a reaction are 300, the percentage and number of moles of converted H₂ can be determined, as defined by equations (2.1)-(2.3):

$$\text{GC Counts of converted } H_2 = 500 - 300 \quad (2.1)$$

$$= 200$$

$$\text{Percentage of converted } H_2 = \frac{200}{500} \quad (2.2)$$

$$= 40 \%$$

$$\text{Number of moles of converted } H_2 = 5.00 \times \frac{40}{100} \quad (2.3)$$

$$= 2.00 \text{ mmoles}$$

The number of moles of H₂ converted and oxime produced were subsequently used to determine 'H₂ selectivity based on oxime.' As one mole of H₂ goes into one mole of H₂O₂ and, by extension, one mole of cyclohexanone oxime, the selectivity of H₂ can be calculated by the difference in the number of moles for both H₂ and cyclohexanone oxime. For example, if 2.00 mmoles of H₂ has been converted and 1.50 mmoles of cyclohexanone oxime has been produced, the H₂ selectivity based on oxime is:

$$\frac{n^{oxime}}{n^{H_2}} = \frac{1.50}{2.00} = 75 \%$$

The retention times for each analyte are described below (Table 2.1).

Table 2.1. Retention times of the chemical species analysed for the gas phase samples from the cyclohexanone ammoximation utilising *in-situ* H₂O₂ synthesis reaction.

Chemical Species	Retention Time / min
H ₂	1.63
O ₂	2.24
N ₂	2.40
CO ₂	9.21

2.1.4.3. Gas Chromatography for Liquid Phase Samples

For the cyclohexanone ammoximation tests, the conversion of cyclohexanone, and the selectivity towards and yield of the cyclohexanone oxime was determined by analysing a sample of the filtrate. The product was collected by solvation with ethanol (6.00 g) to limit the amount of residue left in the PTFE liner. Additionally, the ethanol diluted the reaction mixture (and the calibration solutions) for detection *via* GC analysis. With an internal standard (diethylene glycol monoethyl ether, 0.15 g), the mixture was subsequently filtered.

The filtered samples (0.20 µL) were injected and analysed using a Varian 3800 GC fitted with an FID (~0.04 MPa) and a CP Wax 52 CB (WCOT) column (splitless injection, 353.15-473.15 K at 15 K min⁻¹, 473.15-523.15 K at 20 K min⁻¹, nine-minute total run time, He carrier gas (10 mL min⁻¹)). Calibrations were completed by making standards of the reaction mixture (20 %, 50 % and 80 % conversion).⁵ The retention times for each analyte is described below (Table 2.2).

Table 2.2. Retention times of the chemical species analysed for the gas phase samples from the cyclohexanone ammoximation utilising *in-situ* H₂O₂ synthesis reaction.

Chemical Species	Retention Time / min
Cyclohexanone	4.2
Diethylene glycol monoethyl ether	7.1
Cyclohexanone oxime	8.7

2.1.5. Catalyst Characterisation Techniques

2.1.5.1. Scanning Electron Microscopy

Scanning Electron Microscopy (SEM) is a technique to observe the surface of materials at a scale superior to optical microscopy. The advantage of an electron microscope over an optical microscope is that it is not hindered by wavelength; the electron has a shorter wavelength, meaning that the resolution will be higher. This type of microscopy is based on the principle of the interactions of the atoms within a material, at various depths near its surface, with an electron beam (*i.e.*, incident beam) producing an image. As a result, the electrons from the atoms are emitted in different ways.

Secondary Electrons (SEs) are electrons that have been emitted from the surface or near-surface of the material because of inelastic interactions between the electron beam, with an energy transfer from the beam to the electron of an atom within the material. In this context, an elastic interaction is where there is an insufficient amount of energy provided for an electron to leave the atom, and so returns to the ground state; an inelastic interaction is where there is a sufficient amount of energy provided to leave the atom. Back-Scattered Electrons (BSEs) are high-energy electrons that originated from the electron beam that are back-scattered (*i.e.*, reflected) out of the material, as a result of inelastic interactions. This is often depicted as a space vehicle's slingshot manoeuvre around a celestial body. Of the two types of emissions, BSEs have higher energies, meaning that their mean free path from a solid sample is less restricted than that of SEs. However, SEM heavily relies on SEs as they are highly localised to the point of interaction from the incident beam. Thus, it has the capability of collecting an image of the surface of the sample,

at a significantly higher resolution (<1 nm) than that of optical microscopy (but lower resolution than that of Transmission Electron Microscopy (TEM)).

Light as cathodoluminescence, X-rays, transmitted electrons and absorbed current are other emissions that can occur from a sample interacting with the electron beam. These emissions originate from the interaction volume; a space within a sample material that is affected by the electron beam, with different zones from which the emissions come from. The interaction volume and its associated emission zones differ depending on the element of the atom that is interacting with the electron beam as well as the accelerating voltage of the beam (Fig. 2.2).

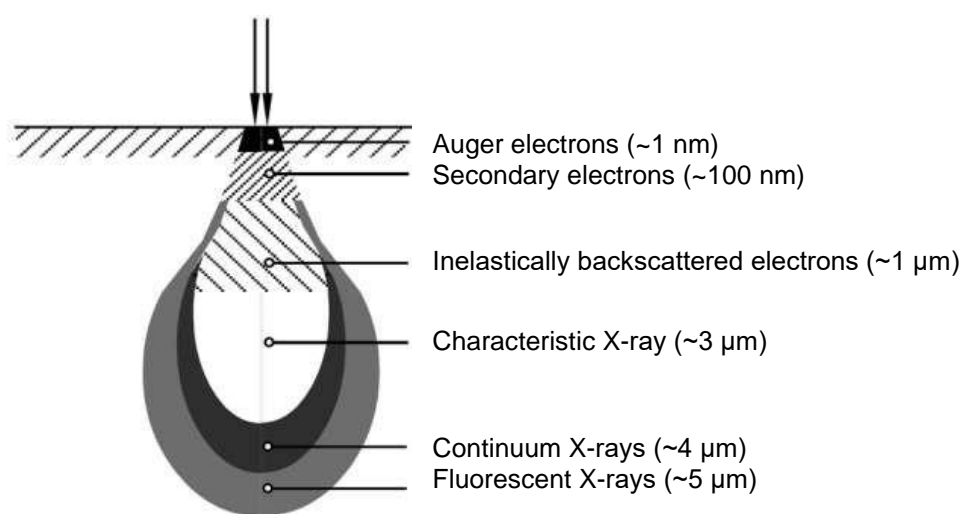


Figure 2.2. A diagram of the interaction volume with the different zones of the emissions from the sample material because of the incident beam. Image reused from publicly accessible reference.⁶

SEM micrographs have a large depth of field because the incident beam is narrow, meaning that an image with a three-dimensional appearance can be collected. This is useful in understanding the topography and contours of the surface of a material. The reason why this is uniquely beneficial for heterogeneous catalysis is that catalysts can be observed on the nanoscale. Observing how a support material and the nanoparticles have interacted as well as how they reacted from post-preparation treatment or after a reaction (*i.e.*, post-reaction) is vital in understanding how the catalysis is performed and how to better improve the catalyst. The morphology of a heterogeneous catalyst is an important part of its ability to function, which is related to its activity and selectivity.

Typically, an SEM has an electron beam emitted thermionically at the top of the column and accelerated down, which is passed through a combination of

apertures and lenses to create a focused beam. This beam is fired from an electron gun fitted with a filament cathode made from tungsten (W) as it has the lowest cost, lowest vapour pressure and highest melting point of all the metals. The range of energy the electron beam can be changed from 0.2-40.0 keV (Fig. 2.3).

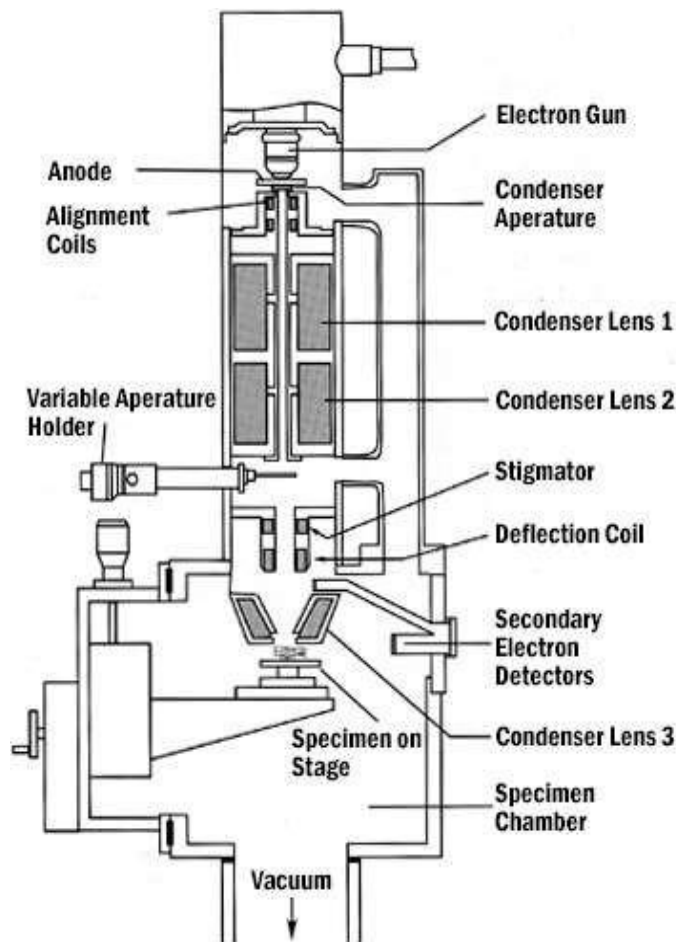


Figure 2.3. Schematic diagram of a scanning electron microscope with the different parts labelled. Image reused from publicly accessible reference.⁷

After passing through the apertures and lenses, the beam moves to the final lens where it can be deflected in the x and y directions to raster scan the surface of the material. This in turn can alter the magnification by modifying the raster scan area. The smaller the raster scan area, the higher the resolution as the number of pixels does not change. In addition, the higher the accelerating voltage, the lower the resolution.

The sample is mounted on a stage, with the chamber and column under vacuum. As the previously described photon and electron emissions occur, amplifiers boost the signals that the emissions generate to produce an image with a variation of

brightness. This image is a signal intensity distribution map because the beam's position over the sample and the computer's pixels are correlated and synchronised.

An Everhart-Thornley detector is used, where SEs are detected by attracting them towards a grid that is electrically influenced ($\sim +400$ V). Subsequently, they are accelerated towards a scintillator that is biased ($\sim +2000$ V), which in turn causes the electrons to emit light as cathodoluminescence, conducted toward a photomultiplier beyond the column. The electrical output or signal is displayed as the image (*i.e.*, distribution map).

In the current work, samples for examination by SEM were prepared by dispersing the catalyst powder over a carbon disc, placed upon a stainless-steel stage. Samples were then subjected to chemical microanalysis in a Hitachi TM3030 Tabletop Microscope operating at 15.0 kV. The instrument was also fitted with a Bruker Nano GmbH EDX analyser. As not all nanoparticles were perfectly hemispherical, the longest length of each nanoparticle analysed was used for the Particle Size Distributions (PSDs) in Chapter 3.

2.1.5.2. Field Emission Gun-Scanning Electron Microscopy

A Field Emission Gun (FEG) can be equipped to an SEM to resolve the issue of signal-to-noise ratio. A FEG is an electron gun held at a negative potential relative to the nearby electrode by several kilovolts difference. This provides the sharply pointed Muller-type emitter to have a sufficient potential gradient to cause a field electron emission. This means that the signal-to-noise ratio and spatial resolution is enhanced, as well as longevity of the emitter. There are two types of emitters: a cold-cathode type and Schottky type. The former is usually comprised of a single crystal of W sharpened to a tip (radius = 100 nm); the latter uses improved thermionic emissions by lowering the barrier in the presence of a high electric field, with a ZrO₂-coated W tip.

Field Emission Gun-Scanning Electron Microscopy (FEG-SEM) was completed using a Tescan MAIA3 Triglav FEG-SEM with an Oxford EDX analyser. The beam operated at 15.0 kV. Samples were prepared using ethanol as a solvent and deposition of the materials onto carbon-supported, 300-mesh copper grid. Excess solvent was subsequently dried.⁸

2.1.5.3. Energy Dispersive X-Ray Spectroscopy

The principle of Energy Dispersive X-ray Spectroscopy (EDS, EDX, EDXS or XEDS) works by analysing the aforementioned X-ray emissions from the sample within an electron microscope. However, the key difference is that X-rays are used instead of the electron beam to excite the electrons. This analytical technique can provide the chemical composition of a material and produce a map of the atoms of the different elements. Each element has a particular X-ray photoemission wavelength, which is converted to a voltage signal that is used to provide a spectrum.

This emission is caused by excitation of a core electron that is subsequently ejected. This leaves a vacancy in the core orbital which is filled by a valence electron. This is known as the Auger effect and this transition from the valence electron to the core releases an X-ray of a particular wavelength. An energy-dispersive spectrometer can measure the energy and number of X-rays emitted.

2.1.5.4. X-Ray Photoelectron Spectroscopy

X-ray Photoelectron Spectroscopy (XPS) is an analytical technique that gives information on the elemental composition and the oxidation states of the elements of a material's surface. The principle of this characterisation technique relies on is the photoelectric effect as a core electron of an atom is emitted due to high energy X-rays (Fig. 2.4).^{9,10}

The identification of the atom is dependent on the binding energy of the core electrons, which is unique to each element. The oxidation state also influences the binding energy as a decreased oxidation state results in a lower binding energy, and vice versa. The energy of the X-ray must be higher than the binding energy of the core electron and the work function of the spectrometer for the atom to have an electron emission. The work function of the spectrometer is the amount of energy needed to emit the core electron into the vacuum from the Fermi level and the kinetic energy of the electron is the excess energy, as defined by equation (2.4):

$$E_K = h\nu - E_B - \varphi \quad (2.4)$$

where E_K is the emitted electron's kinetic energy, h is Planck's constant (6.626×10^{-34} J·s), ν is the frequency of the X-ray photon, E_B is the binding energy of the electron and φ is the work function of the spectrometer.

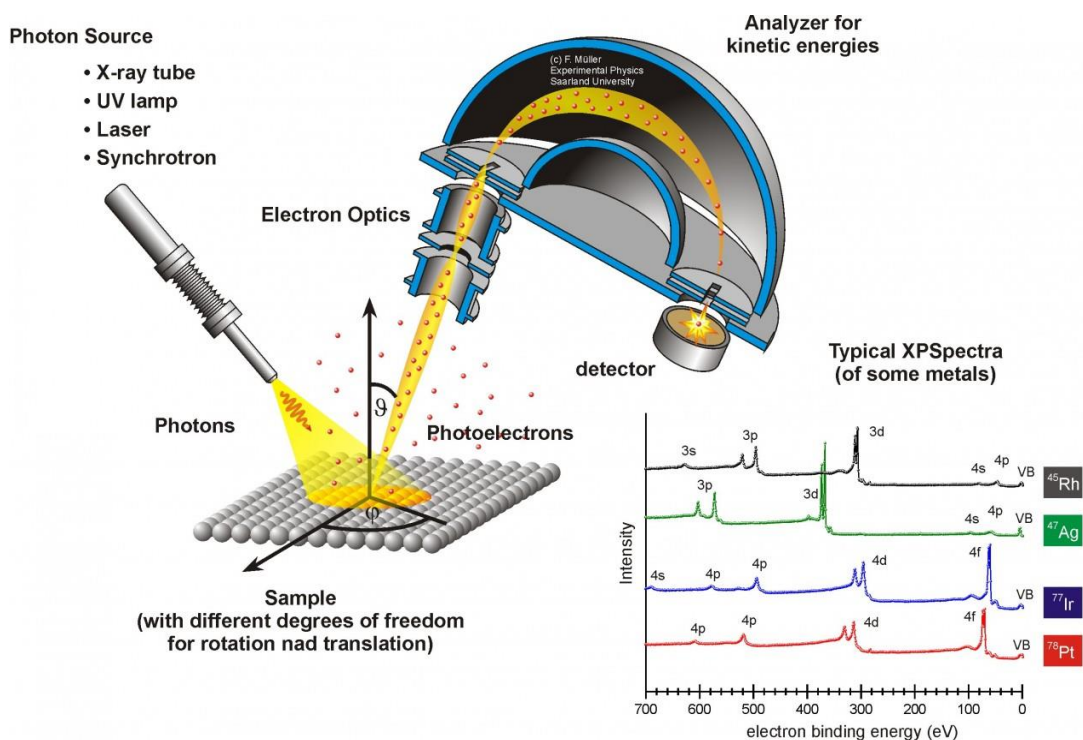


Figure 2.4. Cross-section diagram of an XPS analyser. Image reused from publicly accessible reference.¹⁰

The binding energy is also dependent on the spin of the electrons. If the angular momentum of the electron is in a favourable configuration with the angular momentum of the orbital, this will increase the binding energy, and vice versa. This spin orbital splitting can also be seen at both the core and valence orbitals, where unpaired electrons can exist at both levels. Whether the electrons are opposed or not will also affect the binding energy.^{9,10}

XPS can also provide qualitative data on the dispersion of the surface particles. The signal intensity on the spectra of a low dispersion of particles will be low. However, if the dispersion is high, this will make it distinguishable from the support material. This is ideal for the analysis of heterogeneous catalysts.

XPS was carried out using a Kratos Axis Ultra-DLD photoelectron spectrometer with monochromatic Al *K* α radiation. The device was operated at 144 W power. Survey scans were completed at a pass energy of 160.00 eV and spectra were calibrated to the C (1s) signal (284.80 eV). Subsequently, the CasaXPS v2.3.17 software, with the manufacturer supplied modified Wagner sensitivity factors, was used to quantify the results.^{5,8,11}

2.1.5.5. Powder X-Ray Diffraction

Powder X-Ray Diffraction (XRD) is a technique that analyses the bulk of a material, determining its crystal structure. Elastic scattering of X-rays by atoms in a crystalline lattice occurs as the separation of the atoms and X-ray wavelengths are similar (0.1 nm), giving rise to characteristic patterns of interference. The use of monochromatic X-rays is needed, with an energy range produced by a metal target (usually Mo or Cu). The metal target is subjected to a bombardment of high energy electrons and the collisions cause the metal's electrons to be emitted from the 1s orbital, known as the K-shell. The electrons in the valence orbitals (2p is L and 3p is M) will fill this vacancy for the atom to return to the ground state. In doing so, this releases energy in the form of X-rays that are characteristic to the element of the atom (*i.e.*, K_{α} and K_{β} , corresponding to the L and M electrons filling the core electron vacancy, respectively) as well as Bremsstrahlung (*i.e.*, "braking radiation") of the incident electron beam.

The X-rays need to be passed through a monochromator (*e.g.*, single Ge crystal) to generate an X-ray beam with wavelengths of a narrow range. Interference patterns are created from the interaction of the beam and the sample. Constructive interference of waves causes amplification; destructive interference causes reduction or cancellation of the wavelengths. The former is sometimes known as a "reflection" (Fig. 2.5) and can be expressed mathematically by the Bragg equation, defined in equation (2.5):

$$BD + DC = 2d \sin\theta = n\lambda \quad (2.5)$$

where $BD + DC$ is the additional distance travelled by the lower incident X-ray, d is the lattice spacing, θ is the diffraction angle (*i.e.*, Bragg angle), n is an integer and λ is the wavelength of the X-ray.

If the additional distance is an integer of the wavelengths, the diffraction will be comprehensible and display constructive interference. The detected X-rays are normally observed as a diffraction pattern, much like a spectrum from a spectroscopic technique.

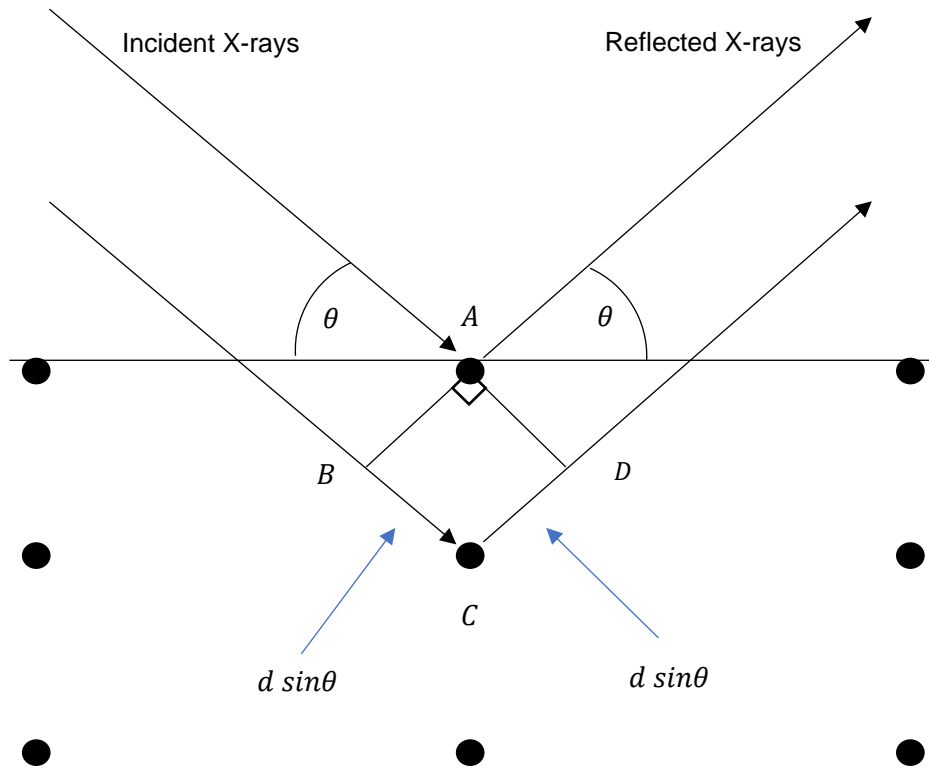


Figure 2.5. Diagram of an XRD reflection depicting the parts used in the Bragg equation, expressed in equation (2.5).

In powder XRD, the detector is mobile, moving around the sample and the X-ray source is stationary. The determination of the Bragg angle where “reflections” occur can lead to the calculation of the lattice spacing, as defined in equation (2.5). This is required as powdered samples have many crystallites that are orientated randomly and only a certain number of them will be orientated correctly to produce a “reflection.” However, the crystallites need to be of a certain size (≥ 5 nm) as a certain amount of lattice planes within the crystal structure are required to give the necessary constructive and destructive interference. Line broadening can occur in the diffraction pattern either from some destructive interference or lack of interference from smaller crystallites. The shape of detected “reflections” provides information on the size of the crystallites, that can then be approximated using the Scherrer equation, as defined in equation (2.6):

$$\tau = \frac{K\lambda}{\beta \cos \theta} \quad (2.6)$$

where τ is the crystallite mean size, K is the dimensionless shape factor, λ is the X-ray wavelength and β is the line broadening (at half of the maximum intensity).

For heterogeneous catalysts, XRD can provide information on elemental composition, identification of phases of the support material, the amount of crystallinity the nanoparticles have, or support material has, and the size of the supported nanoparticles and support material crystallites.

Crystallinity was determined using the crystallinity index (C_I) of each material. This value was calculated by determining the sum of the areas under the crystalline peaks of the XRD pattern and the sum of the areas of all the peaks (both crystalline and amorphous) of the XRD pattern. This value was calculated as percentage (where 100 % would denote a completely crystalline structure) as defined in equation (2.7):

$$C_I = \frac{\Sigma A_c}{\Sigma A_c + \Sigma A_a} \times 100 \quad (2.7)$$

where A_c is the area of a crystalline peak and A_a is the area of an amorphous peak.

Powder XRD was achieved using a PANalytical X'Pert Pro diffractometer, operated at 40.0 mA and 40.0 kV, with a monochromatic Cu- $K\alpha$ source ($\lambda = 0.154$ nm). The 2θ scan range was between 10° and 80° .^{5,8,11} Phase identification was completed using the International Centre for Diffraction Data (ICDD) databases.

2.1.6. Error and Limitations

The standard deviation for each type of datapoint (*i.e.*, conversion, selectivity, and yield) of each catalyst was determined by completing between two and five tests for each catalyst, denoted by the error bars that move away from the averaged values of the datapoints. The standard deviation was a result of the variation from measuring the components of the reaction mixture for both the calibration and experiment solutions. Catalytic tests that gave carbon balances of $\sim 100\%$ were considered acceptable to use and the error from the carbon balances for each experiment were included in the error bars. To garner a selectivity of 100 % is not likely to happen, and from this, there are certain datapoints that appear to exceed 100 %, which is an impossibility.

Consideration for error and deviation that arose from experimental preparation errors and instrumentation limitations (*e.g.*, resolution), such as measuring the

materials for the reaction or small variations along the GC column lining, was required to realise that those results were not necessarily outliers that should be excluded from the data. The range of some of the error bars for the data points appeared to be above 100 % and have been taken into careful consideration.

Oxime selectivity should be based on the GC counts of the cyclohexanone, cyclohexanol, cyclohexanone oxime, nitrocyclohexane, cyclohexenylcyclohexanone and cyclohexanone azine. This was due to the different reaction pathways that can be taken, and most importantly, the subsequent reactions of the oxime with hydrogen peroxide (H₂O₂) (Chapter 3, Scheme 3.1). This cannot be averted in a batch process. The counts for the oxime in the chromatogram could decrease as the oxime was available to further react during each catalytic experiment. Obtaining the correct number of moles of all the by-products would provide a “total and true” value for oxime selectivity.

This obstacle may have been overcome by incorporating the undesirable by-products into the selectivity calculations. However, some of the by-products were not commercially available, and therefore, could not be used for the required GC calibrations and analyses. Nevertheless, the oxime selectivity can be gleaned by accounting for the number of moles of cyclohexanone and oxime. The number of moles of reactant and desirable product were determined using the GC analyses and, as this reaction was 1:1, the conversion of cyclohexanone and the oxime selectivity (and by extension the oxime yield) were calculated for each experiment.

Knowing the amount of H₂ in the reactor was important to determine to provide values for the H₂ conversion and H₂ selectivity based on oxime. Using fundamental physical chemistry equations (2.8)-(2.11) and the chemical species’ physical parameters (Table 2.3), the number of moles of H₂ present in the reactor at the beginning of the experiments using the typical reaction mixture has been estimated through the calculations described below:

$$V_l = \frac{m}{\rho} \tag{2.8}$$

where V_l is volume of liquid reagents, m is mass and ρ is density.

Table 2.3. Quantification of reactant and solvent masses, densities, and volumes. The decimal places have been increased to use standard units for each datapoint.

Species	m / kg (x 10 ³)	ρ / kg m ⁻³	V / mL
H ₂ O	2.90	997	2.91
(CH ₃) ₃ COH	5.60	781	7.17
NH ₄ HCO ₃	0.32	1590	0.20
Cyclohexanone	0.20	948	0.21
Sum of Species	9.02	-	10.49

Using the calculated volumes of the liquid reagents (Table 2.3), the volume of the headspace within the reactor can be determined using the reactor volume and the liner volume (~7.00 mL) as well:

$$\begin{aligned}
 V_H &= V_R - (V_L + \sum V_l) & (2.9) \\
 &= 1.00 \times 10^{-4} - (7.00 \times 10^{-6} + 1.049 \times 10^{-5}) \\
 &= 8.251 \times 10^{-5} \text{ mL}
 \end{aligned}$$

where V_H is headspace volume, V_R is the reactor volume, V_L is the volume of the liner and V_l is the volume of the liquid reagents.

With the headspace estimated, the number of moles of H₂ present can be estimated using the Ideal Gas Law, as defined in equation (2.10), and the partial pressure of H₂ under the reaction conditions:

$$pV = nRT \quad (2.10)$$

$$\begin{aligned}
 n &= \frac{pV}{RT} & (2.11) \\
 &= \frac{(0.05 \times (2.90 \times 10^6)) \times (82.51 \times 10^6)}{8.3145 \times 293.15} \\
 &= 4.91 \times 10^{-3} \text{ moles of } H_2 \\
 &= 4.91 \text{ mmoles of } H_2
 \end{aligned}$$

This was an estimate as the volume of the pipes that feed into the reactor was approximated. Nevertheless, it gave a useful estimate of the amount of H_2 that was present in the reactor vessel headspace for the cyclohexanone ammoximation reaction tests.

Although this value was used to determine H_2 conversion and H_2 selectivity based on oxime, this value did not take into consideration the amount of H_2 that would be dissolved into the solvent/reactant mixture before the experiment was started. An estimate can be determined using the Ostwald coefficient for H_2O , tBA and cyclohexanone. The latter was a reactant, but it would be part of the solvent/reactant mixture at the beginning of each catalytic test.

The Ostwald coefficient (L) is described as the ratio of the volume of gas to the volume of liquid, as defined by equation (2.12):

$$L = \frac{V_{(g)}}{V_{(l)}} \quad (2.12)$$

where $V_{(g)}$ is the volume of gas absorbed and $V_{(l)}$ is the volume of the absorbing liquid.

In this case, the gas (g) would be H_2 . The number of moles of a substance can also be defined by the following equation (2.13):

$$n = \frac{m}{M_r} \quad (2.13)$$

where M_r is the relative molecular mass.

Using the Ostwald coefficient values from the Solubility Data Series for Hydrogen and Deuterium,¹² in conjunction with equations (2.8), (2.13)-(2.29) as well as the values from Table 2.3, the volumes and number of moles of H₂ have been determined (as estimates) for all three components of the solvent/reactant mixture. For certain equations, the liquid (*i.e.*, H₂O, tBA or cyclohexanone) was placed in the superscript of the subject and the gas (*i.e.*, H₂) was placed in the subscript of the subject (*e.g.*, $m_{(H_2)}^{(H_2O)}$ is the mass of H₂ in H₂O).

For the number of moles of H₂ in H₂O:

$$\begin{aligned} V_{(H_2)} &= L \times V_{(H_2O)} & (2.14) \\ &= 194 \times 2.91 \times 10^{-6} \\ &= 0.565 \times 10^{-3} \text{ mL} \end{aligned}$$

$$\begin{aligned} m_{(H_2)}^{(H_2O)} &= \rho_{(H_2)} \times V_{(H_2)} & (2.15) \\ &= 8.988 \times 10^{-2} \times 0.565 \times 10^{-3} \\ &= 5.074 \times 10^{-5} \text{ kg} \\ &= 5.074 \times 10^{-2} \text{ g} \end{aligned}$$

$$\begin{aligned} n_{(H_2)}^{(H_2O)} &= \frac{m_{(H_2)}^{(H_2O)}}{M_{r(H_2)}} & (2.16) \\ &= \frac{5.074 \times 10^{-2}}{2.016} \\ &= 2.52 \times 10^{-2} \text{ moles of } H_2 \\ &= 0.25 \text{ mmoles of } H_2 \end{aligned}$$

For tBA, equation (2.17) describes the mole fraction solubility of a binary system and equation (2.18) describes the relationship between the mole fraction and the Ostwald Coefficient. This was rearranged to make the Ostwald coefficient the subject of equation (2.19):

$$x_{(g)} = \frac{n_{(g)}}{n_{(g)} + n_{(l)}} \quad (2.17)$$

where $x_{(g)}$ is the mole fraction solubility, $n_{(g)}$ is the number of moles of gas (g) and $n_{(l)}$ is the number of moles of liquid (l).

The $x_{(g)}$ for H_2 in the reactor vessel with tBA was as follows:

$$\begin{aligned} x_{(H_2)} &= \frac{n_{(H_2)}}{n_{(H_2)} + n_{(tBA)}} & (2.18) \\ &= \frac{4.91 \times 10^{-3}}{(4.91 \times 10^{-3}) + (\frac{5.60}{74.12})} \\ &= \frac{4.91 \times 10^{-3}}{(4.91 \times 10^{-3}) + (7.56 \times 10^{-2})} \\ &= 6.10 \times 10^{-2} \end{aligned}$$

$$x_{(g)} = \left(\frac{RT}{p_{(g)} L V_{M(l)}} + 1 \right)^{-1} \quad (2.19)$$

where R is the gas constant, T is the temperature, $p_{(g)}$ is the partial pressure of the gas (g), L is the Ostwald coefficient and $V_{M(l)}$ is molar volume of the liquid (l).

$$L = \frac{RTx_{(g)}}{p_{(g)} V_{M(l)} (1 - x_{(g)})} \quad (2.20)$$

$$V_{M(l)} = \frac{V_{(l)}}{n_{(l)}} \quad (2.21)$$

$$V_{M(tBuOH)} = \frac{V_{(tBA)}}{n_{(tBA)}} \quad (2.22)$$

$$= \frac{7.17}{7.56 \times 10^{-2}}$$

$$= 0.95 \text{ m}^3 \text{ mol}^{-1}$$

$$L = \frac{RTx_{(H_2)}}{p_{(H_2)} V_{M(tBA)}(1-x_{(H_2)})} \quad (2.23)$$

$$= \frac{(8.3145 \times 293.15 \times (6.10 \times 10^{-2}))}{((0.05 \times 2.90 \times 10^6) \times 0.95 \times (1 - 6.10 \times 10^{-2}))}$$

$$= 1.15 \times 10^{-5}$$

As L for H_2 in tBA was calculated, this could then be used to determine the number of moles of H_2 dissolved in tBA, in equations (2.24)-(2.26):

$$V_{(H_2)} = L \times V_{(tBA)} \quad (2.24)$$

$$= 1.15 \times 10^{-5} \times 7.17 \times 10^{-6}$$

$$= 8.25 \times 10^{-11} \text{ mL}$$

$$m_{(H_2)}^{(tBA)} = \rho_{(H_2)} \times V_{(H_2)} \quad (2.25)$$

$$= 8.988 \times 10^{-2} \times 8.25 \times 10^{-11}$$

$$= 7.42 \times 10^{-12} \text{ kg}$$

$$= 7.42 \times 10^{-9} \text{ g}$$

$$n_{(H_2)}^{(tBA)} = \frac{m_{(H_2)}^{(tBA)}}{M_{r(H_2)}} \quad (2.26)$$

$$= \frac{7.42 \times 10^{-9}}{2.016}$$

$$= 3.68 \times 10^{-9} \text{ moles of } H_2$$

$$= 3.68 \times 10^{-6} \text{ mmoles of } H_2$$

For the number of moles of H₂ in cyclohexanone:

$$\begin{aligned}
 V_{(H_2)} &= L \times V_{(cyclohexanone)} & (2.27) \\
 &= 0.0501 \times 0.21 \times 10^{-6} \\
 &= 1.052 \times 10^{-8} \text{ mL}
 \end{aligned}$$

$$\begin{aligned}
 m_{(H_2)}^{(cyclohexanone)} &= \rho_{(H_2)} \times V_{(H_2)} & (2.28) \\
 &= 8.988 \times 10^{-2} \times 1.052 \times 10^{-8} \\
 &= 9.456 \times 10^{-10} \text{ kg} \\
 &= 9.456 \times 10^{-7} \text{ g}
 \end{aligned}$$

$$\begin{aligned}
 n_{(H_2)}^{(cyclohexanone)} &= \frac{m_{(H_2)}^{(cyclohexanone)}}{M_{r(H_2)}} & (2.29) \\
 &= \frac{9.456 \times 10^{-7}}{2.016} \\
 &= 4.69 \times 10^{-7} \text{ moles of } H_2 \\
 &= 4.69 \times 10^{-4} \text{ mmoles of } H_2
 \end{aligned}$$

The sum of the number of moles of H₂ in each of the three components of the solvent/reactant mixture was ~0.25 mmoles. Therefore, the total number of moles of H₂ in the reactor vessel was ~5.16 mmoles. However, there were limitations to the calculations described above. These calculations neglected the cosolvation of the other gases present in the reactor vessel (O₂ and N₂) and used the *L* values at ~0.10 MPa (*i.e.*, 1 atm) of pressure and at 293.15 K, which was not representative of the experimental conditions used. In addition, these calculations did not consider gas-liquid behaviours at higher temperatures or pressures as well as any salt effects from the NH₄HCO₃ used. Therefore, the results from these calculations are only estimates of the orders of magnitude of error. For this reason, the number of moles of H₂ in the solvent/reactant mixture have not been included in the H₂ selectivity based on oxime data for the catalytic tests.

Determining the H₂ selectivity was difficult as it was dependent on the “total” amount of oxime (*i.e.*, the counts of all of the aforementioned chemical species to work out the “total” number of moles of products) in the calculations as well as the converted H₂. Not all the gases dissolved, including H₂, would have reacted.

Another issue with H₂ selectivity was to consider the other pathways that ultimately lead to the production of H₂O (*e.g.*, direct synthesis of H₂O). One possibility to resolve this could be to determine the solvent/reactant mixture mass after the reaction, however, some of the gases would most likely still be dissolved in the solvent/reactant mixture, and therefore, be included in those measurements. Additionally, there would most likely be unreacted H₂O₂ and NH₂OH present in the solvent/reactant mixture. Although these chemical species may be present, they have been neglected in the H₂ selectivity data as it was not possible to determine their concentrations. As such, the current work classed the non-selectively converted H₂ as degraded H₂O₂ for a more facile interpretation of the experimental results.

Errors within the characterisation techniques used could also occur. For example, EDX analyses throughout other studies detected C, which is a common problem, even when the sample is under vacuum. This element is a common element and can be found on the surfaces of almost all materials as well as the sample grids being comprised of C.

As with all X-Ray techniques, the samples could be damaged by the beams. For example, in SEM-EDX analysis, the beam damage can cause deformation of nanoparticles as well as reduction of oxidised particles. The former would mean that a rearrangement of the atoms in the nanoparticle could be caused by this technique and not represent what the nanoparticle truly was. The latter would mean that the surface chemistry of the particles would be changed, thus, not provide a true representation of the particle’s original surface composition.

2.2. Computational Methods

As previously described in Chapter 1, Density Functional Theory (DFT) was used as part of the computational methods in the current work. The methods described below rely on the principles, concepts, and approximations of DFT. The methods were also optimised to complete the various calculations to an acceptable level of accuracy in the least amount of time.

2.2.1. Optimisation of Parameters

2.2.1.1. Energy Cut-Off

Before determining the bulk modulus and performing any optimisation calculations, the correct energy cut-off had to be established first. To do this, DFT calculations were completed using the Vienna *ab-initio* Simulation Package (VASP) code and the Perdew-Burke-Ernzerhof (PBE) functional with the energy cut-off incremented (*i.e.*, 300, 400, 500, 600 and 700 eV) at a set *k*-point sampling grid (3×3×3) for bulk Au and Pd. An optimum energy cut-off for both metals was used for the geometry optimisation calculations. The energy from each calculation of each energy cut-off was plotted against its related calculated energy (Fig. 2.6).

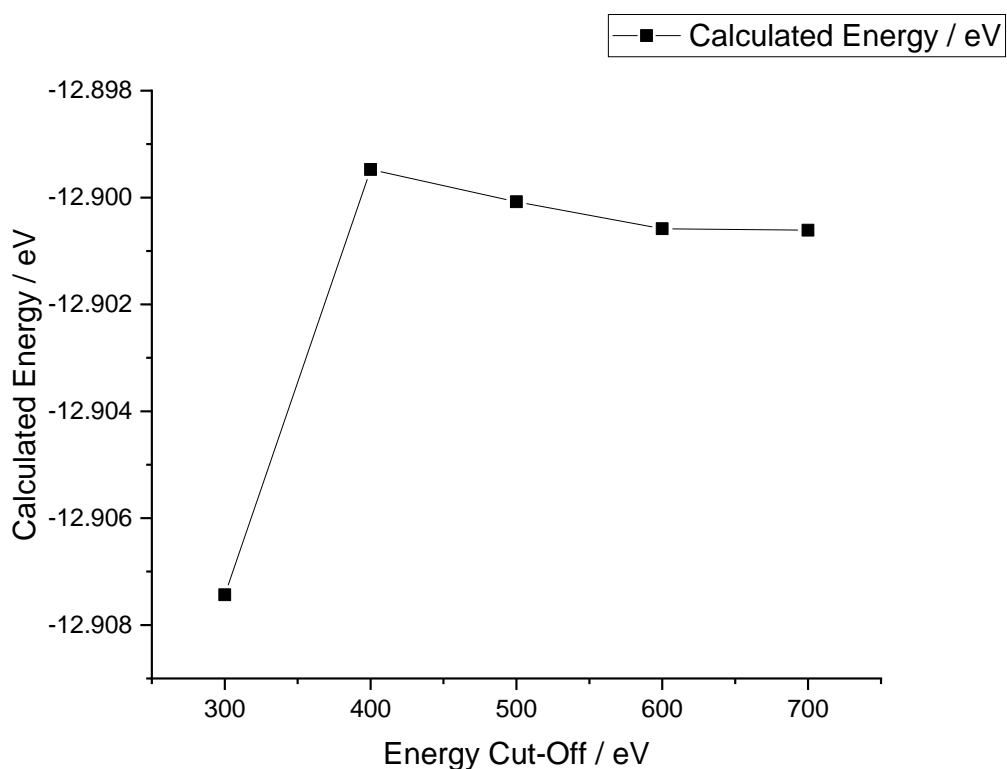


Figure 2.6. Effect of energy cut-off against the calculated energy of bulk Au from its geometry optimisation calculation.

It was observed that there was an increase in accuracy when comparing 300 eV to 400 eV, with a difference of 7.97×10^{-3} eV. However, there was little accuracy gained beyond an energy cut-off of 400 eV. As the energy cut-off increased from 400 eV, the difference in energy compared to the 400 eV energy cut-off was

6.10×10^{-4} eV, 1.11×10^{-3} eV, and 1.14×10^{-3} eV, respectively. This level of convergence is suited to dealing with chemical problems as 10^{-2} eV is approximately 1 kJ mol^{-1} . It was concluded that the energy cut-off at 400 eV was the best compromise between accuracy and computational effort.

2.2.1.2. Bulk Modulus, Expansion Factor and Miller Indices

As the theory and principles of the bulk modulus (B_0) and the Murnaghan equation were discussed explored in the Chapter 1, this chapter will describe how those concepts were put into practice for the theoretical methods involved in the computational research in the current work.

Utilising DFT calculations with the VASP code and the PBE functional, the cell dimensions of a material (*i.e.*, Au and Pd) in its bulk form were incrementally changed as the cell volume was uniformly scaled. Optimisations of the atoms' positions in the fixed cells were carried out. This was repeated at different k -point sampling grids (*i.e.*, $1 \times 1 \times 1$, $3 \times 3 \times 3$, $5 \times 5 \times 5$, $7 \times 7 \times 7$ and $9 \times 9 \times 9$) at the prescribed energy cut-off of 400 eV. Cell scaling was completed once a surface was generated, and the cell of the model was fixed with a 15.00 Å vacuum gap. The vacuum gap would normally collapse if it could move.

All surfaces were “cut” from the same bulk reference, using the determined expansion factor, along the Miller indices (*i.e.*, (100) and (111)). For Au at the k -point sampling grids of $3 \times 3 \times 3$, $5 \times 5 \times 5$, $7 \times 7 \times 7$ and $9 \times 9 \times 9$, the calculated energy of the incremented cell volumes was compared to the calculated Murnaghan energy plot. For each k -point sampling grid, they were aligned and in good agreement, meaning that the material behaved as predicted under pressure. The first k -point sampling grid ($1 \times 1 \times 1$) could not be used as no discernible trough was formed because of the change in cell volume (Fig. 2.7).

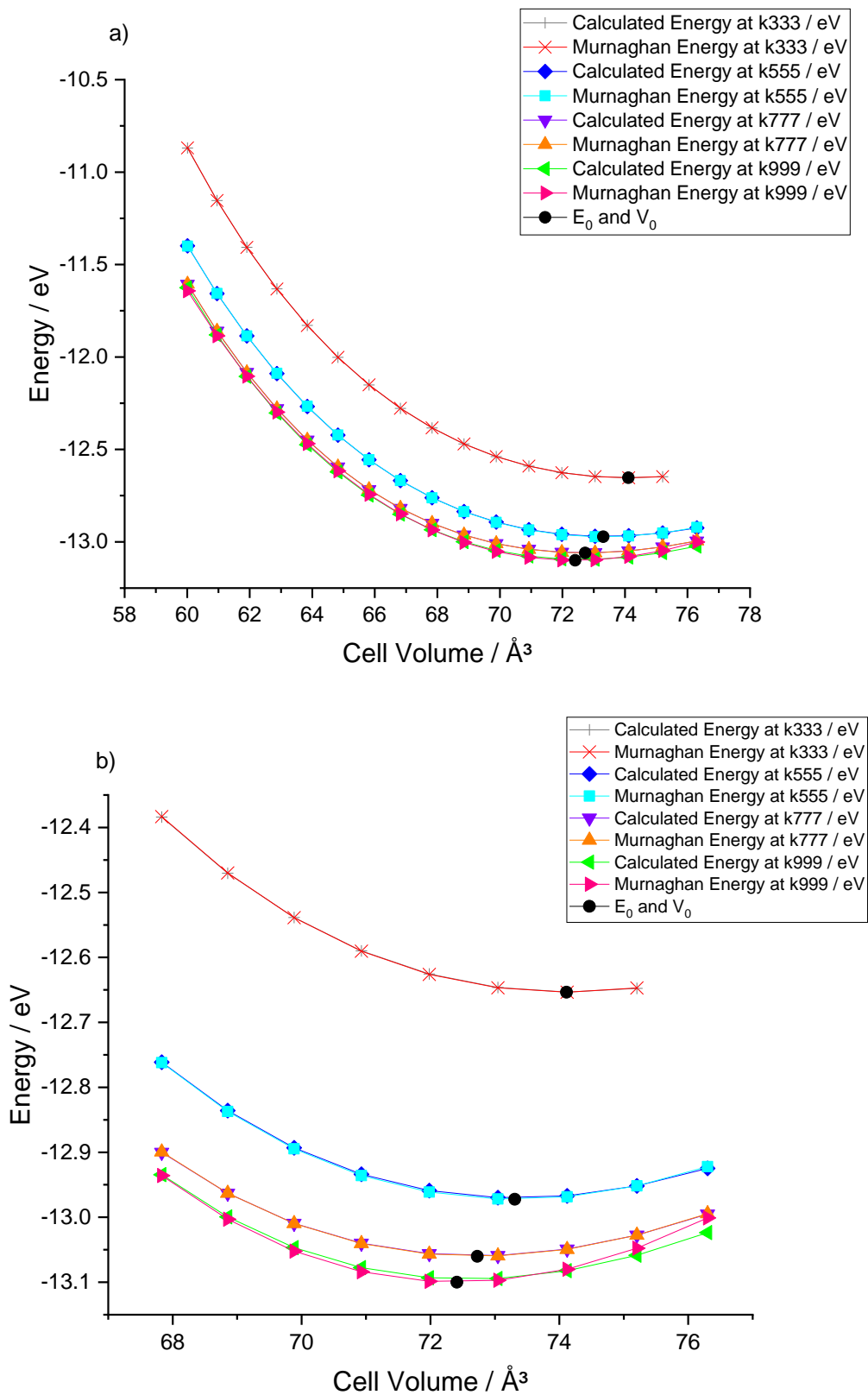


Figure 2.7. Murnaghan plots for Au, where **a)** is with the full data range, and **b)** is an expanded view of the calculated minima energy points.

For the k -point sampling grid $3 \times 3 \times 3$, the bulk cell had an original volume and calculated energy of $\sim 67.83 \text{ \AA}^3$ (which was the same for all k -point sampling grids) and $\sim -12.38 \text{ eV}$, respectively. From Fig. 2.7a, the values for V_0 and E_0 were $\sim 74.11 \text{ \AA}^3$ and $\sim -12.65 \text{ eV}$, respectively. As previously described in Chapter 1, B_0 can be defined by the energy and volume of the cell, as defined by equation (2.30):

$$B_0 = V \frac{\partial^2 E}{\partial V^2} \quad (2.30)$$

where $\frac{\partial^2 E}{\partial V^2}$ is the second derivative of the potential energy with respect to the volume.

This meant that B_0 could be calculated from the calculated energy plots as they were close to the Murnaghan energy plots. Each calculated energy plot showed a clear minimum. For the k -point sampling grid $3 \times 3 \times 3$, B_0 was calculated using V_0 and E_0 ($B_0 = \sim 135 \text{ GPa}$). The V_0 , E_0 and B_0 values were calculated (Table 2.4).

Table 2.4. Table of the effect the k -point sampling grid on the volume, energy, and bulk modulus for a Au cell, with the original energies included for comparison.

k -point Sampling Grid	$V_0 / \text{\AA}^3$	E / eV	E_0 / eV	B_0 / GPa
$3 \times 3 \times 3$	74.11	-12.38	-12.65	135
$5 \times 5 \times 5$	73.31	-12.76	-12.97	142
$7 \times 7 \times 7$	72.73	-12.90	-13.06	133
$9 \times 9 \times 9$	72.41	-12.95	-13.10	164

The trend observed was that with an increasing k -point sampling grid, the V_0 decreased resulting in a more negative E_0 and ultimately B_0 . However, B_0 for the k -point sampling grid $7 \times 7 \times 7$ decreased due to the significantly decreased V_0 as E_0 did not significantly decrease (Table 2.4 and Fig. 2.7).

The experimentally measured value of B_0 for Au is 180 GPa .¹³ In comparison to the literature value of B_0 for Au, it was reported by Dewaele *et al.* that the value of their B_0 was underestimated by $\sim 17 \%$ ($\sim 149 \text{ GPa}$),¹³ whereas the current work

underestimated the B_0 by ~25 %. Although the difference between the current work's value and the experimental value were significant, the difference in error between the current work and the work of Dewaele *et al.* was not (Table 2.4 and Fig. 2.7).¹³

Using a higher value k -point sampling grid would have been the appropriate choice as it provided a more accurate value for B_0 , however, this would have increased the computational effort and time required to complete the calculations. Although using a k -point sampling grid of $3 \times 3 \times 3$ would cause a difference of ~13.51 kJ mol⁻¹ compared to a $5 \times 5 \times 5$ k -point sampling grid, it was more appropriate to use this grid to obtain results quickly (Table 2.4 and Fig. 2.7).

Expansion factors were determined from the volume of the minima point on the Murnaghan cell expansion graph and the original volume, as defined in equation (2.31):

$$EF = \left(\frac{V_0}{V_{bulk}} \right)^{1/3} \quad (2.31)$$

where EF is the expansion factor, V_0 is the volume of the cell at the minimum of the curve of the bulk modulus and V_{bulk} is the original volume of the bulk.

This factor was important as the cell volume for all slabs “cut” at (100) and (111) in the current work needed to be increased by this value. For each viable k -point sampling grid (*i.e.*, $3 \times 3 \times 3$, $5 \times 5 \times 5$, $7 \times 7 \times 7$ and $9 \times 9 \times 9$), EF was determined giving values of ~1.024, ~1.026, ~1.024 and ~1.022, respectively. It was observed that an increasing k -point sampling grid did not affect the EF to a significant degree, averaging at $\sim 1.024 \pm 0.002$ overall.

After calculating the bulk modulus and the expansion factor, the slabs needed to be created from the bulk of the material. As the bulk needed to be “cut” to expose its surface, the use of Miller indices was required to show how the material was “cut”. For the (100) slab, one “cut” along the x axis of the cell was performed and for the (111) slab, one “cut” along all three axes (*i.e.*, x , y , and z) of the cell performed (Fig. 2.8).

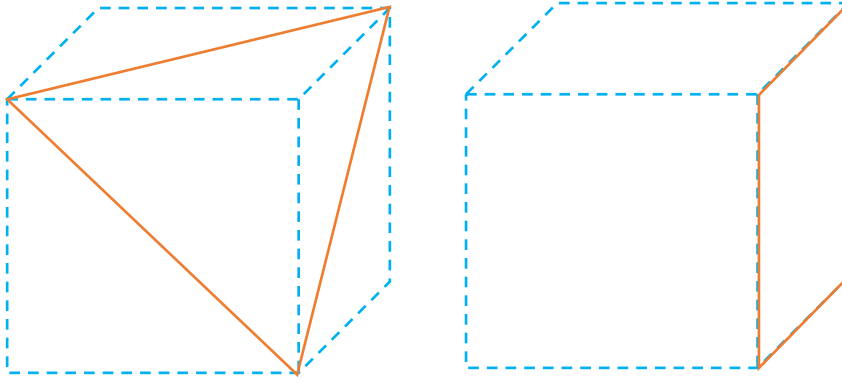


Figure 2.8. Planes of (111) and (100) “cut” from the bulk (1×1×1) cell.

The energy was required to create a surface of a particular Miller index. As the slab was constructed with five layers of atoms, the contribution of the lower, fixed atoms in the bottom three layers and the contribution from the top, relaxed atoms in the top two layers, needed to be determined. To determine the energy of the surface, each component of equation (2.32) must be calculated for the different slabs.

$$E_{surf}^{opt} = \frac{E_{slab} - nE_{bulk}}{S} - E_{surf}^{term} \quad (2.32)$$

where E_{surf}^{opt} is the energy of the optimised exposed surface of the upper section of the slab, E_{slab} is the total energy of the slab, n is the ratio of stoichiometries in the bulk and slab, E_{bulk} is the total energy of the bulk, S is the surface area and E_{surf}^{term} is the energy of the termination of the slab.

The E_{surf}^{term} can be determined using $d(E^{term})$ and S , as defined by equation (2.33):

$$E_{surf}^{term} = \frac{d(E^{term})}{2S} \quad (2.33)$$

For Au: the bulk contained four atoms; the (100) slab contained ten atoms; and the (111) slab contained 20 atoms. This meant the values of n were 2.5 and 5, respectively. Using the lengths of x and y for the periodic boundary conditions of each

slab as well as the largest angle observed in each slab along the two dimensions, the area of the slab (S) could be determined, as defined in equation (2.34):

$$S = x \times y \times \sin \theta \quad (2.34)$$

where x and y denote the length of each dimension and θ is the largest angle of the cell at the x and y lengths using a conversion to radians.

The change in energy for the lower termination surface needed to be calculated before determining the energy, as defined by equation (2.34):

$$d(E^{term}) = E^{term} - nE_{bulk} \quad (2.35)$$

where E^{term} is the energy of the lone termination section of the slab and E^{opt} is the energy of the converged slab.^{14,15}

As all the terms have been determined from equation (2.35), E_{surf}^{opt} can now be calculated. For both slabs, these values have been tabulated (Table 2.5).^{14,15}

Table 2.5. Surface area and energy values for Au(100) and (111). Limited to three significant figures and where E_{bulk} was -13.059 eV.

Slab Type	$S / \text{\AA}^2$	n	$E_{slab} /$ eV	$E^{term} /$ eV	$d(E^{term})$ / eV	$E_{surf}^{term} /$ J m ⁻²	$E_{surf}^{opt} /$ J m ⁻²
(100)	17.424	2.5	-30.815	-30.812	1.836	0.849	0.843
(111)	26.136	5	-62.667	-62.666	2.631	0.801	0.806

For both the (100) and (111) surfaces, the surface energy was lower for the optimised surface than for the terminated surface because the optimised atoms have lowered their energy. The (111) surface energy was lower than the (100) because the (111) was a close-packed configuration, whereas the (100) surface was not close-packed and exposed defects (*i.e.*, hollow sites).^{14,15} This process was repeated

for Pd and all materials used were from the Leibniz Institute for Information Infrastructure Inorganic Crystal Structure Database (ICSD).

2.2.1.3. Calculation Parameters

To determine the best parameters to use in relation to computational effort, the number of cores for the supercomputer and the *k*-point parallelisation needed to be optimised for the calculations. For the former, a “speed test” was completed using propene. The test provided a comparison for the speed at which a certain number of cores completes a Self-Consistent Field (SCF) iteration or ionic step (Fig. 2.9).

It was seen that using only one core was highly inefficient at ~6310 s, but by doubling the number of cores, it reduced the time by almost half (~3470 s). However, doubling or quadrupling the ten cores (~1000 s) did not have this drastic reduction in time and was only decreased by a quarter (~730 s) and by half (~560 s), respectively.

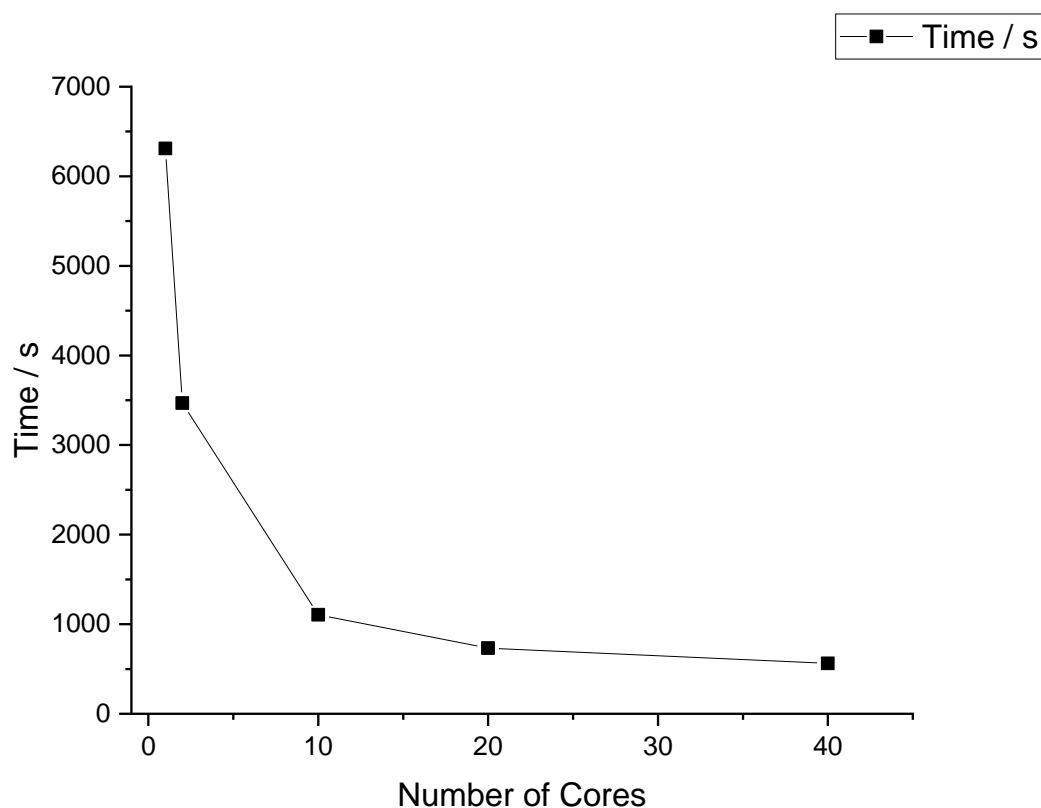


Figure 2.9. Comparison of the performance of the number of cores of the supercomputer to complete one iteration for a propene molecule, using a *k*-point mesh of 3×3×1.

Nevertheless, this test was completed without the k -point parallelisation. To set the correct number for this, the number of irreducible k -points needed to be determined for the $3 \times 3 \times 1$ k -point sampling grid. This was done by symmetry reduction, which makes this k -point sampling grid equal to five (Fig. 2.9).

With the k -point parallelisation activated, the “speed test” was completed again. It was observed that there was a marked improvement when the k -point parallelisation was activated. This was an expected result as a group of cores were assigned a single k -point to calculate. This increased the efficiency of the computing process as all the cores calculated for all of atoms, but with a different periodic pattern. This was unlike the previous “speed test”, which was calculating one orbital at a time utilising all the cores. This was inefficient as communication between cores increased the computational time (Fig. 2.10).

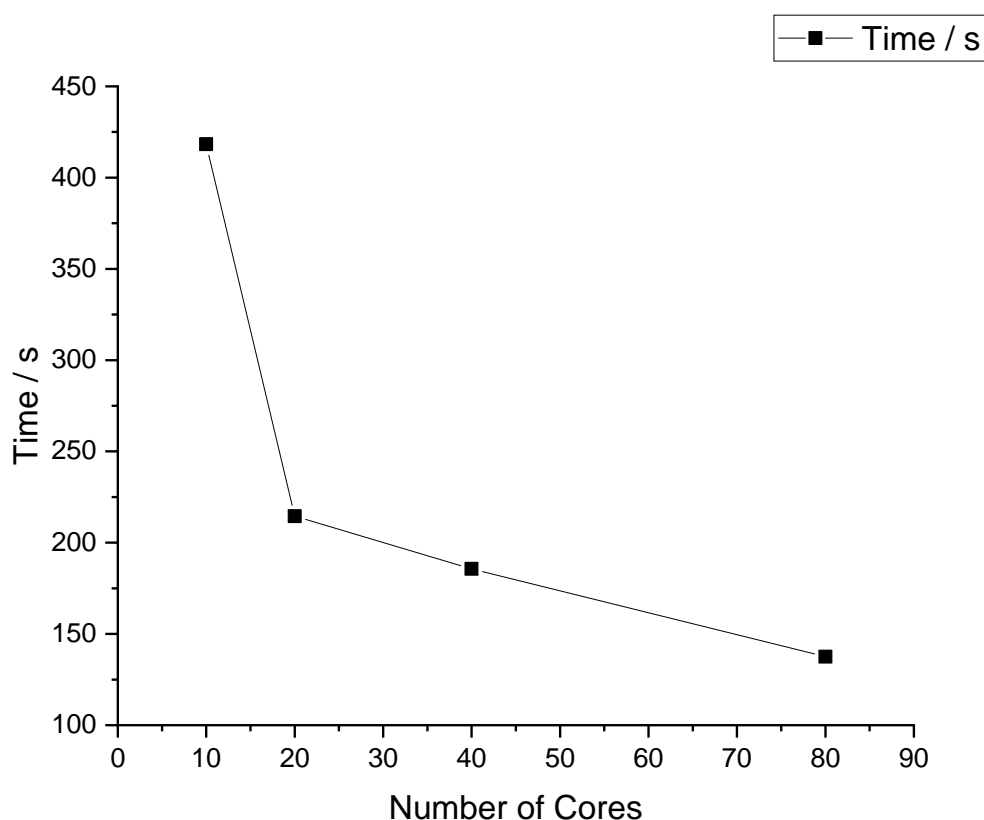


Figure 2.10. Comparison of the performance of the number of cores of the supercomputer to complete one iteration for a propene molecule, with k -point parallelisation activated, using a k -point mesh of $3 \times 3 \times 1$.

Using ten cores with the parallelisation reduced the time by a magnitude of ~ 8.26 compared to using ten cores without it. In a similar fashion, the 20 and 40 cores used with the k -point parallelisation reduced the computational time by ~ 3.40 and ~ 4.10 , respectively, compared to those cores used without it. Additionally, comparing the performance for the number of cores showed that there was a decrease by roughly half from ten (~ 420 s) to 20 cores (~ 210 s), followed by a reduction of $\sim 13\%$ from 20 cores to 40 cores (~ 190 s) (Fig. 2.10).

Further investigation into the use of multiple nodes was conducted. The number of cores was doubled again from 40 to 80 cores, with a reduction in time by almost a quarter (~ 140 s) to complete one ionic step. This finding may have suggested that this was not the most efficient method as doubling the number of cores did not halve the compute time. Even so, 80 cores were used for the geometry optimisation calculations as the number of electrons would increase as the number of metal atoms would be introduced to the cell with a metal surface (*e.g.*, for a Au(111) surface, there would be 80 metal atoms, with 11 electrons, each as the inner core electrons were supplemented by pseudopotentials). The requirement for more cores would increase with an increased number of electrons within the cell.

2.2.2. Geometry Optimisation Calculations

DFT calculations were completed using the VASP code, the PBE functional and the aforementioned optimised calculation parameters. A plane wave energy cut-off of 400 eV was employed. The valence electrons of O, C ($2s, 2p$), Au ($6s, 5d$) and Pd ($5s, 4d$) were treated explicitly with the Projector Augmented Wave (PAW) method used to represent the core electrons of these atoms, except for H. To accommodate the slabs, vacuum gaps of 25.00 Å above the surface of the slab and 1.00 Å below were introduced. The latter gap was to stop the atoms from the bottom layer moving into the cell below, which in effect would look as though the atoms were at the top of the cell. The slabs were 2×2 supercells of five layers, where the bottom three layers were fixed, and the top two layers were allowed to relax.

Four different INCAR files were used for the geometry optimisation calculations, which has been shown as a flow diagram below. The reason for using four INCAR files was to reduce the computing time for each calculation whilst obtaining reasonably accurate results. The first INCAR file carried out a brief search at the Γ -point of the Brillouin zone using the lowest k -sampling Monkhorst pack

(1×1×1). This search using the Conjugate Gradient algorithm located the minima (Fig. 2.11).

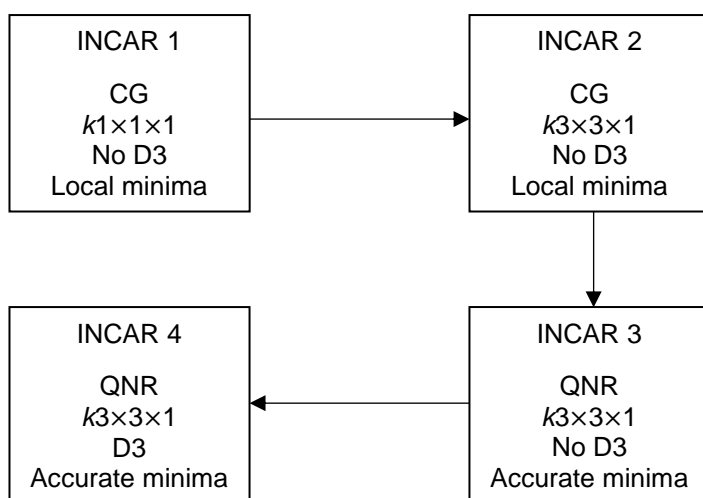


Figure 2.11. Flow diagram of the INCAR files used for the geometry optimisation calculations, with the algorithm, k -point sampling grid and the type of minima that was located. CG denotes the Conjugate Gradient algorithm and QNR is the Quasi-Newton-Raphson algorithm.

The next INCAR file went further by locating the minima for the Brillouin zone using a higher k -sampling Monkhorst pack (3×3×1). After 50 ionic steps, the calculation was halted to find the minima, using the Quasi-Newton-Raphson algorithm, to a greater degree of accuracy. The calculation ran to completion, at which point the final INCAR was used with the information from the converged structures to add the D3 corrections from Grimme *et al.*¹⁶ All INCAR files are presented below (Fig. 2.11, 2.4.2. Settings for INCAR Files).

2.2.3. Interaction, Deformation and Adsorption Energies

For the group's computational work on propene glycerol hydrogenolysis, Coll *et al.*¹⁷ described equations to use for the energy of adsorption (E_{ads}), the energy of interaction between the surface and the molecule (E_{int}) and the energy of deformation of the surface or molecule (E_{def}). These equations are described in equations (2.36)-(2.40):

$$E_{ads} = E_{def} + E_{int} \quad (2.36)$$

$$E_{int} = E_{molecule/surface} - E_{molecule}^{frozen} - E_{surface}^{frozen} \quad (2.37)$$

$$E_{def} = E_{def}^{surface} + E_{def}^{molecule} \quad (2.38)$$

$$E_{def}^{surface} = E_{surface}^{frozen} - E_{surface}^{relaxed} \quad (2.39)$$

$$E_{def}^{molecule} = E_{molecule}^{frozen} - E_{molecule(g)}^{relaxed} \quad (2.40)$$

where $E_{molecule/surface}$ is the energy of the optimised adsorption complex, *frozen* is the geometry of either the molecule or surface at the geometry of the adsorption complex, *relaxed* is the geometry of either the molecule or surface not in adsorption complex, $E_{def}^{surface}$ is the energy of deformation of the surface, $E_{def}^{molecule}$ is the energy of deformation of the molecule and $E_{molecule(g)}^{relaxed}$ is the energy of the relaxed molecule used as the gas phase reference.¹⁷

These equations are important to determine the impact of the E_{int} and E_{def} values on the E_{ads} value. Two examples of the effect of E_{def} had on the E_{ads} were described in Chapter 4 (*i.e.*, adsorption of O₂ and propene to Au(100)). This was done by completing single point calculations of the lone, frozen molecule and lone frozen surface after the geometry optimisation calculations for the molecule adsorbed to the surface, where they were allowed to relax. The difference in energies between the relaxed and frozen O₂, propene and Au(100) surface were ~-138, ~-6 and ~-74 kJ mol⁻¹, respectively.

Additionally, the reference energy for atomic O used in the current work was derived from the energy of an O₂ molecule. The value was halved to represent the energy of an O atom in the calculations. A point to note is that discussions regarding dissociated adsorbing molecules (*e.g.*, H₂O₂ at the HO-OH bond), the E_{ads} describes the adsorption of both species (in this case, two OH groups) and not as adsorption of one species.

2.2.4. Density of States Calculations

From the optimised structures, the DOSCAR file from the D3 corrected calculations and the VASP code were used to produce the total and partial density of

states (DoS) for each surface with and without the adsorbates. The total DoS was all of the density of states for the unit cell and the partial DoS was the density of states for selected atoms within the unit cell (e.g., just the adsorbate atoms in the adsorbate-surface complex, neglecting the surface's atoms). The selected adsorbates of focus with regards to the DoS were H₂, O₂ and propene, using the sites of the lowest E_{ads} value.

In the current work, these calculations provided information on the bonding and anti-bonding orbitals of a multi-atomic system (*i.e.*, the cell of the surface and adsorbate). The data described the effects of adsorption on the orbitals of the surface and the molecules. However, to gain a representative DoS, the DoS profiles needed to go through an integration process to normalise the data. The normalisation takes the area of DoS of the adsorption complex, the frozen molecule, and the molecule from the gas phase reference up to the Fermi level and is divided by the number of electrons within each system. This means that each DoS is calculated as unit area per electron making the DoS of the different systems comparable.

Settings within the INCAR file were activated to be able to use the DOSCAR and generate the DoS files needed (LORBIT = 12, NEDOS = 601). The DoS files for each slab were compiled to produce a graph of the total DoS of the adsorbate-surface complex, the lone, relaxed adsorbate, and the partial DoS of the of the adsorbate-surface complex, focusing on the adsorbate alone. Comparisons of the DoS were made and described in Chapter 4.

2.3. References

- 1 J. K. Edwards, B. Solsona, E. N. N, A. F. Carley, A. A. Herzing, C. J. Kiely and G. J. Hutchings, Switching Off Hydrogen Peroxide Hydrogenation in the Direct Synthesis Process, *Science (80-.)*, 2009, **323**, 1037–1041.
- 2 D. A. Crole, S. J. Freakley, J. K. Edwards and G. J. Hutchings, Direct synthesis of hydrogen peroxide in water at ambient temperature, *Proc. R. Soc. A Math. Phys. Eng. Sci.*, 2016, **472**, 20160156.
- 3 J. K. Edwards, *PhD Thesis Title: Direct synthesis of hydrogen peroxide from hydrogen and oxygen over catalysts containing gold*, Cardiff University, 2006.

- 4 J. K. Edwards, A. F. Carley, A. A. Herzing, C. J. Kiely and G. J. Hutchings, Direct synthesis of hydrogen peroxide from H₂ and O₂ using supported Au-Pd catalysts, *Faraday Discuss.*, 2008, **138**, 225–239.
- 5 R. J. Lewis, *PhD Thesis Title: The application of Cs-exchanged tungstophosphoric acid as an additive in the direct synthesis of hydrogen peroxide and the use of Au-Pd/TS-1 in a one-pot approach to cyclohexanone oxime production*, Cardiff University, 2016.
- 6 Canadian Centre for Welding and Joining, Microscopy, <https://sites.ualberta.ca/~ccwj/teaching/microscopy/#XWerner2012>, (accessed 9 July 2020).
- 7 U. of I. Central Microscopy Research Facility, Scanning Electron Microscopy , <https://cmrf.research.uiowa.edu/scanning-electron-microscopy>, (accessed 9 July 2020).
- 8 I. Orlowski, M. Douthwaite, S. Iqbal, J. S. Hayward, T. E. Davies, J. K. Bartley, P. J. Miedziak, J. Hirayama, D. J. Morgan, D. J. Willock and G. J. Hutchings, The hydrogenation of levulinic acid to Γ -valerolactone over Cu–ZrO₂ catalysts prepared by a pH-gradient methodology, *J. Energy Chem.*, 2019, **36**, 15–24.
- 9 V. Gupta, H. Ganegoda, M. H. Engelhard, J. Terry and M. R. Linford, Assigning Oxidation States to Organic Compounds via Predictions from X-ray Photoelectron Spectroscopy: A Discussion of Approaches and Recommended Improvements, *J. Chem. Educ.*, , DOI:10.1021/ed400401c.
- 10 Saarland University, AG Jacobs - Dusseldorf, https://jacobs.physik.uni-saarland.de/home/index.php?page=steinbeiss/home_cms_steinbeissdet3-1&navi=service, (accessed 5 August 2020).
- 11 D. A. Crole, *PhD Thesis Title: The direct synthesis of hydrogen peroxide in water at ambient temperature: A study of reaction conditions, catalyst design and implementation*, Cardiff University, 2017.
- 12 C. L. Young, Ed., *Hydrogen and deuterium*, Pergamon Press, Oxford ; New York, 1st ed., 1981.
- 13 A. Dewaele, M. Torrent, P. Loubeyre and M. Mezouar, Compression curves of transition metals in the Mbar range: Experiments and projector augmented-wave calculations, , DOI:10.1103/PhysRevB.78.104102.

- 14 K. L. Howard and D. J. Willock, A periodic DFT study of the activation of O₂ by Au nanoparticles on α -Fe₂O₃, *Faraday Discuss.*, 2011, **152**, 135–151.
- 15 N. E. Singh-Miller and N. Marzari, Surface energies, work functions, and surface relaxations of low-index metallic surfaces from first principles, *Phys. Rev. B - Condens. Matter Mater. Phys.*, 2009, **80**, 235407.
- 16 S. Grimme, J. Antony, S. Ehrlich and H. Krieg, A consistent and accurate ab initio parametrization of density functional dispersion correction (DFT-D) for the 94 elements H-Pu, *J. Chem. Phys.*, 2010, **132**, 154104.
- 17 D. Coll, F. Delbecq, Y. Aray and P. Sautet, Stability of intermediates in the glycerol hydrogenolysis on transition metal catalysts from first principles, *Phys. Chem. Chem. Phys.*, 2011, **13**, 1448–1456.

2.4. Appendix

2.4.1. Gas Chromatography Calibrations

GC Calibrations for the liquid-phase samples needed to be completed prior to any testing. This was to establish the Relative Response Factor (RRF) of each component within the reaction mixture against a known quantity of the internal standard. The calibration solutions at 20 %, 50 % and 80 % conversion of cyclohexanone were diluted with the same amount of ethanol (6.00 g) as the reaction mixture for a catalytic reaction test. Thus, the conversion of the cyclohexanone and formation of cyclohexanone oxime in a catalytic reaction test could be calculated (Fig. A2.1 and A2.2). The masses for the cyclohexanone and cyclohexanone oxime needed for the different calibration solutions were calculated by using the percentage of conversion and equation (2.12).

For example, at 20 % conversion, 80 % of the cyclohexanone mass would still be present (0.16 g) and the 20 % of the cyclohexanone that had been converted would, with a high selectivity, become cyclohexanone oxime. This is a 1:1 reaction, with the relative molecular masses (M_r) known for cyclohexanone and cyclohexanone oxime (98.15 and 113.16 g mol⁻¹). Thus, using equations (A2.1)-(A2.3), the masses required for the calibrations can be calculated:

$$n^{cyclo} = \frac{m^{cyclo}}{M_r^{cyclo}} \quad (A2.1)$$

$$= \frac{0.04}{98.15}$$

$$= 4.08 \times 10^{-4} \text{ moles}$$

$$= 40.8 \text{ mmoles}$$

$$n^{cyclo} = n^{oxime} \quad (A2.2)$$

$$m^{oxime} = n^{oxime} \times M_r^{oxime} \quad (A2.3)$$

$$= 4.08 \times 10^{-4} \times 113.16$$

$$= 0.046 \text{ g}$$

where n^{cyclo} is the number of moles of cyclohexanone, m^{cyclo} is the mass of cyclohexanone, M_r^{cyclo} is the relative molecular mass of cyclohexanone, n^{oxime} is the number of moles of cyclohexanone oxime, m^{oxime} is the mass of cyclohexanone oxime, and M_r^{oxime} is the relative molecular mass of cyclohexanone oxime.

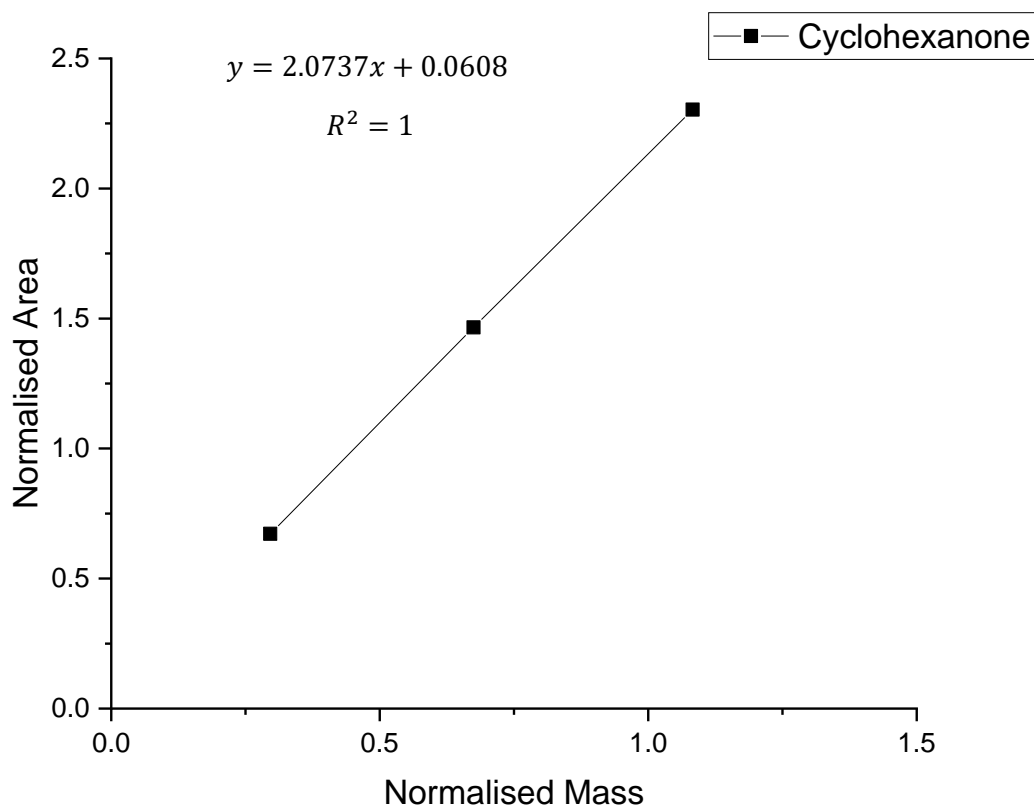


Figure A2.1. Calibration plot for cyclohexanone normalised against the internal standard (diethylene glycol monoethyl ether) at 20 %, 50 % and 80 % conversion.

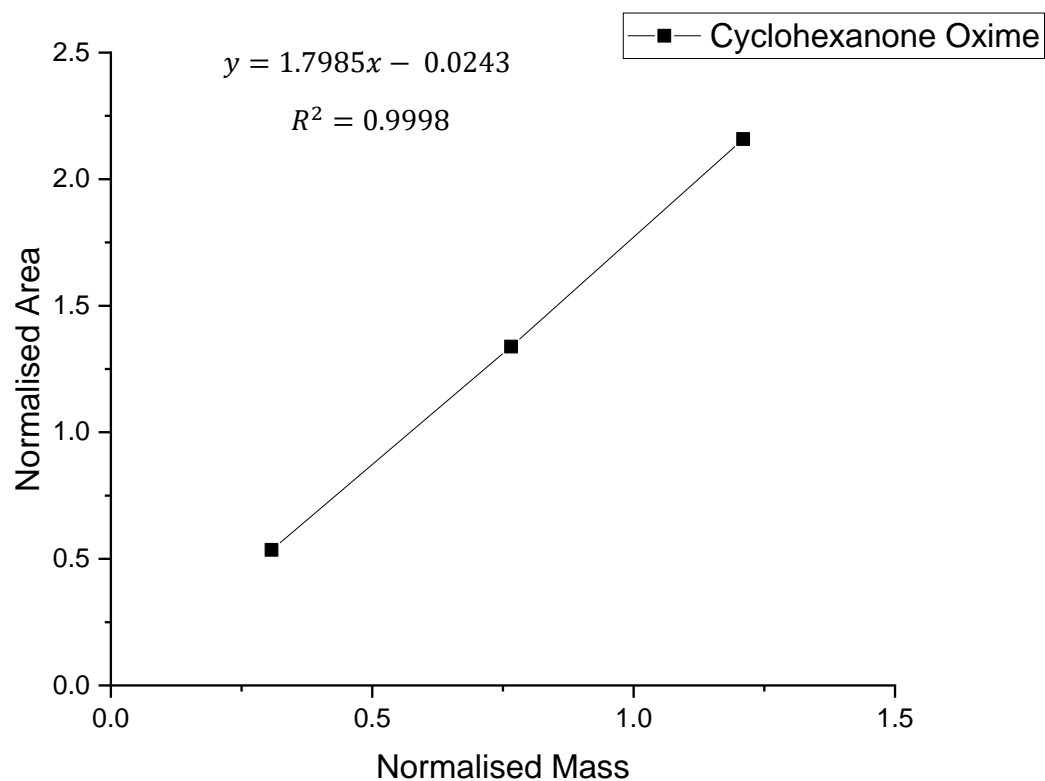


Figure A2.2. Calibration plot for cyclohexanone oxime normalised against the internal standard (diethylene glycol monoethyl ether) at 20 %, 50 % and 80 % conversion.

2.4.2. Settings for INCAR Files

The settings for the four INCAR files used for the geometry optimisation calculations have been provided below.

For the first INCAR:

```
SYSTEM bulk using PBE
ISTART = 0          # 0: New job, 1: Continuation job
PREC = Normal
GGA = PS           # Use the PBE functional
ENCUT = 400        # Set plane wave cut-off
ICHARG = 2         # Initiate charge as superposition of atomic charges
NSW = 4000         # Maximum number of ionic steps
ISYM=0            # Symmetry analysis not allowed

#Optimisation choices
IBRION = 2         # 1: QNR, 2: Conjugate gradient
POTIM = 0.01      # For smaller steps along gradient
#NFREE = 10

EDIFF = 1E-4      # Electronic relaxation threshold, 1E-4 is default
EDIFFG= -1E-2     # Electronic relaxation threshold, 1E-3 is default
ISIF = 2

# Settings for speed
ALGO = Normal     # RMM-DIIS algorithm for electrons
LREAL = .FALSE.   # Evaluate projection operators in real space
NSIM = 4          # Blocked algorithm update, four bands at a time

#ISPIN = 2        # Spin polarisation for O2 triplet state
#MAGMOM = 1 1    # Both O atoms initially spin parallel

ADDGRID = .TRUE.

#NPAR = 20
NCORE = 5
#KPAR = 2

#
#D3 Corrections
#
#IVDW = 11
#VDW_S6 = 1.0
#VDW_SR = 1.217
#VDW_S8 = 0.722
#VDW_RADIUS = 15.0
#VDW_CNRADIUS = 10.0
```

For the second INCAR:

```
SYSTEM bulk using PBE
ISTART = 0          # 0: New job, 1: Continuation job
PREC = Normal
GGA = PE           # Use the PBE functional
ENCUT = 400        # Set plane wave cut-off
ICHARG = 11        # Initiate charge as superposition of atomic charges
NSW = 20           # Maximum number of ionic steps
ISYM=0            # Symmetry analysis not allowed

#Optimisation choices
IBRION = 2         # 1: Quasi NR, 2: Conjugate gradient
POTIM = 0.01      # For smaller steps along gradient
#NFREE = 10

EDIFF = 1E-4      # Electronic relaxation threshold, 1E-4 is default
EDIFFG= -1E-2     # Electronic relaxation threshold, 1E-3 is default
ISIF = 2

# Settings for speed
ALGO = Fast       # RMM-DIIS algorithm for electrons
LREAL = .FALSE.   # Evaluate projection operators in real space
NSIM = 4          # Blocked algorithm update, four bands at a time

#ISPIN = 2        # Spin polarisation for O2 triplet state
#MAGMOM = 1 1     # Both O atoms initially spin parallel

ADDGRID = .TRUE.

#NPAR = 20
NCORE = 5
KPAR = 2

#
#D3 Corrections
#
#IVDW = 11
#VDW_S6 = 1.0
#VDW_SR = 1.217
#VDW_S8 = 0.722
#VDW_RADIUS = 15.0
#VDW_CNRRADIUS = 10.0
```

For the third INCAR:

```
SYSTEM bulk using PBE
ISTART = 1          # 0: New job, 1: Continuation job
PREC = Normal
GGA = PE           # Use the PBE functional
ENCUT = 400        # Set plane wave cut-off
ICHARG = 2         # Initiate charge as superposition of atomic charges
NSW = 4000         # Maximum number of ionic steps
ISYM=0            # Symmetry analysis not allowed

#Optimisation choices
IBRION = 1         # 1: Quasi NR, 2: Conjugate gradient
POTIM = 0.01      # For smaller steps along gradient
#NFREE = 10

EDIFF = 1E-4      # Electronic relaxation threshold, 1E-4 is default
EDIFFG= -1E-2     # Electronic relaxation threshold, 1E-3 is default
ISIF = 2

# Settings for speed
ALGO = Normal     # RMM-DIIS algorithm for electrons
LREAL = .FALSE.   # Evaluate projection operators in real space
NSIM = 4          # Blocked algorithm update, four bands at a time

#ISPIN = 2        # Spin polarisation for O2 triplet state
#MAGMOM = 1 1    # Both O atoms initially spin parallel

ADDGRID = .TRUE.

#NPAR = 20
NCORE = 5
KPAR = 2

#
#D3 Corrections
#
#IVDW = 11
#VDW_S6 = 1.0
#VDW_SR = 1.217
#VDW_S8 = 0.722
#VDW_RADIUS = 15.0
#VDW_CNRADIUS = 10.0
```

For the last INCAR:

```
SYSTEM bulk using PBE
ISTART = 1          # 0: New job, 1: Continuation job
PREC = Normal
GGA = PE           # Use the PBE functional
ENCUT = 400        # Set plane wave cut-off
ICHARG = 2         # Initiate charge as superposition of atomic charges
NSW = 4000         # Maximum number of ionic steps
ISYM=0            # Symmetry analysis not allowed

#Optimisation choices
IBRION = 1         # 1: Quasi NR, 2: Conjugate gradient
POTIM = 0.01      # For smaller steps along gradient
#NFREE = 10

EDIFF = 1E-4      # Electronic relaxation threshold, 1E-4 is default
EDIFFG= -1E-2     # Electronic relaxation threshold, 1E-3 is default
ISIF = 2

# Settings for speed
ALGO = Normal     # RMM-DIIS algorithm for electrons
LREAL = .FALSE.   # Evaluate projection operators in real space
NSIM = 4          # Blocked algorithm update, four bands at a time

#ISPIN = 2        # Spin polarisation for O2 triplet state
#MAGMOM = 1 1    # Both O atoms initially spin parallel

ADDGRID = .TRUE.

#NPAR = 20
NCORE = 5
KPAR = 2

#
#D3 Corrections
#
IVDW = 11
VDW_S6 = 1.0
VDW_SR = 1.217
VDW_S8 = 0.722
VDW_RADIUS = 15.0
VDW_CNRADIUS = 10.0
```


3. Ammoximation of Cyclohexanone utilising *in-situ* Direct Hydrogen Peroxide Synthesis

3.1. Introduction

3.1.1. Cyclohexanone Ammoximation

Cyclohexanone oxime is an important intermediate in the production of Nylon-6. Nylon-6 is an essential chemical to produce as it can be used for a variety of things, such as medical stitching or interior car parts. It is prepared by performing a Beckmann rearrangement on the cyclohexanone oxime to produce ϵ -caprolactam, followed by a ring opening polymerisation to form Nylon-6. The previous method of manufacturing cyclohexanone oxime is the hydroxylammonium sulphate route,¹ where ammonia (NH_3) is added to neutralise sulphuric acid (H_2SO_4) to yield hydroxylamine (NH_2OH). Subsequently, NH_2OH then reacts with cyclohexanone to form the oxime.

Another possible route for producing cyclohexanone oxime is to react manufactured hydrogen peroxide (H_2O_2) with NH_3 to form NH_2OH ,² which can then further react with cyclohexanone to yield the oxime.³ Enichem created this method in 1988, with the use of Titanium Silicalite-1 (TS-1).^{4,5} The oxime is subsequently reacted with H_2SO_4 to produce ϵ -caprolactam, followed by a ring opening polymerisation to produce nylon-6.^{3,6-8}

Meng *et al.*⁸ proposed two mechanisms for the ammoximation of acetaldehyde over TS-1, and consequently, studied the reactions involved. The first pathway explored was the imine route, where an imine was formed from NH_3 and organic reactant over the TS-1 and oxidised to the oxime. The other pathway was the hydroxylamine route, where the NH_3 was oxidised first before reacting with the organic reactant. The research demonstrated that the hydroxylamine route was the mechanism for the ammoximation of acetaldehyde for two reasons: no C=N bond was detected by *in-situ* infrared (IR) spectroscopy at any stage of the reaction; and hydroxylamine was detected. The studies completed by Li *et al.*,⁹ Dal Pozzo *et al.*³ and Raja *et al.*¹⁰ supported the aforementioned research conducted by Meng *et al.*⁸ by their use of Field-Emission Scanning Electron Microscopy (FESEM), Fourier

Transform-Infrared (FT-IR) spectroscopy and Scanning Electron Microscopy (SEM), respectively.

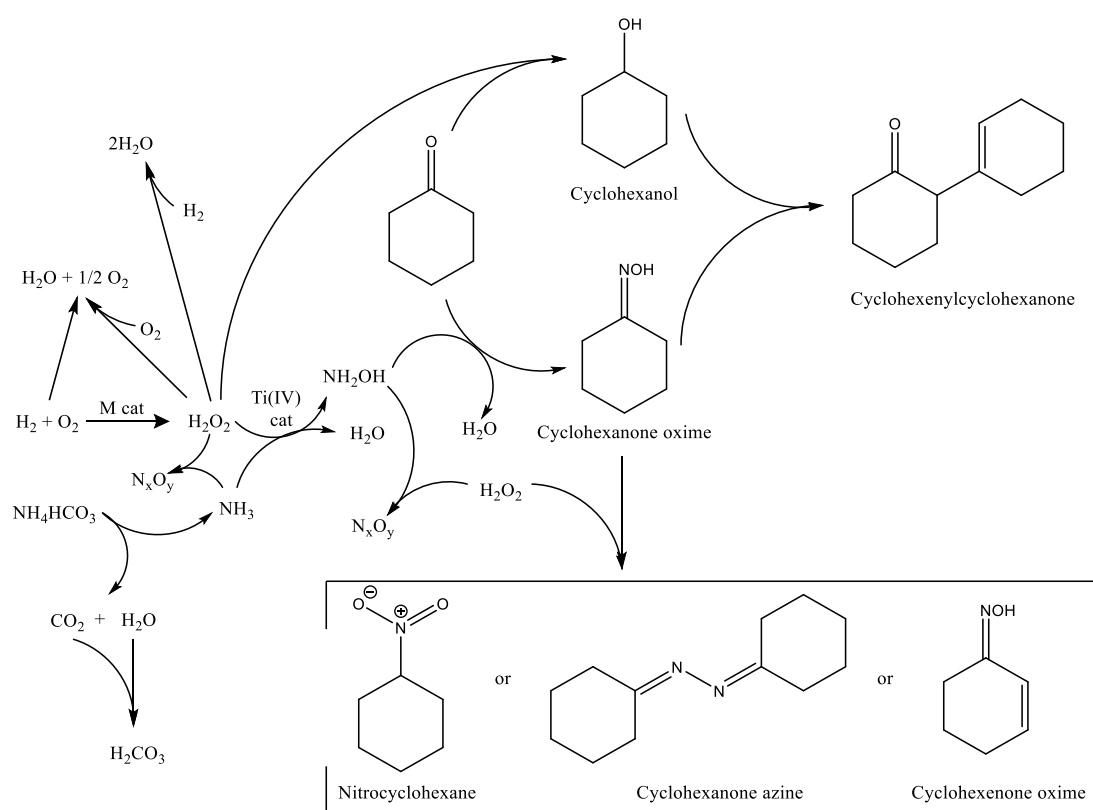
Jin *et al.*¹¹ observed the different effects that temperature, reactant ratios and varying amounts of TS-1 had on acetaldehyde ammoximation. The research showed that increasing the reaction temperature increased the activity and selectivity of the TS-1. However, this was only up to 333.15 K, after which the acetaldehyde conversion and oxime selectivity decreased. The amount of H₂O₂ was critical as there was a narrow range for its concentration in the reaction. Inadequate or excessive amounts would lead to increased decomposition and little acetaldehyde conversion. Based on conversion and selectivity, the best H₂O₂/acetaldehyde and NH₃/acetaldehyde ratios were 1.2-1.3 and 3.0, respectively. Increasing the amount of TS-1 increased the conversion and selectivity. However, the study did not explore excessive amounts of TS-1 to observe the upper limit.¹¹ Although these works use acetaldehyde as the target reactant, it should be noted that similar trends have been observed for cyclohexanone as well as utilising the same reaction mechanism.^{6,12,13}

The key difference between the two pathways is which phase they take place in. Jin *et al.*¹¹ demonstrated that the hydroxylamine pathway occurred in the liquid phase. The imine route occurred in the gas phase. Zhang *et al.*¹⁴ showed this phenomenon and further researched the mechanism of H₂O₂ activation on the Ti⁴⁺ sites of the TS-1 through experimental and theoretical methods. Density Functional Theory (DFT) was utilised to support the experimental Diffuse Reflectance Infrared Fourier Transform Spectroscopy (DRIFTS) results that showed that a Ti-OOH species existed.

In modern industrial manufacturing, H₂O₂ added to the ammoximation reaction is sourced from the anthraquinone oxidation (AO) process. As previously discussed in Chapter 1, the direct synthesis route is a competitor for the AO process and can be utilised for the ammoximation of cyclohexanone.¹⁵ Adding H₂ and O₂ into the system, H₂O₂ can be synthesised *in-situ* using a selective catalyst. Efforts have been made to combine the direct synthesis of H₂O₂ and the ammoximation reaction. Lewis⁶ and Kenji *et al.*¹⁶ showed that it was possible to create a single catalyst that could carry out both reactions. Precious metal nanoparticles were supported on TS-1 (Scheme 3.1).

Direct synthesis of H₂O₂ from dissolved H₂ and O₂, as well as its subsequent hydrogenation and decomposition reactions, occur at the metal nanoparticles (M cat) and the reaction to produce NH₂OH occurs at the Ti⁴⁺ sites. These sites are readily

available in TS-1, which is a titanosilicalite with a Mordenite Framework Inverted (MFI) zeolite structure, similar to the common zeolite ZSM-5.¹⁷ Lewis⁶ carried out this catalytic reaction at 353.15 K and 4.00 MPa of pressure (2.89 MPa of 5 % H₂/N₂ and 1.11 MPa of 25 % O₂/N₂). In addition, this reaction to produce acids (*i.e.*, H₂O₂ and H₂CO₃) was also completed in the presence of a base (*i.e.*, NH₃) (Scheme 3.1).



Scheme 3.1. Reaction pathways for the direct synthesis of H₂O₂ with subsequent NH₂OH and cyclohexanone oxime production in the liquid phase.^{8,18–23}

However, another technique could be used by preparing a separate catalyst for the direct synthesis of H₂O₂ and adding the TS-1 for the subsequent reaction of H₂O₂ and NH₃, making a tandem catalyst system. The aims of the current work are to synthesise a catalyst that yields high activity and selectivity towards direct H₂O₂ synthesis and to do so under the required reaction conditions (*i.e.*, at 353.15 K, 4.00 MPa and under basic conditions). The findings of this new tandem catalyst system are discussed below.

3.2. Results and Discussion

Research was conducted into the set of catalytic reactions for the utilisation of *in-situ* direct H₂O₂ synthesis for cyclohexanone ammoximation. Different studies were completed that explored the effects of the support material of the direct H₂O₂ synthesis catalyst, the amount of TS-1 and the length of the reaction time affected the yield of cyclohexanone oxime and H₂ conversion and selectivity. The results of these studies are described below.

3.2.1. Different Support Study

As a significant amount of research had been carried out for the conventional wet impregnation (C_{IM}) catalysts supported on TS-1,^{6,24–26} catalysts were investigated using different supports other than ACS TS-1 (*i.e.*, P25 TiO₂, ZrO₂ and SiO₂). As two of the three reaction steps were catalytic, the first reaction step was initially tested separately. These catalysts were tested for the catalytic direct H₂O₂ synthesis prior to the cyclohexanone ammoximation tests, with a set amount of ACS TS-1 (1:1, 0.075 g), working as a tandem catalyst system. The primary focus of researching these catalysts was to attempt to obtain a tandem catalyst system that could produce oxime yields and H₂ selectivity values that were acceptable for industrial scale-up (≥95 %).

3.2.1.1. Catalyst Experiments

For the 0.33 wt% Au-0.33 wt% Pd catalysts, four different support materials were selected: P25 TiO₂, ACS TS-1, ZrO₂ and SiO₂. It was important to use different types of support to garner how much the supported influenced the catalyst's overall performance. The ACS TS-1-, P25 TiO₂-, SiO₂- and ZrO₂-supported catalysts gave productivity values of 44, 55, 12 and 16 mol_{H₂O₂} kg_{cat}⁻¹ h⁻¹, respectively. It was clear that P25 TiO₂ was the better support with a higher H₂O₂ productivity value than ZrO₂, SiO₂ and ACS TS-1 (Table 3.1).

For comparison, the 2.50 wt% Au-2.50 wt% Pd/P25 TiO₂ catalyst²⁷ was added to the dataset. No research using exactly the same reaction conditions for this catalyst has been published for the ammoximation of cyclohexanone utilising *in-situ* direct H₂O₂ synthesis, thus, this data is absent from the current work. The ACS

TS-1-supported catalyst in the current work performed better than the previous work by Kenji *et al.*¹⁶ as the yield of oxime was far greater, using the same 0.33 wt% Au-0.33 wt% Pd catalyst on the same ACS TS-1 (67 and 42 %, respectively). A possible reason for this difference could be due to the nuances and rigor in catalyst preparation (Table 3.1).

The reason for the differences between these catalysts in relation to their ability to synthesise H₂O₂ directly may be due to the supports' influence on the size, composition, and morphology of the nanoparticles. It has been well documented that the use of acidic metal precursors has a reduced interaction with acidic supports, such as SiO₂, and do not bind to them because their isoelectric points (pIs) are similar. This means that the charges of the metals and the support's surface was similar, and therefore, were not attractive but repulsive.^{28,29}

Table 3.1. H₂O₂ productivity values and cyclohexanone oxime yields of the 0.33 wt% Au-0.33 wt% Pd/(support) catalysts on different supports (P25 TiO₂, ACS TS-1, SiO₂ and ZrO₂), which were compared to the 2.50 wt% Au-2.50 wt% Pd/P25 TiO₂ catalyst.²⁷

Catalyst	Productivity / mol _{H₂O₂} kg _{cat} ⁻¹ h ⁻¹	Oxime Yield / %
2.50 wt% Au-2.50 wt% Pd/P25 TiO ₂	64 ²⁷	-
0.33 wt% Au-0.33 wt% Pd/ACS TS-1	44	67
0.33 wt% Au-0.33 wt% Pd/ P25 TiO ₂	55	56
0.33 wt% Au-0.33 wt% Pd/SiO ₂	12	62
0.33 wt% Au-0.3 3wt% Pd/ZrO ₂	16	57

Note: Direct H₂O₂ Synthesis conditions - Catalyst (0.01 g), H₂O (2.90 g), CH₃OH (5.60 g), 5% H₂/CO₂ (2.89 MPa), 25% O₂/CO₂ (1.11 MPa), and stirred (0.5 h, 275.15 K, 1200 rpm). Cyclohexanone Ammoximation Conditions - Catalyst (0.075 g) with ACS Materials TS-1 (0.075 g), NH₄HCO₃ (0.32 g), H₂O (7.50 g), (CH₃)₃COH (5.90 g), cyclohexanone (0.20 g), 5 % H₂/N₂ (2.89 MPa) and 25 % O₂/N₂ (1.11 MPa). Heated (353.15 K) and stirred (3.0 h, 800 rpm). Washed with CH₃CH₂OH (6.00 g). Internal Standard (0.15 g).

When the direct H₂O₂ synthesis data was coupled with the cyclohexanone ammoximation reaction data, it became apparent that P25 TiO₂ may not have been the better support to use (H₂ selectivity: 66 %). The direct H₂O₂ synthesis catalyst with the highest H₂ selectivity was the ZrO₂-supported catalyst (H₂ selectivity: 70 %). The

oxime selectivity values for both catalysts were similar because after the NH_2OH had been produced, the synthesis of cyclohexanone oxime would readily occur non-catalytically, with a small number of subsequent undesirable reactions of the cyclohexanone oxime possibly occurring. The cyclohexanone conversion was dependent on the direct synthesis of H_2O_2 by the metal nanoparticles on the support material and the subsequent capture and conversion of H_2O_2 to NH_2OH was dependent on the Ti^{4+} sites of the ACS TS-1 (Table 3.1 and Fig. 3.1).

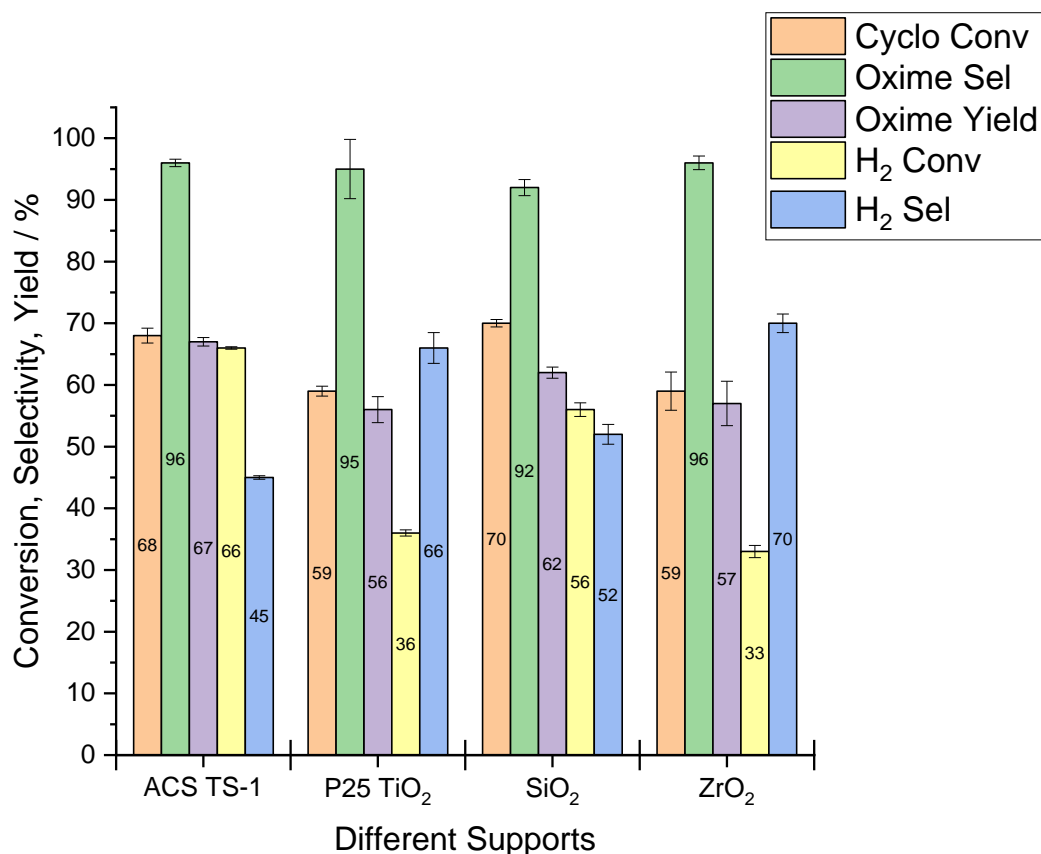


Figure 3.1. Different Support Study using 0.33 wt% Au-0.33 wt% Pd/ACS TS-1 (without additional ACS TS-1), 0.33 wt% Au-0.33 wt% Pd/P25 TiO₂ with ACS TS-1, 0.33 wt% Au-0.33 wt% Pd/SiO₂ with ACS TS-1, and 0.33 wt% Au-0.33 wt% Pd/ZrO₂ with ACS TS-1. Cyclo Conv denotes the conversion of cyclohexanone; Oxime Sel denotes the selectivity towards cyclohexanone oxime; H₂ Conv denotes the conversion of H₂; and H₂ Sel denotes the selectivity of the H₂ utilised to produce the oxime. Cyclohexanone Ammoximation Conditions - Catalyst (0.075 g) with ACS Materials TS-1 (0.075 g), NH₄HCO₃ (0.32 g), H₂O (7.50 g), (CH₃)₃COH (5.90 g), cyclohexanone (0.20 g), 5 % H₂/N₂ (2.89 MPa) and 25 % O₂/N₂ (1.11 MPa). Heated (353.15 K) and stirred (3.0 h, 800 rpm). Washed with CH₃CH₂OH (6.00 g). Internal Standard (0.15 g).

There are a number of competing reactions for cyclohexanone ammoximation utilising *in-situ* direct H₂O₂ synthesis. From the reactants within the ammoximation reaction, the direct synthesis of H₂O₂ or H₂O can occur over the catalyst, followed by

the catalytic hydrogenation or decomposition (collectively known as degradation) of H_2O_2 , which are both in direct competition with the desorption of H_2O_2 and its subsequent capture by TS-1. The rates of each reaction step prior to H_2O_2 capture and conversion by the TS-1 must be less than or equal to the rate of H_2O_2 capture and conversion to obtain higher H_2 selectivity values. Otherwise, the H_2O_2 in excess will go on to degrade (Scheme 3.1, Table 3.1, and Fig. 3.1).

The oxime selectivity values for all the direct H_2O_2 synthesis catalysts were similar (average oxime selectivity for all the catalysts: ~95 %) as these values were solely dependent on the TS-1, regardless of whether it had been used as the support material or not. This meant that the TS-1 had a set rate of H_2O_2 capture and conversion. The rates of direct H_2O_2 synthesis by all the catalysts were most likely higher than the rate of H_2O_2 capture and conversion by the TS-1 because the H_2 selectivity values were still lower than the target H_2 selectivity (*i.e.*, ≥ 95 %). This may have been rectified by a greater amount of TS-1 that could have captured the potential excess of H_2O_2 synthesised by these catalysts. Nevertheless, in the current work, it was assumed that the excess H_2O_2 had degraded, whilst there was the possibility that the excess H_2O_2 synthesised could have remained unreacted in the solvent/reactant mixture or was in the process of being converted into NH_2OH . Likewise, there may have been unreacted NH_2OH present in the solvent/reactant mixture (Table 3.1 and Fig. 3.1).

It was observed in the current work as both the ACS TS-1- and SiO_2 -supported catalysts turned over a similarly high amount of H_2 (H_2 conversion: 66 and 56 %, respectively), with a large proportion of that H_2 not being selectively utilised for the synthesis of cyclohexanone oxime (H_2 selectivity: 45 and 52 %, respectively). Conversely, the P25 TiO_2 - and ZrO_2 -supported catalysts had direct H_2O_2 synthesis rates that were slower than the ACS TS-1- and SiO_2 -supported catalysts as the former pair of catalysts had similar H_2 conversion and selectivity values (H_2 conversion: 36 and 33 %, respectively; H_2 selectivity: 66 and 70 %, respectively) (Table 3.1 and Fig. 3.1).

It was clear that the ACS TS-1-, SiO_2 - and ZrO_2 -supported catalysts could readily degrade H_2O_2 , unlike the P25 TiO_2 -supported catalysts, as both the ACS TS-1- and SiO_2 -supported catalysts produced an excess of H_2O_2 , which was degraded after it was not captured by the saturated TS-1, and both the SiO_2 - and ZrO_2 -supported catalysts gave significantly lower H_2O_2 productivity values (12 and 16 $\text{mol}_{\text{H}_2\text{O}_2} \text{kg}_{\text{cat}}^{-1} \text{h}^{-1}$, respectively). However, as the rate of direct H_2O_2

synthesis of the ZrO₂-supported catalyst was closer to the rate of the capture and conversion of H₂O₂ by the TS-1, akin to the P25 TiO₂-supported catalyst, it could not readily degrade the excess H₂O₂ it had synthesised. This was because the amount of excess H₂O₂ produced by the P25 TiO₂- and ZrO₂ supported catalysts was less than the ACS TS-1- and SiO₂-supported catalysts, which was related to the tandem catalyst system's ability to convert selectively H₂ to cyclohexanone oxime (Table 3.1 and Fig. 3.1).

The rationale for the ACS TS-1-supported catalyst's results can be explained by the higher rate of direct H₂O₂ synthesis compared to its rate of H₂O₂ degradation and its rate of H₂O₂ capture and conversion to NH₂OH (as there was no additional TS-1 for this catalyst's tests). The difference in reaction rates explained this catalyst's higher H₂O₂ productivity (44 mol_{H₂O₂} kg_{cat}⁻¹ h⁻¹) compared to the SiO₂- and ZrO₂-supported catalysts, but the ACS TS-1-supported catalyst had similar cyclohexanone ammoximation results to the SiO₂-supported catalyst (Table 3.1 and Fig. 3.1).

However, because the rate of H₂O₂ degradation by the ACS TS-1-supported catalyst was lower than the SiO₂- and ZrO₂-supported catalysts, the reason for the reduced H₂ selectivity in the cyclohexanone ammoximation reaction was most likely due to the increased H₂ conversion to H₂O₂ that would not have been captured by the already saturated TS-1. Therefore, the excess H₂O₂ went on to degrade. A possible solution to resolve the decreased H₂ selectivity that arises from excess H₂O₂ degrading could be to add a greater amount of TS-1 to capture the H₂O₂ (Table 3.1 and Fig. 3.1).

For the P25 TiO₂-supported catalyst, the rate of H₂ turnover to cyclohexanone oxime was similar to the ZrO₂-supported catalyst (H₂ conversion: 36 and 33 %, respectively; H₂ selectivity: 66 and 70 %, respectively). However, the reason for the difference in H₂O₂ productivity values was mostly likely due to the decreased number of degradation sites on the P25 TiO₂-supported catalyst compared to the ZrO₂-supported catalyst (55 and 16 mol_{H₂O₂} kg_{cat}⁻¹ h⁻¹, respectively) (Table 3.1 and Fig. 3.1).

Nevertheless, the H₂O₂ hydrogenation and decomposition data as well as the reaction rates data for the direct H₂O₂ synthesis catalysts and the TS-1 would be required to prove or disprove the hypotheses proposed above. The data regarding the rate of H₂O₂ turnover by the TS-1 could be acquired by removing the *in-situ* direct H₂O₂ synthesis reaction. The catalytic reaction performed by the TS-1 could be tested

and a rate determined using a set concentration of H₂O₂, without the direct H₂O₂ synthesis catalyst. Additionally, the unreacted H₂O₂ and NH₂OH would also need to be determined to ensure whether the H₂ selectivity based on oxime was accurate as both these intermediate chemicals are used in these catalytic reaction steps to produce cyclohexanone oxime (Scheme 3.1, Table 3.1, and Fig. 3.1).

3.2.1.2. Catalyst Characterisation

Some explanations of the catalytic results may be drawn from the characterisation data obtained for each catalyst. Analyses using Field Emission Gun-Scanning Electron Microscopy (FEG-SEM) and subsequent Energy Dispersive X-ray (EDX) spectroscopy were completed upon the 0.33 wt% Au-0.33 wt% Pd/P25 TiO₂. The detection of C was ignored due to the supporting plate comprising partially of C as well as it being detected on the surface of the catalyst. Even under vacuum, C is difficult to remove from within the analyser (Table 3.2 and Fig. 3.2).

TEM could not detect the range of smaller nanoparticles (<2 nm in length), but an exceptionally large nanoparticle was detected (215 nm in length) using FEG-SEM-EDX. This large nanoparticle was mainly comprised of Ti (from the support) and Au, with an atom concentration percentage ratio for Au/Pd of 37.64. A particle size distribution (PSD) was created from the images collected for the 0.33 wt% Au-0.33 wt% Pd/P25 TiO₂ catalyst. Most of the particles from this distribution had a calculated length of 3-8 nm, however, larger particles were observed (>100 nm in length). The mean particle size and standard deviation from this distribution were determined (6.8 and 17.8 nm, respectively) (Table 3.2 and Fig. 3.2).

Table 3.2. Quantification from EDX Spectra Analysis from of the large nanoparticle in Fig. 3.2a and b from the 0.33 wt% Au-0.33 wt% Pd/P25 TiO₂ catalyst.

Element	Line Type	Atom Conc. %
O	K series	88.35
Ti	K series	7.40
Pd	L series	0.11
Au	L series	4.14

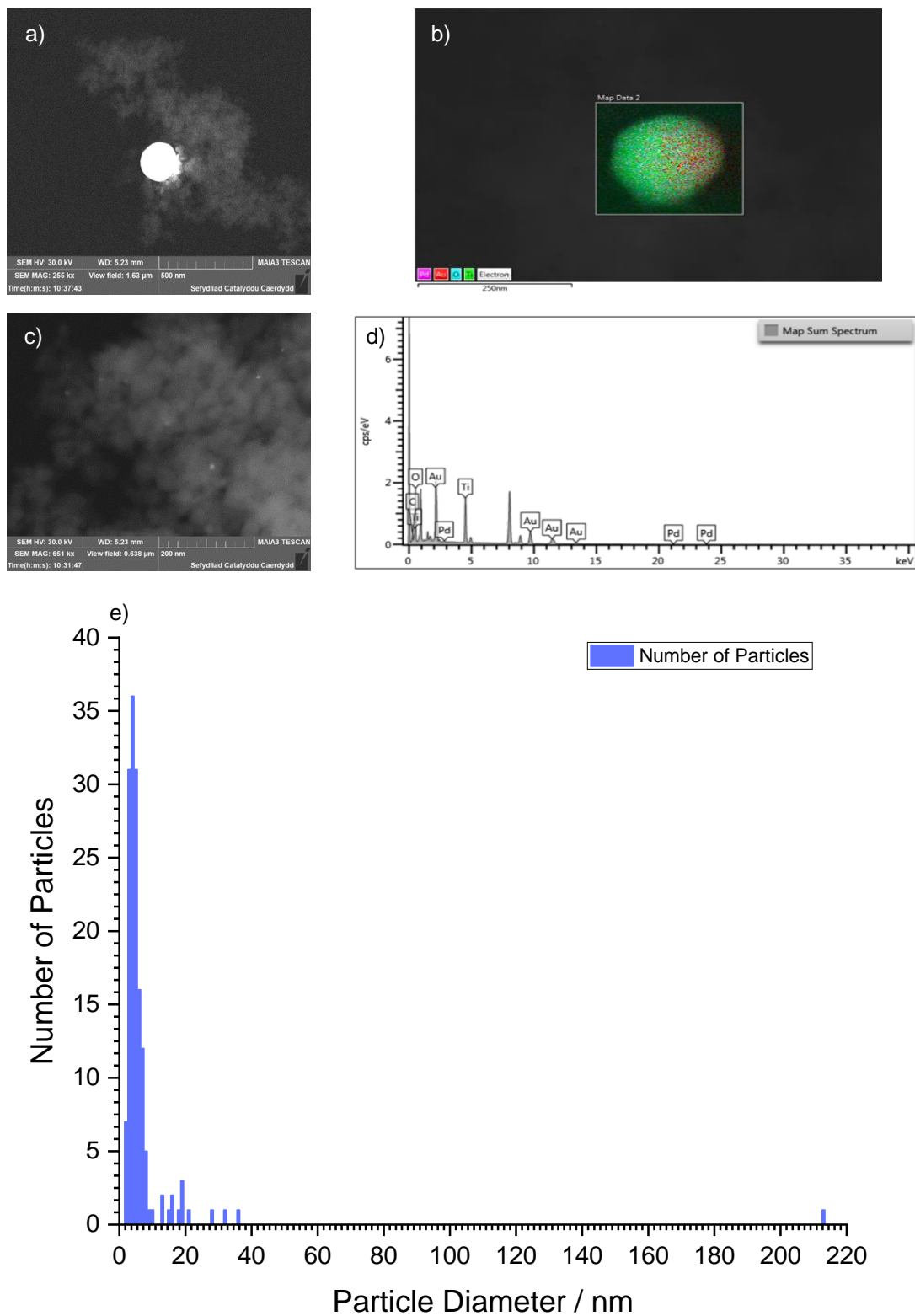


Figure 3.2. FEG-SEM sample image of 0.33 wt% Au-0.33 wt% Pd/P25 TiO₂ catalyst, where **a)** is displaying the large nanoparticle, **b)** is the EDX map of the large nanoparticle in Fig. 3.2a (Ti – green, O – blue, Au – red, Pd – pink), **c)** is displaying the nanoparticles, and **d)** is the EDX Spectra of Fig. 3.2a, and **e)** is the PSD for the 0.33 wt% Au-0.33 wt% Pd/P25 TiO₂ catalyst from the FEG-SEM (30 images, 154 particles, Fig. A3.1), which shows the whole distribution. cps denotes counts per second.

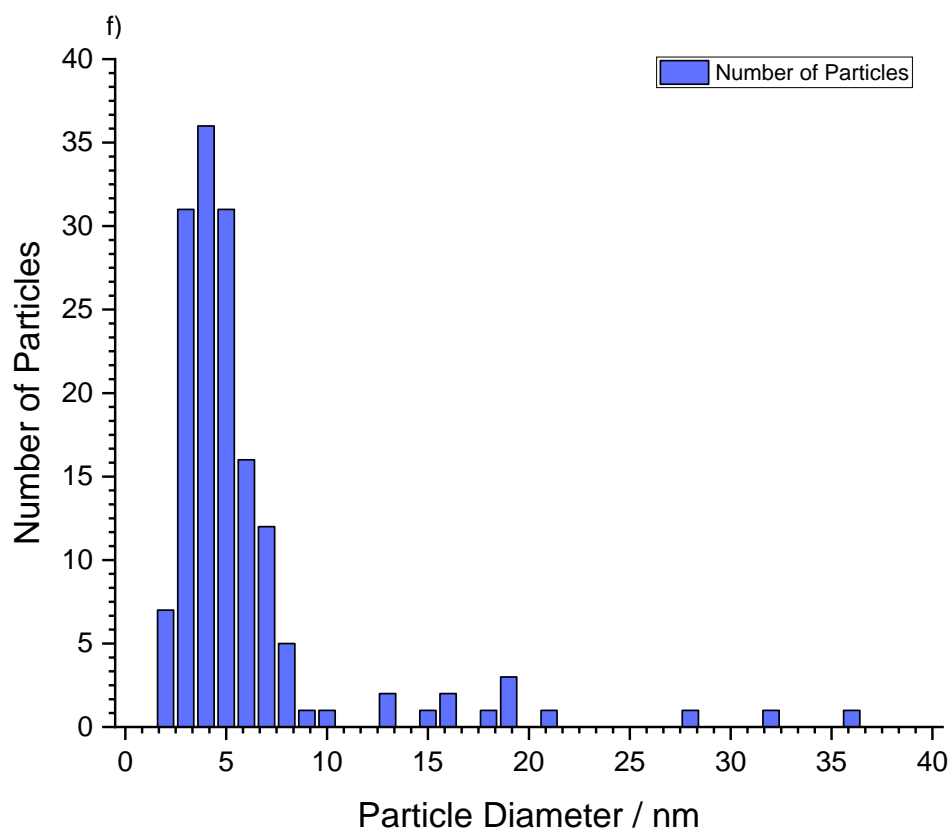


Figure 3.2f. PSD for the 0.33 wt% Au-0.33 wt% Pd/P25 TiO₂ catalyst from the FEG-SEM (30 images, 154 particles, Fig. A3.1), which shows the mode of the distribution.

As with most of the PSDs in the current work, the reason for such a large deviation was due to the small number of larger nanoparticles. Additionally, EDX analyses displayed that the larger particles were Au-rich by a large margin (Au/Pd atom conc.% ratio: 37.64). The factors that most likely attributed to this agglomeration were the Au-Au affinity and the metal atoms' ability to move during calcination (Table 3.2 and Fig. 3.2 e and f).

Using SEM-EDX, the 0.33 wt% Au-0.33 wt% Pd/P25 TiO₂ catalyst showed a homogeneous dispersion of the metals across the support. However, when combining the FEG-SEM-EDX data and SEM-EDX, it became apparent that there may have been some degree of dispersion of the metals as atomic metal and as nanoparticles. The grouping of Pd suggested the existence of large particles and the detection of Au was over most of the sample area. This dispersion was previously observed in the 2.50 wt% Au-2.50 wt% Pd/P25 TiO₂ catalyst in the studies of Edwards *et al.*^{19,27} and of Moreno *et al.*³⁰ (Fig. 3.2 and 3.3).

Nevertheless, the scale of the sample area used for the SEM-EDX was much larger than the FEG-SEM-EDX analysis for the P25 TiO₂-supported catalyst. These points in Fig. 3.3 may not have necessarily been atomic metal, but smaller nanoparticles. Further investigation would be required to confirm this hypothesis (Fig. 3.2 and 3.3).

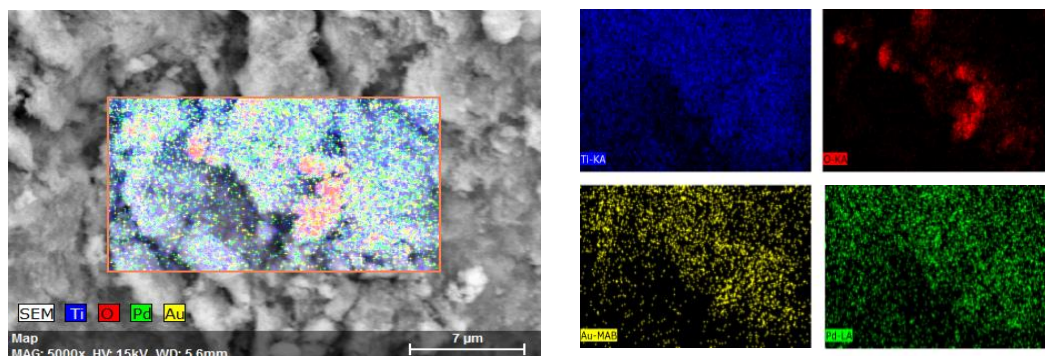


Figure 3.3. SEM-EDX images of the 0.33 wt% Au-0.33 wt% Pd/P25 TiO₂ with individual elemental EDX maps (Ti – blue, O – red, Au – yellow, Pd – green).

Unlike the P25 TiO₂-supported catalyst, the 0.33 wt% Au-0.33 wt% Pd/ZrO₂ catalyst had no nanoparticles from the sample images that were larger than 20 nm in length (Fig. 3.4c). This could have been due to the surface area or the isoelectric point (pI) of the surface relative to the metal precursors' pIs.^{28,29,31} A study by Zhang *et al.*³² demonstrated that the size of the support nanoparticles affected the size of the metal nanoparticles. However, the differences between Zhang *et al.*'s work³² and the current work were that the catalyst preparation method was deposition-precipitation (DP) and used Au only; not bi-metallic AuPd catalysts synthesised *via* the C_{IM} preparation method (Table 3.3 and Fig. 3.4).

Table 3.3. Quantification from EDX Spectra Analysis of the nanoparticles in Fig. 3.4a from the 0.33 wt% Au-0.33 wt% Pd/ZrO₂ catalyst.

Element	Line Type	Atom Conc. %
C	K series	43.00
O	K series	46.19
Zr	K series	10.40
Pd	L series	0.21
Au	L series	0.20

From the PSD for the ZrO₂-supported catalyst, the average length of the nanoparticles was 12.3 nm with a standard deviation of 2.2 nm. It was observed that the nanoparticles larger than 8 nm in length also had a slightly higher atom concentration percentage of Pd than Au (Au/Pd atom conc.% ratio: 0.95) but were approximately equal. This trait was dissimilar to that of the P25 TiO₂-supported catalyst as the Au/Pd atom concentration percentage ratio for the ZrO₂-supported catalyst was significantly lower. However, the EDX analysis on the P25 TiO₂-supported catalyst was completed on a significantly larger nanoparticle, thus, a direct comparison cannot be made (Table 3.3 and Fig. 3.4).

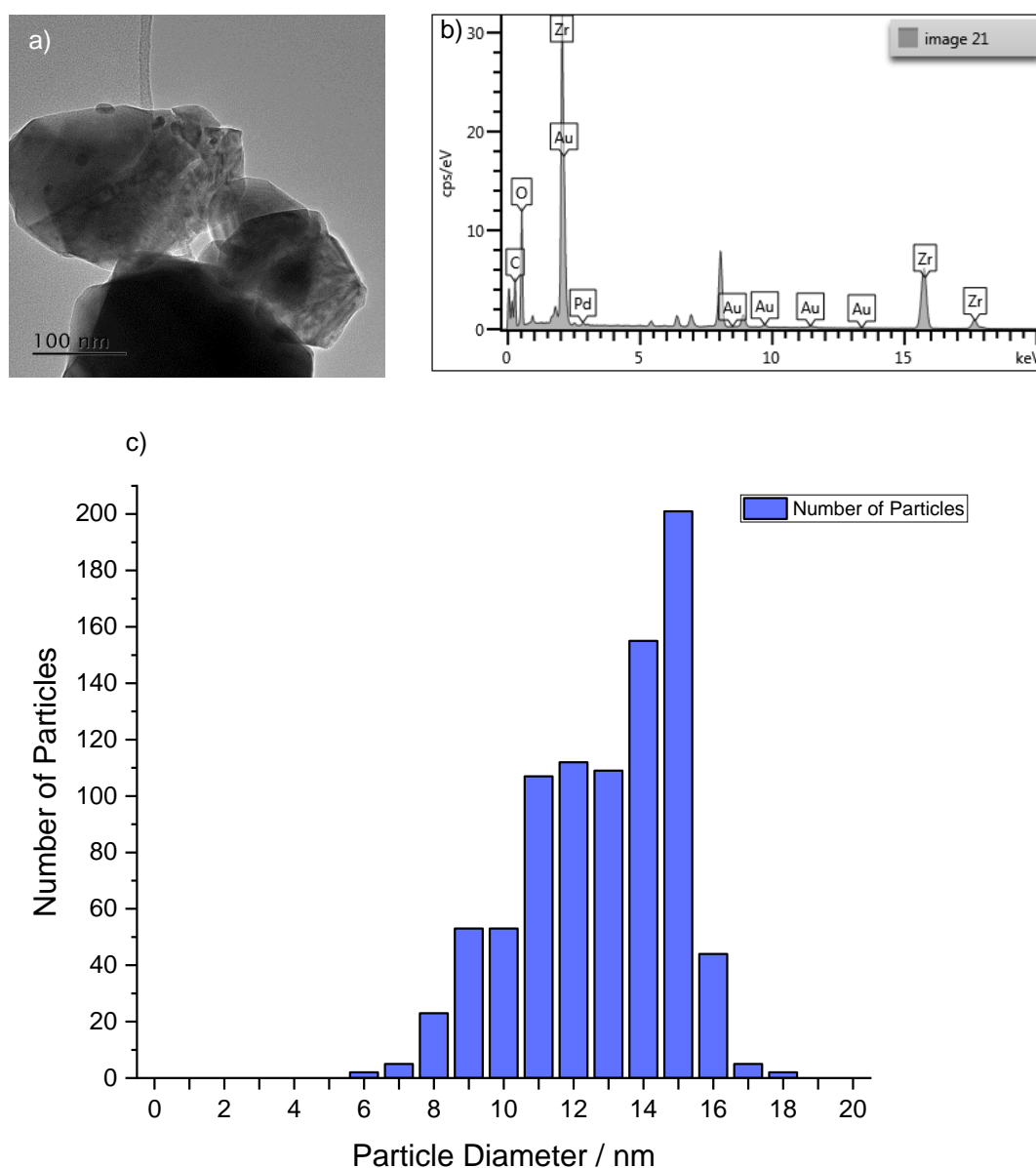


Figure 3.4. FEG-SEM sample image of 0.33 wt% Au-0.33 wt% Pd/ZrO₂ catalyst, where **a)** is displaying the nanoparticles, **b)** is the EDX Spectra of Fig. 3.4a, and **c)** is the PSD for the 0.33 wt% Au-0.33 wt% Pd/ZrO₂ catalyst from the FEG-SEM (12 images, 871 particles, Fig. A3.5), which shows the whole distribution. cps denotes counts per second.

From the current work, there were a limited number of nanoparticles that had a length greater than 16 nm. One possible explanation for this phenomenon could be the metal-support interaction (MSI). The Strong MSI (SMSI) is known to prevent sintering of nanoparticles.^{33–39} Another explanation could be that the morphology of the ZrO₂ support may have dictated the growth of the nanoparticles as the surface structure of the support may be preventing the nanoparticles' growth. Further investigation would be required to determine this phenomenon (Fig. 3.4).

Similar observations were drawn for the second sample image of the ZrO₂-supported catalyst. However, there was a small difference in the amount of the metals (Au increased by 0.70 atom conc.%; Pd increased by 0.14 atom conc.%) as well as their atom concentration percentage ratio (Au/Pd atom conc.% ratio: 0.77). The EDX analyses demonstrated that these particles did not strictly adhere to a set ratio of metals and did vary from particle to particle (Table 3.4 and Fig. 3.5).

Equally, the other elements and their atom concentration percentages must be considered. For example, the key differences between these two EDX analyses for the ZrO₂-supported catalyst was that Si was not present in the first analysis and the atom concentration percentages of O decreased and Zr increased in the second analysis. The appearance of Si can be explained by the window on the detector within the SEM instrumentation (Table 3.4 and Fig. 3.5).

Table 3.4. Quantification from EDX Spectra Analysis of the nanoparticles in Fig. 3.5a from the 0.33 wt% Au-0.33 wt% Pd/ZrO₂ catalyst.

Element	Line Type	Atom Conc.%
C	K series	47.34
O	K series	35.05
Si	K series	3.43
Zr	K series	13.55
Pd	L series	0.35
Au	L series	0.27

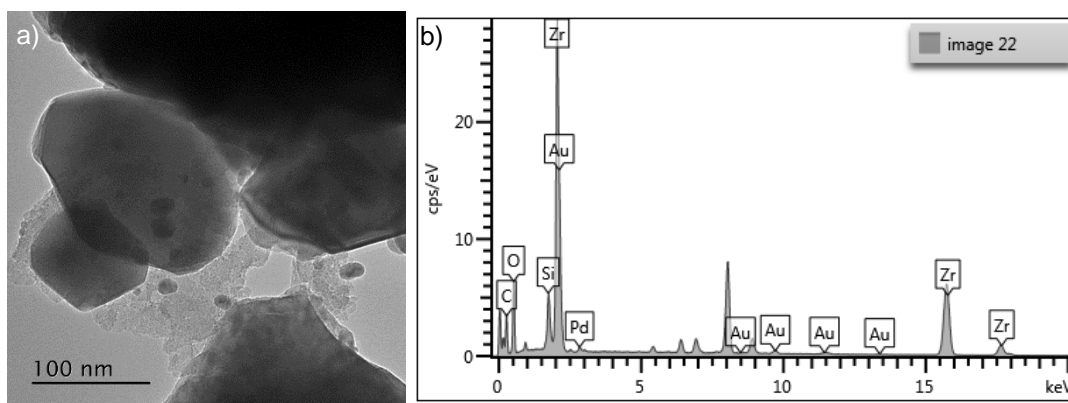


Figure 3.5. FEG-SEM sample image of 0.33 wt% Au-0.33 wt% Pd/ZrO₂ catalyst, where **a)** is displaying the nanoparticles, and **b)** is the EDX Spectra of Fig. 3.5a. cps denotes counts per second.

In relation to the atom concentration percentages of the elements, similar amounts of C, O and Zr were observed in both the first and last EDX analyses. However, there was a large decrease in the amount of Pd in the final analysis and gave a ratio of Au/Pd as 5.00 (Tables 3.3 and 3.5, and Fig. 3.4 and 3.6).

Table 3.5. Quantification from EDX Spectra Analysis of the nanoparticles in Fig. 3.6a from the 0.33 wt% Au-0.33 wt% Pd/ZrO₂ catalyst.

Element	Line Type	Atom Conc. %
C	K series	39.14
O	K series	50.14
Zr	K series	10.49
Pd	L series	0.04
Au	L series	0.20

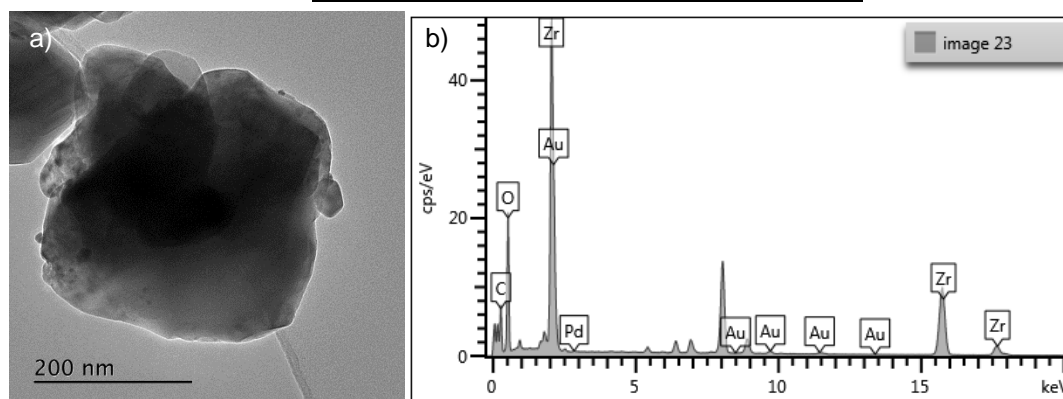


Figure 3.6. FEG-SEM sample image of 0.33 wt% Au-0.33 wt% Pd/ZrO₂ catalyst, where **a)** is displaying the nanoparticles, and **b)** is the EDX Spectra of Fig. 3.6a. cps denotes counts per second.

More of the “larger” nanoparticles within the PSD for the ZrO₂-supported catalyst were observed in the final sample. Larger nanoparticles have been previously attributed to having a greater proportion of Au than Pd, and this phenomenon was supported by the current work.^{40–42} This was akin to the P25 TiO₂-supported catalyst, but the size of the “larger” nanoparticles was different for these different catalysts. The P25 TiO₂-supported catalyst had nanoparticles larger than 20 nm in length, which was not observed for the ZrO₂-supported catalyst. However, it cannot be assumed that nanoparticles larger than 18 nm in length were not present on the ZrO₂-supported catalyst as SEM is a sampling technique and may not have detected these nanoparticles. Overall, the EDX analyses for the ZrO₂-supported catalyst revealed that the atom concentration percentages of Au and Pd in the areas analysed were relatively similar to each other. Only in the last analysis was a significantly smaller quantity of Pd detected. (Tables 3.3-3.5, and Fig. 3.4-3.6).

In the first analysis of the SiO₂-supported catalyst, large nanoparticles were observed and EDX analysis on the lower nanoparticle in Fig. 3.7a (red ring) showed a smaller proportion of Au to Pd (Au/Pd atom conc.% ratio: 1.76) not previously seen for the other catalysts. Again, C was observed from the grid, but an interesting finding was the detection of Cl and Ca. The presence of Cl was mostly likely due to the metal chloride precursors used in the catalyst preparation technique. The presence of Ca could be due to a small impurity from the commercially purchased SiO₂ (Table 3.6 and Fig. 3.7).

From the PSD, the mean particle size and standard deviation from this distribution were determined (12.8 and 14.7 nm, respectively). Akin to the previously discussed catalysts, most of the nanoparticles' lengths were observed between 4-30 nm. Similar to the P25 TiO₂-supported catalyst and unlike the ZrO₂-supported catalyst, nanoparticles with a length greater than 20 nm were observed for the SiO₂-supported catalyst. This demonstrated that a metal oxide (MO_x) and non-MO_x support had a similar range of nanoparticle lengths (Fig. 3.2-3.7).

Table 3.6. Quantification from EDX Spectra Analysis of the large nanoparticle in Fig. 3.7a (red ring) from the 0.33 wt% Au-0.33 wt% Pd/SiO₂ catalyst.

Element	Line Type	Atom Conc.%
C	K series	17.98
O	K series	62.56
Si	K series	18.29
Cl	K series	0.16
Ca	K series	0.07
Pd	L series	0.34
Au	L series	0.60

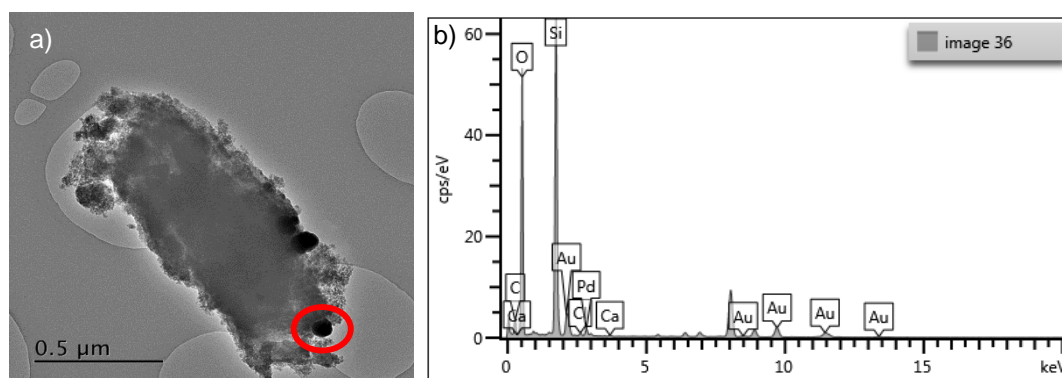


Figure 3.7. FEG-SEM sample image of 0.33 wt% Au-0.33 wt% Pd/SiO₂ catalyst, where **a)** is displaying the large nanoparticle (red ring), and **b)** is the EDX Spectra of the large nanoparticle in Fig. 3.7a (red ring). cps denotes counts per second.

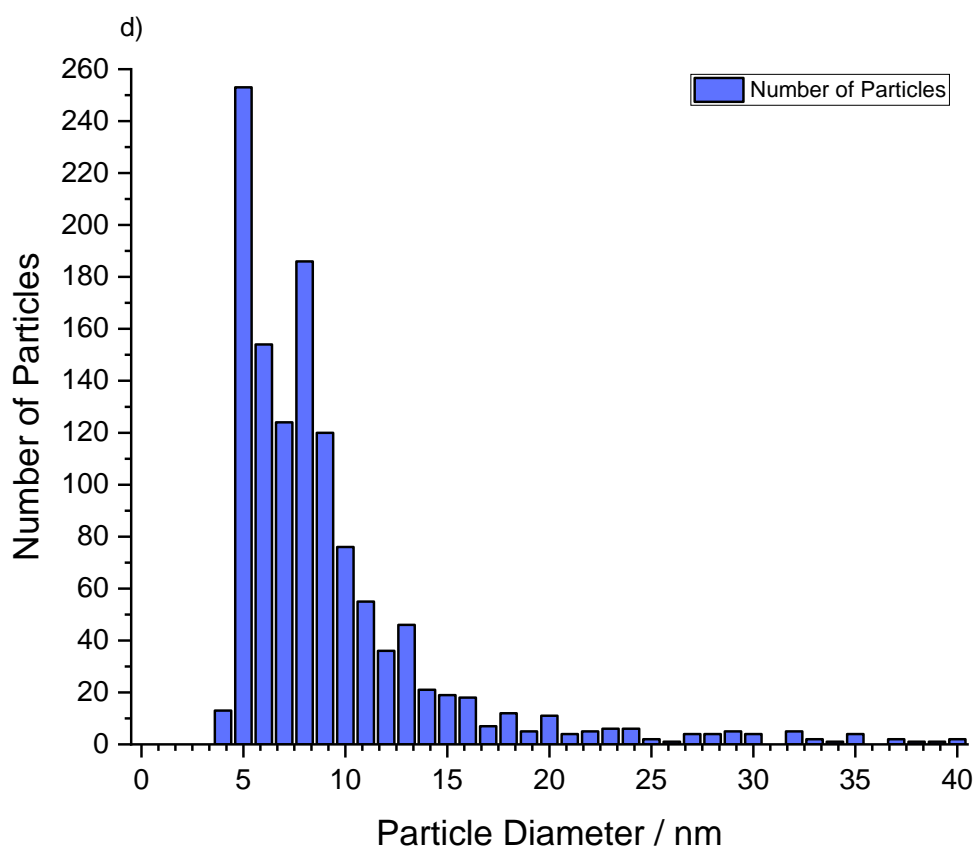
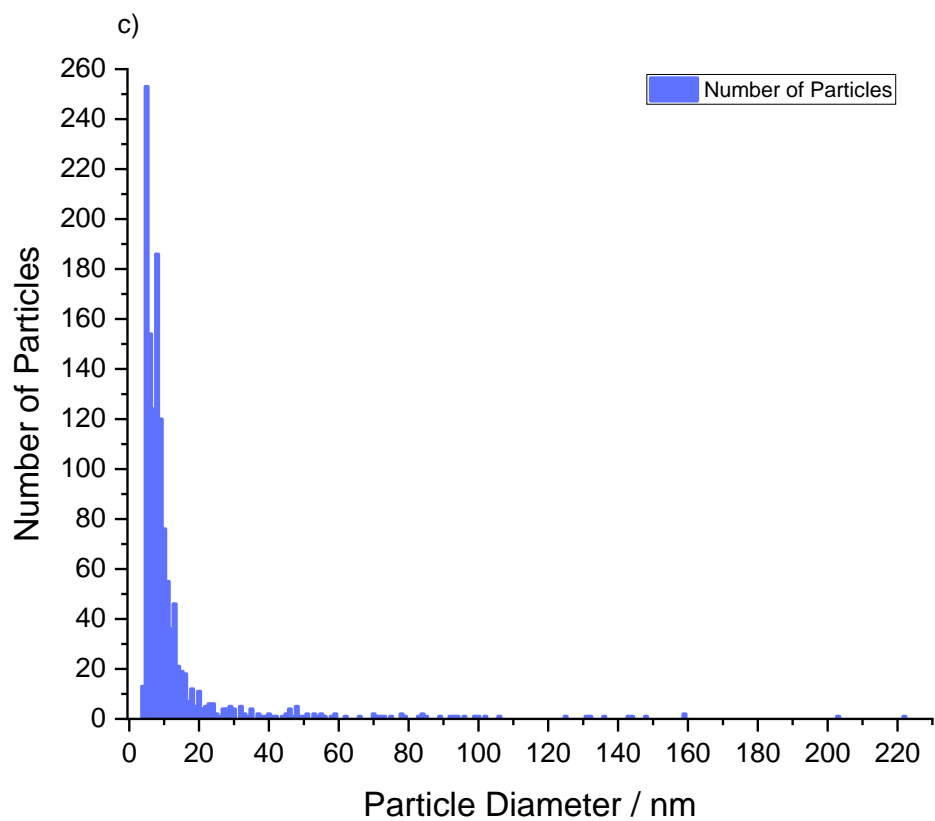


Figure 3.7. PSD for the 0.33 wt% Au-0.33 wt% Pd/SiO₂ catalyst from the FEG-SEM (9 images, 1278 particles, Fig. A3.6), where **c)** shows the whole distribution and **d)** shows the mode of the distribution.

In the second EDX analysis performed on the SiO₂-supported catalyst, the upper right nanoparticle in Fig. 3.8a (blue ring) was observed to contain an atom concentration percentage of 7.14 % for Au, which was approximately 12-fold higher than the first EDX analysis. The atom concentration percentage for Pd increased by ~330 % between the first and second EDX analyses, which was a result of the difference in the size of the nanoparticles analysed (~50 and ~100 nm in length, respectively). These results seemed reasonable as the larger nanoparticle observed in the second EDX analysis would be expected to contain a greater amount of both Au and Pd than the smaller nanoparticle observed in the first EDX analysis. This gave a ratio for Au/Pd of 6.38, which was significantly higher than the ZrO₂-supported catalyst (Tables 3.3-3.5 and 3.7).

There was a small decrease in the atom concentration percentages for Au and a marked decrease for Pd between the EDX analyses for the upper right nanoparticle and the lower right nanoparticle in Fig. 3.8a (blue and red rings, respectively). However, the lower right nanoparticle in Fig. 3.8a was still Au-rich (Au/Pd atom conc.% ratio: 3.54), which was likely because of the Au's affinity for itself and the metal atoms' ability to move during calcination. By atom concentration, the amount of O and Si significantly increased between the analyses. Nevertheless, the atom concentration percentages of these elements were not as high as the first EDX analysis (Tables 3.6-3.8).

Table 3.7. Quantification from EDX Spectra Analysis of the large nanoparticle in Fig. 3.8a (blue ring) from the 0.33 wt% Au-0.33 wt% Pd/SiO₂ catalyst.

Element	Line Type	Atom Conc. %
C	K series	64.25
O	K series	22.93
Si	K series	4.18
Ti	K series	0.39
Pd	L series	1.12
Au	L series	7.14

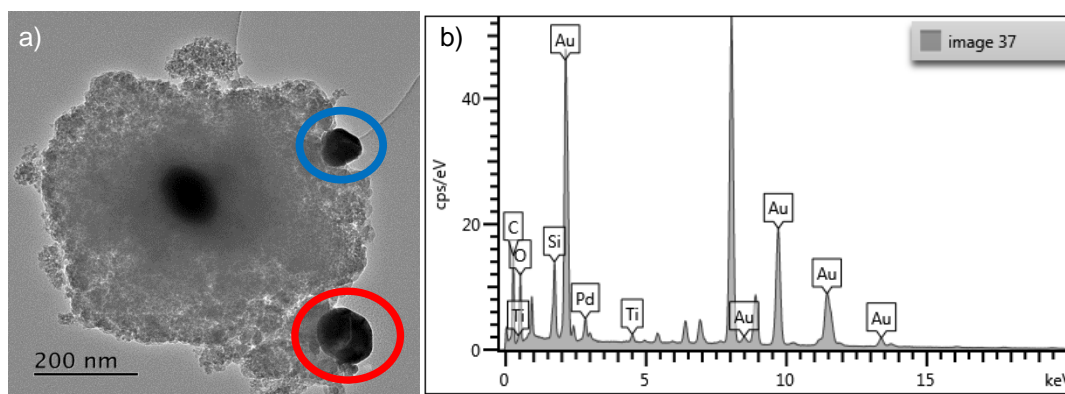


Figure 3.8. FEG-SEM sample image of the 0.33 wt% Au-0.33 wt% Pd/SiO₂ catalyst, where **a)** is displaying two large nanoparticles (blue and red rings), and **b)** is the EDX Spectra of the large nanoparticle in Fig. 3.8a (blue ring). cps denotes counts per second.

Additionally, there also seemed to be a line defect or fracture in the last nanoparticle with two different levels of the lower right nanoparticle visible in Fig 3.8a (red ring). This could have been from the nanoparticle breaking as it was handled, shearing part of the nanoparticle off. Another possibility could be that it had formed that way, however, this seemed unlikely as growth of bi-metallic AuPd nanoparticles *via* the C_{IM} catalyst preparation method usually produces spherical or hemispherical particles (Fig. 3.8).^{15,24,43,44}

Table 3.8. Quantification from EDX Spectra Analysis of the large nanoparticle in Fig. 3.8a (red ring) from the 0.33 wt% Au-0.33 wt% Pd/SiO₂ catalyst.

Element	Line Type	Atom Conc.%
C	K series	39.83
O	K series	45.09
Si	K series	11.12
Pd	L series	0.87
Au	L series	3.08

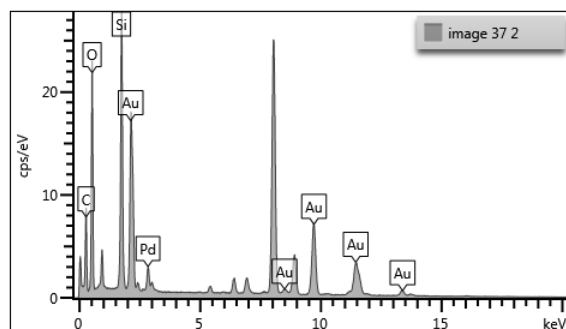


Figure 3.9. EDX Spectra of the large nanoparticle in Fig. 3.8a (red ring). cps denotes counts per second.

To conclude, most of the nanoparticles for the SiO₂-supported catalyst were moderately sized (4-30 nm) and the larger nanoparticles were more Au-rich. The latter trait was similarly observed for both the P25 TiO₂- and ZrO₂-supported catalysts. This was observed to a lesser extent for the ZrO₂-supported catalyst as two EDX analyses showed a more even distribution of the metals within their nanoparticles, but still gave Au/Pd atom concentration percentage ratios greater than 1.00. However, the nanoparticles analysed *via* FEG-SEM-EDX for the P25 TiO₂- and SiO₂-supported catalysts were significantly larger than those of the ZrO₂-supported catalyst (+80 nm difference in length) (Tables 3.2-3.8, and Fig. 3.2-3.9).

The ACS TS-1-supported catalyst was also analysed *via* FEG-SEM-EDX, and a PSD was subsequently created. Initially, large nanoparticles (>100 nm in length) were investigated followed by study of smaller nanoparticles (<20 nm in length). The ACS TS-1 had undergone significant structural changes as they were unlike the uncalcined support.⁴⁵ New “cloud-like” structures had been created as a result of catalyst preparation and subsequent calcination. From the first EDX analysis of the large nanoparticle in Fig. 3.10a (red ring), it was determined that there was a much larger amount of Au than Pd, not unlike the SiO₂- and ZrO₂-supported catalysts. The Au/Pd atom concentration percentage ratio was 6.07. Only small amounts of O and Ti were detected (3.70 and 0.10 atom conc.%, respectively), with no Si detected. The amount of Ti should have been low as the Si/Ti ratio in the ACS TS-1 is ~30.00. As no Si was detected, it may have been possible that during the analysis that only a small portion of the support was captured (Table 3.9 and Fig. 3.10).

The PSD for the ASC TS-1 supported catalyst revealed that it was similar to the P25 TiO₂- and SiO₂-supported catalysts as the size of the nanoparticles ranged from 3-110 nm in length. The average length of the nanoparticles was 6.2 nm, with a standard deviation of 9.1 nm. This meant that this catalyst provided the smallest

average length of the nanoparticles of all the catalysts from the Different Support Study. Again, the nanoparticles below 5 nm in length exhibited by these three catalysts demonstrated that these smaller nanoparticles were responsible more for the direct synthesis of H₂O₂ as opposed to the nanoparticles above 5 nm in length that appeared to be more responsible for its degradation (Tables 3.1, 3.2 and 3.7-3.9, and Fig. 3.1, 3.2, 3.3 and 3.8-3.10).

Table 3.9. Quantification from EDX Spectra Analysis of the large nanoparticle in Fig. 3.10a (red ring) from the 0.33 wt% Au-0.33 wt% Pd/ACS TS-1 catalyst.

Element	Line Type	Atom Conc. %
C	K series	85.53
O	K series	3.70
Ti	K series	0.10
Pd	L series	1.51
Au	L series	9.16

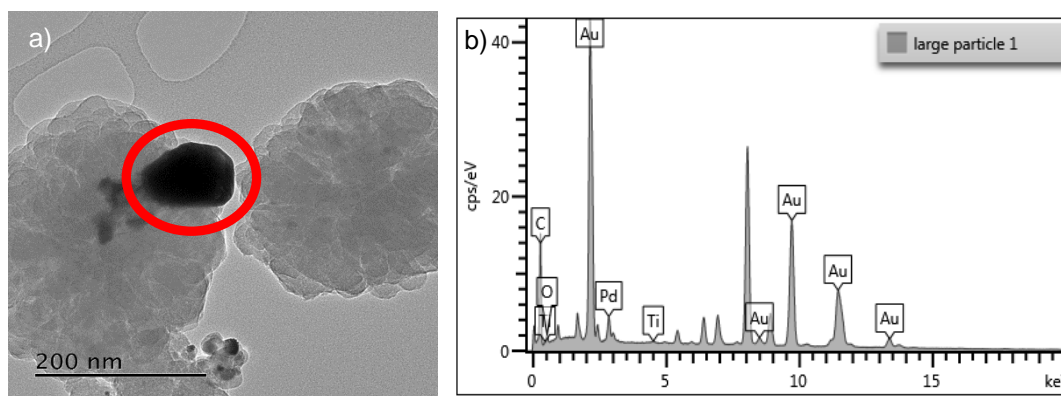


Figure 3.10. FEG-SEM sample image of 0.33 wt% Au-0.33 wt% Pd/ACS TS-1 catalyst, where **a)** is displaying the large nanoparticle (red ring), and **b)** is the EDX Spectra of the large nanoparticle in Fig. 3.10a (red ring). cps denotes counts per second.

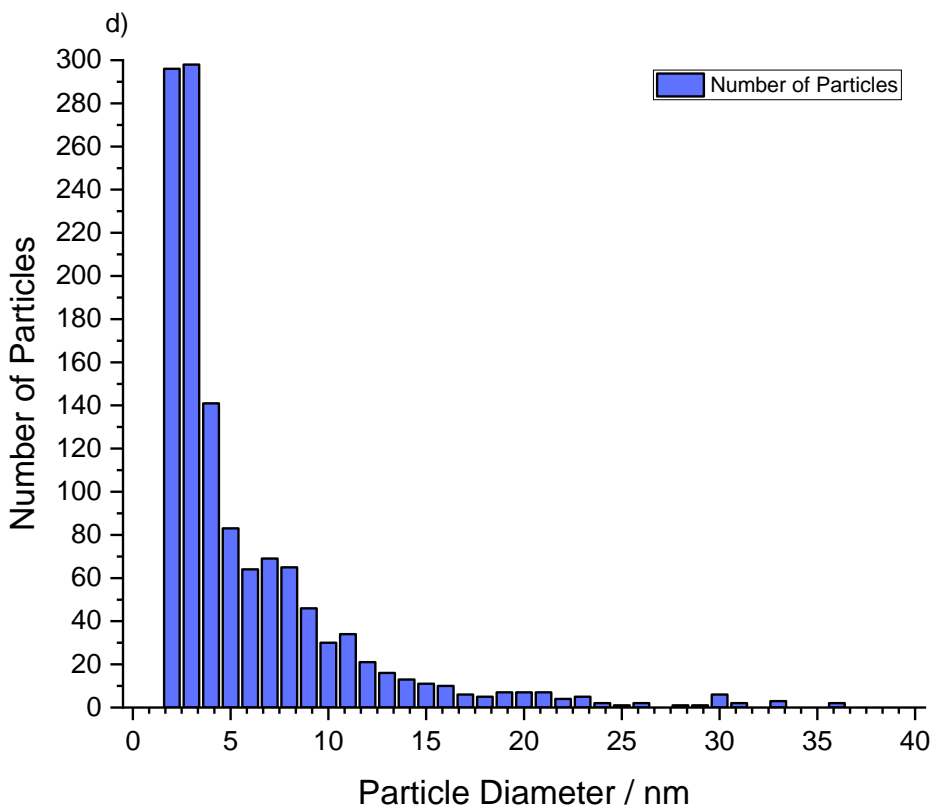
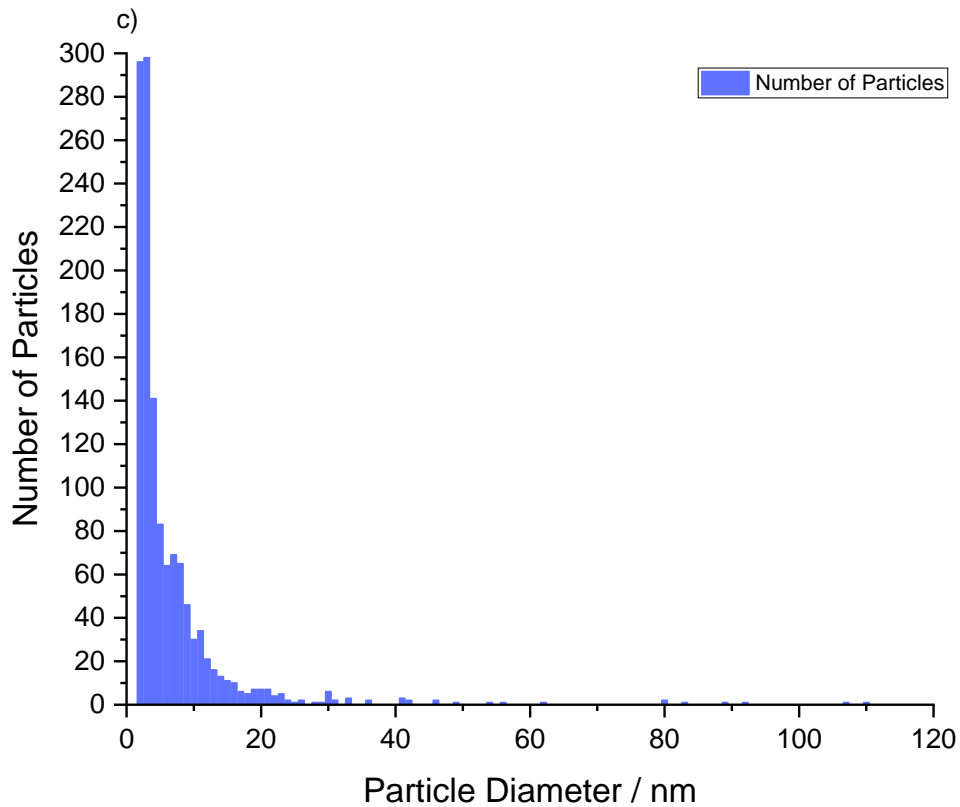


Figure 3.10. PSDs for the 0.33 wt% Au-0.33 wt% Pd/ACS TS-1 catalyst from the FEG-SEM (9 images, 1278 particles, Fig. A3.7), where **c)** shows the whole distribution, and **d)** shows the mode of the distribution.

In the second EDX analysis, another large nanoparticle was detected in Fig. 3.11a (red ring). Interestingly, this nanoparticle appeared to be multifaceted, with an additional level indicated by the lighter area observed. As previously discussed, this could have been due to the nanoparticle cracking and shearing part of itself off or from the way the nanoparticle grew during the catalyst preparation (Fig. 3.11a, red ring).

Table 3.10. Quantification from EDX Spectra Analysis of the large nanoparticle in Fig. 3.11a (red ring) from the 0.33 wt% Au-0.33 wt% Pd/ACS TS-1 catalyst.

Element	Line Type	Atom Conc. %
C	K series	69.96
O	K series	16.78
Si	K series	3.94
Ti	K series	0.09
Pd	L series	2.02
Au	L series	7.22

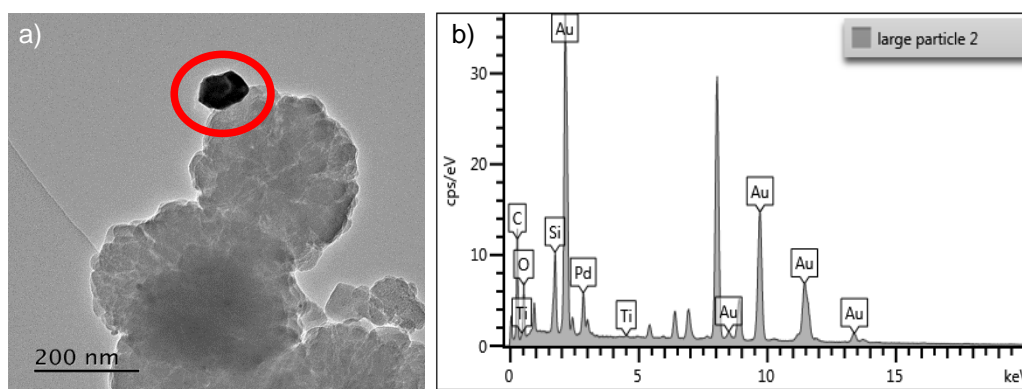


Figure 3.11. FEG-SEM sample image of the 0.33 wt% Au-0.33 wt% Pd/ACS TS-1 catalyst, where **a)** is displaying the large nanoparticle (red ring), and **b)** is the EDX Spectra of the large nanoparticle in Fig. 3.11a (red ring). cps denotes counts per second.

From the spectra and elemental analysis, the presence of Si from the support was detected, as well as O in a slightly larger amount. Again, Ti was not observed to be significant (<0.10 atom conc.%). The amount of Pd had increased slightly (0.51 atom conc.%) and the atom concentration percentage for Au had decreased by

more than half, thus, a significant impact was seen for the Au/Pd ratio in the second analysis (3.57) compared to the first (Table 3.10 and Fig. 3.11).

The third FEG-SEM-EDX analysis was of another large nanoparticle. A larger amount of Si and Ti was detected and more representative of the support. The amount of Au observed had decreased compared to the second analysis by more than half. The atom concentration percentage of Pd had decreased slightly (by 1.09 atom conc.%). The ratio of Au/Pd for this nanoparticle was 2.77, having decreased between the second and third EDX analyses (Tables 3.10 and 3.11, and Fig. 3.11 and 3.12).

Table 3.11. Quantification from EDX Spectra Analysis of the large nanoparticle in Fig. 3.12a (red ring) from the 0.33 wt% Au-0.33 wt% Pd/ACS TS-1 catalyst.

Element	Line Type	Atom Conc.%
C	K series	41.11
O	K series	43.21
Si	K series	11.95
Ti	K series	0.21
Pd	L series	0.93
Au	L series	2.58

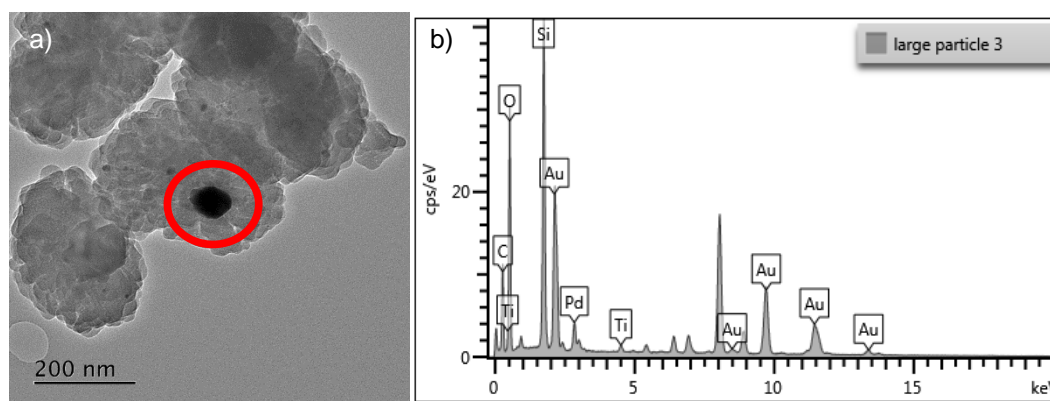


Figure 3.12. FEG-SEM sample image of the 0.33 wt% Au-0.33 wt% Pd/ACS TS-1 catalyst, where **a)** is displaying the large nanoparticle (red ring), and **b)** is the EDX Spectra of the large nanoparticle in Fig. 3.12a (red ring). cps denotes counts per second.

Overall, the large nanoparticles of the ACS TS-1-supported catalyst exhibited similarities to the larger nanoparticles shown in the other catalysts because they all

demonstrated a Au-rich composition. During the catalyst preparation process, the metal atoms will seed onto the support material. Intrinsically, Au has a natural affinity for itself, thus, more Au atoms will be drawn to the Au seed and begin to grow. The metals also have some capacity to move over the support surface and agglomerate during the subsequent heat treatment (Tables 3.9-3.11).

Other analyses were performed on areas of the ACS TS-1-supported catalyst, where smaller nanoparticles (<20 nm in length) were detected. The first analysis detected over half of the atom concentration as O (largely from the support). Almost double the amount of Si/Ti was detected (Si/Ti atom conc.% ratio: 58.56) compared to the stated amount by ACS Materials (Si/Ti atom conc.% ratio: ~30.00). This could be due to the sample area containing more SiO₂ units (Table 3.12 and Fig. 3.13)

The smaller nanoparticles exhibited significantly decreased and more equal amounts of Au and Pd, with an atom concentration percentage ratio for Au/Pd of 1.25. Although Au was still the major constituent, it was not to the same extent as the large nanoparticles (Tables 3.9-3.12).

Table 3.12. Quantification from EDX Spectra Analysis of the nanoparticles in Fig. 3.13a from the 0.33 wt% Au-0.33 wt% Pd/ACS TS-1 catalyst.

Element	Line Type	Atom Conc.%
C	K series	31.75
O	K series	52.08
Si	K series	15.81
Ti	K series	0.27
Pd	L series	0.04
Au	L series	0.05

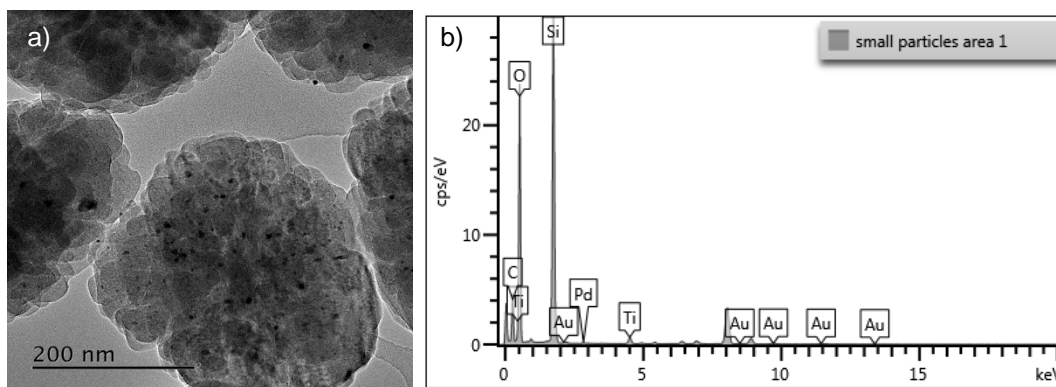


Figure 3.13. FEG-SEM sample image of the 0.33 wt% Au-0.33 wt% Pd/ACS TS-1 catalyst, where **a)** is displaying the nanoparticles, and **b)** is the EDX Spectra of the nanoparticles in Fig. 3.13a. cps denotes counts per second.

The second analysis provided data that was similar to the first analysis. The atom concentration percentage ratios for Si/Ti and Au/Pd were 36.37 and 2.50, respectively. The reason for the different ratios was due to the small decrease in Si and Pd and increase in Ti. The atom concentration percentage for Au was unchanged and the ratio for Ti to Si was closer to the ratio stated by ACS Materials (Tables 3.12 and 3.13, and Fig. 3.13 and 3.14.)

Table 3.13. Quantification from EDX Spectra Analysis of the nanoparticles in Fig. 3.14a from the 0.33 wt% Au-0.33 wt% Pd/ACS TS-1 catalyst.

Element	Line Type	Atom Conc.%
C	K series	34.06
O	K series	50.54
Si	K series	14.91
Ti	K series	0.41
Pd	L series	0.02
Au	L series	0.05

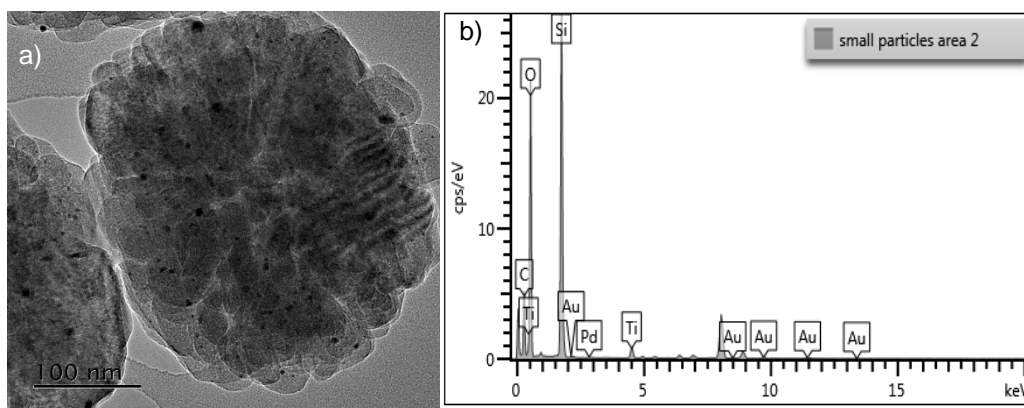


Figure 3.14. FEG-SEM sample image of the 0.33 wt% Au-0.33 wt% Pd/ACS TS-1 catalyst, where **a)** is displaying the nanoparticles, and **b)** is the EDX Spectra of Fig. 3.14a. cps denotes counts per second.

The final analysis of the smaller nanoparticles revealed that although the atom concentration percentage of Au was similar to the first analysis of the smaller nanoparticles, the decreased Pd caused the ratio to be the same as the second analysis, with a Au/Pd ratio of 2.50. Additionally, the atom concentration percentage of Si was similar to the previous analysis of the smaller nanoparticles, yet the results garnered a ratio of Si/Ti that was more akin to the first analysis of the smaller nanoparticles (Si/Ti atom conc.% ratio: 58.81) (Table 3.14 and Fig. 3.15).

Table 3.15. Quantification from EDX Spectra Analysis of the nanoparticles in Fig. 3.15a from the 0.33 wt% Au-0.33 wt% Pd/ACS TS-1 catalyst.

Element	Line Type	Atom Conc. %
C	K series	33.23
O	K series	51.14
Si	K series	15.29
Ti	K series	0.26
Pd	L series	0.02
Au	L series	0.05

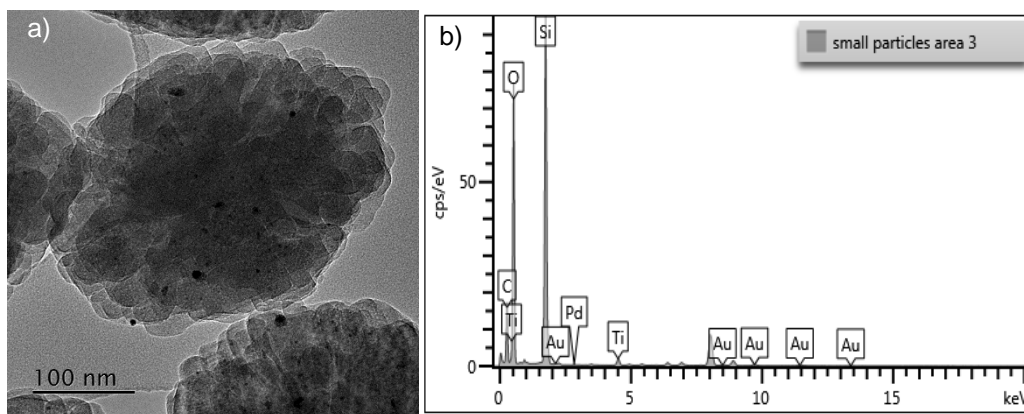


Figure 3.15. FEG-SEM sample image of the 0.33 wt% Au-0.33 wt% Pd/ACS TS-1 catalyst, where **a)** is displaying the nanoparticles, and **b)** is the EDX Spectra of Fig. 3.15a. cps denotes counts per second.

To conclude, throughout all of the EDX analyses for the ACS TS-1-supported catalyst, C was detected at a level of ~20-30 wt% as the sample plates used were made of C and C exists on most surfaces. Although both the types of nanoparticles for the ACS TS-1-supported catalyst had an elemental composition that was Au-rich, the amount of Au was vastly greater in the larger nanoparticles than the smaller nanoparticles (Tables 3.9-3.14, and Fig. 3.10-3.15).

As one quantitative EDX analysis was completed for the P25 TiO₂-supported catalyst, it was difficult to draw strict comparisons with the other catalysts. It was clear that the larger nanoparticles of the ZrO₂-, SiO₂- and ACS TS-1-supported catalysts did not exceed an atom concentration percentage ratio for Au/Pd above 7.00 (Table 3.15).

Nevertheless, the ZrO₂-supported catalyst was unique as there were no nanoparticles that had a length larger than 18 nm. This was unlike the other catalysts that had nanoparticles not only larger than 20 nm but larger than 100 nm in length. In two of the three areas analysed for the ZrO₂-supported catalyst, the Au/Pd atom concentration percentage ratio was lower than 1.00. These ratios were lower than those exhibited by the other catalysts within this study (Table 3.15 and Fig. 3.2-3.15).

The results for the large nanoparticles of the SiO₂-supported catalyst were not dissimilar from the results of the ACS TS-1-supported catalyst's large nanoparticles in relation to their atom concentration percentage ratio of metals. There was a large amount of Au (~7.00 atom conc.%) and approximately the same amount of Pd was detected for both catalysts. The rationale for this similarity could be due to the lack of difference in the composition of the support material as TS-1 is mainly

compromised of SiO₂ units. However, the support structure, the crystallinity and the pls of the support (which are all different between TS-1 and SiO₂) and the pls of the metals also influence nanoparticle morphology and composition (Table 3.15 and Fig. 3.2-3.15).

Table 3.15. Quantification from EDX Spectra Analyses of all of the samples of all the catalysts (0.33 wt% Au-0.33 wt% Pd/(support)) used in the Different Support Study, where the support and size of the metal nanoparticles have been identified and the Au/Pd atom concentration percentage ratios have been determined (Tables 3.3-3.15, and Fig. 3.2-3.15).

Support	Pd Atom Conc.%	Au Atom Conc.%	Au/Pd Atom Conc.% Ratio
P25 TiO ₂ (Large NP)	0.11	4.14	37.64
	0.21	0.20	0.95
ZrO ₂ ("Large" NPs)	0.35	0.27	0.77
	0.04	0.20	5.00
SiO ₂ (Large NPs)	0.34	0.60	1.76
	1.12	7.14	6.38
	0.87	3.08	3.54
ACS TS-1 (Large NPs)	1.51	9.16	6.07
	2.02	7.22	3.57
	0.93	2.58	2.77
ACS TS-1 (Small NPs)	0.04	0.05	1.25
	0.02	0.05	2.50
	0.02	0.05	2.50

Note: NP(s) denotes nanoparticle(s) and, for the purpose of the current work, the nanoparticles of the 0.33 wt% Au-0.33 wt% Pd/ZrO₂ catalyst were considered large ("Large"), despite being smaller than the large nanoparticles of the other catalysts in the Different Support Study.

The key difference between the ACS TS-1-supported catalysts' small and large nanoparticles was that the smaller particles had significantly less metal content that led to smaller atom concentration percentage ratios of the metals. However, two ratios from the small nanoparticles were not dissimilar from one of the ratios of the large nanoparticles (2.50 and 2.50 to 2.77, respectively). It was observed that Au was still the major constituent regardless of nanoparticle size. However, with the smaller nanoparticles supported on ACS TS-1, the limits of detection were observed (~0.05 atom conc.%). Although the Au/Pd atom concentration percentage ratio was stated for these nanoparticle (e.g., 1.25 atom conc.%), careful consideration and due diligence must be undertaken with smaller atom concentration percentages (Table 3.15 and Fig. 3.2-3.15).

Based on the direct H₂O₂ synthesis data and PSDs of the four catalysts, there was a correlation between the pieces of information that suggested that the nanoparticles of lengths greater than 5 nm in length were more responsible for the degradation of H₂O₂ as opposed to the nanoparticles below 5 nm in length. The P25 TiO₂- and ACS TS-1-supported catalysts, which gave higher H₂O₂ productivity values (55 and 44 mol_{H₂O₂} kg_{cat}⁻¹ h⁻¹, respectively) also had a greater number of the smaller nanoparticles (<5 nm in length) compared to the ZrO₂- and SiO₂-supported catalysts.

The mode of the PSDs for the ZrO₂- and SiO₂-supported catalysts had nanoparticles greater than 5 nm in length and low gave productivity values (16 and 12 mol_{H₂O₂} kg_{cat}⁻¹ h⁻¹, respectively), suggesting that these nanoparticles were responsible for the degradation of H₂O₂. However, this did not mean that these nanoparticles could not synthesise H₂O₂ directly. No correlation between the nanoparticle sizes and the cyclohexanone ammoximation data was found (Tables 3.1 and 3.15, and Fig. 3.1-3.15).

Excluding the P25 TiO₂-supported catalyst in this analysis (as quantitative EDX data on its smaller nanoparticles was not collected for this catalyst), there was a correlation between the cyclohexanone ammoximation data and the nanoparticles' composition. The ACS TS-1- and SiO₂-supported catalysts had Au/Pd atom concentration percentage ratios above 1.00 and had significantly lower H₂ selectivity values compared to the ZrO₂-supported catalyst. The latter catalyst had two EDX analyses that detected Au/Pd atom concentration percentage ratios below 1.00 (Tables 3.1-3.15, and Fig. 3.1 and 3.4-3.15).

This suggested that the Au-rich nanoparticles of the ACS TS-1- and SiO₂-supported catalysts were responsible for the increased rates of H₂O₂ synthesis

and its subsequent degradation, whereas the Pd-rich nanoparticles of the ZrO₂-supported catalyst appeared responsible for the slower rate of H₂O₂ synthesis. However, certain studies such as Hutchings *et al.*⁴⁶ suggested that Au was the most selective metal to use for a direct H₂O₂ synthesis catalyst. The current work did not directly support this as the larger Au-rich nanoparticles appeared to lead to a greater amount of H₂O₂ degradation. Nevertheless, this does not mean to say that small Au nanoparticles are not selective. The current work supported the research of Gudarzi *et al.*⁴⁷ and Edwards *et al.*,⁴⁴ who suggested Pd (in the form of PdO) was more selective than Au (Tables 3.1-3.15, and Fig. 3.1-3.15).

Nevertheless, the assumption that the larger nanoparticles were Au-rich, and therefore, the smaller nanoparticles were Pd-rich, cannot be made. Through quantitative FEG-SEM-EDX analysis, only the ZrO₂-supported catalyst produced nanoparticles that were small and Pd-rich, whereas the ACS TS-1-supported catalyst produced small nanoparticles that were still Au-rich. Further study would be required to confirm the composition of the smaller nanoparticles of all the catalysts with different supports.

Additionally, the SEM-EDX analysis of the P25 TiO₂-supported catalyst that may have detected atomic dispersion of the metals. However, the scale of the image has to be taken into consideration and the analysis could have detected nanoparticles instead as suggested by the grouping of the Pd atoms. Further research using FEG-SEM-EDX and TEM-EDX would be required to determine the existence of atomic metal (Tables 3.1-3.15, and Fig. 3.1-3.15).

Nevertheless, the composition and size of the nanoparticles were only two facets to consider. Morphology of nanoparticles was also integral in providing a selective catalyst. It was difficult to determine the difference in morphology between the smaller and larger nanoparticles observed in the current work, but the EDX mapping of the P25 TiO₂-supported catalyst as well as other group's research suggested that using the C_{IM} catalyst preparation method resulted in random alloy nanoparticles (Tables 3.1-3.15, and Fig. 3.1-3.15).^{6,15,44,48,49}

Furthermore, the Si/Ti ratios were also determined for the ACS TS-1-supported catalyst. The ratio for the first EDX analysis on the large nanoparticles could not be verified due to the lack of data for the Si atom concentration percentage. It was observed that only one of the Si/Ti atom concentration percentage ratios throughout the dataset was comparable to the ratio that ACS Materials stated for this support that they manufacture (36.37 and ~30.00, respectively) (Table 3.16).⁴⁵

Table 3.16. Quantification from EDX Spectra Analyses of all the samples of the 0.33 wt% Au-0.33 wt% Pd/ACS TS-1 catalyst, where the size of the nanoparticles has been identified and the Si/Ti atom concentration percentage ratios have been determined (Tables 3.10-3.15, and Fig. 3.10-3.15).

Nanoparticle Size	Ti Atom Conc.%	Si Atom Conc.%	Si/Ti Atom Conc.% Ratio
	0.1	-	n/a
Large NPs	0.09	3.94	43.78
	0.21	11.95	56.90
Small NPs	0.27	15.81	58.56
	0.41	14.91	36.37
	0.26	15.29	58.81

Note: NPs denote nanoparticles.

One reason for the lack of comparable data between this work's data and the manufacturers' data could be due to the way in which the EDX analyses were performed. As this was a sampling technique, the sample area could have had more of the SiO₂ units within its structure than the TiO₂ units that comprise the TS-1 material. Another observation from the results was the O content. As the majority of O was attributed to being a key component of all the support materials (all were oxide supports), there was the possibility that the O could have been an oxide with Pd as PdO. X-ray Photoelectron Spectroscopy (XPS) would confirm whether this was the case (Tables 3.2-3.16).

However, for all the analyses that have been completed, it should be noted that EDX is a bulk technique, that analyses more of the interior of the nanoparticles. It may have been possible that more of the Pd was at the surface of the nanoparticles analysed. A surface technique that could support the elemental composition analyses would be XPS.

Although the entire region within the XPS spectra for each element was considered for quantification by the software used (CasaXPS v2.3.17), the software automatically assigned the binding energies to the most intense peak for an element during the quantification process (Table 3.17).

Table 3.17. XPS Quantification of all the catalysts (0.33 wt% Au-0.33 wt% Pd/(support)) used in the Different Support Study, where the support has been identified (Fig. A3.8, A3.11-A3.13).

Support	Orbital of Element	Binding Energy / eV	Atom Conc. / %
P25 TiO ₂	O 1s	~530	65.7
	C 1s	~285	6.4
	Ti 2p	~459	27.51
	Pd 3d	~337	0.36
	Au 4f	~84	0.04
ZrO ₂	O 1s	~530	66.49
	C 1s	~285	6.73
	Zr 3p	~182	18.02
	Pd 3d	~337	8.74
	Au 4f	~84	0.01
SiO ₂	O 1s	~530	62.49
	Si 2p	~104	37.26
	Pd 3d	~337	0.24
	Au 4f	~84	0.01
ACS TS-1	O 1s	~530	61.19
	C 1s	~285	1.53
	Ti 2p	~459	0.18
	Si 2p	~104	37.10
	Pd 3d	~337	0.00
	Au 4f	~84	0.00

For example, Au 4f would assign the Au_{5/2} spin orbital splitting (~87 eV) if it were a more intense peak than the Au_{7/2} spin orbital splitting (~84 eV), but both peaks were considered for the quantification calculations. In the current work, the binding energies have been assigned to what they should conform to (e.g., Au 4f has been assigned to ~84 eV, not ~87 eV, regardless of peak intensity). All spectra from the XPS analyses of the calcined catalysts displayed Au⁰, which at the binding energy of ~84 eV was indicative of bulk Au, and Pd²⁺ (as PdO). As previously suggested, some of the O content that was detected by FEG-SEM-EDX did come in the form of PdO and the oxide supports used as it was confirmed *via* XPS (Table 3.17).

However, the SiO₂-supported catalysts also displayed Pd⁰, which may have contributed to its increased rates of H₂O₂ synthesis and degradation, which was supported by the previous research of others.^{6,15,44,48,49} Although the Zr 3p peaks were observed in the Pd 3d region for the ZrO₂-supported catalyst, there was no interference. The ACS TS-1-supported catalyst showed no Au or Pd due to the increased noise, thus, a high-resolution scan would be required to determine the amount of surface metal on the support material (Tables 3.1-3.17, and Fig. 3.1-3.15).

The P25 TiO₂-, ZrO₂- and SiO₂-supported catalysts demonstrated the low loading of metals onto the support material. However, XPS is also another sampling technique and may not have been representative of the entire catalyst. From the XPS spectra, Au/Pd atom concentration percentage ratios for the catalysts were determined and showed that the ZrO₂- and SiO₂-supported catalyst had a significantly greater amount of Pd than Au. However, the detection of Au (0.01 atom conc.%) was at the detection limit of the XPS instrument, and although Au/Pd atom concentration percentage ratios have been determined, these should be taken under due consideration. No correlation between the direct H₂O₂ synthesis, cyclohexanone ammoximation and XPS data could be found (Tables 3.1 and 3.18, and Fig. 3.1).

From the samples analysed *via* EDX and XPS, the data suggested that the metals' distributions throughout the catalysts' nanoparticles were not totally homogeneous. This was supported by the results of both techniques as most of the catalysts had a larger amount of Au than Pd within the EDX analyses and a greater amount of Pd compared to Au in the XPS analyses. This suggested that the nanoparticles of the P25 TiO₂-, ZrO₂- and SiO₂-supported catalysts had a mix between a random alloy and a Au core-Pd shell morphology, the latter being supported by the works of Edwards *et al.*^{27,50,51} The core-shell effect was most likely due to the catalysts' post-preparation calcination, but further investigation into the morphology and

composition of the different nanoparticles of all the catalysts in the current work would be required to confirm this (Tables 3.1-3.18, and Fig. 3.1-15).

Table 3.18. Focused XPS Quantification of all the catalysts used in the Different Support Study (0.33 wt% Au-0.33 wt% Pd/(support)), where the support has been identified and the Au/Pd atom concentration percentage ratios have been determined (Fig. A3.8, A3.11-A3.13).

Support	Pd Atom Conc. %	Au Atom Conc. %	Au/Pd Atom Conc. % Ratio
P25 TiO ₂	0.36	0.04	0.11
ZrO ₂	8.74	0.01	1.14 x 10 ⁻³
SiO ₂	0.24	0.01	0.04
ACS TS-1	-	-	-

Due to time constraints, the SiO₂-supported catalyst was not analysed *via* X-ray Diffraction (XRD). From the XRD analyses performed on the catalysts, it was clear that the P25 TiO₂-supported catalyst demonstrated a large peak for Au⁰ ($2\theta = \sim 45^\circ$), which was consistent with previous work.⁵⁰ This was indicative of the large Au-rich nanoparticles observed *via* FEG-SEM. Additionally, an increase in crystallite size was also observed for the anatase phase of the P25 TiO₂ support (~ 30 nm). Wang *et al.* had shown that an increase in crystallite size for P25 TiO₂ as the calcination temperature was increased, however, the crystallite sizes of the P25 TiO₂ in the current work was larger than that of Wang *et al.*'s (~ 55 and ~ 32 nm, respectively).⁵² This could be due to the difference in preparation methodologies and the presence of metals (*i.e.*, Au and Pd) on the P25 TiO₂ support (Table 3.19, and Fig. 3.2 and 3.16).

The most significant observation for the P25 TiO₂ was that the support in the catalyst was more amorphous than the uncalcined support. Based on the crystallinity indices of both materials, a loss of crystallinity was observed upon catalyst preparation and calcination by ~ 13 %. This could be due to the effect of calcination combined with a low loading of metals, but further investigation would be required to confirm this (Table 3.19 and Fig. 3.16).

The only significant differences in peak intensity were observed for the P25 TiO₂ and ACS TS-1 materials as both decreased in intensity with catalyst preparation and calcination. This was likely due to the materials having less

crystallites aligned in the same orientation, meaning less constructive interference of the X-rays. The P25 TiO₂ support material had an increase in crystallite size, meaning that there would be intrinsically less crystallites present, thus, less crystallites that were orientated in the same direction (Table 3.19 and Fig. 3.16).

Table 3.19. Crystallite sizes for the clean support and the supported catalysts.

Support	Crystallite Size of Uncalcined Support / nm	Crystallite Size of Supported Catalyst / nm	Crystallinity Index of Uncalcined Support / %	Crystallinity Index of Supported Catalyst / %
P25 TiO ₂	~25	~55	~83	~70
ZrO ₂	~68	~68	~85	~80
ACS TS-1	~42	~32	~92	~90

Note: only the anatase peaks have been used for the crystallite sizes for the uncalcined P25 TiO₂ and 0.33 wt% Au-0.33 wt% Pd/P25 TiO₂ catalyst.

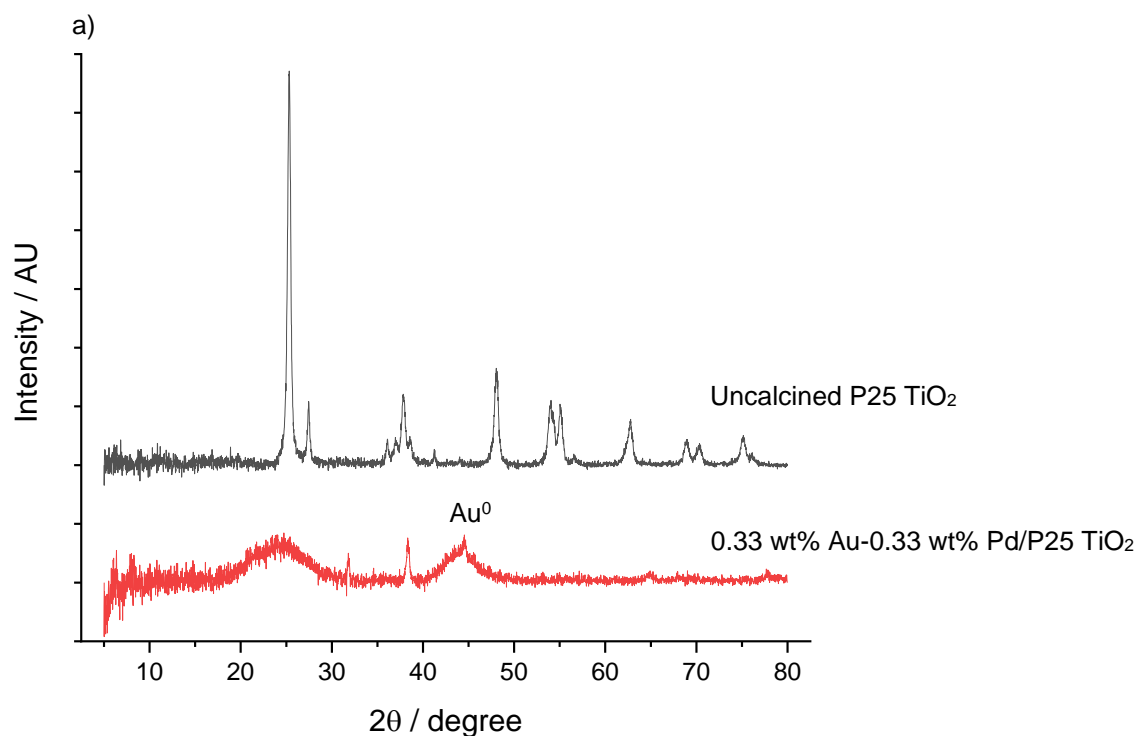


Figure 3.16. XRD patterns of the supports (P25 TiO₂, ZrO₂, ACS TS-1) and the supported catalysts (0.33 wt% Au-0.33 wt% Pd/(support)), where **a)** shows the P25 TiO₂ support and P25 TiO₂-supported catalyst. The peak for Au⁰ has been identified on the XRD pattern.

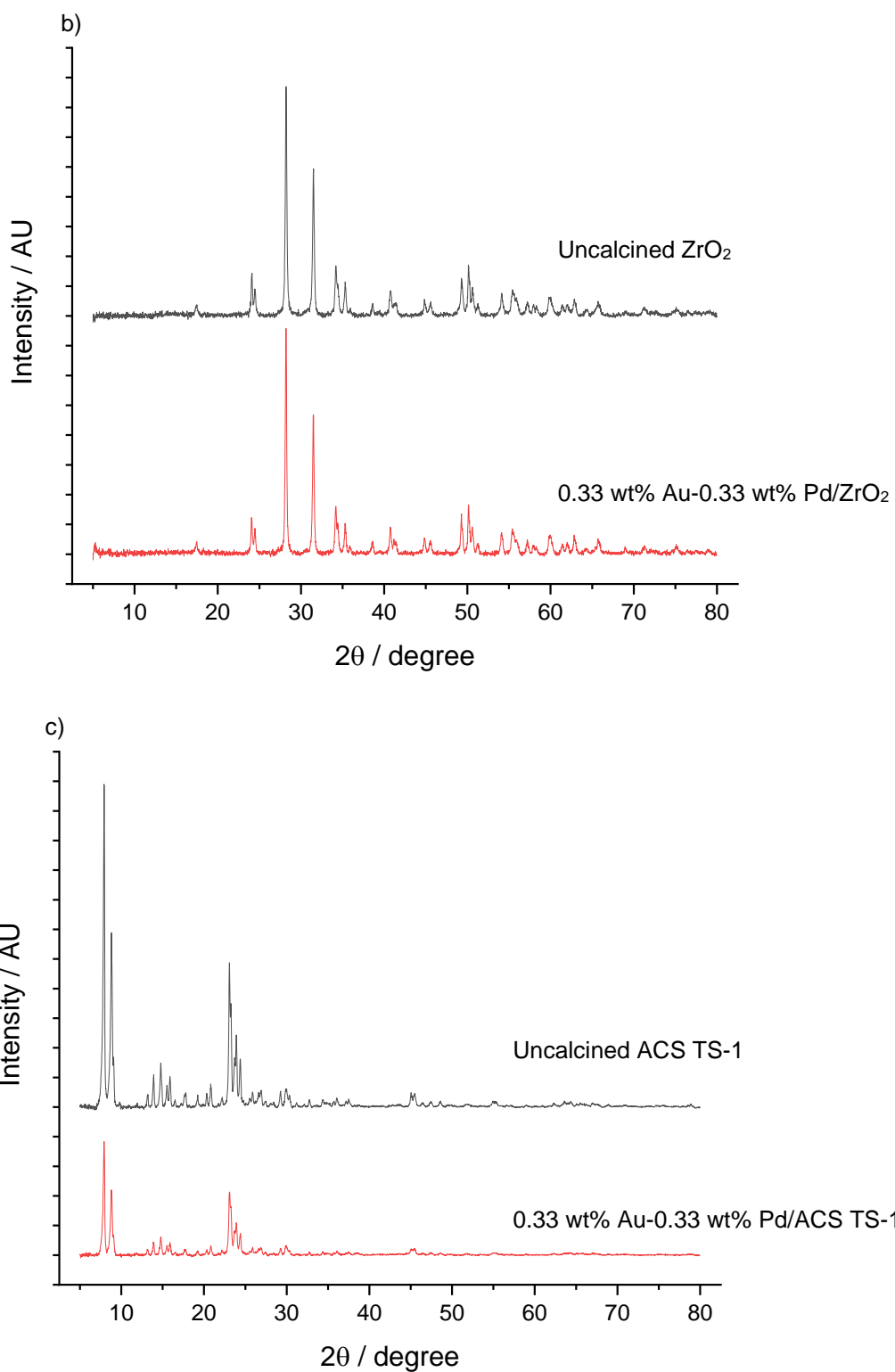


Figure 3.16. XRD patterns of the supports (P25 TiO_2 , ZrO_2 , ACS TS-1) and the supported catalysts (0.33 wt% Au-0.33 wt% Pd/(support)), where **b)** shows the ZrO_2 support and ZrO_2 -supported catalyst, and **c)** shows the ACS TS-1 support and the ACS TS-1-supported catalyst.

For both the ZrO₂ and ACS TS-1 support materials, the catalyst preparation method and calcination had little to no effect on the materials' crystallite sizes and their crystallinity. The ZrO₂ support did not undergo a change in crystallite size and only had a small decrease in crystallinity based on the crystallinity indices of the uncalcined support and supported catalyst (~5 %). The ACS TS-1 support underwent a small change in crystallite size between the uncalcined support and supported catalyst (~10 nm), which may have been due to the restructuring of the crystallites to "cloud-like" particles and had an extremely minimal decrease in crystallinity based on the crystallinity indices of both materials (~2 %).⁴⁵ The reason why the ZrO₂- and ACS TS-1-supported catalysts did not have peaks for Au⁰ could be that XRD is a sampling technique and not enough of the large Au-rich nanoparticles were in the samples (Table 3.19 and Fig. 3.16).

No Pd or PdO was detected, and no phase changes were observed for any of the catalysts in this study based on the pure phase XRD patterns. A correlation was made between the catalysts' performance and their support's crystallite sizes. The two catalysts with supports that gave larger crystallite sizes (*i.e.*, P25 TiO₂ and ZrO₂) gave rise to metal nanoparticles that directly synthesised H₂O₂ more slowly than the catalyst with smaller support crystallite sizes (*i.e.*, ACS TS-1). Further evidence for this would be needed from the XRD patterns of uncalcined SiO₂ and the SiO₂-supported catalyst. However, to determine the effect(s) of the preparation method and the heat treatment had on the support materials, further investigation into the dried-only catalyst would need to be performed. In addition, the differing the heat treatment as well as the heat treatment temperature would also provide vital information of how the support materials change and their influence on catalytic performance (Tables 3.1 and 3.19, and Fig. 3.16 and 3.17).

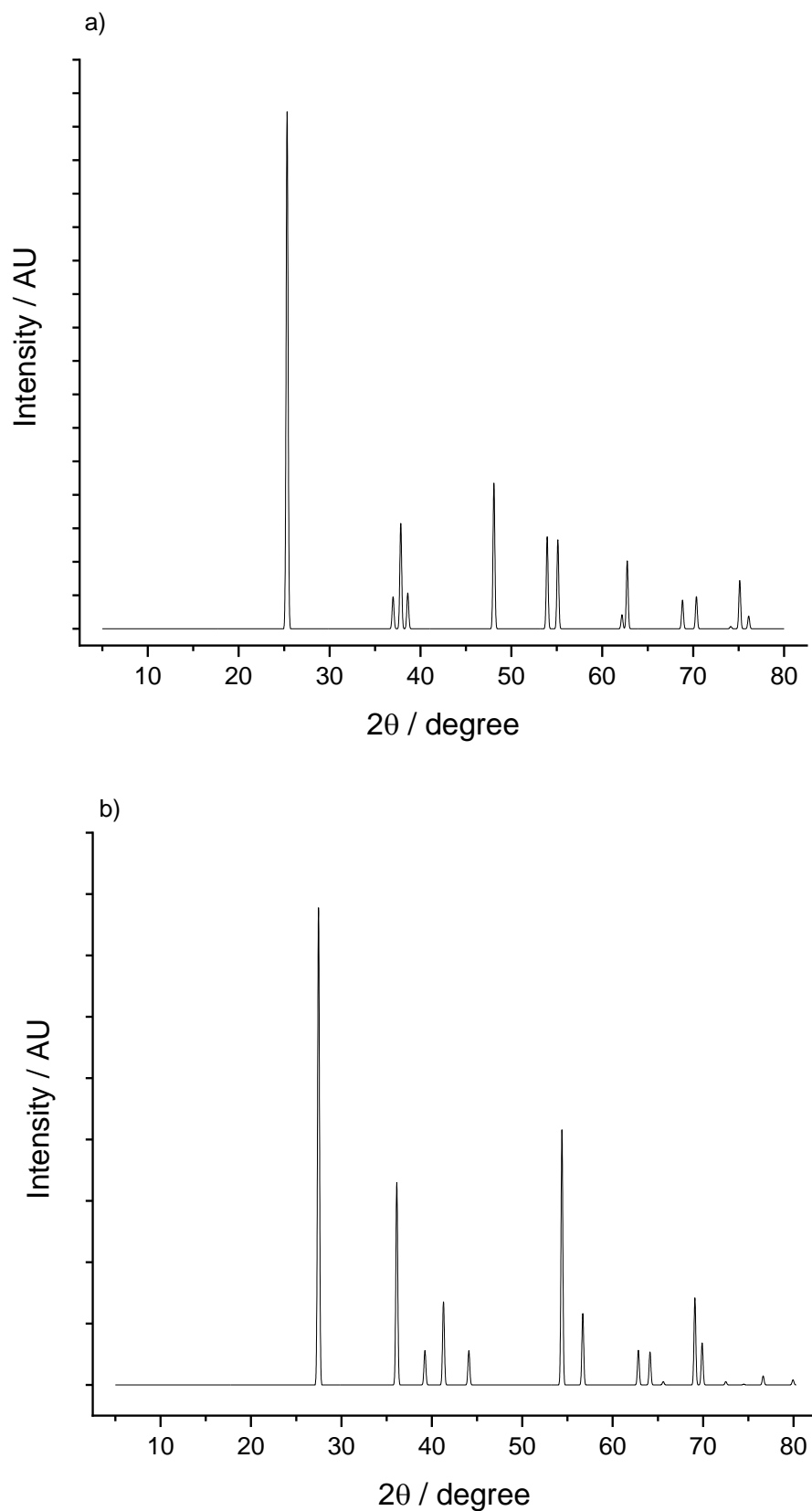


Figure 3.17. XRD patterns of the reference materials, where **a)** shows the anatase TiO₂ phase, and **b)** shows the rutile TiO₂ phase. The images have been adapted from the Inorganic Crystal Structure Database (ICSD), with the original content referenced.⁵³⁻⁵⁵

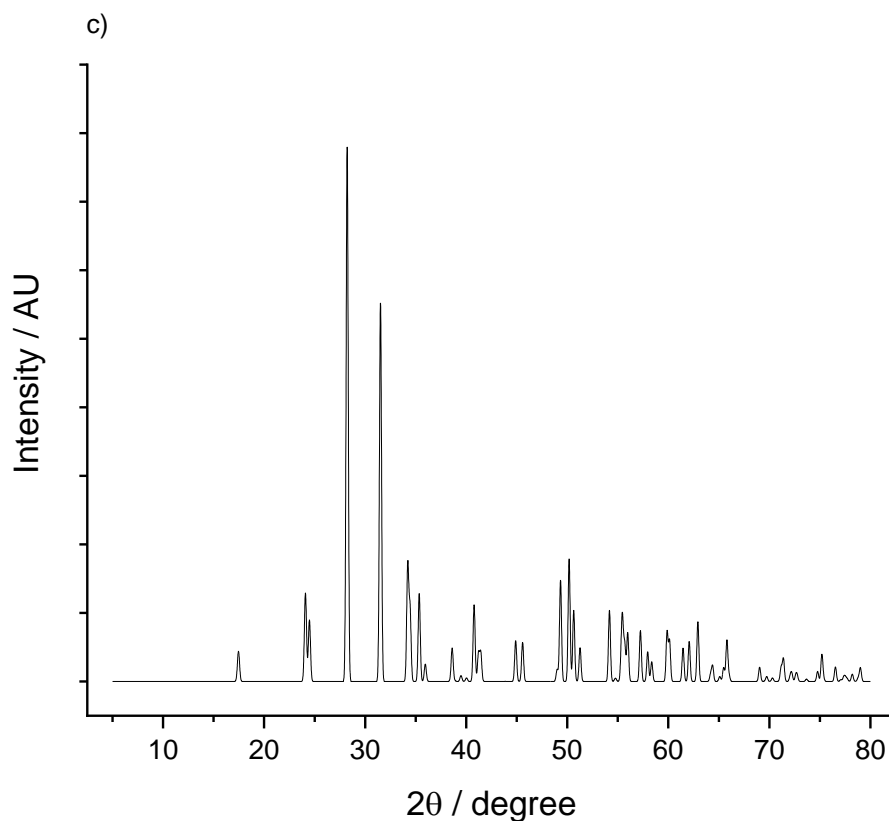


Figure 3.17. XRD patterns of the reference materials, where **c)** shows the monoclinic ZrO₂ phase. The images have been adapted from the Inorganic Crystal Structure Database (ICSD), with the original content referenced.^{53–55}

3.2.2. Reaction Time Study

As P25 TiO₂ was cheaper to purchase in bulk than ZrO₂ and the former supported catalyst gave a high H₂ selectivity with a moderate H₂ conversion and oxime yield, research was continued with this catalyst. This meant that it was a better candidate for large-scale use. To better understand the processes within this set of catalytic reactions and to discover the activity of the catalyst over time, a reaction time study using the 0.33 wt% Au-0.33 wt% Pd/P25 TiO₂ catalyst with added ACS TS-1 was completed.

3.2.2.1. Catalyst Experiments

Different time intervals for the 0.33 wt% Au-0.33 wt% Pd/P25 TiO₂ catalyst were selected. The 1.5 h experiments showed the least amount of turnover of H₂ and cyclohexanone conversion (H₂ conversion: 30 %; cyclohexanone conversion: 41 %) while the 6.0 h experiments showed the greatest amount of turnover of H₂ and

cyclohexanone (H₂ conversion: 71 %; cyclohexanone conversion: 94 %). This was expected as the greatest amount of time would lead to more of the H₂O₂ being synthesised to subsequently react to either form NH₂OH (and then cyclohexanone oxime) or H₂O non-selectively (Fig. 3.18).

The trends observed were that with an increase in reaction time, the cyclohexanone and H₂ conversion values also increased (from 1.5 h to 6 h: 53 and 41 %, respectively). The oxime selectivity should be considered constant as little variation occurred between each reaction time interval (average oxime selectivity with increasing reaction time: ~97 %). A larger decrease in H₂ selectivity based on oxime was observed as the reaction time increased from 3.0 h to 4.5 h (14 %). The rationale for this trend may be due to three possible consequences (Fig. 3.18).

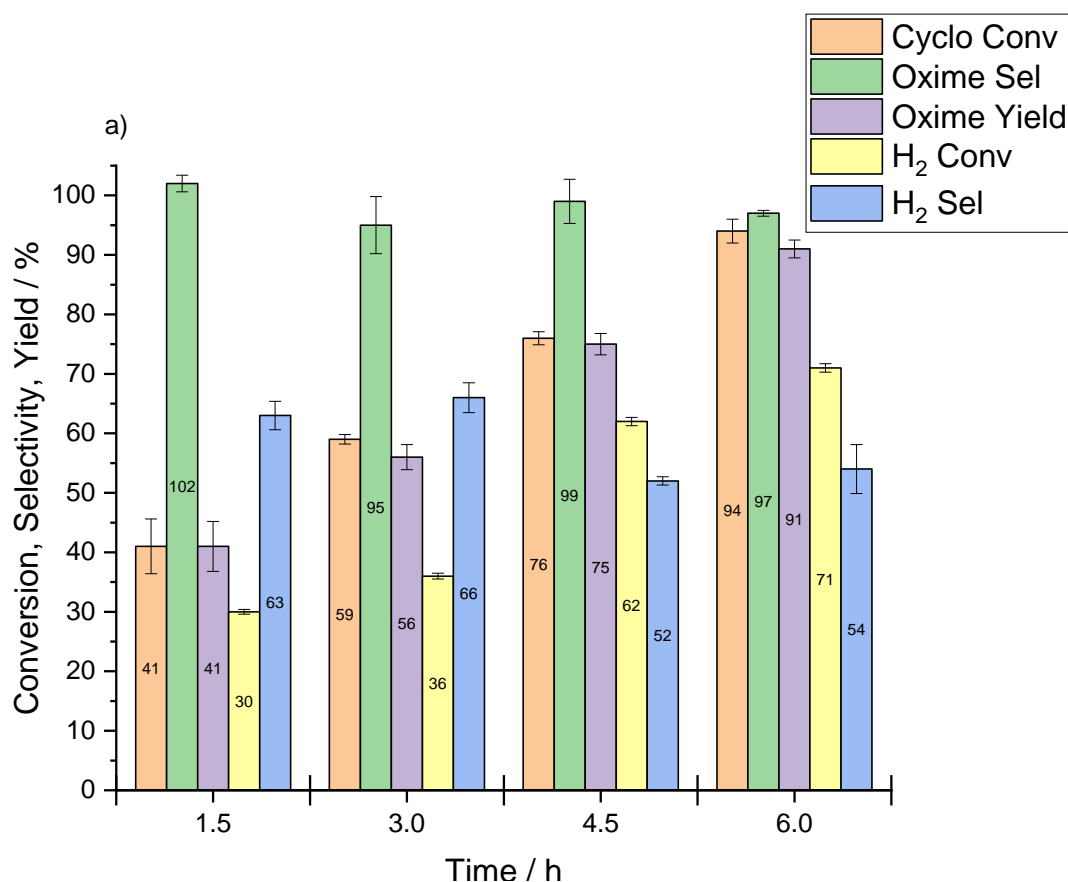


Figure 3.18. Reaction Time Study using 0.33 wt% Au-0.33 wt% Pd/P25 TiO₂ with ACS TS-1, where **a)** shows all of the data. Cyclo Conv denotes the conversion of cyclohexanone; Oxime Sel denotes the selectivity towards cyclohexanone oxime; H₂ Conv denotes the conversion of H₂; and H₂ Sel denotes the selectivity of the H₂ utilised to produce the oxime. Cyclohexanone Ammoximation Conditions - 0.33 wt% Au-0.33 wt% Pd/P25 TiO₂ catalyst (0.075 g) with ACS Materials TS-1 (0.075 g), NH₄HCO₃ (0.32 g), H₂O (7.50 g), (CH₃)₃COH (5.90 g), cyclohexanone (0.20 g), 5 % H₂/N₂ (2.89 MPa) and 25 % O₂/N₂ (1.11 MPa). Heated (353.15 K) and stirred (x h, where x is 1.5, 3.0, 4.5 or 6.0 h, 800 rpm). Washed with CH₃CH₂OH (6.00 g). Internal Standard (0.15 g).

The first possibility was that the catalyst continued to synthesise H_2O_2 , which was subsequently catalysed to produce NH_2OH by TS-1 but did not go on to react with cyclohexanone. An issue of diffusion could occur with the decreased amount of cyclohexanone available for the ammoximation reaction after 3.0 h. This meant the limited amount of cyclohexanone was unable to react with the NH_2OH , which meant that it could subsequently react to form nitrites and nitrates. A ratio of 1:1 between cyclohexanone and H_2 could be used as the cyclohexanone would be in excess compared to the amount of NH_2OH synthesised and the decrease in H_2 selectivity based on oxime observed may not occur (Scheme 3.1 and Fig. 3.18).

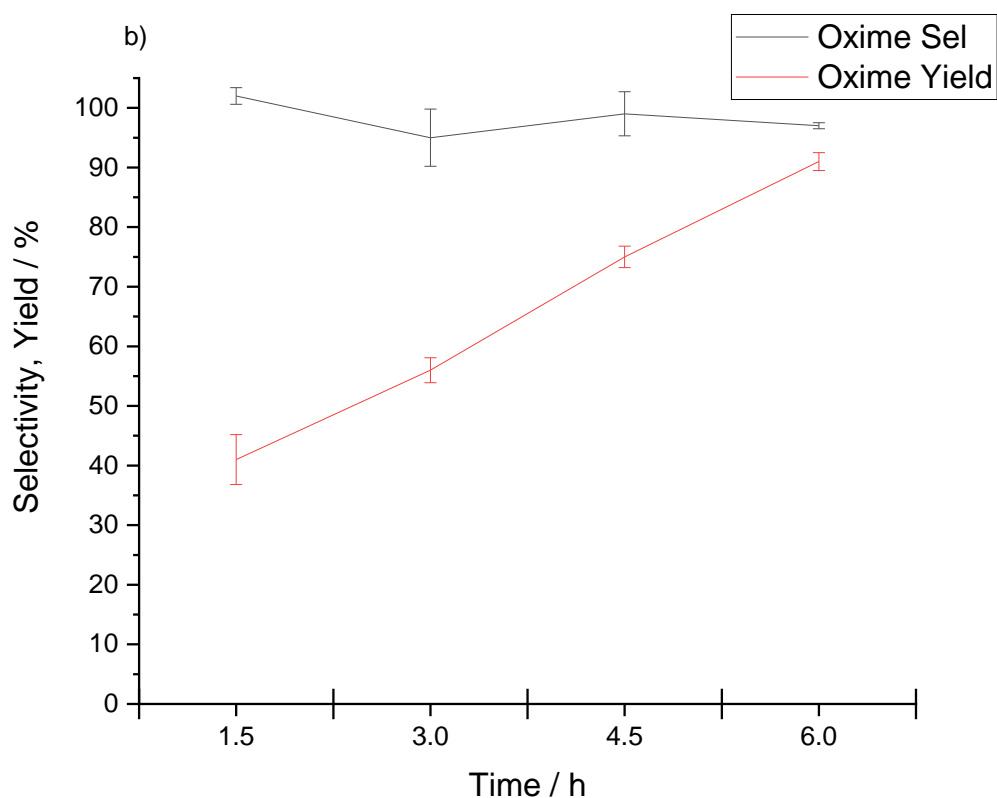


Figure 3.18. Reaction Time Study using 0.33 wt% Au-0.33 wt% Pd/P25 TiO_2 with ACS TS-1, where **b)** focuses on the oxime selectivity and yield trends. Oxime Sel denotes the selectivity towards cyclohexanone oxime. Cyclohexanone Ammoximation Conditions - 0.33 wt% Au-0.33 wt% Pd/P25 TiO_2 catalyst (0.075 g) with ACS Materials TS-1 (0.075 g), NH_4HCO_3 (0.32 g), H_2O (7.50 g), $(\text{CH}_3)_3\text{COH}$ (5.90 g), cyclohexanone (0.20 g), 5 % H_2/N_2 (2.89 MPa) and 25 % O_2/N_2 (1.11 MPa). Heated (353.15 K) and stirred (x h, where x is 1.5, 3.0, 4.5 or 6.0 h, 800 rpm). Washed with $\text{CH}_3\text{CH}_2\text{OH}$ (6.00 g). Internal Standard (0.15 g).

The second possibility could be that the direct H_2O_2 synthesis catalyst was in the process of deactivating after 3.0 h. A change in the oxidation state of one or both of the metals may have occurred. This hypothesis could be confirmed using XPS immediately after a 4.5 h reaction. If this were correct, Pd^0 or Au^{1+} or Au^{3+} may be observed on the surface of the catalyst. However, this may not be feasible as the removal of TS-1 from the direct H_2O_2 synthesis catalyst would be difficult. A strong base could dissolve the TS-1, but the counter cation may affect the direct H_2O_2 synthesis catalyst. Washing the catalyst with deionised H_2O may resolve this issue (Fig. 3.18).

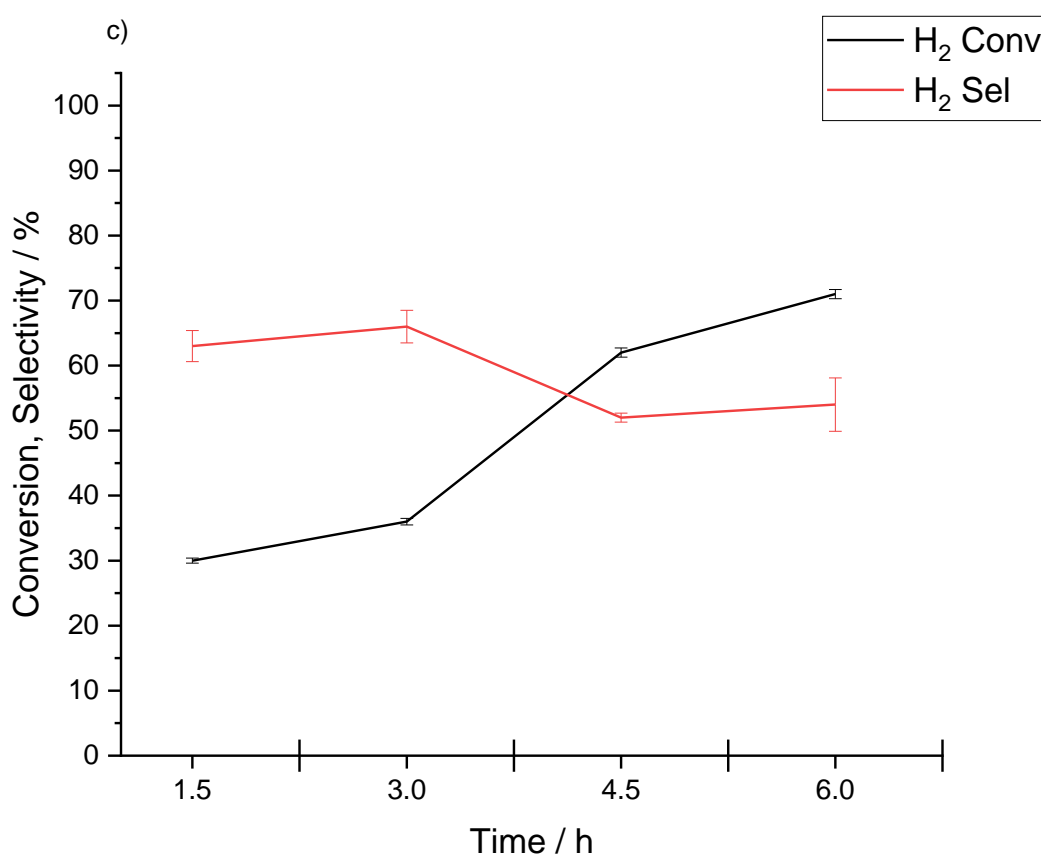


Figure 3.18. Reaction Time Study using 0.33 wt% Au-0.33 wt% Pd/P25 TiO_2 with ACS TS-1, where **c)** focuses on the H_2 conversion and selectivity trends. H_2 Conv denotes the conversion of H_2 ; and H_2 Sel denotes the selectivity of the H_2 utilised to produce the oxime. Cyclohexanone Ammoximation Conditions - 0.33 wt% Au-0.33 wt% Pd/P25 TiO_2 catalyst (0.075 g) with ACS Materials TS-1 (0.075 g), NH_4HCO_3 (0.32 g), H_2O (7.50 g), $(\text{CH}_3)_3\text{COH}$ (5.90 g), cyclohexanone (0.20 g), 5 % H_2/N_2 (2.89 MPa) and 25 % O_2/N_2 (1.11 MPa). Heated (353.15 K) and stirred (x h, where x is 1.5, 3.0, 4.5 or 6.0 h, 800 rpm). Washed with $\text{CH}_3\text{CH}_2\text{OH}$ (6.00 g). Internal Standard (0.15 g).

The third possibility was that the rate of turnover of H_2O_2 to NH_2OH by the TS-1 may have decreased and was significantly lower than the rate of direct H_2O_2 synthesis. The TS-1 may either be in the process of deactivating after 3.0 h (which seemed unlikely with a constant oxime selectivity) or reached a point of total saturation as all the Ti^{4+} sites became unavailable to capture the excess H_2O_2 synthesised. The excess H_2O_2 could not be converted to NH_2OH , and therefore, it either hydrogenated or decomposed. To prove or disprove this hypothesis, a larger amount of TS-1 with the 0.33 wt% Au-0.33 wt% Pd/P25 TiO_2 catalyst (for example, 1:1 to 1:2) for the 4.5 h and 6.0 h reactions would be required (Fig. 3.18).

3.2.3. Different Amounts of TS-1 with P25 TiO_2 -Supported Catalyst Study

This study focused on the effect(s) of increasing the amount of ACS TS-1 in the tandem catalyst system. The direct H_2O_2 synthesis catalyst used was the 0.33 wt% Au-0.33 wt% Pd/P25 TiO_2 catalyst. The rationale for using this support was that it maintained the theme of the current work and that P25 TiO_2 is commercially available in large quantities, which is useful for industrial scale-up.

3.2.3.1. Catalyst Experiments

Increasing the amount of TS-1 increased the yield of oxime and H_2 selectivity. The amount of H_2 conversion was similar throughout as it worked independently of the ACS TS-1 molecular sieve. With a greater amount of TS-1, more of the H_2 that had been converted into H_2O_2 by the P25 TiO_2 -supported catalyst was subsequently captured by the TS-1 and converted to NH_2OH . This improved H_2 selectivity and the subsequent cyclohexanone conversion and yield. Nevertheless, an increase in H_2 selectivity was observed, meaning that for reactions carried out for longer than 3.0 h, a larger amount of TS-1 to the direct H_2O_2 synthesis catalyst (>1) would likely aid in the decreased H_2 selectivity observed after 3.0 h in the Reaction Time Study (Fig. 3.18 and 3.19).

The reason for the decrease in oxime selectivity for the reaction with 0.0325 g of TS-1 was due to the decreased amount of NH_2OH available for the non-catalytic reaction to form the oxime. This was due to the decreased number of Ti^{4+} sites available in 0.0325 g of TS-1 compared to 0.075 g of TS-1. The cyclohexanone

reacted with the H₂O₂ to form cyclohexanol and other by-products (Scheme 3.1 and Fig. 3.19).

Although doubling the amount of TS-1 from 0.075 g to 0.150 g did not result in double the amount of cyclohexanone oxime, the rate of direct H₂O₂ synthesis was better met with an increased number of Ti⁴⁺ sites. This was observed with an increase of H₂ conversion and selectivity (10 and 5 %, respectively), meaning that the yield of the H₂O₂ that was converted selectively towards cyclohexanone oxime increased from ~24 % to ~33 %. In turn, this increased the oxime yield by 19 %. However, the results indicate the 29 % of the converted H₂ was not selectively converted to cyclohexanone oxime, meaning that the P25 TiO₂-supported catalyst degraded some of the H₂O₂ it had synthesised directly.

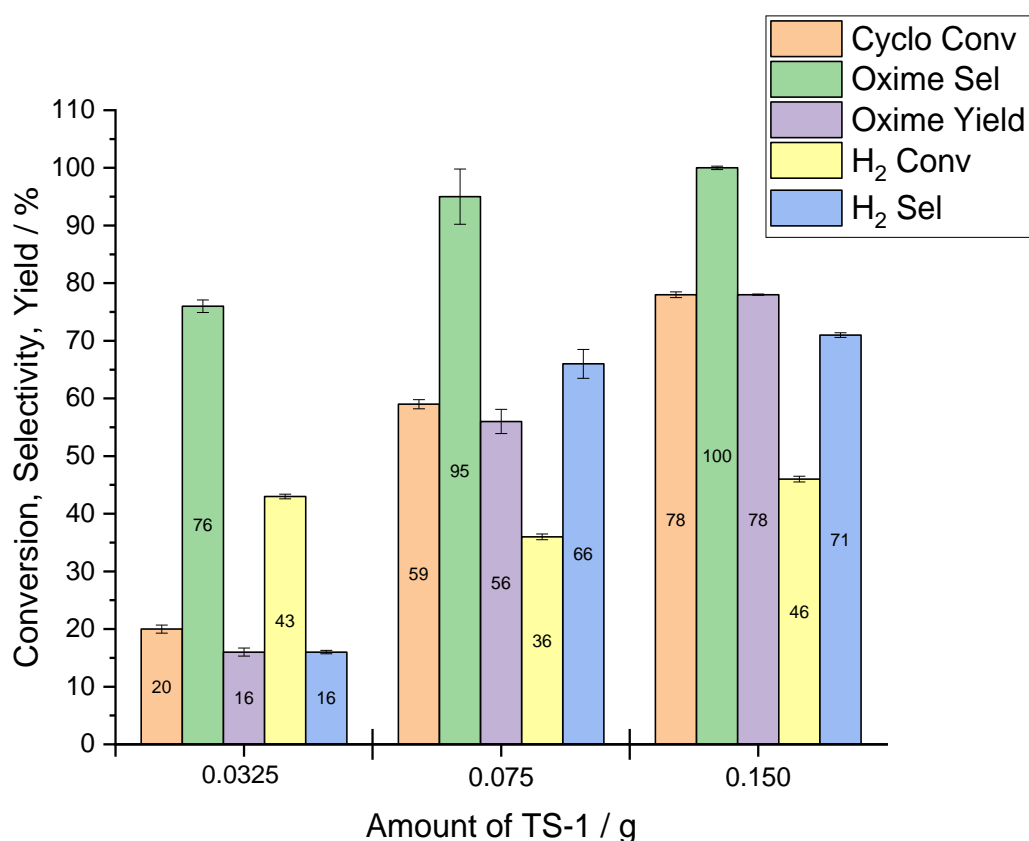


Figure 3.19. Different Amounts of ACS TS-1 Study using 0.33 wt% Au-0.33 wt% Pd/P25 TiO₂ with ACS TS-1. Cyclo Conv denotes the conversion of cyclohexanone; Oxime Sel denotes the selectivity towards cyclohexanone oxime; H₂ Conv denotes the conversion of H₂; and H₂ Sel denotes the selectivity of the H₂ utilised to produce the oxime. Cyclohexanone Ammoximation Conditions - 0.33 wt% Au-0.33 wt% Pd/P25 TiO₂ catalyst (0.075 g) with ACS Materials TS-1 (x g, where x is 0.0325, 0.075 and 0.150 g), NH₄HCO₃ (0.32 g), H₂O (7.50 g), (CH₃)₃COH (5.90 g), cyclohexanone (0.20 g), 5 % H₂/N₂ (2.89 MPa) and 25 % O₂/N₂ (1.11 MPa). Heated (353.15 K) and stirred (3.0 h, 800 rpm). Washed with CH₃CH₂OH (6.00 g). Internal Standard (0.15 g).

The trends observed in this study were similar to those observed in the research by Jin *et al.* This group also found that increasing the number of active sites by increasing the amount of TS-1 aided in the ammoximation reaction. However, their work used acetaldehyde, and not cyclohexanone, for their target reactant (Fig. 3.20).¹¹

3.2.4. Different Phases of TiO₂ Study

To determine the active phase of P25 TiO₂, the individual components of this TiO₂ were investigated. The major component of P25 TiO₂ is anatase at a ratio of 7:3 with rutile. Again, the rationale for using the P25 TiO₂-supported catalyst was to use a commercially available support for the catalyst that could be used at an industrial scale as well as maintaining the theme of the current work.

3.2.4.1. Catalyst Experiments

The results from the direct H₂O₂ synthesis tests and ammoximation reaction tests were completed for the anatase TiO₂-, the P25 TiO₂- and the rutile TiO₂-supported catalysts. From the two sets of data, the rutile TiO₂-supported catalyst had a similar activity to the P25 TiO₂-supported catalyst. The decrease in H₂O₂ productivity for the rutile TiO₂-supported catalyst (45 mol_{H₂O₂} kg_{cat}⁻¹ h⁻¹) compared to the P25 TiO₂-supported catalyst (55 mol_{H₂O₂} kg_{cat}⁻¹ h⁻¹) could be explained by the different hydrogenation and decomposition capabilities of each catalyst, as the rutile TiO₂-supported catalyst may potentially have had a greater number of degradation sites on the surface of the catalyst compared to the P25 TiO₂-supported catalyst (Table 3.20 and Fig. 3.20).

During the cyclohexanone ammoximation reaction, it was clear that both the rutile TiO₂- and P25 TiO₂-supported catalysts were synthesising and desorbing H₂O₂ at approximately the same rate, as the H₂ conversion and selectivity values were exceptionally similar (38 and 67 %, respectively, and 36 and 66%, respectively). The reason for the similarity displayed by these two catalysts was unexpected as the major component of P25 TiO₂ is anatase and not rutile (7:3). This phenomenon could be due to the preparation of P25 by Degussa and the preparation methods of anatase and rutile by Sigma-Aldrich, or it could be due to the P25 TiO₂ having had a different ratio of anatase to rutile (not 7:3). XRD could be used to determine if there was a greater amount of rutile in the P25 than expected. However, the more likely reason

was that the phase of the TiO₂ has little influence on the activity and selectivity for these catalysts (Table 3.20 and Fig. 3.20).

Table 3.20. H₂O₂ productivity values and cyclohexanone oxime yields of the 0.33 wt% Au-0.33 wt% Pd/(support) catalysts on different supports (P25 TiO₂, rutile TiO₂ and anatase TiO₂).

Catalyst	Productivity / mol _{H₂O₂} kg _{cat} ⁻¹ h ⁻¹	Oxime Yield / %
0.33 wt% Au-0.33 wt% Pd / Anatase TiO ₂	21	74
0.33 wt% Au-0.33 wt% Pd / P25 TiO ₂	55	56
0.33 wt% Au-0.33 wt% Pd / Rutile TiO ₂	45	58

Note: Direct H₂O₂ Synthesis conditions - Catalyst (0.01 g), H₂O (2.90 g), CH₃OH (5.60 g), 5% H₂/CO₂ (2.89 MPa), 25% O₂/CO₂ (1.11 MPa), 0.5 h, 275.15 K, 1200 rpm. Cyclohexanone Ammoximation Conditions - Catalyst (0.075 g) with ACS Materials TS-1 (0.075 g), NH₄HCO₃ (0.32 g), H₂O (7.50 g), (CH₃)₃COH (5.90 g), cyclohexanone (0.20 g), 5 % H₂/N₂ (2.89 MPa) and 25 % O₂/N₂ (1.11 MPa). Heated (353.15 K) and stirred (3.0 h, 800 rpm). Washed with CH₃CH₂OH (6.00 g). Internal Standard (0.15 g).

Despite the anatase TiO₂-supported catalyst having a low H₂O₂ productivity value in the absence of TS-1 (21 mol_{H₂O₂} kg_{cat}⁻¹ h⁻¹), it gave a slightly higher H₂ conversion and selectivity than the rutile TiO₂- and P25 TiO₂-supported catalysts. It should be noted that a small change in H₂O₂ yield had a large effect on the cyclohexanone oxime production because there was over double the number of moles of H₂ than to the number of moles of cyclohexanone (Chapter 2), which in the case of the anatase TiO₂-supported catalyst increased the oxime yield considerably (Table 3.20 and Fig. 3.20).

The reason for these results may be due to the rate of direct H₂O₂ synthesis having been slightly higher for the anatase TiO₂-supported catalyst than the rutile TiO₂- and P25 TiO₂-supported catalysts, whilst the rate of H₂O₂ degradation was significantly higher as it exhibited a low H₂O₂ productivity value. The rate of H₂O₂ capture and conversion by the TS-1 was slower than all of the direct H₂O₂ synthesis catalysts' H₂O₂ synthesis and degradation rates, meaning that the TS-1 was saturated and could not turnover the excess H₂O₂. As observed previously in the current work, additional TS-1 may aid in reducing the amount of H₂O₂ degradation, but this will likely only improve the H₂ selectivity slightly (Table 3.20, and Fig. 3.19 and 3.20).

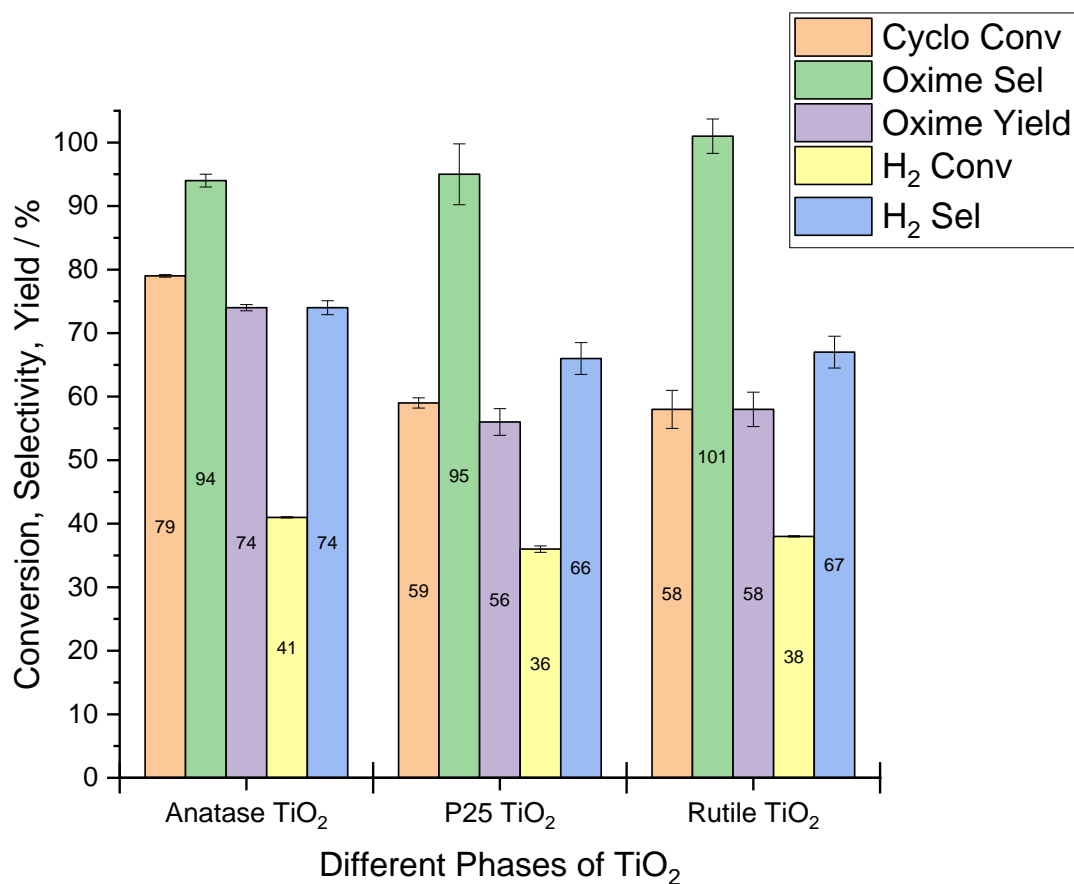


Figure 3.20. Catalyst testing of 0.33 wt% Au-0.33 wt% Pd/anatase TiO₂, 0.33 wt% Au-0.33 wt% Pd/P25 TiO₂ and 0.33 wt% Au-0.33 wt% Pd/rutile TiO₂ with ACS TS-1 for 3.0 h. Cyclo Conv denotes the conversion of cyclohexanone; Oxime Sel denotes the selectivity towards cyclohexanone oxime; H₂ Conv denotes the conversion of H₂; and H₂ Sel denotes the selectivity of the H₂ utilised to produce the oxime. Cyclohexanone Ammoxidation Conditions - Catalyst (0.075 g) with ACS Materials TS-1 (0.075 g), NH₄HCO₃ (0.32 g), H₂O (7.50 g), (CH₃)₃COH (5.90 g), cyclohexanone (0.20 g), 5 % H₂/N₂ (2.89 MPa) and 25 % O₂/N₂ (1.11 MPa). Heated (353.15 K) and stirred (3.0 h, 800 rpm). Washed with CH₃CH₂OH (6.00 g). Internal Standard (0.15 g).

The direct H₂O₂ synthesis and cyclohexanone ammoxidation results for the anatase TiO₂-supported catalyst were similar to those of the ZrO₂-supported catalyst. In relation to the kinetics for the desorption and degradation of H₂O₂ for these catalysts, the rate of desorption must have been marginally higher than the rate of degradation, as a slightly higher amount of H₂O₂ was synthesised by the anatase TiO₂- and ZrO₂-supported catalysts compared to the rutile TiO₂- and P25 TiO₂-supported catalysts. The H₂O₂ that was synthesised and desorbed from these catalysts was subsequently captured and converted by the TS-1. Hydrogenation, decomposition and kinetic data for these catalysts and the TS-1 would be needed to confirm or disprove the proposed hypothesis (Tables 3.1 and 3.20, and Fig. 3.1 and 3.20).

3.2.4.2. Catalyst Characterisation

XPS and elemental composition analyses were completed on the anatase TiO₂-, rutile TiO₂- and P25 TiO₂-supported catalysts. It was confirmed that all three catalysts possessed Au⁰ and Pd²⁺ in the form of PdO, which was a result of being calcined. However, the anatase TiO₂-supported catalyst also displayed Pd⁰ (Table 3.21).

Table 3.21. XPS Quantification of all the catalysts (0.33 wt% Au-0.33 wt% Pd/(support)) used in the Different Phases of TiO₂ Study, where the support has been identified (Fig. A3.8-A3.10).

Support	Orbital of Element	Binding Energy / eV	Atom Conc. / %
Anatase TiO ₂	O 1s	~530	69.31
	C 1s	~285	3.08
	K 2p	~294	1.39
	Ti 2p	~459	25.71
	Pd 3d	~337	0.43
	Au 4f	~84	0.08
Rutile TiO ₂	O 1s	~530	71.76
	C 1s	~285	5.40
	Ti 2p	~459	19.4
	Pd 3d	~337	3.17
	Au 4f	~84	0.27
P25 TiO ₂	O 1s	~530	65.7
	C 1s	~285	6.40
	Ti 2p	~459	27.51
	Pd 3d	~337	0.36
	Au 4f	~84	0.04

The metal atom concentration percentage ratios were also determined. Both the P25 TiO₂- and anatase TiO₂-supported catalysts displayed similar atom concentration percentages for O and Ti, but the rutile TiO₂-supported catalyst exhibited a decreased amount of Ti (19.40 atom conc.%). This decrease could be the result of the technique as XPS is a sampling technique (Tables 3.21 and 3.22).

The data showed that the rutile TiO₂-supported catalyst had a significantly larger amount of Pd than the other catalysts (3.17 atom conc.%), whereas the anatase TiO₂- and P25 TiO₂-supported catalysts had atom concentration percentages around 0.40 %. The rutile TiO₂-supported catalyst had the largest atom concentration percentage of Au with 0.27 %, unlike the anatase TiO₂- and P25 TiO₂-supported catalysts (0.08 and 0.04 atom conc.%, respectively) (Tables 3.21 and 3.22).

Table 3.22. Focused XPS Quantification of all the catalysts used in the Different Phases of TiO₂ Study (0.33 wt% Au-0.33 wt% Pd/(support)), where the support has been identified and the Au/Pd atom concentration percentage ratios have been determined (Fig. A3.8-A3.10).

Support	Pd Atom Conc.%	Au Atom Conc.%	Au/Pd Atom Conc.% Ratio
Anatase TiO ₂	0.43	0.08	0.19
P25 TiO ₂	0.36	0.04	0.11
Rutile TiO ₂	3.17	0.27	0.09

With the Au/Pd atom concentration percentage ratios determined for these catalysts, it was observed that all three catalysts exhibited similar ratios, with the anatase TiO₂-supported catalyst having the highest Au/Pd ratio. This was despite not having the greatest amount of Au, which the rutile TiO₂-supported catalyst had. However, no correlation between the catalyst's activity, selectivity and XPS data could be determined (Tables 3.21-23, and Fig. 3.20).

A finding of interest in the analysis for the anatase TiO₂-supported catalyst was the presence of potassium (K) (1.39 atom conc.%) in the form of K⁺, which is a known promoter (or additive) that can be employed to increase the amount of H₂O₂ a catalyst can synthesise.^{40,56} However, this is disputed in the literature. With K⁺ and Pd⁰ present on the catalyst, this may explain the increased selective conversion of H₂ observed for the cyclohexanone ammoximation reaction in the current work, but a decreased amount of H₂O₂ present in the direct H₂O₂ synthesis reaction. In the

absence of TS-1 during the direct H₂O₂ synthesis reaction, the H₂O₂ synthesised degraded due to the well documented non-selective nature of Pd⁰ (Tables 3.20-3.22, and Fig. 3.20).^{15,24,43,44}

However, when in the presence of TS-1 during the cyclohexanone ammoximation reaction, the H₂O₂ was captured by the Ti⁴⁺ sites before the Pd⁰ could degrade it. This may explain the increase in H₂ selectivity for the anatase TiO₂-supported catalyst compared to the other two catalysts in this study (Tables 3.20-3.22, and Fig. 3.20).

A comparison was drawn between the catalysts of the different supports and the different phases of TiO₂ as a support with their respective XPS data. It was observed that all the catalysts (except for the ACS TS-1-supported catalyst) had a higher atom concentration percentage of Pd than Au. The degree to which the amount of Pd was detected on the surface of the catalyst was most likely dependent on the support material's influence. This could have been due to the differing pls of the supports and the metals used, or possibly due to the metal seeding on the support's surface structure (Table 3.23).

Table 3.23. Focused XPS Quantification of all the catalysts used in the Different Support and Different Phases of TiO₂ Studies (0.33 wt% Au-0.33 wt% Pd/(support)), where the support has been identified and the Au/Pd atom concentration percentage ratios have been determined (Fig. A3.8-A3.13).

Support	Pd Atom Conc.%	Au Atom Conc.%	Au/Pd Atom Conc.% Ratio
ACS TS-1	-	-	-
SiO ₂	0.24	0.01	0.04
ZrO ₂	8.74	0.01	1.14 x 10 ⁻³
P25 TiO ₂	0.36	0.04	0.11
Anatase TiO ₂	0.43	0.08	0.19
Rutile TiO ₂	3.17	0.27	0.09

With the exception of the ZrO₂-supported catalyst, the Au/Pd atom concentration percentage ratios of all the other catalysts could be construed as

similar. Therefore, the XPS results did not provide conclusive evidence of a trend that explained the experimental results observed. Quantitative EDX analyses on the rutile TiO₂- and anatase TiO₂-supported catalysts would be required to determine whether similar observations could be made in respect of the catalysts from the Different Support Study regarding the nanoparticles' mixed random alloy and core-shell morphologies, which was likely due to the catalysts undergoing movement of the metal atoms during calcination (Tables 3.2, 3.20 and 3.23, and Fig. 3.1 and 3.20).

From the XRD analyses performed on the catalysts, it was clear that the P25 TiO₂-supported catalyst demonstrated an increase in crystallite size, which was also observed for the anatase phase of the P25 TiO₂ support, as previously stated in the Different Support Study. Wang *et al.* demonstrated that an increase in crystallite size for P25 TiO₂ was observed as calcination temperature was increased, however, the crystallite sizes of the P25 TiO₂ in the Wang *et al.*'s work was smaller than that of the current work's (~32 and ~55 nm, respectively).⁵² This could be due to the difference in preparation methodologies and the presence of metals (*i.e.*, Au and Pd) upon the P25 TiO₂ support (Table 3.24, and Fig. 3.2 and 3.21).

Table 3.24. Crystallite sizes for the clean support and the supported catalysts.

Support	Crystallite Size of Uncalcined Support / nm	Crystallite Size of Supported Catalyst / nm	Crystallinity Index of Uncalcined Support / %	Crystallinity Index of Supported Catalyst / %
Anatase TiO ₂	~129	~78	~92	~71
P25 TiO ₂	~25	~55	~83	~70
Rutile TiO ₂	~157	~151	~75	~73

Note: only the anatase peaks have been used for the crystallite sizes for the uncalcined P25 TiO₂ and 0.33 wt% Au-0.33 wt% Pd/P25 TiO₂ catalyst.

As previously discussed, a large peak for Au⁰ (2θ = ~45 °) was observed and suggested the presence of large Au-rich nanoparticles, which were observed *via* FEG-SEM. These observations were supported by the work of Edwards *et al.*⁵⁰ The P25 TiO₂ support in the catalyst was more amorphous than its respective uncalcined support. A loss of crystallinity based on the crystallinity indices between both materials

was observed (~13 %). This could be due to effect of calcination combined with a low loading of metals, but further investigation would be required to confirm this (Table 3.24, and Fig. 3.2 and 3.21).

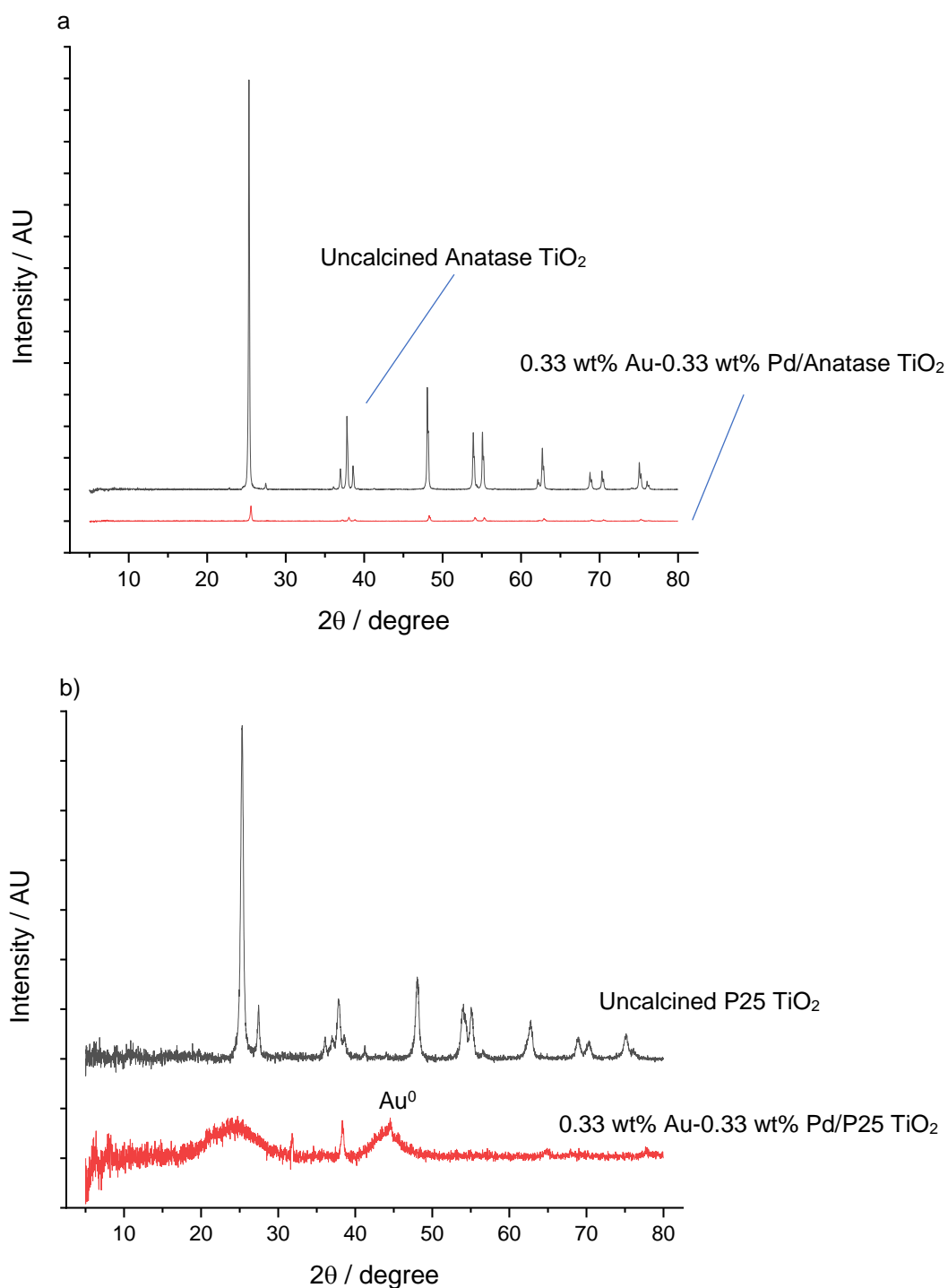


Figure 3.21. XRD patterns of the supports (Anatase, P25 TiO₂, Rutile) and the supported catalysts (0.33 wt% Au-0.33 wt% Pd/(support)), where **a**) shows the Anatase TiO₂ support and Anatase TiO₂-supported catalyst, and **b**) shows the P25 TiO₂ support and P25 TiO₂-supported catalyst. The peak for Au⁰ has been identified on the XRD pattern.

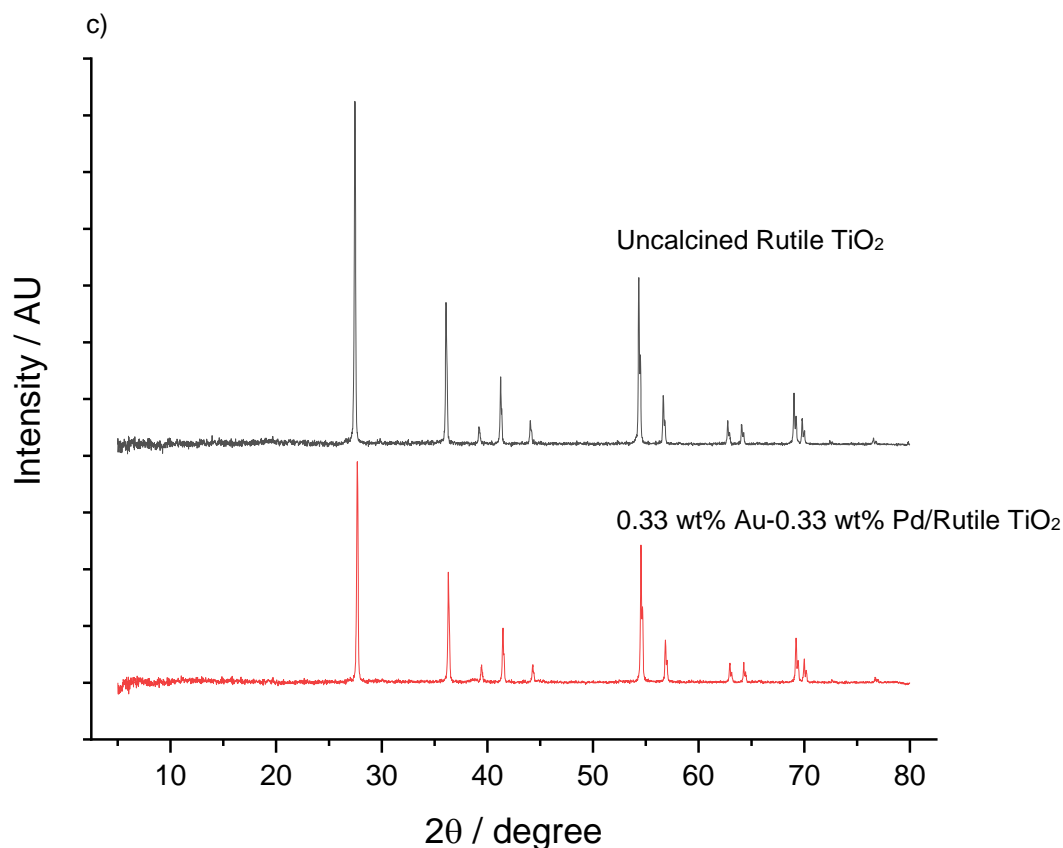


Figure 3.21. XRD patterns of the supports (Anatase, P25 TiO₂, Rutile) and the supported catalysts (0.33 wt% Au-0.33 wt% Pd/(support)), where **c)** shows the Rutile TiO₂ support and Rutile TiO₂-supported catalyst.

Both the anatase TiO₂- and rutile TiO₂-supported catalysts had a decrease in peak intensity, crystallite size and crystallinity from their respective uncalcined support materials. However, the degree to which these attributes decreased was different. For the anatase TiO₂- and rutile TiO₂-supported catalysts, the crystallites decreased by ~51 nm and ~6 nm, respectively, and the crystallinities based on the crystallinity indices decrease by ~21 and ~2 %, respectively. The reason for the greater decrease in crystallite size and crystallinity exhibited by the anatase TiO₂-supported catalyst compared to the rutile TiO₂-supported catalyst may have been due to the influence of K⁺ (detected by XPS) present on this support, aiding in its' decomposition. However, further investigation would be needed to confirm this hypothesis (Tables 3.22-3.24, and Fig. 3.21).

As all three catalysts in this study had similar crystallinities, only the crystallite sizes were drastically different. Again, the observation of larger support crystallites (>50 nm) gave rise to metal nanoparticles that could produce H₂O₂ more slowly. However, the anatase TiO₂-supported catalyst had the distinct advantage of having

both Pd⁰ (and Pd²⁺) and K⁺, both known for increasing the amount of direct H₂O₂ synthesis.^{15,24,40,43,44,56} The decrease in peak intensity for the TiO₂-support catalysts was due to less crystallites orientated in the same direction, but there significantly more crystallites orientated for the rutile TiO₂-supported catalyst than the anatase TiO₂- and P25 TiO₂-supported catalysts. No Pd or PdO was detected, and no phase changes were observed for any of the catalysts in this study (Table 3.24 and Fig. 3.21).

3.3. Conclusions

For cyclohexanone ammoximation utilising *in-situ* direct H₂O₂ synthesis, multiple studies were conducted to discover a tandem catalyst system that could rival the ACS TS-1-supported catalyst for industrial scale-up. From these studies, the 0.33 wt% Au-0.33 wt% Pd/P25 TiO₂ catalyst was exclusively investigated as P25 TiO₂ is commercially available in bulk, and to better understand its high H₂ selectivity compared to other catalysts in the current work. It was determined that anatase TiO₂ was the superior support material for the direct H₂O₂ synthesis catalyst in the tandem catalyst system as it provided the highest H₂ conversion and selectivity as well as the highest oxime yield of all the catalysts that were tested.

Characterisation techniques determined the crystallinity, crystallite size, the surface composition and the nanoparticles' composition and morphology. It was clear that the support influenced these traits, which in turn affected the catalysts' performances. The SEM-EDX, FEG-SEM-EDX and XPS analyses suggested that the nanoparticles' morphology for most of the catalysts in the Different Support Study was a mix between a random alloy and a Au core-Pd shell, the latter of which had most likely occurred during the catalysts' calcination. Larger nanoparticles were detected (>18 nm in length) for the SiO₂-, ACS TS-1- and P25 TiO₂-supported catalysts, unlike the ZrO₂-supported catalyst. The large nanoparticle of the P25 TiO₂-supported catalyst was found to be Au-rich, which was likely due to the Au's affinity for itself and the capacity of metal atoms to move during calcination.

From the FEG-SEM-EDX, two correlations with the experimental results were suggested. Firstly, a correlation between the nanoparticles' size from the catalysts' PSDs and the catalysts' direct H₂O₂ synthesis data was observed. The nanoparticles below 5 nm in length that existed on the P25 TiO₂- and ACS TS-1-supported catalysts were less responsible for the degradation of H₂O₂, whereas those nanoparticles

above 5 nm in length that were on the SiO₂- and ZrO₂-supported catalysts were more responsible for the degradation of H₂O₂. This was due to the former two catalysts' high H₂O₂ productivity values and the latter two catalysts' low H₂O₂ productivity values.

The second correlation found was between the cyclohexanone ammoximation data and the EDX data. If the nanoparticles' composition had a Au/Pd atom concentration percentage ratio greater than 1.00 (*i.e.*, the SiO₂- and ACS TS-1-supported catalysts), that catalyst had increased H₂ conversion but decreased H₂ selectivity towards the oxime. The catalyst that had Au/Pd atom concentration percentage ratios less than 1.00 gave the best H₂ selectivity (and H₂O₂ yield) of the catalysts within the Different Support Study (with the exception of the P25 TiO₂-supported catalyst as no quantitative EDX data was collected on the smaller nanoparticles).

Deformation of the TS-1 support was observed in the SEM analyses. Compared to the ACS Materials SEM images,⁴⁵ there was a drastic change to the structure of the TS-1 after catalyst preparation and calcination. This was not uncommon as other studies have shown that TS-1 is prone to structural changes.^{6,7,25} However, the change observed in the current work was unlike the other studies as the support particles seemed to be arranged in a "cloud" formation. This could be a result of the preparation method or the post-preparation treatment; the latter being the more likely cause.

Furthermore, most of the metal in the large nanoparticles was spectator metal as the large core was unexposed. Thus, not contributing to the catalysis. This in turn would have a negative impact on the catalysts' performance as the spectator metal would not have contributed to any direct H₂O₂ synthesis.

The XRD analyses showed that no Pd or PdO peaks were present, and no phase changes had occurred for the catalysts of the Different Support Study. However, a peak for Au⁰ ($2\theta = \sim 45^\circ$) was observed for the P25 TiO₂-supported catalyst. This was indicative of the large Au-rich nanoparticles.⁵⁰ Furthermore, the crystallite sizes of the P25 TiO₂ and ACS TS-1 support materials changed upon catalyst preparation and calcination. The P25 TiO₂ support crystallites increased in size (not decreased like the ACS TS-1), not unlike the work of Wang *et al.*⁵² A correlation was suggested between the support crystallite size and H₂ selectivity as those support materials that had crystallite sizes above ~50 nm gave better H₂

selectivity values (*i.e.*, P25 TiO₂ and ZrO₂), whereas the ACS TS-1-supported catalyst showed a greater activity towards direct H₂O₂ synthesis. Further investigation upon SiO₂-supported catalyst would be required to confirm this suggestion.

In the Reaction Time Study, the P25 TiO₂-supported tandem catalyst system was used and tested upon for the aforementioned reasons. It was observed that increasing the reaction time increased the conversion of cyclohexanone and H₂, which in turn increased the oxime yield. The oxime selectivity remained constant. The latter result was a measure of the TS-1 catalyst and not the direct H₂O₂ synthesis catalyst. Nevertheless, there was a decrease in H₂ selectivity after 3.0 h. Suggestions for this decrease were made and would need to be further investigated to understand this result and confirm the rationale for this occurrence.

From the Different Amounts of TS-1 Study, increasing the amount of TS-1 increased the production of oxime. These results gave a similar trend to the work completed by Jin *et al.*¹¹ It could be possible that if the TS-1-supported catalyst or SiO₂-supported tandem catalyst system had been provided with a greater amount of TS-1, the decreased H₂ selectivity may not have been observed. The increased amount of TS-1 would result in a greater number of Ti⁴⁺ sites present and available for the capture and conversion of H₂O₂ into NH₂OH. However, the SiO₂-supported catalyst demonstrated its ability to degrade H₂O₂ feasibly. Nevertheless, the increase in H₂ selectivity observed for the P25 TiO₂-supported catalyst was low with increasing the amount of TS-1. Doubling the TS-1 (from 0.075 g to 0.150 g) did not double the capture and conversion of H₂O₂.

Characterisation techniques were performed on the catalysts in both the Different Supports study and the Different Phase of TiO₂ study. The XPS, XRD, and SEM-EDX analyses revealed the nanoparticle and support crystallite sizes of the different catalysts as well as their elemental compositions and metal atom concentration percentage ratios, although, FEG-SEM-EDX data was not collected for the anatase TiO₂- or the rutile TiO₂-supported catalysts. The data alluded to certain hypotheses; however, further characterisation data would be required to confirm them.

The existence of K⁺ and Pd⁰ in the anatase TiO₂-supported catalyst, captured in the XPS analysis, was the most likely reason for the increased activity toward direct H₂O₂ synthesis. For direct H₂O₂ synthesis, Pd⁰ is known for a greater activity towards H₂O₂ production, as opposed to being more selective (which Pd²⁺ is known for), and K⁺ is a known promoter.^{40,56} Although Na⁺ is a known poison for catalysts.⁵⁶ However,

there is literature that contradicts K^+ as a promoter for direct H_2O_2 synthesis.^{15,57} This discovery was of significance as there was an increase in the catalyst's performance, which was a direct result of the oxidation state of the Pd, and the additive used. However, chemical companies are likely to avoid the use of promoters and additives because of their additional cost.

3.4. Future Research

For the continuation of this research, further characterisation would be required. Other tests for the direct synthesis of H_2O_2 and cyclohexanone ammoximation reactions would also be needed to complete certain studies. For example, anatase TiO_2 that did not contain K^+ should be used to determine how much of an effect the K^+ had on the production of H_2O_2 during both of these reactions.

Characterisation of certain catalysts would be required to complete the studies in the current work. For example, the high-resolution XPS analyses for the ACS TS-1-supported catalyst to determine the metals' atom concentration percentages would be needed to complete the Different Supports Study. The FEG-SEM-EDX on the P25 TiO_2 -, rutile TiO_2 - and anatase TiO_2 -supported catalyst would help in explaining the results of the activities of the catalysts in the Different Phases of TiO_2 Study, as well as confirm if the nanoparticles had a similar composition and morphology to those in the Different Support Study. In addition, High Angle Annular Dark Field-Scanning Transmission Electron Microscopy (HAADF-STEM) would also confirm the Au core-Pd Shell morphology observed *via* FEG-SEM-EDX and XPS.

Brunauer-Emmett-Teller (BET) and surface area data could support the observation of the increased crystallite size observed for the P25 TiO_2 -supported. Completion of the TEM analyses would determine the existence of nanoparticles smaller than 2 nm in length on all the catalysts. Although TEM was performed on the P25 TiO_2 -supported catalyst, no small nanoparticles (<2 nm in length) were detected. However, this may not be true of the other catalysts. In addition, Atomic Emission Spectroscopy (AES) would be an ideal analytical technique to use to determine the amount of each metal in each catalyst that seeded and became nanoparticles. This information would support the EDX and XPS analyses.

Other support materials, such as CeO_2 ,⁵⁸ along with different catalyst preparation methods (e.g., M_{IM} or S_{IM}) could be explored.²⁴ Akin to Pritchard *et al.*, the metal loadings could be optimised in this bi-metallic catalyst.⁵⁹ The addition of Pt to

the catalysts would also be another avenue for future research as Edwards *et al.* had investigated.⁴⁴ Researching a flow reactor system that separates each reaction, with each section at their optimum reaction conditions, would be insightful, particularly for the chemical industry.

3.5. References

- 1 G. Rapp and H. Fuchs, *United States Patent: MANUFACTURE OF CYCLOHEXANONE OXIME*, 1976.
- 2 J. Sirijaraensre and J. Limtrakul, Mechanisms of the ammonia oxidation by hydrogen peroxide over the perfect and defective Ti species of TS-1 zeolite, *Phys. Chem. Chem. Phys.*, 2013, **15**, 18093.
- 3 L. Dal Pozzo, G. Fornasari and T. Monti, TS-1, catalytic mechanism in cyclohexanone oxime production, *Catal. Commun.*, 2002, **3**, 369–375.
- 4 P. Roffia, M. Padovan, G. Leofanti, M. A. Mantegazza and G. De Alberti, *United States Patent (19) Roffia et al. (54 CATALYTIC PROCESS FOR THE MANUFACTURE OF OXIMES*, 1987.
- 5 M. Taramasso, S. Donato Milanese, G. Perego and B. Notari, *United States Patent: PREPARATION OF POROUS CRYSTALLINE SYNTHETIC MATERIAL COMPRISED OF SILICON AND TITANIUM OXIDES*, 1982.
- 6 R. J. Lewis, *PhD Thesis Title: The application of Cs-exchanged tungstophosphoric acid as an additive in the direct synthesis of hydrogen peroxide and the use of Au-Pd/TS-1 in a one-pot approach to cyclohexanone oxime production*, Cardiff University, 2016.
- 7 H. Ichihashi and H. Sato, The development of new heterogeneous catalytic processes for the production of epsilon-caprolactam, *Appl. Catal. a-General*, 2001, **221**, 359–366.
- 8 C. Meng, S. Yang, G. He, G. Luo, X. Xu and H. Jin, The Reaction Mechanism of Acetaldehyde Ammoximation to Its Oxime in the TS-1/H₂O₂ System, *Catalysts*, 2016, **6**, 109.
- 9 Z. Li, R. Chen, W. Xing, W. Jin and N. Xu, Continuous acetone ammoximation over TS-1 in a tubular membrane reactor, *Ind. Eng. Chem. Res.*, 2010, **49**, 6309–6316.

- 10 R. Raja and J. M. Thomas, in *Studies in Surface Science and Catalysis*, 2002, vol. 141, pp. 317–328.
- 11 H. Jin, C. Meng, G. He, X. Guo and S. Yang, Green synthesis of acetaldehyde oxime using ammonia oxidation in the TS-1/H₂O₂ system, *React. Kinet. Mech. Catal.*, 2018, **125**, 1113–1125.
- 12 M. E. Potter, D. Sun and R. Raja, The curious effects of integrating bimetallic active centres within nanoporous architectures for acid-catalysed transformations, *Catal. Sci. Technol.*, 2016, **6**, 2616–2622.
- 13 Y. Y. Xu, Z. H. Li, L. Y. Gao, D. S. Zhang, X. Q. Zhao, S. F. Wang and Y. J. Wang, An Integrated Process for the Synthesis of Solid Hydroxylamine Salt with Ammonia and Hydrogen Peroxide as Raw Materials, *Ind. Eng. Chem. Res.*, 2015, **54**, 1068–1073.
- 14 In-situ FTIR study on mechanism of cyclohexanone ammoximation to its oxime on TS-1 in liquid phase, http://en.cnki.com.cn/Article_en/CJFDTotall-HBQJ201106020.htm, (accessed 8 February 2020).
- 15 C. Samanta, Direct synthesis of hydrogen peroxide from hydrogen and oxygen: An overview of recent developments in the process, *Appl. Catal. a- General*, 2008, **350**, 133–149.
- 16 World Intellectual Property Office, WO2018088436A1, 2018, 1–29.
- 17 A. Silvestre-Albero, A. Grau-Atienza, E. Serrano, J. Garcia-Martinez and J. Silvestre-Albero, Desilication of TS-1 zeolite for the oxidation of bulky molecules, *Catal. Commun.*, 2014, **44**, 35–39.
- 18 T. Deguchi, H. Yamano and M. Iwamoto, Kinetic and mechanistic studies on direct H₂O₂ synthesis from H₂ and O₂ catalyzed by Pd in the presence of H⁺ and Br⁻ in water: A comprehensive paper, *Catal. Today*, 2015, **248**, 80–90.
- 19 A. Plauck, E. E. Stangland, J. A. Dumesic and M. Mavrikakis, Active sites and mechanisms for H₂O₂ decomposition over Pd catalysts, *Proc. Natl. Acad. Sci.*, 2016, **113**, E1973–E1982.
- 20 N. M. Wilson and D. W. Flaherty, Mechanism for the Direct Synthesis of H₂O₂ on Pd Clusters: Heterolytic Reaction Pathways at the Liquid-Solid Interface, *J. Am. Chem. Soc.*, 2016, **138**, 574–586, <https://pubs.acs.org/doi/10.1021/jacs.5b1>.

- 21 J. K. Edwards, N. N. Edwin, A. F. Carley, A. A. Herzing, C. J. Kiely and G. J. Hutchings, Direct synthesis of H₂O₂ from H₂ and O₂ over gold, palladium, and gold-palladium catalysts supported on acid-pretreated TiO₂, *Angew. Chemie - Int. Ed.*, 2009, **48**, 8512–8515.
- 22 J. M. Thomas and R. Raja, The materials chemistry of inorganic catalysts, *Aust. J. Chem.*, 2001, **54**, 551–560.
- 23 J. M. Thomas and R. Raja, Design of a 'green' one-step catalytic production of epsilon-caprolactam (precursor of nylon-6), *Proc. Natl. Acad. Sci. U. S. A.*, 2005, **102**, 13732–13736.
- 24 M. Sankar, Q. He, M. Morad, J. Pritchard, S. J. Freakley, J. K. Edwards, S. H. Taylor, D. J. Morgan, A. F. Carley, D. W. Knight, C. J. Kiely and G. J. Hutchings, Synthesis of Stable Ligand-free Gold-Palladium Nanoparticles Using a Simple Excess Anion Method, *ACS Nano*, 2012, **6**, 6600–6613.
- 25 R. J. Lewis, K. Ueura, Y. Fukuta, S. J. Freakley, L. Kang, R. Wang, Q. He, J. K. Edwards, D. J. Morgan, Y. Yamamoto and G. J. Hutchings, The Direct Synthesis of H₂O₂ Using TS-1 Supported Catalysts, *ChemCatChem*, 2019, **11**, 1673–1680.
- 26 R. J. Lewis and G. J. Hutchings, Recent Advances in the Direct Synthesis of H₂O₂, *ChemCatChem*, 2019, **11**, 298–308.
- 27 J. K. Edwards, A. F. Carley, A. A. Herzing, C. J. Kiely and G. J. Hutchings, Direct synthesis of hydrogen peroxide from H₂ and O₂ using supported Au-Pd catalysts, *Faraday Discuss.*, 2008, **138**, 225–239.
- 28 J. W. Bullard and M. J. Cima, Orientation dependence of the isoelectric point of TiO₂ (rutile) surfaces, *Langmuir*, 2006, **22**, 10264–10271.
- 29 M. F. Cuddy, A. R. Poda and L. N. Brantley, Determination of Isoelectric Points and the Role of pH for Common Quartz Crystal Microbalance Sensors, *ACS Appl. Mater. Interfaces*, 2013, **5**, 3514–3518.
- 30 I. Moreno, N. F. Dummer, J. K. Edwards, M. Alhumaimess, M. Sankar, R. Sanz, P. Pizarro, D. P. Serrano and G. J. Hutchings, Selective oxidation of benzyl alcohol using in situ generated H₂O₂ over hierarchical Au-Pd titanium silicalite catalysts, *Catal. Sci. Technol.*, 2013, **3**, 2425–2434.

- 31 S. Muhammad, S. T. Hussain, M. Waseem, A. Naeem, J. Hussain and M. Tariq Jan, *Surface charge properties of zirconium dioxide*, 2012, vol. 4.
- 32 X. Zhang, H. Wang and B. Q. Xu, Remarkable nanosize effect of zirconia in Au/ZrO₂ catalyst for CO oxidation, *J. Phys. Chem. B*, 2005, **109**, 9678–9683.
- 33 S. J. Tauster, S. C. Fung and R. L. Garten, Strong Metal-Support Interactions. Group 8 Noble Metals Supported on TiO₂, *J. Am. Chem. Soc.*, 1978, **100**, 170–175.
- 34 S. J. Tauster, Strong Metal-Support Interactions, *Acc. Chem. Res.*, 1987, **20**, 389–394.
- 35 H. Tang, F. Liu, J. Wei, B. Qiao, K. Zhao, Y. Su, C. Jin, L. Li, J. J. Liu, J. Wang and T. Zhang, Ultrastable Hydroxyapatite/Titanium-Dioxide-Supported Gold Nanocatalyst with Strong Metal–Support Interaction for Carbon Monoxide Oxidation, *Angew. Chemie - Int. Ed.*, 2016, **55**, 10606–10611.
- 36 H. Tang, Y. Su, B. Zhang, A. F. Lee, M. A. Isaacs, K. Wilson, L. Li, Y. Ren, J. Huang, M. Haruta, B. Qiao, X. Liu, C. Jin, D. Su, J. Wang and T. Zhang, Classical strong metal–support interactions between gold nanoparticles and titanium dioxide, *Sci. Adv.*, 2017, **3**, e1700231.
- 37 J. C. Matsubu, S. Zhang, L. DeRita, N. S. Marinkovic, J. G. Chen, G. W. Graham, X. Pan and P. Christopher, Adsorbate-mediated strong metal-support interactions in oxide-supported Rh catalysts, *Nat. Chem.*, 2017, **9**, 120–127.
- 38 T. W. van Deelen, C. Hernández Mejía and K. P. de Jong, *Nat. Catal.*, 2019, **2**, 955–970.
- 39 H. Chen, S. Z. Yang, Z. Yang, W. Lin, H. Xu, Q. Wan, X. Suo, T. Wang, D. E. Jiang, J. Fu and S. Dai, Sinter-Resistant Nanoparticle Catalysts Achieved by 2D Boron Nitride-Based Strong Metal-Support Interactions: A New Twist on an Old Story, *ACS Cent. Sci.*, 2020, **6**, 1617–1627.
- 40 S. Ranganathan and V. Sieber, *Catalysts*, 2018, **8**.
- 41 J. M. Campos-Martin, G. Blanco-Brieva and J. L. G. Fierro, Hydrogen peroxide synthesis: an outlook beyond the anthraquinone process, *Angew. Chem. Int. Ed. Engl.*, 2006, **45**, 6962–6984.

- 42 J. K. Edwards, S. J. Freakley, R. J. Lewis, J. C. Pritchard and G. J. Hutchings, Advances in the direct synthesis of hydrogen peroxide from hydrogen and oxygen, *Catal. Today*, 2015, **248**, 3–9.
- 43 D. A. Crole, S. J. Freakley, J. K. Edwards and G. J. Hutchings, Direct synthesis of hydrogen peroxide in water at ambient temperature, *Proc. R. Soc. A Math. Phys. Eng. Sci.*, 2016, **472**, 20160156.
- 44 J. K. Edwards, J. Pritchard, L. Lu, M. Piccinini, G. Shaw, A. F. Carley, D. J. Morgan, C. J. Kiely and G. J. Hutchings, The Direct Synthesis of Hydrogen Peroxide Using Platinum-Promoted Gold-Palladium Catalysts, *Angew. Chemie-International Ed.*, 2014, **53**, 2381–2384.
- 45 ACS Materials, Titanium Silicalite-1 - TS-1 - Molecular Sieves - Materials, <http://www.acsmaterial.com/titanium-silicalite-55.html>, (accessed 7 June 2017).
- 46 B. Nkosi, N. J. Coville and G. J. Hutchings, Vapour phase hydrochlorination of acetylene with group VIII and IB metal chloride catalysts, *Appl. Catal.*, 1988, **43**, 33–39.
- 47 D. Gudarzi, W. Ratchananusorn, I. Turunen, T. Salmi and M. Heinonen, Preparation and study of Pd catalysts supported on activated carbon cloth (ACC) for direct synthesis of H₂O₂ from H₂ and O₂, *Top. Catal.*, 2013, **56**, 527–539.
- 48 J. K. Edwards, S. F. Parker, J. Pritchard, M. Piccinini, S. J. Freakley, Q. He, A. F. Carley, C. J. Kiely and G. J. Hutchings, Effect of acid pre-treatment on AuPd/SiO₂ catalysts for the direct synthesis of hydrogen peroxide, *Catal. Sci. Technol.*, 2013, **3**, 812–818.
- 49 D. A. Crole, *PhD Thesis Title: The direct synthesis of hydrogen peroxide in water at ambient temperature: A study of reaction conditions, catalyst design and implementation*, Cardiff University, 2017.
- 50 J. K. Edwards, B. E. Solsona, P. Landon, A. F. Carley, A. Herzing, C. J. Kiely and G. J. Hutchings, Direct synthesis of hydrogen peroxide from H₂ and O₂ using TiO₂-supported Au-Pd catalysts, *J. Catal.*, 2005, **236**, 69–79.
- 51 J. Edwards, P. Landon, A. F. Carley, A. A. Herzing, M. Watanabe, C. J. Kiely and G. J. Hutchings, *J. Mater. Res.*, 2007, **22**, 831–837.

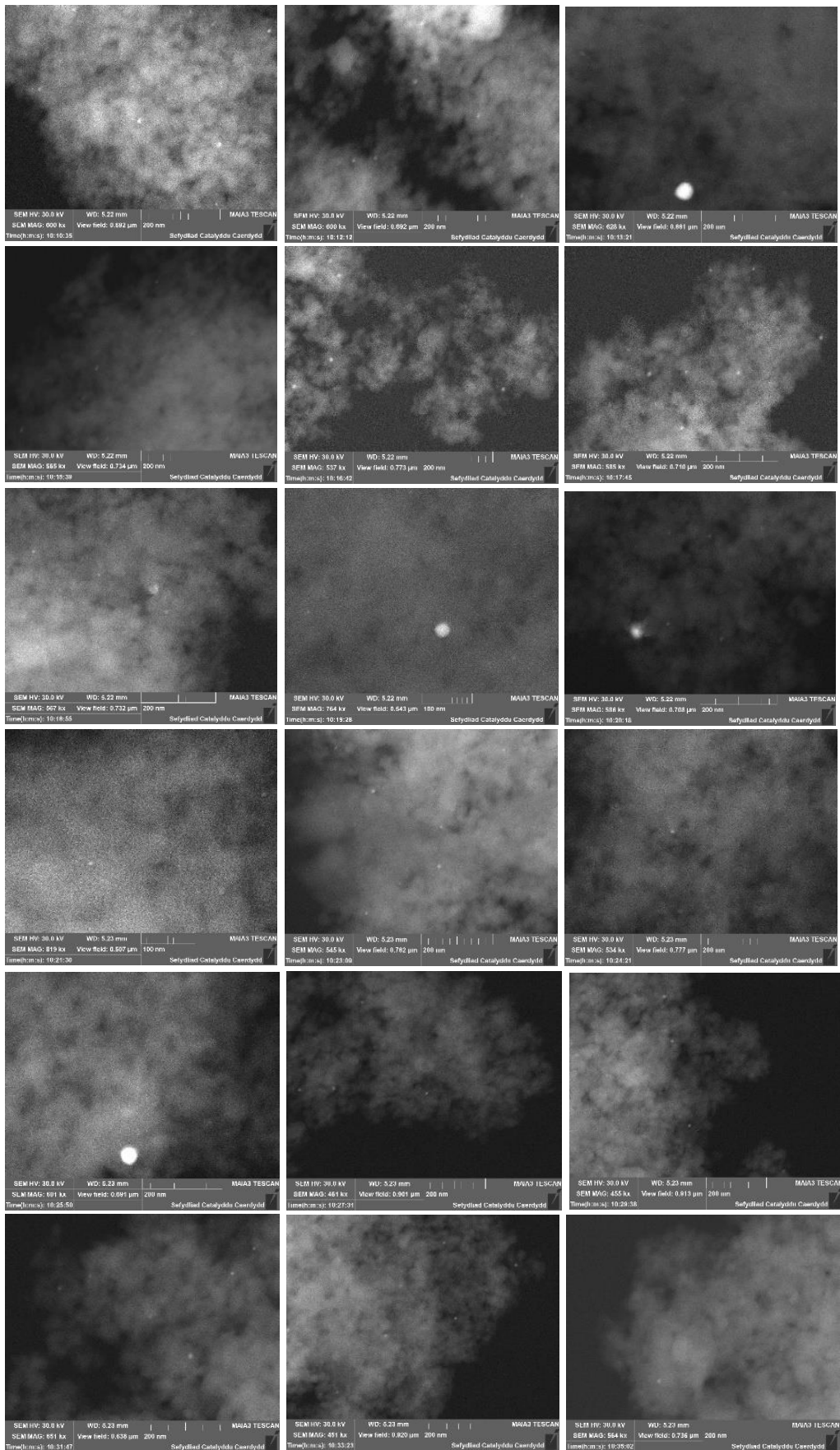
- 52 G. Wang, L. Xu, J. Zhang, T. Yin and D. Han, Enhanced photocatalytic activity of TiO₂ powders (P25) via calcination treatment, *Int. J. Photoenergy*, , DOI:10.1155/2012/265760.
- 53 J. K. Burdett, T. Hughbanks, G. J. Miller, J. V. Smith and J. W. Richardson, Structural-Electronic Relationships in Inorganic Solids: Powder Neutron Diffraction Studies of the Rutile and Anatase Polymorphs of Titanium Dioxide at 15 and 295 K, *J. Am. Chem. Soc.*, 1987, **109**, 3639–3646.
- 54 C. M. B. Henderson, K. S. Knight and A. R. Lennie, Temperature Dependence of Rutile (TiO₂) and Geikielite (MgTiO₃) Structures Determined Using Neutron Powder Diffraction, *Open Mineral. J.*, 2009, **3**, 1–11.
- 55 D. K. Smith and W. Newkirk, The crystal structure of baddeleyite (monoclinic ZrO₂) and its relation to the polymorphism of ZrO₂, *Acta Crystallogr.*, 1965, **18**, 983–991.
- 56 M. Bowker, *The Basis and Applications of Heterogeneous Catalysis*, Oxford University Press, 1998.
- 57 J. K. Edwards, *PhD Thesis Title: Direct synthesis of hydrogen peroxide from hydrogen and oxygen over catalysts containing gold*, Cardiff University, 2006.
- 58 E. N. Ntainjua, M. Piccinini, J. C. Pritchard, J. K. Edwards, A. F. Carley, C. J. Kiely and G. J. Hutchings, Direct synthesis of hydrogen peroxide using ceria-supported gold and palladium catalysts, *Catal. Today*, 2011, **178**, 47–50.
- 59 J. Pritchard, L. Kesavan, M. Piccinini, Q. He, R. Tiruvalam, N. Dimitratos, J. A. Lopez-Sanchez, A. F. Carley, J. K. Edwards, C. J. Kiely and G. J. Hutchings, Direct Synthesis of Hydrogen Peroxide and Benzyl Alcohol Oxidation Using Au-Pd Catalysts Prepared by Sol Immobilization, *Langmuir*, 2010, **26**, 16568–16577.

3.6. Appendix

3.6.1. Scanning Electron Microscopy Images

Below are all the SEM images taken for the catalysts described in 3.2.1. Different Support Study (0.33 wt% Au-0.33 wt% Pd supported on P25 TiO₂, ZrO₂, SiO₂ and ACS TS-1) (Fig. A3.1, A3.5, A3.6 and A3.7. respectively).

3.6.1.1. 0.33 wt% Au-0.33 wt% Pd/P25 TiO₂ Catalyst



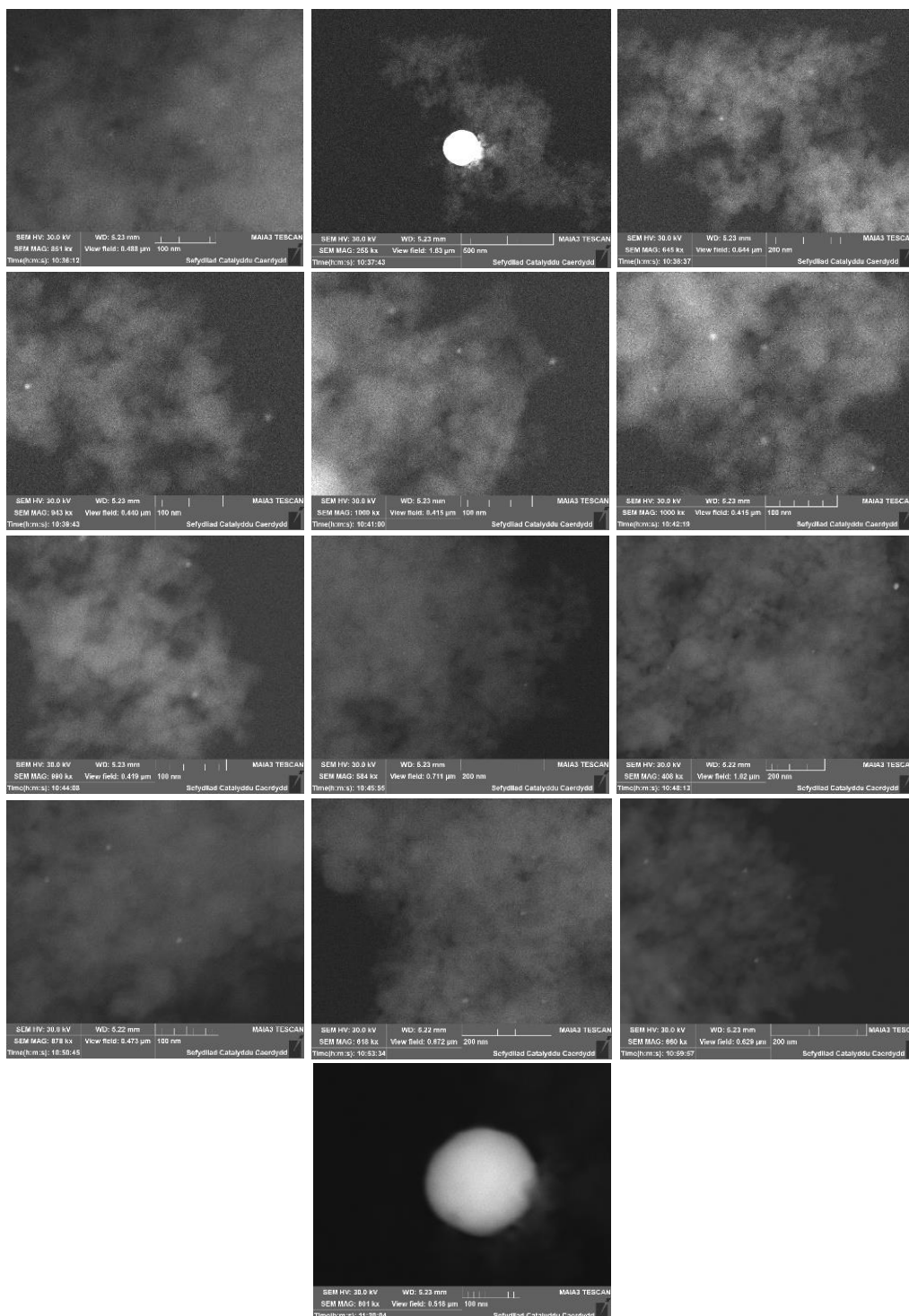


Figure A3.1. All SEM images for the 0.33 wt% Au-0.33 wt% Pd/P25 TiO₂ catalyst.

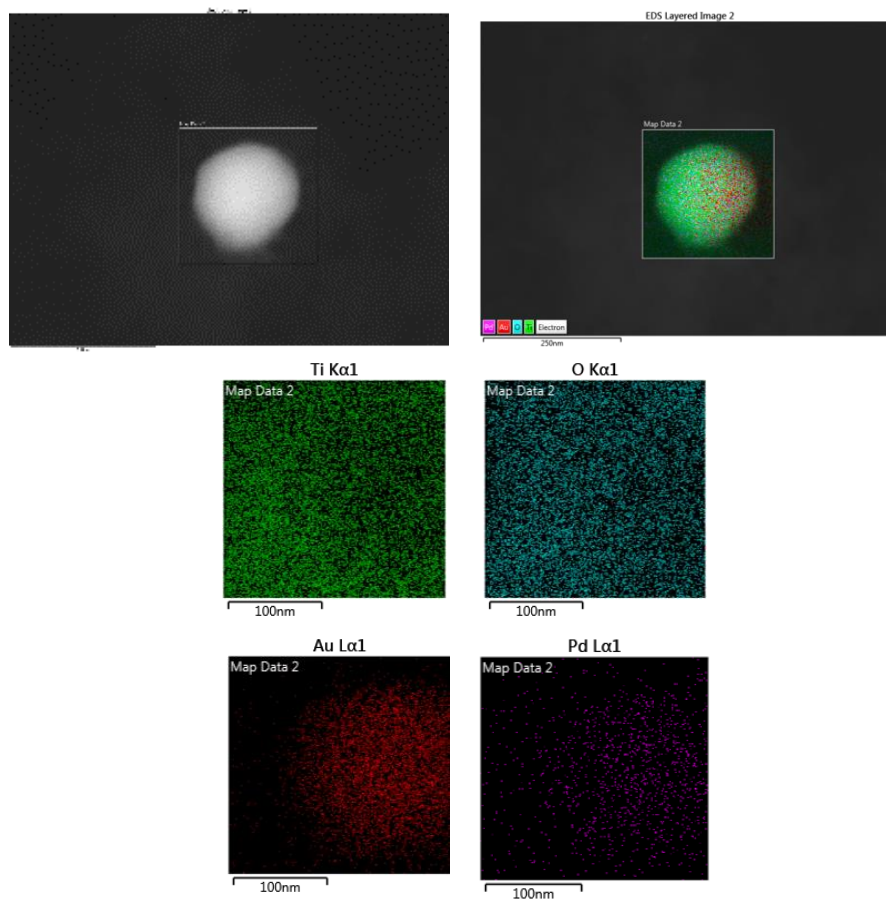


Figure A3.2. All SEM-EDX images and maps for site one of the sample of 0.33 wt% Au-0.33 wt% Pd/P25 TiO₂ catalyst.

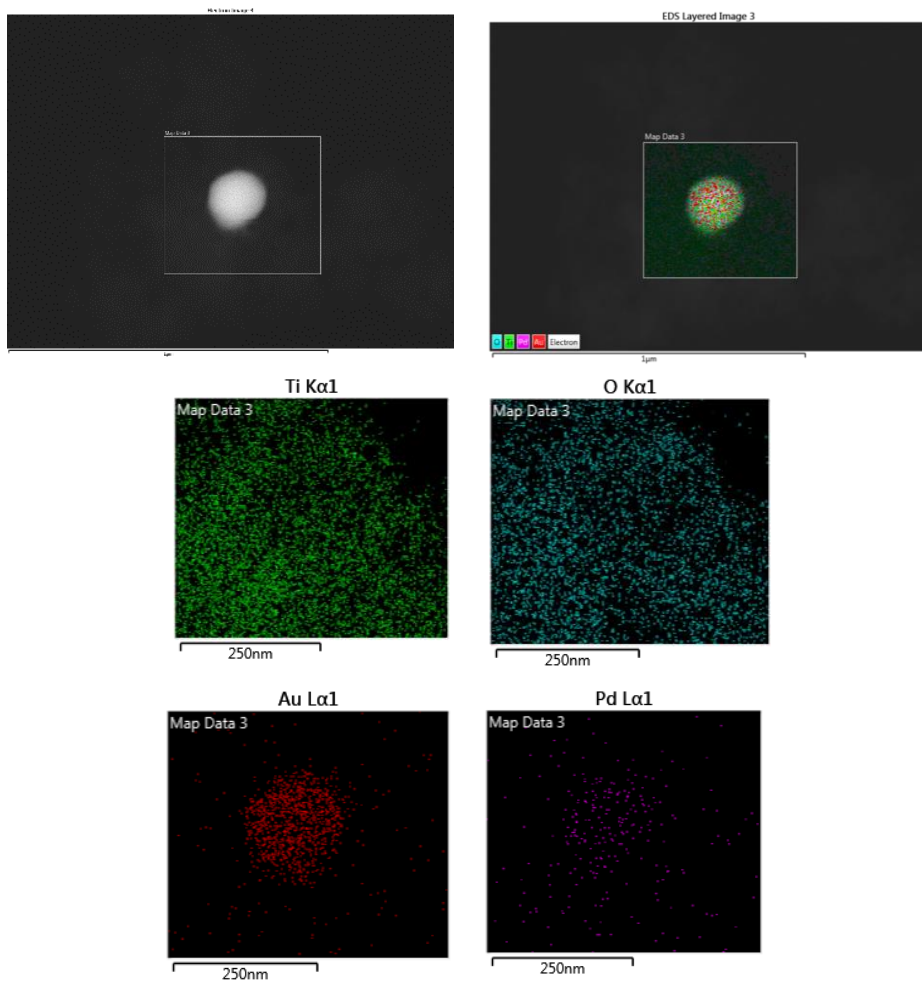


Figure A3.3. All SEM-EDX images and maps for site two of the sample of the 0.33 wt% Au-0.33 wt% Pd/P25 TiO₂ catalyst.

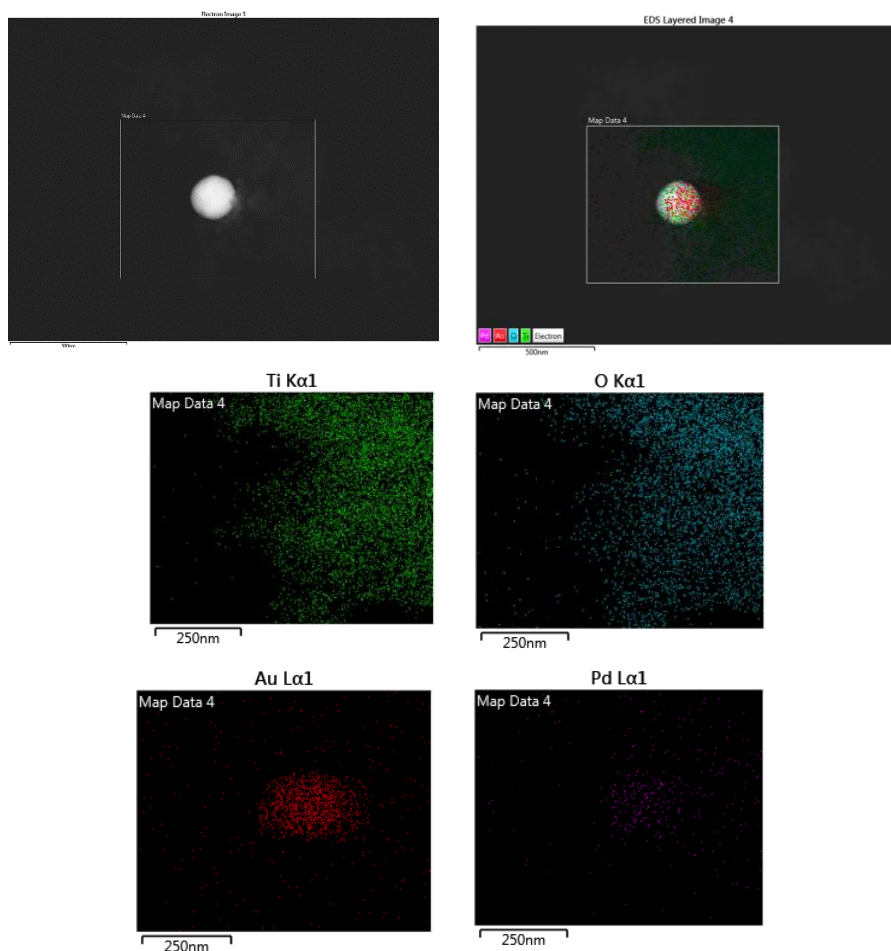


Figure A3.4. All SEM-EDX images and maps for site three of the sample of the 0.33 wt% Au-0.33 wt% Pd/P25 TiO₂ catalyst.

3.6.1.2. 0.33 wt% Au-0.33 wt% Pd/ZrO₂ Catalyst

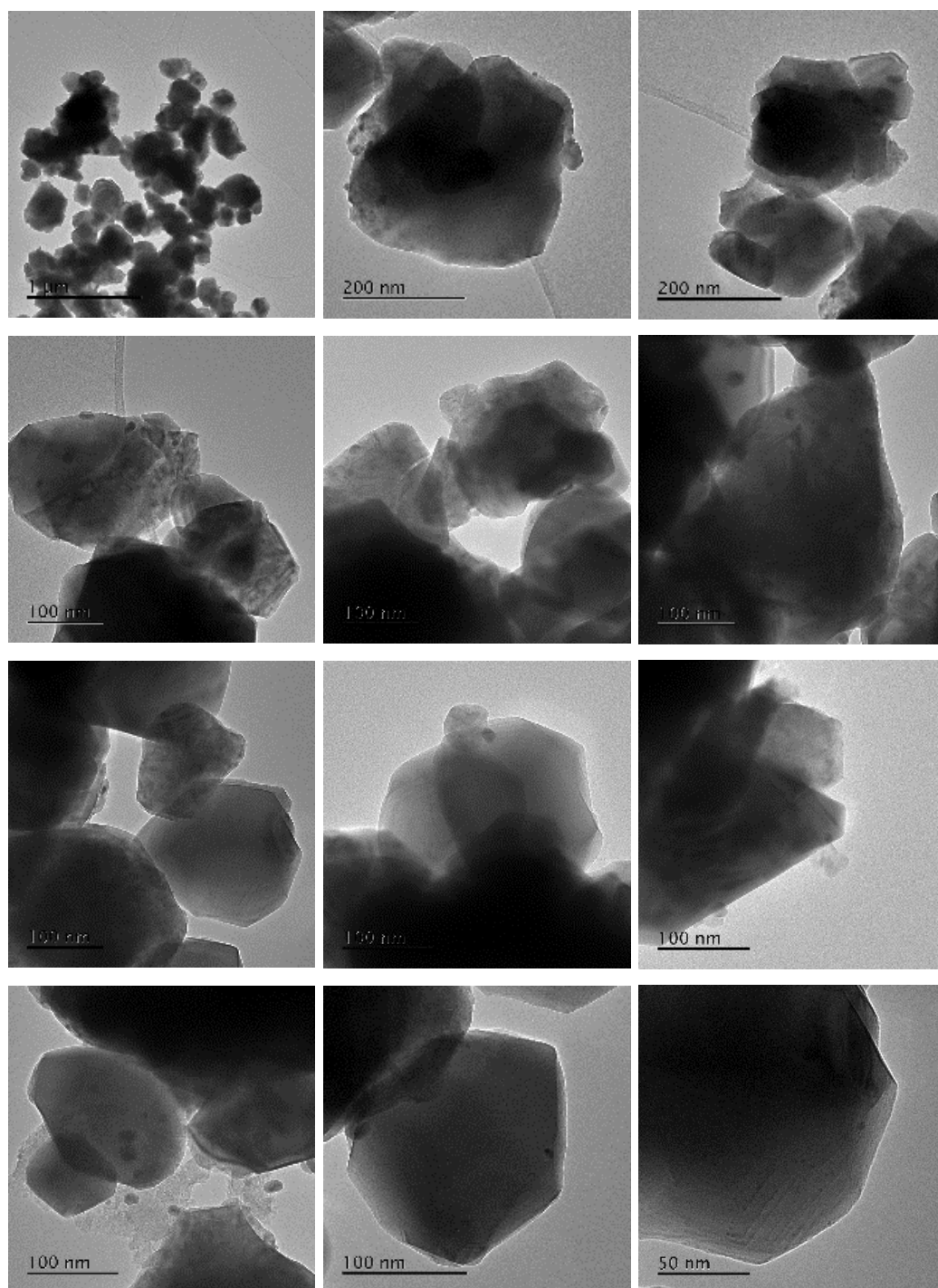


Figure A3.5. All SEM images for the 0.33 wt% Au-0.33 wt% Pd/ZrO₂ catalyst.

3.6.1.3 0.33 wt% Au-0.33 wt% Pd/SiO₂ Catalyst

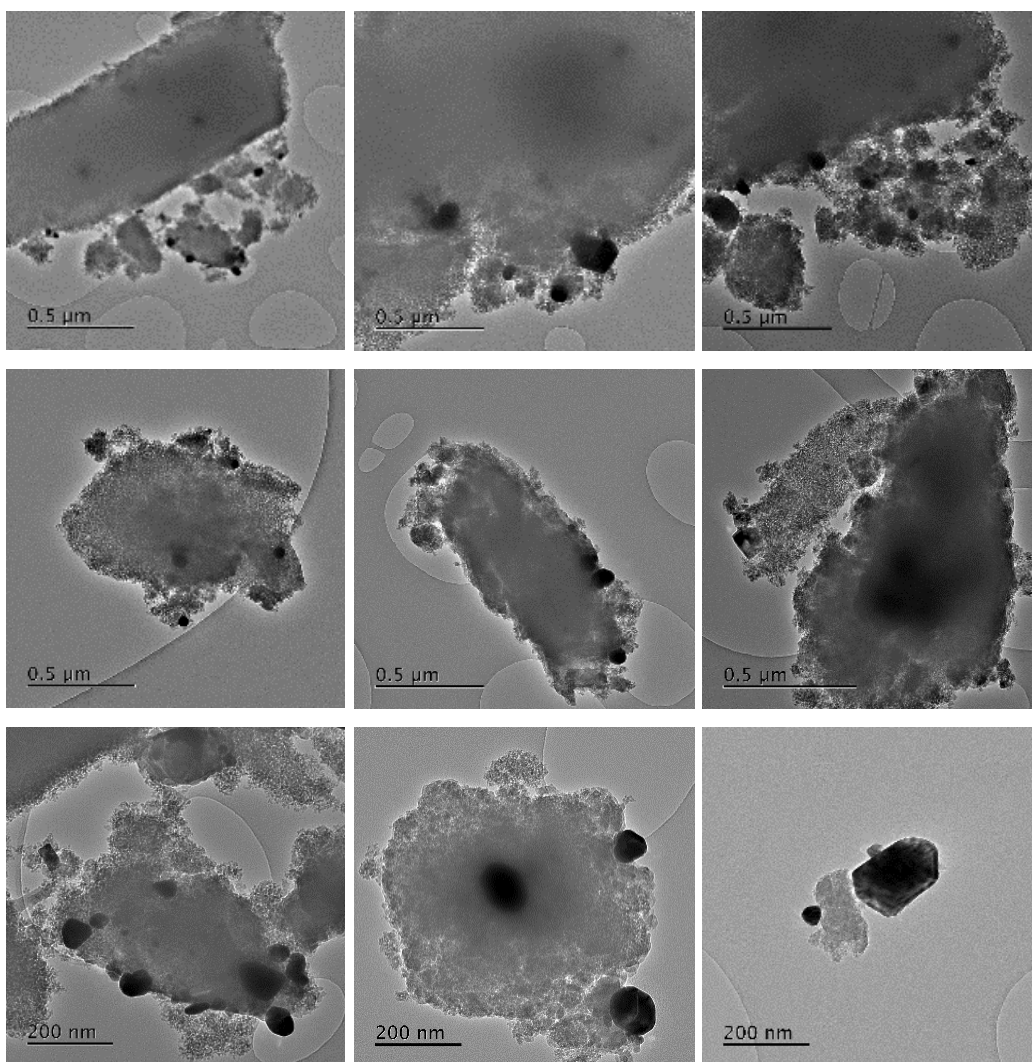
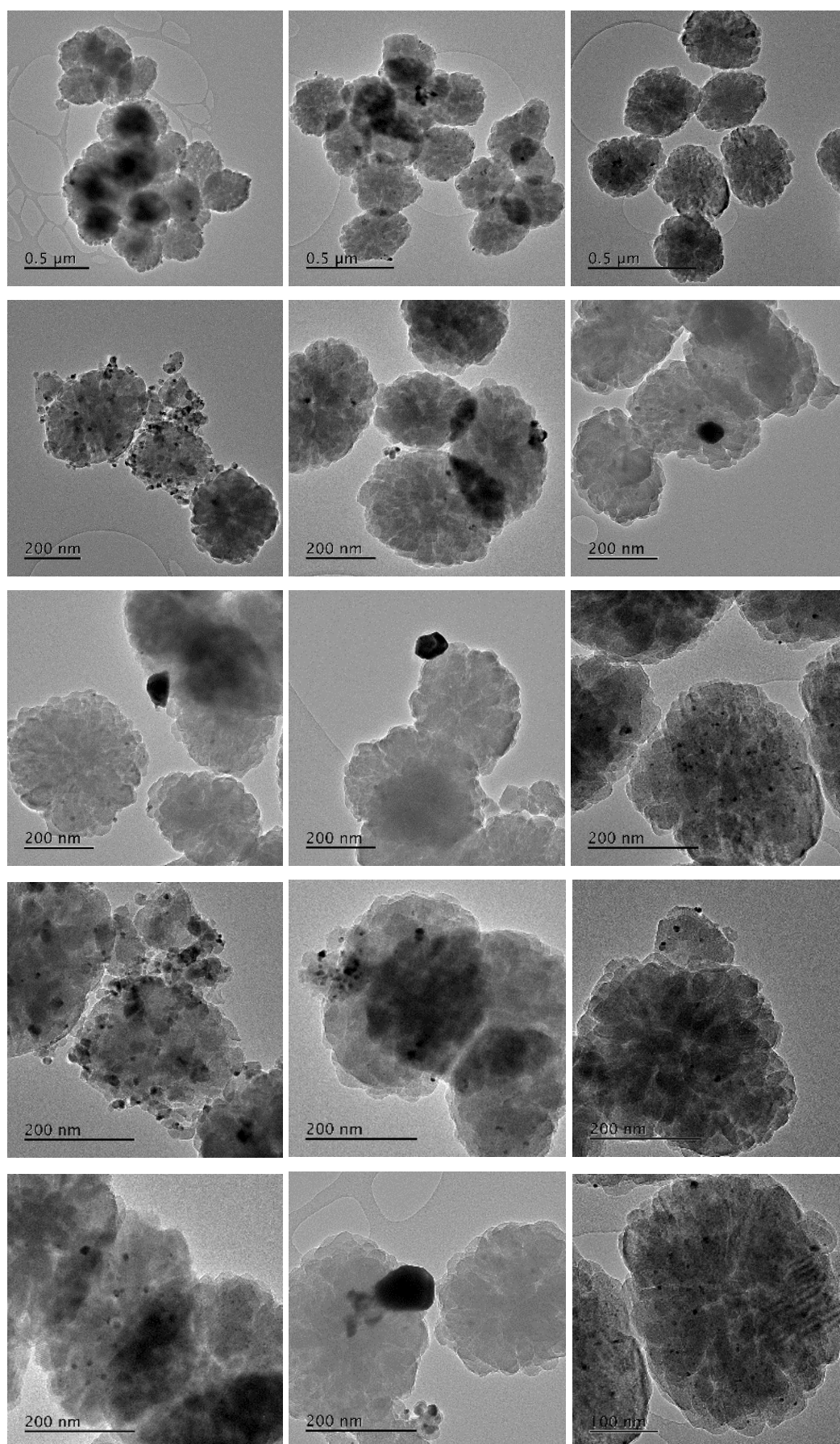


Figure A3.6. All SEM images for the 0.33 wt% Au-0.33 wt% Pd/SiO₂ catalyst.

3.6.1.4. 0.33 wt% Au-0.33 wt% Pd/ACS TS-1 Catalyst



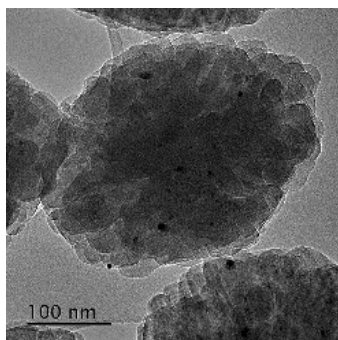


Figure A3.7. All SEM images for the 0.33 wt% Au-0.33 wt% Pd/P25 TiO₂ catalyst.

3.6.2. X-ray Photoelectron Spectroscopy

Below are all the XPS spectra taken for the catalysts described in 3.2.1. Different Support Study and the 3.2.4. Different Phases of TiO₂ Study (0.33 wt% Au-0.33 wt% Pd supported on P25 TiO₂, anatase TiO₂, rutile TiO₂, ZrO₂, SiO₂ and ACS TS-1) (Fig. A3.8, A3.9, A3.10, A3.11, A3.12 and A3.13. respectively).

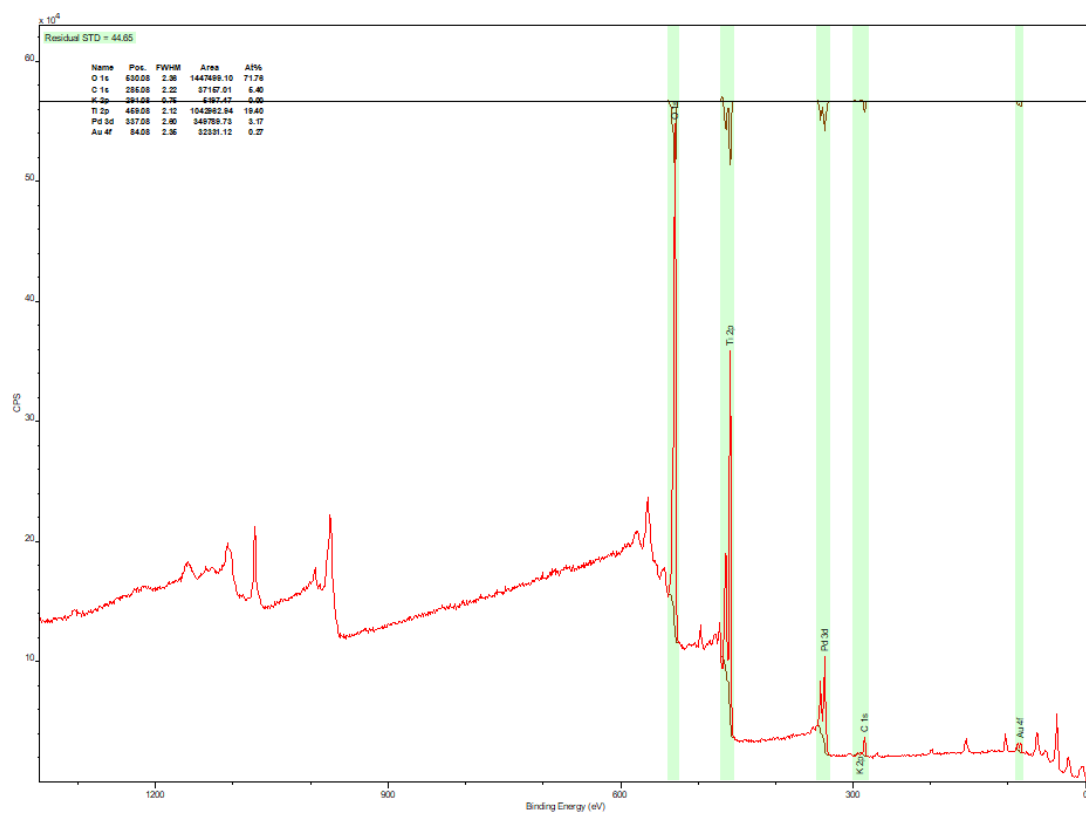


Figure A3.8. XPS spectra for the 0.33 wt% Au-0.33 wt% Pd/P25 TiO₂ catalyst.

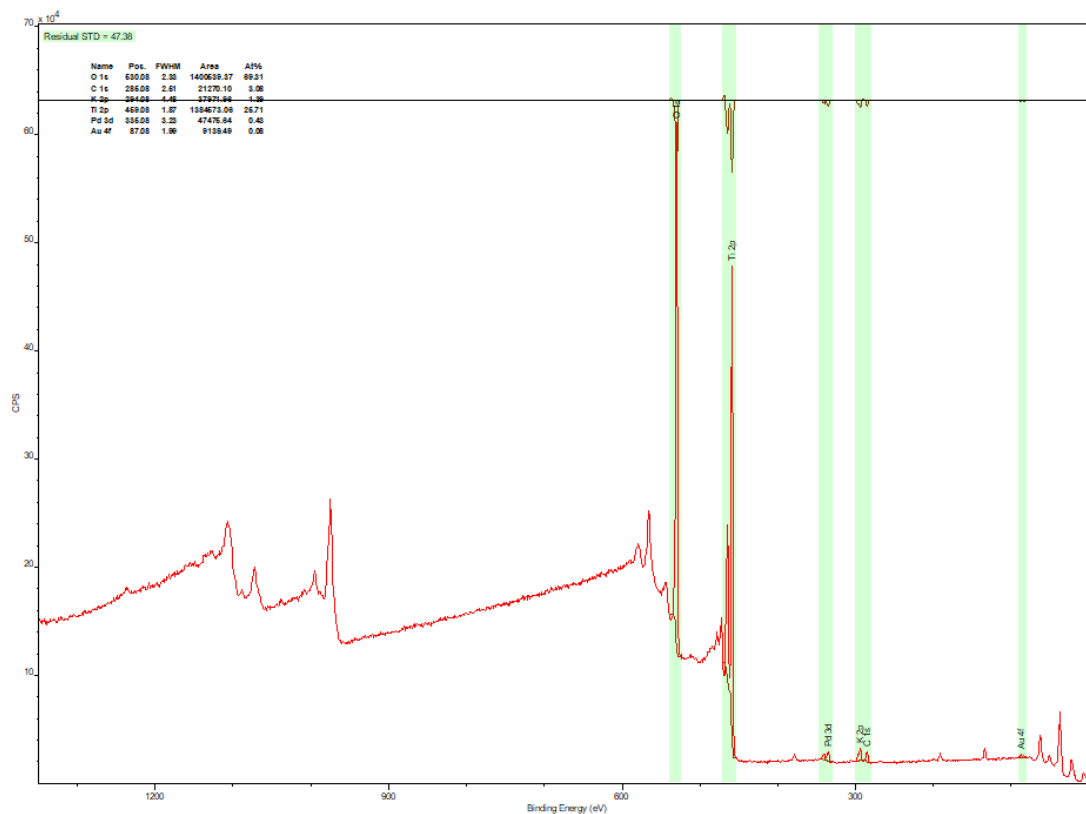


Figure A3.9. XPS spectra for the 0.33 wt% Au-0.33 wt% Pd/anatase TiO₂ catalyst.

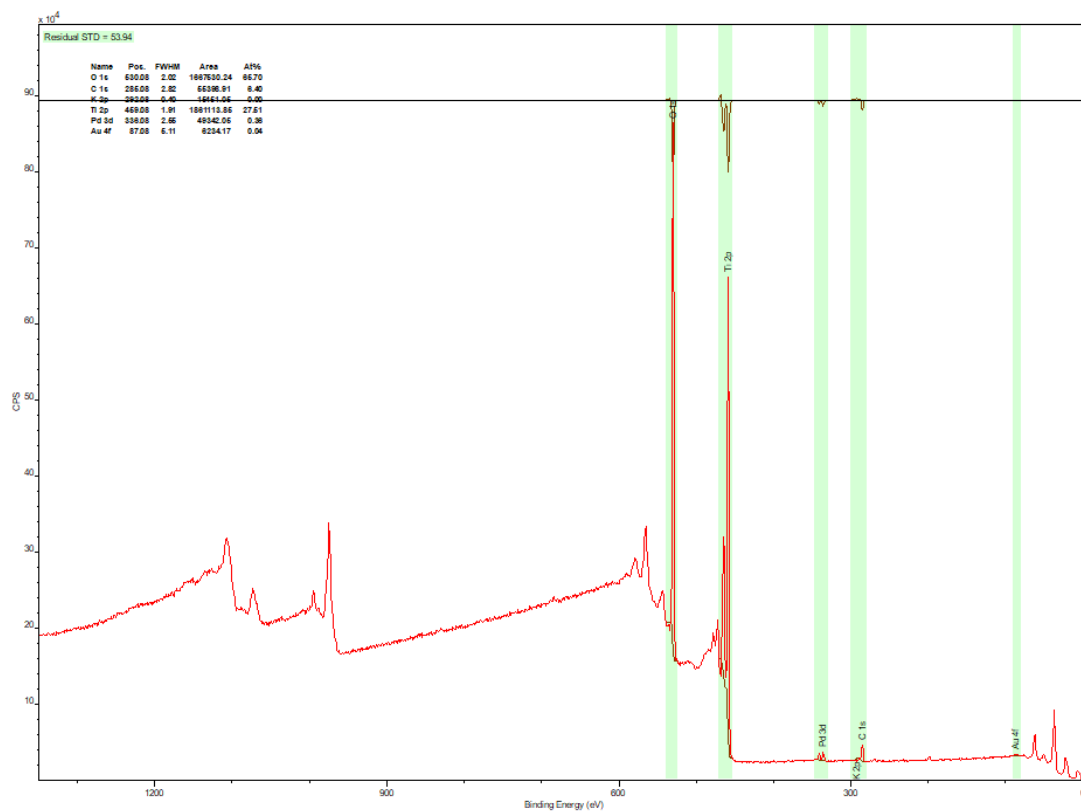


Figure A3.10. XPS spectra for the 0.33 wt% Au-0.33 wt% Pd/rutile TiO₂ catalyst.

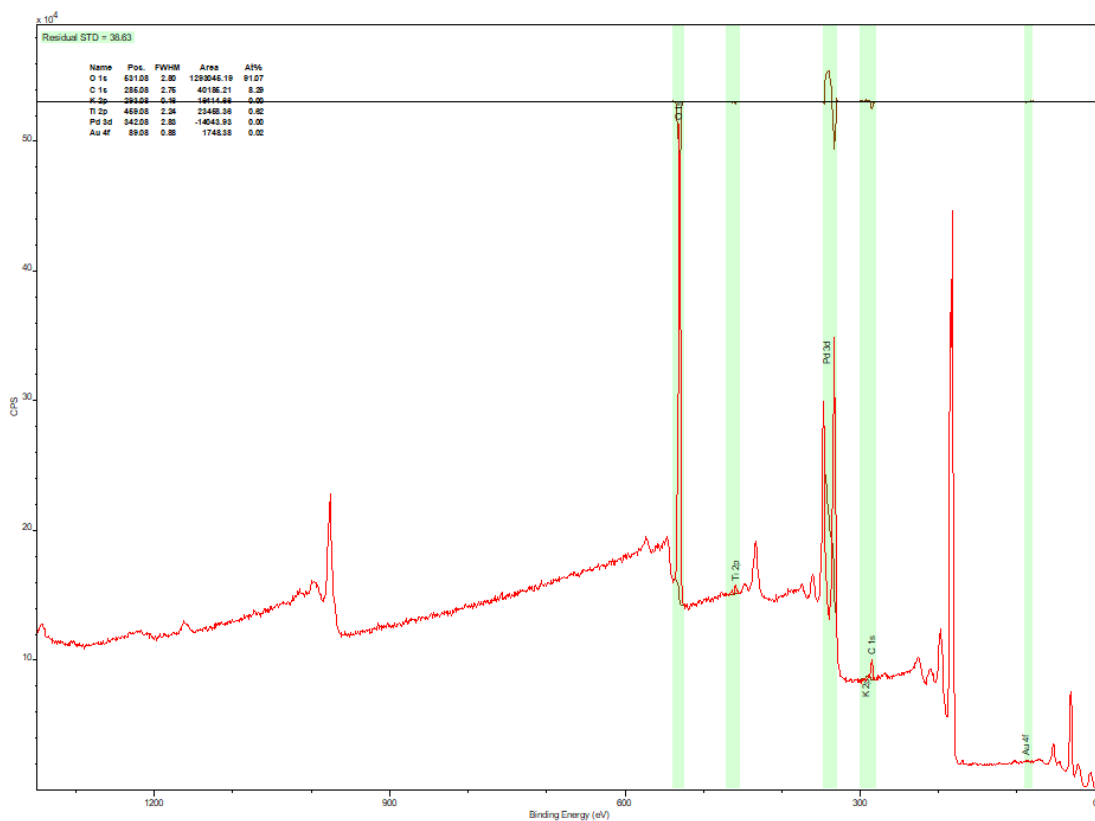


Figure A3.11. XPS spectra for the 0.33 wt% Au-0.33 wt% Pd/ZrO₂ catalyst.

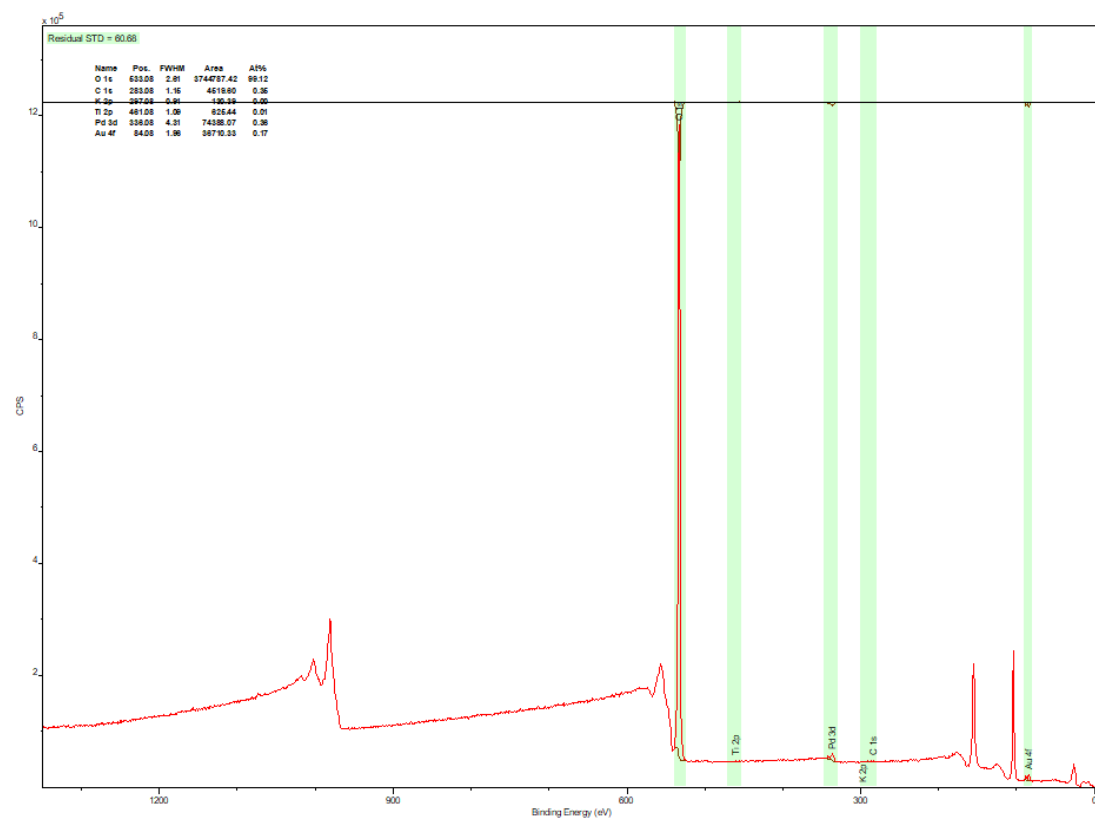


Figure A3.12. XPS spectra for the 0.33 wt% Au-0.33 wt% Pd/SiO₂ catalyst.

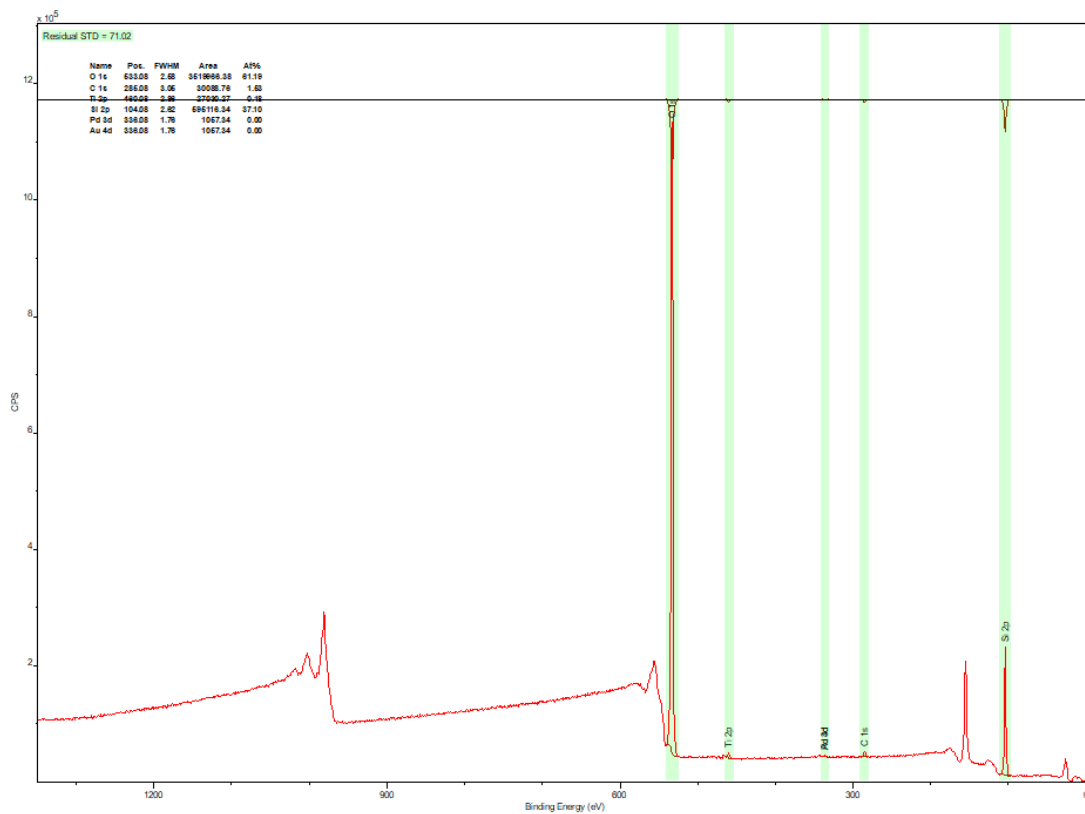


Figure A3.13. XPS spectra for the 0.33 wt% Au-0.33 wt% Pd/ACS TS-1 catalyst.

4. Epoxidation of Propene utilising *in-situ* Direct Hydrogen Peroxide Synthesis

4.1. Introduction

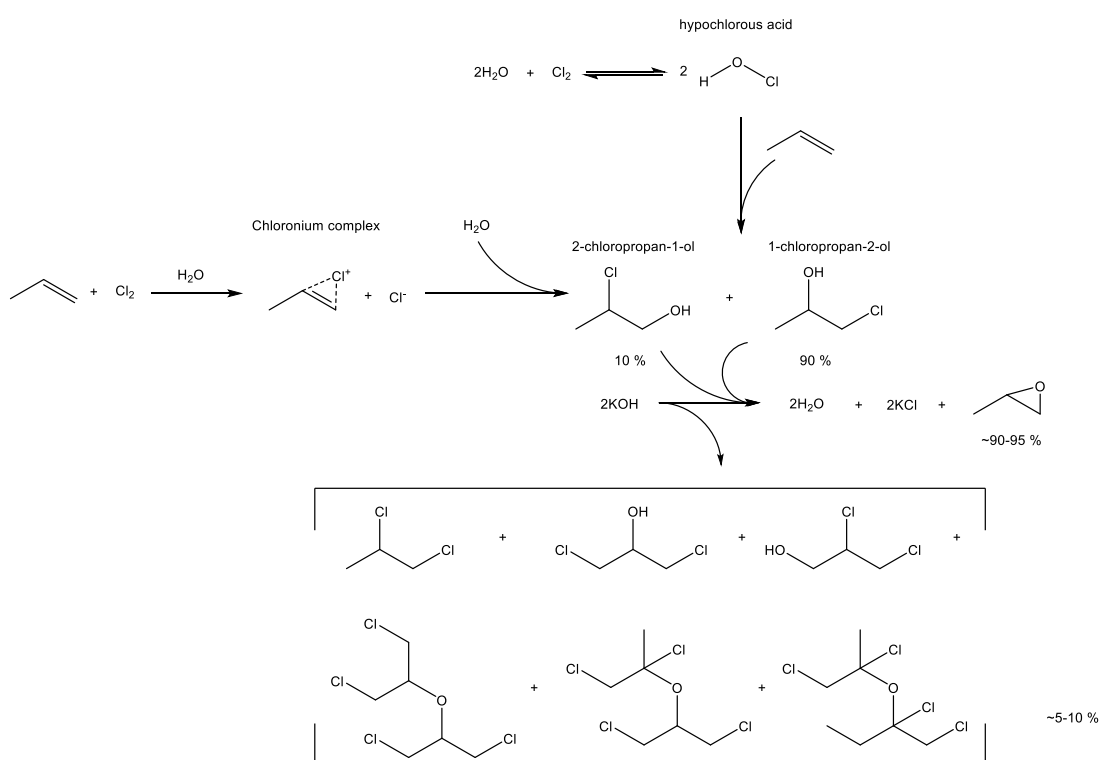
4.1.1. Propene Epoxidation

Propene oxide (PO) is a bulk chemical used to produce polyether polyols, which in turn, are transformed into polyurethane. Polyurethane has many applications such as foams, coatings, adhesives, sealants, injection moulding and more. PO is also used to synthesise propene glycol and propene glycol ethers; the former being a food additive and the latter being a paint and ink solvent, mainly for stripping paint. Propene glycol is also converted into polyesters. These useful products from PO are its largest application, with 65 %, 30 % and 4 % of all PO production dedicated to these products, respectively. PO production utilises 10 % of all propene synthesised, amassing ~5.8 million ton per year of PO from 1999 with a projected ~4-5 % increase each year.^{1,2}

The current processes of production require radical changes due to their acute disadvantages. There are two processes for PO production: the chlorohydrin and the hydroperoxide processes. The chlorohydrin process had a similar production capacity to the hydroperoxide process in the late 1990's. The hydroperoxide process was more favoured due to the negative environmental effects of the chlorohydrin process, thus, the industry has been building hydroperoxide plants. Unfortunately, the hydroperoxide process is not a selective pathway as *tert*-butanol (tBA) or styrene are synthesised along with PO. The quantity of these by-products can yield approximately three times more than that of PO, which means that the market is principally led by the demand of the by-products.^{1,2}

In 1859, Wurtz³ produced ethene oxide and PO using the chlorohydrin process in a bubble column reactor (323.15 K, 0.15 MPa), which in part was similar to Wilkinson's ether synthesis. A bubble column reactor is a column reactor with gas inserted at the bottom causing bubbles to rise within the liquid of the reactor. These reactors are used for gas-liquid chemical reactions.

Hypochlorous acid (HOCl), formed *in-situ* by the equilibrium reaction of the acid with chlorine (Cl) and water (H₂O), reacts with the alkene and forms the chlorohydrin (chloropropanol) from propene. Additionally, Nijhuis *et al.* also found that the reaction can proceed *via* a chloronium complex.¹ With the use of aqueous potassium hydroxide (KOH), this product is then dehydrochlorinated to produce the epoxide. The selectivity from this two-step reaction was ~90-95 %, due to the greater susceptibility the α-carbon has to electrophilic attack than the β-carbon, and the gas phase by-products formed were dichloropropanols, dichloroisopropyl ethers and 1,2-dichloropropane (Scheme 4.1).^{1,2}

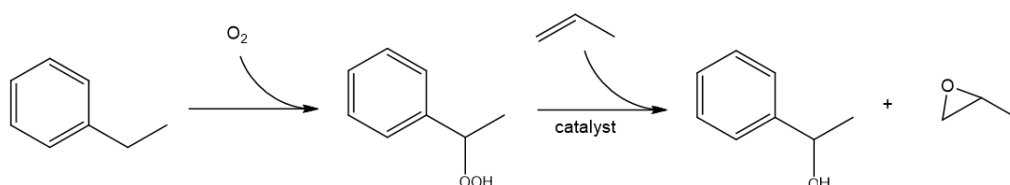


Scheme 4.1. Reaction pathway of the Chlorohydrin Process (some by-products excluded).^{1,2}

From the 1940's, the process for ethene oxide production was phased out due to a more efficient method for its production and the advances with a silver (Ag) catalyst. This resulted in ethene oxide plants being converted to PO plants. However, the enhanced selectivity that was observed for ethene oxide with Ag catalyst was not observed for propene. This was due to the additional methyl (CH₃) group competing with the oxidation pathways *via* H abstraction from the C² to form allyl cation intermediates. The ethene oxide plants that were converted to PO plants have been

gradually transformed to the hydroperoxide process for PO production, which required innovation in PO catalysis.^{1,2}

The hydroperoxide method is based on the peroxidation of an alkane to form an alkyl-hydroperoxide. These chemical species are then reacted with propene to produce an alcohol and the desired PO (product ratio – 2-4:1, respectively) (Scheme 4.2).



Scheme 4.2. Reaction pathway of the Hydroperoxide Process.^{1,2}

There are two derivatives to this method that have been commercially applied. With ~60 % of PO production plants, the major contributing method is the PO-styrene monomer (*i.e.*, PO-SM or SMPO) process (400.15 K, 3.00 MPa). Oxidation of ethylbenzene to ethylbenzene hydroperoxide occurs and this product is then further reacted with propene to form PO and α -phenyl ethanol. The latter species is dehydrated to produce styrene. The minor contributing process is the PO-tBA method (400.15 K, 0.20 MPa). Isobutane is oxidised to *tert*-butyl hydroperoxide (tBHP) and is then reacted with propene to form tBA and PO. Dehydration of the former product can form isobutene or it can be directly converted into methyl-*tert*-butyl ether (MtBE) with methanol.^{1,2}

Both variants of the hydroperoxide process use a bubble column reactor and are more selective than the chlorohydrin process, producing far less waste. The major drawback of the hydroperoxide process is that a larger amount of by-product is formed. The market for PO is dependent on the market for the by-product (SM or tBA). As MtBE is being used less as a fuel additive, the demand for it has decreased significantly, meaning PO production *via* the PO-tBA method has also decreased in favour of the PO-SM method. Should the demand for SM also decrease, PO production will also decrease and possibly cease without an alternate method.^{1,2}

Significant research is being carried out in this area with recent developments in the 'H₂O₂ combination process', with Ag and Au/TiO₂ catalysts. The discovery of Au/TiO₂ catalysts by Haruta *et al.* has been discussed previously in Chapter 1.⁴ With the literature regarding direct H₂O₂ synthesis previously discussed in Chapter 1,⁵⁻⁷ the literature regarding PO production using theoretical methods has been discussed below.

In 2006, Taylor *et al.* conducted kinetic experiments for the epoxidation of propene over a Au/TS-1 catalyst, prepared by the deposition-precipitation (DP) method. The conditions used in the experiments were as close as feasibly possible to industrial conditions without entering the explosive limit of the reactants; (H₂, O₂) and propene.⁸

The study used a hybridised form of a factorial design and a singular approach, where the former observed the effect of the change of multiple parameters and the latter observed the effect of the change of one parameter. This design reduced the amount of time required to test the parameters by involving a sampling technique to determine trends that the experiments would exhibit. Temperature and partial pressures of the reactants were changed to observe the kinetics surrounding PO formation and its resulting selectivity and yield.

From the three catalysts with different weight loadings (0.02, 0.04 and 0.06 wt%) and different TS-1 supports (Si/Ti ratio: 36 and 143) (0.02 and 0.06 wt% Au/TS-1(36) and 0.04 wt% Au/TS-1(143)) examined by Taylor *et al.*, a power rate law was determined for PO production from 33 tests using the 0.02 wt% Au/TS-1(36). However, it underestimated the experimental values acquired and was limited by the O₂ concentration range tested. It was discovered that at least two active sites must work together to produce the observed orders and a mechanism was proposed. The H₂O₂ was synthesised over the Au sites and subsequently reacted with propene that was adsorbed at the Ti⁴⁺ sites. The rate of PO synthesis was largely dependent on H₂ rather than propene and O₂, and the mechanistic insights from the Density Functional Theory (DFT) calculations were coupled with the reaction orders.^{9,10} It was assumed that the hydroperoxy (OOH) species on the Au active sites were the most abundant reactive intermediate; the same assumption was made for propene and the Ti⁴⁺ sites.⁸

The H₂ selectivity was determined, and it was found that it was at its highest (~13 %) when the optimised reactant mixture (10/10/10/70 vol% O₂/H₂/C₃H₆/N₂, respectively) and temperature (473.15 K) were employed, for the greatest catalyst

activation. However, this was considered an extremely low H₂ selectivity by Taylor *et al.* As H₂ concentration was decreased, its efficiency also decreased, and as temperature increased, the H₂ conversion and selectivity increased as well as the rate of PO synthesis. This indicated to the group that the energy required for direct H₂O₂ synthesis was greater than PO production.⁸

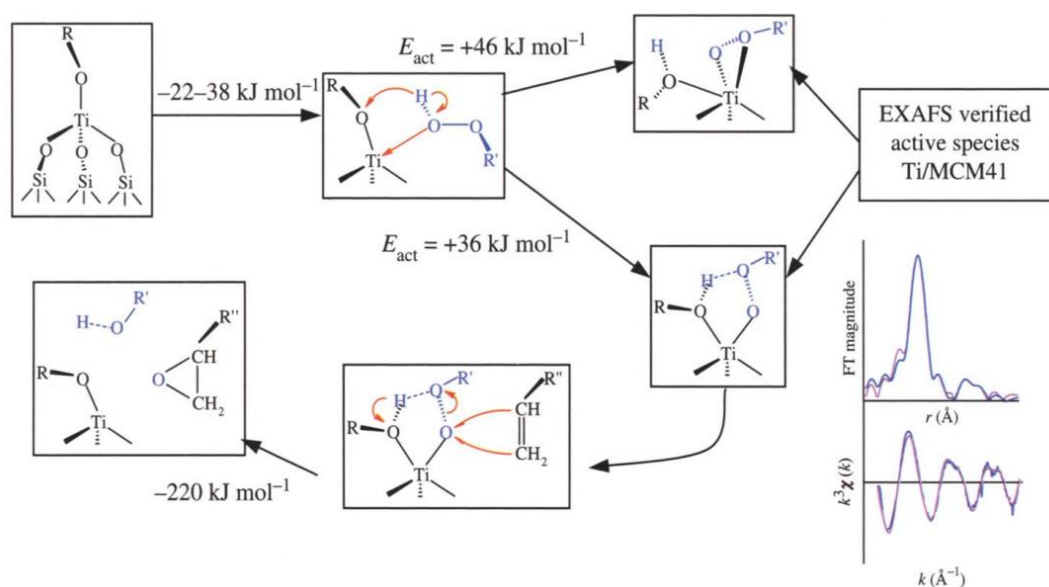
No DFT calculations were performed in this study, however, calculations and results from other studies were used, such as Barton *et al.*'s and Wells *et al.*'s works.^{9,10} Barton *et al.* conducted a kinetic study of direct H₂O₂ synthesis over Au nanoparticles supported on different silicas (amorphous silica, Silicalite-1 and TS-1).⁹ DFT calculations were completed upon the (111) and (211) facets of Au₅, Au₁₃ and Au₅₅ clusters to assess the reactivity and thermodynamic stability of the surface species and to model the different types of surface (rough against smooth).⁸ The DFT calculations utilised the DMol³ code in Materials Studio 2.2 and the double numerical with polarisation (DNP) basis set with the Generalised Gradient Approximation-Perdew-Burke-Ernzerhof (GGA-PBE) functional. Semi-core pseudopotentials were used to represent the tightly bound core electrons and the experimental value of the equilibrium Au lattice constant (4.087 Å) corresponded closely to the calculated value (4.197 Å). The effect of the metal particle size on the stability of the H₂- and O₂-derived adsorbed species were evaluated on a number of model Au surfaces. Small Au clusters with an odd number of atoms were analysed as previous calculations suggested that the adsorbates bind more strongly to the clusters.^{9,10} Clusters of Au (~5.00 Å) were selected to represent the particles in the Mordenite Framework Inverted (MFI) pores of the supports, and clusters that had less than 12 atoms had flat geometries, which conformed to the work of Bonacic-Koutecky *et al.*¹¹

As the top two layers were optimised with an adsorbate to simulate the surface relaxation on adsorption, the bottom four layers of each slab were fixed during the calculations, with a vacuum spacing (25.00 Å) in each unit cell.⁸ The Au(211) structure was used to approximate the activation energy (E_a) through constrained optimisation. Having excluded H₂O₂ decomposition as two hydroxy (OH) groups, the O-H bond distance for bond breaking and forming was constrained incrementally from the reactant structure value to the geometry of the product. The optimisation performed for H₂O₂ decomposition into two OH groups was completed with the HO-OH bond having been constrained. The accuracy of the DFT calculations for predicting E_{ads} was stated (20 kJ mol⁻¹).^{9,10} As this accuracy value depended on the calculation details and the employed surface models' validity, the group compared the different models

to deduce their results in terms of relative energetic trends as a function of particle size. This method was atypical as absolute values for a single model are usually analysed and compared. All reaction, activation and adsorption energies were determined without zero-point energy corrections at 0.00 K.

In 2005, Catlow *et al.*¹² studied multiple systems using hybridised Quantum Mechanics/Molecular Mechanics (QM/MM) and DFT. One of particular interest was the alkene epoxidation over a Ti^{4+} centre, exclusive to titanium silicates such as TS-1. A mechanism for this reaction had been created from this study.

In the proposed mechanism, H_2O_2 is adsorbed by the Ti^{4+} centre and dehydrogenated by a neighbouring O to form an OOH bound to the Ti^{4+} site. The intermediate OOH species was found to have two configurations, both observed experimentally by EXAFS.¹³ The first of the two configurations observed had both O atoms of the OOH bound to the Ti^{4+} centre (η^2) and the second was that the O atom without the H was bound to the Ti^{4+} site (Ti-O-OH) (η^1). The latter configuration had the lower E_a barrier, with the H atom stabilised by two O atoms. Studies from Ford *et al.*⁵ and Staykov *et al.*¹⁴ confirmed the observation that a metal-hydroperoxy intermediate was stable (Scheme 4.3).



Scheme 4.3. Catalytic cycle for epoxidation of alkene by Ti^{4+} centre, involving η^1 and η^2 intermediates, and including calculated energies. Images were reused with permission from reference.¹²

Following this transformation, the alkene donated its electrons from the double bond to the non-hydrogenated O. As this occurred, HO-OR dissociation resulted in the hydrogenated O being hydrogenated further by the H atom that had been bound to the Ti⁴⁺ site's neighbouring O atom, to form H₂O (or if a different functional group (R) was present; ROH). In this step, the alkene epoxide is formed and not bound to the surface of the TS-1.

However, this mechanism opposed the mechanism proposed by Taylor *et al.*⁸ Both utilise the Langmuir-Hinshelwood (LH) mechanism, but Catlow *et al.*¹² observed the H₂O₂ adsorbed to the Ti⁴⁺ site first, unlike Taylor *et al.*⁸ who observed the propene adsorbed first. Additionally, work completed by Harris *et al.*¹⁵ showed a different mechanism with a Au/TS-1 catalyst that this reaction proceeded by. The catalyst produced H₂O₂ and PO on separate, but adjacent, sites with sequential catalysis occurring: the former species produced on Au and the latter at the Ti⁴⁺ sites. Another point from this study was that PO inhibited the production of PO. This disagreement in proposed mechanisms calls for determination by experimental methods.

In 1996, Thiele *et al.* investigated propene epoxidation utilising a titanium silicate catalyst experimentally. The group determined that acidification of coordinated H₂O to the Ti⁴⁺ site and its reversible deprotonation to an ate complex, which inhibited the formation of the active species for epoxidation, explained the high catalytic activity (100 %) and PO selectivity (97 %). Catalyst pre-treatment with acidic or neutral salts enhanced the selectivity without diminishing the catalytic activity. The rationale for this was that the sites of high acidity (silanol groups at crystal defects) were neutralised by these salts. The Ti⁴⁺ sites were stronger in acidity than the silanol groups, meaning that a stronger base, such as sodium acetate, was required to deprotonate the Ti⁴⁺ sites and become site blocked. It was concluded that strong basic salts were detrimental to the catalyst's performance.¹⁶

Deactivation of the catalyst occurred through pore blocking of the TS-1 by PO oligomers, however, this can be resolved through a refluxing method with H₂O₂ as oxidation of these oligomers instigated their breakdown. Calcination (823.15 K) also rejuvenated the catalyst; however, the current work showed a loss of crystallinity for TS-1 upon calcination at 673.15 K. Nevertheless, this was with metal nanoparticles present that may have influenced the crystal structure of the TS-1, and therefore, the X-Ray Diffraction (XRD) patterns (Chapter 3).

The reflux method was more appealing as it can be completed at a lower temperature. Solvents were also tested for their effect on catalytic activity, and it was

found that methanol (CH₃OH) was the superior solvent. From these solvent tests with subsequent Gas Chromatography-Mass Spectrometry (GC-MS) analysis, it demonstrated that PO ring opening was acid catalysed. Therefore, acid sites can lead to loss of the desired product and decrease selectivity.

Joshi *et al.* studied a different mechanism over Au for the epoxidation of propene utilising *in-situ* direct H₂O₂ synthesis. Clusters of Au₃ *via* the B3LYP method were used, where O₂ adsorbed first with H₂ dissociating and forming OOH and H function groups. The O closest to the Au (more electrophilic) attacked the C¹=C² of the propene. At this point, the mechanism continued in two ways. The first way is the formation of H₂O from the OH and H that were bonded to the same Au atom and subsequent desorption. The second possibility is another H₂ is added to form H₂O from the AuOH. The remaining H groups rearrange to separate bridge and terminal sites. Additional O₂ reformed the OOH and H groups previously observed.¹⁷

This study identified that the epoxidation was the rate-determining step (RDS). However, this work was not representative as Au₃ clusters are unlikely to exist on synthesised catalysts, even those prepared *via* sol-immobilisation (S_{IM}). With the lack of a support material, the geometries observed may not occur in the “real world” as the support material would repel the terminal H atom, observed in the second mechanism, into the vacuum. The bridged H atom would move to the other two Au atoms.

Roldan *et al.*¹⁸ studied large Au(111) surfaces for the epoxidation of propene using DFT. The three mechanisms of this reaction were also investigated. The radical mechanisms involved H abstraction of the propene to form the radical (C¹, denoting the first C atom), which was subsequently oxidised by atomic O. The other two mechanisms were formulated based on the formation of an oxametallocycle (*i.e.*, Oxygen-Metal-Metal-Propene (OMMP)) either at C¹ or C² of the propene molecule) (Fig. 4.1).

This group identified that the radical mechanism gave a lower E_a compared to the OMMP intermediates. However, the OMMP gave more stable intermediates, of which the C¹ conformation was the lowest. The H abstraction was more kinetically favourable as the OMMP was more thermodynamically favourable. Although that this was a slab of Au, these mechanisms introduced something different to those studies previously discussed. The studies by Taylor *et al.*, Catlow *et al.*, Harris *et al.* and Joshi *et al.* utilised *in-situ* direct H₂O₂ synthesis for their propene epoxidation studies,^{8,12,15,17} whereas Roldan *et al.*¹⁸ observed ½ O₂ as the oxidant.

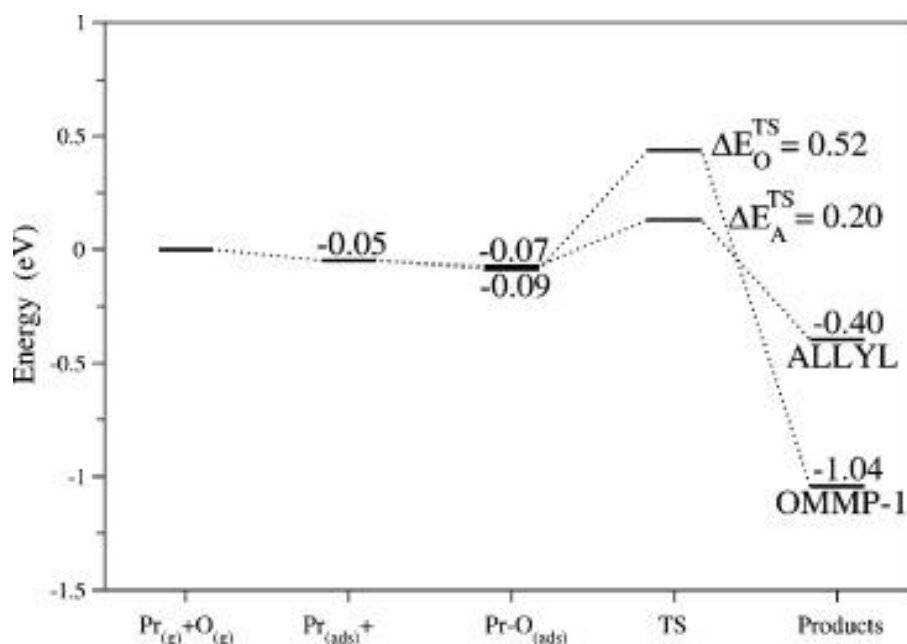
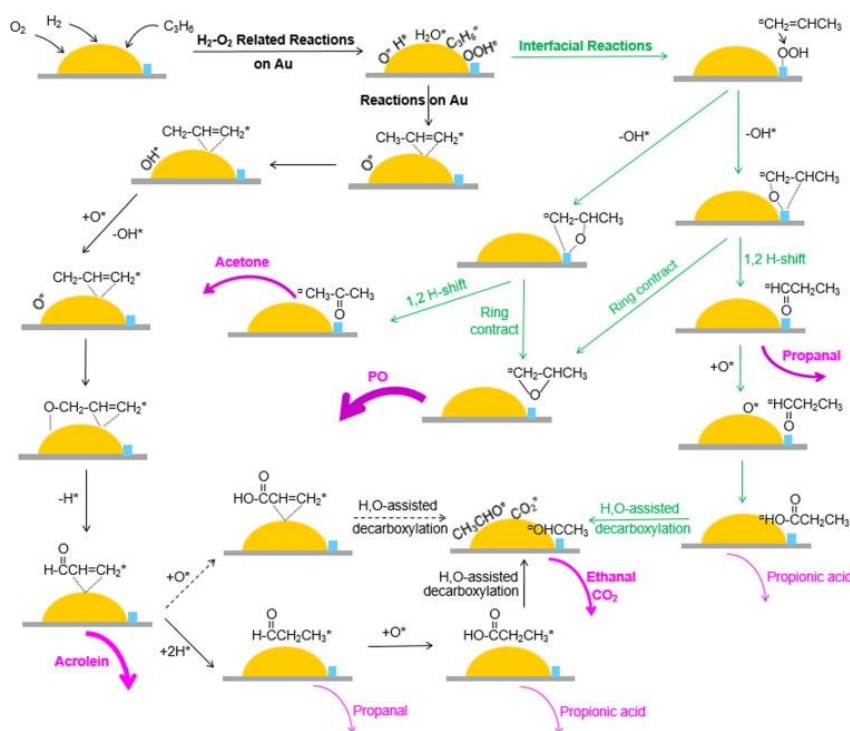


Figure 4.1. Reaction coordinate profile for the epoxidation of propene over the Au(111) surface. Image was reused with permission from reference.¹⁸

Ji *et al.*² studied PO production utilising *in-situ* direct H₂O₂ synthesis over a Au/TiO₂/SiO₂, via kinetic Monte Carlo (KMC) simulations. In particular, the mechanisms of interfacial and bulk Au were investigated (Scheme 4.4).



Scheme 4.4. Proposed reaction scheme for interfacial and surface Au pathways for H₂O₂ synthesis, hydrogenation and decomposition and propene epoxidation. Image reused with permission from reference.²

From the mechanism explored, an oxametallocycle was observed, similar to Roldan *et al.*'s work.¹⁸ The observation of Ti-OOH was also noted, which agreed with the work by Catlow *et al.*,¹² that provided a more favourable pathway at the interface.² It expanded on the further undesirable reactions that PO could undertake whilst in an oxidising environment. A key point that was discovered was that an optimum ratio of H₂/C₃H₆ was required to enhance PO selectivity (14/6 (2.33) H₂/C₃H₆; PO selectivity >91 %). To further enhance the selectivity values, reducing the amount of atomic O on the surface of the catalyst was vital.

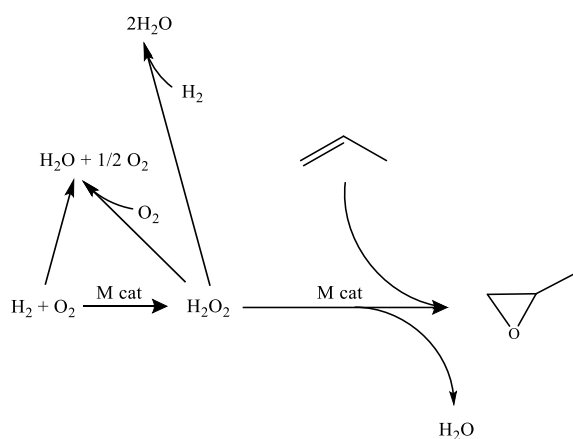
KMC calculations use the elementary reaction energetics to work out how the reaction should proceed on an idealised surface. This means that realistic surface populations of intermediate species can be built up and the overall kinetics of the reaction can be estimated. Although KMC simulations provide greater accuracy to the calculations, a greater amount of computational effort and time is required for these types of calculations. In addition, Prats *et al.* found that the construction of appropriate lattice models was required, which were completed manually, with no automatic process available. The KMC algorithms did not account for the surfaces' processes, with dissimilar reaction rates being noted as well.¹⁹

From the literature, there have been different mechanisms for propene epoxidation utilising an oxidant over the same and different active sites. Thus, a greater amount of research must be conducted to prove or disprove the catalytic mechanisms that the different research groups proposed. The primary focus of the literature thus far has been on Au catalysts, with TS-1 being a favourable support material due to its affinity for H₂O₂ and propene. However, there has been no research for Pd and AuPd catalyst using DFT. Nevertheless, there has been some experimental research of these catalysts in the studies by Shin *et al.*²⁰ and Prieto *et al.*²¹

One of the aims of the current work was to explore the Pd catalyst in comparison to Au. With little agreement on the mechanisms proposed in the literature, this research will highlight how the reactions of direct H₂O₂ synthesis and its subsequent utilisation for propene epoxidation occurs on these two metals. Additionally, Bi-metallic catalysts have often been heralded as a superior compromise between activity and selectivity that is not normally afforded from mono-metallic catalysts.

4.2. Results and Discussion

The aim of the current work was to research the catalytic abilities of Au(111), Au(100), Pd(111) and Pd(100) for the epoxidation of propene utilising *in-situ* direct H₂O₂ synthesis. This required investigation into the adsorption of the reactants, intermediates, and products of each reaction step in the catalytic process (Scheme 4.5).



Scheme 4.5. Reaction scheme of the epoxidation of propene utilising *in-situ* direct H₂O₂ synthesis over a metal catalyst (M cat, where M is Au or Pd).

The key difference to the work of Ji *et al.*² was that the studies of the current work will investigate pure surfaces and not interfacial reactions. Additionally, Ji *et al.* further explored subsequent and side reactions involved in the reactions of direct H₂O₂ synthesis and the epoxidation of propene.² This work will neglect these pathways as well as the hydrogenation and decomposition pathways that could subsequently occur after H₂O₂ has been synthesised on the surface of the catalyst(s).

Using DFT and the Vienna *Ab-initio* Simulation Package (VASP), the thermodynamics of propene epoxidation utilising *in-situ* direct H₂O₂ synthesis were determined, and possible reaction mechanisms were alluded to. This was completed by using geometry optimisation calculations and Densities of States (DoS) calculations. The current work will give the scientific community an insight into these reactions over Au and Pd catalysts, which show how to modify catalysts to achieve a more selective process.

4.2.1. Gold

Gold has been shown in various studies to be a selective element for various catalytic reactions. However, it has been previously reported by Barrio *et al.*^{22,23} that the adsorption of H₂ and O₂ on Au does not readily occur. This was due to their associated positive ΔG values. With this information, it was important to attempt to attain values for adsorption and possible dissociation for the most and second most stable surfaces of Au, not only to draw comparisons, but for future research for alloyed surfaces utilising Au.

4.2.1.1. Gold(111)

Geometry optimisation calculations of Au(111) and the adsorbates at different active sites were completed. The reaction pathways for direct H₂O₂ synthesis were explored as H₂, O₂ and H₂O₂ adsorption and dissociation configurations were created and optimised. Both H₂ and O₂ need to adsorb to form H₂O₂ on the surface. H₂ was the first molecule studied. Au(111) is a stable surface (the most stable of the four studied), which resulted in little interaction with H₂ (Table 4.1 and Fig. 4.2).

Table 4.1. Adsorption energies for the different positions of H₂ adsorbed to Au(111) without and with D3 corrections.

Site	Position	$E_{ads}^{PBE} / \text{kJ mol}^{-1}$	$E_{ads}^{PBE+D3} / \text{kJ mol}^{-1}$
Hollow	fcc	-1	-8
Top	Vertical	-1	-7

From the results observed, it was clear that almost no interaction between Au(111) and H₂ occurred and could be deemed to be site insensitive with only $\sim 1 \text{ kJ mol}^{-1}$ difference between the two sites. Even with the D3 corrections applied, the E_{ads} was above -10 kJ mol^{-1} , meaning that there was no obvious physical interaction. This was consistent with previous work that attempted the same.^{22,23} Moreover, Fig. 4.2 demonstrated that the optimised structures had little interaction because of the increased distances between the surface and the H₂ molecule, confirming the results summarised in Table 4.1 (Fig. 4.2).

It was seen that the Hollow fcc site had an E_{ads} of ~ -8 kJ mol $^{-1}$, resulting in an average distance between the surface and the closest H atom of ~ 4.42 Å. When compared to the other adsorption site, the Top Vertical site had a slightly more positive E_{ads} value than the other site at ~ -7 kJ mol $^{-1}$, with an Au-H interatomic distance of ~ 3.02 Å. No movement of the top layer of Au atoms was observed for either site, which was indicative of weak adsorption as no repulsion between the adsorbate and surface was observed (Table 4.1 and Fig. 4.2).

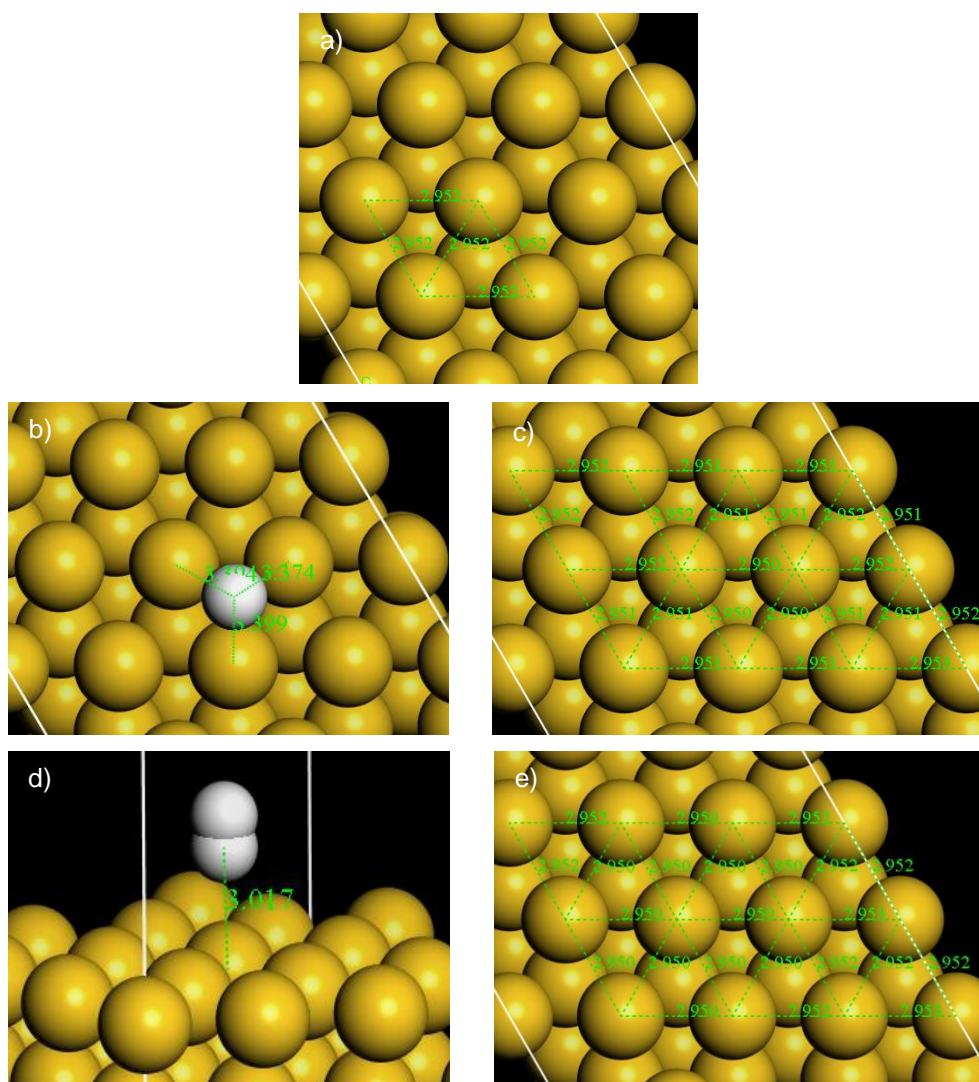


Figure 4.2. Images of the geometry optimisation calculations for H₂ adsorbed to Au(111) calculated with D3 corrections and the adsorbate removed, where **a)** is the clean surface, **b)** is the Hollow fcc site with the adsorbate, **c)** is the Hollow fcc site without the adsorbate, **d)** is the Top Vertical site with the adsorbate, and **e)** is the Top Vertical site without the adsorbate. The yellow atoms represent the Au atoms, and the white atoms represent the H atoms. Interatomic distances in green are in Angstroms (Å).

The reason for this difference was due to the interaction of the H atoms with the surface. If H₂ had adsorbed to the surface, it could very easily desorb, thus, making this interaction unlikely to occur during a catalytic reaction. Furthermore, observations of the top layer of the Au(111) surface revealed that the Au atoms did not move. This was expected as Au has a low affinity for H₂. This was the case regardless of site or orientation of the H₂ molecule (Table 4.1 and Fig. 4.2).

In Fig. 4.3, the DoS of the Hollow fcc site showed that there was the slightest interaction between the Au(111) surface and the H₂. This interaction resulted in the anti-bonding orbital of the H₂ above the Fermi level being reduced to almost nothing with the density being spread out. The bonding orbital had been reduced and shifted towards the Fermi level by ~+5 eV. The small s-orbital peak observed for the adsorbed H₂ suggested that the overlap of bonding orbitals between the surface and adsorbate was weak, which was correlated to the E_{ads} value. The gas phase H₂ reference bonding orbital peak was more negative in energy than that of H₂ adsorbed to Au(111) (Table 4.1, and Fig. 4.2 and 4.3).

Two electrons in the anti-bonding orbital would be needed for the dissociation or scission of the H₂ single bond, which did not break. There was no significant bond lengthening of the adsorbate and remained at ~0.75 Å, which coupled with the adsorption energy data, would confirm that this interaction between H₂ and Au(111) was weak. The H₂ would also desorb easily (Tables 4.1, and Fig. 4.2 and 4.3).

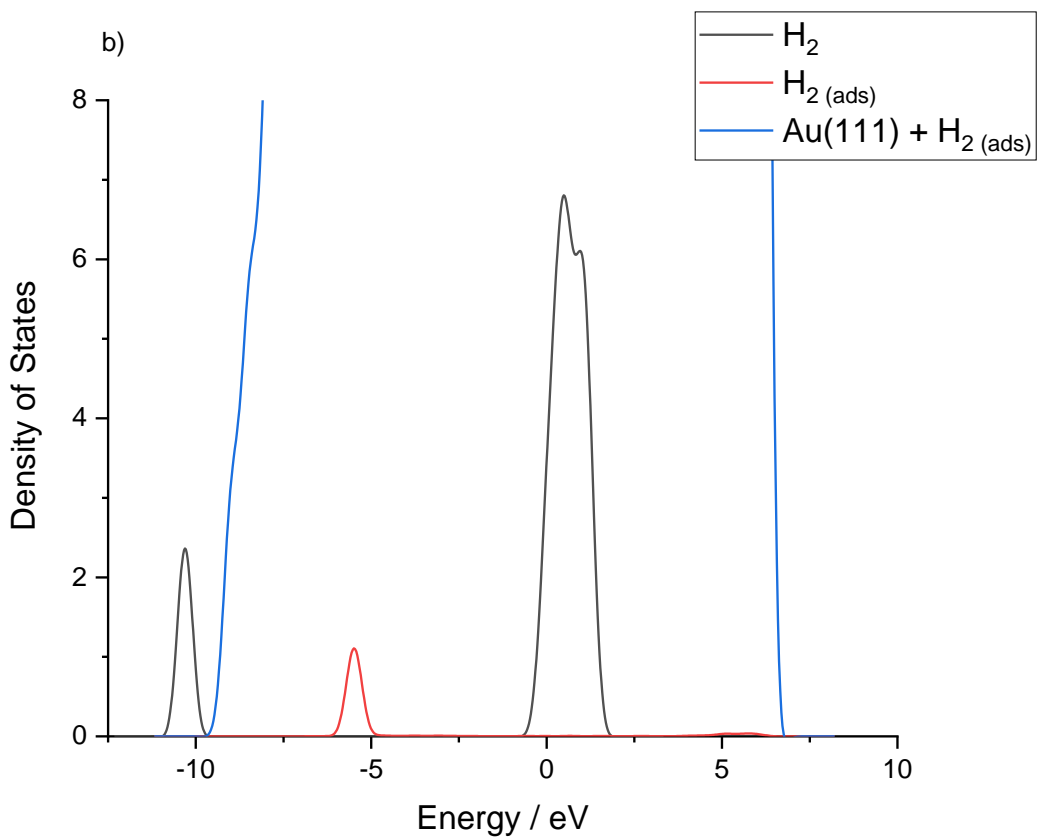
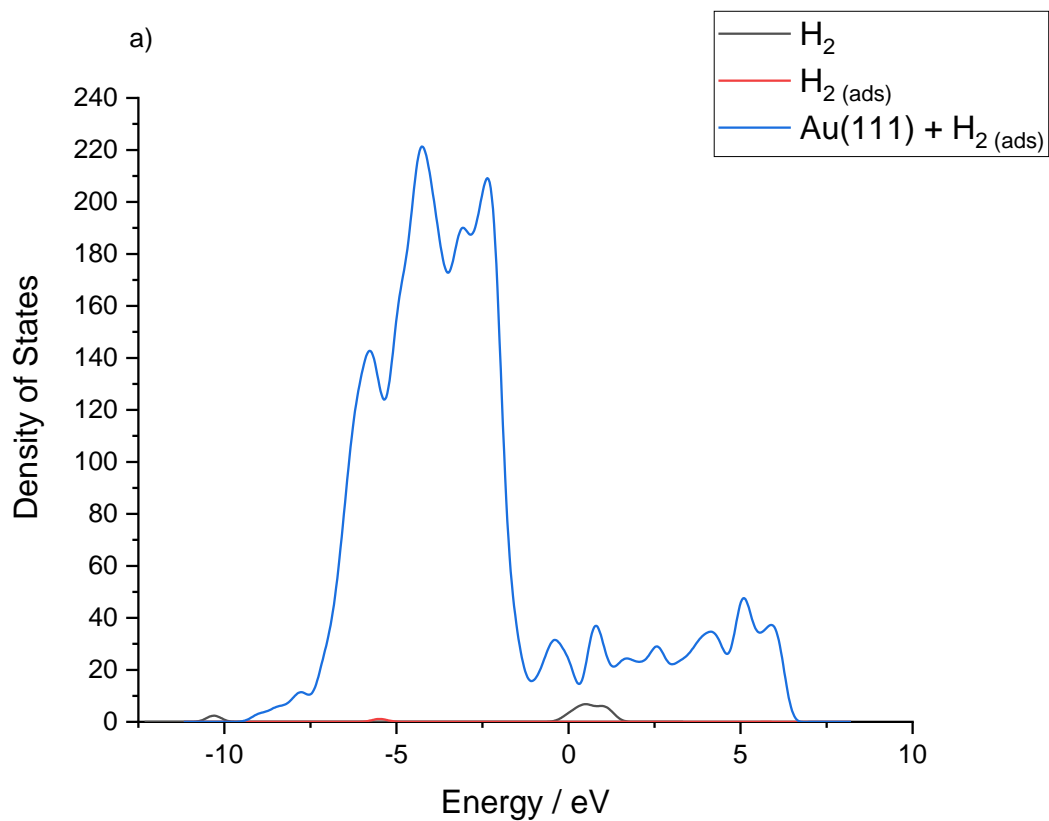


Figure 4.3. Normalised Densities of States for H_2 adsorbed to Au(111), lone H_2 and the partial Densities of States of H_2 adsorbed to Au(111), where **a)** shows all three Densities of States, and **b)** shows a magnified view of the normalised Densities of States with a focus on the lone H_2 and partial Densities of States of H_2 adsorbed to Au(111).

Although H₂ did not adsorb sufficiently to the surface of Au(111), it was important to explore whether dissociated H₂ (*i.e.*, two individual H atoms) would adsorb to the surface. However, the dissociation of H₂ on Au(111) led to unfavourable, positive E_{ads} values and the results confirmed that there was a lack of interaction between Au(111) and H₂ (intact or dissociated). Even with the D3 corrections applied, which decreased the E_{ads} , the values remained positive, meaning that it would require energy for dissociated H₂ to exist on the surface of Au(111). The least positive E_{ads} value, at ~ 5 kJ mol⁻¹, was at the Hollow fcc-fcc sites (Table 4.2 and Fig. 4.4).

Table 4.2. Adsorption energies for the different positions of dissociated H₂ adsorbed to Au(111) without and with D3 corrections.

Site	Position	$E_{\text{ads}}^{\text{PBE}} / \text{kJ mol}^{-1}$	$E_{\text{ads}}^{\text{PBE}+\text{D3}} / \text{kJ mol}^{-1}$
	Diagonal fcc-hcp	29 (29)	12 (12)
Hollow	Straight fcc-hcp	22	5
	fcc-fcc	29	12

Note: Diagonal denotes the position of the adsorbate is over the diamond shape of four top layer metal atoms. Energy values in parentheses indicate that a different site optimised to the same site configuration.

The Top Straight sites collapsed into Hollow fcc-fcc sites at the furthest possible distance. The Hollow fcc-fcc and hcp-hcp sites were not calculated for as the hollow fcc sites at the furthest distance over the central Au atom produced a positive value for E_{ads} , and therefore, it was unlikely that either type of hollow site would provide an E_{ads} of a negative value (Table 4.2 and Fig. 4.4).

Although the Au-H interatomic distances were largely in the range of bonding (~ 1.77 to ~ 2.05 Å), the weak interaction between the surface and the adsorbates caused the top layer of Au atoms to move minimally. The Au-Au bond distances for the Hollow Diagonal fcc-hcp, Hollow Straight fcc-hcp and Hollow fcc-fcc were: $\sim +0.10$ Å, ~ -0.05 – $\sim +0.21$ Å, and ~ -0.10 – $\sim +0.13$ Å, respectively (Table 4.2 and Fig. 4.4).

Although H₂ did not readily adsorb onto the surface of Au(111), it could be possible that O₂ could adsorb to the surface and be reduced by the H₂. Nevertheless, this went against the previous thinking that H₂ should adsorb first as it has a lower molecular energy value compared to O₂.

As intact O₂ interacted with the surface of the Au(111), it was seen in Table 4.3 that without the D3 corrections, it would require energy for the O₂ to adsorb onto the surface. The lowest E_{ads} value without D3 corrections for adsorbed O₂ was ~58 kJ mol⁻¹ on a DB site. Nevertheless, when an O atom adsorbed to the surface, an E_{ads} of a negative value was observed (~-10 kJ mol⁻¹). This value was too low to have true adsorption to the Au(111) surface and it would feasibly desorb before a catalytic reaction could take place (Table 4.3 and Fig. 4.5).

Table 4.3. Adsorption energies for the different positions of O₂ and ½ O₂ adsorbed to Au(111) without and with D3 corrections.

Adsorbate	Site	Position	E_{ads}^{PBE} / kJ mol ⁻¹	E_{ads}^{PBE+D3} / kJ mol ⁻¹
O ₂	DB	-	58	30
	Hollow	fcc	78	-
O	Hollow	fcc	-10	-30
	Top	-	130	-

Note: DB denotes di-bridge.

Of the four optimisation calculations without the use of D3 corrections, only two could be optimised with D3 corrections. When D3 corrections were applied in the optimisation calculations, a similar theme was discerned to that of H₂ adsorption on Au(111). With a decrease of ~27 and ~20 kJ mol⁻¹ for the O₂ DB site and atomic O Hollow fcc site, respectively, when D3 corrections were instigated, it was observed that the adsorption of atomic O occurred on the surface, which was below the maximum threshold for the adsorption of chemical species (~-20 kJ mol⁻¹). The E_{ads} value for an O atom on the surface was ~-30 kJ mol⁻¹. In Fig. 4.5, at approximately 2.28 and 2.15 Å for the O₂ molecule and O atom from the surface, respectively, this interaction seemed reasonable, and the adsorbates would not escape into the vacuum (Table 4.3 And Fig. 4.5).

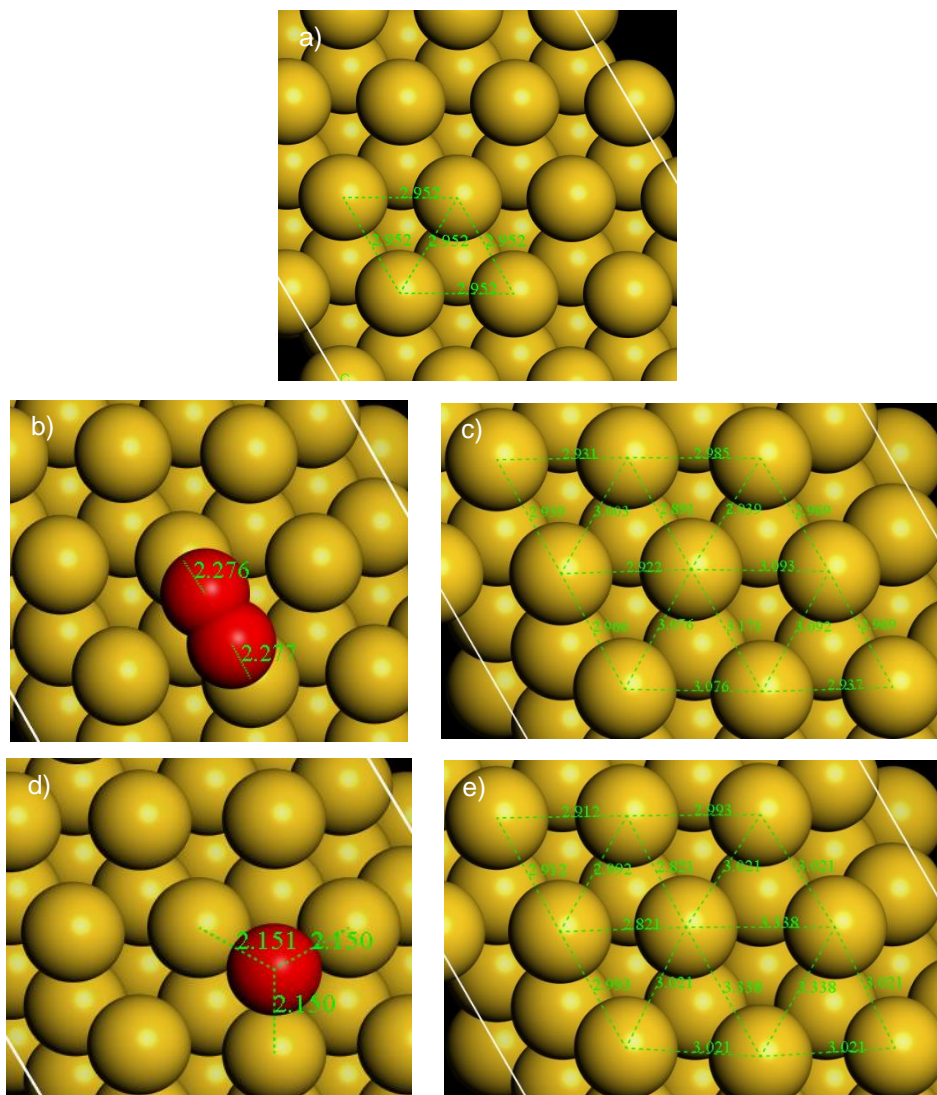


Figure 4.5. Images of the geometry optimisation calculations for O_2 and $\frac{1}{2} O_2$ adsorbed to Au(111) calculated with D3 corrections and the adsorbate removed, where **a)** is the clean surface, **b)** is the DB site, **c)** is the DB sites without the adsorbate, **d)** is the Hollow fcc ($\frac{1}{2} O_2$) site, and **e)** is the Hollow fcc ($\frac{1}{2} O_2$) site without the adsorbate. The yellow atoms represent the Au atoms, and the red atoms represent the O atoms. Interatomic distances in green are in Angstroms (Å). DB denotes di-bridge.

Nevertheless, the adsorption of O_2 was still positive at $\sim 30 \text{ kJ mol}^{-1}$, meaning that dissociation of the O_2 cannot be completed without first adsorbing the O_2 . In response to the interactions of both O_2 and atomic O, the Au(111) surface moved its surface atoms as the Au-Au bond distance moved from the norm. The Au-Au bond ranges of the DB and Hollow fcc ($\frac{1}{2} O_2$) sites were $\sim -0.06 - \sim +0.22 \text{ Å}$, and $\sim -0.13 - \sim +0.39 \text{ Å}$, respectively. This was expected as the surface-adsorbate distances for both sites were relatively close, with Au-O interatomic distances of $\sim 2.28 \text{ Å}$ and $\sim 2.15 \text{ Å}$, respectively (Table. 4.3 and Fig. 4.5).

However, the overriding positive E_{ads} value from the O_2 adsorption meant that the surface could not adsorb and dissociate the O_2 molecule. Therefore, any reaction involving the direct synthesis of H_2O_2 on Au(111) was unlikely to occur, which was in line with previous research.^{22,23} It was therefore logical to not continue the research into O_2 dissociation.

Although Au(111) was proving to be an unlikely candidate for direct H_2O_2 synthesis, it was important to continue with the research into H_2O_2 adsorption and dissociation as well as propene and PO adsorption. It could be possible to include Au as part of an alloy with another metal, which in this research would be Pd. Hence, further investigations of the interactions of Au(111) and H_2O_2 were completed. It was also important to investigate the potential role of Au in both selective and non-selective reaction pathways (e.g., H_2O_2 decomposition) during the direct H_2O_2 synthesis reaction.

Initially, intact H_2O_2 was adsorbed onto the surface of Au(111). Most of the optimisation calculations without D3 corrections revealed that Au(111) was still too stable a surface to have any significant interaction with H_2O_2 . With the different orientations of the H_2O_2 on the surface, the E_{ads} values ranged from ~ -10 – ~ -15 kJ mol^{-1} (Table 4.4 and Fig. 4.6).

There was one exception where there was significant adsorption as the starting position of a top site with both O atoms of the H_2O_2 interacting with the surface (η^2). However, switching on the D3 corrections led to dissociation of the H_2O_2 at the HO-OH bond, meaning that the E_{a} barrier for this dissociation must be low. The only factor stopping this dissociation was the molecule's orientation. This result was discounted from the research. Although most of the calculations could not be completed for this interaction between H_2O_2 and Au(111), it provided insight into how Au behaved (Table 4.4 and Fig. 4.6).

With the D3 corrections applied, the calculations revealed that the DB position resulted in the H_2O_2 moving so that the H^2 atom from the molecule moved to a sloped bridged site (halfway between a Hollow fcc site and a bridge site) with the O^1 atom positioned on a top site. This new position of the H_2O_2 on the surface was called the Top (O^1)-Bridge (H^2) site. The interatomic distance of the bridged H to the Au atoms was ~ 2.59 and ~ 2.87 Å, and the Au-O interatomic distance was ~ 2.78 Å. This was the favoured position of H_2O_2 as this was observed in Nasrallah's work, with a similar E_{ads} value and interatomic distances (~ 45 kJ mol^{-1} , Au-O interatomic distance: ~ 2.77 Å).²⁴ The top layer Au atoms moved minimally with a maximum bond increase

of 0.04 Å, which was due to the increased distance between the surface and adsorbate. This in turn would decrease the repulsive forces involved in this interaction (Table 4.4 and Fig. 4.6).

Table 4.4. Adsorption energies for the different positions of H₂O₂ adsorbed to Au(111) without and with D3 corrections.

Site	Position	E_{ads}^{PBE} / kJ mol ⁻¹	E_{ads}^{PBE+D3} / kJ mol ⁻¹
DB	(OH)	-11	-
	(H)	-10	-
Top	(O)	-15	-
	(OH)	-10	-
	(OO)	-89	-137
Top (O ¹)-Bridge (H ²)	-	-15	-44

Note: DB denotes di-bridge. The species involved in each position are stated in the parentheses.

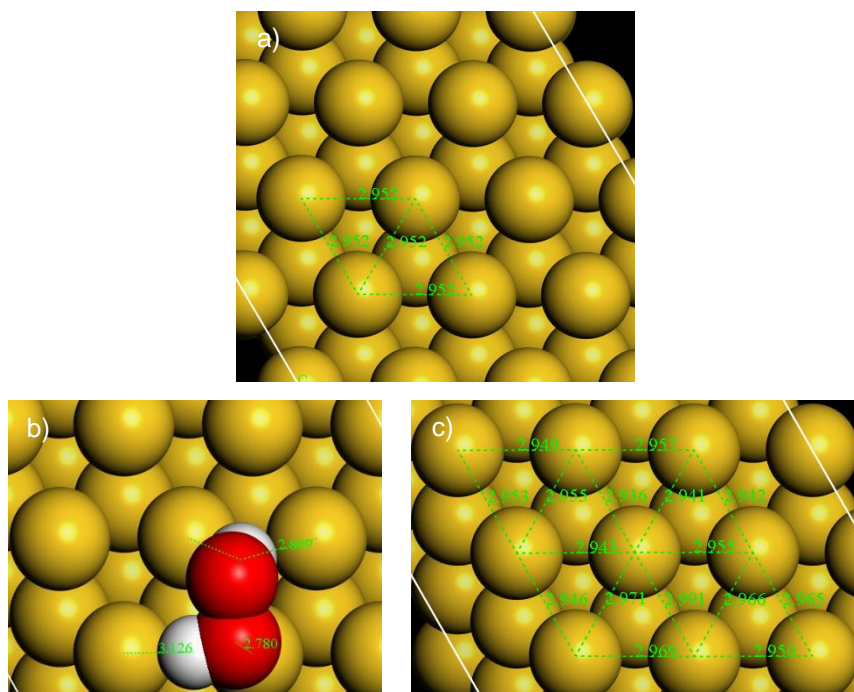


Figure 4.6. Images of the geometry optimisation calculations for H₂O₂ and dissociated H₂O₂ adsorbed to Au(111) calculated with D3 corrections, where **a**) is the clean surface, **b**) is the Top (O¹)-Bridge (H²) site, and **c**) is the Top (O¹)-Bridge (H²) site without the adsorbate. The yellow atoms represent the Au atoms, the red atoms represent the O atoms, and the white atoms represent the H atoms. Interatomic distances in green are in Angstroms (Å). The species involved in each position are stated in the parentheses.

However, Ford *et al.* found that the most favoured position of H₂O₂ was a DB (OO) site for H₂O₂ adsorption.⁵ In the current work, the lower energy observed for the Top site starting position resulted in HO-OH dissociation. This dissociation seemed more favourable than Ford *et al.*'s DB (OO) site, but further investigation will be required to determine this. The Top (OO) site result was discounted for the adsorption of intact H₂O₂. What was gleaned from this was that Au could dissociate H₂O₂, which may be a favourable pathway for further reactions (Fig. 4.6).

Continuing with the theme of H₂O₂ dissociation, there were two possible avenues to explore: the dissociation of the H-OOH bond to form a lone H and an OOH species; and the dissociation of the HO-OH bond to form two OH species. Both forms of H₂O₂ dissociation were investigated. For both without and with D3 corrections applied, the H-OOH bond dissociation of H₂O₂ was summarised in Table 4.5, and it was observed that the adsorption of H and OOH species was unfavourable. This was because all the positions of the species on different sites produced positive E_{ads} values, ranging from ~117 – ~130 kJ mol⁻¹ and ~75 – ~85 kJ mol⁻¹, respectively (Table 4.5 and Fig. 4.7).

The calculations for the Hollow fcc (OOH)-Top (H) and Top Diagonal sites with the D3 corrections applied could not be completed as the OOH adsorbate failed to orientate correctly to enter the Hollow fcc site during the calculations. The resultant energies for the successfully completed optimisation calculations with the D3 corrections applied decreased by ~42 kJ mol⁻¹, but they all remained positive, and therefore, they were unfavourable. This did not support the work of Taylor *et al.* or Joshi *et al.*, however, both groups did not use Au(111) slabs for their work (Table 4.5 and Fig. 4.7).^{8,17}

It was demonstrated in Fig. 4.7 that the average Au-O interatomic distances for the OOH species of each site was ~2.39, ~2.38 and ~2.34 Å for the Hollow fcc (H)-Hollow hcp (OOH), Hollow hcp (H)-Hollow hcp (OOH) and Bridge (H)-Hollow hcp (OOH) sites, respectively. The average Au-H bond lengths for each site was ~1.89, ~1.90 and ~1.77 Å, respectively (Table 4.5 and Fig. 4.7).

Table 4.5. Adsorption energies for the different positions of dissociated H₂O₂ (H-OOH) adsorbed to Au(111) without and with D3 corrections.

Site	Position	E_{ads}^{PBE} / kJ mol ⁻¹	E_{ads}^{PBE+D3} / kJ mol ⁻¹
Hollow-Hollow	fcc (H)-hcp (OOH)	122	85
	hcp (H)-hcp (OOH)	130	84
Hollow-Top (H)	fcc (OOH)	122	-
Top	Diagonal	122	-
Bridge (H)-Hollow	hcp (OOH)	117	75

Note: Diagonal denotes the position of the adsorbate over the diamond shape of four top layer metal atoms. The species involved in each position are stated in the parentheses.

The top layer of Au atoms restructured as the Hollow fcc (H)-Hollow hcp (OOH), Hollow hcp (H)-Hollow hcp (OOH) and Bridge (H)-Hollow hcp (OOH) sites had Au-Au bond length ranges of $\sim -0.04 - \sim +0.39$ Å, $\sim -0.06 - \sim +0.60$ Å, and $\sim -0.15 - \sim +0.48$ Å, respectively. The large movements of the Au atoms were the most likely contributing factor to the positive E_{ads} values as the Au atoms were repelled by the interacting species. As previously discussed, Au has a low affinity for H and O, thus, as the H and OOH species moved toward the surface, the top layer Au atoms moved from their original positions (Table 4.5 and Fig. 4.7).

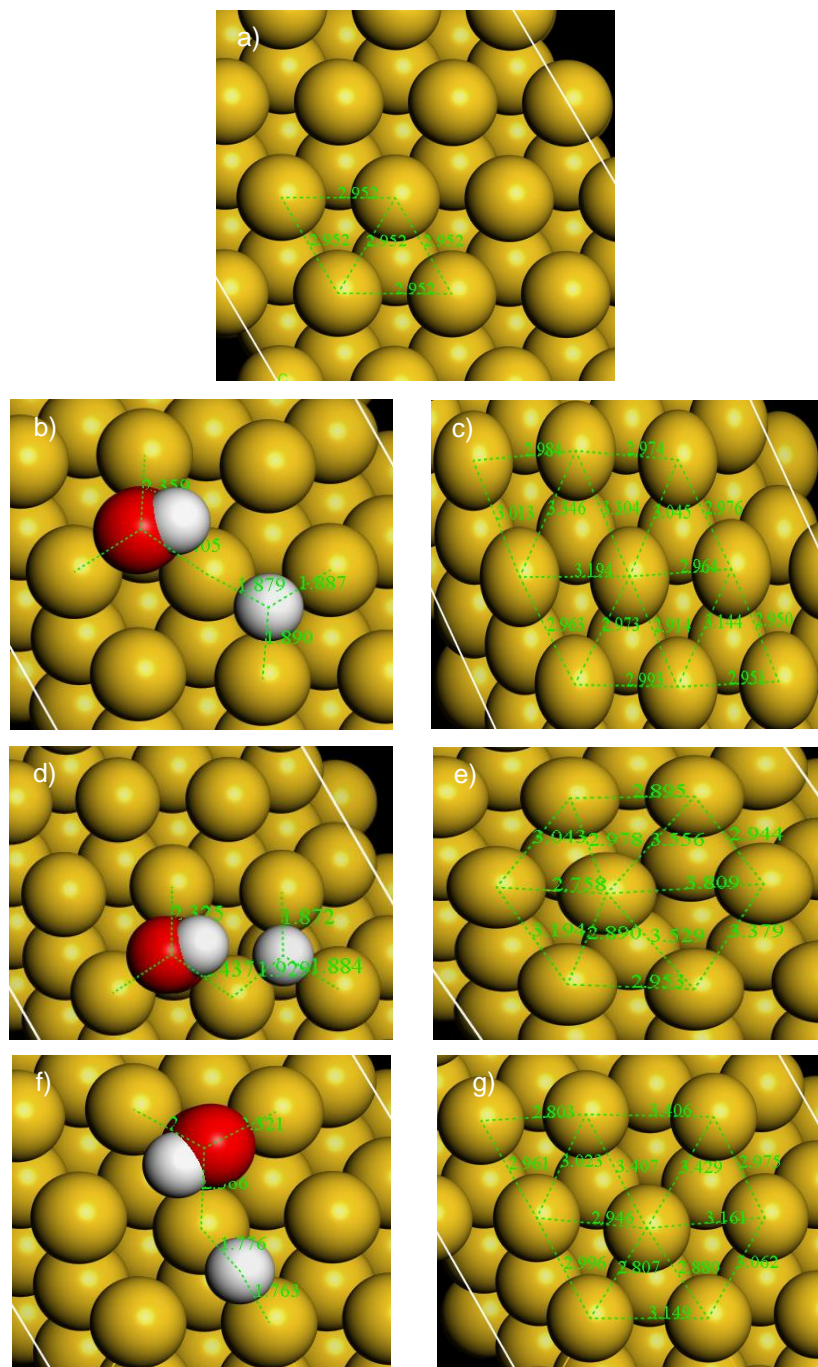


Figure 4.7. Images of the geometry optimisation calculations for dissociated H_2O_2 adsorbed to Au(111) calculated with D3 corrections and the adsorbate removed, where **a)** is the clean surface, **b)** is the Hollow fcc (H)-Hollow hcp (OOH) sites with the adsorbates, **c)** is the Hollow fcc (H)-Hollow hcp (OOH) sites without the adsorbates, **d)** is the Hollow hcp (H)-Hollow hcp (OOH) sites with the adsorbates, **e)** is the Hollow hcp (H)-Hollow hcp (OOH) sites without the adsorbates, **f)** is the Bridge (H)-Hollow hcp (OOH) sites with the adsorbates, and **g)** is the Bridge (H)-Hollow hcp (OOH) sites without the adsorbates. The yellow atoms represent the Au atoms, and the white atoms represent the H atoms. Interatomic distances in green are in Angstroms (\AA). The species involved in each position are stated in the parentheses.

The other type of dissociation that H_2O_2 can undergo is at the HO-OH bond. Even without D3 corrections, it was observed through the optimisation calculations

that this dissociation was favourable as the E_{ads} values were negative. The lowest E_{ads} value observed was ~ -118 kJ mol $^{-1}$ from a Bridge-Bridge site. However, with the D3 corrections applied, the E_{ads} values decreased further by an average value of ~ -50 kJ mol $^{-1}$. Again, the lowest E_{ads} value was observed by the Bridge-Bridge site of the OH groups at ~ -166 kJ mol $^{-1}$ (Table 4.6 and Fig. 4.8).

Table 4.6. Adsorption energies for the different positions of dissociated H₂O₂ (HO-OH) adsorbed to Au(111) without and with D3 corrections.

Site	Position	$E_{\text{ads}}^{\text{PBE}}$ / kJ mol $^{-1}$	$E_{\text{ads}}^{\text{PBE}+D3}$ / kJ mol $^{-1}$
Hollow	fcc	-106	-161
Top-Bridge	-	-117	-163
Hollow-Bridge	fcc	-100	-151
Bridge-Bridge	-	-118	-166

In Fig. 4.8b, one of the OH species moved from an hcp hollow site to an fcc hollow site. The Au-O bonds had average lengths of ~ 2.33 and ~ 2.32 Å for the first and second OH groups, respectively. The result of this was an E_{ads} value of ~ -161 kJ mol $^{-1}$, which went against the trend where bridge sites appeared to be the favoured position of the OH groups (Table 4.6 and Fig. 4.8).

In Fig. 4.8d, the optimised Top-Bridge site resulted in both OH groups pointed away at an angle from the surface and were not completely perpendicular to the surface. The OH on the top site had a Au-O bond length of ~ 2.13 Å and the Au-O bond lengths for the OH on the bridge site were ~ 2.18 Å. Strong hydrogen bonding ($X^{\ominus}\cdots H$, where X is the electronegative species) was observed at a distance, from the H of the Bridge site's OH group to the O atom of the Top site's OH, equal to ~ 1.57 Å. This gave rise to an E_{ads} value of ~ -163 kJ mol $^{-1}$ (Table 4.6 and Fig. 4.8).

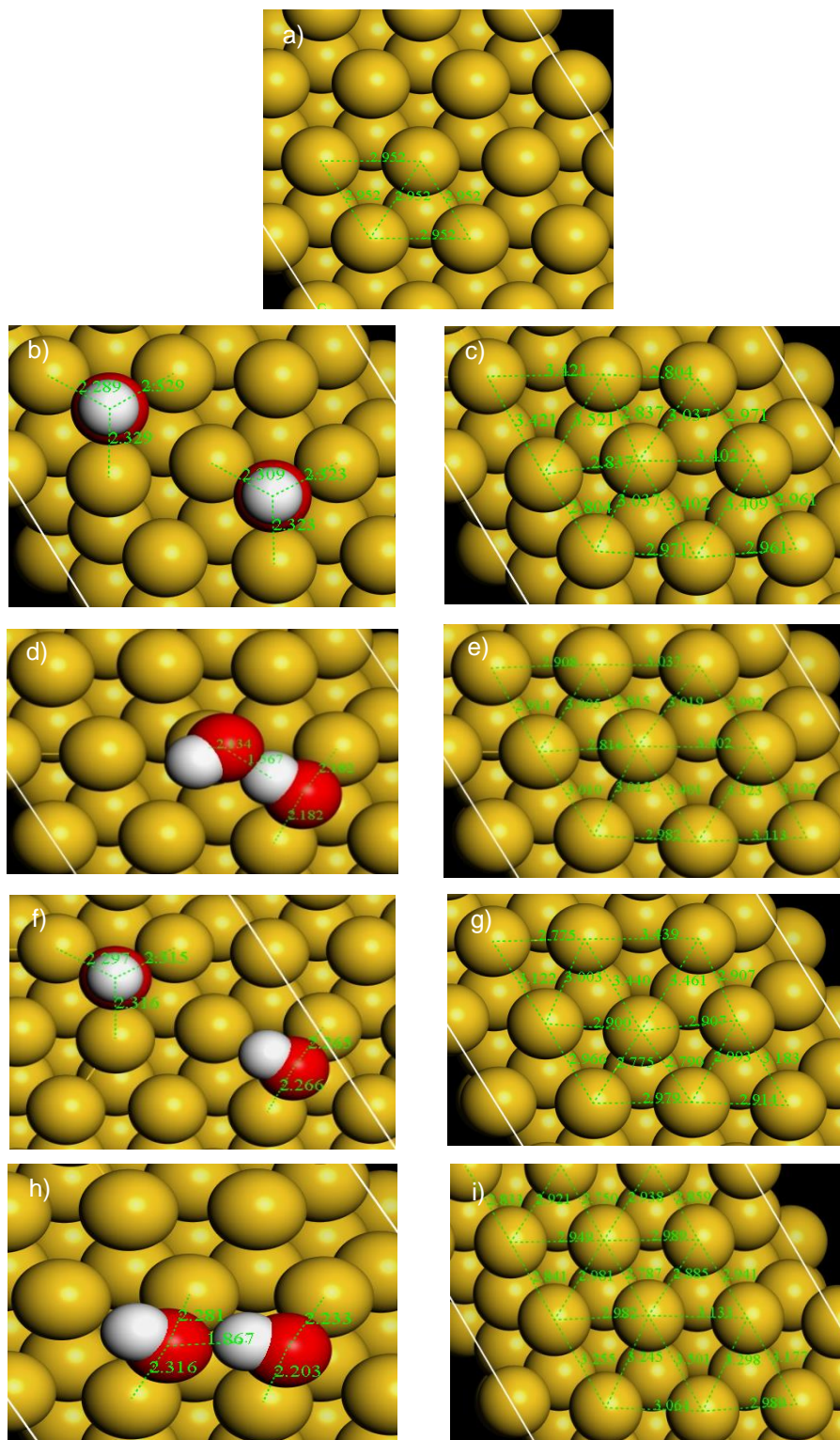


Figure 4.8. Images of the geometry optimisation calculations for dissociated H_2O_2 (HO-OH) adsorbed Au(111) calculated with D3 corrections and the adsorbate removed, where **a**) is the clean surface, **b**) is the Hollow fcc sites with the adsorbates, **c**) is the Hollow fcc sites without the adsorbates, **d**) is the Top-Bridge sites with the adsorbates, **e**) is the Top-Bridge sites without the adsorbates, **f**) is the Hollow fcc-Bridge sites with the adsorbates, **g**) is the Hollow fcc-Bridge sites without the adsorbates, **h**) is the Bridge-Bridge sites with the adsorbates, and **i**) is the Bridge-Bridge sites without the adsorbates. The yellow atoms represent the Au atoms, the red atoms represent the O atoms, and the white atoms represent the H atoms. Interatomic distances in green are in Angstroms (\AA).

In Fig. 4.8f, for the Hollow fcc-Bridge configuration of OH groups, the OH in the hollow fcc site had an average Au-O interatomic distance of ~ 2.31 Å and the OH at the bridge site gave an average Au-O interatomic distance of ~ 2.67 Å. This would explain the decreased adsorption energy (~ 151 kJ mol⁻¹) in comparison to the other adsorption sites. Although the average interatomic distance of the hollow fcc site was approximately the same as the Hollow fcc (far) configuration (difference of 0.01 Å), the average interatomic distance of the bridge site was longer than that of the bridge site of the Top-Bridge configuration (Table 4.6 and Fig. 4.8).

The Bridge-Bridge OH positions in Fig. 4.8h interestingly showed different Au-O bond lengths for the two bridged sites. It was observed that one of the OH groups had Au-O interatomic distances of ~ 2.28 and ~ 2.31 Å, whereas the other OH group had Au-O interatomic distances of ~ 2.23 and ~ 2.20 Å. The O \cdots H bond between the OH groups was ~ 1.87 Å. The O atom donating electron density to the O \cdots H bond caused the increased Au-O bond lengths of the “donating” OH group. This was a difference of ~ 0.30 Å compared to the Top-Bridge configuration. Thus, the decreased O \cdots H bond length observed for the Top-Bridge was the reason for the decreased the E_{ads} value by ~ 3 kJ mol⁻¹ due to increased repulsion (Table 4.6 and Fig. 4.8).

Adsorption of the species to the surface caused the top layer of Au atoms to move. The Hollow fcc, Top-Bridge, Hollow fcc-Bridge and Bridge-Bridge sites gave Au-Au bond length ranges away from the norm of: ~ -0.15 – $\sim +0.57$ Å, ~ -0.14 – $\sim +0.45$ Å, ~ -0.18 – $\sim +0.49$ Å, and ~ -0.17 – $\sim +0.55$ Å, respectively. However, the Au atom movements were most likely a minor contributing factor to the E_{ads} values as all four adsorption sites gave large, negative E_{ads} values. Although the E_{def} value was likely a large, positive number for the deformed surface, the E_{int} value must have been a larger, negative number to gain a negative E_{ads} value. From the results both without and with D3 correction applied, it was concluded that the dissociation of the HO-OH bond was favourable (Table 4.6 and Fig. 4.8).

For propene and PO adsorption on Au(111), a limited number of orientations of the molecule could be completed through the use of calculations both without and with D3 corrections. For the adsorption of propene, the C¹C² is a C¹=C² bond and the interaction(s) between the surface and propene will occur through the π -orbitals of the C¹ and C² atoms. The current work refers to the positions of propene on the adsorption sites as the centre of the C¹C² bond and defines the PO adsorption sites using the position of the molecule's O atom. The nomenclature with regards to the orientation of the methyl group (C³) follows that of Roldan *et al.*'s work, where the

central H atom is either pointed away from the surface or towards the surface (“up” or “down”, respectively).¹⁸

In Table 4.7, without the D3 corrections, the propene Top Up sites of the propene produced positive E_{ads} values of ~ 40 kJ mol⁻¹. However, when D3 corrections were applied for the adsorption of propene, there was a small difference by ~ 2 kJ mol⁻¹ for the E_{ads} values of both Top Up sites in Fig. 4.9b and d, which were ~ -63 and ~ -65 kJ mol⁻¹, respectively. This was consistent with the findings of Roldan *et al.* who observed that propene adsorbed to Au(111) as a Top Up site, however, this group observed that it gave an E_{ads} value of ~ -3 kJ mol⁻¹.¹⁸ Nevertheless, D3 corrections had been applied to the calculations of the current work, which could explain the significant difference in E_{ads} between the two works (Table 4.7 and Fig. 4.9).

Table 4.7. Adsorption energies for the different positions of propene and PO adsorbed to Au(111) without and with D3 corrections.

Adsorbate	Site	Position	$E_{\text{ads}}^{\text{PBE}} / \text{kJ mol}^{-1}$	$E_{\text{ads}}^{\text{PBE}+\text{D3}} / \text{kJ mol}^{-1}$
Propene	Top	Up	40 (40)	-63 (-65)
		Hollow	fcc	-5
PO	Top	-	-6	-
		(OC ² H)	-9	-57

Note: Up denotes the methyl group of the propene is pointed up away from the surface. The species involved in each position are stated in the parentheses. Energy values in parentheses indicate that a different site optimised to the same site configuration.

This decrease in E_{ads} values between *PBE* only and *PBE + D3* calculations demonstrated the fundamental difference between the van der Waals forces exhibited by molecules of differing size. For example, H₂ (two atoms) interacted with the Au(111) surface to give a difference of ~ 7 kJ mol⁻¹ between the calculations without and with D3 corrections applied, whereas propene (nine atoms) adsorbed to the Au(111) surface to give a difference of ~ 104 kJ mol⁻¹ on average for both Top Up adsorption sites (Table 4.1 and 4.7).

The interatomic distances of the C¹ and C² to the central Au atom for the Top Up sites without D3 corrections were ~3.16 and ~3.47 Å, respectively. Compared to those distances after the D3 corrections had been applied, there was a difference of ~0.40 Å. This highlighted the significance of D3 correction as the van der Waals forces played an important part in the adsorption of propene and affected other adsorbates and surfaces in a similar fashion. The interatomic distances of the C¹ and C² atoms to the interacting Au atom for both Top Up sites, with the D3 corrections applied, were ~2.67 and ~3.02 Å, and ~2.68 and ~3.02 Å, respectively. Although the difference was negligible, the difference in the peripheral atoms could be the reason for the slight difference in E_{ads} values. In Fig. 4.9b, the C²-Au interatomic distance with the neighbouring Au atom was ~3.26 Å for the Top Up site, which was shorter than the other Top Up site's C²-Au interatomic distance of ~3.37 Å in Fig. 4.9d (Table 4.7 and Fig. 4.9).

The H-Au interatomic distances for the two peripheral Au atoms interacting with the H in the CH₃ group were shorter for the Top Up site in Fig. 4.9b by ~0.04 and ~0.25 Å than the Top Up site in Fig. 4.10d. The Top Up site in Fig. 4.9b had H-Au interatomic distances of ~2.88 and ~3.37 Å, while the Top Up site in Fig. 4.9d had H-Au interatomic distances of ~2.92 and ~3.62 Å. This could be the reason for the small difference in E_{ads} values for the two positions as the Top Up site in Fig. 4.9d was due to the increased distance of the propene adsorbing to the surface compared to the Top Up site in Fig 4.9b (Table 4.7 and Fig. 4.9).

Propene adsorbed to Au(111) did not cause drastic changes to the top layer of the Au atoms. The Au-Au bond length ranges changed by ~-0.01 – ~+0.06 Å and ~-0.01 – ~+0.04 Å for both Top Up sites in Fig. 4.9b and d, respectively. This difference in Au-Au movements and difference in distance between the propene and Au(111) surface may be the cause for the slight difference in E_{ads} values for both Top Up sites as the repulsion and the E_{def} value would have been higher for the one with the larger Au-Au movements and decreased surface-adsorbate distance than the other (Table 4.7 and Fig. 4.9).

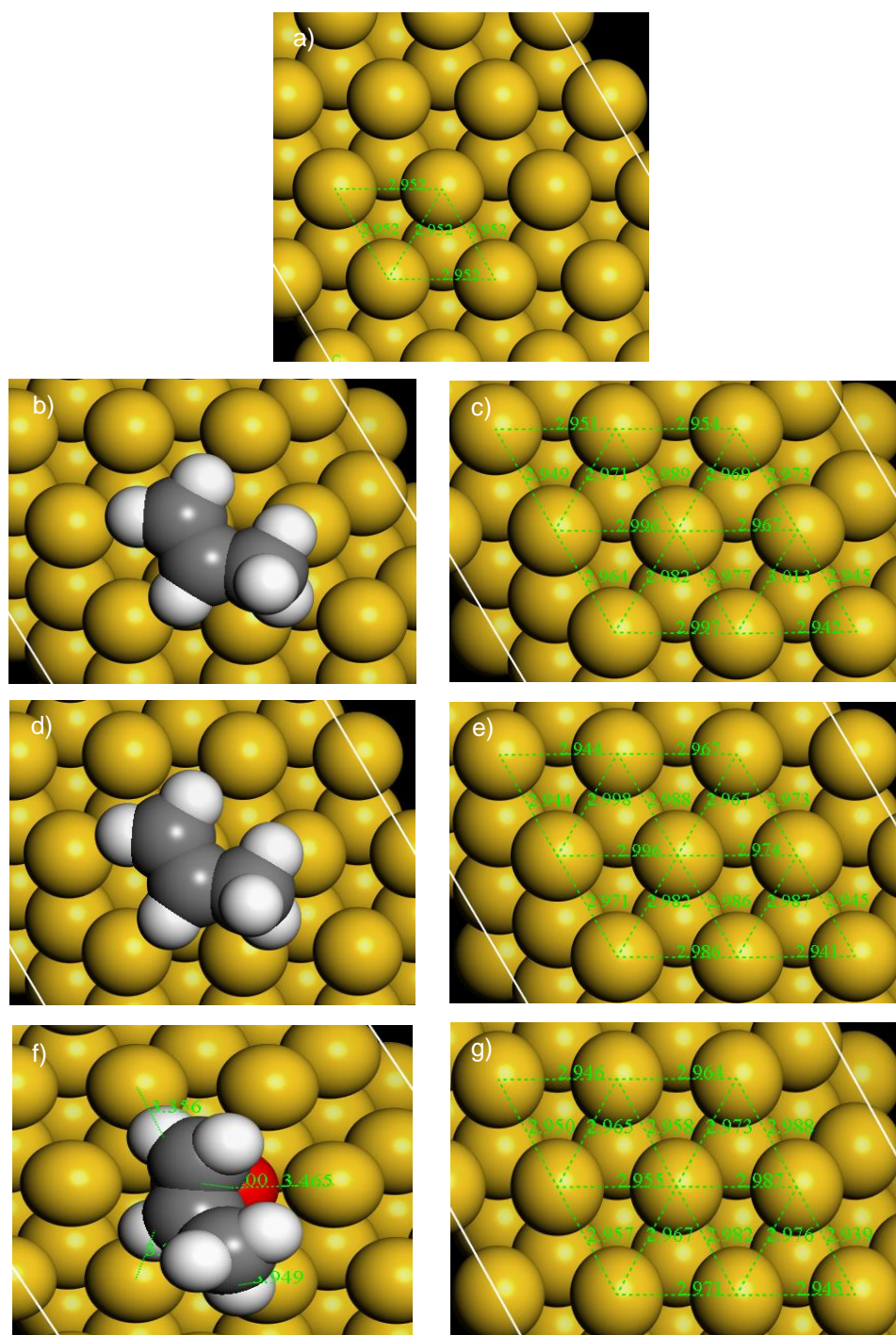


Figure 4.9. Images of the geometry optimisation calculations for propene and PO adsorbed Au(111) calculated with D3 corrections and the adsorbate removed, where **a)** is the clean surface, **b)** is the propene Top Up site with the adsorbate, **c)** is the propene Top Up site without the adsorbate, **d)** is the propene Top Up site with the adsorbate, **e)** is the propene Top Up site without the adsorbate, **f)** is the PO Top (OC²H) site with the adsorbate, and **g)** is the PO Top (OC²H) site without the adsorbate. The yellow atoms represent the Au atoms, the grey atoms represent the C atoms, the red atoms represent the O atoms, and the white atoms represent the H atoms. Interatomic distances in green are in Angstroms (Å). Up denotes the methyl group of the propene is pointed up away from the surface. The species involved in each position are stated in the parentheses.

In Fig. 4.10, the DoS of the Top Up site demonstrated that there was significant interaction between the Au(111) surface and propene. This interaction resulted in the anti-bonding orbital(s) of the propene molecule above the Fermi level being reduced to almost nothing, with the densities being spread out. The bonding orbitals had been reduced and shifted towards the Fermi level by $\sim +1 - \sim +4$ eV. The small sp^2 -orbital peaks for the adsorbed propene molecule at ~ -16 , ~ -13 , ~ -9 and ~ -6 eV overlapped with those of the Au(111) and adsorbed propene, which suggested that there was an overlap of the bonding orbitals between the surface and adsorbate, which correlated with the chemisorption observed for the Top Up site (~ -65 kJ mol $^{-1}$) (Table 4.7, and Fig. 4.9 and 4.10).

There was a small bond lengthening of the adsorbate as the C 1 =C 2 bond length increased from ~ 1.34 Å to ~ 1.36 Å. This bond lengthening was most likely due to the small shift of electron density of the adsorbate and of the surface. Four electrons in the anti-bonding orbitals of the propene C 1 =C 2 bond would be required for its dissociation, which did not occur (Table 4.7, and Fig. 4.9 and 4.10).

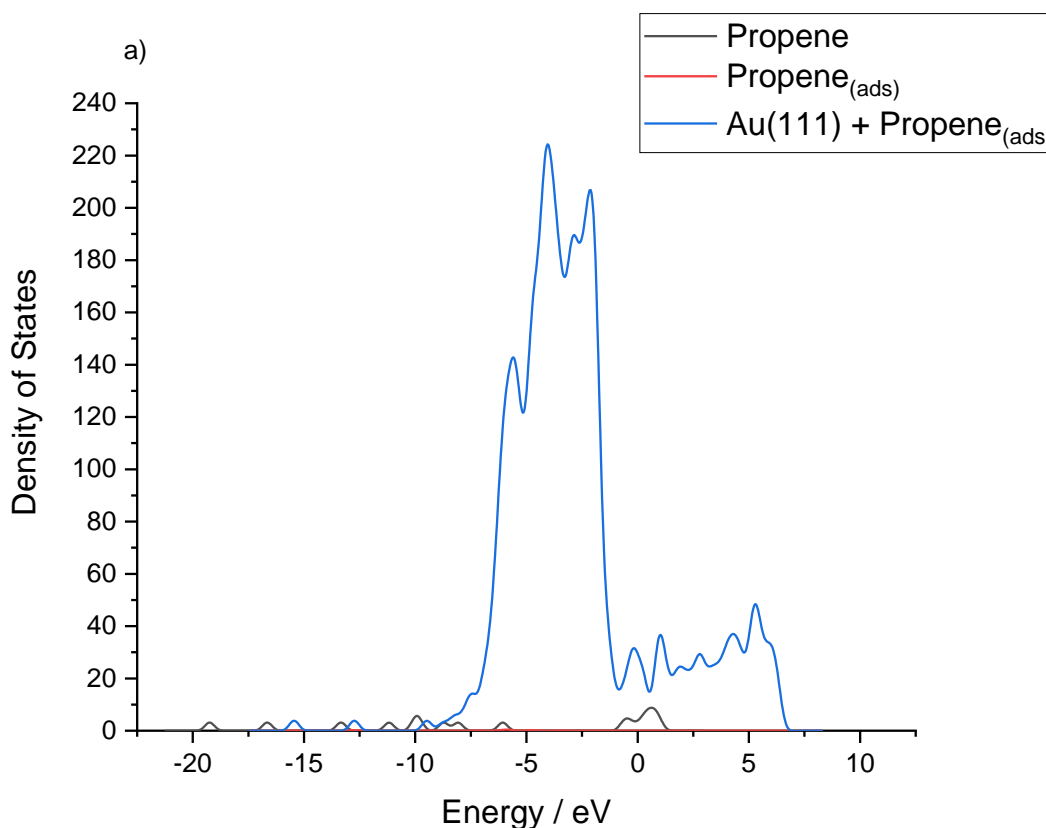


Figure 4.10. Normalised Densities of States for propene adsorbed to Au(111), lone propene and the partial Densities of States of propene adsorbed to Au(111), where **a)** shows all three Densities of States.

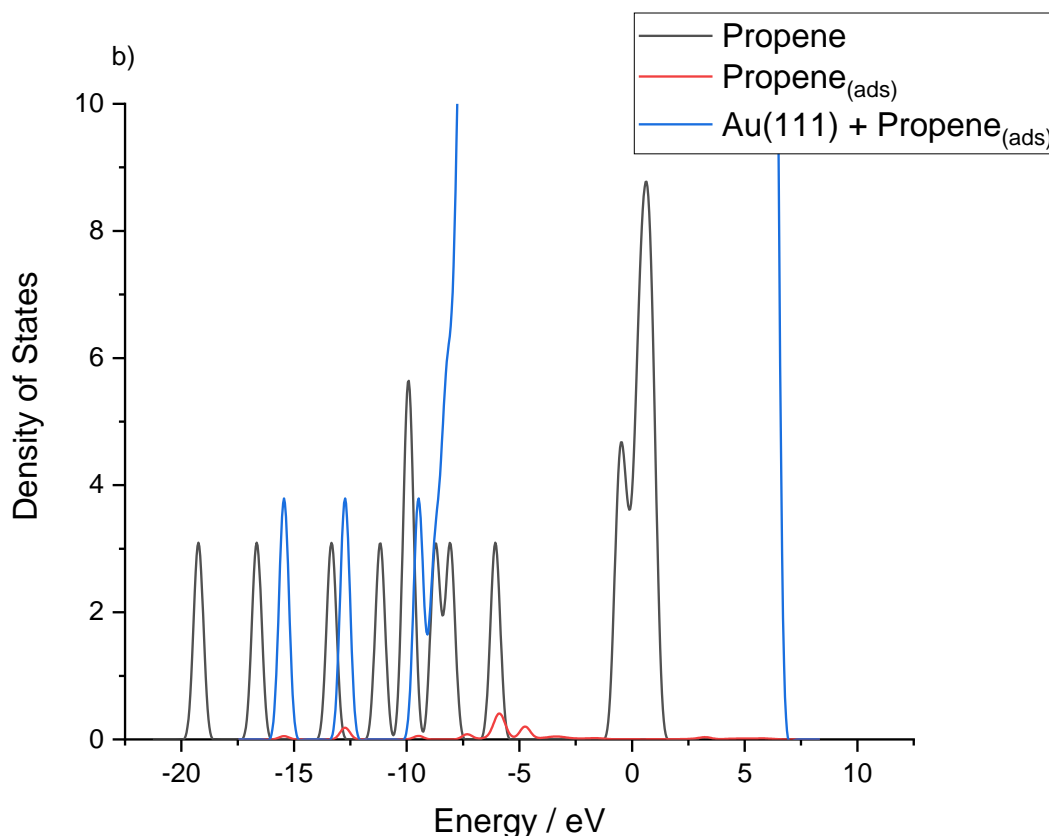


Figure 4.10. Normalised Densities of States for propene adsorbed to Au(111), lone propene and the partial Densities of States of propene adsorbed to Au(111), where **b)** shows a magnified view of the normalised Densities of States with a focus on the lone propene and partial Densities of States of propene adsorbed to Au(111).

The PO Hollow fcc (O) position gave the least negative E_{ads} value at ~ -5 kJ mol $^{-1}$ in comparison to the Top sites. This suggested that the PO Hollow site experienced more repulsion from the surface than the Top sites. The PO Top and Top (OC 2 H) sites gave rise to more negative adsorption values than the Hollow fcc (O) site, at ~ -6 at ~ -9 kJ mol $^{-1}$, respectively. The only calculation with D3 corrections applied that could be completed for PO was the PO Top (OC 2 H) site, which gave an E_{ads} value of ~ -57 kJ mol $^{-1}$. The difference in distance of the PO from the surface between the calculations without and with D3 corrections was that the Au-C 1 bond decreased from 3.16 Å to 2.68 Å and the Au-C 2 bond decreased from 3.47 Å to 2.94 Å. The inclusion of van der Waals forces caused this decreased as changes in polarity of the surface and adsorbate atoms was induced, causing a greater attraction between the Au(111) surface and the PO adsorbate (Table 4.7 and Fig. 4.9).

In Fig. 4.9f, the Au-O interatomic distances for the interacting and neighbouring Au atoms were ~ 2.60 and ~ 3.47 Å, respectively, with a Au-H interatomic

distance of 3.45 Å. For the PO Top (OC²H) site in Fig 4.9f, the changes to the top layer of the Au atoms were minor. The maximum change in Au-Au bond lengths was ~0.04 Å and did not significantly contribute to the E_{ads} value (Table 4.7 and Fig. 4.9).

To summarise, Au(111) was too stable a surface to allow for the adsorption of some of the target molecules. H₂ and O₂ did not readily adsorb because of Au's low affinity for them. Therefore, Au(111) should be considered as an unsuitable candidate as a catalytic material for reactions involved in the direct synthesis of H₂O₂. However, it should be considered as a suitable catalyst for propene epoxidation that could be used together with a direct H₂O₂ synthesis catalyst, combined to form a tandem catalyst system. Additionally, it should not be discounted for its candidacy as an alloyed catalyst for these reactions. This was due to its ability to adsorb H₂O₂, propene and PO effectively. However, E_{a} barriers for the catalytic steps of propene epoxidation utilising H₂O₂ are required to determine if they can be completed feasibly on Au(111).

4.2.1.2. Gold(100)

Although Au(111) demonstrated a low affinity for H₂ and O₂, it was worth investigating what a less stable surface of Au might be able to achieve. If Au(100) could be proved to adsorb H₂ and O₂, Au's candidacy as a catalytic material for direct H₂O₂ synthesis would not be discounted.

Initially, H₂ was adsorbed to the surface of Au(100) both without and with D3 corrections applied within the geometry optimisation calculations. A variety of different sites and positions were used, but those that did not complete their geometry optimisations were discounted from the current work. Without the D3 corrections, it was observed that there was a lack of adsorption. With the lowest E_{ads} at a Hollow site with ~-6 kJ mol⁻¹, it was important to apply the D3 corrections to ensure that the intermolecular forces were included. At first glance, it appeared that the Hollow site decrease in adsorption by ~18 kJ mol⁻¹ to ~-24 kJ mol⁻¹. However, closer examination of this site demonstrated that the H₂ had dissociated with each H on a bridge site. This was not unlike what was observed for Pd(111) by Todorovic *et al.*⁷ This group demonstrated that H₂ automatically dissociated when interacting with the Pd(111) surface (Table 4.8 and Fig. 4.11).

The only viable site within the current work for the molecular adsorption of H₂ was the Top Vertical site as the H₂ remained intact. The adsorption of H₂ to Au(100) was weak (~-7 kJ mol⁻¹) with a Au-H interatomic distance of ~2.88 Å. This was

supported by the work of Barrio *et al.*^{22,23} who also observed a lack of interaction between Au and H₂. No significant movement of the Au atoms of the top layer was observed for this site (Table 4.8 and Fig. 4.11).

Table 4.8. Adsorption energies for the different positions of H₂ adsorbed to the Au(100) without and with D3 corrections.

Site	Position	E_{ads}^{PBE} / kJ mol ⁻¹	E_{ads}^{PBE+D3} / kJ mol ⁻¹
Hollow	-	-6	-24
Top	Vertical	0	-7

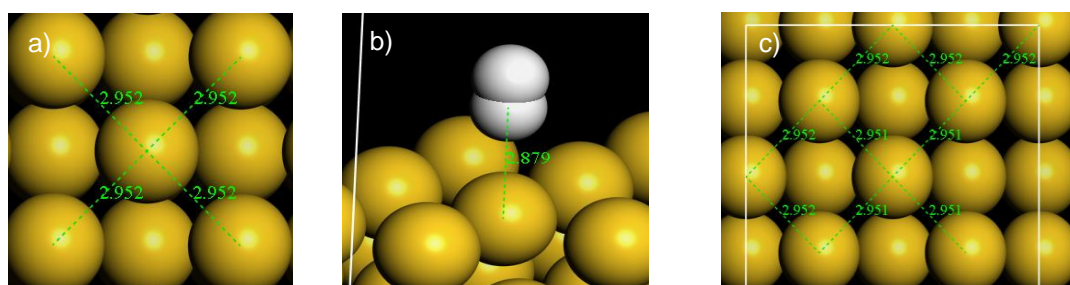


Figure 4.11. Images of the geometry optimisation calculations for H₂ adsorbed to Au(100) calculated with D3 corrections, where **a)** is the clean surface, and **b)** is the Top Vertical site, **c)** is the Top Vertical site without the adsorbate. The yellow atoms represent the Au atoms, and the white atoms represent the H atoms. Interatomic distances in green are in Angstroms (Å).

From the DoS of the Top Vertical site, there was the slightest interaction between the Au(100) surface and the H₂. This interaction resulted in the peak for the anti-bonding orbital of the H₂ above the Fermi level being reduced to almost nothing, with the densities being spread out. The bonding orbital had been reduced and shifted towards the Fermi level by ~+5 eV. The small *s*-orbital peak observed for the adsorbed H₂ suggested that the overlap of bonding orbitals between the surface and adsorbate was weak, which was correlated to the E_{ads} value. Two electrons in the anti-bonding orbital would be needed for H₂ dissociation. There was no significant bond lengthening of the adsorbate and remained at ~0.75 Å, which, with the adsorption energy data, would confirm that this interaction between H₂ and Au(100) was weak. The intact H₂ would also desorb easily (Table 4.8, and Fig. 4.11 and 4.12).

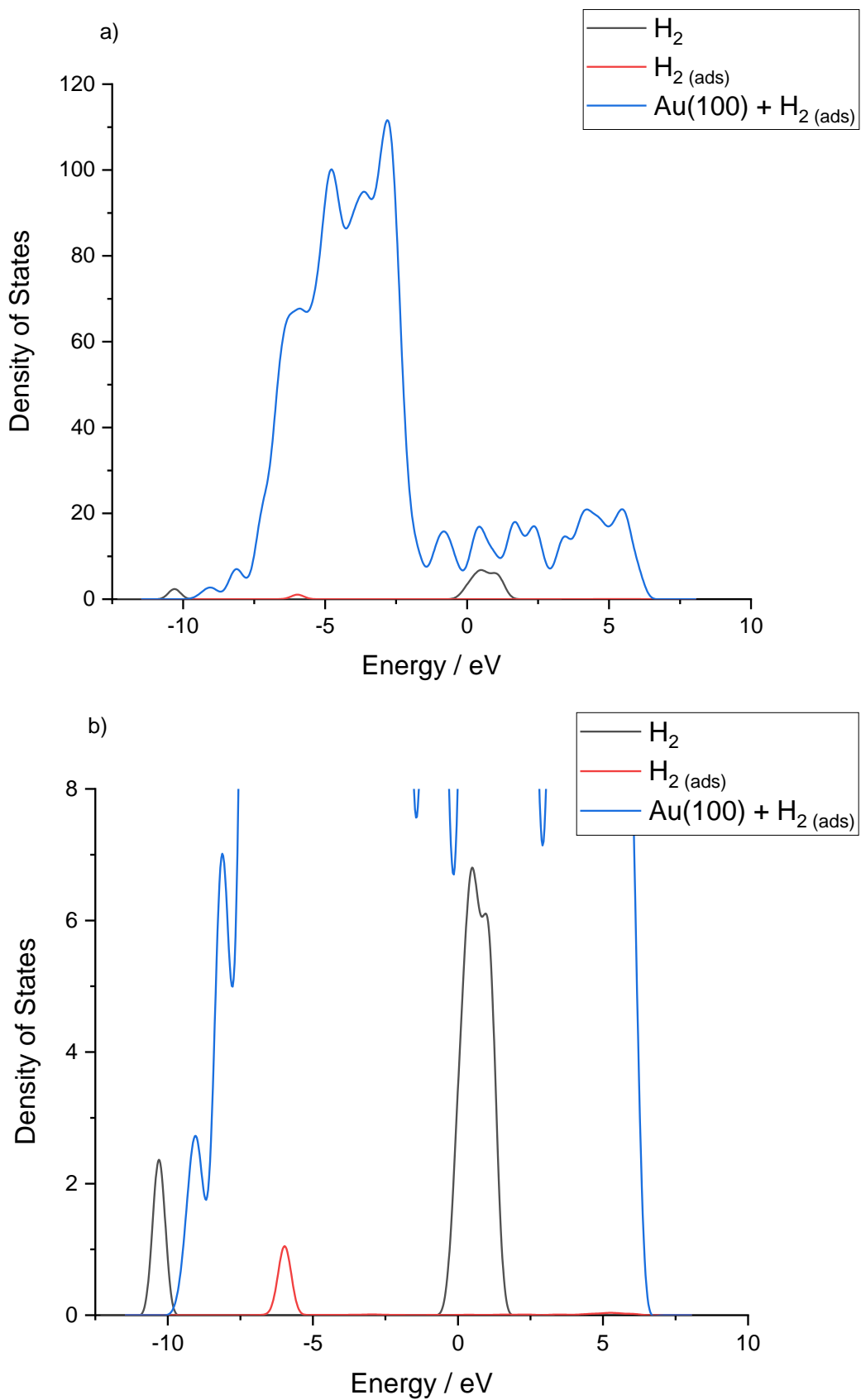


Figure 4.12. Normalised Densities of States for H_2 adsorbed to Au(100), lone H_2 and the partial Densities of States of H_2 adsorbed to Au(100), where **a)** shows all three Densities of States and **b)** shows a magnified view of the normalised Densities of States with a focus on the lone H_2 densities and the partial Densities of States for H_2 adsorbed to Au(100).

Investigating the dissociation of H₂ revealed that the adsorption of H atoms to Au(100) was weak without D3 corrections applied. Each of the sites resulted in Bridge-Bridge sites, however, the H···H interatomic distances were all different. Without the D3 corrections applied, the Bridge-Bridge (1) and (3) sites gave E_{ads} values of ~ -3 and ~ -8 kJ mol⁻¹, respectively. The Bridge-Bridge (2) sites were uncharacteristic as they gave a high positive value for its adsorption (~ 78 kJ mol⁻¹) (Table 4.9 and Fig. 4.13).

Further investigation with the D3 corrections applied in the optimisation calculations showed that the E_{ads} values decreased by ~ 17 , ~ 16 and ~ 16 kJ mol⁻¹ for the Bridge-Bridge (1), (2) and (3) sites, respectively. The reason for the Bridge-Bridge (2) sites' positive E_{ads} value was due to the unusual rearrangement of the top layer of Au atoms. In Fig. 4.13d and e, it appeared that the surface had distorted toward a Au(111) surface (~ 63 kJ mol⁻¹). A direct comparison to either Au(100) and Au(111) could not be made as this new surface was neither. However, it did suggest that Au(100) was a soft, malleable surface (Tables 4.9, and Fig. 4.13).

Table 4.9. Adsorption energies for the different positions of dissociated H₂ adsorbed to Au(100) without and with D3 corrections.

Site	Position	$E_{\text{ads}}^{\text{PBE}}$ / kJ mol ⁻¹	$E_{\text{ads}}^{\text{PBE}+D3}$ / kJ mol ⁻¹	H···H Interatomic Distance / Å
	(1)	-3	-19	3.09
Bridge-Bridge	(2)	78	63	3.72
	(3)	-8	-24	5.90

The Bridge-Bridge (1) sites gave the second lowest E_{ads} value and an average Au-H bond length of ~ 1.78 Å, and the Bridge-Bridge (3) sites gave the lowest E_{ads} and an average Au-H bond length of ~ 1.77 Å. Although the Au-H bond lengths were not significantly different for both Bridge-Bridge (1) and (3) sites, the decreased E_{ads} value observed for the Bridge-Bridge (3) sites was attributed to the increased distance between the H atoms seen in Fig. 4.13f (~ 5.90 Å). This resulted in less repulsion of the H atoms by the surface (Table 4.9 and Fig. 4.13).

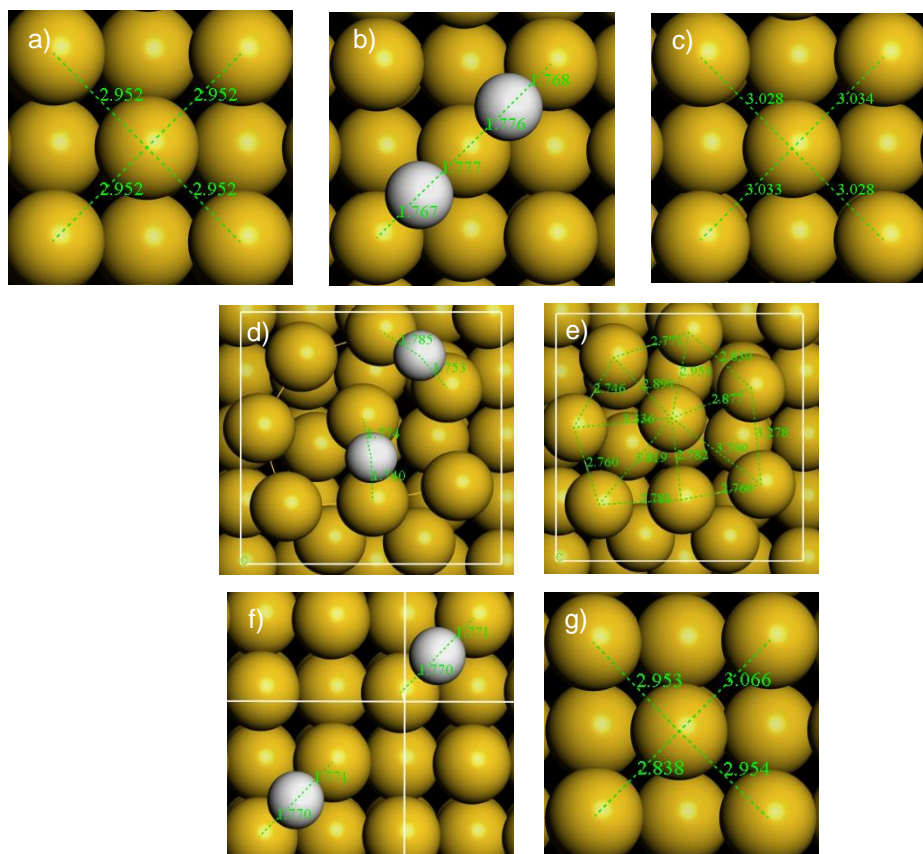


Figure 4.13. Images of the geometry optimisation calculations for dissociated H_2 adsorbed to Au(100) calculated with D3 corrections and the adsorbate removed, where **a**) is the clean surface, **b**) is the Bridge-Bridge (1) sites with the adsorbates, **c**) is the Bridge-Bridge (1) sites without the adsorbates, **d**) is the Bridge-Bridge (2) sites with the adsorbates, **e**) is the Bridge-Bridge (2) sites without the adsorbates, **f**) is the Bridge-Bridge (3) sites with the adsorbates, and **g**) is the Bridge-Bridge (3) sites without the adsorbates. The yellow atoms represent the Au atoms, and the white atoms represent the H atoms. Interatomic distances in green are in Angstroms (\AA).

The Bridge-Bridge (1) sites in Fig. 4.13c caused the Au-Au bond lengths to increase by $\sim 0.08 \text{ \AA}$ to $\sim 3.03 \text{ \AA}$. The surface deformed from the increased proximity of the H atoms, and consequently, increased repulsion of the H atoms being close together. The Bridge-Bridge (3) sites in Fig. 4.13g had a Au-Au bond range of $\sim -0.11 - \sim +0.11 \text{ \AA}$. As previously discussed, H_2 could automatically dissociate upon interaction with Au(100) and the H atoms were at their most stable when bound at the Bridge-Bridge (3) sites (Tables 4.8 and 4.9, and Fig. 4.13).

As intact O_2 was adsorbed onto the surface of the Au(100), it was seen that without the D3 corrections it would require energy for the O_2 to adsorb onto the surface. The lowest E_{ads} value for adsorbed O_2 was $\sim 29 \text{ kJ mol}^{-1}$ on a DB site. However, when atomic O was adsorbed to the surface, the E_{ads} values were drastically higher as the Bridge site gave an E_{ads} value of $\sim 160 \text{ kJ mol}^{-1}$. These values

demonstrated that there was a low affinity between Au and O₂ (and atomic O) as the adsorbates would feasibly desorb before a catalytic reaction could take place (Table 4.10).

Although not all of the geometry optimisation calculations with the D3 corrections applied could be completed for the different sites and positions of O₂ adsorbed onto Au(100), it was observed that the adsorption of O₂ or atomic O was not favourable. The decrease in E_{ads} values between calculations without and with D3 corrections for O₂ for the DB and Quad-Bridge (QB) sites were ~27 and ~12 kJ mol⁻¹, respectively, with the DB site having the lowest E_{ads} value at ~2 kJ mol⁻¹. As seen in Fig. 4.14b and d, the adsorbate moved to its optimum position with a slight angle away from the starting diagonal position of the DB site with Au-O interatomic distances of ~2.18 Å (Table 4.10 and Fig. 4.14).

Table 4.10. Adsorption energies for the different positions of O₂ and ½ O₂ adsorbed to Au(100) without and with D3 corrections.

Adsorbate	Site	Position	$E_{\text{ads}}^{\text{PBE}}$ / kJ mol ⁻¹	$E_{\text{ads}}^{\text{PBE}+\text{D3}}$ / kJ mol ⁻¹
	DB	-	29 (29)	2 (2)
	QB	-	83	70
O ₂	Hollow	-	40	-
		Horizontal	98	-
		Top	59	-
O	Bridge	-	160	32

Note: DB denotes di-bridge and QB is quad-bridge. The species involved in each position are stated in the parentheses. Energy values in parentheses indicate that a different site optimised to the same site configuration.

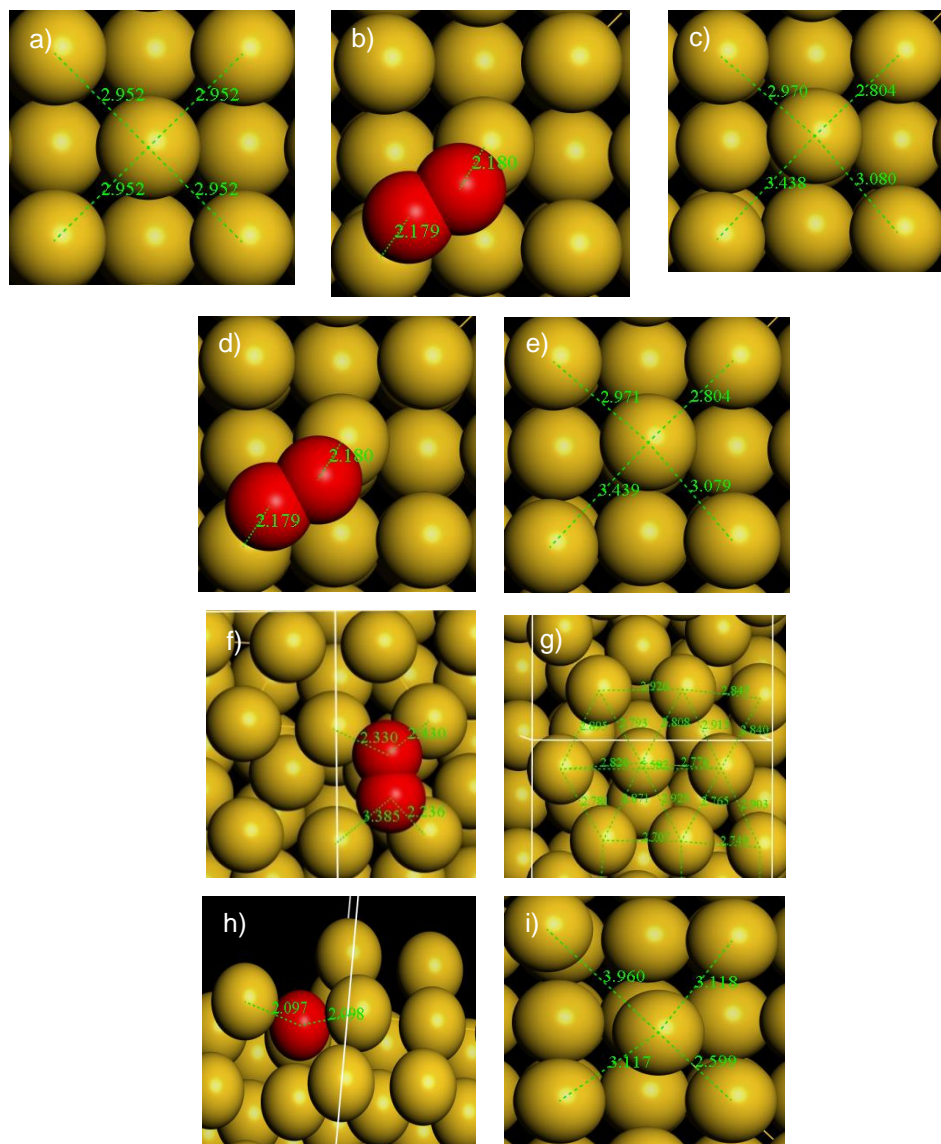


Figure 4.14. Images of the geometry optimisation calculations for O_2 and $\frac{1}{2} O_2$ adsorbed to Au(100) calculated with D3 corrections and the adsorbate removed, where **a)** is the clean surface, **b)** is the DB site with the adsorbate, **c)** is the DB site without the adsorbate, **d)** is the DB site with the adsorbate, **e)** is the DB site without the adsorbate, **f)** is the QB site with the adsorbate, **g)** is the QB site without the adsorbate, **h)** is the Bridge ($\frac{1}{2} O_2$) site with the adsorbate, and **i)** is the Bridge ($\frac{1}{2} O_2$) site without the adsorbate. The yellow atoms represent the Au atoms, and the red atoms represent the O atoms. Interatomic distances in green are in Angstroms (\AA). DB denotes di-bridge and QB is quad-bridge. The species involved in each position are stated in the parentheses.

In Fig. 4.14f, the QB site had undergone an extreme change in the top layer of Au atoms as it became a distorted Au(111) configuration, with a maximum decrease in bond length of $\sim 0.25 \text{\AA}$. A direct comparison between surfaces could not be made. Utilising the equations described in Chapter 2 in tandem with the calculated lone and adsorbed structures, it was determined that the contribution of the deformation of the Au(100) surface and the adsorbate was high, as defined in equations (4.1)-(4.3):

$$\begin{aligned}
E_{def}^{Au(100)} &= E_{Au(100)}^{frozen} - E_{Au(100)}^{relaxed} & (4.1) \\
&= -141.85 - -142.62 \\
&= 0.76 \text{ eV} \approx 74 \text{ kJ mol}^{-1}
\end{aligned}$$

$$\begin{aligned}
E_{def}^{O_2} &= E_{O_2}^{frozen} - E_{O_2}^{relaxed} & (4.2) \\
&= -8.52 - -9.95 \\
&= 1.43 \text{ eV} \approx 138 \text{ kJ mol}^{-1}
\end{aligned}$$

$$\begin{aligned}
E_{def} &= E_{def}^{Au(100)} + E_{def}^{O_2} & (4.3) \\
&= 74 + 138 \\
&= 212 \text{ kJ mol}^{-1}
\end{aligned}$$

where $E_{def}^{Au(100)}$ is the energy of deformation of the Au(100) surface during adsorption, $E_{Au(100)}^{frozen}$ is the energy of the optimised system of the Au(100) during adsorption with the adsorbate removed, $E_{Au(100)}^{relaxed}$ is the energy of the optimised system of the lone Au(100) surface without the adsorbate, $E_{def}^{O_2}$ is the energy of deformation of the O₂ adsorbate during adsorption, $E_{O_2}^{frozen}$ is the energy of the optimised system of the O₂ adsorbate during adsorption with the surface removed, $E_{O_2}^{relaxed}$ is the energy of the optimised system of the lone O₂ molecule, and E_{def} is the total energy of deformation for both the Au(100) surface and the O₂ adsorbate.

As the E_{def} value for the adsorption of O₂ to Au(100) at the QB site in Fig. 4.14f was high at ~212 kJ mol⁻¹, which was a result of the larger Au-Au movements and the increased repulsion between the O₂ and the four Au atoms causing the O₂ to deform (O=O bond increased by ~0.14 Å). This in turn resulted in the highly positive E_{ads} value. The Au-O interatomic distances for the QB site were ~2.24, ~2.33, ~2.43 and ~3.39 Å. The increased distances demonstrated the greater repulsion exhibited as the adsorbate was interacting with more surface atoms, increasing the E_{def} value (Table 4.10 and Fig. 4.14).

There was little variation between the two DB sites top layer Au atoms as the Au-Au bond lengths were ~ 2.80 , ~ 2.97 , ~ 3.08 and ~ 3.44 Å and both maintained a (100) configuration of the top layer. The range in movement compared to the clean surface was marginal with the movement being ~ -0.15 – $\sim +0.49$ Å. Although the movements were moderate, the E_{int} values for these sites were more favourable than the QB site, which was why the E_{ads} values were less positive (Table 4.10 and Fig. 4.14).

In Fig. 4.14h, the adsorbed atomic O on Au(100) showed that it became part of the crystal structure of the Au surface. As gold oxide does not readily occur, this would explain its elevated E_{ads} value (~ 32 kJ mol⁻¹). The Au-Au bond length range in Fig. 4.14i was ~ -0.35 – $\sim +1.01$ Å, which may explain the unfavourable E_{ads} value as a large E_{def} value would have affected the E_{ads} value. The Au atoms were forced closer together, increasing their repulsion (Table 4.10 and Fig. 4.14).

To summarise, the current work was in agreement with the research completed by Barrio *et al.* (~ -4 kJ mol⁻¹)^{22,23} as Au(100) had a low affinity for O₂ and atomic O. As atomic O could not be successfully adsorbed onto Au(100), the research into the adsorption of dissociated O₂ was abandoned.

Although Au(100) proved that it may not have been able to produce H₂O₂ due to its low affinity for O₂, it may have been possible to adsorb and dissociate H₂ first and then become oxidised by the adsorbing O₂ to form H₂O₂ (or reactive oxygen species (ROS)). However, geometry optimisation and E_a barrier calculations would be needed to determine this possibility.

Au(100) could help with the epoxidation reaction and capture the H₂O₂ similarly to the Au(111) surface. Further investigation into H₂O₂ adsorption and dissociation was conducted. Several different positions of the intact H₂O₂ only resulted in two completed calculations as other calculations failed. The DB (OO) site produced an extremely low E_{ads} value of ~ -200 kJ mol⁻¹ without the D3 corrections applied in the calculation, whereas the Sloped Bridge (OH) produced a positive E_{ads} value of ~ 27 kJ mol⁻¹ (Table 4.11 and Fig. 4.15).

With the D3 corrections applied, the E_{ads} values for DB (OO) and Top (OH) sites decreased by ~ 46 and ~ 64 kJ mol⁻¹, respectively. The resultant values were ~ -246 and ~ -37 kJ mol⁻¹, respectively. Both demonstrated an affinity for H₂O₂ with their negative adsorption values, as the former suggested strong chemisorption and the latter suggested a mid-point between physisorption and chemisorption with

Au(100). The DB (OO) site had dissociated the H₂O₂ at the HO-OH bond. And was discounted from the research (Table 4.11 and Fig. 4.15).

Table 4.11. Adsorption energies for the different positions of H₂O₂ adsorbed to Au(100) without and with D3 corrections.

Site	Position	E_{ads}^{PBE} / kJ mol ⁻¹	E_{ads}^{PBE+D3} / kJ mol ⁻¹
DB	(OO)	-200	-246
Sloped Bridge	(OH)	27	-37

Note: DB denotes di-bridge. The species involved in each position are stated in the parentheses.

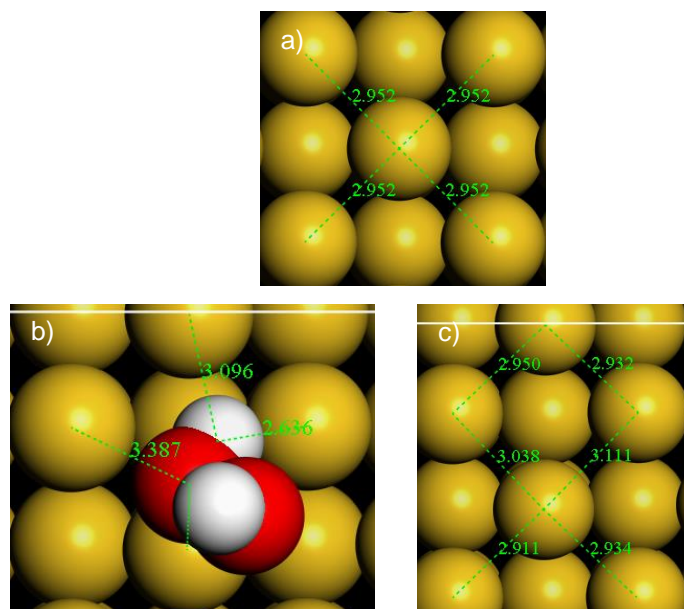


Figure 4.15. Images of the geometry optimisation calculations for H₂O₂ adsorbed to Au(100) calculated with D3 corrections and the adsorbate removed, where **a)** is the clean surface, **b)** is the Sloped Bridge (OH) site with the adsorbate, and **c)** is the Sloped Bridge (OH) site without the adsorbate. The yellow atoms represent the Au atoms, the red atoms represent the O atoms, and the white atoms represent the H atoms. Interatomic distances in green are in Angstroms (Å). The species involved in each position are stated in the parentheses.

The Top (OH) had not remained at the Top site as it moved towards a Sloped Bridge (OH) as it slightly fell into the Hollow site, with the H² atom pointed directly away from the surface. The O¹ atom interacted with the central Au atom and the H¹ atom interacted with a neighbouring Au atom. The Au-O interatomic distance was ~2.68 Å and the Au-H interatomic distance was ~2.64 Å (Table 4.11 and Fig. 4.15).

Analysis of the Au(100) surface without the adsorbate for the Sloped Bridge (OH) site revealed that there was little movement of the top layer of Au atoms. The range of movement for the Au atoms in comparison to the clean surface was $\sim -0.04 - \sim +0.16$ Å. This would explain the reasonable E_{ads} value as little movement was observed, thus, a decreased E_{def} value influenced the E_{ads} value slightly (Table 4.11 and Fig. 4.15).

In summary, H₂O₂ adsorbed to the surface of Au(100), meaning that it could be used as part of an alloy catalyst or tandem catalyst system for the epoxidation process. However, it could also be dissociated automatically depending on the adsorbate orientation and site. It was important to further explore the dissociative capabilities of Au(100). As previously described, there are two possible ways in which H₂O₂ dissociate; either at the H-OOH or HO-OH bonds.

Although not described in the section below, two calculations led to the HO-OH bond dissociating and were discounted from the current work. Irrespective of whether D3 corrections were applied in the geometry optimisation calculations or not, the E_{ads} values were positive. The Bridge (H)-DB (OOH) and Bridge-Bridge sites gave E_{ads} values of ~ 81 and ~ 65 kJ mol⁻¹, respectively, without the D3 corrections. The E_{ads} values with the D3 corrections were ~ 42 and ~ 23 kJ mol⁻¹, respectively (Table 4.12 and Fig. 4.16).

Table 4.12. Adsorption energies for the different positions of dissociated H₂O₂ (H-OOH) adsorbed to Au(100) without and with D3 corrections.

Site	E_{ads}^{PBE} / kJ mol ⁻¹	E_{ads}^{PBE+D3} / kJ mol ⁻¹
Bridge (H)-DB (OOH)	82	42
Bridge-Bridge	65	23

Note: DB denotes di-bridge. The species involved in each position are stated in the parentheses.

The reason for these positive E_{ads} values was most likely due to the low affinity Au has for O. In Fig. 4.16b and d, the Bridge (H)-DB (OOH) and Bridge-Bridge sites had Au-H bond lengths of ~ 1.76 and ~ 1.78 Å, and ~ 1.77 and ~ 1.78 Å, respectively, with Au-O bond lengths of ~ 2.13 and ~ 2.50 Å, and ~ 2.23 and ~ 2.24 Å, respectively. This would explain the more positive E_{ads} value exhibited by the Bridge (H)-DB (OOH)

sites than the Bridge-Bridge sites as one of the Au-O bond lengths was smaller, which in turn, increased repulsion and affected the E_{ads} value (Table 4.12 and Fig. 4.16).

Another contributing factor to the positive E_{ads} value could have been the movement of the top layer Au atoms. The Bridge (H)-DB (OOH) and Bridge-Bridge sites had Au-Au bond length ranges of $\sim -0.13 - \sim +0.43$ Å, and $\sim -0.07 - \sim +0.49$ Å, respectively. Usually, the greater the deformation of the surface (and molecule), the greater the E_{def} value, which in turn affects the E_{ads} value (Table 4.12 and Fig. 4.16).

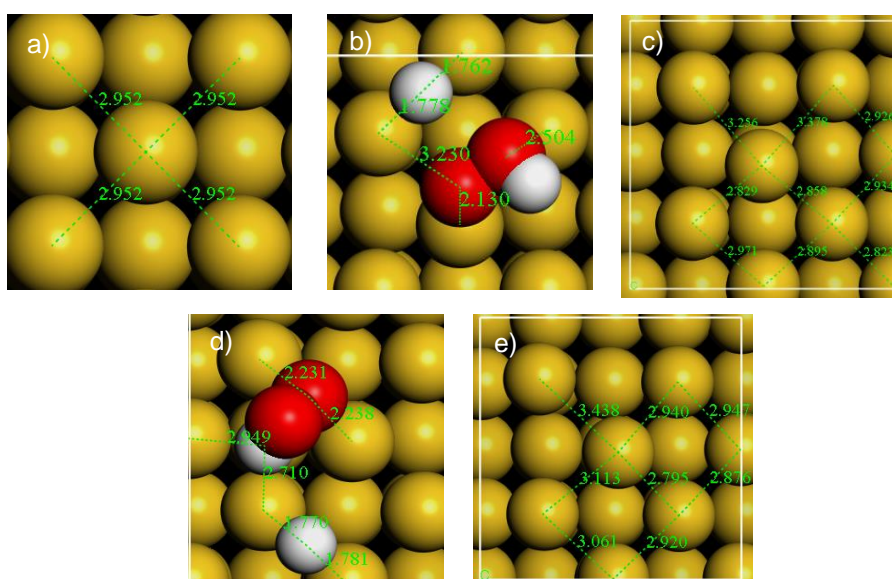


Figure 4.16. Images of the geometry optimisation calculations for dissociated H_2O_2 (H-OOH) adsorbed to Au(100) calculated with D3 corrections and the adsorbate removed, where **a**) is the clean surface, **b**) is the Bridge (H)-DB (OOH) sites with the adsorbates, **c**) is the Bridge (H)-DB (OOH) sites without the adsorbates, **d**) is the Bridge-Bridge sites with the adsorbates, and **e**) is the Bridge-Bridge sites without the adsorbates. The yellow atoms represent the Au atoms, the red atoms represent the O atoms, and the white atoms represent the H atoms. Interatomic distances in green are in Angstroms (Å). DB denotes di-bridge.

In summary, the adsorption of dissociated H_2O_2 (at the H-OOH bond) to Au(100) was unlikely to occur. Therefore, this type of dissociation was unlikely to be a step in the catalytic epoxidation of propene. With some of the previous calculations for H_2O_2 , H and OOH adsorption dissociating at the HO-OH, it was apparent that this type of dissociation was favourable on Au(100), thus, the dissociation at the HO-OH bond was investigated.

It was observed that without D3 corrections, the calculations produced extremely negative E_{ads} values. The Bridge-Bridge (1), Bridge-Bridge (2), Bridge-Bridge (3) and Hollow (O)-Top (H_2O) sites had E_{ads} values of ~ -200 , ~ -169 ,

~-163 and ~-139 kJ mol⁻¹, respectively. With the D3 corrections applied, the E_{ads} values for these sites were ~-246, ~-213, ~-209 and ~-183 kJ mol⁻¹, which was a decrease of ~46, ~44, ~47 and ~44 kJ mol⁻¹, respectively, and were approximately the same (Table 4.13 and Fig. 4.17).

Table 4.13. Adsorption energies for the different positions of dissociated H₂O₂ (HO-OH) adsorbed to Au(100) without and with D3 corrections.

Site	E_{ads}^{PBE} / kJ mol ⁻¹	E_{ads}^{PBE+D3} / kJ mol ⁻¹	O-H Bond Distance / Å
Bridge-Bridge (1)	-200	-246	~1.79
Bridge-Bridge (2)	-169	-213	-
Bridge-Bridge (3)	-163	-209	~2.12
Hollow (O)-Top (H ₂ O)	-139	-183	~1.57

Note: The species involved in each position are stated in the parentheses.

The Bridge-Bridge (1) sites gave Au-O bond lengths of ~2.19, ~2.24 and ~2.25 Å. These bond lengths were similar to the Au-O bond lengths of the Bridge-Bridge (2) sites, which were ~2.21 and ~2.22 Å, and of the Bridge-Bridge (3) sites, which were ~2.16, ~2.19, ~2.27 and ~2.31 Å. In Fig 4.17h and i, it was observed that what were originally OH groups became the Hollow (O)-Top (H₂O) sites, with the top layer of Au atoms reconfiguring to the Au(111) position. Although this result was discounted from this section as the Au(100) configuration was not maintained, it meant that the E_a barrier for H₂O formation was low. Although Bridge-Bridge (2) sites in Fig. 4.17d lacked any O-H bonding, it gave a slightly more negative E_{ads} value than the Bridge-Bridge (3) sites in Fig. 4.17f, by ~4 kJ mol⁻¹. Moreover, the Bridge-Bridge (1) sites with the shorter O-H bond gave the most negative E_{ads} value, meaning that O-H bonding was favourable for the adsorption of the OH groups (Table 4.13 and Fig. 4.17).

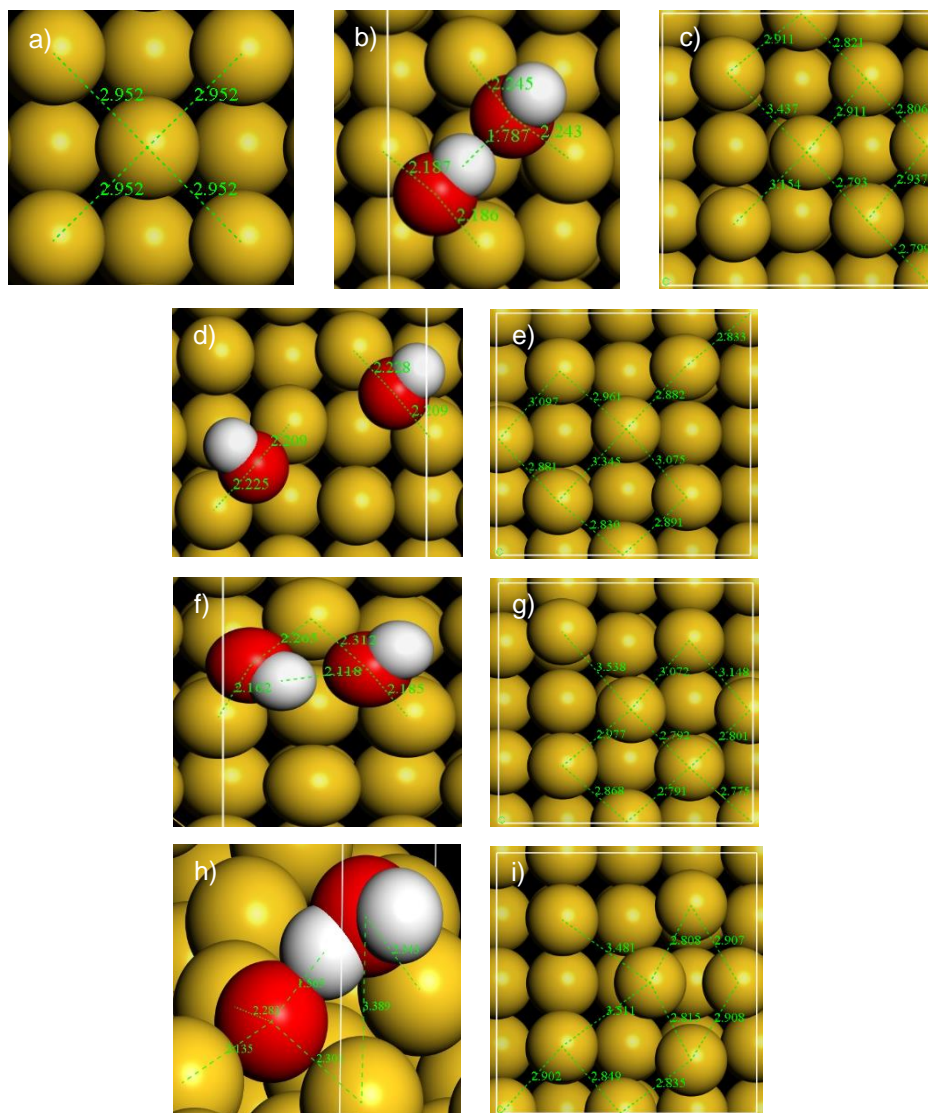


Figure 4.17. Images of the geometry optimisation calculations for dissociated H_2O_2 (HO-OH) adsorbed to Au(100) calculated with D3 corrections and the adsorbate removed, where **a**) is the clean surface, **b**) is the Bridge-Bridge (1) sites with the adsorbates, **c**) is the Bridge-Bridge (1) sites without the adsorbates, **d**) is the Bridge-Bridge (2) sites with the adsorbates, **e**) is the Bridge-Bridge (2) sites without the adsorbates, **f**) is the Bridge-Bridge (3) sites with the adsorbates, **g**) is the Bridge-Bridge (3) sites without the adsorbates, **h**) is the Hollow (O)-Top (H_2O) sites with the adsorbates, and **i**) is the Hollow (O)-Top (H_2O) sites without the adsorbates. The yellow atoms represent the Au atoms, the red atoms represent the O atoms, and the white atoms represent the H atoms. Interatomic distances in green are in Angstroms (\AA).

The OH groups caused major changes to the top layer of Au atoms when compared to the clean surface. It was observed that for the Bridge-Bridge (1) sites in Fig. 4.17c the range in Au-Au bond lengths were $\sim 2.79 - \sim 3.44 \text{ \AA}$. For the Bridge-Bridge (2) sites in Fig. 4.17e, this range was $\sim 2.82 - \sim 3.10 \text{ \AA}$ and for the Bridge-Bridge (3) sites in Fig. 4.17g, this range was $\sim 2.78 - \sim 3.54 \text{ \AA}$. The latter showed a large increase up to $\sim 0.59 \text{ \AA}$ in one of Au-Au bond lengths. However, the

changes to the Au(100) were not detrimental to the adsorption of the OH groups. Au(100) should be considered for the possible integration into an alloy catalyst as the Au atoms could capture or maintain the binding of H₂O₂ and subsequently dissociate it to aid the catalytic epoxidation of propene (Table 4.13 and Fig. 4.17).

Continuing with the research into the epoxidation of propene, it was vital to understand the adsorption of both propene and PO. Initially, propene adsorption was researched, and it was found that various orientations of the molecule could adsorb to the surface of Au(100). All orientations of propene were on Top sites with reference to the C¹=C² bond, unless stated otherwise. Without D3 corrections, the geometry optimisation calculations revealed that adsorption of propene was weak, with the lowest adsorption at ~-1 kJ mol⁻¹ in Fig. 4.18d at the Top Up site. The Top Down site in Fig. 4.18b produced the most unfavourable E_{ads} value with ~29 kJ mol⁻¹. With the D3 corrections applied, the Down, (HC¹), Up and both (HC³) sites decreased in energy by ~45, ~26, ~70, ~28 and ~30 kJ mol⁻¹, respectively. This gave E_{ads} values of ~-16, ~-25, ~-71, ~-29, and ~-30 kJ mol⁻¹, respectively. The fact that the E_{ads} value only became negative when the D3 corrections were applied indicated that the adsorption of propene only involved van der Waals forces (Table 4.14 and Fig. 4.18).

Table 4.14. Adsorption energies for the different positions of propene and PO adsorbed to Au(100) without and with D3 corrections.

Adsorbate	Site	Position	E_{ads}^{PBE} / kJ mol ⁻¹	E_{ads}^{PBE+D3} / kJ mol ⁻¹
Propene	Top	Down	29	-16
		Up	-1	-71
		(HC ¹)	0	-25
		(HC ³)	-1 (0)	-29 (-30)
PO	Top	(HC ³)	0 (0)	-31 (-32)
		(O)	-8 (35)	-59 (5)

Note: Down denotes the methyl group of the propene is pointed down into the surface and Up is the methyl group of the propene pointed away from the surface. The species involved in each position are stated in the parentheses. Energy values in parentheses indicate that a different site optimised to the same site configuration.

Utilising the equations described in Chapter 2 in tandem with the calculated lone and adsorbed structures, it was determined that the contribution of the deformation of the Au(100) surface and the adsorbate was high for the Top Down site, as defined in equations (4.4)-(4.6):

$$\begin{aligned}
 E_{def}^{Au(100)} &= E_{Au(100)}^{frozen} - E_{Au(100)}^{relaxed} & (4.4) \\
 &= -141.85 - -142.62 \\
 &= 0.78 \text{ eV} \approx 75 \text{ kJ mol}^{-1}
 \end{aligned}$$

$$\begin{aligned}
 E_{def}^{prop} &= E_{prop}^{frozen} - E_{prop}^{relaxed} & (4.5) \\
 &= -48.62 - -48.68 \\
 &= 0.06 \text{ eV} \approx 6 \text{ kJ mol}^{-1}
 \end{aligned}$$

$$\begin{aligned}
 E_{def} &= E_{def}^{Au(100)} + E_{def}^{prop} & (4.6) \\
 &= 75 + 6 \\
 &= 81 \text{ kJ mol}^{-1}
 \end{aligned}$$

where E_{def}^{prop} is the energy of deformation of the propene adsorbate during adsorption, E_{prop}^{frozen} is the energy of the optimised system of the propene adsorbate during adsorption with the surface removed, $E_{prop}^{relaxed}$ is the energy of the optimised system of the lone propene molecule, and E_{def} is the total energy of deformation for both the Au(100) surface and the propene adsorbate.

The E_{def} value for the adsorption of propene to Au(100) at the Top Down site in Fig. 4.18b was high at $\sim 81 \text{ kJ mol}^{-1}$. However, the Au-Au movements and the increased repulsion between the propene and the seven Au atoms, as opposed to a maximum of three for the other adsorption sites, led to the small, negative E_{ads} value as the E_{int} value was somewhat favourable. There was also less contribution from the propene adsorbate than observed for the O₂ adsorbate (Table 4.14 and Fig. 4.18).

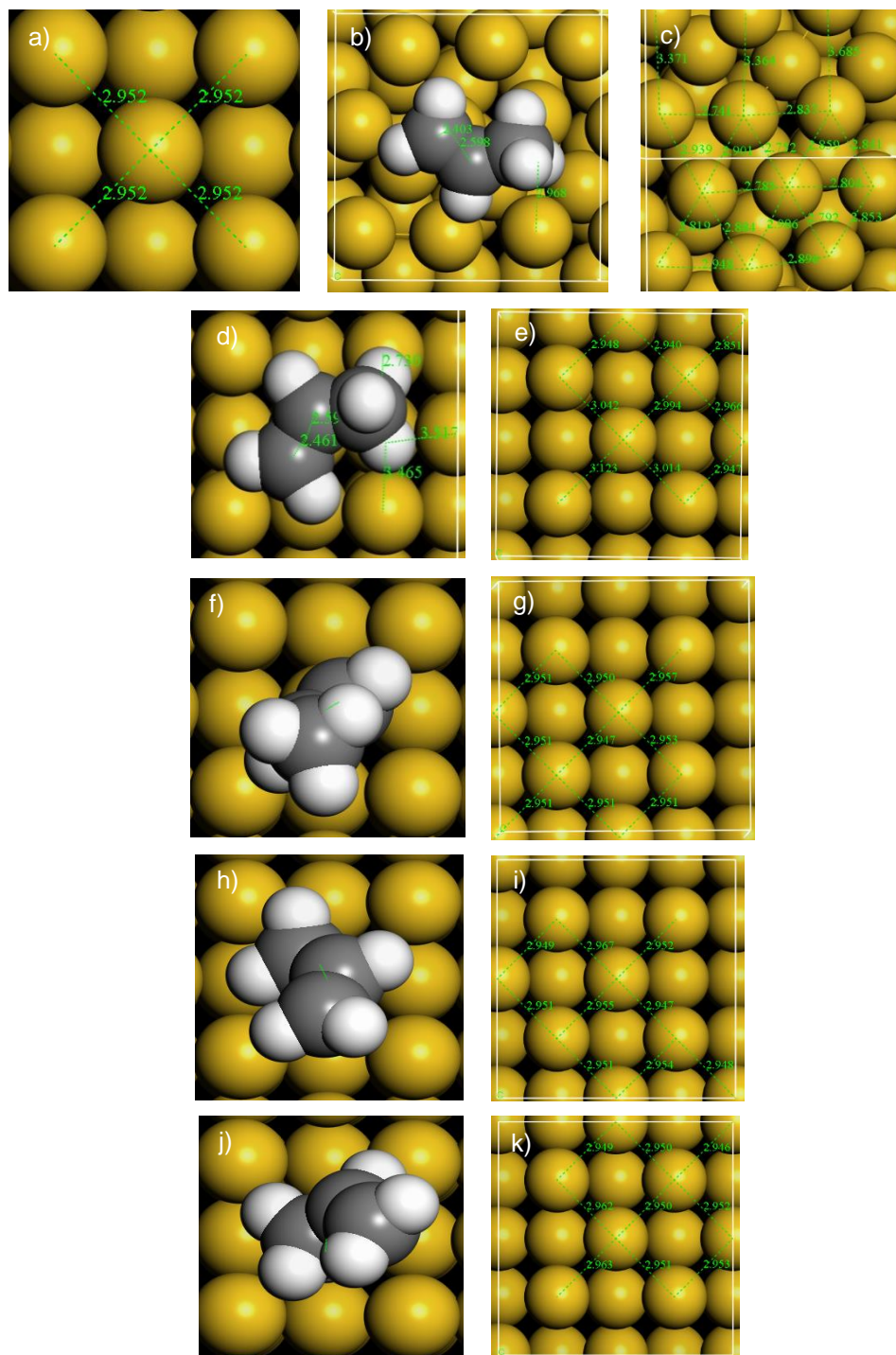


Figure 4.18. Images of the geometry optimisation calculations for propene adsorbed to Au(100) calculated with D3 corrections and the adsorbate removed, where **a)** is the clean surface, **b)** is the Top Down site with the adsorbate, **c)** is the Top Down site without the adsorbate, **d)** is the Top Up site with the adsorbate, **e)** is the Top Up site without the adsorbate, **f)** is the Top (HC¹) site with the adsorbate, **g)** is the Top (HC¹) site without the adsorbate, **h)** is the Top (HC³) site with the adsorbate, **i)** is the Top (HC³) site without the adsorbate, **j)** is the Top (HC³) site with the adsorbate, and **k)** is the Top (HC³) site without the adsorbate. The yellow atoms represent the Au atoms, the grey atoms represent the C atoms, and the white atoms represent the H atoms. Interatomic distances in green are in Angstroms (Å). Down denotes the methyl group of the propene is pointed down into the surface, and Up is the methyl group pointed up and away from the surface. The species involved in each position are stated in the parentheses.

The Au-C interatomic distances for the Top Up site in Fig. 4.18d were ~ 2.46 and ~ 2.59 Å. It was observed that there were some minor interactions between the Au(100) and some of the H atoms. The C¹H atom had an Au-H interatomic distance of ~ 2.89 Å, and with the CH₃ group pointed away from the surface, another of the H atoms had an Au-H interatomic distance of ~ 2.73 Å. Interestingly, the Top (HC¹), and both (HC³) sites in Fig. 4.18f, h and j, respectively, showed similar E_{ads} values and interactions with Au(100) as only one H atom was interacting with the surface, with Au-H interatomic distances of ~ 2.59 , ~ 2.46 and ~ 2.47 Å, respectively (Table 4.14 and Fig. 4.18).

The Top Down site showed an extreme change in the surface Au atoms in Fig. 4.18b and c. The Au atoms repositioned to form a distorted Au(111) configuration with a range of Au-Au bond lengths from ~ 2.79 to ~ 3.69 Å. Although the Au-C interatomic distances were ~ 2.40 and ~ 2.60 , the E_{ads} value was low. This was due to the C³H atom pointed down into the surface. There was no movement of the top layer Au atoms for the Top (HC¹) and Top (HC³) site in Fig. 4.18g and i, but there was the smallest movement for the Top (HC³) site in Fig. 4.18k ($\sim \pm 0.01$ Å), which may explain the slight difference in E_{ads} values between the two sites (~ 1 kJ mol⁻¹). In Fig. 4.18d, only the Top Up site had the most significant change in the top layer Au atom positions, with the range of Au-Au bond lengths of ~ 2.85 – ~ 3.12 Å. It was concluded that the influence of the surface atoms' positions was small for the Top Up site and that the contributing factor to the E_{ads} value of the Top Up site was due to the decreased repulsion as the CH₃ group was pointed away from the surface (Table 4.14 and Fig. 4.18).

In Fig. 4.19, the DoS of the Top Up site showed that there was significant interaction between the Au(100) surface and propene. This interaction resulted in the anti-bonding orbital of the propene molecule above the Fermi level being reduced to almost nothing, with the densities being spread out. The bonding orbitals had been reduced and shifted towards the Fermi level by $\sim +1$ – $\sim +2$ eV. Two of the sp^2 -orbital peaks for the adsorbed propene at ~ -10 and ~ -8 eV overlapped with the peaks for the adsorbate-surface complex, which suggested an overlap of bonding orbitals between the surface and adsorbate. This seemed reasonable with an E_{ads} value of ~ -71 kJ mol⁻¹. There was a small bond lengthening of the adsorbate as the C¹=C² bond length increased from ~ 1.34 Å to ~ 1.37 Å, which was most likely due to a shift of the electron density in the double bond upon interaction with the surface. The DoS demonstrated a partially filled anti-bonding orbital of the adsorbate (Table 4.14, and Fig. 4.18 and 4.19).

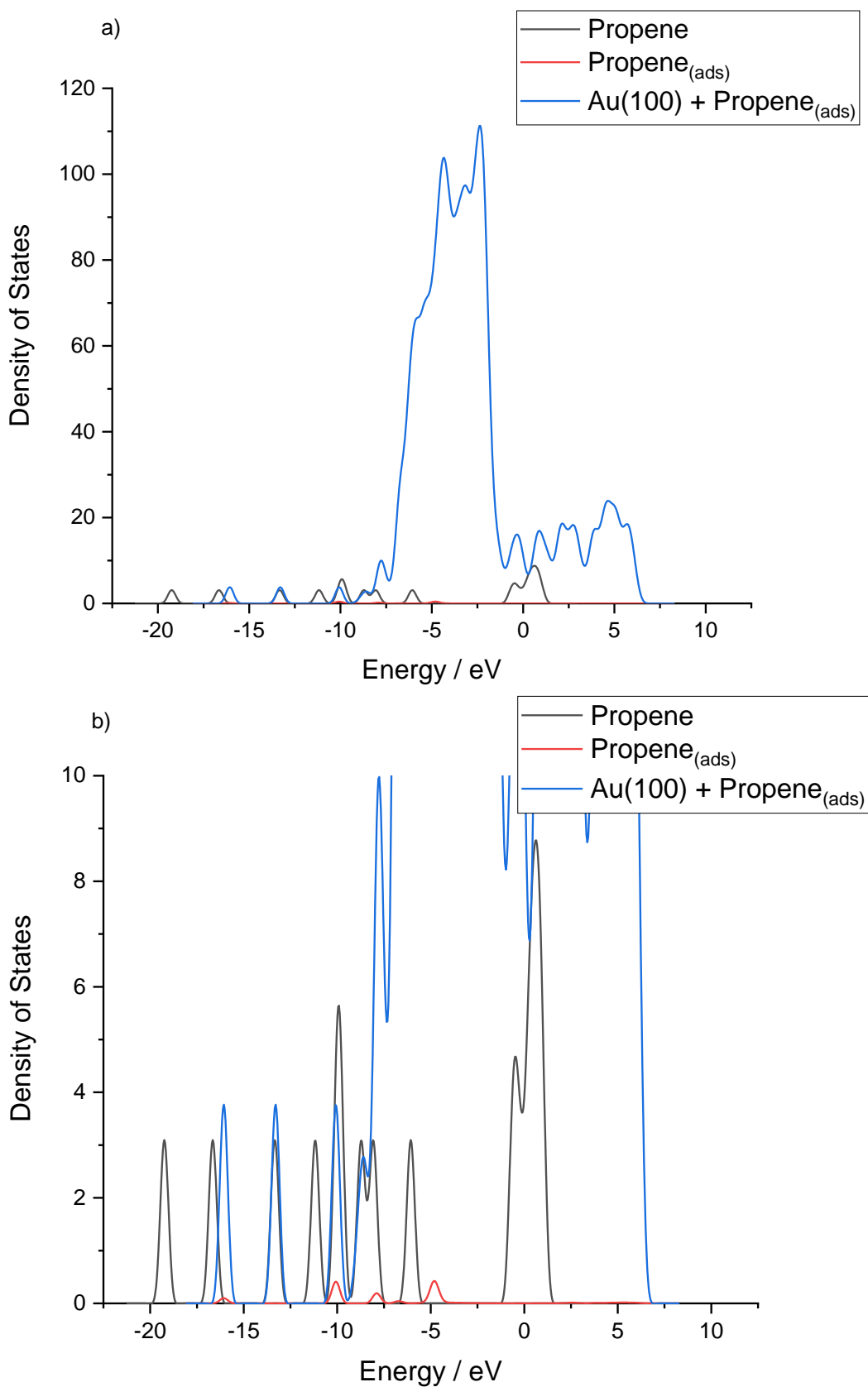


Figure 4.19. Normalised Densities of States for propene adsorbed to Au(100), lone propene and the partial Densities of States of propene adsorbed to Au(100), where **a)** shows all three Densities of States, and **b)** shows a magnified view of the normalised Densities of States with a focus on the lone propene densities and the partial Densities of States for propene adsorbed to Au(100).

All the adsorption sites for PO adsorption were Top sites, and it was observed that without the D3 corrections applied, most of the E_{ads} values were positive except for one of the Top (O) site, which had an E_{ads} value of ~ -8 kJ mol⁻¹. However, when the D3 corrections were applied, the E_{ads} value for all the sites decreased. Both of the Top (HC³) and both Top (O) sites decreased by ~ 31 , ~ 32 , ~ 51 and ~ 30 kJ mol⁻¹, respectively, to ~ -31 , ~ -32 , ~ -59 and ~ 5 kJ mol⁻¹, respectively (Table 4.14 and Fig. 4.20).

The Top (O) site in Fig. 4.20f had one Au-O interatomic distance of ~ 2.63 Å and Au-H interatomic distances of ~ 3.21 , ~ 3.23 and ~ 3.41 Å, where the C¹H and two of the C³Hs were interacting with the Au(100) surface. Regardless, this interaction was the most favourable with an E_{ads} value of ~ -59 kJ mol⁻¹. The Top (O) site in Fig. 4.20h was not a favourable adsorption site as it required energy to adsorb PO in this manner. Although the Au-O interatomic distance was ~ 2.60 Å and the Au-H interatomic distances for the C²H were ~ 2.92 and ~ 3.08 Å, which were comparable to that of the Top (O) site in Fig. 4.20f, the positive E_{ads} value was most likely due to the rearrangement of the Au atoms. The top layer Au atoms for the Top (O) site in Fig. 4.20h reconfigured to a distorted Au(111) structure with a range of Au-Au bond lengths from ~ 2.75 to ~ 3.65 Å (Table 4.14 and Fig. 4.20).

Both Top (HC³) sites and the Top (O) site in Fig. 4.20f had only minor changes to surface atoms, remaining in a (100) configuration. Both Top (HC³) sites did not significantly change ($\sim \pm 0.01$ Å), and the Top (O) site had a range of Au-Au bond lengths from ~ 2.92 to ~ 3.03 Å. These three sites for PO adsorption demonstrated that the site with the largest changes in Au-Au bond distances was the site with the most negative E_{ads} value. Thus, it was concluded that the movement of the top layer Au atoms did influence the E_{ads} value, especially when the surface was completely distorted, as was the case for the Top (O) site in Fig. 4.20h (Table 4.14 and Fig. 4.20).

To summarise, the adsorption of propene and PO occurred on the surface of Au(100). This meant that it could be considered as a viable catalytic material within an alloy catalyst or tandem catalyst system that would benefit the epoxidation of propene. PO can be bound and remain stable to its surface, but energy would be required to desorb it from the surface. From Roldan *et al.*'s work,¹⁸ it could be presumed that Au(100) would have a similar propensity to that of Au(111) when considering the reaction pathways and transition states. Further research would be required to confirm this.

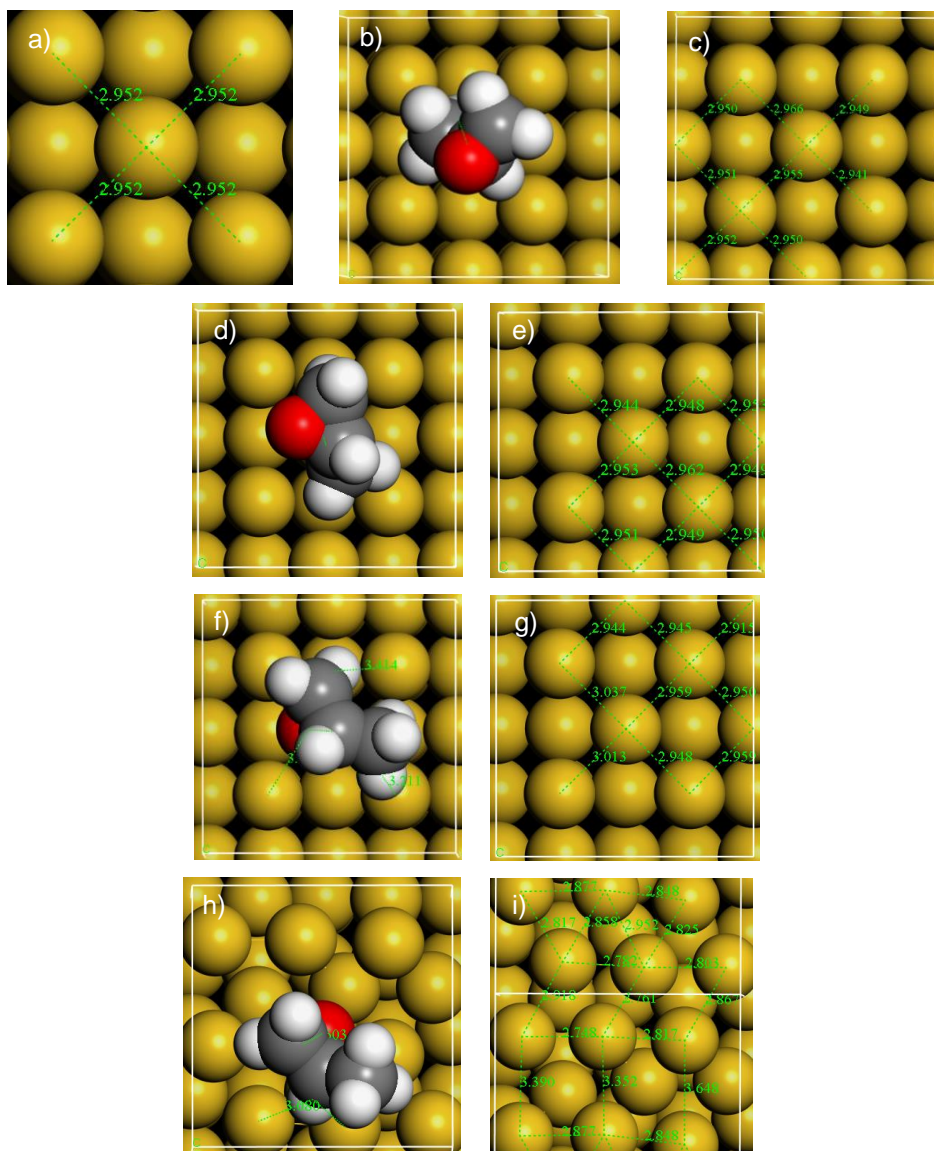


Figure 4.20. Images of the geometry optimisation calculations for PO adsorbed to Au(100) calculated with D3 corrections and the adsorbate removed, where **a)** is the clean surface, **b)** is the Top (HC^3) site with the adsorbate, **c)** is the Top (HC^3) site without the adsorbate, **d)** is the Top (HC^3) site with the adsorbate, **e)** is the Top (HC^3) site without the adsorbate, **f)** is the Top (O) site with the adsorbate, **g)** is the Top (O) site without the adsorbate, **h)** is the Top (O) site with the adsorbate, and **i)** is the Top (O) site without the adsorbate. The yellow atoms represent the Au atoms, the grey atoms represent the C atoms, the red atoms represent the O atoms, and the white atoms represent the H atoms. Interatomic distances in green are in Angstroms (\AA). The species involved in each position are stated in the parentheses.

4.2.2. Palladium

Research into Pd catalysts for the direct synthesis of H_2O_2 , and its possible subsequent decomposition and hydrogenation reactions, is a well-established field, both experimentally and theoretically. However, there are a lack of studies on the catalytic epoxidation of propene using Pd. The adsorption of the reactants,

intermediates, and products for these reactions over the Pd(111) and (100) surfaces have been studied in the current work.

4.2.2.1. Palladium(111)

Initially, Pd was studied for its catalytic properties for the direct synthesis of H₂O₂. For the adsorption of H₂ onto Pd(111), it was seen that without the D3 corrections applied, all of the adsorption sites yielded negative E_{ads} values. However, only the Top Horizontal site could be considered as the adsorbate remained intact, whereas other sites led to dissociation, and therefore, were discounted from this research. This was unsurprising as Pd has the propensity to dissociate H₂ feasibly. This has been well documented by Ford *et al.*⁵ and Todorovic *et al.*⁷ as the E_{a} barrier for dissociation is low (Table 4.15 and Fig. 4.21).

Table 4.15. Adsorption energies for the different positions of H₂ adsorbed to Pd(111) without and with D3 corrections.

Site	Position	$E_{\text{ads}}^{\text{PBE}} / \text{kJ mol}^{-1}$	$E_{\text{ads}}^{\text{PBE}+\text{D3}} / \text{kJ mol}^{-1}$
Bridge	-	-95	-107
DB	-	-115	-128
	fcc	-115	-128
Hollow	hcp	-95	-107
	Top Horizontal	-30	-43

Note: DB denotes di-bridge.

The Top Horizontal site in Fig 4.21b gave the least negative E_{ads} value at $\sim -30 \text{ kJ mol}^{-1}$, without the D3 corrections applied. When they had been applied to the geometry calculations, the E_{ads} value decreased by $\sim 13 \text{ kJ mol}^{-1}$ to $\sim -43 \text{ kJ mol}^{-1}$, which was in the region of chemisorption. This was significant as H₂ readily dissociates over Pd,^{5,7} but in this instance, it remained intact and could be the step that precedes dissociation. This meant that that the only parameter that stopped this dissociation was the orientation of the H₂ molecule. This finding demonstrated the

importance of including intermolecular forces in any geometry calculations performed (Table 4.15 and Fig. 4.21).

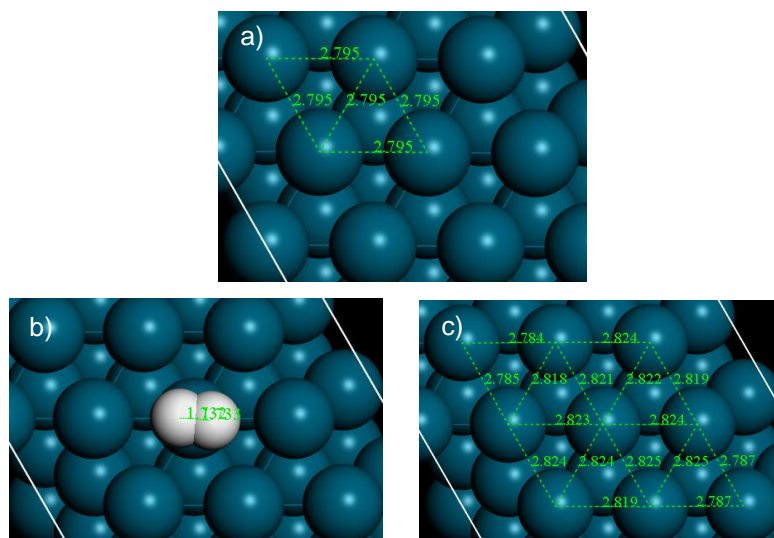


Figure 4.21. Images of the geometry optimisation calculations for H_2 adsorbed to Pd(111) calculated with D3 corrections and the adsorbate removed, where **a)** is the clean surface, **b)** is the Top Horizontal site with the adsorbate, and **c)** is the Top Horizontal site without the adsorbate. The dark blue atoms represent the Pd atoms, and the white atoms represent the H atoms. Interatomic distances in green are in Angstroms (\AA).

Additionally, the Top Horizontal site gave Pd-H bond distances of $\sim 1.73 \text{ \AA}$, which were concurrent with the high E_{ads} value. In Fig. 4.21c, the top layer Pd atoms moved slightly in comparison to the clean Pd(111) surface. From $\sim 2.80 \text{ \AA}$, the range of the Pd-Pd bond distance was from ~ 2.78 to $\sim 2.83 \text{ \AA}$. This was a small range and most likely had little effect on the E_{def} or E_{ads} values (Table 4.15 and Fig. 4.21).

In Fig. 4.22, the DoS of the Top Vertical site showed that there was the slightest interaction between the Pd(111) surface and the H_2 . This interaction resulted in the anti-bonding orbital of the H_2 above the Fermi level being reduced to nothing, whilst the bonding orbital DoS had been reduced, and shifted towards the Fermi level by $\sim +1 \text{ eV}$. Clearly, there was overlap of the bonding orbitals as the corresponding peaks for the adsorbed H_2 and adsorbate-surface complex at $\sim -9 \text{ eV}$ overlapped. This was supported by the E_{ads} value of the Top Vertical site ($\sim -43 \text{ kJ mol}^{-1}$). A shift in electron density upon adsorption resulted in significant bond lengthening of the adsorbate as it increased from $\sim 0.75 \text{ \AA}$ to $\sim 0.87 \text{ \AA}$ (Table 4.15, and Fig. 4.21 and 4.22).

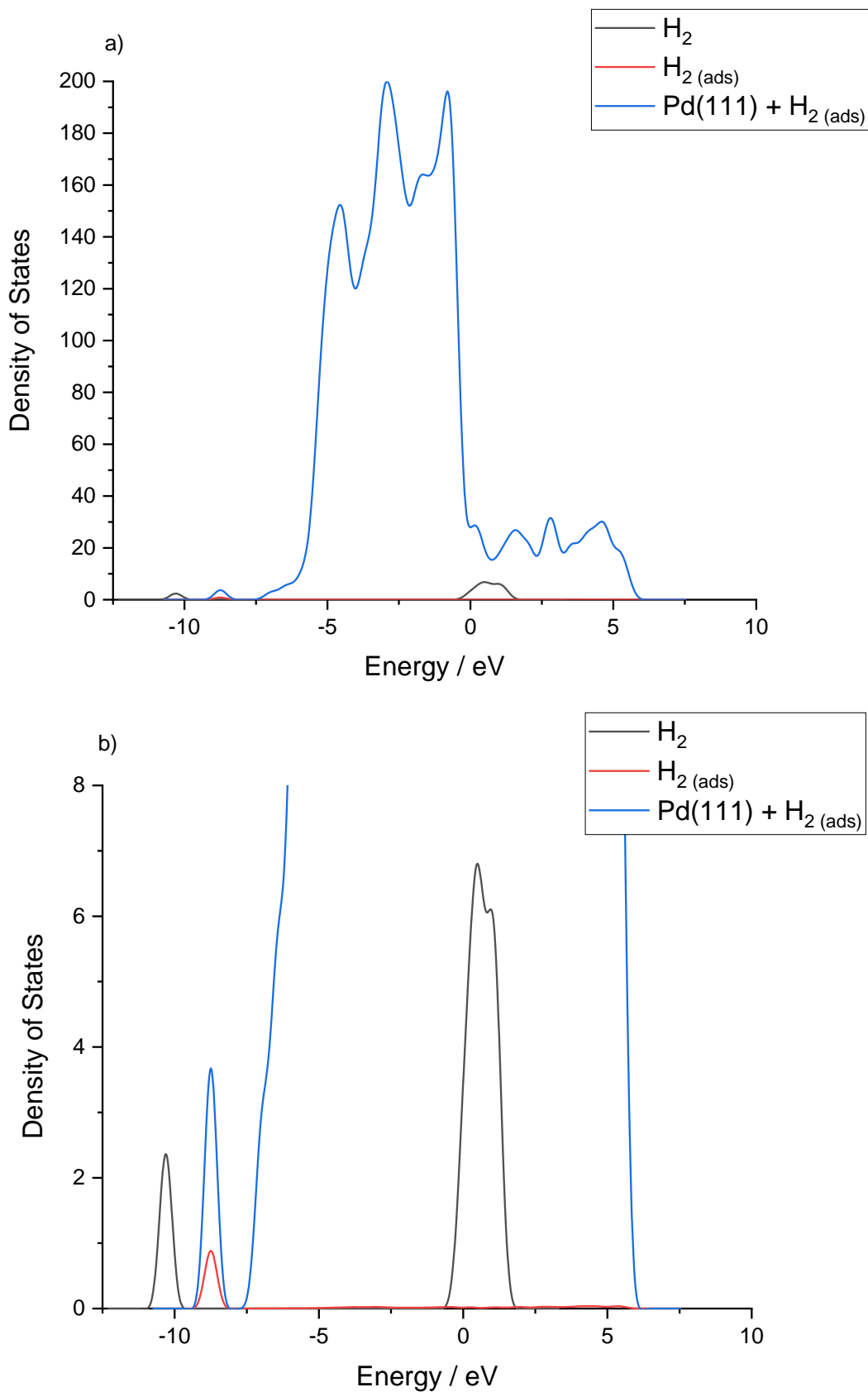


Figure 4.22. Normalised Densities of States for H_2 adsorbed to Pd(111), lone H_2 and the partial Densities of States of H_2 adsorbed to Pd(111), where **a)** shows all three Densities of States and **b)** shows a magnified view of the normalised Densities of States with a focus on the lone H_2 and partial Densities of States of H_2 adsorbed to Pd(111).

As H₂ readily dissociated on Pd(111), it was important to verify which adsorption sites were the most favourable for dissociated H₂. It has been well documented that the Hollow fcc sites are the favoured site of adsorption.^{5,7} The current work also confirmed this, as the Hollow Straight fcc (1) and (2) sites provided the lowest E_{ads} values, both without and with D3 corrections applied to the calculations (~-115 and ~-128 kJ mol⁻¹, respectively). With the D3 corrections applied for the Hollow Diagonal hcp-fcc, Hollow Straight fcc-fcc (1) and (2), hcp-fcc and hcp-hcp and the Top Diagonal sites, the E_{ads} values were reduced by ~13 kJ mol⁻¹, to ~-124, ~-128, ~-128 ~-107, ~-119 and ~-27 kJ mol⁻¹, respectively. All other adsorption sites were less favourable than the Hollow Straight fcc (1) and (2) sites (Table 4.16 and Fig. 4.23).

Table 4.16. Adsorption energies for the different positions of dissociated H₂ adsorbed to Pd(111) without and with D3 corrections.

Site	Position	E_{ads}^{PBE} / kJ mol ⁻¹	E_{ads}^{PBE+D3} / kJ mol ⁻¹
	Diagonal hcp-fcc	-112	-124
	Straight fcc-fcc (1)	-115	-128
Hollow	Straight fcc-fcc (2)	-115	-128
	Straight hcp-fcc	-95	-107
	Straight hcp-hcp	-107	-119
Top	Diagonal	-15	-27

Note: Diagonal denotes the position of the adsorbate over the diamond shape of four top layer metal atoms, and Straight is the position of the adsorbate over the just one length of the diamond shape of four top layer atoms.

With a top site, the distance between one Pd atom and one H atom was shorter (~1.55 Å) than a hollow site, meaning the interaction to bind the H atom had to be stronger than a hollow site, which had three Pd atoms to interact with one H atom. The Hollow fcc sites were less repulsive than the hcp sites, which in turn was due to the distance between the Pd and H atoms. Within a hollow site, three Pd atoms interact directly with the H atom, but a fourth also influences that interaction (Table 4.16 and Fig. 4.23).

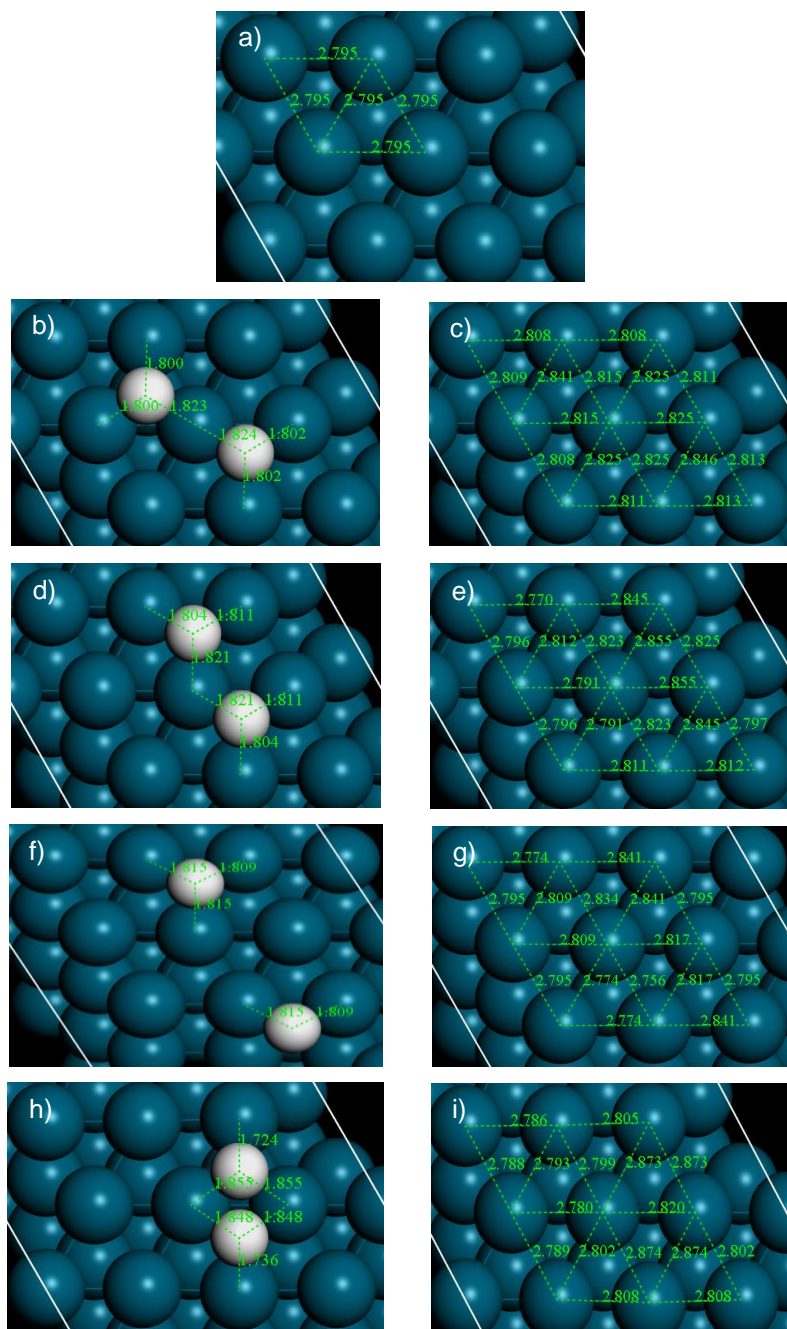


Figure 4.23. Images of the geometry optimisation calculations for dissociated H_2 adsorbed to Pd(111) calculated with D3 corrections and the adsorbate removed, where **a)** is the clean surface, **b)** is the Hollow Diagonal hcp-fcc sites with the adsorbates, **c)** is the Hollow Diagonal hcp-fcc sites without the adsorbates, **d)** is the Hollow Straight fcc-fcc (1) sites with the adsorbates, **e)** is the Hollow Straight fcc-fcc (1) sites without the adsorbates, **f)** is the Hollow Straight fcc-fcc (2) sites with the adsorbates, **g)** is the Hollow Straight fcc-fcc (2) sites without the adsorbates, **h)** is the Hollow Straight fcc-hcp sites with the adsorbates, and **i)** is the Hollow Straight fcc-hcp sites without the adsorbates. The dark blue atoms represent the Pd atoms, and the white atoms represent the H atoms. Interatomic distances in green are in Angstroms (\AA). Straight denotes the position of the adsorbate over the just one length of the diamond shape of four top layer atoms.

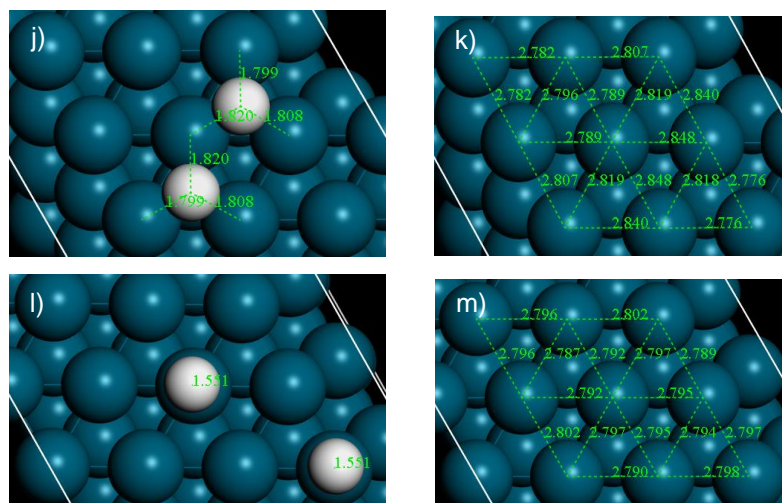


Figure 4.23. Images of the geometry optimisation calculations for dissociated H_2 adsorbed to Pd(111) calculated with D3 corrections and the adsorbate removed, where **j)** is the Hollow Straight hcp-hcp sites with the adsorbates, **k)** is the Hollow Straight hcp-hcp sites without the adsorbates, **l)** is the Top Diagonal sites with the adsorbates, and **m)** is the Top Diagonal sites without the adsorbates. The dark blue atoms represent the Pd atoms, and the white atoms represent the H atoms. Interatomic distances in green are in Angstroms (\AA). Straight denotes the position of the adsorbate over one length of the diamond shape of four top layer atoms.

In a hcp site, a second layer Pd atom in the hollow site interacts with the H atom, whereas the fcc site had a third layer Pd atom. The second layer Pd atom repelled more than the third layer Pd atom. The increased distance reduced the repulsion between the third layer atom Pd, and the H atom compared to the second layer Pd atom of the hcp hollow site. This in turn, made the adsorption to this hollow site more favourable than a hcp site and more negative in E_{ads} (Table 4.16 and Fig. 4.23).

However, it was observed that the E_{ads} value for the Hollow Straight hcp-hcp sites was more negative than that of the fcc-hcp sites because the H atoms were close to each other, in opposite sites, as opposed to sites at a distance away from each other. The repulsion of the H atoms would be included within the E_{ads} value for the Hollow Straight fcc-hcp sites in Fig. 4.23h (Table 4.16 and Fig. 4.23).

For the Hollow Diagonal fcc-hcp, Hollow Straight fcc-fcc (1) and (2), fcc-hcp, hcp-hcp and the Top Straight sites, the Pd-H bond lengths were: ~ 1.80 and ~ 1.82 \AA ; ~ 1.80 , ~ 1.81 and ~ 1.82 \AA ; ~ 1.81 and ~ 1.82 \AA ; ~ 1.72 , ~ 1.73 , ~ 1.85 and ~ 1.86 \AA ; ~ 1.80 , ~ 1.81 and ~ 1.82 \AA ; and ~ 1.55 \AA , respectively. It was observed that the increased Pd-H bonds lengths contributed to the less negative E_{ads} value. For example, the Top Diagonal sites had a Pd-H bond length of ~ 1.55 \AA , whereas the Hollow Straight fcc-fcc sites had Pd-H bond lengths of ~ 1.80 to ~ 1.82 \AA . As previously

stated, this was due to the number of Pd atoms interacting with one H atom; the more Pd atoms there were to interact with the H atom, the longer the distance between them was as the interaction becomes shared between the Pd atoms. Additionally, all Pd-Pd movements were minimal for all sites (maximum change observed: $\sim\pm 0.08 \text{ \AA}$), which may explain the favourable adsorption as the E_{def} value would have been low (Table 4.16 and Fig. 4.23).

In summary, H_2 dissociation readily occurred on the surface of Pd(111) and was extremely favourable. However, it was crucial to investigate the adsorption of O_2 following the promising results of H_2 adsorption and dissociation. This was to determine whether Pd(111) was a suitable candidate for catalytic direct H_2O_2 synthesis.

For the calculations without D3 corrections, it was observed that the most negative E_{ads} value for O_2 was on the Bridge (O^1)-Top (O^2) site in Fig. 4.24b, at $\sim -83 \text{ kJ mol}^{-1}$. Both DB and Top sites collapsed to Bridge (O^1)-Top (O^2) sites and have been consolidated into a single result in the data (Table 4.17 and Fig. 4.24).

Table 4.17. Adsorption energies for the different positions of O_2 and $\frac{1}{2} \text{O}_2$ adsorbed to Pd(111) without and with D3 corrections.

Adsorbate	Site	Position	$E_{ads}^{PBE} / \text{kJ mol}^{-1}$	$E_{ads}^{PBE+D3} / \text{kJ mol}^{-1}$
O_2	Bridge (O^1)-Top (O^2)	-	-83	-107
		fcc	-20	-44
	Hollow	hcp	-13	-36
O	Hollow	fcc ($\frac{1}{2} \text{O}_2$)	-131	-143
		hcp ($\frac{1}{2} \text{O}_2$)	-115	-126

Note: DB denotes di-bridge. The species involved in each position are stated in the parentheses.

The Bridge (O^1)-Top (O^2) site (which adsorbed over a hollow fcc site) had a similar E_{ads} value to that of the research conducted by Tian *et al.* This group showed that this adsorption site gave an energy of $\sim -0.89 \text{ eV}$ ($\sim -86 \text{ kJ mol}^{-1}$),²⁵ similar to the

current work's ~ -83 kJ mol⁻¹. The Hollow fcc and hcp sites gave less negative E_{ads} values with ~ -20 and ~ -12 kJ mol⁻¹, respectively. With the D3 corrections applied, the E_{ads} values decreased by ~ 24 kJ mol⁻¹ to ~ -107 , ~ -44 , ~ -36 kJ mol⁻¹ for the Bridge (O¹)-Top (O²), Hollow fcc and hcp sites, respectively (Table 4.17 and Fig. 4.24).

For the Bridge (O¹)-Top (O²) site in Fig. 4.24b, the O₂ arched over a hollow fcc site. As previously discussed, hollow hcp sites exhibit increased repulsion compared to the hollow fcc sites, thus, the position of the adsorption site was more beneficial than if it had been over a hollow hcp site. This rationale also explained the difference between the E_{ads} values for O₂ adsorbed to the Hollow fcc and hcp sites in Fig. 4.24d and f (Table 4.17). The Hollow fcc and hcp sites showed a decreased E_{ads} value because of the lack of interaction the whole molecule had in comparison to the Bridge (O¹)-Top (O²) sites. Only one of the O atoms of the adsorbate was interacting with the surface (Table 4.17 and Fig. 4.24).

The effect the adsorbates had on the surface Pd atoms was minor. In Fig. 4.24b, the Bridge (O¹)-Top (O²) sites gave a Pd-Pd interatomic distance range of ~ 2.76 to ~ 2.97 Å. There was less movement of the top layer Pd atoms for the Hollow fcc and hcp sites compared to the Bridge (O¹)-Top (O²) site. The Hollow fcc and hcp sites in Fig 4.24 d and f, respectively, had Pd-Pd bond distance ranges of $\sim 2.75 - \sim 2.92$ Å, and $\sim 2.76 - \sim 2.90$ Å, respectively. The latter result was to be expected as the E_{ads} value was less negative than that of the Hollow fcc or the Bridge (O¹)-Top (O²) sites. This was attributed to the increased repulsion exhibited by a hollow hcp site (Table 4.17 and Fig. 4.24).

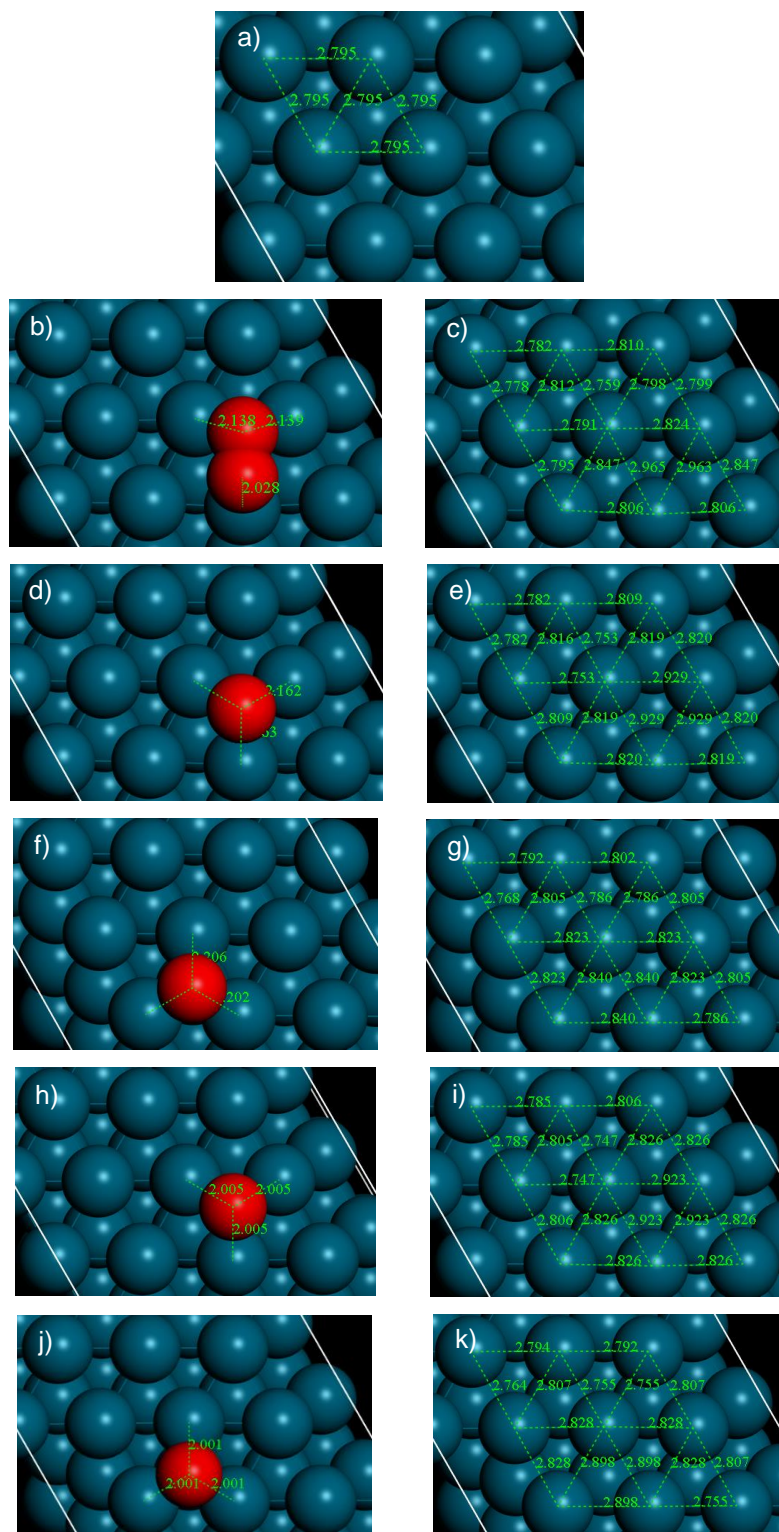


Figure 4.24. Images of the geometry optimisation calculations for O_2 and $\frac{1}{2} O_2$ adsorbed to Pd(111) calculated with D3 corrections and the adsorbate removed, where **a)** is the clean surface, **b)** is the Bridge (O^1)-Top (O^2) site with the adsorbate, **c)** is the Bridge (O^1)-Top (O^2) site without the adsorbate, **d)** is the Hollow fcc site with the adsorbate, **e)** is the Hollow fcc site without the adsorbate, **f)** is the Hollow hcp site with the adsorbate, **g)** is the Hollow hcp site without the adsorbate, **h)** is the Hollow fcc ($\frac{1}{2} O_2$) site with the adsorbate, **i)** is the Hollow fcc ($\frac{1}{2} O_2$) site without the adsorbate, **j)** is the Hollow hcp ($\frac{1}{2} O_2$) site with the adsorbate and **k)** is the Hollow hcp ($\frac{1}{2} O_2$) site without the adsorbate. The dark blue atoms represent the Pd atoms, and the red atoms represent the O atoms. Interatomic distances in green are in Angstroms (\AA). The species involved in each position are stated in the parentheses.

In Fig. 4.25, the DoS of the Bridge (O^1)-Top (O^2) site showed that there was significant interaction between the Pd(111) surface and the O_2 molecule. This interaction resulted in the anti-bonding orbital(s) of the O_2 above the Fermi level being drastically decreased. The bonding orbitals being shifted towards the Fermi level by $\sim +1 - \sim +7$ eV. The p -orbitals of the adsorbed O_2 molecule at ~ -24 , ~ -16 , ~ -9 , and ~ -8 eV overlapped with the peaks of the adsorbate-surface complex, which suggested an overlap of the bonding orbitals of the adsorbate and surface, supported by the large, negative E_{ads} value (~ -107 kJ mol $^{-1}$) (Table 4.17, and Fig. 4.24 and 4.25).

There was a sizeable bond lengthening of the adsorbate as the O=O bond length increased from ~ 1.24 Å to ~ 1.37 Å. This showed that the Pd(111) surface was destabilising the O=O bond (as well as a greater amount of electron repulsion). This also affirms the explanations given with regards to the strong chemisorption at ~ -107 kJ mol $^{-1}$ (Table 4.17, and Fig. 4.24 and 4.25).

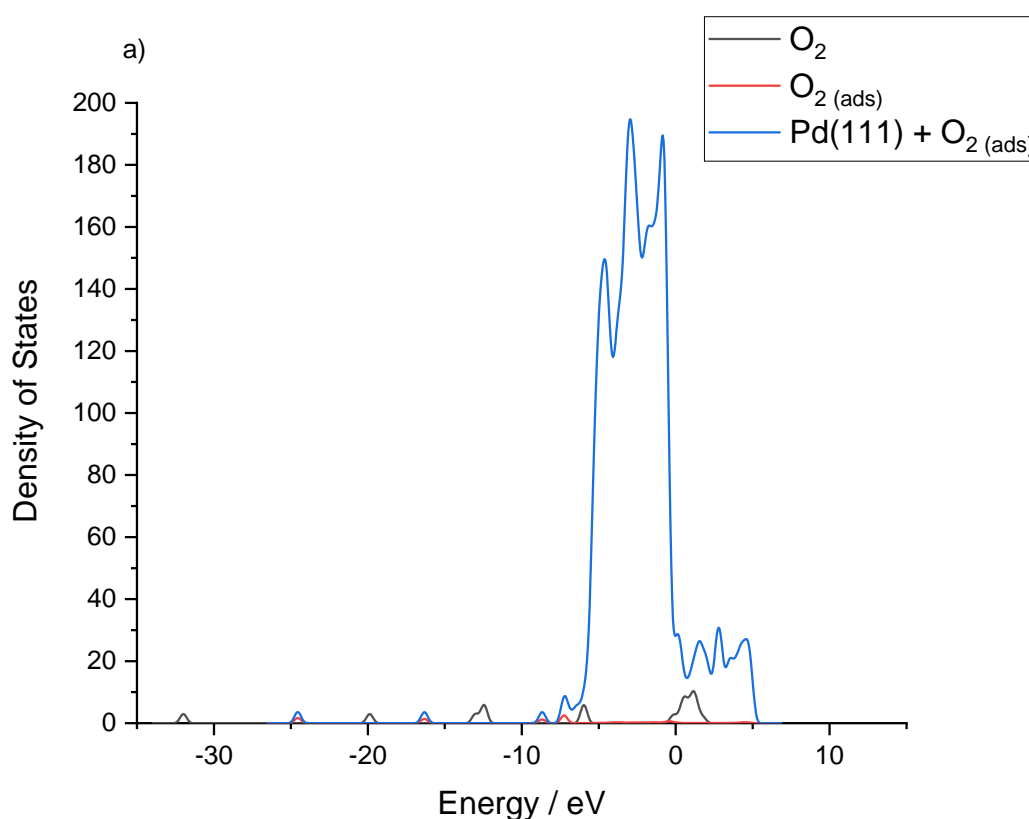


Figure 4.25. Normalised Densities of States for O_2 adsorbed to Pd(111), lone O_2 and the partial Densities of States of O_2 adsorbed to Pd(111), where **a)** shows all three Densities of States.

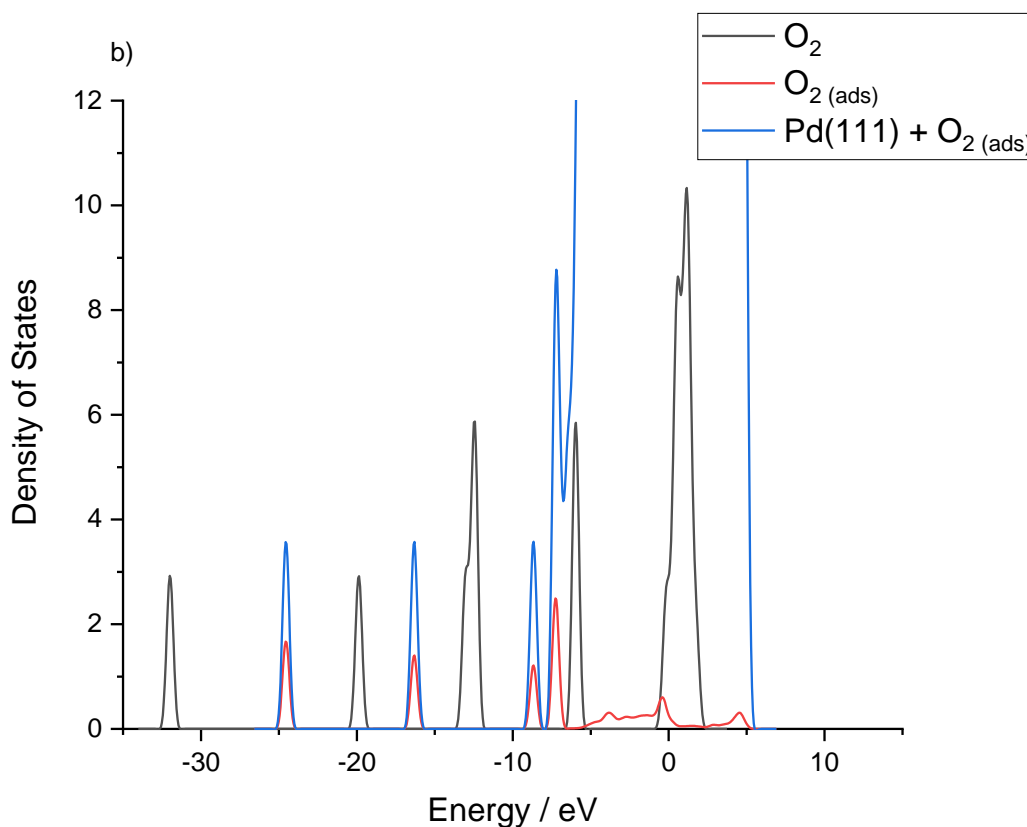


Figure 4.25. Normalised Densities of States for O_2 adsorbed to Pd(111), lone O_2 and the partial Densities of States of O_2 adsorbed to Pd(111), where **b)** shows a magnified view of the normalised Densities of States with a focus on the lone O_2 and partial Densities of States of O_2 adsorbed to Pd(111).

For the adsorption of atomic O, the Top site collapsed to a Hollow fcc site and has been consolidated into a single result in the data. Interestingly, the adsorption of atomic O was more energetically favourable than the adsorption of O_2 . Without D3 corrections applied, the Hollow fcc and hcp sites gave E_{ads} values of ~ -131 and ~ -115 kJ mol^{-1} , respectively, and with the D3 corrections applied, the E_{ads} values decreased to ~ -143 , ~ -126 and ~ -143 kJ mol^{-1} , respectively. Both sets of results were, at minimum, ~ 19 kJ mol^{-1} lower than their O_2 counterpart. This was most likely due to the propensity of Pd to form PdO rather than adsorb O_2 , however automatic dissociation did not occur (Table 4.17 and Fig. 4.24).

Furthermore, the adsorption of atomic O revealed that there was approximately the same amount of movement of the Pd atoms for the Hollow fcc site in Fig. 4.24i as there was for the Hollow fcc site for O_2 , with a Pd-Pd bond length range of $\sim 2.75 - \sim 2.92$ Å. Nevertheless, the decreased adsorption of atomic O for the Hollow hcp site in Fig. 4.24k resulted in a decreased range of Pd-Pd bond lengths,

with $\sim 2.76 - \sim 2.90$ Å. This was most likely due to the same reason stated before: hollow hcp sites are less favourable than hollow fcc sites because of the increased repulsion they exhibit. Both Hollow fcc and hcp for atomic O adsorption gave Pd-O bond lengths of ~ 2.00 Å (Table 4.17 and Fig. 4.24).

As it was observed that the hollow sites were the most favoured for both dissociated H_2 and $\frac{1}{2} O_2$ adsorption (in particular, the Hollow fcc sites), it was sensible to study the hollow sites only for dissociated O_2 adsorbed to Pd(111). Without the D3 corrections, the Hollow fcc-fcc, fcc-hcp and hcp-hcp sites gave E_{ads} values of ~ -236 , ~ -215 and ~ -203 kJ mol $^{-1}$, respectively. A decrease of ~ 24 , ~ 19 and ~ 22 kJ mol $^{-1}$ was observed as the D3 corrections were applied, respectively. This resulted in E_{ads} values at ~ -260 , ~ -235 and ~ -225 kJ mol $^{-1}$, respectively (Table 4.18 and Fig. 4.26).

Table 4.18. Adsorption energies for the different positions of dissociated O_2 adsorbed to Pd(111) without and with D3 corrections.

Site	Position	E_{ads}^{PBE} / kJ mol $^{-1}$	E_{ads}^{PBE+D3} / kJ mol $^{-1}$
	fcc-fcc	-236	-260
Hollow	fcc-hcp	-215	-235
	hcp-hcp	-203	-225

A trend was observed that demonstrated the stepped increase towards a less negative E_{ads} value as the O atoms moved to less favourable adsorption sites. The steps from Hollow fcc-fcc to fcc-hcp to hcp-hcp showed a change in energy by ~ 26 and ~ 10 kJ mol $^{-1}$, respectively. As previously discussed, the rationale for this was due to the nature of the fcc and hcp sites as the former was a less repulsive site than the latter because of the third layer atom in the hollow fcc site being further away than the second layer atom in the hollow hcp site (Table 4.18 and Fig. 4.26).

There was little change in the Pd-O bond lengths between the different adsorption sites. The Pd-O bond distances: for the Hollow fcc-fcc sites in Fig. 4.26b were ~ 1.98 , ~ 2.00 and ~ 2.01 Å; for the Hollow fcc-hcp sites in Fig. 4.26d, they were ~ 1.95 , ~ 1.96 and ~ 1.99 Å; and for the Hollow hcp-hcp sites in Fig. 4.26f, they were ~ 1.98 , ~ 1.99 and ~ 2.05 Å. The Pd-O bond lengths could not be linked to the trend observed for the E_{ads} values stated (Table 4.19 and Fig. 4.26).

Additionally, there was a significant change in the top layer Pd surface atoms for these sites. It was seen that the range of Pd-Pd bond lengths: for the Hollow fcc-fcc sites were ~ 2.73 to ~ 2.94 Å; for the Hollow fcc-hcp sites, they were ~ 2.79 to ~ 3.09 Å; and for the Hollow hcp-hcp sites, they were ~ 2.75 to ~ 2.98 Å. No trend could be found between the Pd-Pd bond lengths and the E_{ads} values (Table 4.18 and Fig. 4.26).

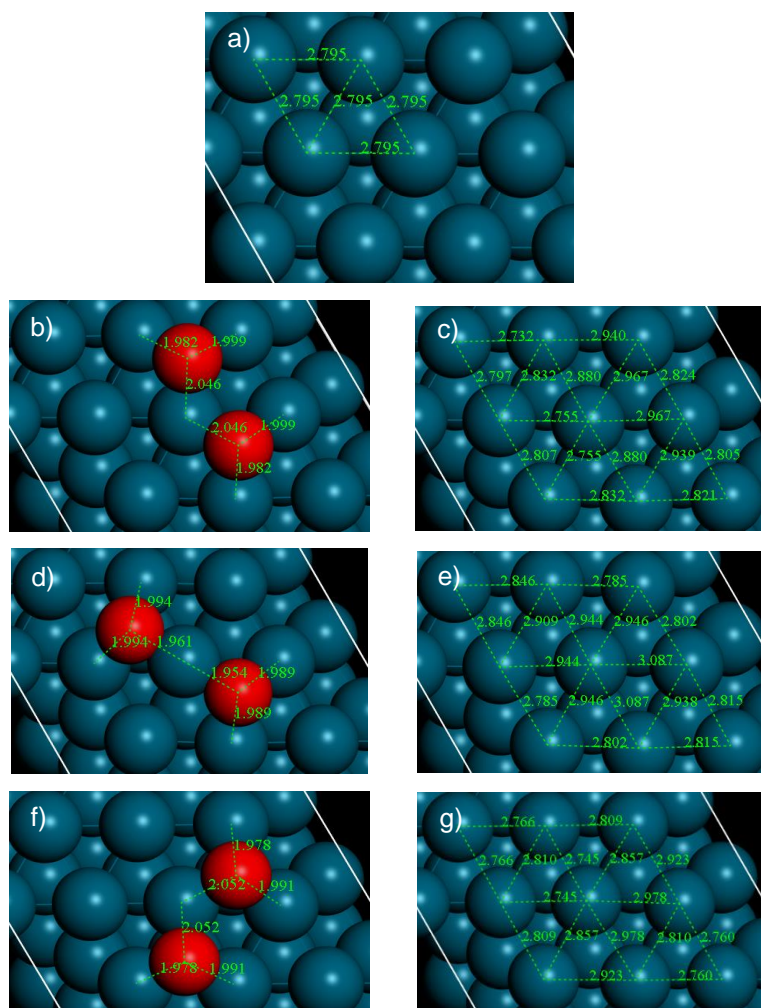


Figure 4.26. Images of the geometry optimisation calculations for dissociated O_2 adsorbed to Pd(111) calculated with D3 corrections and the adsorbate removed, where **a)** is the clean surface, **b)** is the Hollow fcc-fcc sites with the adsorbates, **c)** is the Hollow fcc-fcc sites without the adsorbates, **d)** is the Hollow fcc-hcp sites with the adsorbates, **e)** is the Hollow fcc-hcp sites without the adsorbates, **f)** is the Hollow hcp-hcp sites with the adsorbates, and **g)** is the Hollow hcp-hcp sites without the adsorbates. The dark blue atoms represent the Pd atoms, and the red atoms represent the O atoms. Interatomic distances in green are in Angstroms (Å).

To confirm that direct H_2O_2 synthesis could occur on the surface of Pd(111) and by what route it could be used for the epoxidation of propene, H_2O_2 adsorption

and dissociation on the surface was explored. The former was initially investigated, with a variety of different positions and sites for the molecule to adsorb. However, only four of the geometry optimisation calculations that were completed had returned that could be viably used (Table 4.19 and Fig. 4.27).

The results from the calculations without the D3 corrections applied demonstrated that H₂O₂ adsorption was favourable on Pd(111). As both Top sites collapsed to Top (O¹)-Bridge (H²) sites, these have been consolidated into one result in the data. The least favourable adsorption sites were the Triple DB and DB (OH) sites with an E_{ads} value of ~ -27 kJ mol⁻¹. The most favourable adsorption site was the Top (O¹)-Bridge (H²) site with an E_{ads} value of ~ -33 kJ mol⁻¹. This was a small difference of ~ 6 kJ mol⁻¹. When the D3 corrections were applied, the E_{ads} values decreased by ~ 30 kJ mol⁻¹ for each site and indicate that H₂O₂ weakly adsorbed to the Pd(111) surface as well as being relatively site-insensitive (Table 4.19 and Fig. 4.27).

Table 4.19. Adsorption energies for the different positions of H₂O₂ adsorbed to Pd(111) without and with D3 corrections.

Site	Position	E_{ads}^{PBE} / kJ mol ⁻¹	E_{ads}^{PBE+D3} / kJ mol ⁻¹
Triple DB	-	-27	-59
DB	(OH)	-27	-53
Top (O ¹)-Bridge (H ²)	-	-33	-63

Note: DB denotes di-bridge. The species involved in each position are stated in the parentheses.

The Triple DB site in Fig. 4.27b had the O¹-H¹, O¹-O² and O²-H² bonds of the H₂O₂ adsorbate bound to a pair of Pd atoms each. This site gave Pd-O interatomic distances of ~ 2.50 and ~ 2.64 Å and Pd-H interatomic distances of ~ 2.51 and ~ 2.55 Å. The DB (OH) site in Fig. 4.27d gave Pd-O and Pd-H interatomic distances of ~ 2.28 and ~ 2.69 Å, respectively. The reason for the increased E_{ads} value observed for the Triple DB site in comparison to the DB (OH) site was due to the increased number of atoms interacting with the Pd(111) surface. The former had four adsorbate atoms interacting with the surface, whereas the latter had only two of the adsorbate atoms interacting with the surface, irrespective of the decreased Pd-O bond. The

increased repulsion arose from the van der Waals forces as the change in E_{ads} value(s) was observed when the D3 corrections had been applied. The Top (O^1)-Bridge (H^2) site was the most favourable adsorption site for H_2O_2 , which was indicated by its shorter interatomic distances. The Pd-O interatomic distance was $\sim 2.31 \text{ \AA}$ and the Pd-H interatomic distances were ~ 2.43 and $\sim 2.83 \text{ \AA}$ (Table 4.19 and Fig. 4.27).

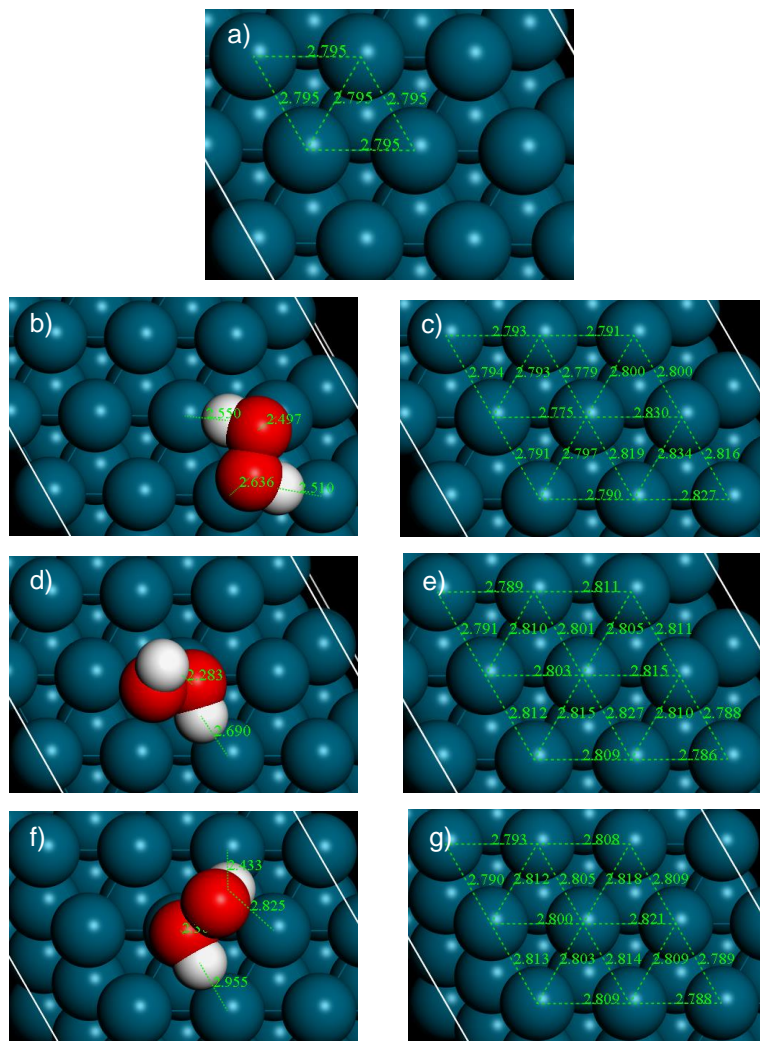


Figure 4.27. Images of the geometry optimisation calculations for H_2O_2 adsorbed to Pd(111) calculated with D3 corrections and the adsorbate removed, where **a)** is the clean surface, **b)** is the Triple DB site with the adsorbates, **c)** is the Triple DB site without the adsorbate, **d)** is the DB (OH) site with the adsorbate, **e)** is the DB (OH) site without the adsorbate, **f)** is the Top (O^1)-Bridge (H^2) site with the adsorbate and **g)** is the Top (O^1)-Bridge (H^2) site without the adsorbate. The dark blue atoms represent the Pd atoms, the red atoms represent the O atoms, and the white atoms represent the H atoms. Interatomic distances in green are in Angstroms (\AA). DB denotes di-bridge. The species involved in each position are stated in the parentheses.

The changes to the top layer Pd atoms were minimal as Pd-Pd bond lengths did not go beyond ± 0.04 Å from the norm (~ 2.80 Å) (Fig. 4.27a). The Triple DB and DB (OH) sites, in Fig. 4.27c and e, respectively, had Pd-Pd bond distance ranges of ~ 2.78 to ~ 2.83 Å, and ~ 2.79 to ~ 2.83 Å, respectively. The Top (O^1)-Bridge (H^2) site in Fig. 4.27g gave a Pd-Pd bond length range of ~ 2.79 to ~ 2.82 Å. The difference in Pd-Pd bond lengths between the different adsorption sites was negligible, which was a likely contributing factor to the lack of difference observed for the E_{ads} values for the adsorption sites (Table 4.19 and Fig. 4.27).

As previously discussed, there are two forms of H_2O_2 dissociation. The first to be investigated was the H-OOH bond dissociation. The H atom always optimised toward a hollow site and the OOH species always optimised toward a bridge-top site that arched over a hollow site (*i.e.*, the type indicated in parentheses). Without D3 corrections applied, the most negative E_{ads} value (~ -41 kJ mol $^{-1}$) was the Hollow fcc (H)-Bridge (O^1)-Top (O^2) (fcc) sites in Fig. 4.28d, and the Hollow fcc (H)-Bridge (O^1)-Top (H) (fcc) site in Fig. 4.28h was the least favourable site at ~ -25 kJ mol $^{-1}$ (Table 4.20 and Fig. 4.28).

As the D3 corrections were applied, the E_{ads} values for these sites decreased by approximately the same amount (~ 36 kJ mol $^{-1}$), and it was found that these species were moderately chemisorbed to the surface of Pd(111). Again, the trend showed that hollow fcc sites were the superior adsorption sites compared to the hollow hcp site for both the H and OOH species. The Bridge-Top sites for OOH were more favourable when the O atoms were adsorbing as opposed to Bridge (O^1)-Top (H) sites, as seen in Fig. 4.28h. This demonstrated that Pd had a greater affinity for O than H (Table 4.20).

Table 4.20. Adsorption energies for the different positions of dissociated H_2O_2 (H-OOH) adsorbed to Pd(111) without and with D3 corrections.

Site	E_{ads}^{PBE} / kJ mol $^{-1}$	E_{ads}^{PBE+D3} / kJ mol $^{-1}$
Hollow fcc (H)-Bridge (O^1)-Bridge (O^2) (hcp)	-27	-66
Hollow fcc (H)-Bridge (O^1)-Top (O^2) (fcc)	-41	-77
Hollow fcc (H)-Bridge (O^1)-Top (H) (fcc)	-25	-60
Hollow hcp (H)-Bridge (O^1)-Top (O^2) (fcc)	-37	-72

Note: The species involved in each position are stated in the parentheses.

The Pd-O bond lengths for the Hollow fcc (H)-Bridge (O¹)-Bridge (O²) (hcp) sites in Fig. 4.28b, Hollow fcc (H)-Bridge (O¹)-Top (O²) (fcc) sites in Fig. 4.28d, Hollow fcc (H)-Bridge (O¹)-Top (H) (fcc) sites in Fig. 4.28f and Hollow hcp (H)-Bridge (O¹)-Top (O²) (fcc) sites in Fig. 4.28h were: ~2.11 and ~2.13 Å; ~2.12, ~2.15 and ~2.24 Å; ~2.11 and ~2.13 Å; and ~2.11, ~2.16 and ~2.26 Å, respectively. It was observed that for the Bridged (O) sites, the Pd-O bond lengths were ~2.12 Å on average and the Top (O²) Pd-O bond lengths were longer at ~2.25 Å. This increase between the different sites' Pd-O bond lengths could be attributed to the fact that the O¹ was bound to two Pd atoms as opposed to one, which was a consequence of the O² having part of its electron density dedicated to the bond with the H², hence, the difference in affinity between the O atoms (Table 4.20 and Fig. 4.28).

The Pd-H bond lengths for the Hollow fcc (H)-Bridge (O¹)-Bridge (O²) (hcp) sites in Fig. 4.28b, Hollow fcc (H)-Bridge (O¹)-Top (O²) (fcc) sites in Fig. 4.28d, Hollow fcc (H)-Bridge (O¹)-Top (H) (fcc) sites in Fig. 4.28f and Hollow hcp (H)-Bridge (O¹)-Top (O²) (fcc) sites in Fig. 4.28h were: ~1.80, ~1.81 and ~1.82 Å; ~1.81 Å; ~1.81 and ~2.34 Å; and ~1.81 Å, respectively. As previously discussed, the Hollow fcc (H)-Bridge (O¹)-Top (H) (fcc) sites were the least favourable because the H atom was in a hollow hcp site and the OOH was bound by one of the H atoms and O¹ as opposed to both O atoms. At ~2.34 Å, this seemed to be a weak intermolecular force rather than a strict Pd-H bond (Table 4.20 and Fig. 4.28).

The variation of the Pd-Pd bond lengths for the four sites was relatively small. The ranges of the bond lengths for the Hollow fcc (H)-Bridge (O¹)-Bridge (O²) (hcp) sites in Fig. 4.28c, Hollow fcc (H)-Bridge (O¹)-Top (O²) (fcc) sites in Fig. 4.28e, Hollow fcc (H)-Bridge (O¹)-Top (H) (fcc) sites in Fig. 4.28g and Hollow hcp (H)-Bridge (O¹)-Top (O²) (fcc) sites in Fig. 4.28i were: ~-0.03 – ~+0.12 Å; ~-0.03 – ~+0.18 Å; ~-0.04 – ~+0.14 Å; and ~-0.05 – ~+0.10 Å, respectively. Again, a trend cannot be definitively confirmed based on the Pd-Pd bond lengths, however, an observation regarding the most negative E_{ads} value and the greatest Pd-Pd bond length change can be made as the Hollow fcc (H)-Bridge (O¹)-Top (O²) (fcc) sites in Fig. 4.28e gave an E_{ads} value ~-77 kJ mol⁻¹ and a range of ~0.21 Å in Pd-Pd bond length (Table 4.20 and Fig. 4.28).

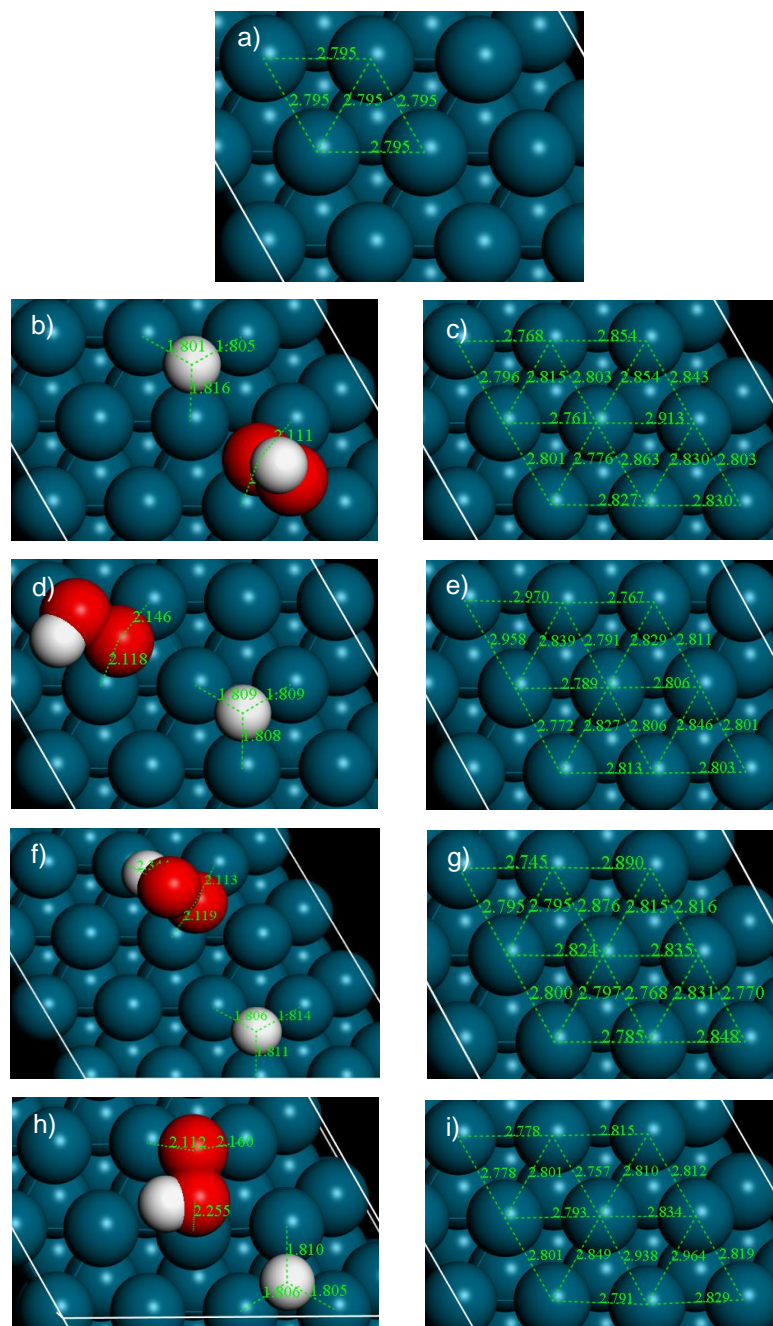


Figure 4.28. Images of the geometry optimisation calculations for dissociated H_2O_2 (H-OOH) adsorbed to Pd(111) calculated with D3 corrections and the adsorbate removed, where **a**) is the clean surface, **b**) is the Hollow fcc (H)-Bridge (O^1)-Bridge (O^2) (hcp) sites with the adsorbates, **c**) is the Hollow fcc (H)-Bridge (O^1)-Bridge (O^2) (hcp) sites without the adsorbates, **d**) is the Hollow fcc (H)-Bridge (O^1)-Top (O^2) (fcc) sites with the adsorbates, **e**) is the Hollow fcc (H)-Bridge (O^1)-Top (O^2) (fcc) sites without the adsorbates, **f**) is the Hollow fcc (H)-Bridge (O^1)-Top (H) (fcc) sites with the adsorbates, **g**) is the Hollow fcc (H)-Bridge (O^1)-Top (H) (fcc) sites without the adsorbates, **h**) is the Hollow hcp (H)-Bridge (O^1)-Top (O^2) (fcc) sites with the adsorbates, and **i**) is the Hollow hcp (H)-Bridge (O^1)-Top (O^2) (fcc) sites without the adsorbates. The dark blue atoms represent the Pd atoms, the red atoms represent the O atoms, and the white atoms represent the H atoms. Interatomic distances in green are in Angstroms (\AA). The species involved in each position are stated in the parentheses.

The other type of dissociation for H₂O₂ at the HO-OH bond was also studied. Although a variety of sites and orientations of the OH groups were researched, only three of them completed their geometry optimisation calculations. Although all these sites were within ~8 kJ mol⁻¹ without the D3 corrections applied, with the most negative E_{ads} value was found at the Bridge-Bridge (2) sites (~-233 kJ mol⁻¹) (Table 4.21 and Fig. 4.29).

Table 4.21. Adsorption energies for the different positions of dissociated H₂O₂ (HO-OH) adsorbed to Pd(111) without and with D3 corrections.

Site	E_{ads}^{PBE} / kJ mol ⁻¹	E_{ads}^{PBE+D3} / kJ mol ⁻¹	O-H Bond Distance / Å
Bridge-Bridge (1)	-225	-260	-
Bridge-Bridge (2)	-233	-269	1.94
Bridge-Top	-227	-263	1.58

With the D3 corrections applied, the E_{ads} value for the Bridge-Bridge (1), Bridge-Bridge (2) and the Bridge-Top sites decreased by approximately the same amount (~36 kJ mol⁻¹), resulting in E_{ads} values of ~-260, ~-269 and ~-263 kJ mol⁻¹, respectively. This suggested that the OH groups were bound tightly to the Pd(111) surface. Although thermodynamically stable (and more stable than the H-OOH adsorption sites), these OH adsorption sites would require a large amount of energy to release the OH groups, which could be problematic for catalytic processes on this surface (Table 4.21 and Fig. 4.29).

The Pd-O bond lengths for the Bridge-Bridge (1) sites in Fig. 4.29b, the Bridge-Bridge (2) sites in Fig. 4.29d and the Bridge-Top sites in Fig. 4.29f were: ~2.12 and ~2.13 Å; ~2.11, ~2.12, ~2.16 and ~2.17 Å; and ~2.09 and ~2.04 Å, respectively. No apparent trend was observed between the E_{ads} values and the Pd-O bond lengths for the different adsorption sites. However, the differences between these sites (and their E_{ads} values) were revealed by the O-H bonding. There was no O-H bonding for the Bridge-Bridge (1) sites, which explained its less negative E_{ads} value. The Bridge-Bridge (2) and Bridge-Top sites had O-H bonding, with O-H bond distances of ~1.94 and ~1.58 Å, respectively. The difference in E_{ads} values for these two sites could be explained by the fact that the O-H bond was longer for the Bridge-Bridge (2)

sites, with decreased repulsion between the OH groups, which in turn, was more favourable (Table 4.21 and Fig. 4.29).

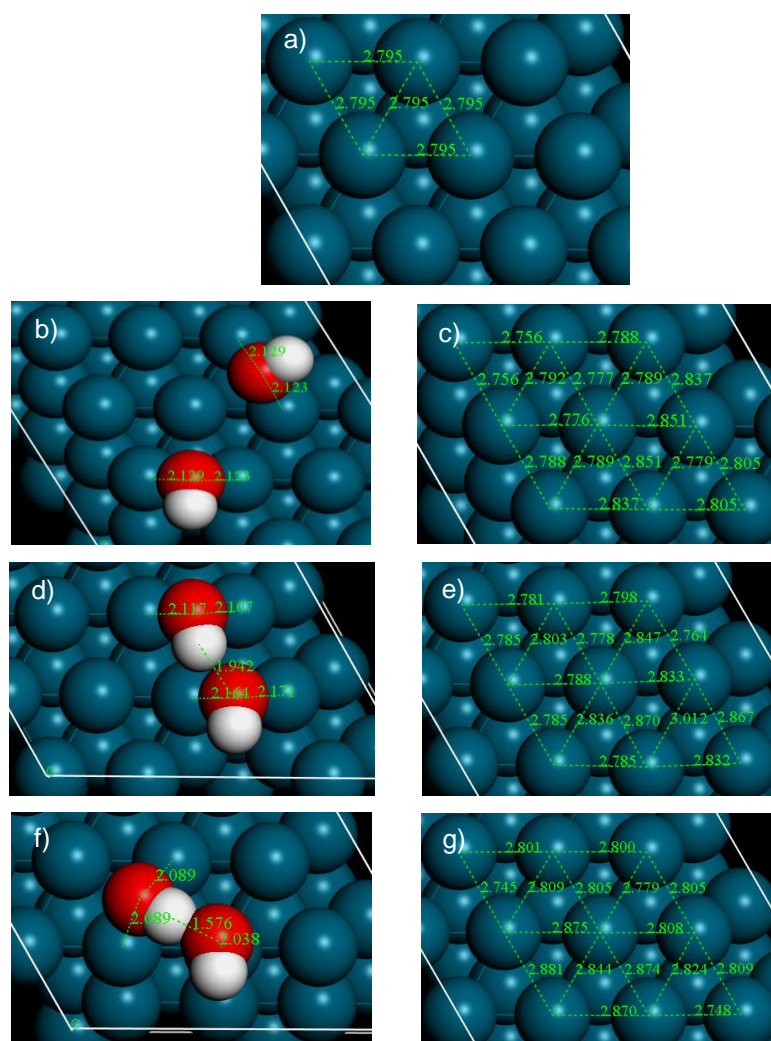


Figure 4.29. Images of the geometry optimisation calculations for dissociated H_2O_2 (HO-OH) adsorbed to Pd(111) calculated with D3 corrections and the adsorbate removed, where **a**) is the clean surface, **b**) is the Bridge-Bridge (1) sites with the adsorbates, **c**) is the Bridge-Bridge (1) sites without the adsorbates, **d**) is the Bridge-Bridge (2) sites with the adsorbates, **e**) is the Bridge-Bridge (2) sites without the adsorbates, **f**) is the Bridge-Top sites with the adsorbates, and **g**) is the Bridge-Top sites without the adsorbates. The dark blue atoms represent the Pd atoms, the red atoms represent the O atoms, and the white atoms represent the H atoms. Interatomic distances in green are in Angstroms (\AA). The species involved in each position are stated in the parentheses.

The Pd-Pd bond length ranges for the Bridge-Bridge (1) sites in Fig. 4.29c, Bridge-Bridge (2) in Fig. 4.29e and Bridge-Top sites in Fig. 4.29g were as follows: $\sim 2.76 - \sim 2.85 \text{ \AA}$; $\sim 2.76 - \sim 3.01 \text{ \AA}$; and $\sim 2.75 - \sim 2.88 \text{ \AA}$, respectively. The most significant Pd-Pd bond length change was exhibited by the Pd(111) surface for the Bridge-Bridge (2) sites ($\sim 3.01 \text{ \AA}$). This was due to the OH groups and their Bridge

sites being so close together, and to reach their energy minima, these Pd-Pd bond needed to increase in length (Table 4.21 and Fig. 4.29).

The current work supported the research conducted by Todorovic *et al.* and showed that the formation of OH groups over Pd(111) was part of the lowest energy pathway for the direct synthesis of H₂O₂. Todorovic *et al.* observed a value of ~270 kJ mol⁻¹ (~2.80 eV), which was within ~7 kJ mol⁻¹ of the current work. In addition, the E_a of H₂O₂ dissociation to two OH groups was ~4 kJ mol⁻¹ (0.04 eV), which for the current work would mean that this dissociation would be feasible and favourable (Table 4.21 and Fig. 4.29).⁷

Propene and PO adsorption was investigated to determine if the target molecules could adsorb, and which orientation(s) of the molecules were the most favourable. Adsorption sites for these molecules were in reference to the C¹=C² bond and O atom, respectively. Multiple variations of propene adsorption sites and positions were investigated, however, only four geometry optimisation calculations completed. Of those four sites, three optimised to the same site with the same E_{ads} values and have been consolidated as one result in the data. Without the D3 corrections applied, the DB and Top Up sites with E_{ads} values of ~-76 kJ mol⁻¹ and ~-67 kJ mol⁻¹, respectively (Table 4.22 and Fig. 4.30).

With the D3 corrections applied, the E_{ads} values decreased by approximately the same amount (~58 kJ mol⁻¹), resulting in strong chemisorption (~-134 and ~-125 kJ mol⁻¹, respectively), with a degree of site insensitivity. The reason for the slight difference in adsorption energy was likely due to the difference of interacting Pd atoms with the C¹=C² bond. With the DB site, a greater amount of electron density was available to be shared as there were two Pd atoms as opposed to the Top Up site's single Pd atom (Table 4.22 and Fig. 4.30).

Table 4.22. Adsorption energies for the different positions of propene and PO adsorbed to Pd(111) without and with D3 corrections.

Adsorbate	Site	Position	E_{ads}^{PBE} / kJ mol ⁻¹	E_{ads}^{PBE+D3} / kJ mol ⁻¹
Propene	DB	-	-76	-134
	Top	Up	-67	-125
PO	Top	-	-27	-79

Note: DB denotes di-bridge, and Up is the methyl group pointed up and away from the surface.

Both adsorption sites in Fig. 4.30b and d had the CH₃ groups pointed away from the surface. As previously observed by Roldan *et al.*,¹⁸ the preferred position of the propene molecule was to have the CH₃ group pointed away from the surface, not into it, because the repulsion between the CH₃ group and surface were reduced in this orientation. However, the work of Roldan *et al.* was conducted on Au(111) and not Pd(111), but the rationale was the same (Table 4.22 and Fig. 4.30).

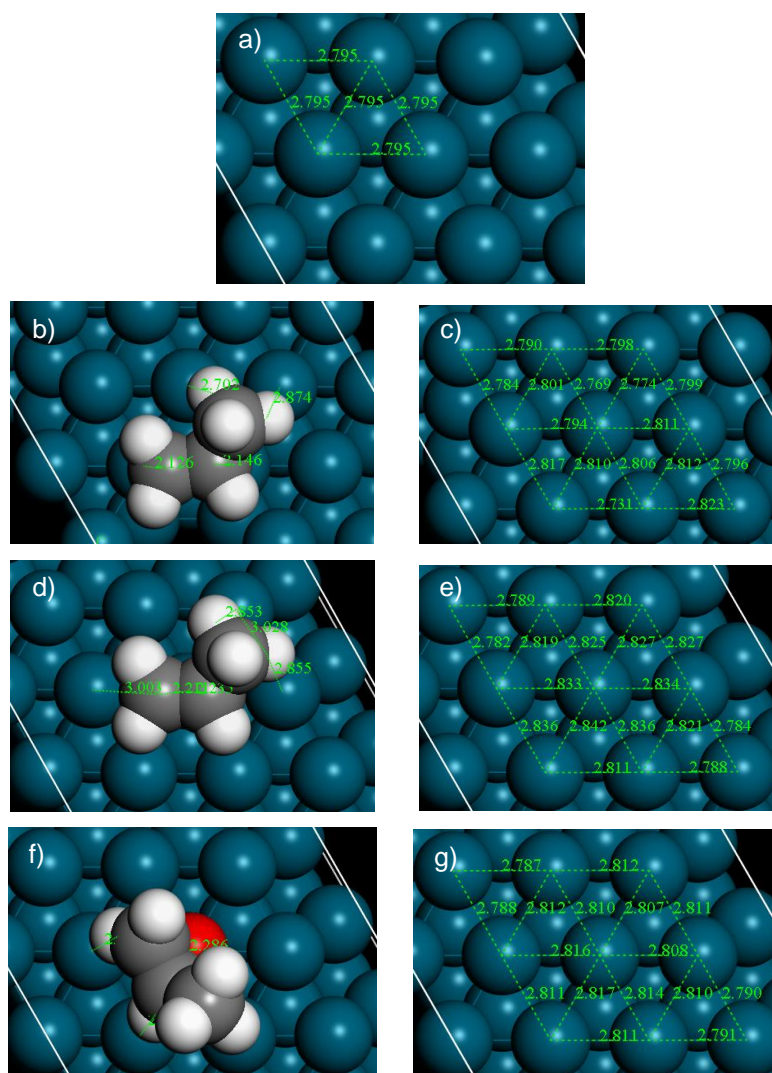


Figure 4.30. Images of the geometry optimisation calculations for propene and PO adsorbed to Pd(111) calculated with D3 corrections and the adsorbate removed, where **a)** is the clean surface, **b)** is the propene DB site with the adsorbate, **c)** is the propene DB site without the adsorbate, **d)** is the propene Top Up site with the adsorbate, **e)** is the propene Top Up site without the adsorbate, **f)** is the PO Top site with the adsorbate and **g)** is the PO Top site without the adsorbate. The dark blue atoms represent the Pd atoms, the grey atoms represent the C atoms, the red atoms represent the O atoms, and the white atoms represent the H atoms. Interatomic distances in green are in Angstroms (Å). DB denotes di-bridge, and Up is the methyl group pointed up and away from the surface.

The Pd-C interatomic distances for the DB site in Fig. 4.30b and the Top Up site in Fig. 4.30d following the order of Pd-C¹ and Pd-C² were: ~2.13 and ~2.15 Å; and ~2.21 and ~2.24 Å, respectively. The rationale for the difference in the E_{ads} values between the two sites was due to the increased Pd-C interatomic distances exhibited by the Top Up site, which in turn, was due to the C¹ and C² atoms competing for the same electron density of one Pd atom. The DB site had one Pd atom interacting with each C atom. Minor changes were observed for the top layer of Pd atoms. The Pd-Pd bond length ranges for the DB and Top Up sites, compared to the clean surface were as follows: ~-0.06 – ~+0.03 Å; and ~-0.01 – ~+0.05 Å, respectively. These minor deformations of the surfaces were unlikely to contribute significantly to the E_{ads} values for these sites (Table 4.22 and Fig. 4.30).

In Fig. 4.31, the DoS of the DB site demonstrated that there was significant interaction observed between the Pd(111) surface and propene. This interaction resulted in the anti-bonding orbital(s) of the propene molecule above the Fermi level being reduced to nothing as the densities spread out. (Table 4.22, and Fig. 4.30 and 4.31).

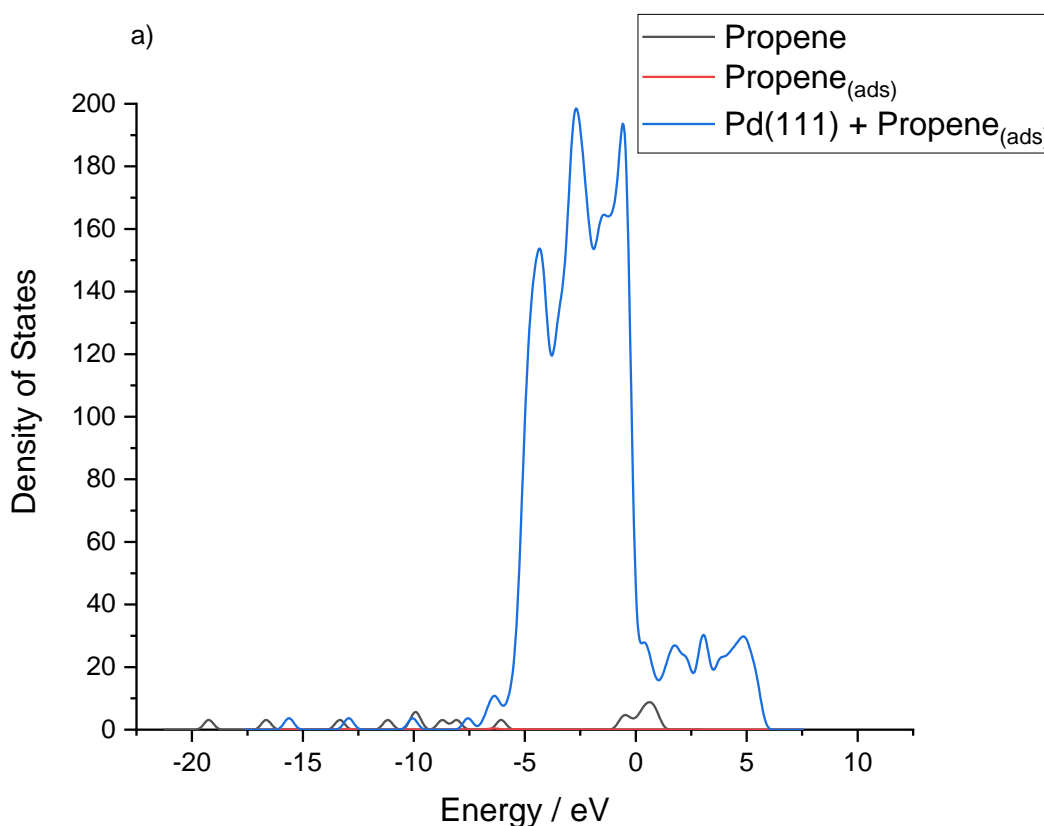


Figure 4.31. Normalised Densities of States for propene adsorbed to Pd(111), lone propene and the partial Densities of States of propene adsorbed to Pd(111), where **a)** shows all three Densities of States.

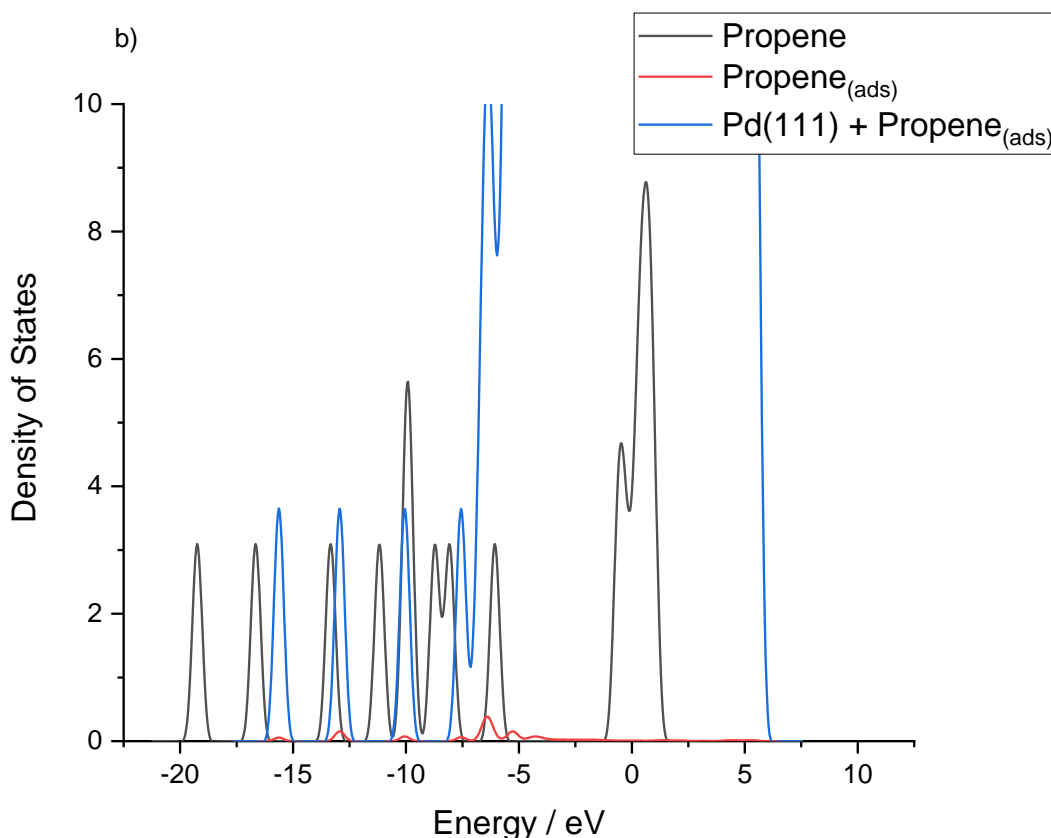


Figure 4.31. Normalised Densities of States for propene adsorbed to Pd(111), lone propene and the partial Densities of States of propene adsorbed to Pd(111), where **b)** shows a magnified view of the normalised Densities of States with a focus on the lone propene and partial Densities of States of propene adsorbed to Pd(111).

The bonding orbitals had been reduced and shifted towards the Fermi level by $\sim +1$ eV. Overlap of the sp^2 -orbital peaks of the adsorbed propene overlapped with peaks of the adsorbate-surface complex at ~ -16 , ~ -10 , ~ -8 , and ~ -6 eV. This suggested that the bonding orbitals of the adsorbate surface overlapped, supported by the negative E_{ads} value (~ -134 kJ mol $^{-1}$). There was significant bond lengthening of the adsorbate as the $C^1=C^2$ bond length increased from ~ 1.34 Å to ~ 1.45 Å, but the bond did not break as a total of eight electrons would be required to completely fill the anti-bonding orbitals of the $C^1=C^2$ bond. The electron densities of both the surface and double bond shifted towards each other. Thus, the strong chemisorption at ~ -134 kJ mol $^{-1}$ was established (Table 4.22, and Fig. 4.30 and 4.31).

Although propene was bound tightly to the surface of the Pd(111), this may not have a detrimental effect on the catalytic reaction upon the surface. This was because the propene was the target molecule to adsorb, and not to desorb. One step of the overall reaction mechanism for propene epoxidation to consider was the adsorption of PO (Table 4.22 and Fig. 4.30).

While a variety of different sites and orientations of the PO were considered, most calculations failed to complete, with only one calculation completing. The Top site gave an E_{ads} value of $\sim -27 \text{ kJ mol}^{-1}$ without the D3 corrections applied, and with the D3 corrections applied, the E_{ads} value decreased by $\sim 53 \text{ kJ mol}^{-1}$ to a value of $\sim -79 \text{ kJ mol}^{-1}$. This highly negative E_{ads} value indicated that the binding between the surface and the adsorbate was tight and within the region of chemisorption ($\geq 40 \text{ kJ mol}^{-1}$). Although the thermodynamics suggested that the binding was strong, this did not provide any information regarding the E_{a} . If the E_{a} barrier was low, this surface could still be a viable candidate for catalysis as the release of PO from the surface would be facile. This adsorption site in Fig. 4.30f gave Pd-H interatomic distances of ~ 2.65 and $\sim 2.75 \text{ \AA}$ and a Pd-O interatomic distance of $\sim 2.29 \text{ \AA}$. In Fig. 4.30g, the Pd-Pd movements of the top layer of the surface were minor, with minimal effect on the E_{ads} value (Table 4.22 and Fig. 4.30).

Overall, Pd(111) was proved to be a viable candidate for the catalytic processes involved in both the direct synthesis of H_2O_2 and the epoxidation of propene as it adsorbed the target species. It also provided an insight into how the intermediate chemical species were likely to move and react. For example, H_2 and O_2 both adsorbed to the surface in an Eley-Rideal (ER) mechanism and would most likely go on to react to form two OH groups. However, the E_{a} barriers for these catalytic reactions were not determined, thus, reaction pathways had not been produced. Further research was required.

4.2.2.2. Palladium(100)

The last surface that was investigated in the current work was Pd(100). As the second most stable surface of Pd, the E_{ads} values of the target molecules would likely be different to that of the Pd(111) surface. In addition, this surface may have possibly provided lower E_{a} values, and therefore, better reaction pathways from a catalytic perspective.

Adsorption of H_2 was explored first. Two geometry optimisation calculations completed both without and with D3 corrections. The Sloped DB and Top Horizontal sites gave E_{ads} values of $\sim -21 \text{ kJ mol}^{-1}$ without the corrections applied. With the D3 corrections applied, the E_{ads} decreased by approximately the same amount for the Sloped DB and Top Horizontal sites ($\sim 16 \text{ kJ mol}^{-1}$). This resulted in the E_{ads} values for both sites becoming $\sim -37 \text{ kJ mol}^{-1}$. These E_{ads} values were in the region between

chemisorption ($\geq 40 \text{ kJ mol}^{-1}$) and the Kubas interaction ($\sim 30 \text{ kJ mol}^{-1}$) (Table 4.23 and Fig. 4.32).

Table 4.23. Adsorption energies for the different positions of H_2 adsorbed to Pd(100) without and with D3 corrections.

Site	Position	$E_{ads}^{PBE} / \text{kJ mol}^{-1}$	$E_{ads}^{PBE+D3} / \text{kJ mol}^{-1}$
Sloped DB	-	-21	-37
Top	Horizontal	-21	-37

Note: DB denotes di-bridge.

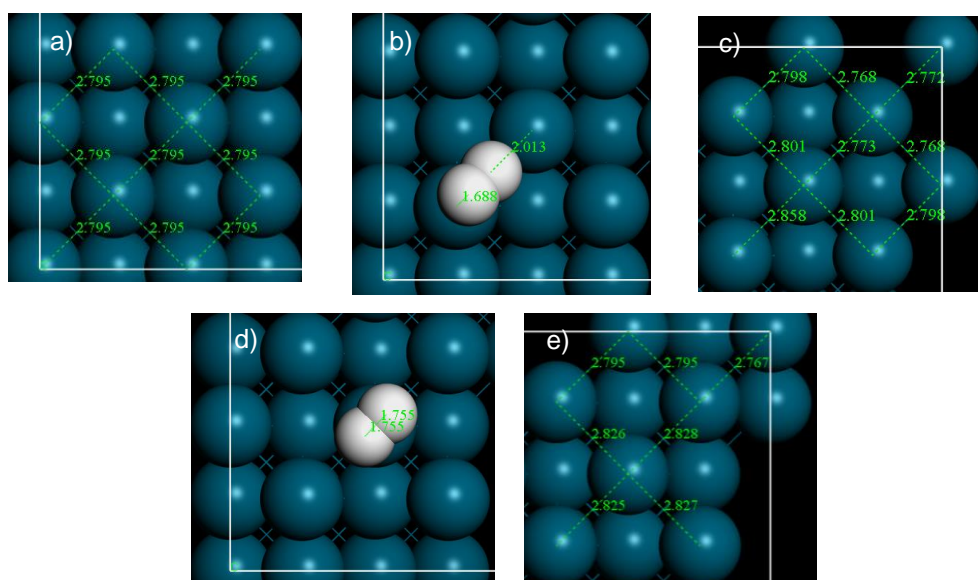


Figure 4.32. Images of the geometry optimisation calculations for H_2 adsorbed to Pd(100) calculated with D3 corrections and the adsorbate removed, where **a)** is the clean surface, **b)** is the Sloped DB site with the adsorbate, **c)** is the Sloped DB site without the adsorbate, **d)** is the Top Horizontal site with the adsorbate, and **e)** is the Top Horizontal site without the adsorbate. The dark blue atoms represent the Pd atoms, and the white atoms represent the H atoms. Interatomic distances in green are in Angstroms (\AA). DB denotes di-bridge.

The sloped DB site in Fig. 4.32b had a Pd-H^1 interatomic distance of $\sim 2.01 \text{ \AA}$ and the Pd-H^2 interatomic distance was $\sim 1.69 \text{ \AA}$. The latter interatomic distance was extremely short for a Pd-H bond and was akin to a lone H atom. Additionally, the electron density from the H_2 molecule was being shared by two Pd atoms. This was unlike the Top Horizontal site in Fig. 4.32d that had only one Pd atom to adsorb the H_2 molecule (Pd-H interatomic distances: $\sim 1.76 \text{ \AA}$), and therefore, slightly less of the electron density was shared with the Pd atom, leading to a longer bond. Even with

the minor Pd-Pd movements for both sites in Fig. 4.32c and e (maximum Pd-Pd bond change $\sim +0.06$ Å), coupled with the differences in Pd-H interatomic distances, these variations had little effect on the E_{ads} values. Thus, H₂ adsorption on Pd(100) was site insensitive. It was important to note that automatic H₂ dissociation did not occur, unlike on Pd(111) (Table 4.23 and Fig. 4.32).

In Fig. 4.33, the DoS of the Sloped DB site demonstrated that there was considerable interaction between the Pd(100) surface and the H₂. This interaction resulted in the anti-bonding orbital of the H₂ above the Fermi level being reduced. The bonding orbital DoS also decreased and shifted $\sim +1$ eV toward the Fermi level. Overlap of the *s*-orbital of the H₂ and the *d*-orbital of the Pd was suggested by the peak overlap observed at ~ -9 eV, supported by the negative E_{ads} value (~ -37 kJ mol⁻¹). There was significant bond lengthening of the adsorbate, with an increase from ~ 0.75 Å to ~ 0.86 Å, due to the shift in electron density of the H₂ and the surface upon adsorption (Table 4.23, and Fig. 4.32 and 4.33).

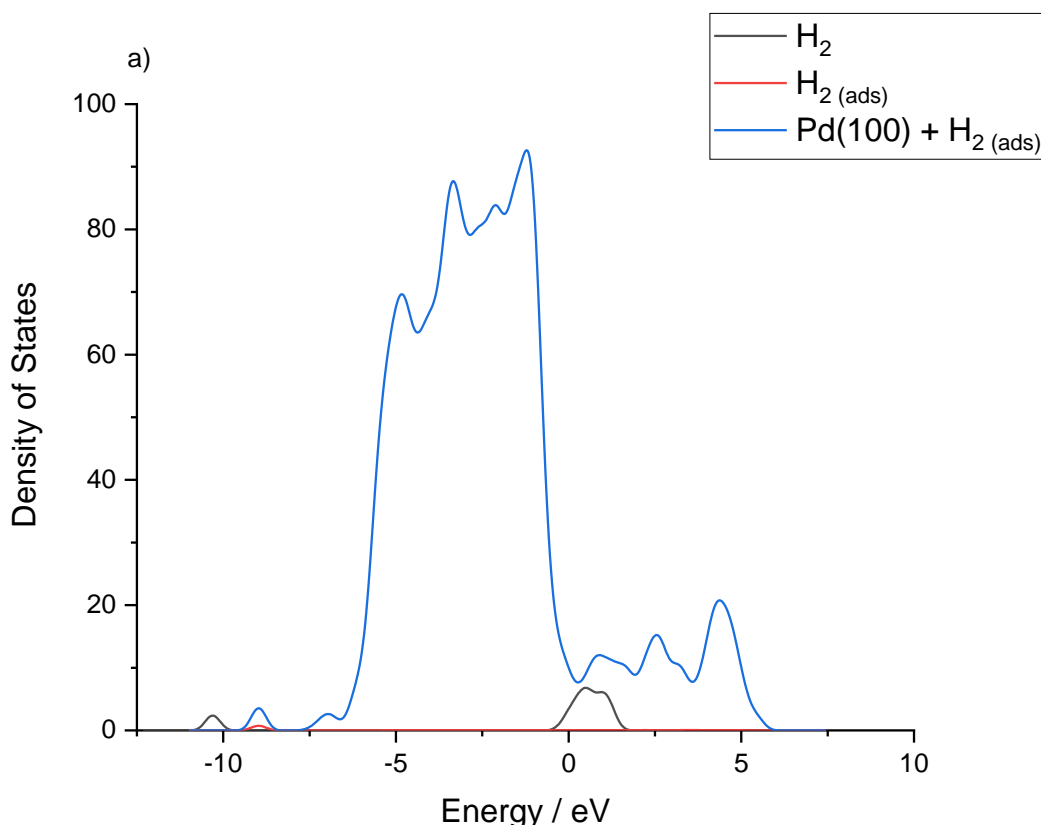


Figure 4.33. Normalised Densities of States for H₂ adsorbed to Pd(100), lone H₂ and the partial Densities of States of H₂ adsorbed to Pd(100), where **a)** shows all three Densities of States.

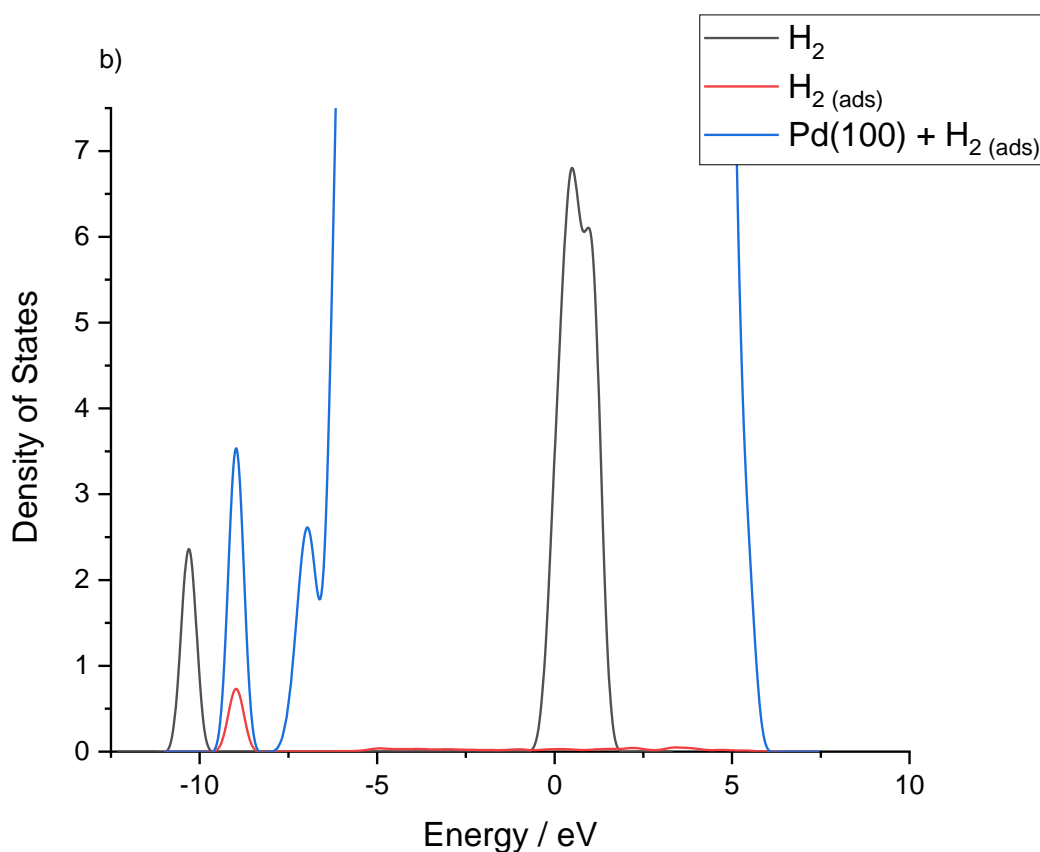


Figure 4.33. Normalised Densities of States for H_2 adsorbed to Pd(100), lone H_2 and the partial Densities of States of H_2 adsorbed to Pd(100), where **b)** shows a magnified view of the normalised Densities of States with a focus on the lone H_2 and partial Densities of States of H_2 adsorbed to Pd(100).

The binding energy for the different adsorption sites of the dissociated H_2 molecule were determined through the geometry optimisation calculations. As three of these calculations resulted in the same adsorption site, they have been consolidated into a single result in the data. It was seen that the H atoms that were originally positioned on Top sites all fell into Hollow sites. The rationale for this occurrence was due to the adsorbate atoms moving into their most thermodynamically stable sites and positions. This has also been supported by the works of Ford *et al.* and Todorovic *et al.*^{5,7} It could be possible that the bridging adsorption sites in Fig. 4.34f were sites preceding the H atoms falling into the hollow sites, but further investigation would be required (Table 4.24 and Fig. 4.34).

The Hollow Diagonal, Hollow Straight, and Bridge-Bridge sites gave E_{ads} values of ~ -79 , ~ -80 , and ~ -74 kJ mol^{-1} , respectively, without the D3 corrections applied. When the D3 corrections were applied, the E_{ads} values decreased by approximately the same amount (~ 15 kJ mol^{-1}). This led to the following E_{ads} values: ~ -94 , ~ -95 , and ~ -91 kJ mol^{-1} , respectively. Again, the minor difference in E_{ads} values

demonstrated that the chemisorption of H₂ or H atoms was site insensitive (Table 4.24 and Fig. 4.34).

Table 4.24. Adsorption energies for the different positions of dissociated H₂ adsorbed to Pd(100) without and with D3 corrections.

Site	Position	E_{ads}^{PBE} / kJ mol ⁻¹	E_{ads}^{PBE+D3} / kJ mol ⁻¹
Hollow	Diagonal	-79	-94
	Straight	-80	-95
Bridge-Bridge	-	-74	-91

Note: Diagonal denotes the position of the adsorbate perpendicular to the direction of the rows of top layer metal atoms, and Straight is the position of the adsorbate parallel to the rows of the top layer metal atoms.

For all adsorption sites in Fig. 4.34 c, e and g, the top layer Pd atoms moved minimally from the norm of the clean surface in Fig. 4.34a. The Hollow Straight sites in Fig. 4.34d showed that Pd-H bond lengths were ~1.98 and ~1.99 Å. The Hollow Diagonal and Bridge-Bridge sites had Pd-H bond lengths of ~1.87 and ~2.12 Å, and ~1.71 Å, respectively. For the adsorption of dissociated H₂, the Pd-H bond lengths had a small effect on the E_{ads} values of the sites. This was because the site with the shortest bond length gave the weakest E_{ads} value (Table 4.24 and Fig. 4.34).

The only reason for the small difference between the Hollow Diagonal and Straight sites with regards to their E_{ads} values could be that there was a slight increase in repulsion from the H atoms, causing the shorter and longer Pd-H bond lengths exhibited by the Hollow Diagonal sites compared to the Hollow Straight sites. This in turn made the E_{ads} value slightly less negative, but this was negligible, and all three types of sites had approximately the same E_{ads} value (Table 4.24 and Fig. 4.34).

The Pd-Pd bonds moved minimally for the three sites (no greater than ± 0.03 Å), which was unexpected considering the level of chemisorption. However, because of the lack of movement of the top layer Pd atoms, the E_{ads} value could be highly negative as the E_{def} value would likely be small (Table 4.24 and Fig. 4.34).

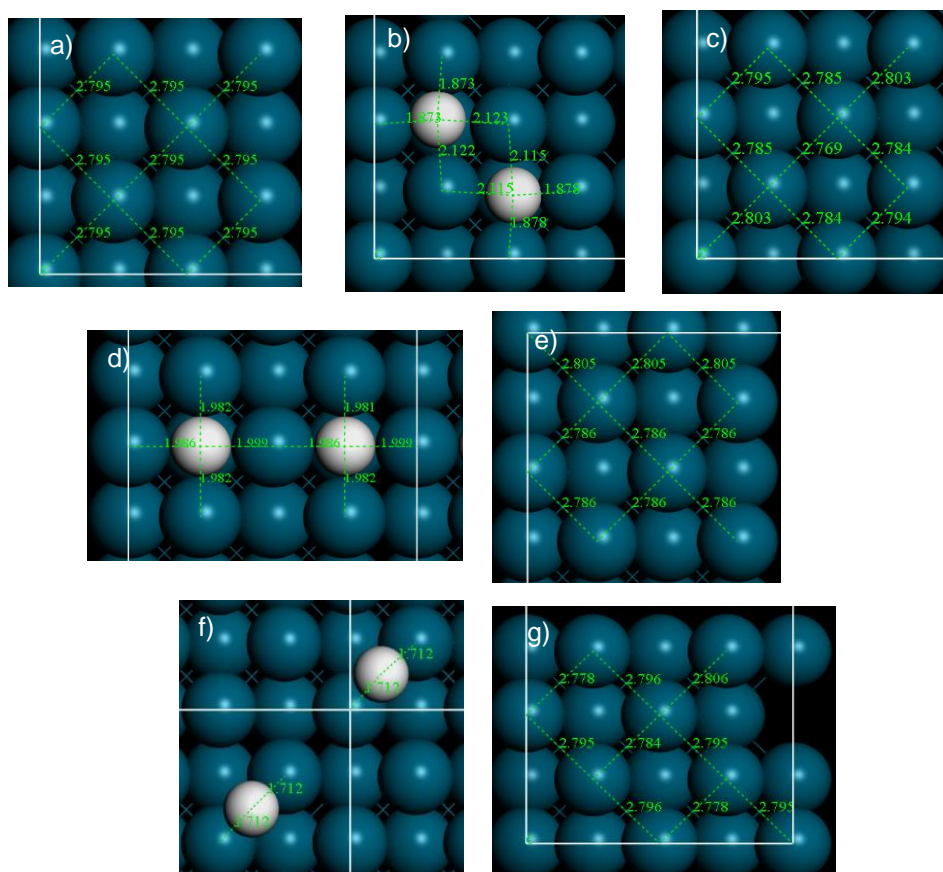


Figure 4.34. Images of the geometry optimisation calculations for dissociated H_2 adsorbed to Pd(100) calculated with D3 corrections and the adsorbate removed, where **a)** is the clean surface, **b)** is the Hollow Diagonal sites with the adsorbates, **c)** is the Hollow Diagonal sites without the adsorbates, **d)** is the Hollow Straight sites with the adsorbates, **e)** is the Hollow Straight sites without the adsorbates, **f)** is the Bridge-Bridge sites with the adsorbates and **g)** is the Bridge-Bridge sites without the adsorbates. The dark blue atoms represent the Pd atoms, and the white atoms represent the H atoms. Interatomic distances in green are in Angstroms (\AA). Diagonal denotes the position of the adsorbate perpendicular to the direction of the rows of top layer metal atoms, and Straight is the position of the adsorbate parallel to the rows of the top layer metal atoms.

As the results for Pd(100) showed that the adsorption of H_2 and dissociated H_2 readily occurred, the adsorption of O_2 on this surface also needed to be investigated as it is a key step in direct H_2O_2 synthesis. Only certain calculations for O_2 and atomic O adsorption to Pd(100) completed due to failure of the calculations. The O atom for the Top site fell into the Hollow site, and as such, they have been consolidated into one result in the data (Table 4.25 and Fig. 4.35).

Without the D3 corrections, the E_{ads} values for the DB, QB and Hollow ($\frac{1}{2} O_2$) sites were ~ -75 , ~ -120 and ~ -95 kJ mol^{-1} , respectively. With the D3 corrections applied, the calculations decreased the E_{ads} values by ~ 25 , ~ 25 and ~ 13 kJ mol^{-1} , respectively, to ~ -100 , ~ -145 , and ~ -108 kJ mol^{-1} , respectively. Although both adsorption sites for the O_2 molecule were strong, and could be considered

chemisorbed, the reason for the significant difference between the DB and QB sites in Fig. 4.35b and d, respectively, was due to the increased interaction of the O₂ molecule with the Pd(100) surface. The former adsorption site only had one Pd atom interacting with one O atom each, whereas the latter site had two Pd atoms to one O atom. This increased interaction stabilised the adsorption of O₂ for the QB site compared to the DB site (Table 4.25 and Fig. 4.35).

Table 4.25. Adsorption energies for the different positions of O₂ and ½ O₂ adsorbed to Pd(100) without and with D3 corrections.

Adsorbate	Site	Position	$E_{ads}^{PBE} / \text{kJ mol}^{-1}$	$E_{ads}^{PBE+D3} / \text{kJ mol}^{-1}$
O ₂	DB	-	-75	-100
	QB	-	-120	-145
O	Hollow	(½ O ₂)	-95	-108

Note: DB denotes di-bridge and QB is quad-bridge. The species involved in each position are stated in the parentheses.

The Pd-O interatomic distances for the DB and QB sites in Fig. 4.35b and d were ~2.00 and ~2.12 Å, respectively. The O atoms had to be closer to the Pd atoms of the DB site as there were less of them to interact with, and therefore, less electron density to share. The QB site had double the number of interacting Pd atoms, and therefore, double the electron density to share. This explained the difference of ~45 kJ mol⁻¹ in E_{ads} values for the two sites (Table 4.25 and Fig. 4.35).

The Hollow ½ O₂ site in Fig. 4.35f had the same Pd-O bond lengths of ~2.16 Å, which was slightly longer than that of the QB site due to the same rationale; the greater the number of interacting Pd atoms, the greater the electron density available for the interaction (in this case, chemisorption). The QB site could be the site that may be responsible for direct H₂O₂ synthesis as two H atoms could bond to the adsorbed O₂, rather than the O₂ molecule dissociating. Further investigation would be required to determine the E_a barriers for each scenario (Table 4.25 and Fig. 4.35).

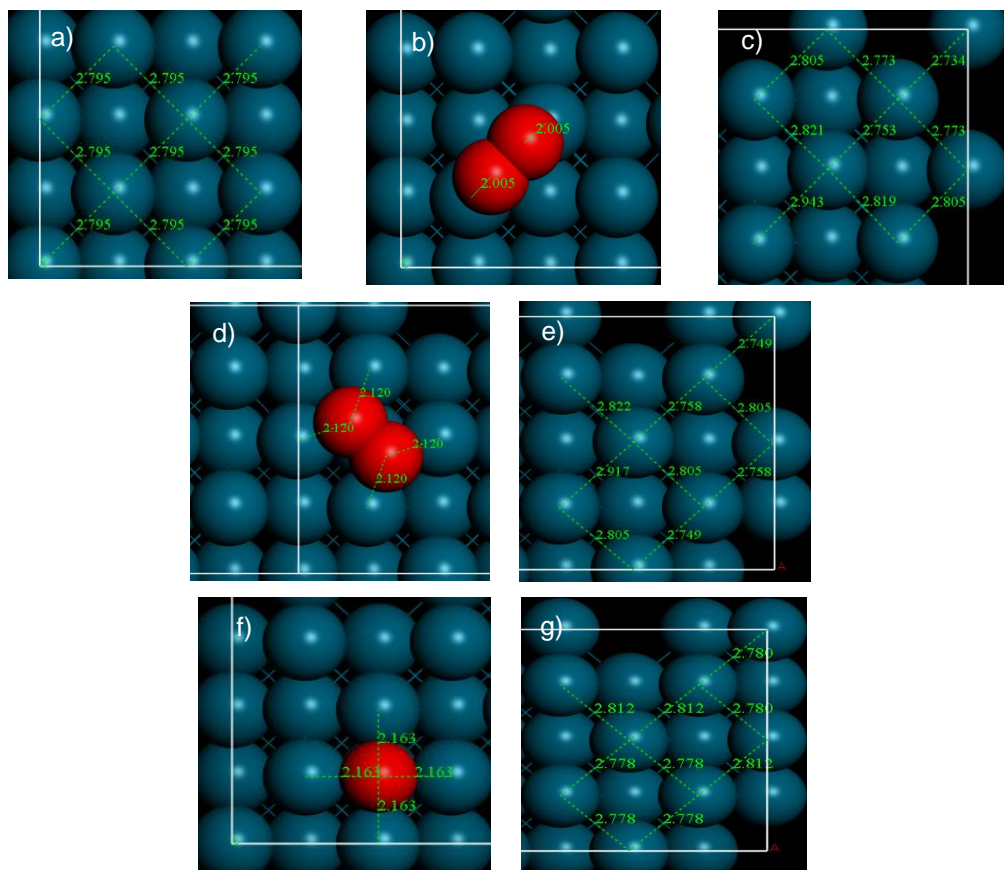


Figure 4.35. Images of the geometry optimisation calculations for O_2 and $\frac{1}{2} O_2$ adsorbed to Pd(100) calculated with D3 corrections and the adsorbate removed, where **a)** is the clean surface, **b)** is the DB site with the adsorbate, **c)** is the DB site without the adsorbate, **d)** is the QB site with the adsorbate, **e)** is the QB site without the adsorbate, **f)** is the Hollow ($\frac{1}{2} O_2$) site with the adsorbate, and **g)** is the Hollow ($\frac{1}{2} O_2$) site without the adsorbate. The dark blue atoms represent the Pd atoms, and the red atoms represent the O atoms. Interatomic distances in green are in Angstroms (\AA). DB denotes di-bridge and QB is quad-bridge. The species involved in each position are stated in the parentheses.

The top layer surface atoms for each of the sites had moved partially as the Pd-Pd bond length ranges for the DB, QB and Hollow ($\frac{1}{2} O_2$) sites in Fig. 4.35 c, e, and g, respectively, were as follows: $\sim -0.04 - \sim +0.15 \text{ \AA}$; $\sim -0.05 - \sim +0.12 \text{ \AA}$; and $\sim \pm 0.02 \text{ \AA}$, respectively. Clearly, the trend was that the increase in the Pd-Pd bond length changes caused the E_{def} value to increase, thus, making the E_{ads} value more positive (Table 4.25 and Fig. 4.35).

In Fig. 4.36, the DoS of the QB site demonstrated that there was significant interaction between the Pd(100) surface and the O_2 . This interaction resulted in the bonding and anti-bonding orbital(s) of the O_2 above the Fermi level being drastically decreased, with the bonding orbitals being shifted towards the Fermi level by $\sim +1 - \sim +7 \text{ eV}$. The peaks that corresponded with the s- and p-orbitals of the adsorbed O_2 overlapped the peaks of the adsorbate-surface complex at ~ -24 , ~ -18 , ~ -9 , and

~-8 eV. This would suggest that the bonding orbitals of the adsorbate and surface overlapped, supported by the negative E_{ads} value (~-145 kJ mol⁻¹). Interestingly, there was also peak overlap above the Fermi level (at ~+4 eV), which would suggest an overlap of anti-bonding orbitals between the surface and adsorbed O₂ (Table 4.25, and Fig. 4.35 and 4.36).

In addition, there was a sizeable bond lengthening of the adsorbate as the O=O bond length increased from ~1.24 Å to ~1.42 Å. This showed that the Pd(100) was destabilising the O=O bond, which can be attributed to the shift in electron densities for both the Pd(100) surface and the adsorbate, supported by the overlap of anti-bonding orbitals between the surface and adsorbed O₂ (Table 4.25, and Fig. 4.35 and 4.36).

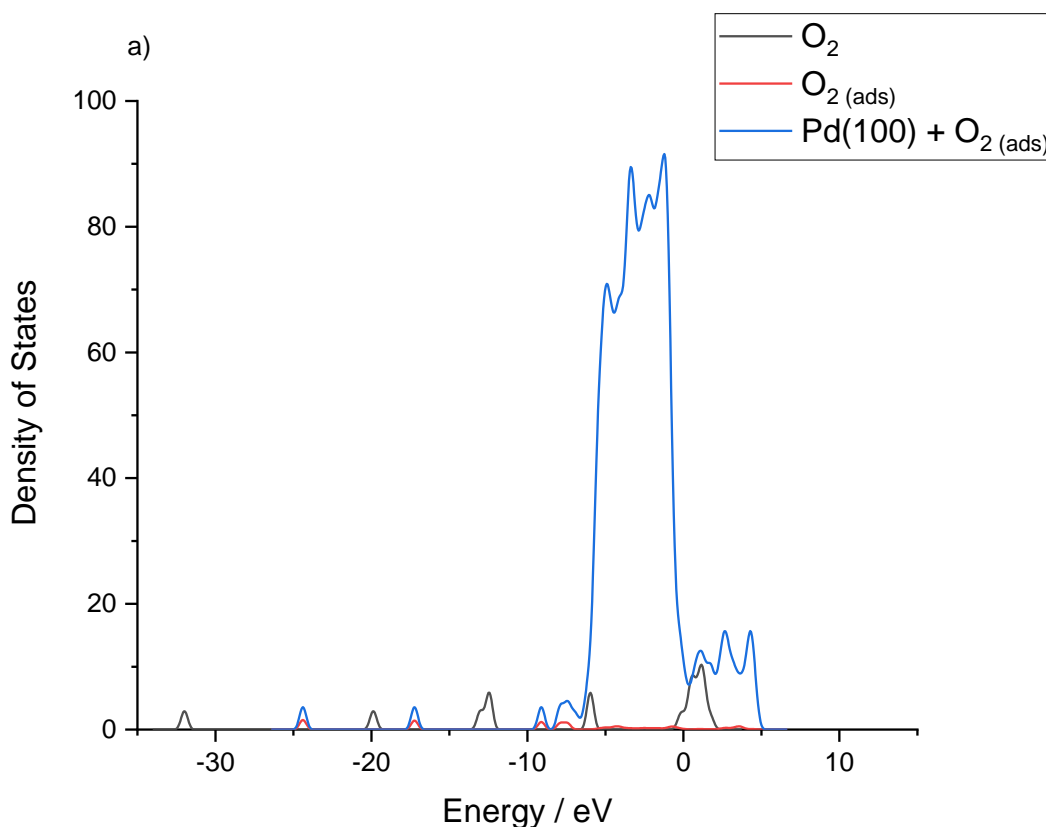


Figure 4.36. Normalised Densities of States for O₂ adsorbed to Pd(100), lone O₂ and the partial Densities of States of O₂ adsorbed to Pd(100), where **a)** shows all three Densities of States.

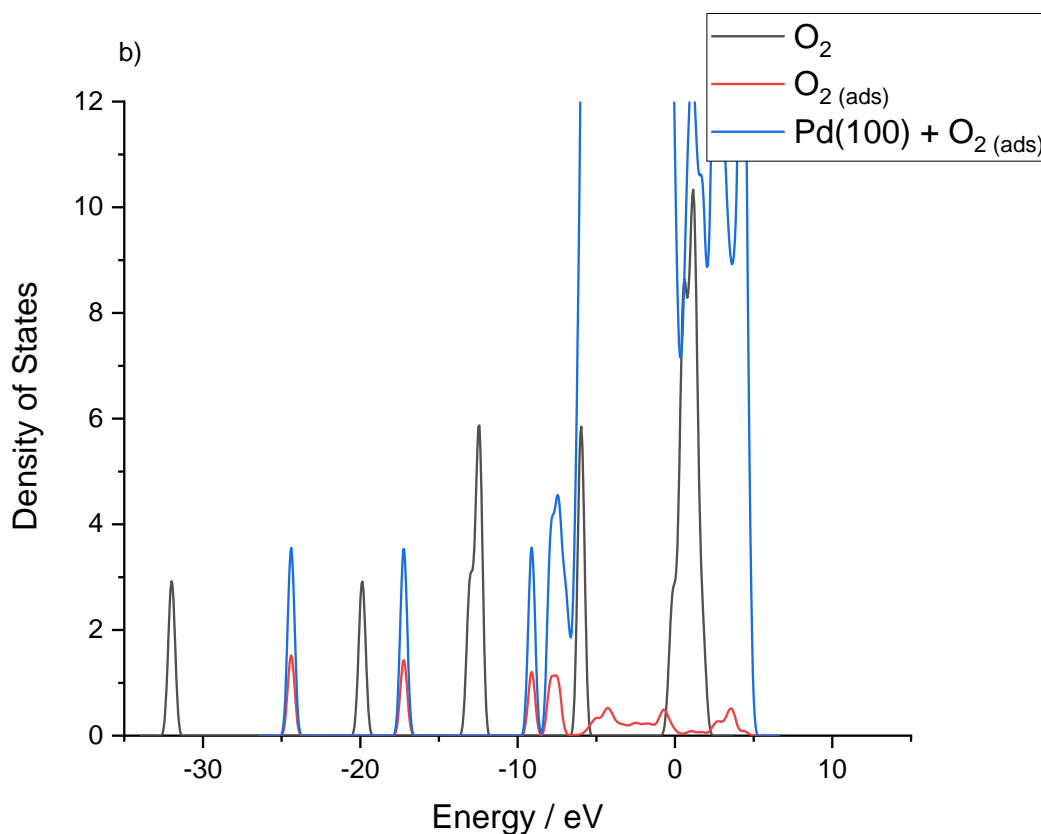


Figure 4.36. Normalised Densities of States for O_2 adsorbed to Pd(100), lone O_2 and the partial Densities of States of O_2 adsorbed to Pd(100), where **b)** shows a magnified view of the normalised Densities of States with a focus on the lone O_2 and partial Densities of States of O_2 adsorbed to Pd(100).

As the adsorption of O_2 and atomic O was strong on Pd(100), the next step in the direct synthesis of H_2O_2 to investigate was the dissociation of O_2 . Geometry optimisation calculations were completed both without and with D3 corrections, where two of the optimised structures collapsed into Hollow Straight sites. These results have been consolidated into a single result in the data. The Top Diagonal site caused the reformation of the O=O bond to make a DB site, and therefore, it was discounted from the current work (Table 4.26 and Fig. 4.37).

The calculations that were completed without the D3 corrections gave E_{ads} values of ~ -174 and ~ -196 kJ mol^{-1} for the Hollow Diagonal and Hollow Straight sites, respectively. With the D3 corrections applied, the calculations decreased the E_{ads} values by approximately the same amount (~ 23 and ~ 19 kJ mol^{-1} , respectively), which led to the E_{ads} values becoming ~ -197 and ~ -215 kJ mol^{-1} , respectively (Table 4.26 and Fig. 4.37).

Table 4.26. Adsorption energies for the different positions of dissociated O₂ adsorbed to Pd(100) without and with D3 corrections.

Site	Position	E_{ads}^{PBE} / kJ mol ⁻¹	E_{ads}^{PBE+D3} / kJ mol ⁻¹
Hollow	Diagonal	-174	-197
	Straight	-196	-215

Note: Diagonal denotes the position of the adsorbate perpendicular to the direction of the rows of top layer metal atoms, and Straight is the position of the adsorbate parallel to the rows of the top layer metal atoms.

The Pd-O bond lengths for the Hollow Diagonal sites in Fig. 4.37b and the Hollow Straight sites in Fig. 4.37d were: ~2.06, ~2.29 and ~2.31 Å; and ~2.07, ~2.17 and ~2.18, respectively. A similar rationale used to explain the trend for the adsorption of dissociated H₂ to Pd(100) can be used to explain the trend for dissociated O₂ adsorbed to Pd(100). As there was another Pd atom involved in the Hollow Straight sites, there was a greater amount of electron density that could interact with the adsorbate(s) than that of the Hollow Diagonal sites (seven and six Pd atoms, respectively) (Table 4.26 and Fig. 4.37).

The top layer Pd atoms did not move significantly. In relation to the clean surface, the Hollow Diagonal and Hollow Straight sites in Fig. 4.37c and e, respectively, had the following Pd-Pd bond lengths ranges: ~-0.07 – ~+0.05 Å; and ~-0.02 – ~+0.04 Å, respectively. The reason for the slightly larger Pd-Pd bond length range exhibited by the Hollow Diagonal sites was most likely due to the marginally increased repulsion from the proximity of a decreased number of atoms compared to the Hollow Straight sites. The O atoms were in the closest hollow sites next to each other for the former sites. This explanation coupled with the previous rationale regarding the number of interacting Pd atoms better defined the difference in E_{ads} values displayed by the Hollow Diagonal and Hollow Straight sites (Table 4.26 and Fig. 4.37).

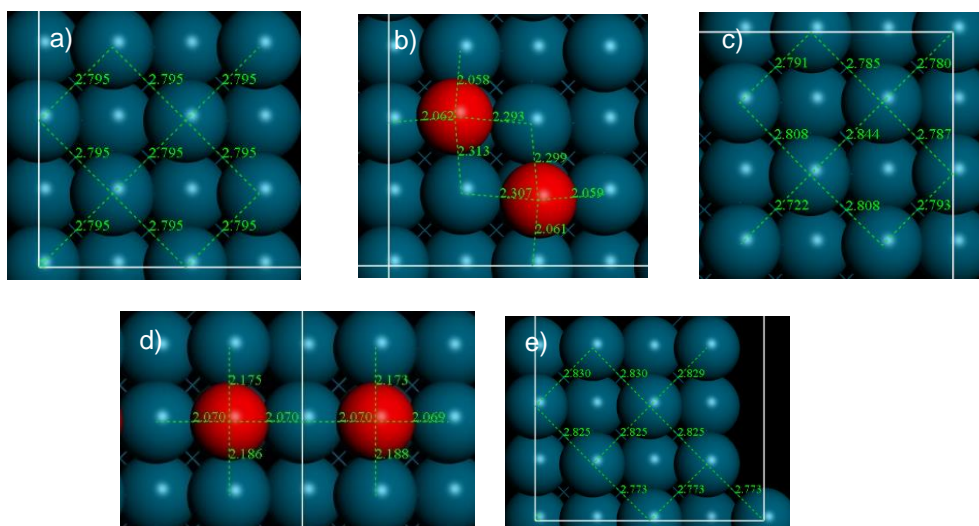


Figure 4.37. Images of the geometry optimisation calculations for dissociated O_2 adsorbed to Pd(100) calculated with D3 corrections and the adsorbate removed, where **a)** is the clean surface, **b)** is the Hollow Diagonal sites with the adsorbates, **c)** is the Hollow Diagonal sites without the adsorbates, **d)** is the Hollow Straight sites with the adsorbates, and **e)** is the Hollow Straight sites without the adsorbates. The dark blue atoms represent the Pd atoms, and the red atoms represent the O atoms. Interatomic distances in green are in Angstroms (Å). Diagonal denotes the position of the adsorbate perpendicular to the direction of the rows of top layer metal atoms, and Straight is the position of the adsorbate parallel to the rows of the top layer metal atoms.

As Pd(100) showed that it had the ability to adsorb and dissociate H_2 and O_2 , the adsorption and dissociation of H_2O_2 was investigated. It was observed that only three sites and orientations of the H_2O_2 molecule adsorbed onto the surface of Pd(100). The geometry optimisation calculations for the DB and Cross-Bridge (CB) sites resulted in the dissociation of the H_2O_2 molecule to form two OH groups. These results have been discounted from the current work.

For the QB (OH) site without D3 corrections applied, it gave an E_{ads} value of $\sim -23 \text{ kJ mol}^{-1}$, which decreased by $\sim 28 \text{ kJ mol}^{-1}$ when the D3 corrections were applied. This resulted in an E_{ads} value of $\sim -51 \text{ kJ mol}^{-1}$. Considering that H_2O_2 dissociation can readily occur on this surface, it can be presumed that the E_a barrier for this was low and was only dependent on the orientation of the molecule and the adsorption site (Table 4.27 and Fig. 4.38).

The QB (OH) site in Fig. 4.38b had Pd-O and Pd-H interatomic distances of ~ 2.35 and 2.71 Å , and ~ 2.56 and $\sim 2.70 \text{ Å}$, respectively. The reason for this difference in interatomic distances between the two types of bond was due to the greater affinity Pd has for O than H. The Pd-Pd bond lengths for this site in Fig. 4.38c changed

minimally compared to the clean surface. The range of Pd bond length changes was $\sim -0.04 - \sim +0.09 \text{ \AA}$ (Table 4.27 and Fig. 4.38).

Table 4.27. Adsorption energies for the different positions of H_2O_2 adsorbed to Pd(100) without and with D3 corrections.

Site	Position	$E_{ads}^{PBE} / \text{kJ mol}^{-1}$	$E_{ads}^{PBE+D3} / \text{kJ mol}^{-1}$
QB	(OH)	-23	-51

Note: QB denotes quad-bridge. The species involved in each position are stated in the parentheses.

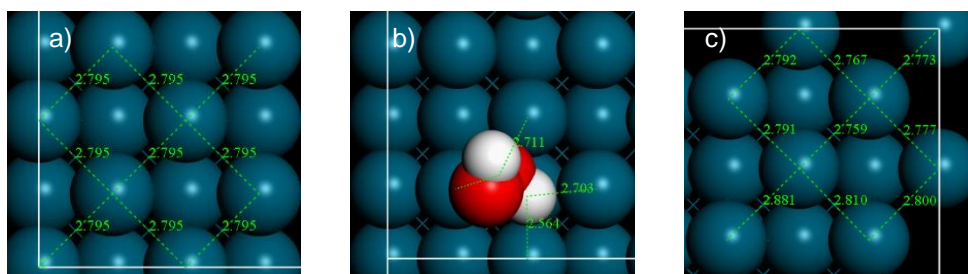


Figure 4.38. Images of the geometry optimisation calculations for H_2O_2 and dissociated H_2O_2 adsorbed to Pd(100) calculated with D3 corrections and the adsorbate removed, where **a**) is the clean surface, **b**) is the QB (OH) site with the adsorbate, and **c**) is the QB (OH) site without the adsorbate. The dark blue atoms represent the Pd atoms, the red atoms represent the O atoms, and the white atoms represent the H atoms. Interatomic distances in green are in Angstroms (\AA). QB denotes quad-bridge. The species involved in each position are stated in the parentheses.

The first type of H_2O_2 dissociation that was investigated was the H-OOH bond scission. Six sites and orientations of the dissociated H_2O_2 species adsorbed onto the surface of Pd(100), but one calculation failed to complete with the D3 corrections applied, and three other calculations resulted in dissociation at the HO-OH bond. The results of these four calculations have been discounted from the current work. Nevertheless, the three calculations suggested that the E_a barrier for this type of dissociation was low. A key intermediate step in the catalytic epoxidation of propene utilising *in-situ* direct H_2O_2 synthesis may have been discovered from the HO-OH dissociation. The free H atom could bond with the OOH or H atom from one of the OH groups could bind with the other OH to form H_2O and O. The H_2O could subsequently desorb, and the O atom could be used as the oxidative species for the propene. Further investigation will be required to determine the validity of this hypothesis.

The geometry optimisation calculations without the D3 corrections applied for the Hollow Straight and Bridge (H)-Hollow (OOH) sites gave E_{ads} values of ~ 16 and ~ 15 kJ mol⁻¹. When the D3 correction were applied to the calculations, the E_{ads} values decreased by approximately the same amount (~ 35 kJ mol⁻¹), which resulted in E_{ads} values of ~ 50 kJ mol⁻¹. Interestingly, the key difference between the Hollow Straight and Bridge (H)-Hollow (OOH) sites in Fig. 4.39b and d, respectively, was the adsorption site of the H atom, but this had little effect on the E_{ads} values as both were the same. Clearly, this type of adsorption was site insensitive (Table 4.28 and Fig. 4.39).

Table 4.28. Adsorption energies for the different positions of dissociated H₂O₂ (H-OOH) adsorbed to Pd(100) without and with D3 corrections.

Site	Position	$E_{\text{ads}}^{\text{PBE}}$ / kJ mol ⁻¹	$E_{\text{ads}}^{\text{PBE}+D3}$ / kJ mol ⁻¹
Hollow	Straight	-16	-50
Bridge (H)-Hollow (OOH)	-	-15	-50

Note: Straight denotes the position of the adsorbate parallel to the rows of the top layer metal atoms. The species involved in each position are stated in the parentheses.

The Pd-O bond lengths for the Hollow Straight sites in Fig. 4.39b and the Bridge (H)-Hollow (OOH) sites in Fig. 4.39d were as follows: ~ 2.29 , ~ 2.31 , ~ 2.32 and ~ 2.43 Å; and ~ 2.24 , ~ 2.29 , ~ 2.36 and ~ 2.46 Å, respectively. These bond lengths were approximately the same because the OOH species was adsorbed to a Hollow site for both cases. The Pd-H bond lengths for these sites were as follows: ~ 1.86 , ~ 1.89 , ~ 1.97 and ~ 2.24 Å; ~ 1.71 Å; and ~ 1.71 Å, respectively. The reason for the difference in Pd-H bond lengths was due to the difference in the number of interacting Pd atoms. The Hollow Straight sites had four Pd atoms interact with the H atom, and therefore, saw increased Pd-H bond lengths as more electron density was available for that interaction, whereas the Bridge site only had two Pd atoms with less electron density available for chemisorption. The top layer Pd atoms had moved marginally for the Pd(100) surface at the Hollow Straight and Bridge (H)-Hollow (OOH) sites. The Pd-Pd bond length changes in relation to the clean surface in Fig. 4.39a were both reported ~ 0.05 – ~ 0.07 Å. This was expected as the E_{ads} values and sites were relatively similar (Table 4.28 and Fig. 4.39).

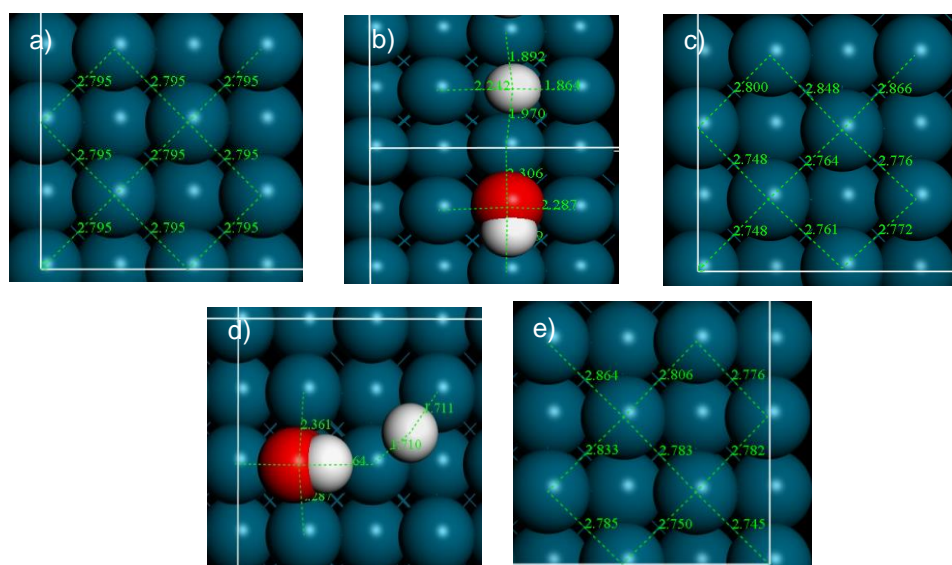


Figure 4.39. Images of the geometry optimisation calculations for dissociated H_2O_2 (H-OOH) adsorbed to Pd(100) calculated with D3 corrections and the adsorbate removed, where **a**) is the clean surface, **b**) is the Hollow Straight sites with the adsorbates, **c**) is the Hollow Straight sites without the adsorbates, **d**) is the Bridge (H)-Hollow (OOH) sites with the adsorbates, and **e**) is the Bridge (H)-Hollow (OOH) sites without the adsorbates. The dark blue atoms represent the Pd atoms, the red atoms represent the O atoms, and the white atoms represent the H atoms. Interatomic distances in green are in Angstroms (Å). Straight denotes the position of the adsorbate parallel to the rows of the top layer metal atoms. The species involved in each position are stated in the parentheses.

As previously discussed in the current work, the dissociation of H_2O_2 via the scission of the HO-OH bond was observed during the investigation into H_2O_2 adsorption and dissociation of H_2O_2 (H-OOH) to the Pd(100) surface. The dissociated H_2O_2 at the HO-OH bond was investigated, and it was found that the geometry optimisation calculations without the D3 corrections applied showed that the binding of the OH groups to the surface was strong. The Bridge-Hollow (1), Bridge-Hollow (2), Bridge-Hollow (3), Hollow Diagonal and Hollow Straight sites gave E_{ads} values of ~ -236 , ~ -235 , ~ -243 , ~ -231 and ~ -216 kJ mol^{-1} , respectively. With the D3 corrections applied, the E_{ads} values decreased by an approximately similar amount (~ 37 kJ mol^{-1}), causing the E_{ads} values for these sites to be ~ -273 , ~ -273 , ~ -281 , ~ -267 and ~ -253 kJ mol^{-1} , respectively (Table 4.29 and Fig. 4.40).

Table 4.29. Adsorption energies for the different positions of dissociated H₂O₂ (HO-OH) adsorbed to Pd(100) without and with D3 corrections.

Site	Position	E_{ads}^{PBE} / kJ mol ⁻¹	E_{ads}^{PBE+D3} / kJ mol ⁻¹
Bridge-Hollow (1)	-	-236	-273
Bridge-Hollow (2)	-	-235	-273
Bridge-Hollow (3)	-	-243	-281
Hollow	Diagonal	-231	-267
Hollow	Straight	-216	-253

Note: Diagonal denotes the position of the adsorbate perpendicular to the direction of the rows of top layer metal atoms, and Straight is the position of the adsorbate parallel to the rows of the top layer metal atoms.

It was observed that the Pd-O bond lengths for the Bridge sites were ~2.01 and ~2.12 Å for the Bridge-Hollow (1), Bridge-Hollow (2) and Bridge-Hollow (3) sites. The Pd-O bond lengths for the hollow sites of the Bridge-Hollow (1), Bridge-Hollow (2), Bridge-Hollow (3), Hollow Diagonal and Hollow Straight sites in Fig. 4.40b, d, f, h, and j, respectively, were as follows: ~2.30, ~2.33, ~2.43 and ~2.56 Å; ~2.16, ~2.32, ~2.42 and ~2.57 Å; ~2.34 Å; ~2.32 and ~2.33 Å; and ~2.31, ~2.32, ~2.35, ~2.41 and ~2.45 Å. The Pd-O bond lengths for the bridge sites were approximately the same and the Pd-O bond lengths for the hollow sites were also similar to each other, however, the Pd-O bond lengths were generally larger for the hollow sites than they were for the bridge sites (Table 4.29 and Fig. 4.40).

The rationale for this was that there were more Pd atoms in the hollow sites than the bridge sites, and therefore, more electron density for adsorption. Thus, the Pd-O bonds were longer as the OH groups could share from a greater amount of electron density. In addition, the OH group on the bridge sites influenced the OH group in the hollow site due to their proximity to each other, forcing the OH out of its hollow site and causing the Pd-O bond lengths to increase (Table 4.29 and Fig. 4.40).

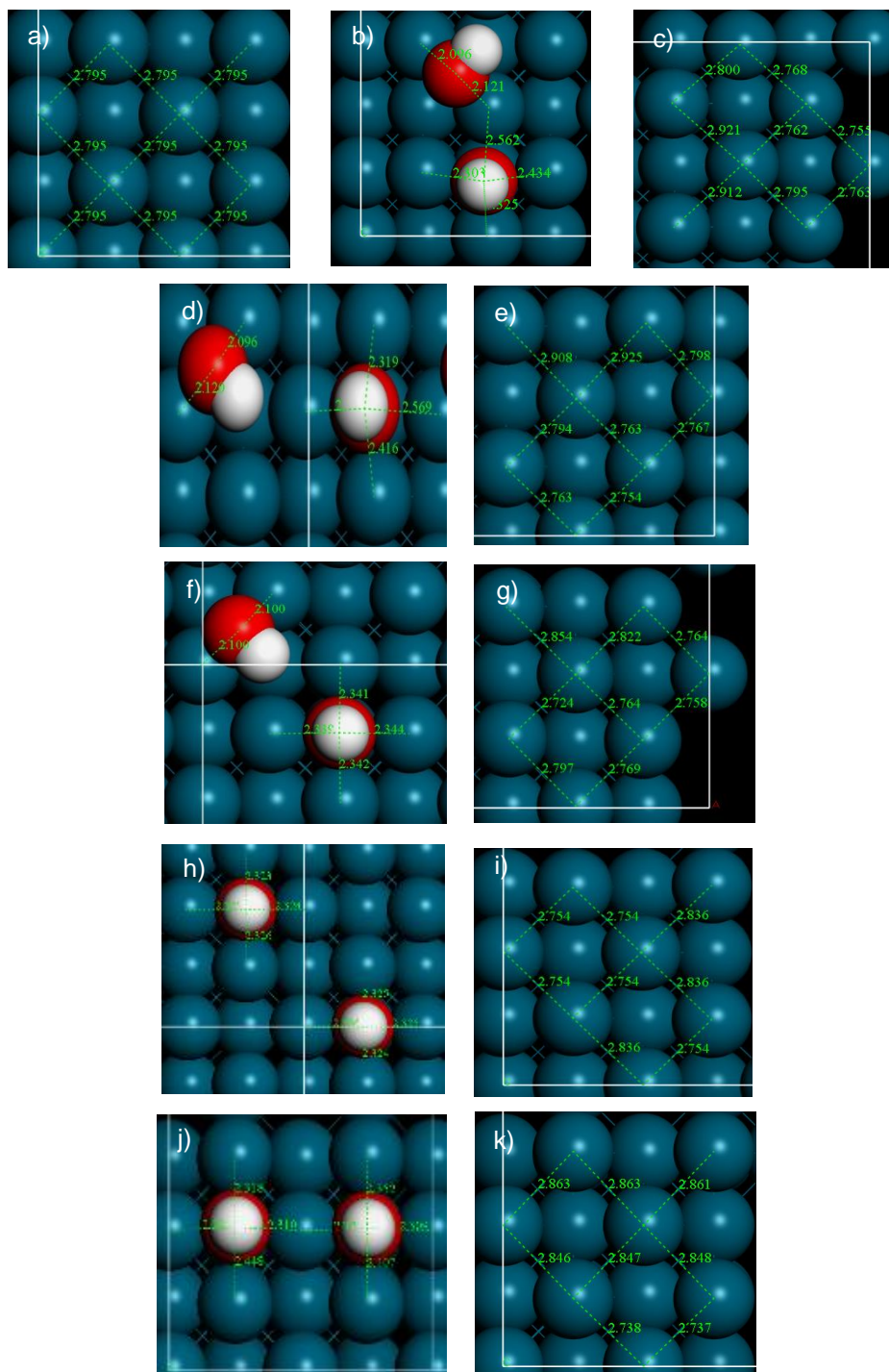


Figure 4.40. Images of the geometry optimisation calculations for dissociated H_2O_2 (HO-OH) adsorbed to $\text{Pd}(100)$ calculated with D3 corrections and the adsorbate removed, where **a**) is the clean surface, **b**) is the Bridge-Hollow (1) sites with the adsorbates, **c**) is the Bridge-Hollow (1) sites without the adsorbates, **d**) is the Bridge-Hollow (2) sites with the adsorbates, **e**) is the Bridge-Hollow (2) sites without the adsorbates, **f**) is the Bridge-Hollow (3) sites with the adsorbates, **g**) is the Bridge-Hollow (3) sites without the adsorbates, **h**) is the Hollow Diagonal sites with the adsorbates, and **i**) is the Hollow Diagonal sites without the adsorbates, **j**) is the Hollow Straight sites with the adsorbates, and **k**) is the Hollow Straight sites without the adsorbates. The dark blue atoms represent the Pd atoms, the red atoms represent the O atoms, and the white atoms represent the H atoms. Interatomic distances in green are in Angstroms (\AA). Diagonal denotes the position of the adsorbate perpendicular to the direction of the rows of top layer metal atoms, and Straight is the position of the adsorbate parallel to the rows of the top layer metal atoms.

The Pd atoms of the top layer of the Pd(100) surface adsorbing dissociated H₂O₂ moved slightly. The ranges for the change in Pd-Pd bond lengths from the norm (*i.e.*, the clean surface in Fig. 4.40a) for the Bridge-Hollow (1) sites in Fig. 4.40c, the Bridge-Hollow (2) sites in Fig. 4.40e, the Bridge-Hollow (3) sites in Fig. 4.40g, the Hollow Diagonal sites in Fig. 4.40i, and Hollow Straight sites in Fig. 4.40k, were as follows: $\sim -0.04 - \sim +0.13$ Å; $\sim -0.04 - \sim +0.13$ Å; $\sim -0.07 - \sim +0.06$ Å; $\sim -0.04 - \sim +0.04$ Å; and $\sim -0.06 - \sim +0.07$ Å, respectively. These small movements accurately reflected the E_{ads} values observed as greater movements would result in larger E_{def} values, which in turn, would cause less negative E_{ads} values (Table 4.29 and Fig. 4.40).

From the results obtained for both types of H₂O₂ dissociation on Pd(100), the HO-OH bond scission was the dissociation type that led to the most negative E_{ads} values. The most negative E_{ads} value recorded for the HO-OH bond dissociation was at the Bridge-Hollow (3) sites, with an energy of ~ -281 kJ mol⁻¹, whereas the most negative E_{ads} recorded for the H-OOH bond dissociation was at the Bridge (H)-Hollow (OOH) sites with ~ -233 kJ mol⁻¹. This gave no accurate determination of the E_{a} barrier for the dissociation. However, the fact that certain orientations of both H₂O₂ and OOH led to HO-OH bond scission would indicate that this barrier was low, and that this dissociation could occur readily.

The adsorption of propene and PO to Pd(100) was investigated as it was for the other surfaces in the current work. A variety of different sites and orientations of propene were considered, but only two geometry optimisation calculations completed as others failed to complete. Both calculations resulted in optimising to the same adsorption site; Top Up. As previously discussed, this is in reference to the C¹=C² double bond.

As such, the current work will only consider one in the data. The calculation without D3 corrections demonstrated a strong chemisorption of the propene on the Pd(100) surface. The Top Up site gave an E_{ads} value of ~ 63 kJ mol⁻¹. With the D3 corrections applied in the calculations, the E_{ads} value decreased (by ~ 60 kJ mol⁻¹) to a value ~ -123 kJ mol⁻¹. This demonstrated that the size of the molecule has a greater effect on the adsorption of the molecule as the van der Waals forces were incorporated into latter calculations. For example, a smaller molecule like H₂ only decreased in E_{ads} by ~ 16 kJ mol⁻¹ (Tables 4.23 and 4.30, and Fig. 4.32 and 4.41).

Table 4.30. Adsorption energies for the different positions of propene and PO adsorbed to Pd(100) without and with D3 corrections.

Adsorbate	Site	Position	E_{ads}^{PBE} / kJ mol ⁻¹	E_{ads}^{PBE+D3} / kJ mol ⁻¹
Propene	Top	Up	-63	-123
	DB	(OC ² H)	-	-63
PO	DB	(C ¹ OC ³ H)	-	-72
	TB	(HC ¹ OC ³ H)	-	-73
	QB	(HC ¹ OC ³ HH)	-	-72

Note: DB denotes di-bridge, TB is tri-bridge, QB is quad-bridge, and Up is the methyl group is pointed up and away from the surface. The species involved in each position are stated in the parentheses.

The Pd-C¹H, Pd-C²H and Pd-C³H interatomic distances for the Top Up site in Fig. 4.41b were ~2.41, ~2.68 and ~2.41 Å, respectively, as the Pd-C¹ and Pd-C² interatomic distances were ~2.21 and ~2.20 Å, respectively. In Fig. 4.41c, the Pd-Pd bond length ranges for the Top Up site was minimal, with a small increase in bond length observed (~+0.04 Å), which had little effect on the E_{ads} value (Table 4.30 and Fig. 4.41).

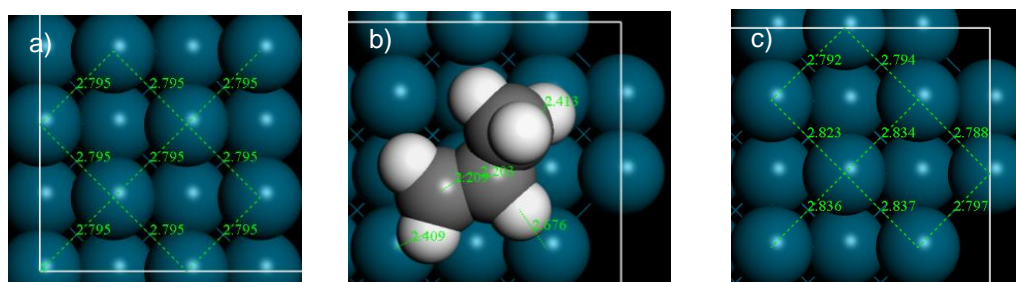


Figure 4.41. Images of the geometry optimisation calculations for propene adsorbed to Pd(100) calculated with D3 corrections and the adsorbate removed, where **a)** is the clean surface, **b)** is the propene Top Up site with the adsorbate, and **c)** is the propene Top Up site without the adsorbate. The dark blue atoms represent the Pd atoms, the grey atoms represent the C atoms, and the white atoms represent the H atoms. Interatomic distances in green are in Angstroms (Å). Up denotes the methyl group is pointed up and away from the surface. The species involved in each position are stated in the parentheses.

In Fig. 4.42, the DoS of the Top Up site demonstrated that there was significant interaction observed between the Pd(100) surface and propene. This interaction

resulted in the anti-bonding orbital(s) of the propene molecule above the Fermi level being reduced to almost nothing, as the densities had been spread out. The bonding orbitals' DoS had been reduced and shifted by a maximum of $\sim +4$ eV (Table 4.30, and Fig. 4.41 and 4.42).

Overlap of the peaks for the adsorbed propene and the adsorbate-surface complex was observed at ~ -17 , ~ -13 , ~ -11 , and ~ -7 eV. This would suggest that the bonding orbitals of the adsorbed propene and surface had overlapped, supported by the negative E_{ads} value (~ -123 kJ mol $^{-1}$). There was a small bond lengthening of the adsorbate as the C 1 =C 2 bond length increased from ~ 1.34 Å to ~ 1.40 Å. The bond did not break, as a total of eight electrons would be required to completely fill the anti-bonding orbitals of the C 1 =C 2 bond. Thus, the strong chemisorption at ~ -123 kJ mol $^{-1}$ was established (Table 4.30, and Fig. 4.41 and 4.42).

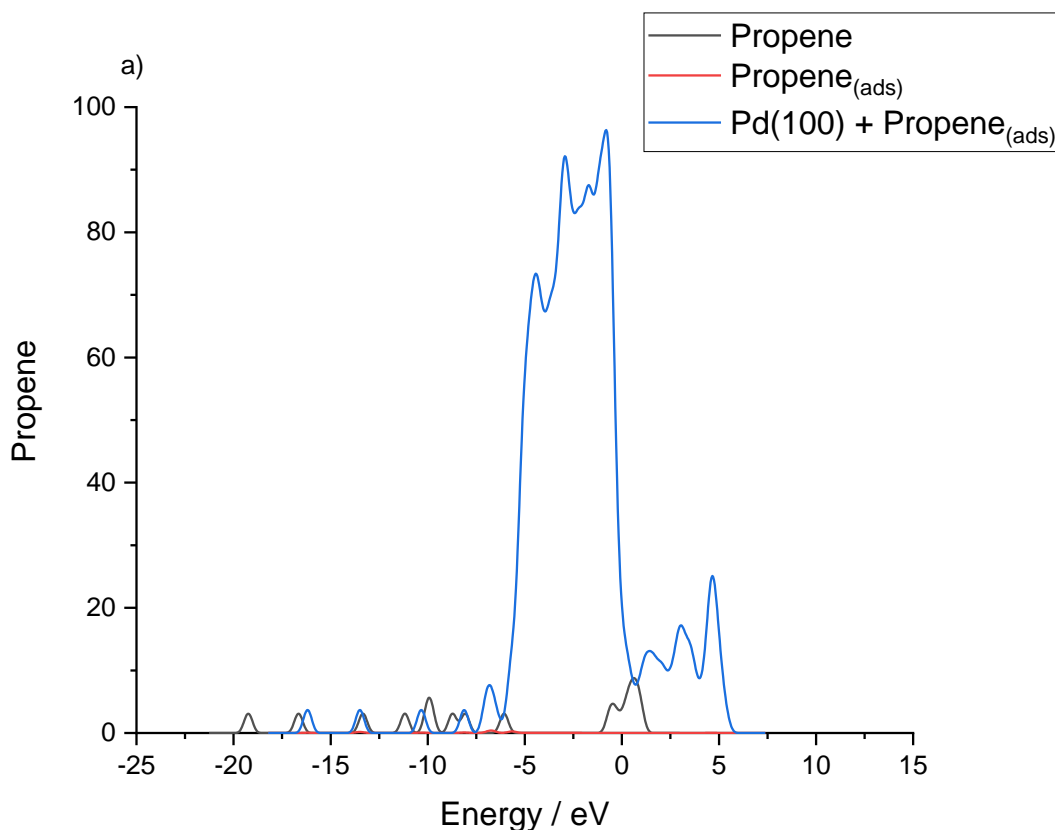


Figure 4.42. Normalised Densities of States for propene adsorbed to Pd(100), lone propene and the partial Densities of States of propene adsorbed to Pd(100), where **a)** shows all three Densities of States of propene adsorbed to Pd(100).

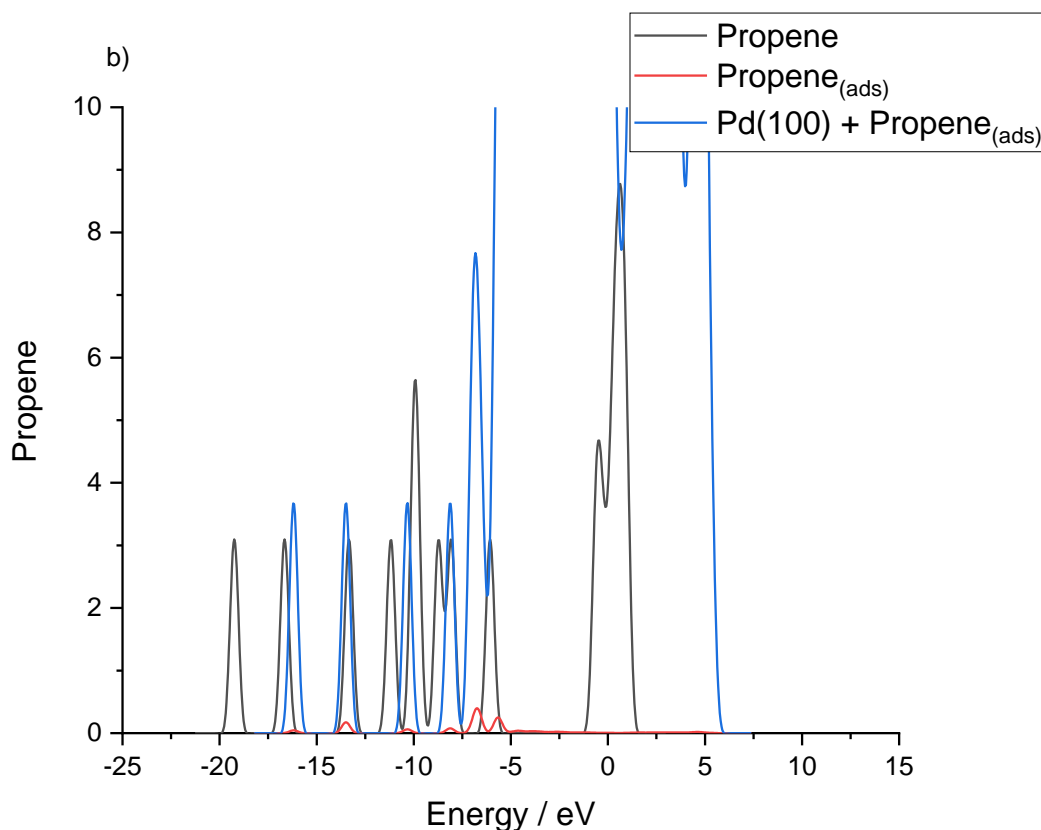


Figure 4.42. Normalised Densities of States for propene adsorbed to Pd(100), lone propene and the partial Densities of States of propene adsorbed to Pd(100), where **b)** shows a magnified view of the normalised Densities of States with a focus on the lone propene and partial Densities of States of propene adsorbed to Pd(100).

Geometry optimisation calculations were completed for the adsorption of PO to Pd(100). Although none of the calculations without D3 corrections completed, some of the calculations with D3 corrections applied did complete. The DB (OC²H), DB (C¹OC³H), TB (HC¹OC³H) and QB (HC¹OC³HH) sites had E_{ads} values of \sim -63, \sim -72, \sim -73, and \sim -72 kJ mol⁻¹, respectively (Table 4.30 and Fig. 4.43).

The DB (OC²H) site in Fig. 4.43b had Pd-O and Pd-C²H interatomic distances of \sim 2.38 and \sim 2.28 Å, respectively, and the DB (C¹OC³H) site in Fig. 4.43d had Pd-O and Pd-C³H interatomic distances of \sim 2.37 and \sim 2.49 Å, respectively. The TB (HC¹OC³H) site in Fig. 4.43f had Pd-O, Pd-C¹H and Pd-C³H interatomic distances of \sim 2.39, \sim 2.64 and \sim 2.45 Å, respectively, and the QB (HC¹OC³HH) site in Fig. 4.43h had Pd-O, Pd-C¹H, Pd-C³H¹ and Pd-C³H² interatomic distances of \sim 2.36, \sim 2.72, \sim 2.51 and \sim 2.56 Å, respectively (Table 4.30 and Fig. 4.43).

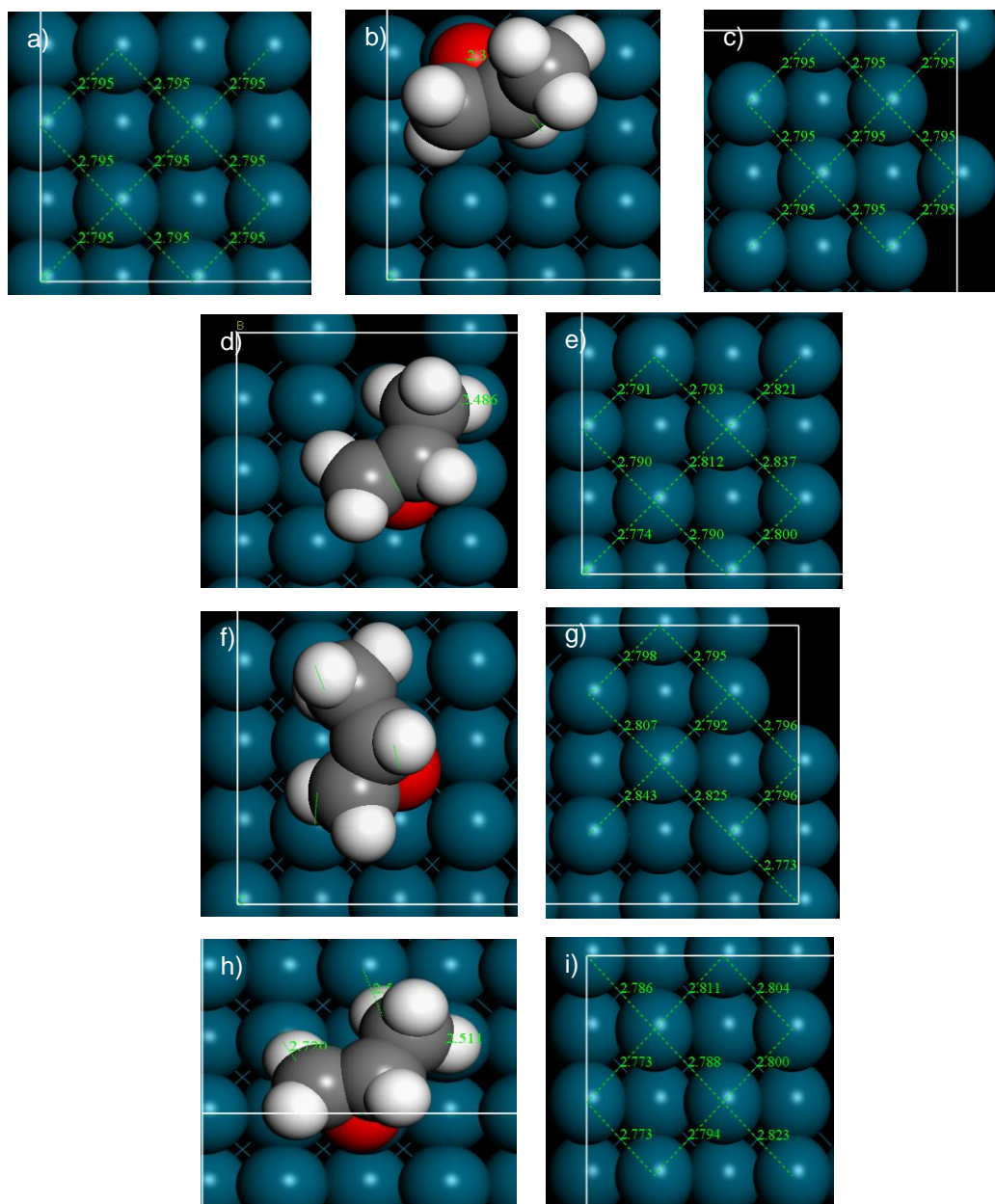


Figure 4.43. Images of the geometry optimisation calculations for propene and PO adsorbed to Pd(100) calculated with D3 corrections and the adsorbate removed, where **a)** is the clean surface, **b)** is the PO DB (OC²H) site with the adsorbate, **c)** is the PO DB (OC²H) site without the adsorbate **d)** is the PO DB (C¹OC³H) site with the adsorbate, **e)** is the PO DB (C¹OC³H) site without the adsorbate, **f)** is the PO TB (HC¹OC³H) site with the adsorbate, **g)** is the PO TB (HC¹OC³H) site without the adsorbate, **h)** is the PO QB (HC¹OC³HH) site with the adsorbate, and **i)** is the PO QB (HC¹OC³HH) site without the adsorbate. The dark blue atoms represent the Pd atoms, the grey atoms represent the C atoms, the red atoms represent the O atoms, and the white atoms represent the H atoms. Interatomic distances in green are in Angstroms (Å). DB denotes di-bridge, TB is tri-bridge, QB is quad-bridge, and Up is the methyl group is pointed up and away from the surface. The species involved in each position are stated in the parentheses.

The most likely reason for the decreased E_{ads} value for the DB (OC²H) site was because the PO was not stabilised by an additional adsorbate atom (H), regardless of the similar Pd-O interatomic distance (~ 2.38 Å). This lack of stabilisation

meant that the Pd-C²H interatomic distance was shorter in length (~2.28 Å) than the other Pd-H interatomic distances exhibited by the other sites. When comparing the other three sites, it was observed that they were site insensitive as they had similar E_{ads} values. The reason for the slightly less negative E_{ads} value exhibited by the DB (C¹OC³H) and the QB (HC¹OC³HH) sites could be due to the slightly smaller Pd-O interatomic distance, causing slightly more repulsion (Table 4.30 and Fig. 4.43).

The Pd-Pd bond lengths for the DB (C¹OC³H) site in Fig. 4.43e, TB (HC¹OC³H) site in Fig. 4.43g and QB (HC¹OC³HH) site in Fig. 4.43i moved minimally (no greater than ±0.05 Å), whereas the top layer Pd atoms of the DB (OC²H) site in Fig. 4.43c did not move. These observations showed a trend that when adsorption was stronger, the Pd atoms moved when interacting with the PO, whereas the DB (OC²H) site had a weaker interaction (by ~10 kJ mol⁻¹) and the Pd atoms did not move (Table 4.30 and Fig. 4.43).

Although the adsorption of PO was strong on Pd(100), this could be problematic when considering the catalytic properties of Pd(100). If adsorption is too strong to the surface, energy will be required to release the adsorbate from the surface. This is undesirable for catalysis. The most stable adsorption site was the TB (HC¹OC³H) site at ~-73 kJ mol⁻¹ (Table 4.30 and Fig. 4.43).

4.2.3. Gold and Palladium Adsorption Site Analysis

4.2.3.1. Adsorption of Hydrogen

For H₂ adsorption, the Pd(111) Top site was the favoured adsorption site, whereas either site for the Pd(100) surface (Sloped DB or Top Horizontal) produced the same E_{ads} value. The difference in energy between the two surfaces' adsorption of H₂ was not significant (~6 kJ mol⁻¹), thus, the adsorption was surface (and site) insensitive. In comparison to Au(100), the most stable configuration was the Top Vertical site. As previously stated, the adsorption of H₂ by Au was weak, supported by the work of Barrio *et al.*^{22,23} (Tables 4.1, 4.8, 4.15 and 4.23, and Fig. 4.2, 4.11, 4.21 and 4.32).

The top layer atoms did not move for the Au(111) and (100) surfaces because of the lack of adsorption of H₂. In comparison to Pd(111), the Top Horizontal sites for both Pd(100) and (111) had the same range of top layer Pd atom movements and had similar energies of adsorption. The amount of deformation of the top layer that

contributed to the E_{ads} values was most likely small for both Au and Pd (Tables 4.1, 4.8, 4.15 and 4.23, and Fig. 4.2, 4.11, 4.21 and 4.32).

Although Pd(111) could automatically dissociate H_2 upon adsorption (prevented only by the site and orientation of H_2), this was not the case for Pd(100). This suggested that there was an E_a barrier for the dissociation of H_2 on Pd(100), as the none of the geometry optimisation calculations for the adsorption of H_2 led to automatic dissociation. Surprisingly, the Au(100) surface could automatically dissociate H_2 upon adsorption. The reason that this occurred was due to the hollow sites between the Au atoms, as a result of the reduced number of surface atoms (less M neighbouring atoms) inherent of a (100) surface, with Au atoms having less Au-Au bonds, and therefore, could bond to the H atoms.²⁶ The affinity that Au has for itself is greater than its affinity for H (and O) when it is in its bulk form. Coupled with the fact that Au is a soft material, this is the reason that in certain instances in the current work a Au(100) surface distorted toward a (111) configuration (Tables 4.8, 4.15 and 4.23, and Fig. 4.11, 4.21 and 4.32).

All four surfaces behaved somewhat similarly with regards to the DoS calculations that were performed for the adsorption of intact H_2 . As a result of the shift of electron density during adsorption, the DoS for the metal surfaces and the adsorbate alike decreased. By what amount depended on where the electron density had shifted to, which was different for each case. In addition, the H-H bond lengths increased significantly on both Pd(111) and (100) by ~ 0.12 and ~ 0.11 Å, respectively. This coupled with the overlap of bonding orbitals, demonstrated by the peak overlap of the s-orbital peak and the adsorbate-surface peak, supported the strong interaction between the Pd surfaces and the H_2 (Fig. 4.3, 4.12, 4.21, 4.22, 4.32 and 4.33).

4.2.3.2. Dissociation of Hydrogen

For the adsorption of dissociated H_2 on the four surfaces studied, the E_{ads} value was more negative on the Pd(111) surface than on Au(100) and Pd(100) (~ -128 , ~ -24 and ~ -95 kJ mol⁻¹, respectively). Although the Hollow sites for Pd(100) were larger than those of Pd(111), there were fewer Pd atoms interacting with each H atom on the Pd(111) surface, meaning that there was likely less repulsion from the surface. This was evidenced by the Pd-H bond lengths as those for the Pd(111) (average Pd-H bond length: ~ 1.81 Å) were shorter by ~ 0.18 Å than those of the Pd(100) (average Pd-H bond length: ~ 1.99 Å). The shorter bond lengths showed that

the H atoms could be closer to the surface as there was less repulsion from the surface. Another argument for this case could be that the Pd-H bond lengths were longer on the Pd(100) surface because more Pd atoms were interacting with the H atoms on the Pd(100), and therefore, more electron density was available to share. However, the E_{ads} value for the Pd(111) surface was more negative than the Pd(100), which demonstrated that the Pd(111) was the more stable surface (Tables 4.9, 4.16 and 4.24, and Fig. 4.13, 4.23, and 4.34).

The most favourable adsorption site for dissociated H_2 on Au(100) was different to that of Pd(111) and Pd(100), which were both Hollow Straight sites. The Bridge-Bridge (3) sites for Au(100) led to a relatively strong adsorption (but not chemisorption) to the surface. There were a decreased number of M atoms interacting with the H atoms on the Au(100) surface (two per H atom) than the Pd(100) surface, meaning that there was less repulsion between the surface and the H atoms, hence, the shorter bond lengths (Au-H bond length: $\sim 1.77 \text{ \AA}$). However, the difference in E_{ads} values arose because Pd has a greater affinity for H than Au does for H. From the four surfaces studied, only Au(111) did not adsorb dissociated H_2 exceedingly well (Tables 4.9, 4.16 and 4.24, and Fig. 4.13, 4.23, and 4.34).

Although both Pd(100) and (111) surface had only minor changes to the top layer atoms, the latter had a larger change in Pd-Pd bond lengths than the former. Although, this did not significantly impact on the E_{ads} as Pd(111) provided the more favourable adsorption site. While adsorption of dissociated H_2 was favourable on Pd, it was not for Au(111) and this surface was seen to have larger movements of the top layer metal atoms (maximum bond length change: $\sim 0.21 \text{ \AA}$) than all other surfaces studied. The Au(100) surface had favourable adsorption sites for dissociated H_2 and small top layer Au atom movements (maximum bond length change: $\sim 0.13 \text{ \AA}$), which were larger than the Pd atom bond length changes observed for both Pd(100) and (111). One of the Au(100) had become distorted and shifted towards a (111) configuration, and therefore, had the largest change to the top layer atoms. However, this adsorption site was unfavourable. This demonstrated that Au(111) was more thermodynamically stable than Au(100) (Tables 4.2, 4.9, 4.16 and 4.24, and Fig. 4.4, 4.13, 4.23, and 4.34).

4.2.3.3. Adsorption of Oxygen

Analysis of the Pd surfaces showed that the Pd(100) surface produced an adsorption site of superior E_{ads} to that of Pd(111), with an approximate difference between the sites of the lowest E_{ads} values of the two different surfaces of $\sim 38 \text{ kJ mol}^{-1}$. The Pd(100) QB site most likely produced a lower E_{ads} value than the Pd(111) Bridge (O^1)-Top (O^2) site because of the difference in interaction between the O_2 molecule and the Pd atoms. The Pd(100) QB site had four Pd atoms sharing its electron density with the O_2 molecule, whereas the Pd(111) Bridge (O^1)-Top (O^2) site only had three Pd atoms to share electron density (Tables 4.17 and 4.25, and Fig. 4.24 and 4.35).

The power of electron density sharing was observed by the difference in the Pd-O interatomic distances of these two surfaces. The Pd(100) QB site and Pd(111) Bridge (O^1)-Top (O^2) site had Pd-O interatomic distances of $\sim 2.12 \text{ \AA}$, and ~ 2.03 and $\sim 2.14 \text{ \AA}$, respectively. Although the Bridge (O^1) site had a slightly longer Pd-O interatomic distance than the QB site, the Top (O^2) site had a shorter interatomic distance. This was because the Top (O^2) site of the Pd(111) Bridge (O^1)-Top (O^2) site only had one Pd atom interacting with the O^2 atom, and therefore, more of the electron density had to be shifted toward the two interacting (Pd and O^2) atoms rather than being shared as it was for the Bridge (O^1) and QB sites (Tables 4.17 and 4.25, and Fig. 4.24 and 4.35).

However, when atomic O was considered, the Pd(111) Hollow fcc ($\frac{1}{2} \text{O}_2$) site was the more favourable adsorption site than the Pd(100) Hollow ($\frac{1}{2} \text{O}_2$) site (~ -143 and $\sim -108 \text{ kJ mol}^{-1}$, respectively). Although the Pd-O bond lengths were shorter on the Pd(111) surface than the Pd (100) surface (~ 2.00 and $\sim 2.16 \text{ \AA}$, respectively), the tighter binding exhibited was indicative of there being less Pd atoms to repel the H atoms, hence a more negative E_{ads} value displayed (Tables 4.17 and 4.25, and Fig. 4.24 and 4.35).

In comparison to Au, neither Au(111) or Au(100) adsorbed molecular O_2 . Only the Au(111) surface adsorbed atomic O. The reason for the difference in the Au(111) Hollow fcc ($\frac{1}{2} \text{O}_2$) site and Pd(100) Hollow ($\frac{1}{2} \text{O}_2$) site E_{ads} values ($\sim 78 \text{ kJ mol}^{-1}$) was due to the greater affinity Pd has for O than Au has for O. The difference between the Au(111) Hollow fcc ($\frac{1}{2} \text{O}_2$) site and Pd(100) Hollow ($\frac{1}{2} \text{O}_2$) site was that the former had slightly shorter M-O bond lengths ($\sim 0.10 \text{ \AA}$) than the latter, which may have affected their E_{ads} values. This rationale was supported by the work of Ford *et al.*⁵ and Barrio *et al.*^{22,23} (Tables 4.3, 4.10, 4.17 and 4.25, and Fig. 4.5, 4.14, 4.24 and 4.35).

The Pd(111) surface had slightly smaller movements of the top layer Pd atoms than the Pd(100) surface for both O₂ and atomic O adsorption. This was because both species were interacting with more Pd atoms on the Pd(100) surface than the Pd(111) surface, thus, a greater amount of repulsion (affecting E_{def}) was exhibited for the Pd(100) adsorption sites than the Pd(111) sites. However, the larger Pd-Pd movements did not affect the adsorption of O₂ to Pd(100) adversely, as it had the more negative E_{ads} value (Tables 4.17 and 4.25, and Fig. 4.24 and 4.35).

In comparison to Au, both the Au(111) and (100) surfaces did not favourably adsorb O₂. However, the Au(111) surface did adsorb atomic O. The change in metal bond lengths for this surface at the Au(111) Hollow fcc ($\frac{1}{2}$ O₂) site was significantly larger (maximum bond length change: ~ 0.44 Å) than those of either Pd surface. As the E_{ads} values for atomic O adsorbed to both Pd(111) and (100) were more negative than that of the Au(111) surface, the E_{def} value for the Au(111) surface must have been greater than those of either Pd surface. This in turn would have made the E_{ads} value more positive for the Au(111) surface (Tables 4.3, 4.10, 4.17 and 4.25, and Fig. 4.5, 4.14, 4.24 and 4.35).

The O=O bond lengths increased on Au(111), Au(100), Pd(111) and Pd(100) by ~ 0.06 , ~ 0.07 , ~ 0.07 and ~ 0.18 Å, respectively. The DoS calculations had only been completed on the Pd surfaces due to the lack of interaction of Au and O. It was clear that Pd interacted with O₂ as the peaks for the adsorbed O₂ and the adsorbate-surface complex overlapped, which suggested an overlap of bonding orbitals between the surface and O₂. For the case of the Pd(100) QB site, there was peak overlap of the adsorbed O₂ and the adsorbate-surface complex above the Fermi level, which may suggest the possibility of overlap of anti-bonding orbitals. Further investigation would be required to confirm this. The reason for the difference in E_{ads} values could be due to the amount of electron density available as Pd(100) would have the greatest amount of electron density available for the O₂ molecule compared to the other surfaces, with a greater number of interacting M atoms (Tables 4.3, 4.10, 4.17 and 4.25, and Fig. 4.5, 4.14, 4.24, 4.25, 4.35 and 4.36).

It has not been previously reported that automatic dissociation of O₂ on either Au or Pd surfaces can occur. The current work also does not report this phenomenon. The reason for this was most likely due to the energy required to break the double bond, whereas H₂ has only a single bond.

4.2.3.4. Dissociation of Oxygen

The adsorption of dissociated O₂ to Pd(100) (Hollow Straight: ~-215 kJ mol⁻¹) was weaker than Pd(111) (Hollow fcc-fcc: ~-260 kJ mol⁻¹) by ~45 kJ mol⁻¹. This was due to the increased repulsion between the O atoms and Pd atoms. The Pd-O bond lengths for the Pd(100) Hollow Straight sites and the Pd(111) Hollow fcc-fcc sites were: ~2.07 and ~2.18 Å; and 1.98, ~2.00 ~2.05 Å, respectively. There were more Pd atoms (five each) repelling the O atoms in the Pd(100) Hollow Straight sites than the Pd(111) Hollow fcc-fcc sites (three each). The increased repulsion demonstrated by the Pd(100) Hollow Straight sites would explain the less negative E_{ads} value compared to the Pd(111) Hollow fcc-fcc sites (Tables 4.18 and 4.26, and Fig. 4.26 and 4.37).

The Pd(111) Hollow fcc-fcc sites for dissociated O₂ had a more negative E_{ads} value than the Pd(100) Hollow Straight sites but had greater movements of the top layer Pd atoms (maximum bond length changes: ~0.17 and ~0.03 Å, respectively). The larger Pd-Pd movements did not negatively impact the E_{ads} value, and therefore, the E_{def} value must have been significantly smaller than E_{int} value.

Au(111) was not investigated for the dissociation of O₂ due to its low affinity for O. Au(100) was investigated, however, the E_{ads} value was positive, and therefore, not favourable. This was due to its low affinity for O, which increased the deformation of the surface-adsorbate complex (Tables 4.10, 4.18 and 4.26, and Fig. 4.14, 4.26 and 4.37).

4.2.3.5. Adsorption of Hydrogen Peroxide

For the adsorption of H₂O₂, the Pd(111) Top (O¹)-Bridge (H²) site and the Pd(100) QB (OH) site were the most favourable adsorption sites for H₂O₂. The H₂O₂ adsorbed to Pd(111) was slightly more strongly bound than it was to Pd(100), with a difference in E_{ads} value of ~12 kJ mol⁻¹. The Pd-O interatomic distances for the Pd(111) Top (O¹)-Bridge (H²) site and the Pd(100) QB (OH) site were: ~2.31 Å; and ~2.35 and ~2.71 Å, respectively. The first Pd-O bond for the Pd(100) QB site was similar in length to that of the Pd(111) Top (O¹)-Bridge (H²) site, but the second Pd-O bond was not. The Pd-H interatomic distances for both sites were as follows: ~2.43 and ~2.83 Å; and ~2.56 and ~2.70 Å, respectively. These interatomic distances were similar, with only minor variations. This was because, for both cases, the H¹ was bridged between two Pd atoms (Tables 4.19 and 4.27, and Fig. 4.27 and 4.38).

The difference in E_{ads} values may be explained by the amount of repulsion that there may have been for these sites. The Pd(111) Top (O^1)-Bridge (H^2) site had only three interacting Pd atoms of the top layer, whereas the Pd(100) QB site was observed to have four interacting Pd atoms. This repulsion must have been small as there was not a significant difference between the Pd(111) and (100) sites' E_{ads} values or certain Pd-O and Pd-H interatomic distances (Tables 4.19 and 4.27, and Fig. 4.27 and 4.38).

By comparison, Au(111) adsorbed H_2O_2 in a similar fashion to Pd(111). Although the Top (O^1)-Bridge (H^2) sites for Au(111) and Pd(111) had comparable M-H interatomic distances, the M-O interatomic distances were not (~ 2.78 and ~ 2.31 Å, respectively). The longer Au-O bond in comparison to the Pd-O bond would explain the less negative E_{ads} value that was exhibited by the Au(111) Top (O^1)-Bridge (H^2) site (~ -44 kJ mol $^{-1}$), which could be attributed to the low affinity for O and H exhibited by Au (Tables 4.4 and 4.19, and Fig. 4.6 and 4.27).

The Au(100) Sloped Bridge (OH) adsorption site had similar Au-O interatomic distances to the Au(111) Top (O^1)-Bridge (H^2) site and similar M-H interatomic distances to the Pd(100) QB (OH) site. However, the E_{ads} value for the Au(100) Sloped Bridge (OH) site was less negative than all the most favourable sites of all the other surfaces studied (~ -37 kJ mol $^{-1}$). This was most likely due to the increased M-M movements, as they were more significant for the Au surfaces than they were for the Pd surfaces, meaning that the influence of the E_{def} values were greater for these surfaces (Tables 4.4, 4.11, 4.19, and 4.27, and Fig. 4.6, 4.15, 4.27 and 4.38).

Clearly, the trend for the adsorption of H_2O_2 was that the tighter the binding, the more negative the E_{ads} value was. This was dependent on the stability of the surface, the number of interacting metal atoms (and therefore, the amount of electron density available to share), the repulsion exhibited between interacting atoms, the repulsion of the surface atoms, and the surface's affinity to O- and H-containing species (H_2O_2 adsorption strength: Pd(111) > Pd(100) > Au(111) > Au(100)). In addition, there was an obvious barrier for the dissociation of H_2O_2 on the Pd(111) surface as there were multiple sites for its adsorption. The Pd(100) surface had a small E_a barrier for HO-OH scission as it automatically dissociated in two of the three cases for H_2O_2 adsorption (Tables 4.4, 4.11, 4.19, and 4.27, and Fig. 4.6, 4.15, 4.27 and 4.38).

The findings of the current work agreed with the work of Nasrallah, however, variations in the studies were seen as all of Nasrallah's work showed a

Hollow (H¹)-Top (O²) site on the Au and Pd(100) surfaces and a Top (H¹)-Top (O²) site on the Au and Pd(111) surfaces. This would suggest that the surfaces have a degree of insensitivity with regards to the adsorption site and the orientation of the adsorbate.²⁴

4.2.3.6. Dissociation of Hydrogen Peroxide

Neither Au(111) or (100) adsorbed H and OOH, thus, a comparison could not be made between these surfaces and Pd(111) and (100). The reason for this was due to their low affinity for H and O, and therefore, the OOH species. A comparison could be made between Pd(111) and (100); the Pd(111) surface had a lower E_{ads} value for its most favourable adsorption site compared to Pd(100) by $\sim 27 \text{ kJ mol}^{-1}$ (~ -77 and $\sim -50 \text{ kJ mol}^{-1}$, respectively). The Pd(111) Hollow fcc (H)-Bridge (O¹)-Top (O²) (fcc) sites stabilised the OOH far better than the Pd(100) Hollow Straight or Bridge (H)-Hollow (OOH) sites. This was due to the decreased repulsion by the Pd(111) surface compared to the Pd(100) surface as there were less Pd atoms interacting with the adsorbate for the former than the latter (Tables 4.5, 4.13, 4.20, and 4.28, and Fig. 4.8, 4.16, 4.28 and 4.39).

The maximum change in Pd-Pd bond length for the Pd(111) Bridge (O¹)-Top (O²) (fcc) site was $\sim 0.17 \text{ \AA}$, which was significantly larger than the maximum change seen for the Pd(100) Hollow Straight and Bridge (H)-Hollow (OOH) sites at $\sim 0.06 \text{ \AA}$. This could be due to the increased repulsion between the surface and the adsorbate as the Pd-O bonds were longer for the Pd(111) site, as opposed to the Pd(100) sites. However, the E_{def} value must have been significantly smaller than the E_{int} value to produce a more negative E_{ads} value (Tables 4.20, and 4.28, and Fig. 4.28 and 4.39).

For the adsorption of dissociated H₂O₂ at the HO-OH bond, the Au(111) and (100) surfaces went against the previous trends and adsorbed the OH groups strongly to their surfaces. The most favourable sites for these two surfaces were the Au(111) Bridge-Bridge and Au(100) Bridge-Bridge (1) sites, with E_{ads} values of ~ -166 and $\sim -246 \text{ kJ mol}^{-1}$, respectively. The latter site was comparable to that of the Pd(111) Bridge-Bridge (2) and the Pd(100) Bridge-Hollow (3) sites, with E_{ads} values of ~ -269 and $\sim -281 \text{ kJ mol}^{-1}$, respectively. Normally, Au has a low affinity for both H and O, but the reason for the extraordinary affinity of OH by Au in the current work could be explained by its ability to make Au(OH)_x (where x is an integer greater than one).

Another contributing factor could be that the Au had the capacity to bond with the OH groups far better on the Au(100) than the Au(111) because there were less Au-Au bonds. This meant that the Au(100) had the capacity to form bonds with the OH groups (Tables 4.6, 4.13, 4.21, and 4.29, and Fig. 4.8, 4.16, 4.29 and 4.40).^{27,28}

For all four surfaces studied within the current work, it was clear that the Bridge sites for OH adsorption were the most favourable. The M-O bond lengths were also similar as Au(111) and (100) sites exhibited average bond lengths of ~ 2.26 and ~ 2.22 Å, respectively, and the Pd(111) and (100) sites exhibited average bond lengths of ~ 2.14 and ~ 2.37 Å, respectively. Although the Pd(100) Bridge-Hollow sites did not have any O^{III}H bonding unlike the other three surfaces' adsorption sites for dissociated H₂O₂, this adsorption site had the lowest E_{ads} value of the four surfaces. This could be due to the increased amount of energy required for O^{III}H bonding to occur. This would also shift the electron density requirements of the OH groups as the O² would require more electron density as it loses some of the electron density from the bonded H², whereas the electron density of O¹ would have a greater dependence on the electron density of the H². This would result in O¹ needing less electron density from the interacting metal atom(s) as it was stabilised by the H², and the O² would require more electron density for stabilisation. Further investigation would be required to determine this (Tables 4.6, 4.13, 4.21, and 4.29, and Fig. 4.8, 4.16, 4.29 and 4.40).

In addition, what was also made clear was that the (100) surfaces, irrespective of the element of the surface, gave more negative E_{ads} values than the (111) surfaces. This could be due to the decreased repulsion from having fewer neighbouring atoms on the surface. Another possibility to consider would be that the (111) surfaces were more stable than their (100) counterparts, which in turn, could have made their E_{ads} values less negative. Again, this rationale was linked to the influence that more metal atoms will have more M-M bonds in the (111) surfaces compared to the (100) surfaces (Tables 4.6, 4.13, 4.21, and 4.29, and Fig. 4.8, 4.16, 4.29 and 4.40).

By comparison, the Pd(111) Bridge-Bridge (2) sites had somewhat dissimilar ranges in Pd-Pd movements to the Pd(100) Bridge-Hollow (3) sites, with maximum Pd-Pd bond lengths changing by ~ 0.21 and ~ 0.08 Å, respectively. However, as most of the Pd-Pd bonds had decreased in length for the Pd(111) Bridge-Bridge (2) sites, these larger increases were expected. In both cases, the OH groups were attracting the Pd atoms towards them, but as there was a greater amount of Pd atoms in close proximity in the top layer of the Pd(111) surface, this consequently decreased more

of the Pd-Pd bond lengths. This may explain the key difference in E_{ads} values between Pd(111) and Pd(100) ($\sim 12 \text{ kJ mol}^{-1}$) as the E_{def} value was most likely larger for the Pd(111) surface than it was for the (100) surface (Tables 4.21, and 4.29, and Fig. 4.29 and 4.40).

In comparison to the Au surfaces, the Au(111) Bridge-Bridge sites had Au-Au movements that were significantly larger than those of the Pd-Pd movements exhibited by the Pd(111) and (100) surfaces. The Au(111) Bridge-Bridge sites had a maximum Au-Au bond length change of $\sim 0.55 \text{ \AA}$, whereas the Au(100) Bridge-Bridge sites had a maximum Au-Au bond length change of $\sim 0.20 \text{ \AA}$, which was similar to the Pd(111) Bridge-Bridge (2) sites' Pd-Pd movements. Again, these larger M-M movements exhibited by the Au(111) could explain the less negative E_{ads} value in relation to its Pd equivalent, as an increased amount of repulsion would occur as the neighbouring metal atoms were forced closer together, increasing the E_{def} value. However, this was most likely in tandem with the differing affinities of the OH species with Au and Pd. Regardless, this supported the fact that the Pd surfaces were more stable than the Au surfaces (Tables 4.6, 4.13, 4.21, and 4.29, and Fig. 4.8, 4.16, 4.29 and 4.40).

This type of dissociation at the HO-OH bond was clearly superior to the dissociation at the H-OOH bond of H_2O_2 for all four surfaces. Moreover, for the Au(100), Pd(100) and Pd(111) surfaces, H_2O_2 could automatically dissociate, which suggested that the E_{a} barrier for this was low. One possibility to explore further would be the reaction of the OH groups to form H_2O , leaving an O atom on the surface that could be used in the epoxidation of propene.

4.2.3.7. Adsorption of Propene

The Au(111) and (100) had similar E_{ads} values for their most favourable adsorption sites for propene, which were the Au(111) Top Up site at $\sim -65 \text{ kJ mol}^{-1}$ and the Au(100) Top Up site at $\sim -71 \text{ kJ mol}^{-1}$. The Pd surfaces had similar E_{ads} values to each other as the Pd(111) DB site had an E_{ads} value of $\sim -134 \text{ kJ mol}^{-1}$ and the Pd(100) Top Up site had an E_{ads} value of $\sim -123 \text{ kJ mol}^{-1}$. It could be construed that the element of the surface had a far greater effect than the cut of the surface. Interestingly, the Top Up sites were the most favoured adsorption site for Au(111), Au(100) and Pd(100) surfaces (Tables 4.7, 4.14, 4.22 and 4.30, and Fig. 4.9, 4.18, 4.30 and 4.41).

The E_{ads} values could be explained by the M-C or M-H interatomic distances as the weakest E_{ads} values observed for the most favourable sites for all the surfaces had the largest interatomic distances between the surface and the adsorbate. The main Au-C² interatomic distance for the Au(111) Top Up (C¹C²) site had a length of ~3.05 Å, whereas the Au(100) Top Up (C¹C²), Pd(100) Top Up (C¹C²) and Pd(111) DB sites had M-C² interatomic distances of ~2.59, ~2.20 and ~2.15 Å, respectively (Tables 4.7, 4.14, 4.22 and 4.30, and Fig. 4.9, 4.18, 4.30 and 4.41).

The reason for the relationship between the E_{ads} values and the M-C interatomic distances could be associated with the affinity that the element of the surface has for the adsorbate as well as the increased repulsion between the surface and the adsorbate. Pd has a greater amount of electron density to share than Au and, with the electron dense C¹=C² bond of the propene, the Pd interacted more strongly with the electron density of propene than Au did. In turn, this caused greater interactions and more negative E_{ads} values for the Pd surfaces than the Au surfaces with propene (Tables 4.7, 4.14, 4.22 and 4.30, and Fig. 4.9, 4.18, 4.30 and 4.41).

The Au(100) surface provided a hollow site for one of the C³H atoms to partially reside in, which may have contributed to the more negative E_{ads} value compared to the Au(111) Top Up site. Although the Pd atoms were closer together for the Pd(100) surface than the Au atoms of the Au(100) surface, which resulted in the Pd(100) surface having a smaller hollow site for the C³H, the smaller hollow site did not adversely affect the E_{ads} value, as the overriding factor in this case was the stronger affinity for propene by Pd than compared to Au (Tables 4.7, 4.14, 4.22 and 4.30, and Fig. 4.9, 4.18, 4.30 and 4.41).

Both Au(111) and (100) surfaces had significantly larger movements of the top layer atoms ($>\pm 0.50$ Å) compared to either the Pd(111) or (100) surfaces ($<\pm 0.40$ Å). This was reflected in their E_{ads} values as the Au(111) Top Up and (100) Top Up sites were less negative by ~52 and ~58 kJ mol⁻¹, respectively, compared to Pd(100) Top Up site. The Pd(100) Top Up site was ~11 kJ mol⁻¹ more positive than the Pd(111) DB site (Tables 4.7, 4.14, 4.22 and 4.30, and Fig. 4.9, 4.18, 4.30 and 4.41).

Interestingly, the Pd(100) Top Up site had significantly less movements of the top layer Pd atoms than the Pd(111) DB site, and yet, the former had the slightly less negative E_{ads} value of the two. The rationale for this observation was that the Pd(111) surface was more stable than the (100) surface, hence the more negative E_{ads} value. In this case, the Pd atom movements were necessary to maintain this stability (Tables 4.7, 4.14, 4.22 and 4.30, and Fig. 4.9, 4.18, 4.30 and 4.41).

With regards to the DoS for the adsorption of propene, all surfaces had a reduction in the anti-bonding orbitals (positioned above the Fermi level) and a small shift in the bonding orbital densities toward the Fermi level. It was clear that there was significant interaction between the adsorbate and the surface, as overlap of the propene and adsorbate-surface complex peaks occurred, which suggested bonding orbital overlap of the adsorbate and surface atoms. In addition, the C¹=C² bond lengths increased when propene was adsorbed to Au(111), Au(100), Pd(111) and Pd(100) by ~0.02, ~0.03, ~0.12 and ~0.06 Å, respectively. The rationale for this trend was due to the increased electron density that was shifted towards the C¹=C² bond from the Pd(111) DB site, as there were more metal atoms interacting with the adsorbate. This in turn was related to the E_{ads} as this site had the most negative E_{ads} value at ~-134 kJ mol⁻¹. (Fig. 4.10, 4.19, 4.31 and 4.42).

The Au surfaces interacted with the adsorbate well, which was contradictory to what Davis *et al.* claimed. This group saw chemisorption of propene to both Au(111) and (100) at ~39 kJ mol⁻¹ (and claimed that this interaction was “weak”).²⁹ Although all three pieces of research can attribute the lack of interaction between Au and other adsorbates to Au-Au affinity being much greater, further investigation is required as the studies with the work of Davis *et al.*²⁹ and Roldan *et al.*¹⁸, and the current work provided different results for the adsorption of propene to Au. However, the work conducted by Roldan *et al.* did not introduce any dispersion corrections to their calculations, which would explain this difference in E_{ads} value.¹⁸

4.2.3.8. Adsorption of Propene Oxide

The adsorption of PO did not follow the trends of the previous adsorbates. Where the normal trend was that Au(111) was more stable with a more negative E_{ads} value than Au(100), this was not the case for PO adsorption. The Au(111) Top (OC²H) site was slightly less negative in E_{ads} than the Au(100) Top (O) site. However, because both sites were within ~2 kJ mol⁻¹ of each other, they should be considered site insensitive. The same could be said of the Pd surfaces as they were only within ~6 kJ mol⁻¹ of each other with regards to their respective E_{ads} values (Tables 4.7, 4.14, 4.22 and 4.30, and Fig. 4.9, 4.20, 4.30 and 4.41).

The largest difference was observed between Au and Pd as the Au(111) and Au(100) Top (O) sites produced E_{ads} values of ~-57 and ~-59 kJ mol⁻¹, respectively, and the Pd(111) Top and Pd(100) TB (HC¹OC³H) sites gave E_{ads} values of ~-79 and

$\sim -73 \text{ kJ mol}^{-1}$, respectively. Again, this demonstrated that Pd(111) had the greater affinity for the adsorbate and was the more stable surface of the four studied (Tables 4.7, 4.14, 4.22 and 4.30, and Fig. 4.9, 4.20, 4.30 and 4.41).

There was no obvious trend with regards to the M-M movements of the surfaces as the Pd(111) surface experienced a maximum M-M interatomic distance change of $\sim 0.20 \text{ \AA}$, whereas the other three surfaces experienced a significantly less change at a maximum of $\sim 0.04 \text{ \AA}$. However, the M-O interatomic distance for the Pd(111) Top (OC^2H) site was the shortest at $\sim 2.29 \text{ \AA}$. This suggested that a greater amount of electron density was shifted towards the adsorbate and bound more tightly than the other surfaces. The trend observed for the other surfaces was that the Pd(100) TB ($\text{HC}^1\text{OC}^3\text{H}$) site had a Pd-O interatomic distance of $\sim 2.39 \text{ \AA}$ and the Au(111) Top (OC^2H) and the Au(100) Top (O) sites had similar Au-O interatomic distances of (~ 2.60 and $\sim 2.63 \text{ \AA}$, respectively) and similar E_{ads} values. A small difference in M-O interatomic distance marginally affected the E_{ads} value (Tables 4.7, 4.14, 4.22 and 4.30, and Fig. 4.9, 4.20, 4.30 and 4.41).

Although the adsorption of PO was strong on both Au and Pd, this could be problematic when considering their catalytic properties. If the adsorption is too strong to the surface, energy will be required to release the adsorbate from the surface. This is undesirable for a catalyst.

4.3. Conclusions

For the epoxidation of propene utilising *in-situ* direct H_2O_2 synthesis, multiple surfaces were studied with various sites and orientations of the adsorbate molecules explored. This was done to discover which surfaces may provide the best routes to synthesising H_2O_2 directly (or the ROS) that would ultimately oxidise propene. From the results, the Au and Pd(111) surfaces generally outperformed their (100) counterparts and the Pd(111) surfaces generally performed better than Au(111), Au(100) and Pd(100) surfaces, with some of the most negative E_{ads} values observed.

Various rationales were used to explain the results. A balance between electron density sharing, surface and adsorbate deformation, repulsion, affinity, and adsorbate orientation were significant attributes to each of the surfaces' adsorption sites and E_{ads} values. In addition, it was found that the Au-Au affinity was stronger than that of the Pd-Pd affinity as the Au(100) moved in several cases to a distorted Au(111), whereas Pd(100) remained (100) in all cases. This was attributed to the

increased repulsion between neighbouring metal atoms, which in turn affected the E_{def} and E_{ads} values.

Both Pd surfaces adsorbed all the adsorbates in the current work, whereas Au interacted negligibly with H_2 or O_2 . This was supported by the work of Ford *et al.*⁵ and Barrio *et al.*^{22,23} This meant that Au(111) and (100) would not be able to synthesise H_2O_2 directly as the reactant molecules required for this reaction would not adsorb. Nevertheless, atomic O did adsorb to Au(111), but more importantly, automatic dissociation of H_2 over Au(100) did occur in the current work. The latter adsorption may offer a pathway to produce H_2O_2 as a surface covered with H may be possible and adsorb O_2 . In addition, the OH groups could readily form H_2O and O, which may be a crucial step prior to propene epoxidation, as the H_2O could desorb, the propene adsorb and then react. However, these reaction steps would require further investigation.

Some E_a barriers were low or non-existent as automatic dissociation of certain adsorbates occurred. For example, the dissociation of H_2 on Pd(111) or the dissociation of H_2O_2 on Pd(100) (HO-OH scission). The former example was supported by Todorovic *et al.*'s work.⁷ Interestingly, Pd(111) could adsorb H_2 intact (~ -43 kJ mol⁻¹), meaning that there was an E_a barrier for the automatic dissociation of H_2 observed on Pd(111), which must be low. It also demonstrated the importance of including van der Waals forces in the geometry optimisation calculations as most (but not all) cases resulted in automatic dissociation.

There had been no significant research completed on Pd(100) prior to the current work. Although less stable than its (111) counterpart, it may offer an alternative to both the catalytic direct synthesis of H_2O_2 and the epoxidation of propene. This was highlighted by the adsorption of the dissociated H_2O_2 (HO-OH) as no O||H bonding was observed between the OH groups and gave the lowest E_{ads} value of the four surfaces (~ -281 kJ mol⁻¹). However, kinetic information would be required to verify this possibility.

Propene adsorbed sufficiently to Au(111) as the E_{ads} value was ~ -25 kJ mol⁻¹ above the threshold for chemisorption (≥ 40 kJ mol⁻¹). However, the other three surfaces studied produced even greater chemisorption values. This suggested that the adsorption of propene was stable to these surfaces. Moreover, in all cases of propene adsorption, the molecule was always in the Up position. This meant that H abstraction leading to the allyl radical mechanism would not occur as this required the propene to be in the Down position.¹⁸ Thus, the epoxidation of propene on the

surfaces within the current work could only proceed *via* the OMMP mechanism. This again highlighted the significance of the D3 corrections, which included the intermolecular forces in the calculations.

The adsorption of PO was weaker for all four surfaces with Au(111) producing the weakest interaction of them all (~ -57 kJ mol⁻¹). The Au(111), (100) and Pd(100) had E_{ads} values in the chemisorption region (> -57 kJ mol⁻¹). This may not be beneficial catalytically as it would require more energy to release the adsorbate and desorb from these surfaces. As PO is the target molecule, it would be necessary for this adsorbate to desorb easily from the surface to prevent undesirable, non-selective further reactions on the surface.

DoS calculations were performed on the sites with the greatest adsorption for the main reactants (H₂, O₂ and propene) on all four surfaces. Generally, Pd(111) and (100) outperformed their Au counterparts due to their innate ability to transfer two electrons as opposed to just one electron like the latter. This meant that binding was largely stronger on the Pd surfaces as the interactions were akin to near-dissociation (as adsorbate bond lengths increased) and chemisorption occurred, with greater overlap of the bonding orbitals for the Pd surfaces compared to the Au surfaces.

4.4. Future Research

For the continuation of this research, further analyses would be required. For completeness, the E_{def} values for each adsorbate for all surfaces should be calculated. This would show the significant effect that M-M movements and adsorbate distortion had on the E_{ads} values. More of the DoS calculations would need to be performed on PO and H₂O₂, with both its dissociative products. Completion of the DoS calculations for these adsorbates would provide greater understanding and aid the rationales described in the current work. More detailed analyses of the DoS would also be beneficial in understanding the adsorbate-surface complex (*e.g.*, d -orbital signature(s) of interacting metal atom(s) and using the down spin DoS to determine if a peroxo or superoxo species was present for the O₂). In addition to this, Bader charge analyses would demonstrate the movement of charge for the surfaces and adsorbates, which in turn, would benefit the rationales that explained the results observed.

Kinetic information for the E_{a} barriers from reactants to products would also be another important avenue of research to undertake. This data would help in

solidifying which of the four surfaces would be the better candidate for the catalytic epoxidation of propene utilising *in-situ* direct H₂O₂ synthesis, as well as the undesirable reaction pathways for both H₂O₂ degradation and PO transformation. From the work conducted by Roldan *et al.*¹⁸ and Ji *et al.*², there are clearly more pathways that PO can take and should be explored, not only for Au, but for Pd as well.

Spectrum-wide research on the adsorption and dissociation of H₂O would also be required as it is an important chemical species for these reactions. The product of H₂O₂ degradation pathways is H₂O, and propene epoxidation is a condensation reaction, meaning the by-product is also H₂O. Understanding how H₂O interacts with a surface would be crucial for any kinetic study as it would alter the interaction between the surface and the other adsorbates. In addition, studies on alloys and nanoparticles would be advantageous as the results would be comparable to experimental values.

Another consideration is the possibility that direct H₂O₂ synthesis could occur on Au(100) after H₂ adsorbs and dissociates on the surface first. Although Au(100) did not adsorb O₂, it might adsorb with a surface coverage of H and subsequently react to form the OH groups. Whether the reaction pathway continues to form H₂O₂ would need to be researched further.

4.5. References

- 1 T. A. Nijhuis, M. Makkee, J. A. Moulijn and B. M. Weckhuysen, *Ind. Eng. Chem. Res.*, 2006, 45, 3447–3459.
- 2 J. Ji, Z. Lu, Y. Lei and C. H. Turner, Mechanistic insights into the direct propylene epoxidation using Au nanoparticles dispersed on TiO₂/SiO₂, *Chem. Eng. Sci.*, 2018, **191**, 169–182.
- 3 A. Kundu, T., Kroschwitz, J.I., Seidel, *Nondestructive Evaluation, Kirk-Othmer Encyclopedia of Chemical Technology*, Wiley-Interscience, 5th edn., 2004.
- 4 S. J. Freakley, R. J. Lewis, D. J. Morgan, J. K. Edwards and G. J. Hutchings, Direct synthesis of hydrogen peroxide using Au-Pd supported and ion-exchanged heteropolyacids precipitated with various metal ions, *Catal. Today*, 2015, **248**, 10–17.

- 5 D. C. Ford, A. U. Nilekar, Y. Xu and M. Mavrikakis, Partial and complete reduction of O₂ by hydrogen on transition metal surfaces, *Surf. Sci.*, 2010, **604**, 1565–1575.
- 6 J. S. Jirkovský, I. Panas, E. Ahlberg, M. Halasa, S. Romani and D. J. Schiffrin, Single atom hot-spots at Au-Pd nanoalloys for electrocatalytic H₂O₂ production, *J. Am. Chem. Soc.*, 2011, **133**, 19432–19441.
- 7 R. Todorovic and R. J. Meyer, A comparative density functional theory study of the direct synthesis of H₂O₂ on Pd, Pt and Au surfaces, *Catal. Today*, 2011, **160**, 242–248.
- 8 B. Taylor, J. Lauterbach, G. E. Blau and W. N. Delgass, Reaction kinetic analysis of the gas-phase epoxidation of propylene over Au/TS-1, *J. Catal.*, 2006, **242**, 142–152.
- 9 D. G. Barton and S. G. Podkolzin, Kinetic study of a direct water synthesis over silica-supported gold nanoparticles, *J. Phys. Chem. B*, 2005, **109**, 2262–2274.
- 10 D. H. Wells, W. N. Delgass and K. T. Thomson, Formation of hydrogen peroxide from H₂ and O₂ over a neutral gold trimer: a DFT study, *J. Catal.*, 2004, **225**, 69–77.
- 11 V. Bonafilc-Koutecky, P. Fantucci and J. Koutecky, Quantum Chemistry of Small Clusters of Elements of Groups Ia, Ib, and I la: Fundamental Concepts, Predictions, and Interpretation of Experiments.
- 12 C. R. A. Catlow, S. A. French, A. A. Sokol and J. M. Thomas, Computational approaches to the determination of active site structures and reaction mechanisms in heterogeneous catalysts, *Philos. Trans. R. Soc. London A Math. Phys. Eng. Sci.*, 2005, **363**, 913–936.
- 13 J. M. Thomas and G. Sankar, The role of synchrotron-based studies in the elucidation and design of active sites in titanium - Silica epoxidation catalysts, *Acc. Chem. Res.*, 2001, **34**, 571–581.
- 14 A. Staykov, T. Kamachi, T. Ishihara and K. Yoshizawa, Theoretical study of the direct synthesis of H₂O₂ on Pd and Pd/Au surfaces, *J. Phys. Chem. C*, 2008, **112**, 19501–19505.

- 15 J. W. Harris, J. Arvay, G. Mitchell, W. N. Delgass and F. H. Ribeiro, Propylene oxide inhibits propylene epoxidation over Au/TS-1, *J. Catal.*, 2018, **365**, 105–114.
- 16 G. F. Thiele and E. Roland, Propylene epoxidation with hydrogen peroxide and titanium silicalite catalyst: Activity, deactivation and regeneration of the catalyst, *J. Mol. Catal. A Chem.*, 1997, **117**, 351–356.
- 17 A. M. Joshi, W. N. Delgass and K. T. Thomson, Partial oxidation of propylene to propylene oxide over a neutral gold trimer in the gas phase: A density functional theory study, *J. Phys. Chem. B*, 2006, **110**, 2572–2581.
- 18 A. Roldan, D. Torres, J. M. Ricart and F. Illas, On the effectiveness of partial oxidation of propylene by gold: A density functional theory study, *J. Mol. Catal. A Chem.*, 2009, **306**, 6–10.
- 19 H. Prats, F. Illas and R. Sayós, General concepts, assumptions, drawbacks, and misuses in kinetic Monte Carlo and microkinetic modeling simulations applied to computational heterogeneous catalysis, *Int. J. Quantum Chem.*, 2018, **118**, e25518.
- 20 S. B. Shin, D.-W. Lee and D. Chadwick, The effects of impregnation of precious metals on the catalytic activity of titanium silicate (TS-1) in epoxidation of propene using hydrogen peroxide, *J. Mol. Catal. A Chem.*, 2016, **423**, 478–488.
- 21 A. Prieto, M. Palomino, U. Díaz and A. Corma, One-pot two-step process for direct propylene oxide production catalyzed by bi-functional Pd(Au)@TS-1 materials, *Appl. Catal. A Gen.*, 2016, **523**, 73–84.
- 22 L. Barrio, P. Liu, J. A. Rodríguez, J. M. Campos-Martín and J. L. G. Fierro, A density functional theory study of the dissociation of H₂ on gold clusters: Importance of fluxionality and ensemble effects, *J. Chem. Phys.*, , DOI:10.1063/1.2363971.
- 23 L. Barrio, P. Liu, J. A. Rodríguez, J. M. Campos-Martin and J. L. G. Fierro, Effects of hydrogen on the reactivity of O₂ toward gold nanoparticles and surfaces, *J. Phys. Chem. C*, 2007, **111**, 19001–19008.
- 24 A. Nasrallah, *PhD Thesis Title: Au & Pd Surfaces: From Capping Agents to Methane Oxidation*, 2020.

- 25 P. Tian, L. Ouyang, X. Xu, J. Xu and Y. F. Han, Density functional theory study of direct synthesis of H₂O₂ from H₂ and O₂ on Pd(111), Pd(100), and Pd(110) surfaces, *Cuihua Xuebao/Chinese J. Catal.*, 2013, **34**, 1002–1012.
- 26 M. Mavrikakis, P. Stoltze and J. K. Nørskov, Making gold less noble, *Catal. Letters*, 2000, **64**, 101–106.
- 27 R. Coquet, 2005.
- 28 R. Meyer, C. Lemire, S. K. Shaikhutdinov and H. J. Freund, Surface chemistry of catalysis by gold, *Gold Bull.*, 2004, **37**, 72–124.
- 29 K. A. Davis and D. W. Goodman, Propene adsorption on clean and oxygen-covered Au(111) and Au(100) surfaces, *J. Phys. Chem. B*, 2000, **104**, 8557–8562.

5. Conclusions and Future Work

5.1. Conclusions

The current work was split into primarily two sections: one experimental (Chapter 3) and one theoretical (Chapter 4). Although the target molecules were different (cyclohexanone oxime and propene oxide (PO)) within these different sections, important information regarding the direct synthesis and utilisation of H₂O₂ for the catalytic oxidation processes involved in producing these target molecules was discovered.

Returning to the aims outlined in Chapter 1, most of the aims were successfully accomplished. Dealing with the first and second aims defined, the ammoximation of cyclohexanone was studied using heterogeneous catalysts (0.33 wt% Au-0.33 wt% Pd/(support)) on various supports (*i.e.*, TS-1, SiO₂, ZrO₂, P25 TiO₂, anatase TiO₂ and rutile TiO₂). Through catalyst design, tandem catalyst systems were created that comprised of a direct H₂O₂ synthesis catalyst and a NH₂OH synthesis catalyst (TS-1), which was compared with the 0.33 wt% Au-0.33 wt% Pd/TS-1 without additional TS-1 that had been previously studied.^{1,2}

Not only was the catalysis involved in these reactions better appreciated, the physical chemistry (*i.e.*, kinetics) was also better understood. Although the P25 TiO₂-supported catalyst was more thoroughly investigated, as P25 TiO₂ is commercially available in bulk, the catalysts studied with a support that was completely comprised of a metal oxide (MO_x) showed marked increases in H₂ selectivity based on oxime and decreases in H₂ conversion compared to the catalysts with SiO₂-based support materials. A contributing factor to this was the greater difference in isoelectric points between the MO_x supports and the metals (*i.e.*, Au and Pd) compared to the SiO₂-based supports, which affected the metals' ability to seed onto the surface. As the charge on the surface was less positive on the MO_x supports, there was a greater attraction to the positive metal ions.

The supports used also influenced the nanoparticle size, composition, and morphology, which in turn affected catalytic performance. For most of the catalysts, the amount of cyclohexanone that was converted, the oxime selectivity and the

cyclohexanone oxime yield were approximately the same, although the SiO₂-based catalyst gave slightly better oxime yields because of the increased amount of H₂O₂ these catalysts produced.

Field Emission Gun-Scanning Electron Microscopy-Energy Dispersive X-ray (FEG-SEM-EDX) spectroscopy, X-ray Photoelectron Spectroscopy (XPS) and X-Ray Diffraction (XRD) analyses were completed on the direct H₂O₂ synthesis catalysts and retrieved information on the nanoparticle and support crystallite sizes of the different catalysts as well as their chemical compositions and metal ratios. Only suggestions regarding the explanations for the observed data were offered as further characterisation would be required to confirm the hypotheses that had been offered.

For most of the direct H₂O₂ synthesis catalysts, there was a smaller amount of Au detected using FEG-SEM-EDX and XPS than Pd. However, this could be due to the smaller nanoparticles containing more Pd and the larger nanoparticles (>18 nm in length) being more Au-rich. From these two characterisation techniques, it appeared as though a Au core-Pd shell morphology for these nanoparticles had been synthesised, which would make sense as Au atoms agglomerate due to their high affinity for themselves upon calcination. However, SEM-EDX data for the TiO₂-supported catalyst may have demonstrated more of a random alloy as the metals were spread widely over the support meaning that there was likely a mixture of both types of morphology for these catalysts.

Coupled with the direct H₂O₂ synthesis data, both sets of results revealed that the rates of the direct H₂O₂ synthesis reaction greatly impacted the selectivity of H₂ based on oxime. If the direct H₂O₂ synthesis catalysts were generating too much H₂O₂, the TS-1 would eventually become saturated and unable to transform the excess H₂O₂. The uncaptured H₂O₂ would subsequently hydrogenate or decompose (collectively known as degrade), thus, producing a decreased H₂ selectivity based on oxime. The FEG-SEM-EDX data revealed that the nanoparticles' sizes influenced the rate of synthesis and degradation as nanoparticles below 5 nm in length (that existed on the P25 TiO₂- and ACS TS-1-supported catalysts) were less responsible for the degradation of H₂O₂, whereas the nanoparticles above 5 nm in length (that were on the SiO₂- and ZrO₂-supported catalysts) were more responsible for the degradation of H₂O₂. High productivity values were observed for the catalysts that had a large proportion of these smaller nanoparticles, unlike those that did not.

In addition, the FEG-SEM-EDX data coupled with the cyclohexanone ammoximation data indicated that if the nanoparticles of a catalyst had a Au/Pd atom

concentration percentage ratio less than 1.00, that catalyst would have the best H₂ selectivity (and H₂O₂ yield) of the catalysts. The catalysts that had Au/Pd atom concentration percentage ratios greater than 1.00 had an increased H₂ conversion but decreased H₂ selectivity towards the oxime within the Different Support Study (with the exception of the P25 TiO₂-supported catalyst as no quantitative EDX data was collected).

However, the reaction and characterisation data along with the rationales described need to be taken under due consideration. The beneficial acid effects from the carbonic acid (H₂CO₃, in equilibrium with the CO₂ diluent) within the direct H₂O₂ synthesis reaction, unlike the cyclohexanone ammoximation reaction, promotes H₂O₂ synthesis. A direct comparison could not be made due to differing solvent mixtures, gas compositions and reaction conditions. The amount of CO₂ in the direct H₂O₂ synthesis reaction would be far greater than that of the cyclohexanone ammoximation as only a small amount of CO₂ is released from the NH₄HCO₃, which would also be in equilibrium with gaseous CO₂. Higher temperatures are also detrimental to H₂O₂ synthesis.

Continuing with the characterisation data, the XRD analyses revealed the presence of Au⁰ on the P25 TiO₂-supported catalyst, which would be indicative of the large Au-rich nanoparticles observed *via* SEM.³ The ZrO₂- and ACS TS-1-supported catalysts did not display the Au⁰ peak ($2\theta = 45^\circ$), although XRD is a sampling technique, with the possibility that there were no large Au-rich nanoparticles in the samples used, as well as the possibility that not enough of the crystallites orientated in the same direction. No catalysts displayed Pd or PdO. The P25 TiO₂-supported catalyst also showed an increase in crystallite size, but this was not unlike previous work.⁴ In addition, a correlation between the reaction data and XRD data was found as the ACS TS-1-supported catalyst had a support crystallite size of 32 nm and was not as selective as the P25 TiO₂- or ZrO₂-supported catalyst at synthesising H₂O₂, whereas the latter catalyst had support crystallite sizes of greater than 50 nm.

From the FEG-SEM analyses, the TS-1 support underwent deformation of its structure. After catalyst preparation and the subsequent calcination, the TS-1-supported catalyst experienced significant changes to its lattice compared to the ACS Materials SEM images.⁵ This phenomenon was not uncommon as other studies have shown that TS-1 is susceptible to structural changes after heat-treating.^{1,6,7} However, the altered lattice (“cloud” formation) seen in the current work was not akin to the observations within the other studies.

With the P25 TiO₂-supported catalyst, increasing the amount of TS-1 increased the production of oxime. These results were similar to work of Jin *et al.*⁸ For the TS-1-supported catalyst or SiO₂-supported tandem catalyst systems, if additional TS-1 had been introduced to the former and more TS-1 introduced to the latter, it may have increased H₂ selectivity as a greater number of Ti⁴⁺ sites would be available for the capture of H₂O₂ and subsequent conversion into NH₂OH. However, when considering the direct H₂O₂ synthesis data, the SiO₂-based supports produced catalysts that appeared to be inherently non-selective towards H₂O₂ synthesis (12 mol_{H₂O₂} kg_{cat}⁻¹ h⁻¹). Thus, the hypothesis proposed may not be correct and can only be confirmed with further research.

Increasing the reaction time increased the cyclohexanone conversion, H₂ conversion, which ultimately increased the yield of oxime. The oxime selectivity remained almost constant, which reflected the performance of the TS-1. However, a decrease in H₂ selectivity after the 3.0 h point was observed. Hypotheses for the observed decrease were suggested and would need to be investigated.

With regards to the third aim described in Chapter 1, an increase in additional TS-1 showed that more H₂O₂ could be captured and converted, increasing both H₂ conversion and selectivity. However, doubling the amount of TS-1 did not double the yield of oxime. To increase the throughput of this multi-step reaction, a direct H₂O₂ synthesis catalyst that could produce a larger amount of H₂O₂ with a high selectivity (*i.e.*, not degrade the H₂O₂ on the catalyst's surface) would be required with additional TS-1. In other words, an optimum ratio of H₂O₂ production, selectivity and subsequent conversion needed to be established. With the current work, however, the results in the studies were not competitive in comparison to the Sumitomo process (Sumitomo oxime yield in 5.5 h: 98.6 %; current work's highest oxime yield in 3.0 h: 74 %).^{2,9}

It was determined that anatase TiO₂ was the superior support material for the H₂O₂ synthesis catalyst because it provided the highest H₂ conversion and selectivity of all the catalysts that were tested. XPS analysis revealed that the presence of Pd⁰ in the nanoparticles of the catalyst and K⁺ within the anatase TiO₂. This was the most likely reason for the increased activity in the tandem catalyst system as Pd⁰ is known for being more active (and less selective) than Pd²⁺, and K⁺ is a known promoter for the direct synthesis of H₂O₂.^{10,11}

The reason for the difference in the reactions investigated experimentally and computationally was to study the oxidation processes involving *in-situ* direct H₂O₂ synthesis more generally. Additionally, the active sites for the H₂O₂ utilisation for these

reactions were different (*i.e.*, cyclohexanone ammoximation utilised H_2O_2 at the Ti^{4+} sites of the TS-1 and propene epoxidation utilised H_2O_2 on the Au and Pd surfaces). For propene epoxidation utilising *in-situ* direct H_2O_2 synthesis, the aims from Chapter 1 were completed as various surfaces were researched with different sites and orientations of the adsorbate molecules investigated. This was to determine which surface(s) may provide the best pathways to synthesising H_2O_2 or the reactive oxygen species (ROS) that would ultimately oxidise propene. The Au and Pd(111) surfaces generally surpassed their (100) counterparts in adsorbing the different species explored (H_2 , O_2 , H_2O_2 , propene and PO). The Pd(111) surface generally performed better than Au(111), Au(100) and Pd(100) surfaces, with some of the most negative adsorption energies observed. For example, the adsorption of H_2O_2 gave rise to adsorption energies of ~ -63 , ~ -44 , ~ -37 , and ~ -51 kJ mol^{-1} , respectively.

Several rationales explained the results observed as a balance between electron density sharing, repulsion, affinity, and molecule (ultimately orbital) orientation was established within each case, which attributed to each of the surfaces' results. In addition, it was found that the Pd-Pd affinity was weaker (as the bonding was stronger) than the Au-Au affinity as the Au(100) atoms moved in several cases to a distorted Au(111) configuration, whereas Pd(100) remained in a (100) configuration in all cases.

Both Pd surfaces adsorbed all the adsorbates well in the current work, except for Au that interacted weakly with H_2 and O_2 . This was supported by the work of Barrio *et al.*^{12,13} and Ford *et al.*¹⁴ This meant that Au(111) and (100) would not be able to synthesise H_2O_2 directly as the reactant molecules required could not adsorb. Atomic O did adsorb to Au(111), and atomic H adsorbed to Au(100) in the current work. The latter adsorption may offer a reaction pathway to synthesise H_2O_2 directly as a surface coverage of H over the Au(100) surface may be possible and could subsequently adsorb O_2 . Additionally, the OH groups could feasibly produce H_2O and O, which may be a crucial step prior to propene epoxidation (*i.e.*, H_2O and O formation, H_2O desorption, propene adsorption and subsequent reaction). Nevertheless, these reaction steps would require further study.

In some instances, certain activation energy (E_a) barriers were non-existent or extremely low as automatic dissociation occurred. For example, the dissociation of H_2O_2 on Pd(100) (HO-OH scission) or the dissociation of H_2 on Pd(111). The latter example was supported by Todorovic *et al.*'s work but there was an orientation and site of the H_2 that did not lead to automatic dissociation.¹⁵ This emphasised the

importance of the D3 corrections as previous work had not included the intermolecular forces and did not find this adsorption.

There had been no substantial research completed on Pd(100) prior to this work for the epoxidation of propene. Although Pd(111) was more stable than its (100) counterpart, Pd(100) could be a potential candidate for the catalytic synthesis of H₂O₂ and epoxidation of propene, as the OH groups observed for dissociated H₂O₂ provided the most negative adsorption energy (~ -281 kJ mol⁻¹). However, this would require kinetic data to confirm this.

Propene adsorption to Au(111) was significant (~ -25 kJ mol⁻¹) but was above the threshold for chemisorption (~ -40 kJ mol⁻¹). However, the other three surfaces studied produced even greater chemisorption values. This suggested that the adsorption of propene was stable. PO adsorption was weaker than propene adsorption for all four surfaces as Pd(111) produced the weakest interaction of them all (~ -27 kJ mol⁻¹). The Au(111), (100) and Pd(100) had adsorption energies in the chemisorption region (more negative than -57 kJ mol⁻¹). It would require more energy to release the adsorbate and desorb from these surfaces. This may not be catalytically beneficial, especially when considering these reactions at an industrial scale. As PO was the target molecule, it would be critical to prevent undesirable, non-selective further reactions on the surface, and therefore, facile desorption of PO is considered necessary.

Density of States (DoS) calculations were completed on the sites with the greatest adsorption for the main reactants of the direct H₂O₂ synthesis and the subsequent propene epoxidation reactions (H₂, O₂ and propene) upon Au(111), Au(100), Pd(111) and Pd(100). In most cases, overlap of peaks within the DoS occurred, which suggested an overlap of bonding orbitals between the surface and the adsorbate. In the current work, Pd(111) and (100) generally outperformed their Au equivalents as Pd can share two electrons as it has two electrons in its outermost orbital, whereas Au, with a full *d*-band, only has one to share. This meant that the adsorption was greater on the Pd surfaces than on the Au surfaces as the interactions were similar to the near-dissociation (as the adsorbate bond lengths increased) and chemisorption occurred.

Through the studies of the different surfaces, the last two aims set out in Chapter 1 were mostly achieved. Ideas regarding the kinetic and mechanistic properties of Au(111), Au(100), Pd(111) and Pd(100) for the direct H₂O₂ synthesis and propene epoxidation reactions (from the local geometric and electronic

properties) have been suggested in some cases. However, no data in relation to these ideas had been obtained to support them. Thus, further research would be required to ascertain the kinetic data, which in turn, should aid in finding suitable catalytic candidates for these reactions.

5.2. Future Research

For the continuance of the research into catalytic cyclohexanone ammoxidation utilising *in-situ* direct H₂O₂ synthesis, further characterisation of the direct H₂O₂ synthesis catalysts would be needed. Brunauer-Emmett-Teller (BET) and surface area data could support the observation of the increased crystallite size observed for the P25 TiO₂-supported catalyst. Both XRD and BET together would explain this phenomenon. The hypothesis that thermal annealing had taken place could be supported if a decrease in surface area was observed between uncalcined and calcined support. The hypothesis that the metals had become part of the support material could be validated if there was no decrease in surface area between the uncalcined support and the calcined support.

Characterisation of certain catalysts would be required to complete the studies, such as the high-resolution XPS analyses for the ACS TS-1-supported catalyst. This would determine the metals' atom concentration percentages to complete the Different Supports study. Further FEG-SEM-EDX analyses on the P25 TiO₂-, rutile TiO₂- and anatase TiO₂-supported catalysts would provide greater support in explaining the results observed for the catalysts within the Different Supports Study and Different Phases of TiO₂ Study. Transmission Electron Microscopy (TEM) on all the catalysts would also be required to detect nanoparticles smaller than 2 nm. Although TEM was performed on the P25 TiO₂-supported catalyst, small nanoparticles were not detected. However, this may not be true of the other catalysts.

High Angle Annular Dark Field-Scanning Transmission Electron Microscopy (HAADF-STEM) would also potentially support the findings of the FEG-SEM-EDX and XPS regarding the morphology of the nanoparticles of the catalysts (Au core-Pd shell). Microwave Plasma-Atomic Emission Spectroscopy (MP-AES) analyses would aid in determining the exact amount of Au and Pd that bound to the support materials in the catalyst preparation stage. This would further help in selecting which type of supports that should be used, as those that do not have a strong affinity for either metal should

be eliminated from future studies. Wasting precious metals would not be acceptable at an industrial scale.

Reuse tests and rejuvenation methodologies would provide vital information regarding the performance of a catalyst over its lifetime. The financial impact of not being able to reuse catalysts would be recognised at an industrial level. Consideration of the feasibility of these processes would require careful planning as two solid materials were mixed in the reactor (the H₂O₂ synthesis catalyst and TS-1). A strong base could dissolve the TS-1, but this would also affect the direct H₂O₂ synthesis catalyst. Further investigation into the separation of these materials would be required.

Tri-metallic catalysts, such as the AuPdPt catalysts utilised by Edwards *et al.*¹⁶ described in Chapter 1, would be another possible research avenue to explore as the addition of Pt increased H₂O₂ synthesis, whilst decreasing the degradation of H₂O₂. Different support materials (*e.g.*, CeO₂)¹⁷, different metal loadings,¹⁸ and different catalyst preparation techniques (*e.g.*, the modified impregnation (M_{IM}) technique used by Sankar *et al.*¹⁹), different ratios of Si/Ti in the TS-1 as well as different Ti⁴⁺-containing catalysts should also be investigated as they may reveal optimum parameters to achieve the highest H₂ conversion and selectivity, which would ultimately provide better cyclohexanone oxime yields. Different heat treatments, such as oxidation-reduction-oxidation (ORO), should also be explored. In addition, exploring photo- and electrocatalysis may enhance the formation of the desirable products for both the direct H₂O₂ synthesis catalyst and the H₂O₂-utilising catalyst.

Other tests for the direct synthesis of H₂O₂ and cyclohexanone ammoximation reactions would also be needed to complete certain studies. For example, anatase TiO₂ that does not contain K⁺ should be used ascertain how much of an effect the K⁺ had on the production of H₂O₂ during both reactions and obtain the performance of an anatase TiO₂-supported catalyst without an additive.

Additionally, the limiting factors with cyclohexanone ammoximation utilising *in-situ* direct H₂O₂ synthesis are as follows: mass transfer, H₂ selectivity, H₂O₂ production, subsequent turnover by the catalyst(s) used for each step, and an optimum ratio of the direct H₂O₂ synthesis catalyst to the TS-1 or Ti⁴⁺-containing material. How the catalysts perform and how the reaction proceeds under flow reactor conditions would also need to be investigated, as a three-reaction one-pot synthesis may not be the best conditions for these reactions. This would be crucial if this catalytic process were to be scaled up for industrial use.

For the continuance of the research into catalytic propene epoxidation utilising *in-situ* direct H₂O₂ synthesis, further analyses would be necessary. Kinetic data for the E_a barriers from reactants to products would be required to better complete the research. This data would help determine which of the four surfaces would be the better candidate for the catalytic epoxidation of propene utilising *in-situ* direct H₂O₂ synthesis. Additionally, the undesirable reaction pathways of both H₂O₂ degradation and PO transformation should also be explored. From the work conducted by Roldan *et al.*²⁰ and Ji *et al.*,²¹ there are clearly more pathways that PO can take and should be investigated for all four surfaces within in the current work.

Dopants and additives could provide a different reaction pathway with lower E_a barriers than those alluded to in the current work and would require further investigation. In addition, the inclusion of a solvent or solvent mixture would provide a greater representation of a catalytic reaction. Depending on the solvent(s) used, they may affect the reaction pathways taken to produce H₂O₂ and PO.

More DoS calculations would also be needed for PO, H₂O₂ and both types of the dissociated H₂O₂ that were explored in the current work. These further DoS calculations would offer greater understanding and support the rationales described in Chapter 4. Further investigation into the automatic dissociation of H₂ on the Au(111) would also be required as this had not been observed previously. The DoS calculations would support the adsorption energy calculations. Additionally, Bader charge analyses would show the movement of charge between the adsorbates and surfaces, which in turn, would benefit the explanations for the results observed.

Research on the adsorption and dissociation of H₂O would also be required as it is a crucial chemical species for these reactions. The product of the H₂O₂ degradation pathways is H₂O, and propene epoxidation is a condensation reaction, meaning the by-product is H₂O as well. Understanding the surfaces' interactions with H₂O would be important for any kinetic study as it would alter the interaction between the other adsorbates and the surface. Additionally, studies on nanoparticles made of Au and Pd as well as alloys would be valuable, as the results would be more comparable to experimental results.

5.3. References

- 1 R. J. Lewis, *PhD Thesis Title: The application of Cs-exchanged tungstophosphoric acid as an additive in the direct synthesis of hydrogen peroxide and the use of Au-Pd/TS-1 in a one-pot approach to cyclohexanone oxime production*, Cardiff University, 2016.
- 2 World Intellectual Property Organisation, WO2018088436A1, 2018, 1–29.
- 3 J. K. Edwards, B. E. Solsona, P. Landon, A. F. Carley, A. Herzing, C. J. Kiely and G. J. Hutchings, Direct synthesis of hydrogen peroxide from H₂ and O₂ using TiO₂-supported Au-Pd catalysts, *J. Catal.*, 2005, **236**, 69–79.
- 4 G. Wang, L. Xu, J. Zhang, T. Yin and D. Han, Enhanced photocatalytic activity of TiO₂ powders (P25) via calcination treatment, *Int. J. Photoenergy*, , DOI:10.1155/2012/265760.
- 5 ACS Materials, Titanium Silicalite-1 - TS-1 - Molecular Sieves - Materials, <http://www.acsmaterial.com/titanium-silicalite-55.html>, (accessed 7 June 2017).
- 6 R. J. Lewis, K. Ueura, Y. Fukuta, S. J. Freakley, L. Kang, R. Wang, Q. He, J. K. Edwards, D. J. Morgan, Y. Yamamoto and G. J. Hutchings, The Direct Synthesis of H₂O₂ Using TS-1 Supported Catalysts, *ChemCatChem*, 2019, **11**, 1673–1680.
- 7 H. Ichihashi and H. Sato, The development of new heterogeneous catalytic processes for the production of epsilon-caprolactam, *Appl. Catal. a-General*, 2001, **221**, 359–366.
- 8 H. Jin, C. Meng, G. He, X. Guo and S. Yang, Green synthesis of acetaldehyde oxime using ammonia oxidation in the TS-1/H₂O₂ system, *React. Kinet. Mech. Catal.*, 2018, **125**, 1113–1125.
- 9 European Patent Office, EP1375473A1, 2004, 1–8.
- 10 M. Bowker, *The Basis and Applications of Heterogeneous Catalysis*, Oxford University Press, 1998.
- 11 S. Ranganathan and V. Sieber, *Catalysts*, 2018, 8.

- 12 L. Barrio, P. Liu, J. A. Rodríguez, J. M. Campos-Martín and J. L. G. Fierro, A density functional theory study of the dissociation of H₂ on gold clusters: Importance of fluxionality and ensemble effects, *J. Chem. Phys.*, , DOI:10.1063/1.2363971.
- 13 L. Barrio, P. Liu, J. A. Rodríguez, J. M. Campos-Martin and J. L. G. Fierro, Effects of hydrogen on the reactivity of O₂ toward gold nanoparticles and surfaces, *J. Phys. Chem. C*, 2007, **111**, 19001–19008.
- 14 D. C. Ford, A. U. Nilekar, Y. Xu and M. Mavrikakis, Partial and complete reduction of O₂ by hydrogen on transition metal surfaces, *Surf. Sci.*, 2010, **604**, 1565–1575.
- 15 R. Todorovic and R. J. Meyer, A comparative density functional theory study of the direct synthesis of H₂O₂ on Pd, Pt and Au surfaces, *Catal. Today*, 2011, **160**, 242–248.
- 16 J. K. Edwards, J. Pritchard, L. Lu, M. Piccinini, G. Shaw, A. F. Carley, D. J. Morgan, C. J. Kiely and G. J. Hutchings, The Direct Synthesis of Hydrogen Peroxide Using Platinum-Promoted Gold-Palladium Catalysts, *Angew. Chemie-International Ed.*, 2014, **53**, 2381–2384.
- 17 E. N. Ntainjua, M. Piccinini, J. C. Pritchard, J. K. Edwards, A. F. Carley, C. J. Kiely and G. J. Hutchings, Direct synthesis of hydrogen peroxide using ceria-supported gold and palladium catalysts, *Catal. Today*, 2011, **178**, 47–50.
- 18 J. Pritchard, L. Kesavan, M. Piccinini, Q. He, R. Tiruvalam, N. Dimitratos, J. A. Lopez-Sanchez, A. F. Carley, J. K. Edwards, C. J. Kiely and G. J. Hutchings, Direct Synthesis of Hydrogen Peroxide and Benzyl Alcohol Oxidation Using Au-Pd Catalysts Prepared by Sol Immobilization, *Langmuir*, 2010, **26**, 16568–16577.
- 19 M. Sankar, Q. He, M. Morad, J. Pritchard, S. J. Freakley, J. K. Edwards, S. H. Taylor, D. J. Morgan, A. F. Carley, D. W. Knight, C. J. Kiely and G. J. Hutchings, Synthesis of Stable Ligand-free Gold-Palladium Nanoparticles Using a Simple Excess Anion Method, *ACS Nano*, 2012, **6**, 6600–6613.
- 20 A. Roldan, D. Torres, J. M. Ricart and F. Illas, On the effectiveness of partial oxidation of propylene by gold: A density functional theory study, *J. Mol. Catal. A Chem.*, 2009, **306**, 6–10.

- 21 J. Ji, Z. Lu, Y. Lei and C. H. Turner, Mechanistic insights into the direct propylene epoxidation using Au nanoparticles dispersed on TiO₂/SiO₂, *Chem. Eng. Sci.*, 2018, **191**, 169–182.